frontiers | Research Topics

Advances in imaging and imaging-directed interventions in hepatic cancers

Edited by
Xiankai Sun and Chandan Guha

Published in
Frontiers in Oncology

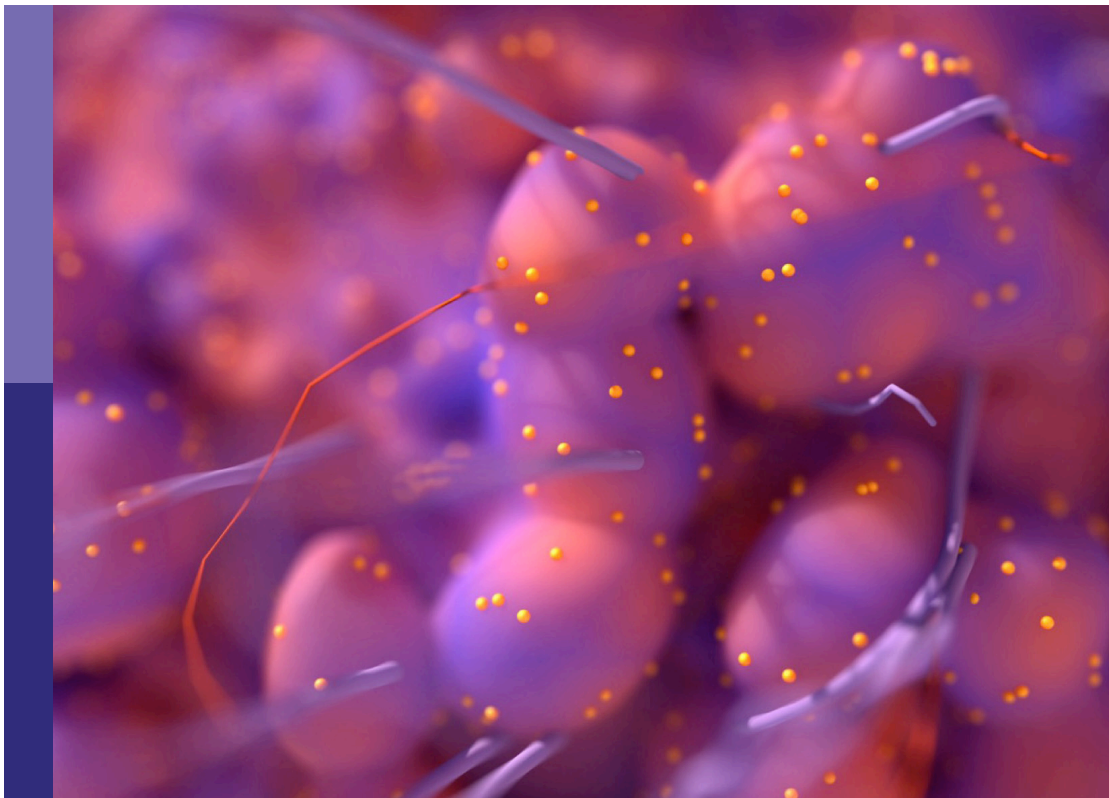

ISSN 1664-8714
ISBN 978-2-8325-3279-9
DOI 10.3389/978-2-8325-3279-9

About Frontiers

Frontiers is more than just an open access publisher of scholarly articles: it is a pioneering approach to the world of academia, radically improving the way scholarly research is managed. The grand vision of Frontiers is a world where all people have an equal opportunity to seek, share and generate knowledge. Frontiers provides immediate and permanent online open access to all its publications, but this alone is not enough to realize our grand goals.

Frontiers journal series

The Frontiers journal series is a multi-tier and interdisciplinary set of open-access, online journals, promising a paradigm shift from the current review, selection and dissemination processes in academic publishing. All Frontiers journals are driven by researchers for researchers; therefore, they constitute a service to the scholarly community. At the same time, the *Frontiers journal series* operates on a revolutionary invention, the tiered publishing system, initially addressing specific communities of scholars, and gradually climbing up to broader public understanding, thus serving the interests of the lay society, too.

Dedication to quality

Each Frontiers article is a landmark of the highest quality, thanks to genuinely collaborative interactions between authors and review editors, who include some of the world's best academicians. Research must be certified by peers before entering a stream of knowledge that may eventually reach the public - and shape society; therefore, Frontiers only applies the most rigorous and unbiased reviews. Frontiers revolutionizes research publishing by freely delivering the most outstanding research, evaluated with no bias from both the academic and social point of view. By applying the most advanced information technologies, Frontiers is catapulting scholarly publishing into a new generation.

What are Frontiers Research Topics?

Frontiers Research Topics are very popular trademarks of the *Frontiers journals series*: they are collections of at least ten articles, all centered on a particular subject. With their unique mix of varied contributions from Original Research to Review Articles, Frontiers Research Topics unify the most influential researchers, the latest key findings and historical advances in a hot research area.

Find out more on how to host your own Frontiers Research Topic or contribute to one as an author by contacting the Frontiers editorial office: frontiersin.org/about/contact

Advances in imaging and imaging-directed interventions in hepatic cancers

Topic editors

Xiankai Sun — University of Texas Southwestern Medical Center, United States

Chandan Guha — Albert Einstein College of Medicine, United States

Citation

Sun, X., Guha, C., eds. (2023). *Advances in imaging and imaging-directed interventions in hepatic cancers*. Lausanne: Frontiers Media SA.

doi: 10.3389/978-2-8325-3279-9

Table of contents

frontiers in Oncology

ORIGINAL RESEARCH
published: 24 February 2022
doi: 10.3389/fonc.2022.838701

A Multi-Parametric Radiomics Nomogram for Preoperative Prediction of Microvascular Invasion Status in Intrahepatic Cholangiocarcinoma

Xianling Qian[1,2,3†], *Xin Lu*[1,2,3†], *Xijuan Ma*[4], *Ying Zhang*[4], *Changwu Zhou*[1,2,3], *Fang Wang*[5], *Yibing Shi*[4*] and *Mengsu Zeng*[1,2,3*]

[1] Department of Radiology, Zhongshan Hospital, Fudan University, Shanghai, China, [2] Shanghai Institute of Medical Imaging, Shanghai, China, [3] Department of Cancer Center, Zhongshan Hospital, Fudan University, Shanghai, China, [4] Department of Radiology, Xuzhou Central Hospital, Xuzhou Clinical School of Xuzhou Medical University, Xuzhou, China, [5] Department of Research and Development, Shanghai United Imaging Intelligence Co., Ltd., Shanghai, China

Background: Intrahepatic cholangiocarcinoma (ICC) is the second most common primary liver cancer with increasing incidence in the last decades. Microvascular invasion (MVI) is a poor prognostic factor for patients with ICC, which correlates early recurrence and poor prognosis, and it can affect the selection of personalized therapeutic regime.

Purpose: This study aimed to develop and validate a radiomics-based nomogram for predicting MVI in ICC patients preoperatively.

Methods: A total of 163 pathologically confirmed ICC patients (training cohort: n = 130; validation cohort: n = 33) with postoperative Ga-DTPA-enhanced MR examination were enrolled, and a time-independent test cohort (n = 24) was collected for external validation. Univariate and multivariate analyses were used to determine the independent predictors of MVI status, which were then incorporated into the MVI prediction nomogram. Least absolute shrinkage and selection operator logistic regression was performed to select optimal features and construct radiomics models. The prediction performances of models were assessed by receiver operating characteristic (ROC) curve analysis. The performance of the MVI prediction nomogram was evaluated by its calibration, discrimination, and clinical utility.

Results: Larger tumor size (p = 0.003) and intrahepatic duct dilatation (p = 0.002) are independent predictors of MVI. The final radiomics model shows desirable and stable prediction performance in the training cohort (AUC = 0.950), validation cohort (AUC = 0.883), and test cohort (AUC = 0.812). The MVI prediction nomogram incorporates tumor size, intrahepatic duct dilatation, and the final radiomics model and achieves excellent predictive efficacy in training cohort (AUC = 0.953), validation cohort (AUC = 0.861), and

OPEN ACCESS

Edited by:
Xiankai Sun,
University of Texas Southwestern Medical Center, United States

Reviewed by:
Duilio Pagano,
Mediterranean Institute for Transplantation and Highly Specialized Therapies (ISMETT), Italy
Weiqi Rong,
Chinese Academy of Medical Sciences and Peking Union Medical College, China

***Correspondence:**
Mengsu Zeng
zengmengsu1963@163.com
Yibing Shi
shiyibing70496@163.com

[†]*These authors have contributed equally to this work and share first authorship*

Specialty section:
This article was submitted to Cancer Imaging and Image-directed Interventions, a section of the journal Frontiers in Oncology

Received: *18 December 2021*
Accepted: *24 January 2022*
Published: *24 February 2022*

Citation:
Qian X, Lu X, Ma X, Zhang Y, Zhou C, Wang F, Shi Y and Zeng M (2022) A Multi-Parametric Radiomics Nomogram for Preoperative Prediction of Microvascular Invasion Status in Intrahepatic Cholangiocarcinoma. Front. Oncol. 12:838701. doi: 10.3389/fonc.2022.838701

test cohort (AUC = 0.819), fitting well in calibration curves ($p > 0.05$). Decision curve and clinical impact curve further confirm the clinical usefulness of the nomogram.

Conclusion: The nomogram incorporating tumor size, intrahepatic duct dilatation, and the final radiomics model is a potential biomarker for preoperative prediction of the MVI status in ICC patients.

Keywords: intrahepatic cholangiocarcinoma, microvascular invasion, prognosis, magnetic resonance imaging, radiomics, nomogram

1 INTRODUCTION

Intrahepatic cholangiocarcinoma (ICC) is the second most common primary liver cancer and accounts for 10%–15% of all cases, which arises from cholangiocytes of intrahepatic bile ducts or bile ductules (1–3). ICC has three predominant macroscopic growth patterns: mass-forming type, periductal infiltrating type, and intraductal papillary type (4). Several studies have reported increasing incidence of ICC in the last decades (5, 6) and the 5-year survival rate is still lower than 10% (7). At present, hepatectomy is still the most effective treatment for long-term survival of ICC patients (8, 9), and several poor prognostic factors have been reported, including lymph node metastasis, microvascular invasion (MVI), tumor size ≥5 cm, and multiple nodules (10).

MVI is an important histopathological feature and refers to the cancer cell nest in vessels of the surrounding hepatic tissue lined with endothelial cells (11). As a poor prognostic factor, MVI correlates early recurrence and poor outcomes and is an independent factor for overall survival in ICC patients (12, 13). However, the status of MVI is difficult to detect by radiographic images and can only be determined by histological evaluation after hepatectomy (14). In addition, MVI can affect the selection of personalized therapeutic regime, for instance, ICC patients without MVI do not need to receive adjuvant chemotherapy after R0 resections (10). Herein, the preoperative determination of MVI status is of great value in ICC patients, and it holds promises for effective patient management and estimation of outcomes.

Radiomics is a powerful and sophisticated image mining tool, and it can improve diagnostic accuracy and predict prognosis by high-throughput selecting imaging features from medical images (15). Also, several studies have constructed radiomics-based nomogram in distinguishing different pathological types of primary liver cancer (16) and predicting MVI of hepatocellular carcinoma preoperatively (17, 18). Recently, radiomics nomograms have been established for the prediction of lymph node metastasis (19), early recurrence (20), and prognosis after hepatectomy (21) in ICC patients. For MVI prediction of ICC, Zhou et al. showed the promise of seven wavelet features extracted from preoperative dynamic contrast-enhanced (DCE) MR images with an area under curve (AUC) of 0.873 (22).

In the present study, we focused on mass-forming ICCs and aimed to develop and validate a radiomics nomogram integrating clinical, imaging, and radiomics features for preoperative prediction of MVI in ICC. In order to verify the accuracy, the radiomics nomogram will be further validated by a test cohort.

2 MATERIALS AND METHODS

2.1 Patients

Zhongshan Hospital, Fudan University, and Xuzhou Central Hospital ethics committees approved this retrospective study, and patient informed consent was waived. Between June 2015 and June 2019, 163 pathologically confirmed ICC patients (118 men and 45 women; 60.48 ± 11.42 years) after hepatectomy with postoperative Ga-DTPA-enhanced MRI examination from Zhongshan Hospital were enrolled by the following inclusion criteria (**Figure 1**): (a) without previous history of liver cancer treatment (including hepatectomy, transcatheter arterial chemoembolization, radiofrequency ablation, chemotherapy, radiotherapy, and immunosuppressive therapy); (b) single mass-forming type ICC with the longest diameter ≥1.0 cm, and without macrovascular invasion and lymphatic metastasis;

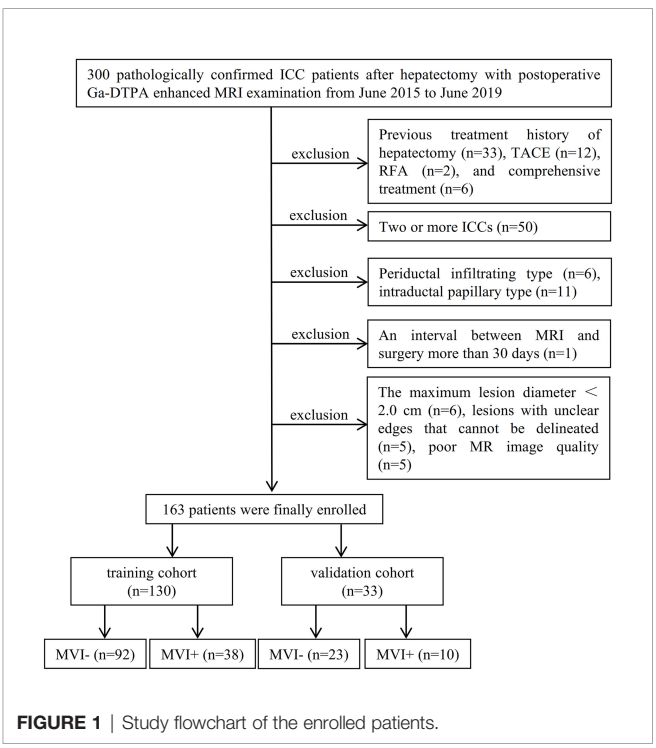

FIGURE 1 | Study flowchart of the enrolled patients.

(c) complete histopathologic description of ICC; (d) MRI scanned within 30 days before surgery; (e) sufficient MR image quality satisfied the diagnostic criteria. All enrolled patients from June 2015 to June 2019 were divided into training cohort (n = 130, 38 MVI positive and 92 MVI negative) and validation cohort (n = 33, 10 MVI positive and 23 MVI negative) in a ratio of 8:2. Importantly, between July 2019 and October 2021, a time-independent test cohort (n = 24, 12 MVI positive and 12 MVI negative) from Zhongshan Hospital and Xuzhou Central Hospital was collected for external validation (**Supplementary Table S1**).

2.2 Laboratory Tests and Histopathology

Demographic and preoperative laboratory indexes (**Table 1**) including serum alpha-fetoprotein (AFP), carcinoembryonic antigen (CEA), carbohydrate antigen 19-9 (CA199), hepatitis B

TABLE 1 | Comparison of MVI status and clinicoradiologic characteristics in ICC patients of training and validation cohorts.

Characteristics	Training cohort (n = 130)			Validation cohort (n = 33)			p-Inter
	MVI (–), (n = 92)	MVI (+), (n = 38)	p-Intra	MVI (–), (n = 23)	MVI (+), (n = 10)	p-Intra	
Clinical features							
Age (years)[a]	60.05 (11.72)	61.21 (10.32)	0.598	60.91 (11.92)	60.70 (12.91)	0.964	0.838
Gender			0.920			0.444	0.698
Female	25 (27.2)	10 (26.3)		6 (26.1)	4 (40.0)		
Male	67 (72.8)	28 (73.7)		17 (73.9)	6 (60.0)		
HBV			0.541			0.707	0.535
Negative	49 (53.3)	18 (47.4)		14 (60.9)	5 (50.0)		
Positive	43 (46.7)	20 (52.6)		9 (39.1)	5 (50.0)		
AFP			0.808			1.000	0.930
<20 ng/ml	79 (85.9)	32 (84.2)		20 (87.0)	9 (90.0)		
≥20 ng/ml	13 (14.1)	6 (15.8)		3 (13.0)	1 (10.0)		
CEA			**0.031**			1.000	0.641
<5 ng/ml	80 (87.0)	27 (71.1)		18 (78.3)	8 (80.0)		
≥ 5ng/ml	12 (13.0)	11 (28.9)		5 (21.7)	2 (20.0)		
CA199			**0.028**			0.707	0.946
<34 U/ml	58 (63.0)	16 (42.1)		14 (60.9)	5 (50.0)		
≥34 U/ml	34 (37.0)	22 (57.9)		9 (39.1)	5 (50.0)		
Edmondson-Steiner grade			**0.017**			0.109	0.777
I–II	34 (37.0)	6 (15.8)		10 (43.5)	1 (10.0)		
III–IV	58 (63.0)	32 (84.2)		13 (56.5)	9 (90.0)		
MR imaging features							
Tumor size (mm)[a]	40.92 (21.66)	59.93 (26.55)	**<0.001**	42.70 (21.79)	46.34 (19.53)	0.653	0.568
Tumor morphology			0.168			0.279	0.713
(Hemi-)spherical and oval	40 (43.5)	10 (26.3)		12 (52.2)	3 (30.0)		
Lobulated	36 (39.1)	18 (47.4)		7 (30.4)	6 (60.0)		
Irregular	16 (17.4)	10 (26.3)		4 (17.4)	1 (10.0)		
SI on T1WI			0.236			1.000	0.693
Low	91 (98.9)	36 (94.7)		22 (95.7)	10 (100.0)		
Moderate	1 (1.1)	1 (2.6)		1 (4.3)	0 (0.0)		
High	0 (0.0)	1 (2.6)		0 (0.0)	0 (0.0)		
SI on T2WI-FS			0.699			1.000	0.474
Low	1 (1.1)	0 (0.0)		0 (0.0)	0 (0.0)		
Moderate	2 (2.2)	1 (2.6)		2 (8.7)	0 (0.0)		
High	89 (96.7)	37 (97.4)		21 (91.3)	10 (100.0)		
Target sign on T2WI-FS			0.560			0.444	0.583
Negative	58 (63.0)	26 (68.4)		17 (73.9)	6 (60.0)		
Positive	34 (37.0)	12 (31.6)		6 (26.1)	4 (40.0)		
Target sign on DWI			0.552			0.707	0.701
Negative	48 (52.2)	22 (57.9)		14 (60.9)	5 (50.0)		
Positive	44 (47.8)	16 (42.1)		9 (39.1)	5 (50.0)		
Rim enhancement on AP			0.735			0.673	0.522
Negative	17 (18.5)	8 (21.1)		5 (21.7)	3 (30.0)		
Positive	75 (81.5)	30 (78.9)		18 (78.3)	7 (70.0)		
Complete rim on AP			0.288			0.378	0.580
Negative	29 (38.7)	15 (50.0)		10 (55.6)	2 (28.6)		
Positive	46 (61.3)	15 (50.0)		8 (44.4)	5 (71.4)		
Enhancement pattern			0.423			0.195	0.376
Gradual and filling	70 (76.1)	29 (76.3)		14 (60.9)	8 (80.0)		
Arterial and persistent	13 (14.1)	3 (7.9)		4 (17.4)	0 (0.00)		

(Continued)

TABLE 1 | Continued

Characteristics	Training cohort (*n* = 130)			Validation cohort (*n* = 33)			*p*-Inter
	MVI (–), (*n* = 92)	MVI (+), (*n* = 38)	*p*-Intra	MVI (–), (*n* = 23)	MVI (+), (*n* = 10)	*p*-Intra	
Wash-in and wash-out	9 (9.8)	6 (15.8)		5 (21.7)	2 (20.0)		
LI-RADS			0.087			1.000	0.242
LR-3	1 (1.1)	0 (0.0)		0 (0.0)	0 (0.0)		
LR-4	5 (5.4)	0 (0.0)		0 (0.0)	0 (0.0)		
LR-5	4 (4.3)	4 (10.5)		4 (17.4)	1 (10.0)		
LR-M	82 (89.1)	33 (86.8)		19 (82.6)	9 (90.0)		
LR-TIV	0 (0.0)	1 (2.6)		0 (0.0)	0 (0.0)		
Intrahepatic duct dilatation			**<0.001**			0.686	0.114
Negative	64 (69.6)	11 (28.9)		16 (69.6)	8 (80.0)		
Positive	28 (30.4)	27 (71.1)		7 (30.4)	2 (20.0)		
Hepatic capsular retraction			0.806			0.139	0.702
Negative	53 (57.6)	21 (55.3)		16 (69.6)	4 (40.0)		
Positive	39 (42.4)	17 (44.7)		7 (30.4)	6 (60.0)		
Visible vessel penetration			0.599			1.000	0.618
Negative	36 (39.1)	13 (34.2)		10 (43.5)	4 (40.0)		
Positive	56 (60.9)	25 (65.8)		13 (56.5)	6 (60.0)		
Peripherally hepatic enhancement			0.146			1.000	0.351
Negative	38 (41.3)	21 (55.3)		8 (34.8)	4 (40.0)		
Positive	54 (58.7)	17 (44.7)		15 (65.2)	6 (60.0)		

Data are shown as number of patients and percentage in parentheses, unless otherwise stated.

[a]*Data are means and standard deviations in parentheses.*

MVI, microvascular invasion; OR, odds ratio; HBV, hepatitis B; AFP, α-fetoprotein; CEA, carcinoembryonic antigen; CA199, carbohydrate antigen 199; SI, signal intensity; T1WI, T1-weighted imaging; T2WI, T2-weighted imaging; FS, fat suppression; DWI, diffusion-weighted imaging; LI-RADS, the liver imaging reporting and data system; AP, arterial phase.

The bold values are statistically significant with p <0.05.

virus (HBV), and HBV-DNA loads were collected from our electronic medical records system. ICC specimens were sampled using 7-point baseline sampling protocol (11). Pathological characteristics including tumor number, Edmondson-Steiner grade, and MVI status were assessed in consensus by two experienced abdominal pathologists. MVI was defined as the presence of tumor cell nest (the number of suspended tumor cell more than 50) in the portal vein, hepatic vein, or large capsular vessel of the surrounding hepatic tissue that was only visible by microscopy (11, 23).

2.3 Gd-DTPA MR Imaging

All patients underwent MR imaging with intravenous injection of 0.2 mmol/kg gadopentetate dimeglumine (Gd-DTPA; Bayer HealthCare, Berlin, Germany) and immediately followed by a 20-ml saline flush at a speed of 2 ml/s. Taking Magnetom Aera 1.5T scanner (Siemens Healthcare, Erlangen, Germany) as an example, imaging sequences included axial T2-weighted imaging with fat suppression (T2WI-FS), diffusion-weighted imaging (DWI), in-phase and opposed-phase T1-weighted imaging (IP-OP T1WI), axial precontrast three-dimensional volumetric-interpolated breath-hold examination T1-weighted imaging (3D-VIBE T1WI) with fat suppression, and postcontrast dynamic-enhanced 3D-VIBE-T1WI at arterial phase (AP, 20–30 s), portal venous phase (PVP, 60–70 s), and delayed phase (DP, 180 s). Detailed parameters of each acquisition sequence are shown in **Supplementary Table S2**.

2.4 MR Images Analysis

All MR images were reviewed independently on a picture archiving and communication system (PACS; Pathspeed, GE Medical Systems Integrated Imaging Solutions, Chicago, IL, USA) by 2 experienced abdominal radiologists (XM and XL with 10 and 15 years of experience, respectively). Both radiologists were blinded to all demographic, clinical, laboratory, and histopathologic information. If any discrepancies occurred, a consensus was reached after discussion. The following imaging features were assessed by 2 abdominal radiologists: (a) tumor size, defined as the maximum diameter on transverse T1WI image; (b) tumor morphology, including spherical/hemispherical/oval, lobulated and irregular; (c) signal intensity on T1WI, T2WI-FS, and DWI, including hypointense, isointense, and hyperintense; (d) target sign on T2WI-FS and DWI, defined as peripheral hyperintense with central isointense/hypointense (24); (e) rim enhancement on AP, defined as peripheral enhancement of the lesion on AP, including complete and incomplete rim; (f) enhancement pattern, including gradual and filling, arterial and persistent, and wash-in and wash-out enhancement; (g) the liver imaging reporting and data system (LI-RADS), defined as LR category based on LI-RADSv2018 (25); (h) intrahepatic duct dilatation, defined as intrahepatic duct dilatation within or outside of the lesion; (i) hepatic capsular retraction, defined as retraction of hepatic capsular adjacent to the lesion; (j) visible vessel penetration, defined as the presence of penetrating vessels in the lesion, including hepatic artery, portal vein, and hepatic vein (26); and (k) peripherally hepatic enhancement, defined as enhancement of liver parenchyma around the lesion on any phase.

2.5 Radiomics Analysis

2.5.1 Workflow

The workflow of the radiomics analysis included tumor segmentation, feature extraction, feature selection, model construction, model analysis, and evaluation (**Figure 2**).

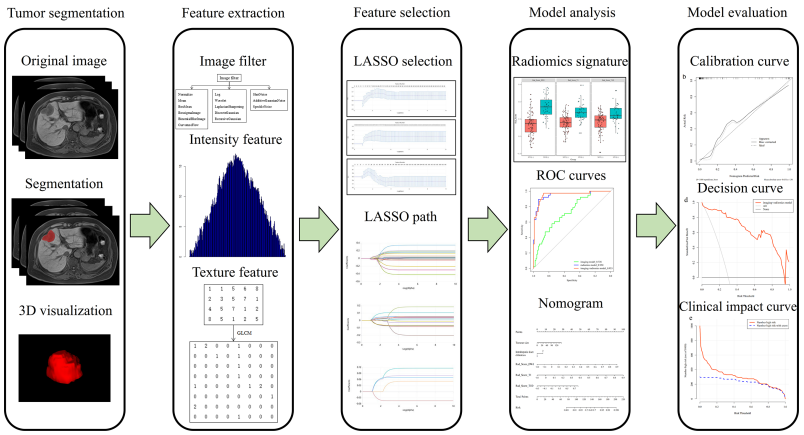

FIGURE 2 | Study flowchart of the radiomics analysis.

2.5.2 Image Segmentation

The whole tumor segmentation was manually delineated in ITK-SNAP (http://www.itksnap.org/pmwiki/pmwiki.php) by an abdominal radiologist with 6 years of experience (XQ) and validated by a senior abdominal radiologist with 15 years of experience (XL). Volumes of interests (VOIs) were drawn on 6 sequences: DWI with *b*-values of 500 s/mm^2, T2WI-FS, 3D-VIBE T1WI, AP, PVP, and DP.

2.5.3 Feature Extraction

Radiomics features were extracted from the VOIs using uAI Research Portal (Version: 20210730), and 2,600 radiomics features were extracted from each sequence (**Supplementary Table S3**). These radiomics features were classified into First Order, Shape, Gray-Level Co-occurrence Matrix (GLCM), Gray-Level Size Zone Matrix (GLSZM), Gray-Level Run Length Matrix (GLRLM), Neighboring Gray Tone Difference Matrix (NGTDM), and Gray-Level Dependence Matrix (GLDM) features.

2.5.4 Feature Selection

To eliminate index dimension difference, the extracted radiomics features of each sequence were standardized into a normal distribution with z-scores. A test-retest procedure was performed on 30 randomly selected tumors, reproducible radiomics features were considered features with intraclass correlation coefficient greater than 0.75 and included in the following feature selection procedures. The variance threshold, SelectKBest and least absolute shrinkage and selection operator (LASSO) methods were performed to select optimal features of each sequence (**Supplementary Table S3** and **Supplementary Figure S1**). The corresponding radiomics score (Rad-score) of each sequence in the training and validation cohorts was calculated (**Supplementary Table S4** and **Supplementary Figure S2**).

2.5.5 Model Construction

To construct clinical and imaging models, the univariate analysis was used to assess the potential predictors of MVI status, and the multivariate logistic regression analysis was used to determine the independent predictors of MVI status. Radiomics models of each sequence were constructed by the corresponding optimal features. The sequences with Rad-scores showed significant differences between MVI-positive and MVI-negative ICCs in both the training cohort and validation cohort were selected for the final radiomics model construction. The MVI prediction model incorporated imaging model and the final radiomics model. All models were constructed with logistic regression (LR), random forest (RF), and support vector machine (SVM) classifiers respectively for comparison.

2.5.6 Model Analysis and Evaluation

The receiver operating characteristic curves were plotted, and the AUC, accuracy, sensitivity, specificity, F1-score, and precision were calculated to quantify the predictive efficacy of each model in training, validation, and test cohorts. The comparison of predictive performances between multiple models was performed by the Delong test. A radiomics nomogram was built on the MVI prediction model with the LR classifier. Hosmer-Lemeshow test was performed to identify the agreement between nomogram-predicted MVI status and actual MVI status, and calibration curves in the training and validation cohorts were plotted. Decision curve and clinical impact curve were plotted for assessing the clinical usefulness of the nomogram by quantifying the net benefits at different risk thresholds.

2.6 Statistical Analysis

Clinical and imaging features were analyzed for statistical differences in the training, validation, and test cohorts by Student's *t*-test, Mann-Whitney *U* test, Wilcoxon test, Chi-square test, or Fisher's exact test, as appropriate. The statistical analyses were conducted using the IBM SPSS Statistics (version 20) and R software (version 3.4.1). A two-tailed *p*-value of less than 0.05 was considered statistically significant.

3 RESULTS

3.1 Clinicoradiologic Characteristics and Performances

Comparison of MVI status and clinicoradiologic characteristics in training and validated ICC patients are shown in **Table 1**. The final cohort of 163 patients with single ICC was divided into training cohort (n = 130, 92 patients were MVI negative and 38 patients were MVI positive) and validation cohort (n = 33, 23 patients were MVI negative and 10 patients were MVI positive). There is no significant difference of the status of MVI between training and validation cohort (p = 0.904). Univariate analysis of clinicoradiologic characteristics indicates that serum CEA level (p = 0.035; OR = 2.716, 95% CI: 1.065–6.918), serum CA199 level (p = 0.030; OR = 2.346, 95% CI: 1.092–5.139), Edmondson-Steiner grade (p = 0.021; OR = 3.126, 95% CI: 1.254–8.977), tumor size (p < 0.001; OR = 1.033, 95% CI: 1.016–1.052), tumor morphology (p= 0.071; OR = 1.604, 95% CI: 0.964–2.708), and intrahepatic duct dilatation (p < 0.001; OR =5.610, 95% CI: 2.505–13.308) are significantly associated with MVI. At the multivariate analysis, tumor size (p = 0.003; OR = 1.032, 95% CI: 1.011–1.055) and intrahepatic duct dilatation (p = 0.002; OR = 4.552, 95% CI: 1.777–12.259) are independent predictors of MVI (**Table 2**). The imaging model constructed with two predictors has an AUC of 0.726 in the training cohort and 0.522 in the validation cohort (**Table 3**). Examples of representative radiological characteristics of MVI-positive and MVI-negative ICCs are shown in **Figure 3**.

3.2 Performance of Radiomics Features From Single MR Sequence

Robust radiomics features of each single MR sequence were selected by reproducibility analysis and LASSO analysis (**Supplementary Table S3** and **Supplementary Figure S1**). The predictive performance of radiomics features on each MR sequence is shown in **Table 3**. However, all single sequences show overfit predictive performance in the training cohort (AUCs = 1.000) and poor predictive performance in the validation cohort (AUCs: 0.422–0.665). The Rad-score of each MR sequence in the training and validation cohorts are shown in **Supplementary Table S4**, and Rad-scores of the diffusion-weighted imaging, precontrast T1-weighted imaging, and delayed phase imaging show significant differences between MVI-positive and MVI-negative ICCs in both the training cohort (p < 0.001) and validation cohort (p_{DWI} = 0.025, p_{T1} = 0.003, p_{T1D} = 0.001) (**Supplementary Table S4** and **Supplementary Figure S2**). Therefore, further analysis about diffusion-weighted imaging, precontrast T1-weighted imaging, and delayed phase imaging was conducted. The detailed information of 22 radiomics features in diffusion-weighted imaging, 17 radiomics features in precontrast T1-weighted imaging, and 5 radiomics features in delayed phase imaging are shown in **Supplementary Table S5**.

3.3 Performance of Radiomics Features From Multiple MR Sequences

Three pairwise combination models of the diffusion-weighted images, precontrast T1-weighted images, and delayed phase images are constructed, and all show a satisfying performance in both the training cohort (AUC = 0.883–0.941) and validation cohort (AUC = 0.817–0.874) (**Table 3**). The final radiomics model incorporates these three sequences, and it performs better in predicting MVI of ICC in both the training cohort (AUC = 0.950, accuracy = 0.862, sensitivity = 0.921, and specificity = 0.837) and validation cohort (AUC = 0.883, accuracy = 0.788,

TABLE 2 | Univariate and multivariate analyses of predictive characteristics related with MVI status in ICC.

Characteristics	Univariate		Multivariate	
	p-value	OR (95% CI)	*p*-value	OR (95% CI)
Age	0.595	1.009 (0.976–1.045)		
Gender	0.920	0.957 (0.394–2.211)		
HBV	0.541	1.266 (0.594–2.717)		
AFP	0.808	1.139 (0.373–3.157)		
CEA	**0.035**	2.716 (1.065–6.918)	0.463	1.517 (0.491–4.629)
CA199	**0.030**	2.346 (1.092–5.139)	0.973	0.984 (0.365–2.541)
Edmondson-Steiner grade	**0.021**	3.126 (1.254–8.977)		
Tumor size	**<0.001**	1.033 (1.016–1.052)	**0.003**	1.032 (1.011–1.055)
Tumor morphology	**0.071**	1.604 (0.964–2.708)	0.440	0.757 (0.362–1.504)
SI on T1WI	0.175	4.225 (0.715–80.403)		
SI on T2WI-FS	0.701	1.455 (0.282–24.396)		
Target sign on T2WI-FS	0.541	0.776 (0.337–1.723)		
Target sign on DWI	0.552	0.793 (0.366–1.695)		
Rim enhancement on AP	0.735	0.850 (0.339–2.273)		
Enhancement pattern	0.659	1.130 (0.640–1.926)		
LI-RADS	0.715	0.912 (0.521–1.447)		
Intrahepatic duct dilatation	**<0.001**	5.610 (2.505–13.308)	**0.002**	4.552 (1.777–12.259)
Hepatic capsular retraction	0.806	1.100 (0.510–2.355)		
Visible vessel penetration	0.599	1.236 (0.567–2.780)		
Peripherally hepatic enhancement	0.148	0.570 (0.263–1.217)		

The bold values are statistically significant with p <0.05.

TABLE 3 | The performance of imaging, radiomics of single and multiple MR sequences, and final fusion models for predicting MVI in ICC patients.

Models	Classifier and cohort	AUC	Accuracy	Sensitivity	Specificity	Precision
Imaging model	LR (TD/VD)	0.726/0.522	0.669/0.545	0.605/0.400	0.696/0.609	0.451/0.308
	RF (TD/VD)	0.742/0.578	0.731/0.697	0.211/0.100	0.946/0.957	0.615/0.500
	SVM (TD/VD)	0.726/0.483	0.708/0.697	0.000/0.000	1.000/1.000	0.000/0.000
DWI model	LR (TD/VD)	1.000/0.530	1.000/0.485	1.000/0.600	1.000/0.435	1.000/0.316
	RF (TD/VD)	0.943/0.530	0.800/0.697	0.316/0.000	1.000/1.000	1.000/0.000
	SVM (TD/VD)	1.000/0.774	1.000/0.697	1.000/0.000	1.000/1.000	1.000/0.000
T1 model	LR (TD/VD)	1.000/0.643	1.000/0.636	1.000/0.700	1.000/0.609	1.000/0.438
	RF (TD/VD)	0.949/0.687	0.823/0.697	0.395/0.100	1.000/0.957	1.000/0.500
	SVM (TD/VD)	1.000/0.513	1.000/0.697	1.000/0.000	1.000/1.000	1.000/0.000
T1A model	LR (TD/VD)	1.000/0.443	1.000/0.636	1.000/0.500	1.000/0.304	1.000/0.238
	RF (TD/VD)	0.967/0.700	1.000/0.364	0.158/0.000	1.000/1.000	1.000/0.000
	SVM (TD/VD)	1.000/0.500	0.754/0.697	1.000/0.000	1.000/1.000	1.000/0.000
T1D model	LR (TD/VD)	1.000/0.665	1.000/0.606	1.000/0.700	1.000/0.565	1.000/0.412
	RF (TD/VD)	0.978/0.765	0.738/0.697	0.105/0.000	1.000/1.000	1.000/0.000
	SVM (TD/VD)	1.000/0.574	1.000/0.697	1.000/0.000	1.000/1.000	1.000/0.000
T1V model	LR (TD/VD)	1.000/0.430	1.000/0.424	1.000/0.600	1.000/0.348	1.000/0.286
	RF (TD/VD)	0.979/0.661	0.738/0.697	0.105/0.000	1.000/1.000	1.000/0.000
	SVM (TD/VD)	1.000/0.426	1.000/0.697	1.000/0.000	1.000/1.000	1.000/0.000
T2 model	LR (TD/VD)	1.000/0.422	1.000/0.424	1.000/0.100	1.000/0.565	1.000/0.091
	RF (TD/VD)	0.969/0.383	0.746/0.697	0.132/0.000	1.000/1.000	1.000/0.000
	SVM (TD/VD)	1.000/0.448	1.000/0.697	1.000/0.000	1.000/1.000	1.000/0.000
DWI+T1 model	LR (TD/VD)	0.941/0.817	0.892/0.758	0.895/0.800	0.891/0.739	0.773/0.571
	RF (TD/VD)	0.963/0.854	0.908/0.848	0.895/0.900	0.913/0.826	0.810/0.692
	SVM (TD/VD)	0.941/0.826	0.892/0.788	0.816/0.800	0.924/0.783	0.816/0.615
DWI+T1D model	LR (TD/VD)	0.901/0.852	0.846/0.788	0.684/0.700	0.913/0.826	0.765/0.636
	RF (TD/VD)	0.897/0.852	0.792/0.636	0.816/0.800	0.783/0.565	0.608/0.444
	SVM (TD/VD)	0.890/0.835	0.815/0.788	0.474/0.600	0.957/0.870	0.818/0.667
T1+T1D model	LR (TD/VD)	0.883/0.874	0.846/0.818	0.711/0.600	0.902/0.913	0.705/0.750
	RF (TD/VD)	0.905/0.878	0.869/0.818	0.816/0.800	0.891/0.826	0.756/0.667
	SVM (TD/VD)	0.884/0.835	0.777/0.727	0.237/0.100	1.000/1.000	1.000/1.000
Radiomics model	LR (TD/VD)	0.950/0.883	0.862/0.788	0.921/0.900	0.837/0.739	0.700/0.600
	RF (TD/VD)	0.967/0.891	0.908/0.879	0.895/0.900	0.913/0.870	0.801/0.750
	SVM (TD/VD)	0.947/0.865	0.869/0.818	0.579/0.700	0.989/0.870	0.957/0.700
Imaging+radiomics model	LR (TD/VD)	0.953/0.861	0.892/0.818	0.974/0.900	0.859/0.783	0.740/0.643
	RF (TD/VD)	0.988/0.878	0.946/0.909	0.895/0.800	0.967/0.957	0.919/0.889
	SVM (TD/VD)	0.898/0.878	0.869/0.909	0.763/0.900	0.913/0.913	0.784/0.818
Radiomics model	LR (test)	0.812 (0.617–1.000)	0.792	0.750	0.833	0.818
	RF (test)	0.757 (0.532–0.982)	0.792	0.667	0.917	0.889
	SVM (test)	0.812 (0.617–1.000)	0.708	0.500	0.917	0.857
Imaging+radiomics model	LR (test)	0.819 (0.620–1.000)	0.875	0.833	0.917	0.909
	RF (test)	0.771 (0.556–0.986)	0.750	0.583	0.917	0.875
	SVM (test)	0.771 (0.555–0.987)	0.792	0.667	0.917	0.889

LR, logistic regression; RF, random forest; SVM, support vector machine; TD, training dataset; VD, validation dataset; AUC, area under the curve.

sensitivity = 0.900, and specificity = 0.739) than three pairwise combination models (**Tables 3**, **4**). Notably, the final radiomics model also performs desirably and stably in the test cohort with AUC, accuracy, sensitivity, and specificity of 0.812 (95% CI: 0.617–1.000), 0.792, 0.750, and 0.833, respectively (**Table 3**).

3.4 Performance of MVI Prediction Model

The MVI prediction model includes imaging model and final radiomics model, and it achieves excellent predictive efficacy in the training cohort (AUC = 0.953, accuracy = 0.892, sensitivity = 0.974, and specificity = 0.859), validation cohort (AUC = 0.861, accuracy = 0.818, sensitivity = 0.900, and specificity = 0.783), and test cohort (AUC = 0.819, accuracy = 0.875, sensitivity = 0.833, and specificity = 0.917) (**Table 3**).

Moreover, the MVI prediction model performs better than imaging model in the training cohort (AUCs: 0.953 vs. 0.726, $p < 0.001$) and validation cohort (AUCs: 0.861 vs. 0.522, $p = 0.018$). However, there is no statistical difference between the MVI prediction model and final radiomics model in the training cohort (AUCs: 0.953 vs. 0.950, $p = 0.629$), validation cohort (AUCs: 0.861 vs. 0.883, $p = 0.202$), and test cohort (AUCs: 0.819 vs. 0.812, $p = 0.732$) (**Table 4**, **Figure 4** and **Supplementary Figure S3**).

3.5 Development and Verification of the Nomogram

The nomogram of the MVI prediction model is presented in **Figure 5A**, and the formula is as follows. It achieves satisfying performance with AUCs of 0.953 in the training cohort and 0.861 in the validation cohort. Calibration curves (**Figures 5B, C**) of the nomogram exhibiting satisfactory predictive performances are aligned with the actual MVI

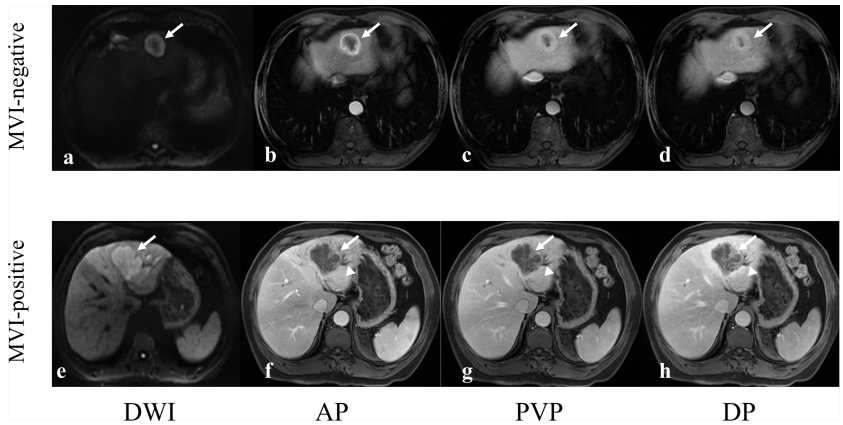

FIGURE 3 | Two examples of representative MVI-negative and MVI-positive ICCs. **(A–D)** A 62-year-old man with a well-circumscribed MVI-negative ICC in hepatic segment II (arrows). DWI image showed target sign **(A)**, axial arterial phase image showed rim enhancement **(B)**, and portal vein phase image **(C)** and delayed phase image **(D)** showed the typical enhancement type of ICC: gradual and filling enhancement. **(E–H)** A 62-year-old man with a lobulated MVI-positive ICC in hepatic segment IV (arrows). DWI image showed hyperintensity **(E)**, axial arterial phase image showed marginal moderate enhancement with no internal enhancement **(F)** and dilated bile ducts next to tumor (arrowheads), and portal vein phase image **(G)** and delayed phase image **(H)** showed the typical enhancement type of ICC: gradual and filling enhancement.

estimates in the training ($p = 0.364$) and validation ($p = 0.543$) cohorts. Decision curve (**Figure 5D**) of the nomogram shows that the net benefit is higher than that assuming all patients have MVI. Clinical impact curve (**Figure 5E**) shows that the predicted probabilities of the nomogram is close to actual high risk with event when risk threshold is 0.2–0.7 and is consistent when risk threshold is over 0.7.

$$Y = -11.420 + 0.020 \times \text{Imaging}_{\text{Tumor size}} + 0.723 \times \text{Imaging}_{\text{Intrahepatic duct dilatation}} + 9.130 \times \text{Rad Score}_{\text{DWI}} + 10.835 \times \text{Rad Score}_{\text{T1}} + 4.690 \times \text{Rad Score}_{\text{T1D}}$$

DISCUSSION

In this study, we established a radiomics-based nomogram for preoperatively predicting MVI in patients with ICC. The final MVI prediction model achieves a satisfying prediction performance, and it incorporates Ga-DTPA-enhanced MRI-based radiomics features of the diffusion-weighted images, precontrast T1-weighted images, and delayed phase images and imaging features including tumor size and intrahepatic duct dilatation.

High serum level of CEA and CA199 (>100 U/ml) can predict the diagnosis of ICC (27, 28), but the predictive value in predicting MVI status of ICC is still unknown. Although univariate analysis shows elevated serum CEA and CA199 level are significant clinical

TABLE 4 | The comparison of models in training, validation, and test cohorts.

Models for comparison	Classifier	$p_{\text{training cohort}}$	$p_{\text{validation cohort}}$	$p_{\text{test cohort}}$
Radiomics model vs. DWI+T1 model	LR	0.222	0.013	0.591
	RF	0.674	0.217	0.260
	SVM	0.636	0.197	0.151
Radiomics model vs. DWI+T1D model	LR	0.014	0.527	0.766
	RF	0.003	0.522	0.493
	SVM	0.012	0.421	0.214
Radiomics model vs. T1+T1D model	LR	0.018	0.888	0.092
	RF	0.006	0.751	0.659
	SVM	0.027	0.572	0.334
Radiomics model vs. imaging model	LR	<0.001	0.018	0.193
	RF	<0.001	0.023	0.071
	SVM	<0.001	0.003	0.294
Imaging+radiomics model vs. imaging model	LR	<0.001	0.023	0.206
	RF	<0.001	0.021	0.055
	SVM	<0.001	0.002	0.306
Imaging+radiomics model vs. radiomics model	LR	0.629	0.202	0.732
	RF	0.032	0.505	0.569
	SVM	0.018	0.757	0.325

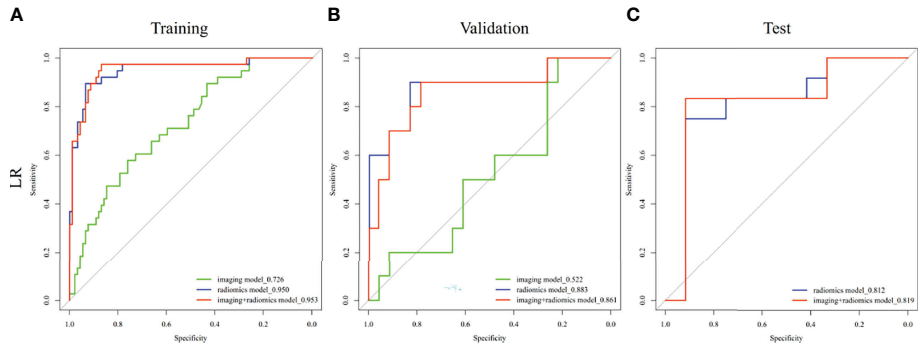

FIGURE 4 | Comparison of receiver operating characteristic (ROC) curves for prediction of MVI in ICC. ROC curves of imaging model constructed with tumor size and intrahepatic duct dilatation, radiomics model constructed with diffusion-weighted image, precontrast T1-weighted image, and delayed phase image, and MVI prediction model constructed imaging model and radiomics model in the **(A)** training, **(B)** validation, and **(C)** test cohorts.

features, there are no statistical difference between the MVI-positive and MVI-negative groups by multivariate analysis, which are consistent with the studies of Zhou et al. (22) and Ma et al. (29). As other studies on preoperative MVI prediction in HCC (30–32) and ICC (14, 22, 33), tumor size is also an independent predictor of MVI in ICC patients in our study, but intrahepatic duct dilatation is another important imaging predictor, which is different from the studies of Zhou et al. (22). This may be due to the different MVI predictor screening methods; in his study, intrahepatic duct dilatation was excluded because there was no significant difference between MVI-positive and MVI-negative groups in the validation cohort (p = 0.279), but a p-value with 0.097 in the training cohort indicated this predictor should be further analyzed by multivariate analysis. Although hepatic capsular retraction and progressive centripetal enhancement in the venous phase have been described as classical imaging features of ICC (34), there are no statistical difference between MVI-positive and MVI-negative groups. In general, the imaging model constructed with tumor size and intrahepatic duct dilatation yields a good performance in the training cohort, but an unsatisfying performance in the validation cohort limits its application in preoperatively predicting MVI. Therefore, a combined model based on radiomics is necessary.

Of 44 radiomics features, 6 are considered optimal features with the absolute values of LASSO coefficients being greater than 0.1, including First Order _Uniformity, GLCM _Maximum Probability, GLCM _Inverse Difference, GLCM _ Informational Measure of Correlation 1, GLDM _Dependence Variance, and GLRLM _Long Run Emphasis. Histologically, ICC often shows aggressive trait, and inflammation, necrosis, and fibrosis are common (2); therefore, heterogeneous signal intensity in MR images are found to be more frequent for MVI-positive ICC, which is in concordance with First Order _Uniformity. Additionally, other 5 radiomics features indicate the higher the neighboring intensity value, variance, and gray-level value of VOI, the higher is the probability of MVI. Compared with the 100 radiomics features pool constructed by Zhou et al. (22), 42 of 44 radiomics features in our study are repeatable, and 3 of 7 optimal radiomics features in his study are also detected in our study. Both three pairwise combination models and the final radiomics model based on the diffusion-weighted images, precontrast T1-weighted images, and delayed phase images have solved the defect of overfit predictive performance in the training cohort and poor predictive performance in the validation cohort of single MR sequence models.

As far as we know, this study is the first to establish a nomogram based on clinicoradiologic and radiomics features. The MVI prediction model incorporates the final radiomics model, and imaging model exhibits excellent performance in both the training cohort (AUC = 0.953) and validation cohort (AUC = 0.861) with good calibration, which are better than the previous study ($AUC_{training}$ = 0.873, $AUC_{validation}$ = 0.850) (22). Also, the MVI prediction model achieves better efficacy than the imaging model in our study, suggesting radiomics features are indispensable in MVI prediction. More importantly, the nomogram in our study also exhibits a desirable prediction performance in the test cohort (AUC = 0.819) and performs better than clinical factor model constructed by Tang et al. (35) with AUCs of 0.739, 0.717, and 0.709 in training, validation, and test cohorts. Hence, the use of our nomogram preoperatively may be a noninvasive and robust method of assisting personalized treatment making, and patients with ICCs may suffer a higher net benefit from it.

There are some limitations in our study. Firstly, selection bias is inevitable in our retrospective study. Secondly, compared with MVI-negative ICCs, the number of MVI-positive ICCs is relatively small. Thirdly, the association between radiomics features and complex tumor biological features needs to be further explained. Fourthly, the study about whether the preoperative prediction of overall survival (OS) and disease-free survival (DFS) based on our MVI prediction model has the same effect as the postoperative prediction of OS and DFS based on pathological MVI after surgery is needed. Finally, although the nomogram has achieved a desirable prediction performance in the test cohort, larger cohorts from other centers are needed to be collected for the prospective validation of our nomogram.

In conclusion, radiomics features extracted from diffusion-weighted images, precontrast T1-weighted images, and delayed phase images of Ga-DTPA-enhanced MR imaging can assist in predicting MVI status of ICC patients. The MVI prediction

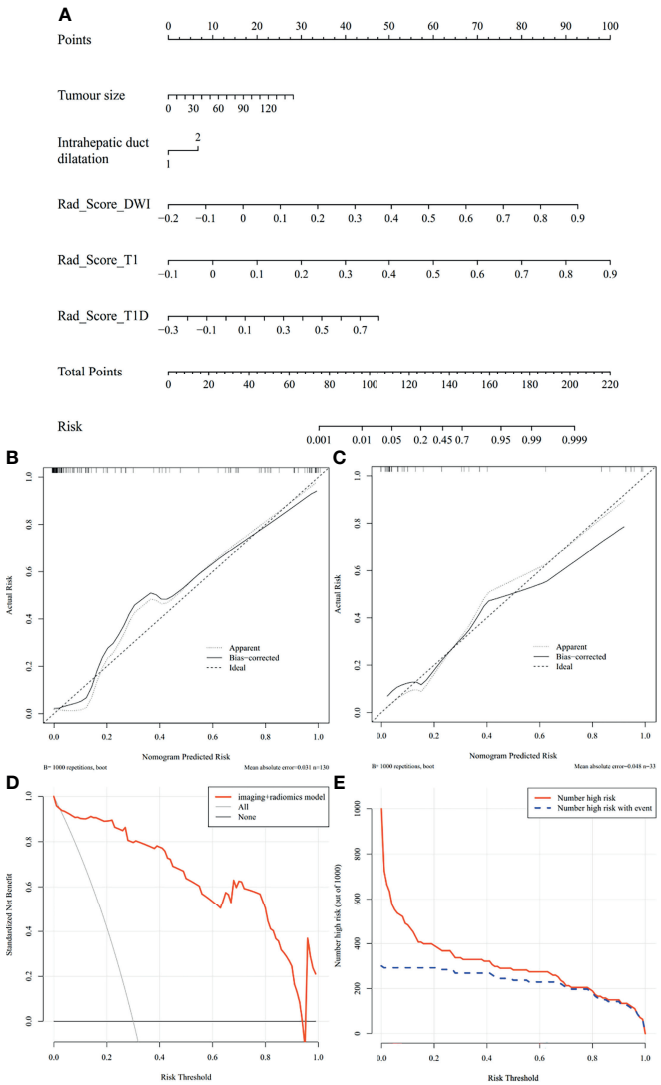

FIGURE 5 | Nomogram of MVI prediction model, calibration curves of the nomogram in the training and validation cohort, decision curve, and clinical impact curve in the overall ICC patients. **(A)** A nomogram integrates imaging factors including tumor size and intrahepatic duct dilatation, and radiomics factors includes Rad-scores of diffusion-weighted images, precontrast T1-weighted images, and delayed phase images. **(B, C)** Calibration curves of the nomogram in the training and validation cohort. *x*-axis is a nomogram-predicted risk of MVI. *y*-axis is actual risk of MVI, and the diagonal dashed line indicates the ideal prediction by an ideal model. **(D)** Decision curve for the nomogram in the overall patients. The gray line is the net benefit of assuming that all patients have MVI; the black line is the net benefit of assuming no patients have MVI; and the red line is the expected net benefit of per patient based on the nomogram. **(E)** Clinical impact curve for the nomogram in the 1,000 simulated samples. The blue dashed line is the actual number of high risk, and the red line is the number of high risk based on nomogram.

nomogram incorporating radiomics features and imaging features including tumor size and intrahepatic duct dilatation is a potential biomarker and clinical tool in MVI stratification of ICC patients preoperatively.

DATA AVAILABILITY STATEMENT

The original contributions presented in the study are included in the article/**Supplementary Material**. Further inquiries can be directed to the corresponding authors.

ETHICS STATEMENT

The studies involving human participants were reviewed and approved by the Zhongshan Hospital, Fudan University ethics committee and Xuzhou Central Hospital ethics committee. The patients/participants provided their written informed consent to participate in this study. Written informed consent was obtained from the individual(s) for the publication of any potentially identifiable images or data included in this article.

AUTHOR CONTRIBUTIONS

Conceptualization: MZ and YS. Methodology: MZ, XQ, and FW. Software: XQ, XL, and FW. Validation: XM, YZ, and CZ. Formal analysis: XQ and XL. Resources: XQ, XL, and MZ. Data curation: XQ and XL. Writing—original draft preparation: XQ and XL. Writing—review and editing: MZ and YS. Supervision: MZ and YS. Project administration: MZ. Funding acquisition: MZ and YS. All authors listed have made a substantial, direct, and intellectual contribution to the work and approved it for publication.

FUNDING

This study was supported by grants from the National Natural Science Foundation of China (No. 82171897), Shanghai Municipal Key Clinical Specialty (No. shslczdzk03202), Clinical Research Plan of SHDC (No. SHDC2020CR1029B), Clinical Research Project of Zhongshan Hospital, Fudan University (No. 2020ZSLC61), "the Development Research Foundation of Affiliated Hospital" of Xuzhou Medical University (No. XYFM2020020), and the Medical Scientific Research Program of Jiangsu Commission of Health (No. M2021014).

ACKNOWLEDGMENTS

We sincerely thank Chun Yang for the assistance of radiomics analysis.

SUPPLEMENTARY MATERIAL

The Supplementary Material for this article can be found online at: https://www.frontiersin.org/articles/10.3389/fonc.2022.838701/full#supplementary-material

REFERENCES

1. Sung H, Ferlay J, Siegel RL, Laversanne M, Soerjomataram I, Jemal A, et al. Global Cancer Statistics 2020: GLOBOCAN Estimates of Incidence and Mortality Worldwide for 36 Cancers in 185 Countries. *CA Cancer J Clin* (2021) 71(3):209–49. doi: 10.3322/caac.21660
2. Sempoux C, Jibara G, Ward SC, Fan C, Qin L, Roayaie S, et al. Intrahepatic Cholangiocarcinoma: New Insights in Pathology. *Semin Liver Dis* (2011) 31 (1):49–60. doi: 10.1055/s-0031-1272839
3. Massarweh NN, El-Serag HB. Epidemiology of Hepatocellular Carcinoma and Intrahepatic Cholangiocarcinoma. *Cancer Control* (2017) 24 (3):1073274817729245. doi: 10.1177/1073274817729245
4. Brindley PJ, Bachini M, Ilyas SI, Khan SA, Loukas A, Sirica AE, et al. Cholangiocarcinoma. *Nat Rev Dis Primers* (2021) 7(1):65. doi: 10.1038/s41572-021-00300-2
5. Utada M, Ohno Y, Tamaki T, Sobue T, Endo G. Long-Term Trends in Incidence and Mortality of Intrahepatic and Extrahepatic Bile Duct Cancer in Japan. *J Epidemiol* (2014) 24(3):193–9. doi: 10.2188/jea.je20130122
6. Bergquist A, von Seth E. Epidemiology of Cholangiocarcinoma. *Best Pract Res Clin Gastroenterol* (2015) 29(2):221–32. doi: 10.1016/j.bpg.2015.02.003
7. Everhart JE, Ruhl CE. Burden of Digestive Diseases in the United States Part III: Liver, Biliary Tract, and Pancreas. *Gastroenterology* (2009) 136(4):1134–44. doi: 10.1053/j.gastro.2009.02.038
8. Wang K, Zhang H, Xia Y, Liu J, Shen F. Surgical Options for Intrahepatic Cholangiocarcinoma. *Hepatobiliary Surg Nutr* (2017) 6(2):79–90. doi: 10.21037/hbsn.2017.01.06
9. Rahnemai-Azar AA, Weisbrod AB, Dillhoff M, Schmidt C, Pawlik TM. Intrahepatic Cholangiocarcinoma: Current Management and Emerging Therapies. *Expert Rev Gastroenterol Hepatol* (2017) 11(5):439–49. doi: 10.1080/17474124.2017.1309290
10. Tsukamoto M, Yamashita YI, Imai K, Umezaki N, Yamao T, Okabe H, et al. Predictors of Cure of Intrahepatic Cholangiocarcinoma After Hepatic Resection. *Anticancer Res* (2017) 37(12):6971–5. doi: 10.21873/anticanres.12164
11. Cong WM, Bu H, Chen J, Dong H, Zhu YY, Feng LH, et al. Practice Guidelines for the Pathological Diagnosis of Primary Liver Cancer: 2015 Update. *World J Gastroenterol* (2016) 22(42):9279–87. doi: 10.3748/wjg.v22.i42.9279
12. Surov A, Pech M, Omari J, Fischbach F, Damm R, Fischbach K, et al. Diffusion-Weighted Imaging Reflects Tumor Grading and Microvascular Invasion in Hepatocellular Carcinoma. *Liver Cancer* (2021) 10(1):10–24. doi: 10.1159/000511384
13. Shao C, Chen J, Chen J, Shi J, Huang L, Qiu Y. Histological Classification of Microvascular Invasion to Predict Prognosis in Intrahepatic Cholangiocarcinoma. *Int J Clin Exp Pathol* (2017) 10(7):7674–81.
14. Zhou Y, Wang X, Xu C, Zhou G, Liu X, Gao S, et al. Mass-Forming Intrahepatic Cholangiocarcinoma: Can Diffusion-Weighted Imaging Predict Microvascular Invasion? *J Magn Reson Imaging* (2019) 50(1):315–24. doi: 10.1002/jmri.26566
15. Lambin P, Leijenaar RTH, Deist TM, Peerlings J, de Jong EEC, van Timmeren J, et al. Radiomics: The Bridge Between Medical Imaging and Personalized Medicine. *Nat Rev Clin Oncol* (2017) 14(12):749–62. doi: 10.1038/nrclinonc.2017.141
16. Wang X, Wang S, Yin X, Zheng Y. MRI-Based Radiomics Distinguish Different Pathological Types of Hepatocellular Carcinoma. *Comput Biol Med* (2021) 141:105058. doi: 10.1016/j.compbiomed.2021.105058
17. Wang Q, Li C, Zhang J, Hu X, Fan Y, Ma K, et al. Radiomics Models for Predicting Microvascular Invasion in Hepatocellular Carcinoma: A Systematic Review and Radiomics Quality Score Assessment. *Cancers (Basel)* (2021) 13(22):5864. doi: 10.3390/cancers13225864
18. Yang Y, Fan W, Gu T, Yu L, Chen H, Lv Y, et al. Radiomic Features of Multi-ROI and Multi-Phase MRI for the Prediction of Microvascular Invasion in Solitary Hepatocellular Carcinoma. *Front Oncol* (2021) 11:756216. doi: 10.3389/fonc.2021.756216
19. Ji GW, Zhu FP, Zhang YD, Liu XS, Wu FY, Wang K, et al. A Radiomics Approach to Predict Lymph Node Metastasis and Clinical Outcome of Intrahepatic Cholangiocarcinoma. *Eur Radiol* (2019) 29(7):3725–35. doi: 10.1007/s00330-019-06142-7
20. Liang W, Xu L, Yang P, Zhang L, Wan D, Huang Q, et al. Novel Nomogram for Preoperative Prediction of Early Recurrence in Intrahepatic Cholangiocarcinoma. *Front Oncol* (2018) 8:360. doi: 10.3389/fonc.2018.00360
21. Wang Y, Li J, Xia Y, Gong R, Wang K, Yan Z, et al. Prognostic Nomogram for Intrahepatic Cholangiocarcinoma After Partial Hepatectomy. *J Clin Oncol* (2013) 31(9):1188–95. doi: 10.1200/jco.2012.41.5984
22. Zhou Y, Zhou G, Zhang J, Xu C, Wang X, Xu P. Radiomics Signature on Dynamic Contrast-Enhanced MR Images: A Potential Imaging Biomarker for Prediction of Microvascular Invasion in Mass-Forming Intrahepatic Cholangiocarcinoma. *Eur Radiol* (2021) 31(9):6846–55. doi: 10.1007/s00330-021-07793-1
23. Lei Z, Li J, Wu D, Xia Y, Wang Q, Si A, et al. Nomogram for Preoperative Estimation of Microvascular Invasion Risk in Hepatitis B Virus-Related Hepatocellular Carcinoma Within the Milan Criteria. *JAMA Surg* (2016) 151(4):356–63. doi: 10.1001/jamasurg.2015.4257
24. Lewis S, Besa C, Wagner M, Jhaveri K, Kihira S, Zhu H, et al. Prediction of the Histopathologic Findings of Intrahepatic Cholangiocarcinoma: Qualitative and Quantitative Assessment of Diffusion-Weighted Imaging. *Eur Radiol* (2018) 28(5):2047–57. doi: 10.1007/s00330-017-5156-6

25. Marrero JA, Kulik LM, Sirlin CB, Zhu AX, Finn RS, Abecassis MM, et al. Diagnosis, Staging, and Management of Hepatocellular Carcinoma: 2018 Practice Guidance by the American Association for the Study of Liver Diseases. *Hepatology* (2018) 68(2):723–50. doi: 10.1002/hep.29913
26. Haradome H, Unno T, Morisaka H, Toda Y, Kwee TC, Kondo H, et al. Gadoxetic Acid Disodium-Enhanced MR Imaging of Cholangiolocellular Carcinoma of the Liver: Imaging Characteristics and Histopathological Correlations. *Eur Radiol* (2017) 27(11):4461–71. doi: 10.1007/s00330-017-4811-2
27. Squadroni M, Tondulli L, Gatta G, Mosconi S, Beretta G, Labianca R. Cholangiocarcinoma. *Crit Rev Oncol Hematol* (2017) 116:11–31. doi: 10.1016/j.critrevonc.2016.11.012
28. Razumilava N, Gores GJ. Cholangiocarcinoma. *Lancet* (2014) 383 (9935):2168–79. doi: 10.1016/s0140-6736(13)61903-0
29. Ma X, Liu L, Fang J, Rao S, Lv L, Zeng M, et al. MRI Features Predict Microvascular Invasion in Intrahepatic Cholangiocarcinoma. *Cancer Imaging* (2020) 20(1):40. doi: 10.1186/s40644-020-00318-x
30. Xu X, Zhang HL, Liu QP, Sun SW, Zhang J, Zhu FP, et al. Radiomic Analysis of Contrast-Enhanced CT Predicts Microvascular Invasion and Outcome in Hepatocellular Carcinoma. *J Hepatol* (2019) 70(6):1133–44. doi: 10.1016/j.jhep.2019.02.023
31. Chong HH, Yang L, Sheng RF, Yu YL, Wu DJ, Rao SX, et al. Multi-Scale and Multi-Parametric Radiomics of Gadoxetate Disodium-Enhanced MRI Predicts Microvascular Invasion and Outcome in Patients With Solitary Hepatocellular Carcinoma ≤ 5 Cm. *Eur Radiol* (2021) 31(7):4824–38. doi: 10.1007/s00330-020-07601-2
32. Yang L, Gu D, Wei J, Yang C, Rao S, Wang W, et al. A Radiomics Nomogram for Preoperative Prediction of Microvascular Invasion in Hepatocellular Carcinoma. *Liver Cancer* (2019) 8(5):373–86. doi: 10.1159/000494099
33. Spolverato G, Ejaz A, Kim Y, Sotiropoulos GC, Pau A, Alexandrescu S, et al. Tumor Size Predicts Vascular Invasion and Histologic Grade Among Patients Undergoing Resection of Intrahepatic Cholangiocarcinoma. *J Gastrointest Surg* (2014) 18(7):1284–91. doi: 10.1007/s11605-014-2533-1
34. Oliveira IS, Kilcoyne A, Everett JM, Mino-Kenudson M, Harisinghani MG, Ganesan K. Cholangiocarcinoma: Classification, Diagnosis, Staging, Imaging Features, and Management. *Abdom Radiol (NY)* (2017) 42(6):1637–49. doi: 10.1007/s00261-017-1094-7
35. Tang Z, Liu WR, Zhou PY, Ding ZB, Jiang XF, Wang H, et al. Prognostic Value and Predication Model of Microvascular Invasion in Patients With Intrahepatic Cholangiocarcinoma. *J Cancer* (2019) 10(22):5575–84. doi: 10.7150/jca.32199

Conflict of Interest: Author FW is employed by Shanghai United Imaging Intelligence Co., Ltd. Shanghai, China.

The remaining authors declare that the research was conducted in the absence of any commercial or financial relationships that could be construed as a potential conflict of interest.

Publisher's Note: All claims expressed in this article are solely those of the authors and do not necessarily represent those of their affiliated organizations, or those of the publisher, the editors and the reviewers. Any product that may be evaluated in this article, or claim that may be made by its manufacturer, is not guaranteed or endorsed by the publisher.

frontiers | Frontiers in Oncology

SYSTEMATIC REVIEW
published: 07 April 2022
doi: 10.3389/fonc.2022.831996

Radiomics for the Preoperative Evaluation of Microvascular Invasion in Hepatocellular Carcinoma: A Meta-Analysis

Liujun Li[1,2], *Chaoqun Wu*[1,2], *Yongquan Huang*[1,2], *Jiaxin Chen*[1], *Dalin Ye*[1] *and Zhongzhen Su*[1,2]*

[1] Department of Ultrasound, The Fifth Affiliated Hospital of Sun Yat-Sen University, Zhuhai, China, [2] Guangdong Provincial Key Laboratory of Biomedical Imaging and Guangdong Provincial Engineering Research Center of Molecular Imaging, The Fifth Affiliated Hospital of Sun Yat-sen University, Zhuhai, China

OPEN ACCESS

Edited by:
Xiankai Sun,
University of Texas Southwestern Medical Center, United States

Reviewed by:
Alessandro Granito,
University of Bologna, Italy
Jesyin Lai,
University of Memphis, United States

***Correspondence:**
Zhongzhen Su
suzhzh3@mail.sysu.edu.cn

Specialty section:
This article was submitted to Cancer Imaging and Image-directed Interventions, a section of the journal Frontiers in Oncology

Received: 09 December 2021
Accepted: 11 March 2022
Published: 07 April 2022

Citation:
Li L, Wu C, Huang Y, Chen J, Ye D and Su Z (2022) Radiomics for the Preoperative Evaluation of Microvascular Invasion in Hepatocellular Carcinoma: A Meta-Analysis. Front. Oncol. 12:831996. doi: 10.3389/fonc.2022.831996

Background: Microvascular invasion (MVI) is an independent risk factor for postoperative recurrence of hepatocellular carcinoma (HCC). To perform a meta-analysis to investigate the diagnostic performance of radiomics for the preoperative evaluation of MVI in HCC and the effect of potential factors.

Materials and Methods: A systematic literature search was performed in PubMed, Embase, and the Cochrane Library for studies focusing on the preoperative evaluation of MVI in HCC with radiomics methods. Data extraction and quality assessment of the retrieved studies were performed. Statistical analysis included data pooling, heterogeneity testing and forest plot construction. Meta-regression and subgroup analyses were performed to reveal the effect of potential explanatory factors [design, combination of clinical factors, imaging modality, number of participants, and Quality Assessment of Diagnostic Accuracy Studies 2 (QUADAS-2) applicability risk] on the diagnostic performance.

Results: Twenty-two studies with 4,129 patients focusing on radiomics for the preoperative prediction of MVI in HCC were included. The pooled sensitivity, specificity and area under the receiver operating characteristic curve (AUC) were 84% (95% CI: 81, 87), 83% (95% CI: 78, 87) and 0.90 (95% CI: 0.87, 0.92). Substantial heterogeneity was observed among the studies (I^2=94%, 95% CI: 88, 99). Meta-regression showed that all investigative covariates contributed to the heterogeneity in the sensitivity analysis ($P < 0.05$). Combined clinical factors, MRI, CT and number of participants contributed to the heterogeneity in the specificity analysis ($P < 0.05$). Subgroup analysis showed that the pooled sensitivity, specificity and AUC estimates were similar among studies with CT or MRI.

Conclusion: Radiomics is a promising noninvasive method that has high preoperative diagnostic performance for MVI status. Radiomics based on CT and MRI had a

comparable predictive performance for MVI in HCC. Prospective, large-scale and multicenter studies with radiomics methods will improve the diagnostic power for MVI in the future.

Systematic Review Registration: https://www.crd.york.ac.uk/prospero/display_record.php?RecordID=259363, identifier CRD42021259363.

Keywords: radiomics, microvascular invasion, hepatocellular carcinoma, diagnosis, meta-analysis

INTRODUCTION

Hepatocellular carcinoma (HCC) is the fourth leading cause of cancer-related deaths and the second most lethal tumor (1), with 905,677 new cases and 830,180 new deaths in 2020 worldwide (2). New HCC cases and deaths in China account for approximately 50% of the cases in the world (3). Surgical and local ablative therapies are recognized as the radical treatment for HCC (4). However, the postoperative 5-year recurrence rate is still as high as 70% (5). Studies have shown the relationship between the high recurrence rate and microvascular invasion (MVI), which is recognized as an independent risk factor for postoperative recurrence of HCC (6–8). Postoperative pathology is the gold standard for MVI, but it is a lagging indicator. Therefore, the preoperative evaluation of MVI status will contribute to inform decision-making about the extent of surgical resection or ablation treatment for patients with HCC.

Biopsy is the preoperative reference standard for the diagnosis of MVI. Nevertheless, it is an invasive operation that may cause correlative complications and tumor seeding (9). In addition, there are some false negative results due to specimen limitation and tumor heterogeneity. Therefore, a noninvasive evaluation system is needed for preoperatively identifying MVI. Ultrasound (US), computed tomography (CT), and magnetic resonance imaging (MRI) have been used to assess the MVI status of HCC based on morphological features, such as size, number, shape, boundary, edge, capsule and enhancement characteristics (10–12). Unfortunately, the results have been inconsistent. The reasons are that the spatial resolution is too low to detect microvessels, and the reviews of medical images rely on subjective experience. Thus, there is an unmet clinical need to objectively, standardly and quantitatively evaluate the MVI status of HCC.

In 2012, Dutch scholar Lambin (13) proposed the concept of radiomics. It could extract massive quantitative imaging features from medical images by the statistics methods or machine learning algorithms. Radiomics has been used to construct predictive models for MVI by extracting quantitative features from US, CT, MRI, or positron emission tomography (PET). However, these studies differed in the diagnostic performance of the preoperative evaluation of MVI due to the differences in imaging modalities, research methods, sample size and so on. The reported diagnostic power ranged from 68% to 98% in the above studies (14–35). For these reasons, the diagnostic performance of radiomics for the preoperative identification of MVI in clinical practice remains uncertain. Therefore, we collected relevant studies and performed this meta-analysis to investigate the diagnostic performance of radiomics for the preoperative evaluation of MVI in HCC and the effect of potential factors.

MATERIALS AND METHODS

Literature Search and Study Selection

The present study followed the Preferred Reporting Items for Systematic reviews and Meta-Analysis of Diagnostic Test Accuracy (PRISMA-DTA) (36), and it was registered in the International Prospective Register of Systematic Reviews (number CRD42021259363). All papers were screened independently by two authors (LL and CW, radiologists with 8 and 2 years of experience, respectively). Any disagreements were resolved by discussion, and if the disagreement could not be resolved, a consensus was reached through arbitration by a third reviewer (YH, a radiologist with 11 years of experience).

We selected published relevant studies by systematically searching the PubMed, Embase and Cochrane Library databases without language, nation, or time restrictions. The deadline for searching the databases was June 06, 2021. We used subject words and free words such as "hepatocellular carcinoma", "microvascular invasion", and "radiomics" and their variations. A detailed search strategy is described in the **Supplementary Materials**. After the elimination of duplicate papers, the titles and abstracts of all remaining articles were reviewed. When it was ambiguous whether an article should be included, the full-text content had to be accessible online or in print and reviewed. Furthermore, we scrutinized the reference lists of each identified primary study and previous systematic reviews to identify additional related articles.

The inclusion criteria were as follows: diagnosis of HCC by pathology after hepatectomy or liver transplantation; presence or absence of MVI by pathologic diagnosis; US, CT, MRI or PET-CT performed one month before surgery; and imaging analysis based on a radiomics algorithm. The exclusion criteria were as follows: antitumor therapy was performed preoperatively; the studies did not have enough information to construct a two-by-two contingency table; the type of study included animal experiments, nondiagnostic tests, case reports, reviews, expert opinions and conference abstracts.

Data Extraction and Quality Assessment

Data extraction and quality assessment of the retrieved studies were completed by two authors independently (LL and JC,

radiologists with 8 and 5 years of experience, respectively). Any discrepancies were resolved by consensus with a senior author (ZS, a radiologist with 22 years of experience). We extracted data on patient characteristics, imaging modalities, and study characteristics from each selected study. Patient characteristics included the total number of participants, the number of participants with MVI present and MVI absent, sensitivity and specificity. We tabulated the number of true positives (TPs), false positives (FPs), false negatives (FNs) and true negatives (TNs) by the number of MVI-present and MVI-absent cases, sensitivity and specificity reported in each included study. If there were two or more predictive models based on the same cohort of patients in one study, the best model reported in the study was included in our meta-analysis.

We evaluated the methodological quality of the included studies by using the standard Quality Assessment of Diagnostic Accuracy Studies 2 (QUADAS-2) tool (Bristol University, Bristol, UK) (37). We followed the guidelines for scoring each item of the checklist to assess the risk of bias and concerns regarding applicability by the software Review Manager 5.4 (Cochrane Library Software, Oxford, UK). The four domains assessed are as follows: patient selection, index test, reference standard, and flow and timing. Each individual question was categorized as "yes", "no" or "unclear" for the risk of bias and "high risk", "low risk" or "unclear risk" for applicability concerns.

Statistical Analysis

We used the MIDAS module for STATA version 16 (Stata Corp LP, College Station, Texas, USA) to analyze the raw data. We calculated the pooled sensitivity, specificity, positive likelihood ratio (PLR), negative likelihood ratio (NLR), and diagnostic odds ratio (DOR) and their corresponding 95% confidence intervals (CI) using a bivariate regression model. Moreover, we plotted the results on a summary receiver operating characteristic (SROC) curve, and the area under the receiver operating characteristic curve (AUC) exhibited the diagnostic power of the included studies (38). AUCs of 0.5–0.7, 0.7–0.9 and > 0.9 show low, moderate and high diagnostic value, respectively. In addition, we plotted the Fagan nomogram by the MIDAS module and used the pretest probability (the ratio of MVI-positive cases to all cases in the included studies), PLR and NLR to calculate the posttest probability.

We drew forest plots to show the variation among studies and to detect heterogeneity for the pooled sensitivity and specificity. Heterogeneity due to the threshold effect was tested with the STATA MIDAS module. Heterogeneity caused by nonthreshold effects was measured using Cochrane's Q-test and inconsistency index I^2, and the difference was considered significant when $P < 0.05$, with $I^2 \geq 50\%$ regarded as being indicative of moderate-to-high heterogeneity among studies (39). Meta-regression and subgroup analysis were performed to investigate the potential sources of heterogeneity. We performed univariable meta-regression analysis of several relevant covariates: design (retrospective or prospective), combined clinical factors (yes or no), imaging modality (MRI, CT or US), number of participants (≥100 or <100), and QUADAS-2 applicability risk (absence or presence of high risk). In addition, the possible presence of publication bias was further assessed by using a Deeks' regression test of asymmetry (40). Slope coefficients with a P value < 0.10 indicate significant publication bias.

RESULTS

Literature Selection

The literature search and study selection are shown in **Figure 1** (36). All included studies were published between 2017 and 2021, and nine radiomics studies based on CT, nine radiomics studies based on MRI, three radiomics studies based on US and one radiomics study based on PET-CT were eligible for inclusion in this meta-analysis. A total of 4,129 HCC patients were included. Among them, 1,668 (40.4%) patients were pathologically diagnosed as MVI-positive and 2,461 (59.6%) as MVI-negative.

Extracted and Quality Assessment

The relevant characteristics and details of the 22 included studies are shown in **Table 1**. **Figure 2** displays the distribution based on the QUADAS-2 scale of the methodological quality assessment of the included studies. The majority of studies were judged to have a low risk of bias and minimal concerns regarding applicability. None of the studies were excluded from the analysis according to the quality assessment. The slope coefficients of Deeks' funnel plot asymmetry test for the presence of publication bias (P=.38) are presented in **Figure 3**, which suggested no publication bias.

Data Analysis

The forest plots and comprehensive results of all studies included in this diagnostic meta-analysis are shown in **Figure 4** and **Table 2**. The primary analysis showed that the pooled sensitivity, specificity, PLR, NLR and DOR for the preoperative prediction of MVI in HCC were 84% (95% CI: 81%, 87%), 83% (95% CI: 78, 87), 5.0 (95% CI: 3.7, 6.6), 0.19 (95% CI: 0.16, 0.24) and 25.5 (95% CI: 16.7, 39.0), respectively. The AUC was 0.90 (95% CI: 0.87, 0.92), which suggested high diagnostic value (**Figure 5**). In addition, the pretest probability of MVI positive was 0.40 in our study, and both the likelihood ratio and posttest probability were high. A PLR of 5 implies an increase in the posttest probability for a positive test result to 77%. Likewise, an NLR of 0.19 reduced the posttest probability to 11% for a negative test result (**Figure 6**).

Meta-regression

Considerable heterogeneity existed among the studies (overall I^2 94%; 95% CI: 88, 99; $P < 0.001$). Similarly, the forest plots indicated high heterogeneity with I^2 values > 50% for sensitivity (I^2 62%; 95% CI: 44, 80; $P< 0.001$) and specificity (I^2 88%; 95% CI: 83, 92; $P < 0.001$). The proportion of heterogeneity likely due to the threshold effect was small (8%). Therefore, we recorded no evidence of a threshold effect. To identify the source of heterogeneity, we performed univariable meta-regression analysis. **Table 3** shows the results of univariable meta-regression and subgroup analyses to

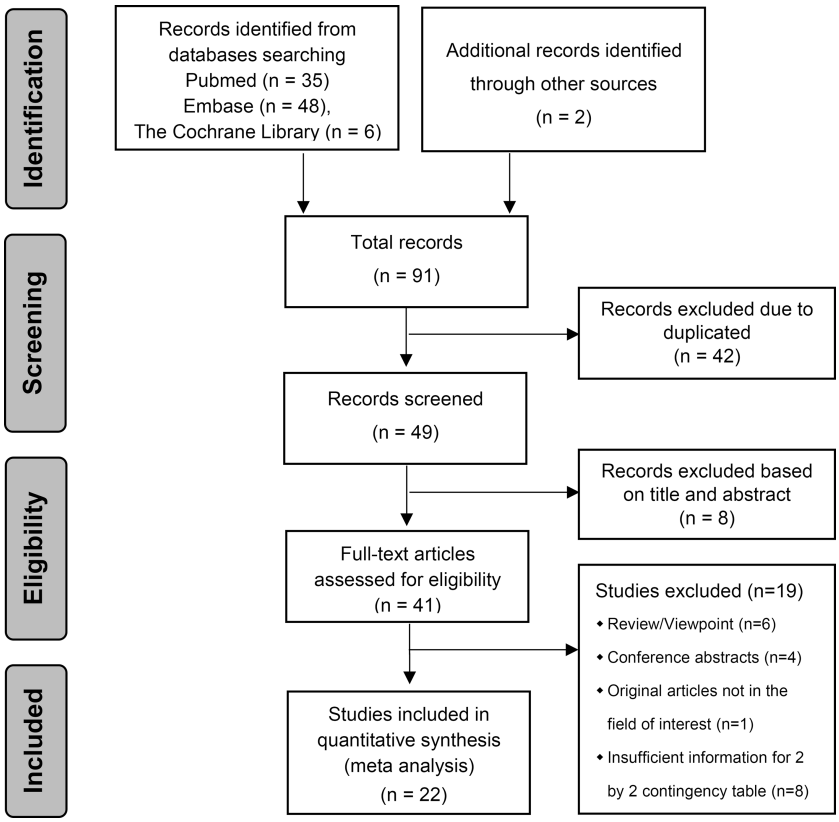

FIGURE 1 | PRISMA flowchart of the study selection procedure.

explore the influence of patient characteristics, imaging modality, and study characteristics on the pooled sensitivity and specificity estimates. The results showed that all investigative covariates contributed to the heterogeneity in the sensitivity analysis ($P < 0.05$). In addition, combined clinical factors, MRI, CT and number of participants contributed to the heterogeneity in the specificity analysis ($P < 0.05$).

Subgroup Analysis

In terms of research design, prospective studies (n=2) had higher sensitivity (88%; 95% CI: 78, 99) and specificity (100%; 95% CI: 100, 100) than retrospective studies (n=20; sensitivity, 83% [95% CI: 80, 86]; specificity, 81% [95% CI: 77, 86]). Regardless of whether radiomics was combined with clinical risk factors to construct a predictive diagnostic model, the sensitivity (84%; 95% CI: 81, 88 vs. 83%; 95% CI: 78, 88) was basically equivalent for both. However, radiomics alone had a slightly higher specificity (n=10; 86%; 95% CI: 80, 93) than radiomics combined with clinical risk factors (n=12; 81%; 95% CI: 74, 87).

In terms of different imaging modalities, US (n=3) had a higher sensitivity (87%; 95% CI: 80, 95) and specificity (87%; 95% CI: 74, 100) than CT (n=9; sensitivity, 84% [95% CI: 79, 88]; specificity, 80% [95% CI: 72, 88]) and MRI (n=9; sensitivity, 84% [95% CI: 79, 88]; specificity, 84% [95% CI: 77, 90]). On the other hand, the pooled sensitivity, specificity and AUC (0.89; 95% CI: 0.86, 0.91 vs. 0.88; 95% CI: 0.85, 0.91) estimates were similar among studies with CT or MRI.

In addition, the pooled sensitivity estimates were higher in studies with 100 participants or more (n=15; 84%; 95% CI: 81, 87) than in studies with fewer than 100 participants (n=7; 81%; 95% CI: 74, 88), but the pooled specificity (80%; 95% CI: 74, 85 vs. 91%; 95% CI: 86, 97) showed the opposite trend. Similarly, studies without high risk according to QUADAS (n=17) had a higher pooled sensitivity (85%; 95% CI: 83, 88) but a lower specificity (82%; 95% CI: 77, 87) than studies with high risk according to QUADAS (n=5; sensitivity, 74% [95% CI: 66, 82]; specificity, 87% [95% CI: 79, 95]).

DISCUSSION

Our meta-analysis showed high pooled sensitivity (84%; 95% CI: 81, 87), specificity (83%; 95% CI: 78, 87), and AUC (0.90; 95% CI: 0.87, 0.92) values. which demonstrated that radiomics has the potential ability to preoperatively differentiate MVI status in HCC. The confirmation of this evidence will be beneficial to the formulation of optimal preoperative therapeutic strategies for patients with MVI of HCC. For example, if the presence of MVI

TABLE 1 | Basic characteristics and details of the 22 included studies.

Study ID	First Author	Year	N	MVI-Present	MVI-Absent	TP	FP	FN	TN	Imaging Modality	Design	Combine Clinical Factors (Yes/No)	Cohort Detail
1	Chong et al. (14)	2021	356	90	266	80	22	10	244	MRI	retrospective	Yes	Training and Validation cohort
2	Dai et al. (15)	2021	69	29	40	27	7	2	33	MRI	retrospective	No	/
3	Dong et al. (16)	2019	42	21	21	18	0	3	21	US	prospective	No	/
4	Dong et al. (17)	2020	322	144	178	121	78	23	100	US	retrospective	No	/
5	Feng et al. (18)	2019	160	62	98	47	11	15	87	MRI	retrospective	No	Training and Validation cohort
6	Jiang et al. (19)	2021	81	44	37	34	2	10	35	CT	retrospective	Yes	Validation cohort
7	Li et al. (20)	2021	50	22	28	15	1	7	27	PET-CT	retrospective	No	Training cohort
8	Ma et al. (21)	2019	157	55	102	48	29	7	73	CT	retrospective	Yes	Training and Validation cohort
9	Ni et al. (22)	2019	58	23	35	19	5	4	30	CT	retrospective	No	Validation cohort
10	Peng et al. (23)	2018	304	201	103	157	25	44	78	CT	retrospective	Yes	Training and Validation cohort
11	Song et al. (24)	2021	601	225	376	191	50	34	326	MRI	retrospective	Yes	Training and Validation cohort
12	Wang et al. (25)	2019	125	41	84	29	18	12	66	MRI	retrospective	No	Test cohort
13	Xu et al. (26)	2019	495	149	346	132	78	17	268	CT	retrospective	Yes	Training/Validation and Test cohort
14	Yang et al. (27)	2019	208	53	155	47	22	6	133	MRI	retrospective	Yes	Training and Validation cohort
15	Yao et al. (28)	2018	43	21	22	19	0	2	22	US	prospective	No	/
16	Yu et al. (29)	2021	148	88	60	84	4	4	56	CT	retrospective	No	Training and Validation cohort
17	Zhang et al. (30)	2019	267	90	177	74	53	16	124	MRI	retrospective	Yes	Training and Validation cohort
18	Zhang et al. (31)	2021	111	57	54	41	16	16	38	CT	retrospective	No	Training/Validation and Test cohort
19	Zhang et al. (32)	2020	75	37	38	26	9	11	29	CT	retrospective	Yes	Validation cohort
20	Zhang et al. (33)	2021	195	110	85	91	20	19	65	MRI	retrospective	Yes	Training and Validation cohort
21	Zheng et al. (34)	2017	120	53	67	48	22	5	45	CT	retrospective	Yes	Tumor size: ≤ 5 cm and >5cm
22	Zhu et al. (35)	2019	142	53	89	43	17	10	72	MRI	retrospective	Yes	Training and Validation cohort

N, nubmer of patients; MVI, microvascular invasion; TP, true positive; FP, false positive; TN, true negative; FN, false negative; US, Ultrasound; CT, computed tomography; MRI, magnetic resonance imaging; PET, positron emission tomography.

is confirmed preoperatively, the extent of resection or ablation will be expanded. So it has great clinical value in reducing recurrence and improving the survival rate of HCC patients.

Likelihood ratios and posttest probabilities can also provide important information about the likelihood that a patient with a positive or negative test actually has MVI or not. Through our meta-analysis, a PLR of 5 indicates that the test is five times more likely to correctly judge a positive result than incorrectly judge a positive result, and the posttest probability for a positive test result is 77%. Similarly, an NLR of 0.19 indicates that the test is 0.19 times more likely to incorrectly judge a negative result than correctly judge a negative result, and the posttest probability for a negative test result is 11%. These results further indicate that radiomics has important clinical value in preoperatively evaluating the MVI status in HCC.

A previous meta-analysis reported that the sensitivity, specificity, and AUC of MVI prediction in HCC were 78% (95% CI: 75, 80), 78% (95% CI: 76, 81) and 0.855 for radiomics and 73% (95% CI: 0.71, 0.75), 82% (95% CI: 80, 83) and 0.860 for non-radiomics, respectively (41). The results indicated that the diagnostic performance for predicting MVI status in HCC was equivalent between radiomics and non-radiomics. However, the results reported above were all lower than those of our meta-analysis. A reasonable interpretation is that the number of included studies was not enough for radiomics (n=9) in the previous meta-analysis. This meta-analysis included 22 studies, showing that radiomics had a higher performance than non-radiomics for the preoperative prediction of MVI status in HCC.

Substantial heterogeneity among the studies was observed, so we performed meta-regression and subgroup analyses to detect the sources of heterogeneity. Due to the limitation of the number of included studies, we only performed univariable meta-regression analysis instead of multivariable meta-regression analysis. The results showed that all the observed indicators contributed to the source of heterogeneity. In addition, each included study used a different methodological design, which was only a part of the heterogeneity, and it was not possible to find all sources of heterogeneity.

We used five key factors for subgroup analysis. In the study design subgroup analysis, prospective studies were better than retrospective studies. This result is reasonable given that prospective studies have a clear purpose, a thorough design, proper observational indicators and so on, suggesting that more prospective studies in the future will improve the predictive performance for MVI. However, only 2 prospective studies addressed the use of radiomics for the evaluation of MVI status in HCC, and more high-quality evidence is needed to reach more definitive conclusions. Some previous studies have shown that an MVI predictive model with combined clinical risk factors had higher diagnostic performance (26, 27, 42). However, the results of our meta-analysis showed that the combination of clinical risk factors with radiomics did not improve the diagnostic ability. This indicates that radiomics alone could also achieve high diagnostic performance, which was consistent with the results of other previous studies (14, 19, 33).

FIGURE 2 | Stacked bar charts of the QUADAS-2 scale of methodological quality assessment. Risk of bias and applicability concerns of each included study. **(A)** Individual studies, **(B)** summary. For each quality domain, the proportions of included studies that suggest low, high, or unclear risk of bias and applicability concerns are displayed in green, red and yellow, respectively.

We performed subgroup analysis to compare the diagnostic performance of radiomics based on different imaging modalities. The results showed that CT and MRI were essentially equivalent, consistent with previous studies (41, 43). However, due to multiparameter imaging and hepatobiliary phase-specific imaging agents, MRI has greater advantages in the diagnostic sensitivity of HCC. For example, a prospective study by Granito A, et al. showed that the diagnostic sensitivity of the hepatobiliary phase for the diagnosis of small HCC was 100% (95% CI: 90-100) with Gd-EOB-DTPA enhanced magnetic resonance, which had a higher sensitivity than contrast-enhanced CT and US (44). In our meta-analysis, US was superior to CT or MRI, but only three studies focusing on grayscale US were included, and two of them were prospective studies. Additionally, another US study with a retrospective design reported an AUC of only 0.68 (17). So the pooled result is incompletely convincing showing ultrasound superior to CT or MRI. However, again, prospective studies can significantly

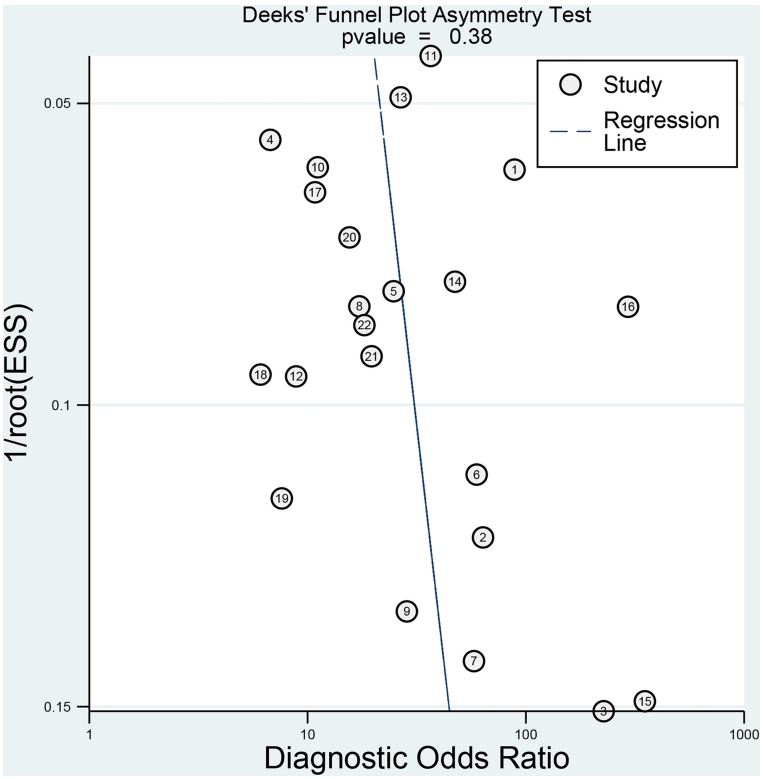

FIGURE 3 | Deeks' funnel plot shows no asymmetry and the presence of publication bias. Numbers in circles refer to the study ID. ESS, effective sample size.

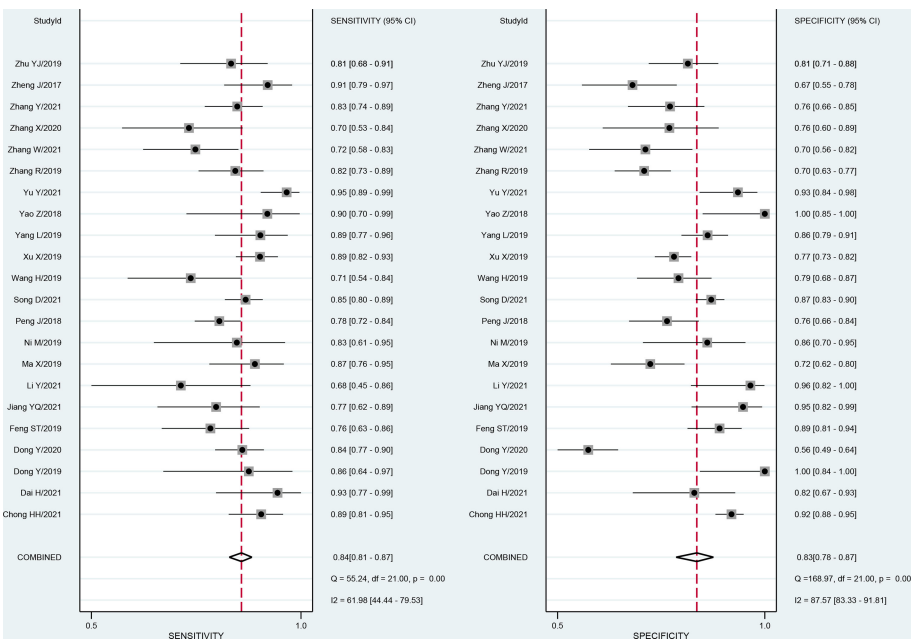

FIGURE 4 | Forest plots show the performance estimates (sensitivity and specificity) of each study based on radiomics for the preoperative prediction of MVI in HCC. Vertical lines in the forest plots show the pooled estimates of sensitivity and specificity. $I^2 > 50\%$ indicates substantial heterogeneity in the diagnostic parameters across studies.

TABLE 2 | Sensitivity analysis based on radiomics for the preoperative prediction of microvascular invasion in hepatocellular carcinoma.

Author	ACC (%)	SEN (%)	SPE (%)	PLR	NLR	DOR
Chong HH	91	89 (81, 95)	92 (88, 95)	10.75 (7.16, 16.14)	0.12 (0.07, 0.22)	88.7 (40.3, 195.3)
Dai H	87	93 (77, 99)	82 (67, 93)	5.32 (2.69, 10.50)	0.08 (0.02, 0.32)	63.6 (12.2, 332.0)
Dong Y*	93	86 (64, 97)	100 (84, 100)	37.00 (2.37, 576.55)	0.16 (0.06, 0.43)	227.3 (11.0, 1000.0)
Dong Y†	69	84 (77, 90)	56 (49, 64)	1.92 (1.60, 2.30)	0.28 (0.19, 0.42)	6.7 (4.0, 11.5)
Feng ST	84	76 (63, 86)	89 (81, 94)	6.75 (3.80, 11.99)	0.27 (0.17, 0.43)	24.8 (10.5, 58.3)
Jiang YQ	85	77 (62, 89)	95 (82, 99)	14.30 (3.68, 55.55)	0.24 (0.14, 0.42)	59.5 (12.1, 291.7)
Li Y	84	68 (45, 86)	96 (82, 100)	19.09 (2.73, 133.61)	0.33 (0.18, 0.61)	57.9 (6.5, 516.1)
Ma X	77	87 (76, 95)	72 (62, 80)	3.07 (2.22, 4.24)	0.18 (0.09, 0.36)	17.3 (7.0, 42.6)
Ni M	84	83 (61, 95)	86 (70, 95)	5.78 (2.51, 13.30)	0.20 (0.08, 0.50)	28.5 (6.8, 119.7)
Peng J	77	78 (72, 84)	76 (66, 84)	3.22 (2.27, 4.56)	0.29 (0.22, 0.38)	11.1 (6.4, 19.5)
Song D	86	85 (80, 89)	87 (83, 90)	6.38 (4.90, 8.31)	0.17 (0.13, 0.24)	36.6 (22.9, 58.7)
Wang H	76	71 (54, 84)	79 (68, 87)	3.30 (2.10, 5.20)	0.37 (0.23, 0.61)	8.9 (3.8, 20.8)
Xu X	81	89 (82, 93)	77 (73, 82)	3.93 (3.21, 4.82)	0.15 (0.09, 0.23)	26.7 (15.2, 46.9)
Yang L	87	89 (77, 96)	86 (79, 91)	6.25 (4.19, 9.31)	0.13 (0.06, 0.28)	47.4 (18.1, 123.9)
Yao Z	95	90 (70, 99)	100 (85, 100)	40.77 (2.62, 634.99)	0.12 (0.04, 0.37)	351.0 (15.9, 1000.0)
Yu Y	95	95 (89, 99)	93 (84, 98)	14.32 (5.55, 36.94)	0.05 (0.02, 0.13)	294.0 (70.6, 1000.0)
Zhang R	74	82 (73, 89)	70 (63, 77)	2.75 (2.15, 3.51)	0.25 (0.16, 0.40)	10.8 (5.8, 20.3)
Zhang W	71	72 (58, 83)	70 (56, 82)	2.43 (1.56, 3.78)	0.40 (0.25, 0.63)	6.09 (2.7, 13.8)
Zhang X	73	70 (53, 84)	76 (60, 89)	2.97 (1.62, 5.45)	0.39 (0.23, 0.66)	7.6 (2.7, 21.3)
Zhang Y	80	83 (74, 89)	76 (66, 85)	3.52 (2.37, 5.21)	0.23 (0.15, 0.35)	15.6 (7.7, 31.5)
Zheng J	78	91 (79, 97)	67 (55, 78)	2.76 (1.94, 3.93)	0.14 (0.06, 0.33)	19.6 (6.9, 56.3)
Zhu YJ	81	81 (68, 91)	81 (71, 88)	4.25 (2.72, 6.64)	0.23 (0.13, 0.41)	18.2 (7.7, 43.4)

*Data in parentheses are 95% CIs. *Published in 2019; †Published in 2020.*

ACC, accuracy; SEN, sensitivity; SPE, specificity; PLR, positive likelihood ratio; NLR, negative likelihood ratio; DOR, diagnostic odds ratio.

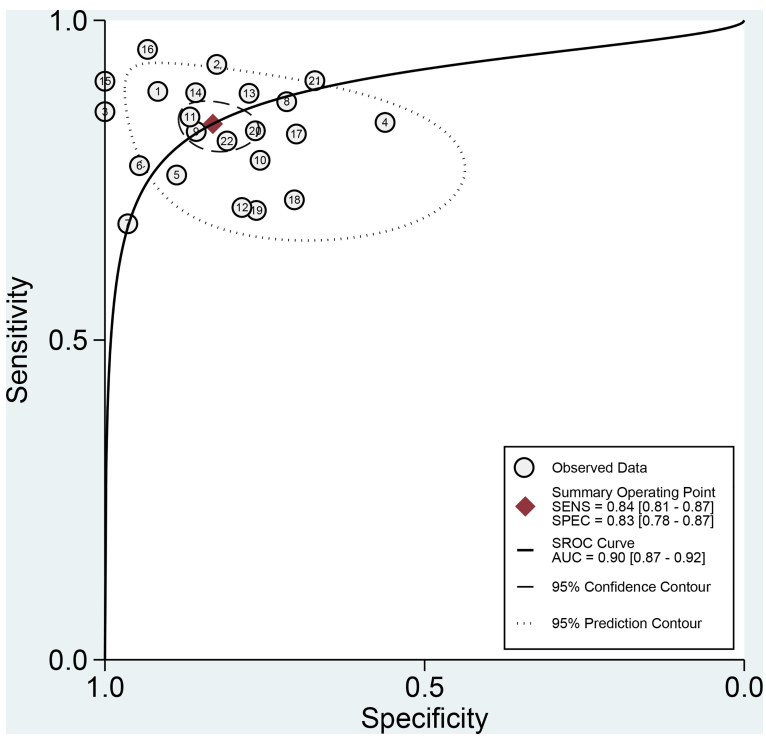

FIGURE 5 | Summary receiver operating characteristic (SROC) plots of radiomics for the preoperative identification of microvascular invasion in hepatocellular carcinoma. Each circle indicates one included study. Values in brackets are 95% CIs. AUC, area under the receiver operating characteristic curve.

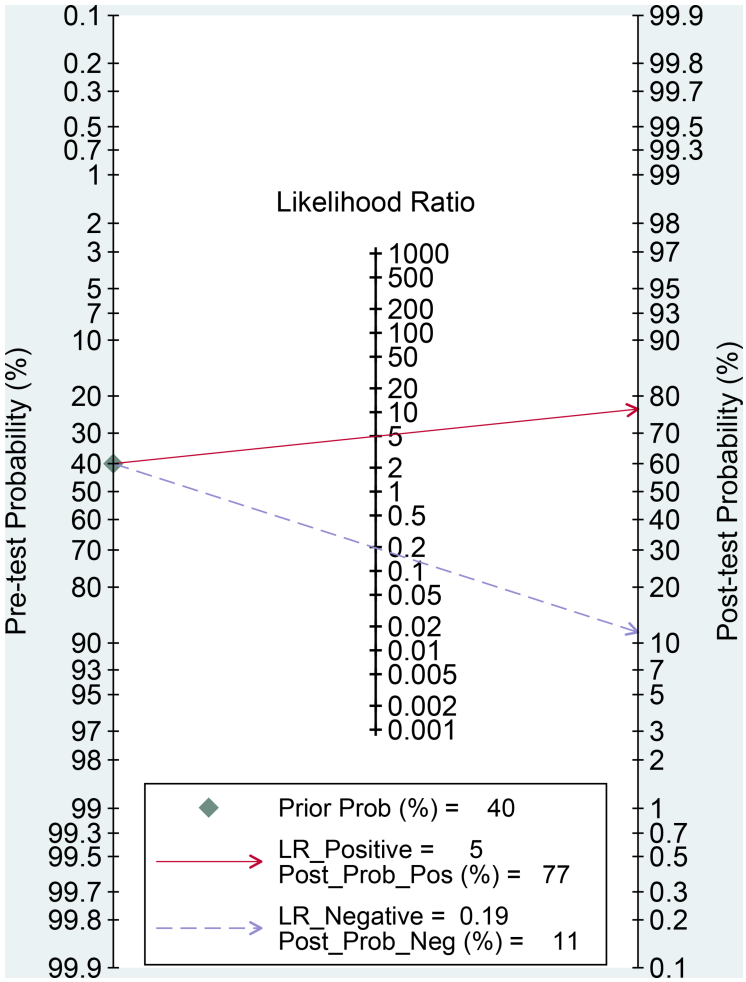

FIGURE 6 | Fagan nomogram of radiomics for the preoperative identification of microvascular invasion in hepatocellular carcinoma. LR, likelihood ratio; Prob, probability; Pos, positive; Neg, negative.

TABLE 3 | Univariable meta-regression and subgroup analyses.

Parameter	Category	No. of Studies	Sensitivity (%)	P_1	Specificity (%)	P_2
Design	retrospective	20	83 (80, 86)	0.04	81 (77, 86)	0.15
	prospective	2	88 (78, 99)		100 (100, 100)	
Combine clinical factors	Yes	12	84 (81, 88)	0.00	81 (74, 87)	0.00
	no	10	83 (78, 88)		86 (80, 93)	
MRI	Yes	9	84 (79, 88)	0.00	84 (77, 90)	0.00
	no	13	84 (80, 88)		83 (76, 89)	
CT	Yes	9	84 (79, 88)	0.00	80 (72, 88)	0.00
	no	13	84 (80, 88)		85 (79, 90)	
US	Yes	3	87 (80, 95)	0.02	87 (74, 100)	0.44
	no	19	83 (80, 86)		83 (78, 88)	
No. of participants	≥100	15	84 (81, 87)	0.00	80 (74, 85)	0.00
	<100	7	81 (74, 88)		91 (86, 97)	
QUADAS	QUADAS high risk	5	74 (66, 82)	0.00	87 (79, 95)	0.08
	QUADAS no high risk	17	85 (83, 88)		82 (77, 87)	

Data in parentheses are 95% CIs. MRI, magnetic resonance imaging; CT, computed tomography; US, ultrasound; QUADAS, quality assessment of diagnostic accuracy studies.

improve the predictive performance. Only one study on PET-CT was not included in the subgroup analysis. In addition, the results showed that the studies with large samples and without a high risk of bias had higher sensitivity. Therefore, in future studies, increasing the sample size and reducing bias will improve the ability to identify MVI.

We recognize that our meta-analysis has several limitations. First, mostly retrospective studies were included in our analysis, and patient selection could introduce some bias. Second, all included studies were from China. Studies from other countries were excluded for various reasons; for example, 2 studies from the United States were excluded because we could not reconstruct the 2×2 contingency table (45, 46). Thus, some characteristic populations may have been missed, which could affect the general applicability of the results in clinical practice. Finally, although radiomics models aid in the identification of MVI, the modeling method used might affect the predictive results of radiomics analysis. Each included study would have resulted in a different radiomics model, so it does not currently elucidate a clear modeling method to determine presence of MVI. However, multiple modeling methods can be attempted to achieve optimal model selection.

CONCLUSION

In summary, our meta-analysis demonstrated that radiomics is a promising noninvasive method, and it has high preoperative identification performance for MVI status, which has crucial guiding significance for surgical planning of HCC patients in clinical practice. CT and MRI had a comparable predictive performance for MVI, but US and PET-CT still need to be conducted in more studies for further analysis based on radiomics methods. Moreover, it is necessary to carry out additional prospective, large-scale and multicenter studies with radiomics methods to improve the preoperative diagnostic performance of MVI in the future.

DATA AVAILABILITY STATEMENT

The original contributions presented in the study are included in the article/**Supplementary Material**. Further inquiries can be directed to the corresponding author.

AUTHOR CONTRIBUTIONS

Study design: LL, CW, YH, JC, DY, and ZS. Literature search and study selection: LL, CW and YH. Data extraction and quality assessment: LL, CW, JC and ZS. Statistical analysis: LL, DY and YH. Study supervision: ZS and YH. ZS obtained the research fund. Editing and review of the manuscript: all authors. All authors contributed to the article and approved the submitted version.

FUNDING

This study was supported by the National Natural Science Foundation of China (Grant No. 82072038) and the Natural Science Foundation of Guangdong Province, China (Grant No. 2018A0303130070).

SUPPLEMENTARY MATERIAL

The Supplementary Material for this article can be found online at: https://www.frontiersin.org/articles/10.3389/fonc.2022.831996/full#supplementary-material

REFERENCES

1. Villanueva A. Hepatocellular Carcinoma. *N Engl J Med* (2019) 380:1450–62. doi: 10.1056/NEJMra1713263
2. Sung H, Ferlay J, Siegel RL, Laversanne M, Soerjomataram I, Jemal A, et al. Global Cancer Statistics 2020: GLOBOCAN Estimates of Incidence and Mortality Worldwide for 36 Cancers in 185 Countries. *CA Cancer J Clin* (2021) 71:209–49. doi: 10.3322/caac.21660
3. Zhou M, Wang H, Zeng X, Yin P, Zhu J, Chen W, et al. Mortality, Morbidity, and Risk Factors in China and its Provinces, 1990-2017: A Systematic Analysis for the Global Burden of Disease Study 2017. *Lancet* (2019) 394:1145–58. doi: 10.1016/S0140-6736(19)30427-1
4. Department of Medical Administration and National Health and Health Commission of the People's Republic of China. Guidelines for Diagnosis and Treatment of Primary Liver Cancer in China (2019 Edition). *Chin J Hepatol* (2020) 28:112–28. doi: 10.3760/cma.j.issn.1007-3418.2020.02.004
5. Vitale A, Peck-Radosavljevic M, Giannini EG, Vibert E, Sieghart W, Van Poucke S, et al. Personalized Treatment of Patients With Very Early Hepatocellular Carcinoma. *J Hepatol* (2017) 66:412–23. doi: 10.1016/j.jhep.2016.09.012
6. Wang H, Wu MC, Cong WM. Microvascular Invasion Predicts a Poor Prognosis of Solitary Hepatocellular Carcinoma Up to 2 Cm Based on Propensity Score Matching Analysis. *Hepatol Res* (2019) 49:344–54. doi: 10.1111/hepr.13241
7. Zhang XP, Wang K, Wei XB, Li LQ, Sun HC, Wen TF, et al. An Eastern Hepatobiliary Surgery Hospital Microvascular Invasion Scoring System in Predicting Prognosis of Patients With Hepatocellular Carcinoma and Microvascular Invasion After R0 Liver Resection: A Large-Scale, Multicenter Study. *Oncologist* (2019) 24:e1476–88. doi: 10.1634/theoncologist.2018-0868
8. Zhang XP, Zhou TF, Wang ZH, Zhang F, Zhong CQ, Hu YR, et al. Association of Preoperative Hypercoagulability With Poor Prognosis in Hepatocellular Carcinoma Patients With Microvascular Invasion After Liver Resection: A Multicenter Study. *Ann Surg Oncol* (2019) 26:4117–25. doi: 10.1245/s10434-019-07504-7
9. Szpakowski JL, Drasin TE, Lyon LL. Rate of Seeding With Biopsies and Ablations of Hepatocellular Carcinoma: A Retrospective Cohort Study. *Hepatol Commun* (2017) 1:841–51. doi: 10.1002/hep4.1089
10. Renzulli M, Brocchi S, Cucchetti A, Mazzotti F, Mosconi C, Sportoletti C, et al. Can Current Preoperative Imaging be Used to Detect Microvascular Invasion of Hepatocellular Carcinoma? *Radiology* (2016) 279:432–42. doi: 10.1148/radiol.2015150998
11. Lee S, Kim SH, Lee JE, Sinn DH, Park CK. Preoperative Gadoxetic Acid-Enhanced MRI for Predicting Microvascular Invasion in Patients With Single

Hepatocellular Carcinoma. *J Hepatol* (2017) 67:526–34. doi: 10.1016/j.jhep.2017.04.024
12. Zhu W, Qing X, Yan F, Luo Y, Li Y, Zhou X. Can the Contrast-Enhanced Ultrasound Washout Rate be Used to Predict Microvascular Invasion in Hepatocellular Carcinoma? *Ultrasound Med Biol* (2017) 43:1571–80. doi: 10.1016/j.ultrasmedbio.2017.04.003
13. Lambin P, Rios-Velazquez E, Leijenaar R, Carvalho S, van Stiphout RG, Granton P, et al. Radiomics: Extracting More Information From Medical Images Using Advanced Feature Analysis. *Eur J Cancer* (2012) 48:441–6. doi: 10.1016/j.ejca.2011.11.036
14. Chong HH, Yang L, Sheng RF, Yu YL, Wu DJ, Rao SX, et al. Multi-Scale and Multi-Parametric Radiomics of Gadoxetate Disodium-Enhanced MRI Predicts Microvascular Invasion and Outcome in Patients With Solitary Hepatocellular Carcinoma ≤ 5 Cm. *Eur Radiol* (2021) 31:4824–38. doi: 10.1007/s00330-020-07601-2
15. Dai H, Lu M, Huang B, Tang M, Pang T, Liao B, et al. Considerable Effects of Imaging Sequences, Feature Extraction, Feature Selection, and Classifiers on Radiomics-Based Prediction of Microvascular Invasion in Hepatocellular Carcinoma Using Magnetic Resonance Imaging. *Quant Imaging Med Surg* (2021) 11:1836–53. doi: 10.21037/qims-20-218
16. Dong Y, Wang QM, Li Q, Li LY, Zhang Q, Yao Z, et al. Preoperative Prediction of Microvascular Invasion of Hepatocellular Carcinoma: Radiomics Algorithm Based on Ultrasound Original Radio Frequency Signals. *Front Oncol* (2019) 9:1203. doi: 10.3389/fonc.2019.01203
17. Dong Y, Zhou L, Xia W, Zhao XY, Zhang Q, Jian JM, et al. Preoperative Prediction of Microvascular Invasion in Hepatocellular Carcinoma: Initial Application of a Radiomic Algorithm Based on Grayscale Ultrasound Images. *Front Oncol* (2020) 10:353. doi: 10.3389/fonc.2020.00353
18. Feng ST, Jia Y, Liao B, Huang B, Zhou Q, Li X, et al. Preoperative Prediction of Microvascular Invasion in Hepatocellular Cancer: A Radiomics Model Using Gd-EOB-DTPA-Enhanced MRI. *Eur Radiol* (2019) 29:4648–59. doi: 10.1007/s00330-018-5935-8
19. Jiang YQ, Cao SE, Cao S, Chen JN, Wang GY, Shi WQ, et al. Preoperative Identification of Microvascular Invasion in Hepatocellular Carcinoma by XGBoost and Deep Learning. *J Cancer Res Clin Oncol* (2021) 147:821–33. doi: 10.1007/s00432-020-03366-9
20. Li Y, Zhang Y, Fang Q, Zhang X, Hou P, Wu H, et al. Radiomics Analysis of [18F] FDG PET/CT for Microvascular Invasion and Prognosis Prediction in Very-Early- and Early-Stage Hepatocellular Carcinoma. *Eur J Nucl Med Mol Imaging* (2021) 48:2599–614. doi: 10.1007/s00259-020-05119-9
21. Ma X, Wei J, Gu D, Zhu Y, Feng B, Liang M, et al. Preoperative Radiomics Nomogram for Microvascular Invasion Prediction in Hepatocellular Carcinoma Using Contrast-Enhanced CT. *Eur Radiol* (2019) 29:3595–605. doi: 10.1007/s00330-018-5985-y
22. Ni M, Zhou X, Lv Q, Li Z, Gao Y, Tan Y, et al. Radiomics Models for Diagnosing Microvascular Invasion in Hepatocellular Carcinoma: Which Model is the Best Model? *Cancer Imaging* (2019) 19:60. doi: 10.1186/s40644-019-0249-x
23. Peng J, Zhang J, Zhang Q, Xu Y, Zhou J, Liu L. A Radiomics Nomogram for Preoperative Prediction of Microvascular Invasion Risk in Hepatitis B Virus-Related Hepatocellular Carcinoma. *Diagn Interv Radiol* (2018) 24:121–7. doi: 10.5152/dir.2018.17467
24. Song D, Wang Y, Wang W, Wang Y, Cai J, Zhu K, et al. Using Deep Learning to Predict Microvascular Invasion in Hepatocellular Carcinoma Based on Dynamic Contrast-Enhanced MRI Combined With Clinical Parameters. *J Cancer Res Clin Oncol* (2021) 147:3757–67. doi: 10.1007/s00432-021-03617-3
25. Wang H, Zeng M, Rao S, Sheng R, Yang C, Weng X, et al. Radiomic Features to Predict Microvascular Invasion in Hepatocellular Carcinoma Based on Conventional MRI: Preliminary Findings. *Chin J Radiol* (2019) 53:292–8. doi: 10.3760/cma.j.issn.1005-1201.2019.04.010
26. Xu X, Zhang HL, Liu QP, Sun SW, Zhang J, Zhu FP, et al. Radiomic Analysis of Contrast-Enhanced CT Predicts Microvascular Invasion and Outcome in Hepatocellular Carcinoma. *J Hepatol* (2019) 70:1133–44. doi: 10.1016/j.jhep.2019.02.023
27. Yang L, Gu D, Wei J, Yang C, Rao S, Wang W, et al. A Radiomics Nomogram for Preoperative Prediction of Microvascular Invasion in Hepatocellular Carcinoma. *Liver Cancer* (2019) 8:373–86. doi: 10.1159/000494099
28. Yao Z, Dong Y, Wu G, Zhang Q, Yang D, Yu JH, et al. Preoperative Diagnosis and Prediction of Hepatocellular Carcinoma: Radiomics Analysis Based on Multi-Modal Ultrasound Images. *BMC Cancer* (2018) 18:1089. doi: 10.1186/s12885-018-5003-4
29. Yu Y, Hu C, Wang X, Fan Y, Hu M, Shi C, et al. Value of the Application of Enhanced CT Radiomics and Machine Learning in Preoperative Prediction of Microvascular Invasion in Hepatocellular Carcinoma. *Natl Med J China* (2021) 101:1239–45. doi: 10.3760/cma.j.cn112137-20200820-02425
30. Zhang R, Xu L, Wen X, Zhang J, Yang P, Zhang L, et al. A Nomogram Based on Bi-Regional Radiomics Features From Multimodal Magnetic Resonance Imaging for Preoperative Prediction of Microvascular Invasion in Hepatocellular Carcinoma. *Quant Imaging Med Surg* (2019) 9:1503–15. doi: 10.21037/qims.2019.09.07
31. Zhang W, Yang R, Liang F, Liu G, Chen A, Wu H, et al. Prediction of Microvascular Invasion in Hepatocellular Carcinoma With a Multi-Disciplinary Team-Like Radiomics Fusion Model on Dynamic Contrast-Enhanced Computed Tomography. *Front Oncol* (2021) 11:660629. doi: 10.3389/fonc.2021.660629
32. Zhang X, Ruan S, Xiao W, Shao J, Tian W, Liu W, et al. Contrast-Enhanced CT Radiomics for Preoperative Evaluation of Microvascular Invasion in Hepatocellular Carcinoma: A Two-Center Study. *Clin Transl Med* (2020) 10:e111. doi: 10.1002/ctm2.111
33. Zhang Y, Shu Z, Ye Q, Chen J, Zhong J, Jiang H, et al. Preoperative Prediction of Microvascular Invasion in Hepatocellular Carcinoma *via* Multi-Parametric MRI Radiomics. *Front Oncol* (2021) 11:633596. doi: 10.3389/fonc.2021.633596
34. Zheng J, Chakraborty J, Chapman WC, Gerst S, Gonen M, Pak LM, et al. Preoperative Prediction of Microvascular Invasion in Hepatocellular Carcinoma Using Quantitative Image Analysis. *J Am Coll Surg* (2017) 225:778–88.e1. doi: 10.1016/j.jamcollsurg.2017.09.003
35. Zhu YJ, Feng B, Wang S, Wang LM, Wu JF, Ma XH, et al. Model-Based Three-Dimensional Texture Analysis of Contrast-Enhanced Magnetic Resonance Imaging as a Potential Tool for Preoperative Prediction of Microvascular Invasion in Hepatocellular Carcinoma. *Oncol Lett* (2019) 18:720–32. doi: 10.3892/ol.2019.10378
36. McInnes MDF, Moher D, Thombs BD, McGrath TA, Bossuyt PMand the PRISMA-DTA Group, et al. Preferred Reporting Items for a Systematic Review and Meta-Analysis of Diagnostic Test Accuracy Studies: The PRISMA-DTA Statement. *JAMA* (2018) 319:388–96. doi: 10.1001/jama.2017.19163
37. Whiting PF, Rutjes AW, Westwood ME, Mallett S, Deeks JJ, Reitsma JB, et al. QUADAS-2: A Revised Tool for the Quality Assessment of Diagnostic Accuracy Studies. *Ann Intern Med* (2011) 155:529–36. doi: 10.7326/0003-4819-155-8-201110180-00009
38. Moses LE, Shapiro D, Littenberg B. Combining Independent Studies of a Diagnostic Test Into a Summary ROC Curve: Data-Analytic Approaches and Some Additional Considerations. *Stat Med* (1993) 12:1293–316. doi: 10.1002/sim.4780121403
39. Higgins JP, Thompson SG, Deeks JJ, Altman DG. Measuring Inconsistency in Meta-Analyses. *BMJ* (2003) 327:557–60. doi: 10.1136/bmj.327.7414.557
40. Deeks JJ, Macaskill P, Irwig L. The Performance of Tests of Publication Bias and Other Sample Size Effects in Systematic Reviews of Diagnostic Test Accuracy was Assessed. *J Clin Epidemiol* (2005) 58:882–93. doi: 10.1016/j.jclinepi.2005.01.016
41. Huang J, Tian W, Zhang L, Huang Q, Lin S, Ding Y, et al. Preoperative Prediction Power of Imaging Methods for Microvascular Invasion in Hepatocellular Carcinoma: A Systemic Review and Meta-Analysis. *Front Oncol* (2020) 10:887. doi: 10.3389/fonc.2020.00887
42. Hu HT, Wang Z, Huang XW, Chen SL, Zheng X, Ruan SM, et al. Ultrasound-Based Radiomics Score: A Potential Biomarker for the Prediction of Microvascular Invasion in Hepatocellular Carcinoma. *Eur Radiol* (2019) 29:2890–901. doi: 10.1007/s00330-018-5797-0
43. Meng XP, Wang YC, Zhou JY, Yu Q, Lu CQ, Xia C, et al. Comparison of MRI and CT for the Prediction of Microvascular Invasion in Solitary Hepatocellular Carcinoma Based on a Non-Radiomics and Radiomics Method: Which Imaging Modality Is Better? *J Magn Reson Imaging* (2021) 54:526–36. doi: 10.1002/jmri.27575
44. Granito A, Galassi M, Piscaglia F, Romanini L, Lucidi V, Renzulli M, et al. Impact of Gadoxetic Acid (Gd-EOB-DTPA)-Enhanced Magnetic Resonance on the non-Invasive Diagnosis of Small Hepatocellular Carcinoma: A Prospective Study. *Aliment Pharmacol Ther* (2013) 37(3):355–63. doi: 10.1111/apt.12166

45. Wilson GC, Cannella R, Fiorentini G, Shen C, Borhani A, Furlan A, et al. Texture Analysis on Preoperative Contrast-Enhanced Magnetic Resonance Imaging Identifies Microvascular Invasion in Hepatocellular Carcinoma. *HPB (Oxf)* (2020) 22:1622–30. doi: 10.1016/j.hpb.2020.03.001
46. Bakr S, Echegaray S, Shah R, Kamaya A, Louie J, Napel S, et al. Noninvasive Radiomics Signature Based on Quantitative Analysis of Computed Tomography Images as a Surrogate for Microvascular Invasion in Hepatocellular Carcinoma: A Pilot Study. *J Med Imaging (Bellingham)* (2017) 4:41303. doi: 10.1117/1.JMI.4.4.041303

Conflict of Interest: The authors declare that the research was conducted in the absence of any commercial or financial relationships that could be construed as a potential conflict of interest.

Publisher's Note: All claims expressed in this article are solely those of the authors and do not necessarily represent those of their affiliated organizations, or those of the publisher, the editors and the reviewers. Any product that may be evaluated in this article, or claim that may be made by its manufacturer, is not guaranteed or endorsed by the publisher.

frontiers | Frontiers in Oncology

REVIEW
published: 10 May 2022
doi: 10.3389/fonc.2022.871829

Rabbit VX2 Liver Tumor Model: A Review of Clinical, Biology, Histology, and Tumor Microenvironment Characteristics

Florentina Pascale[1], Jean-Pierre Pelage[2,3†], Michel Wassef[4†], Saïda H. Ghegediban[1†], Jean-Pierre Saint-Maurice[5†], Thierry De Baere[6,7†], Alban Denys[8†], Rafael Duran[8†], Frédéric Deschamps[6,7†], Olivier Pellerin[9†], Noboru Maeda[10†], Alexandre Laurent[5†] and Julien Namur[1]*

[1] Research and Development Department, Archimmed Société à responsabilité limtée Limited liability Company (SARL), Jouy-en-Josas, France, [2] Université de Caen Normandie (UNICEAN), Centre d'Energie atomique (CEA), Centre National de la Recherche Scientifique, Imagerie et Stratégies Thérapeutiques pour les Cancers et Tissus Cérébraux CERVOxy (ISTCT-CERVOxy) Normandie University, Caen, France, [3] Department of Interventional and Diagnostic Imaging, University Hospital of Caen, Avenue de la Côte de Nacre, Caen, France, [4] Service d'Anatomie et Cytologie Pathologiques, Hôpital Lariboisière, Assistance Publique Hopitaux de Paris (APHP); Unité de Formation et de Recherche (URF) de Médecine Paris Nord, Université de Paris, Paris, France, [5] Department of Neuroradiology, Hôpital Lariboisière, Assistance Publique Hopitaux de Paris (APHP); Unité de Formation et de Recherche (URF) de Médecine Paris Nord, Université de Paris, Paris, France, [6] Department of Interventional Radiology, Gustave Roussy Cancer Center, Villejuif, France, [7] Unité de Formation et de Recherche (URF) Médecine Le Kremlin-Bicêtre, Université Paris-Saclay, Le Kremlin-Bicêtre, France, [8] Department of Radiology and Interventional Radiology, Centre Hospitalier Universitaire Vaudois, University of Lausanne, Lausanne, Switzerland, [9] Department of Interventional Radiology, Hôpital Européen Georges Pompidou, Assistance Publique Hopitaux de Paris (APHP) Université de Paris, Paris, France, [10] Department of Diagnostic and Interventional Radiology, Osaka International Cancer Institute, Osaka, Japan

The rabbit VX2 is a large animal model of cancer used for decades by interventional radiologists to demonstrate the efficacy of various locoregional treatments against liver tumors. What do we know about this tumor in the new era of targeted therapy and immune-oncology? The present paper describes the current knowledge on the clinics, biology, histopathology, and tumor microenvironment of VX2 based on a literature review of 741 publications in the liver and in other organs. It reveals the resemblance with human cancer (anatomy, vascularity, angiogenic profile, drug sensitivity, immune microenvironment), the differences (etiology, growth rate, histology), and the questions still poorly explored (serum and tissue biomarkers, genomic alterations, immune checkpoint inhibitors efficacy).

Keywords: embolization, locoregional treatments, imaging, immune oncology, angiography, tumor microenvironment

OPEN ACCESS

Edited by:
Xiankai Sun, University of Texas Southwestern Medical Center, United States

Reviewed by:
Guiyang Hao, University of Texas Southwestern Medical Center, United States
Samuel Rice, University of Texas Southwestern Medical Center, United States

***Correspondence:**
Florentina Pascale
florentina.pascale@archimmed.com
orcid.org/0000-0003-3942-3521

†These authors have contributed equally to this work

Specialty section:
This article was submitted to Cancer Imaging and Image-directed Interventions, a section of the journal Frontiers in Oncology

Received: *08 February 2022*
Accepted: *05 April 2022*
Published: *10 May 2022*

Citation:
Pascale F, Pelage J-P, Wassef M, Ghegediban SH, Saint-Maurice J-P, De Baere T, Denys A, Duran R, Deschamps F, Pellerin O, Maeda N, Laurent A and Namur J (2022) Rabbit VX2 Liver Tumor Model: A Review of Clinical, Biology, Histology, and Tumor Microenvironment Characteristics. Front. Oncol. 12:871829. doi: 10.3389/fonc.2022.871829

INTRODUCTION

The rabbit VX2 is a well-known animal tumor model in interventional radiology. Initially developed by Kid and Rous in the late 1930s (1), it is an anaplastic squamous cell carcinoma derived from *Shope papillomavirus* infection in rabbit. The tumor can be serially transplanted from one animal to another by allograft implantation and may grow in any organ or grafted tissue. A distinctive feature of VX2 is the fact that it does not request genetically modified or immunocompromised subjects but can be transplanted to normal immunocompetent animals. Sizeable tumors are obtained within a couple of weeks with up to >95% efficiency and good reproducibility. Another reason why

interventionalists have been using the rabbit VX2 is the larger size of the animal compared to the conventional rodent tumor model allowing the use of similar medical devices and an interventional procedure as in patients. For decades, VX2 has been used successfully to demonstrate the efficacy of various locoregional treatments such as transarterial chemoembolization (TACE), thermoablative therapies, radioembolization, and combinatory approaches (2–7).

The first immune checkpoint inhibitors have just entered treatment algorithms for primary and metastatic liver tumors (8), and many trials combining immunotherapies and locoregional treatments have been initiated (9). In this new era, researchers expect more from their translational model besides a growing mass that responds to physical or chemical aggression. Is the VX2 tumor a relevant model to evaluate these new tools and to what extent? The answer is not straightforward.

Among the 1,487 publications related to the VX2 model in the PubMed database, basic research articles are very few. Most investigative papers focus on the safety or efficacy of a new treatment and give a sparse and superficial description of the tumor. However, this literature search also reveals many trials, past and recent, that used the model and provides significant information about tumor growth characteristics, its biology, its genetic expression, or even its immunobiology.

The present paper will give a comprehensive review of the current knowledge on the VX2 tumor model with regard to clinical and imaging characteristics, macro- and microvascularization, histopathology, and microenvironment.

1 CLINICS

1.1 Tumor Induction, Growth, and Spread

The methods to induce the development of VX2 tumors in the liver have been described in detail in several review and investigation papers (10–12). Different types of inoculum and modalities of grafting of the tumor cells into the liver may be used that will affect tumor growth and tumor seeding. Briefly, the implantation of fragments dissected from fresh tumor grown in the muscle of a donor animal and placed surgically in the liver by laparotomy gives a satisfactory tumor take rate (90%–100%) and limits the risk of early extrahepatic dissemination. It is most commonly used in trials evaluating locoregional therapies. On the other hand, the injection of a cell suspension seems to provide a lower tumor take rate, accelerated tumor development, and earlier development of lung metastases due to accidental infusion of tumor cells into vessels. This approach may be considered for studying the antitumor effects of systemic therapies.

Regarding the number of tumor nodules, the large majority of studies induce a single VX2 tumor because it is easier to create and follow. Multiple VX2 nodules can still be grown successfully, either by implanting several fragments in different locations of the organ or by injecting the inoculum in a vessel irrigating the liver (13–16) (**Figures 1A–F**). These approaches have been developed to mimic metastases to the liver. They also seem relevant as a model of primary cancer since the population treated by locoregional or systemic therapies are generally patients with multifocal disease (18).

Tumor growth is fast, with a doubling of their volume every week (**Figure 2**). Two weeks after inoculation which is usually the time when the experiment is performed, the tumor reaches approximately 2.0 cm in length (2.5–5 cc in volume) (19–21). A size of 3 cm, which is considered a threshold for surgery/ablation vs. TACE allocation in hepatocellular carcinoma (HCC) patients, is reached after approximately 15 days, depending on the modality of tumor induction. At 6 weeks after implantation, rabbits may present very large tumors measuring 7.5 cm in length and 115 cc in volume (7, 12, 17, 19, 22, 23).

1.2 Animal Follow-Up

Rabbits generally show no clinical signs of the disease for a period of 1 month after tumor inoculation. They have a normal behavior and appetite, and no clinical signs of pain are observed. Liver function is not impaired despite tumor burden. The biochemical parameters of the liver and kidney (liver enzymes alanine transaminase (ALT) and alkaline phosphatase (ALP), creatinine, and urea nitrogen) remain in the normal range for that period of observation (17, 22, 24). After 36 days, animals become less brisk with a selective appetite. They may show signs of abdominal pain, due to possible ascites, peritoneal metastases, and tumor-associated cytokines (17, 25) and trouble breathing because of pulmonary invasion. Neutrophils are highly increased at 36 days (>10,000/μl), and this neutrophilia is strongly associated with the development of lung metastasis (22, 26). Other biology parameters appear unaffected.

1.3 Metastatic Spread

Although rarely described in literature, abdominal and pulmonary metastases should be expected (**Figures 3A–D**). Early discovery is likely due to tumor seeding at the time of implantation and may be detected in 16% for lungs and 8% for peritoneum 2 weeks after liver inoculation. Extra-hepatic nodules may also develop due to tumor spread at later time points. After 6 weeks, 89% to 100% of animals not receiving any treatment will develop metastases (17). They are the main factor limiting the duration of follow-up of the animals.

1.4 Survival

Survival is the most important outcome of an anticancer therapy. This is rarely an endpoint reported in VX2 preclinical trials because the tumor growth and metastases are life-threatening for the control untreated animals. The reported average survival time for the untreated animals is 45 days after tumor inoculation (12, 21, 24, 25, 27). After this period, the general state of the animal becomes impaired by the tumor burden and/or by the complications associated with pulmonary spread.

VX2 animals undergoing anticancer therapy are fine at 45 days without any clinical sign of the disease and can survive much longer than 45 days. The lifespan of VX2-bearing animals was extended up to 300 days in a study comparing different routes of administration of an anticancer agent mixture (28).

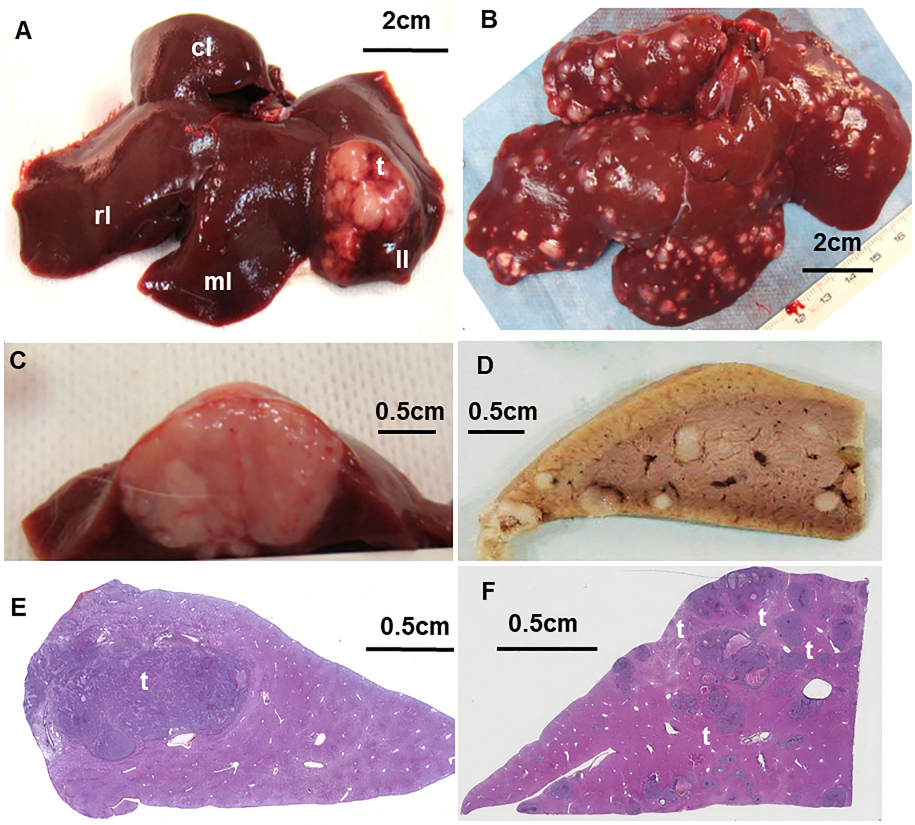

FIGURE 1 | **(A)** Macroscopic aspect of the uninodular VX2 tumor into the left lobe of the liver and **(B)** multinodular tumors, explanted at D14 after grafting. **(C)** Cross section of the uninodular tumor into the left liver and **(D)** of the multinodular liver lobe fixed in formalin. **(E)** Digitized histology section of the liver left lobe bearing uninodular or multinodular tumors **(F)** of different sizes stained with hematein–eosin–saffron showing the tumor in liver parenchyma. T, tumor; LL, left lobe; ML, median lobe; RL, right lobe; CL, caudate lobe. From (16, 17).

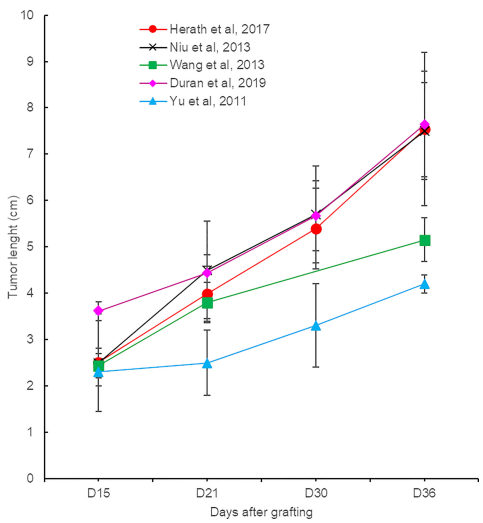

FIGURE 2 | Evolution of VX2 liver tumor size from different reports.

2 VASCULARIZATION

As in patients, the liver parenchyma in rabbit receives dual vascularization with 75%–80% of the blood supply coming from the portal system and 20%–25% from the hepatic artery while tumors are vascularized mainly by the hepatic artery (13). The liver arterial anatomy is also very close between rabbits and human. In patients, the hepatic artery commonly arises from the celiac trunk but may originate from the superior mesenteric artery in 3% of cases (29). In rabbit, angiography shows that the common hepatic artery also emerges from the celiac trunk in the majority of cases (98%) and in a few cases from the cranial mesenteric artery (2%) (30). In the two species, the common hepatic artery gives some digestive branches before ending into the liver as a proper hepatic artery (31). Inside the liver, the proper hepatic artery divides into two main branches, right and left hepatic arteries distributed to the right and left lobes, respectively. In rabbits, the left hepatic artery measures approximately 1 mm (0.6–1.5 mm) and divides into one or two branches that feed the tumor (30). The main tumor feeding artery measures 0.7 mm (0.5–0.9 mm), and the second feeding

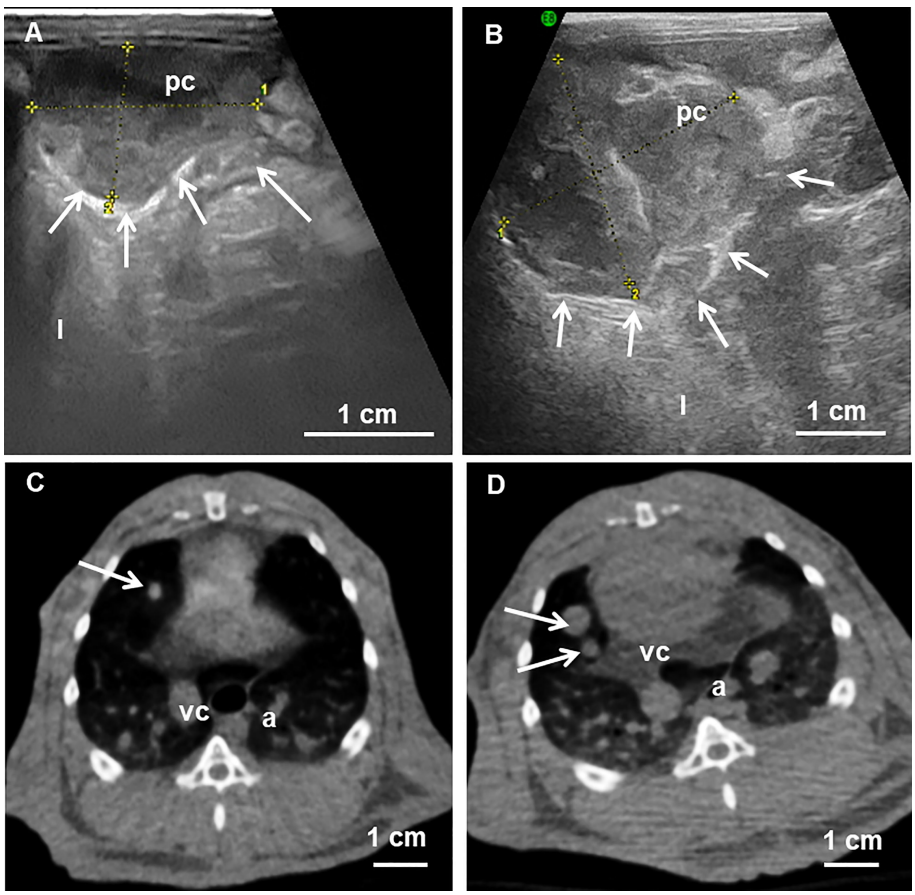

FIGURE 3 | **(A, B)** Abdominal ultrasound examination 30 and 36 days after tumor inoculation showing abdominal peritoneal metastases and peritoneum surrounding the carcinosis (arrows). The metastases increased in size and became more invasive over time. **(C, D)** Cone beam CT at the thoracic level shows small pulmonary nodules (arrows) at 18 days that have increased in size one week later. pc, peritoneal carcinosis; l, liver; vc, vena cava; a, aorta. From (22).

artery, arising from the left hepatic or from the principal feeder artery, has a diameter around 0.5 mm (0.3–0.8 mm). For comparison, the mean diameter of the main artery irrigating HCC nodules in human with a diameter of 7–63 mm was measured between 0.1 and 1.8 mm (32).

The diameter of intratumoral vessels can be deduced from embolization trials that have evaluated the distribution of embolic particles in histology or imaging (33–35). In VX2, beads with a caliber below 100 μm are mostly located inside the tumor nodule, microspheres with a size between 100 and 300 μm are evenly distributed inside and outside the tumor, and particles larger than 300 μm may not penetrate inside the tumor bed. Interestingly, two studies demonstrated a similar distribution of beads in HCC explants (36, 37), suggesting that the size of intratumoral vessels may be in the same range for patient hepatomas and VX2 tumors.

Tumor vascularization depends on the tumor size. Below a diameter of 2.5 cm, the vessels are homogenously distributed into the tumor core and capsule (38). When the tumor size exceeds 3 cm, the feeding artery becomes larger and the vessels are dense at the tumor edges but the core of the tumor becomes poorly vascularized. In patients, this aspect is frequently observed for the liver metastases from gastrointestinal adenomas (39).

3 IMAGING

3.1 Morphology

The aspect of VX2 tumors under different imaging modalities has been described in many different publications (**Figures 4A–J**). For morphology assessment, ultrasound is usually preferred due to the easy access to the equipment, affordability, and the fact that the examination can be executed on an awake rabbit. Tumors are identified as a heterogenous mass with hyperechogenic and hypoechogenic areas that correspond to viable and necrotic areas, respectively, and the hypoechogenic aspect of the tumor boundaries. The liver around appears as a uniform, sponge-like texture of low-level gray. The demarcation between the tumor and normal liver parenchyma is sometimes difficult and needs an experienced operator or the injection of contrast (40).

In computed tomography (CT), VX2 liver tumors have a low-density appearance which resembles the normal liver and cannot

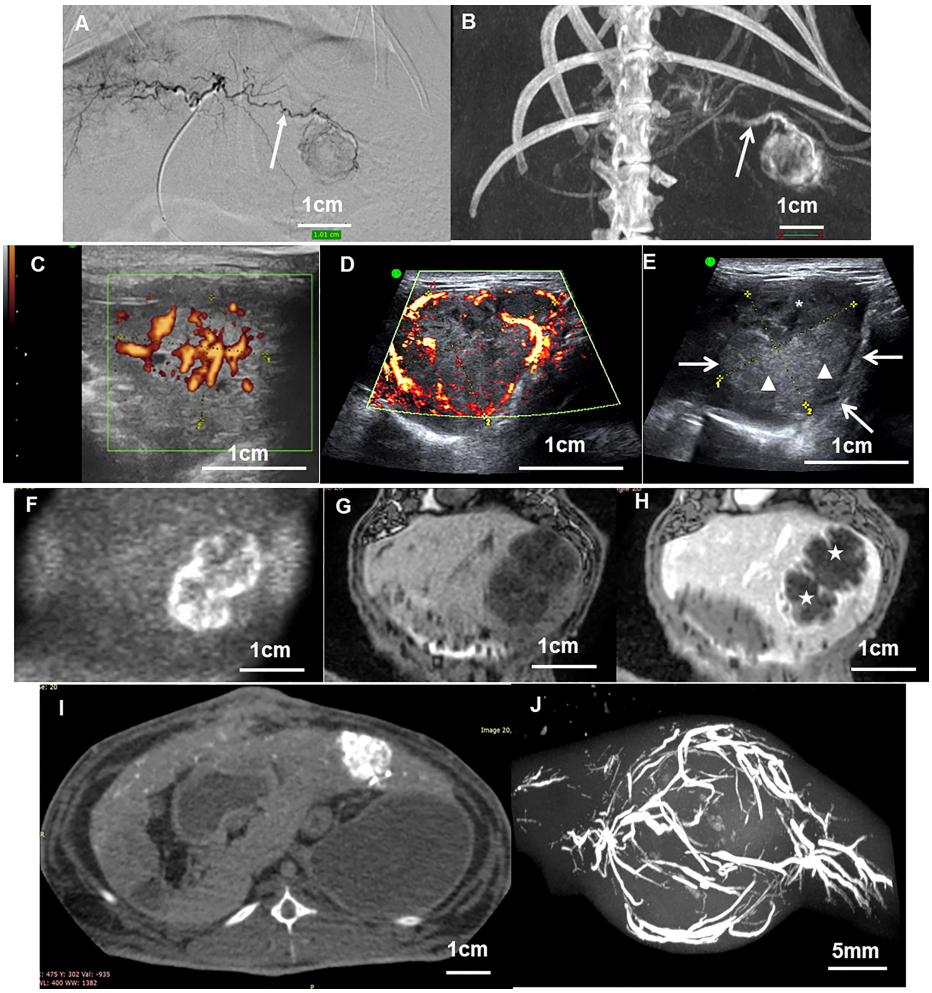

FIGURE 4 | **(A)** Angiography and **(B)** cone beam CT acquisitions of a VX2 tumor after 13 days of tumor development showing the main tumor feeding artery (arrow). **(C)** Ultrasound image in Power Doppler mode of VX2 tumor at 13 days showing vessels inside the tumor core. **(D)** The same examination of the same tumor at 21 days showing vessels at the periphery of the nodule. **(E)** The same tumor in B mode gray scale showing the tumor as a heterogenous mass with hyperechogenic (arrow heads) and hypoechogenic (stars) areas that correspond to viable and necrotic areas respectively, and hypoechogenic aspect of the tumor boundaries (arrows). **(F–H)** Coronal MRI view of a 21-day tumor with diffusion weight imaging **(F)**, T1-weighted before **(G)** and after **(H)** intravenous Dotarem contrast injection. The vessels are enhanced by gadolinium injection at the tumor boundaries while the necrotic core of the tumor remains unenhanced (stars). **(I)** Axial slice of a cone beam CT abdominal acquisition of a rabbit showing enhanced VX2 liver tumor after intra-arterial contrast injection. **(J)** Maximum intensity projection of a micro-CT acquisition of a VX2 tumor injected intra-arterially with radiopaque beads. Beads are seen with high attenuation in the vessels inside and around the nodule. All figure parts are from (16, 22).

be clearly distinguished from surrounding parenchyma without contrast injection (41).

In magnetic resonance imaging (MRI), the VX2 morphology is better depicted by T2-weighted imaging, as a mass with well-defined margins and areas of high and low signals corresponding to viable and necrotic portions, respectively (42). The liver around appears in the lower signal compared to the tumor.

3.2 Viability

Recent papers have tried to develop functional imaging tools mainly to evaluate the viability of the tumor or its perfusion after treatment.

Viability may be investigated by different MRI protocols with or without exogenous markers. The apparent diffusion coefficient (ADC) in diffusion-weighted imaging (DWI) is increased in areas of tumor necrosis compared to viable tumor regions at the tumor margin (38, 42). The concentration of choline and lipids as determined by hydrogen-1 proton MR spectroscopy may also reflect the percentage of tumor necrosis (43). The use of contrast agents specific for components of the extracellular matrix allowed a finer visualization of baseline tumor morphology as well as fibrotic remodeling of the periablation zone after radiofrequency treatment (44). VX2 tumors have an increased glucose metabolism and reduced oxidative metabolism, resulting in acidosis of the

tumor microenvironment that promotes the tumor growth, metastasis, and resistance to therapy. By generating an extracellular pH map by specific MRI procedures, the proliferating portions of the tumor or areas that do not respond to treatment can be visualized (45). Apoptosis could also be evaluated *in vivo* in VX2 tumors by positron emission tomography (PET) with the use of ^{18}F-labeled Annexin V targeting the phosphatidylserine exposed on damaged cellular membranes (46).

3.3 Vascularity

The vascularization and perfusion of VX2 liver tumors can be evaluated by many imaging modalities. Power and color Doppler sonography provides a basic and easy-to-perform macrovascular assessment in a semiquantitative approach and has been shown to anticipate tumor response after chemoembolization (17). A quantitative assessment of the tumor angiogenesis was established by quantitative three-dimensional (3D) dynamic contrast-enhanced ultrasound (DCE-US) (40).

Tumor vascularity can also be assessed by contrast-enhanced CT using a perfusion protocol. Quantitative parameters can be evaluated such as arterial flow, portal flow, and perfusion index (47). The VX2 tumors display a marked enhancement in the arterial phase, while the necrotic core of the tumor and the surrounding normal liver parenchyma appear unenhanced. In the portal phase, the tumors show low opacity and the liver around is strongly enhanced, giving the best visualization of the tumor (41). Spectral CT can be used for the quantitative evaluation of tumor angiogenesis (27).

Dynamic contrast-enhanced MRI (DCE-MRI) measures several parameters to quantitatively assess tissue vessel density, integrity, and permeability (48, 49) and further allows the visualization of hypoxic areas of the tumors (50). Transcatheter intra-arterial perfusion (TRIP) MRI was developed as an arterial analog to DCE-MRI to help quantify hepatic arterial perfusion in tumors (51).

Finally, the microvascularity and neo-angiogenesis of VX2 tumors could be nicely pictured by MRI using contrast media that target molecules involved in endothelial cell sprouting (52).

4 HISTOPATHOLOGY

4.1 Histology

The histology of VX2 is well known (1, 53, 54). Tumors are generally well delineated and composed of sheets and lobules of large undifferentiated cells with a high nucleo-cytoplasmic ratio (**Figures 5A–E**). Their nuclei are large, round, and with

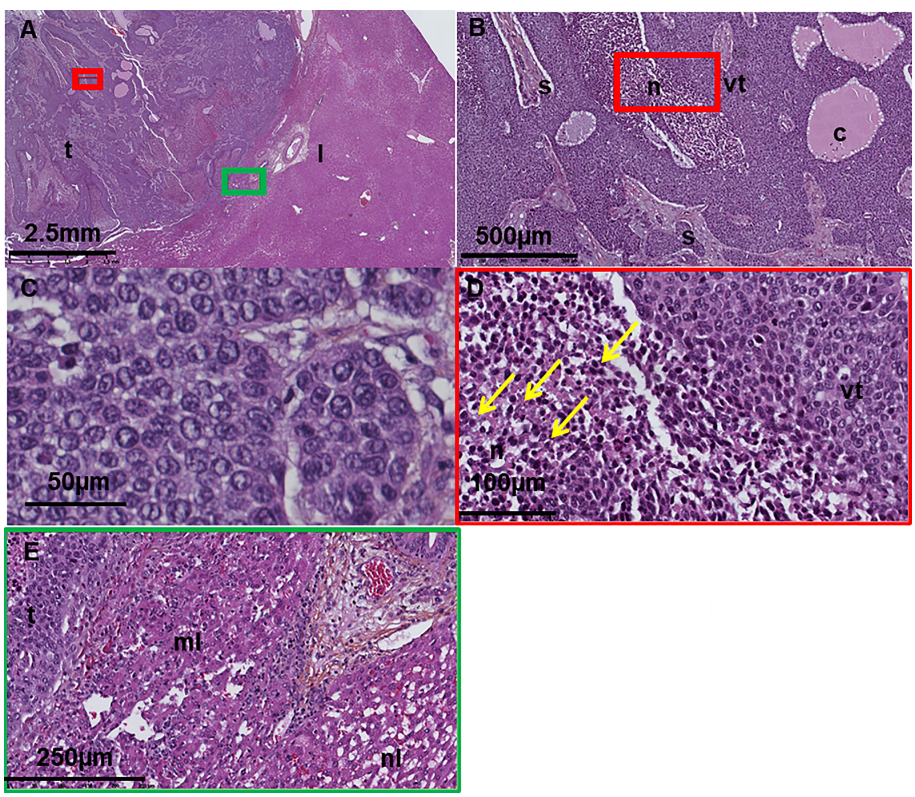

FIGURE 5 | **(A–E)** Digitized histology section of a VX2 tumor in the liver at different magnification showing **(A)** normal liver and tumor, **(B)** areas of viable tumor, necrosis, cystic cavities and fibrous stroma, **(C)** large undifferentiated tumor cells with high nucleo-cytoplasmic ratio, eosinophilic/pale cytoplasm, and ill-defined borders. **(D)** Apoptotic cell debris (arrows) in the necrotic areas. **(E)** Compressed and normal liver in the vicinity of the tumor t, tumor; l, liver; n, necrosis; vt, viable tumor; c, cyst. From (22, 55).

moderate anisocaryosis, coarse chromatin, and inconspicuous nucleolus. Their cytoplasms are eosinophilic or pale with ill-defined borders resulting in a pseudo-syncytial aspect. Mitosis and apoptotic bodies are numerous, the later tending to concentrate in the center of the lobules. The largest tumor sheets or lobules are generally centered by necrotic areas containing apoptotic-cell debris. Cystic cavities of various sizes, containing a proteinaceous eosinophilic fluid and some apoptotic/necrotic debris, are often present. The tumors are surrounded and penetrated by various, generally low, amounts of fibrous stroma, containing some blood vessels and few inflammatory cells, mostly macrophages and lymphocytes (56). The surrounding liver is normal or may show compression-distorted hepatic plates in the vicinity of the tumor.

Control non-treated animals will show a fraction of dead tumor due to spontaneous necrosis that may reach 30%–40% of the tumor surface the third week after tumor development (34, 38). The percentage of necrotic tumor may increase with tumor size (38). This spontaneous necrosis is often considered a limitation of the model and requests the inclusion of a non-treated or sham group to discriminate the effects of the tested therapy itself.

4.2 Immunohistochemistry

In immunohistochemistry, VX2 tumors are positive for cytokeratin AE1/AE3 and high molecular weight cytokeratin (HCK) labeling and negative for low molecular weight cytokeratins and CK18 (57, 58), as reported for the majority of squamous cell carcinomas (**Figure 6**). They also show strong, diffuse staining for the proliferation markers Ki-67 and PCNA all over the tumor surface and positive scattered labeling for vimentin, which are characteristic of aggressive cancers. The VX2 tumors are also positive for ALDH1 and CD44, two markers of cancer stem cells (59).

Regarding the tumor microenvironment, a positive immunohistochemical signal could be detected for different members of the matrix metallopeptidase family (MMP2, MMP3, MMP9, TIMP2, TIMP3) which are key players in the tumor invasion neovascularization processes, especially where tumors actively proliferated (60, 61). In non-treated tumors, epithelial cancer cells may represent 75% of viable cells, while CD11b+ macrophages and CD8+ T cells compose the majority of the non-tumoral cells (58, 62). To our knowledge, subtyping of other immune cells has not been explored.

Immunohistochemistry with CD31 and CD34 markers for endothelial cells has also shed light on the microvascularity of the liver tumors. Vessels are mostly present in the capsule and outer part of the tumor while the microvascular density is lower in the center of the tumor (40, 63). As a consequence, overexpression of hypoxia-inducible factor 1 alpha (HIF1α) is primarily found in tumor cells in proximity to the tumor core (45). Histopathologic markers indicative of glycolysis (GLUT-1) and chronic acidosis (LAMP-2) were found to be upregulated in untreated VX2 tumors (45).

Contrary to HCC, the basal levels of heat-shock protein HSP70 in VX2 tumors are low (64). The expression of other diagnostic markers for primary [glypican 3 (GPC3), glutamine synthetase (GS), arginase 1, hepatocyte paraffin 1 antigen (Hep Par-1)] and secondary [caudal-type homeobox 2 (CDX2), special AT-rich sequence-binding protein 2 (SATB2)] liver tumors has not been explored by immunohistochemistry.

5 TUMOR MICROENVIRONMENT

The last two decades reported a switch in concept of cancer therapy, from therapies focusing on the tumor itself to therapies centered on its microenvironment. The tumor microenvironment (TME) designates cancer cells, stromal cells, blood vessels, nerve fibers, extracellular matrix, and associated acellular components located at the center, at the margin, or within the vicinity of the tumor lesion. It can be classified into different specialized microenvironments (65), namely, immune microenvironment, hypoxic and acidic niche, mechanical microenvironment, innervated niche, and metabolism microenvironment. The VX2 tumor model is scarcely used for basic research on TME. However, several early and recent therapeutic studies have revealed some of the signaling pathways and molecules involved in the TME of this tumor (**Figure 7**). We will focus on the three first types of microenvironment which have been more explored in VX2.

5.1 Immune Microenvironment

Livers bearing primary or secondary tumors are characterized by multiple immune regulatory changes that act in favor of (liver intrinsic immunotolerance, immunosuppression of chronic inflammation) or against (antitumor response) disease progression. The goal of cancer immunotherapy is to shift that balance toward immunity against the tumor, using different non-exclusive strategies: blocking the suppressor lymphocytes that maintain the tolerance of the immune system for the tumors (checkpoint inhibitors), making some hidden tumor antigens visible to immune cells, or repopulating the tumors with cytotoxic lymphocytes and turn "cold" cancers into "hot" ones. Several of these approaches have been tested in VX2 tumors, as presented below.

5.1.1 Blockade of Immune Checkpoint Inhibitors

The role of several immune checkpoints including programmed cell death 1/programmed death-ligand 1 (PD-1/PD-L1), cytotoxic T-lymphocyte-associated protein 4 (CTLA-4), lymphocyte-activation gene 3 (LAG-3), adenosine A2a receptor (A2aR), or T-cell immunoglobulin and mucin domain-3 (TIM-3) has been highlighted in the immune tolerance for HCC (66). All these markers are highly upregulated on CD4+ and CD8+ cells infiltrating the HCC and are predictive of poorer disease outcome and postoperative recurrence. The first success of immunotherapy has been recently achieved in HCC with the approval of the anti-PD-L1 atezolizumab in combination with anti-VEGF bevacizumab as first-line treatment for advanced diseases.

In VX2, the expression of PD-L1, CTLA-4, LAG-3, and A2aR is significantly upregulated inside the tumors compared to the host liver tissue (67), suggesting that VX2 could potentially respond to immune checkpoint inhibitors. To our knowledge,

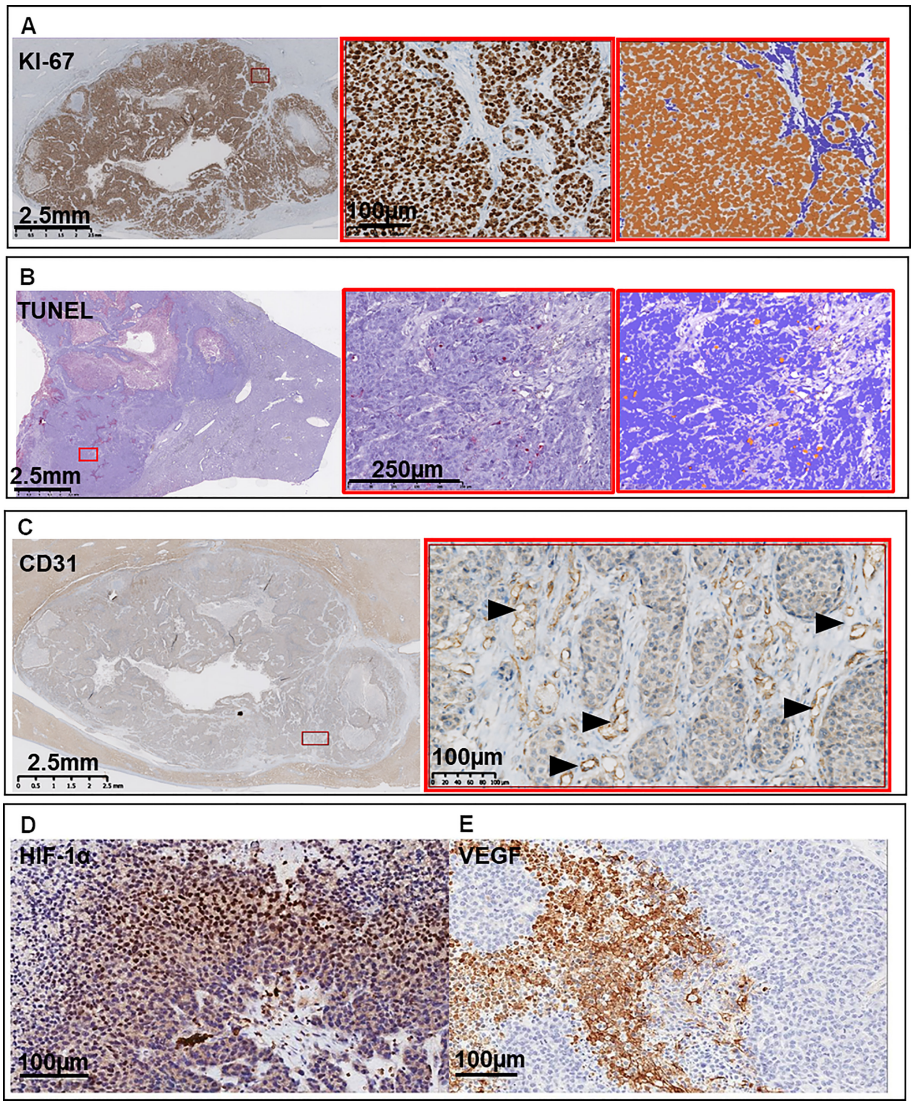

FIGURE 6 | Representative immunohistochemistry images of **(A)** Ki-67 labeling for proliferating cells at low magnification, high magnification, and automatic counting with ImmunoRatio plug-in for ImageJ. **(B)** TUNEL for apoptotic cells at low magnification, high magnification, and automatic counting with ImmunoRatio plug-in for ImageJ. **(C)** CD31 for endothelial cells (arrow heads), **(D)** hypoxia-inducible factor HIF-1α, and **(E)** vascular endothelial growth factor VEGF. From (7, 22).

no investigation on immune checkpoint inhibitors has been reported in VX2. One study did investigate the effects of combined blocking of PD-1 and LAG-3 in a rabbit model of ocular herpes. They showed an increased number of functional tissue-resident antivirus-specific CD8+ T cells, associated with a protection against further infection (68).

5.1.2 Unmasking Tumoral Antigens

Despite its immunotolerance, VX2 is an immunogenic tumor. In 1978, Shah et al. demonstrated several key facts on the immunocompetence after locoregional therapy using the rabbit VX2 liver model (69). First, the local hyperthermia treatment of the tumor elicits an immune response against tumor extracts. This response is both cellular and humoral. It disappears over time in animals not showing a complete response and is maintained in respondent animals which do not show any tumor development upon rechallenging with *de novo* inoculation of VX2 cells. Since then, the immunomodulatory and abscopal effects of the locoregional treatments have been confirmed with different therapies. Radiofrequency ablation (RFA) induced prolonged survival of the treated animals versus controls. This survival advantage was correlated with the presence of an antitumoral T-cell response after RFA that made some cryptic tumoral antigens accessible to antigen-presenting cells (APC) (70). Locally, CD3+ T cells were observed infiltrating the tumor nodule. Peripheral blood cells from these animals further showed an increase in activation when exposed to tumor lysates as well as specific increased

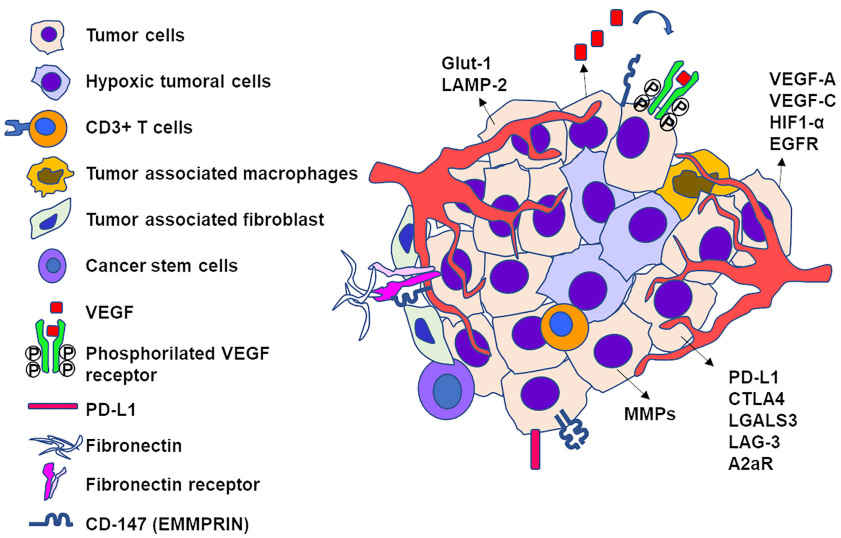

FIGURE 7 | Schematic representation of elements of tumor microenvironment of an untreated VX2 tumor. Viable tumor cells are found at the periphery of the nodule while hypoxic cells locate in the center. The following non-tumor cells have been found in tumor microenvironment: CD3+ T cells, tumor-associated macrophages, tumor-associated fibroblasts, and cancer stem cells. The mediators and receptors overexpressed by the tumor include markers of angiogenesis (VEGF-A, VEGF-C, EGFR, HIF-1α), immunologic checkpoints (PDL-1, CTLA-4, Gal-3, LAG-3, A2aR), extracellular matrix (fibronectin receptor, MMPs, CD147).

cytotoxicity when co-incubated with tumor cells. This immune stimulation is most likely directed against tumor antigens and not against transplantation alloantigens from donor animals, since non-treated VX2 animals do not show any immune reaction to tumor cells or tumor lysates. Adding a stimulation of dendritic cells by Toll-like receptor 9 (TLR9) ligands to RFA further potentiated antitumor T-cell response: tumor spread to other organs was prevented, survival was significantly prolonged compared to single treatments, and animals receiving a secondary tumor cell injection did not develop any tumor (25), suggesting a memory immune response against the tumor (**Figure 8**).

In another study, peritoneum-ozonized oxygen insufflation was applied to rabbits with VX2 auricular tumors. Regressing tumors showed an increased number of intratumoral CD3+ T cells and overexpression of genes coding for antigen presentation, T-cell activation, and inflammatory mediators. Most interestingly, the injection of peripheral blood leukocytes from responder rabbits to newly implanted animals resulted in tumor regression, showing that this oncolytic immune response may be adoptively transferred (71).

5.1.3 Stimulation the Homing of T Cells

Another immunomodulatory approach has been tested in VX2 tumors, that is, the reinforcing of the impotent immune system of the host. The delivery of interferon gamma inside the tumor led to a significant increase in natural killer cell infiltration *via* C–X–C motif chemokine ligand 10 (CXCL10)-mediated migration (72). Peritumoral injection of interleukin 2 (IL2), a potent stimulator of the helper and cytotoxic T cells, caused complete rejection for 33% of animals of both the treated auricular tumors and the non-treated contralateral tumors, and acquired immune rejection upon rechallenging. Similar results were obtained after intra-arterial injection of IL2 to rabbits with liver metastases of colorectal cancer (73). Several studies have also achieved better tumor response and systemic antitumor immunity when a locoregional therapy was associated with an immunostimulant treatment (74–76).

5.2 Hypoxia Niche and Angiogenesis

Hypoxia is an important hallmark of cancer and its microenvironment. It is involved in tumor angiogenesis, progression, stemness, intercellular communication, or resistance to treatment. It is described as a common feature of solid tumors including hepatocellular carcinoma and globally associated with poor prognosis. Two mediators have been particularly emphasized, vascular endothelial growth factor (VEGF) and hypoxia-inducible factor 1 alpha (HIF-1α). Overexpression of VEGF has been observed in HCC, and the concentration of circulating VEGF correlates with advanced HCC tumor stage, with the highest level observed in patients with metastases (77). The protein level of HIF-1α is significantly elevated in HCC samples and associated with worse prognosis, but the expression of mRNA shows variations. Intravascular therapies may induce an elevation of VEGF serum levels which is a negative prognostic factor for treatment outcome (77).

The basal expression of VEGF and HIF-1α in VX2 tumors has been evaluated at transcriptomic and protein levels. VX2 tumors constitutively express VEGF-A, the main type of growth factor and target for bevacizumab involved in tumor angiogenesis and growth (56, 78), as well as VEGF-C, responsible for the morphogenesis of lymphatic vessels and metastasis development (67, 79). The protein may be found in the plasma at very low concentrations (<10 pg/ml). VEGF

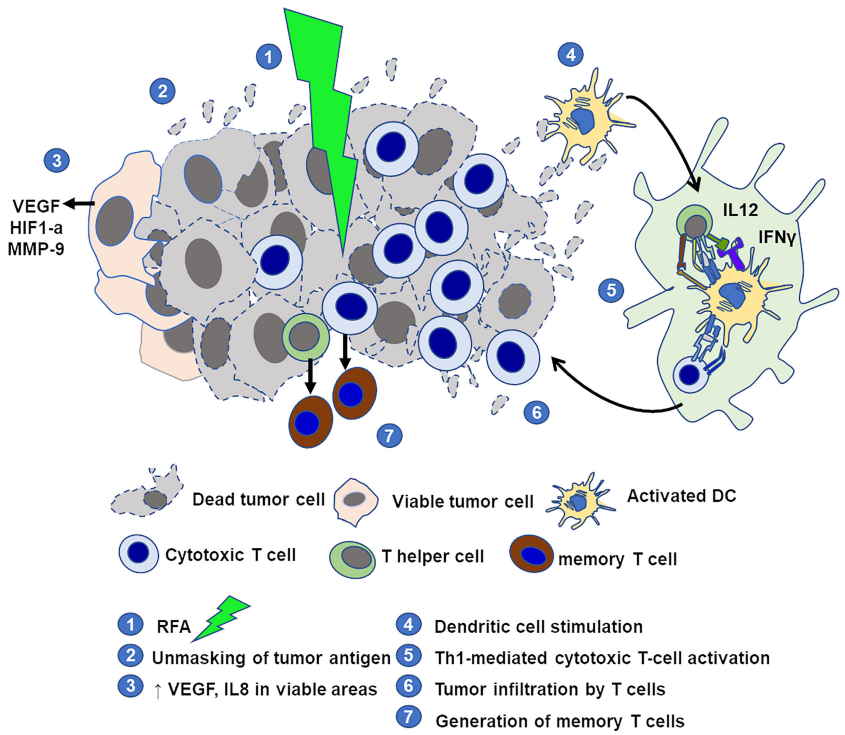

FIGURE 8 | Schematic representation of elements of immune microenvironment in VX2 tumor treated by RFA with immunostimulation. RFA destroys the tumor and produces tumor-specific antigens. Areas at the periphery of the tumor may remain viable and show increased expression of pro-angiogenic factors. Adjuvant stimulation of dendritic cells with CpG promotes a tumor-specific Th1 and cytotoxic T-cell reaction, increases the number of lymphocytes infiltrating the tumor, and allows the generation of memory T cells.

receptor 2 is also present in active phosphorylated form in non-treated tumors (55), showing the activation of angiogenesis *via* p38 MAPK, PI3K/AKT, and/or PLC-MEK/ERK pathways. HIF-1α is overexpressed in proximity to the necrotic tumor core which is poorly vascularized and deprived of oxygen supply (45, 80). Similarly to patients, chemoembolization of VX2 liver tumors induces ischemia, an increase in HIF-1α, and hypoxia which trigger the synthesis of VEGF (81, 82). These effects actually depend on the aggressiveness of treatment. The expression of HIF-1α may decrease immediately after cTACE and remain undetectable several weeks after TACE along with the onset and increasing extent of tumor necrosis. On the contrary, undertreated tumor portions after incomplete treatment have characteristic viable tumor features with the overexpression of HIF-1α and other markers of tumor progression (45). Perfusion maps of embolized VX2 tumors proved that embolization until angiographic stasis eliminated perfusion in only 56% of microvessels (83), further suggesting that partial response of the tumor and pro-angiogenic effects of embolization may be due to incomplete devascularization of the tumor.

Several therapies that block the induction of angiogenesis pathway have been tested in VX2, e.g., by combining chemoembolization with an oral tyrosine kinase inhibitor or by delivering an antiangiogenic drug rather than a cytotoxic drug through TACE procedure. TACE with sorafenib, sunitinib, apatinib, or vandetanib was successful at inhibiting the angiogenesis, tumor growth, and metastatic spread of VX2 tumors (22, 55, 84, 85). Interestingly, groups treated with the anti-angiogenic drug in these trials often showed partial efficacy, suggesting that the drugs are active in this preclinical model. A more recent therapeutic approach has proposed to take advantage of this adverse hypoxic effect of TACE and inject prodrugs which will be activated by the non-normoxic environment, with promising results in the VX2 model (7).

The hypoxic niche inside the tumor also has a negative impact on its immune microenvironment, by excluding effective immune cells from the acidic and poorly vascularized regions of the nodule (**Figure 9**). Normalization of tumor extracellular pH using bicarbonate or oxygen-generating catalase during TACE counteracted these immunosuppressive effects and triggered the homing of the cytotoxic lymphocytes, resulting in tumor regression (45, 86).

5.3 Mechanical Microenvironment

The tumor microenvironment also includes the factors of the extracellular matrix (ECM). Matrix metalloproteinases (MMPs), the principal ECM-degrading enzymes, are often overexpressed in cancer and are associated with a poor prognosis. The MMP receptor CD147 (EMMPRIN) is a glycoprotein initially known as

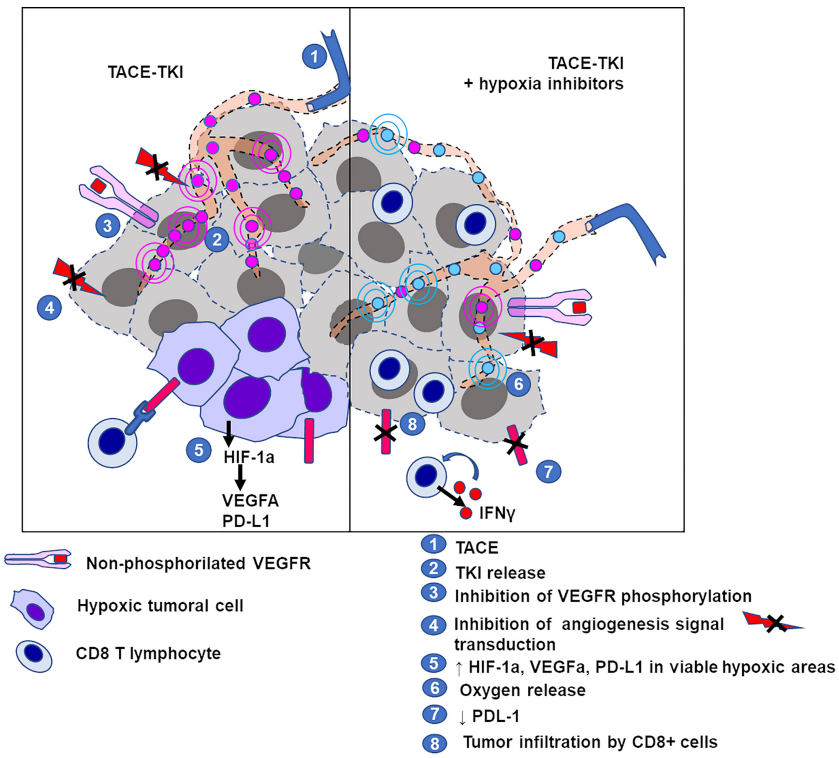

FIGURE 9 | Schematic representation of elements of the tumor microenvironment in VX2 tumor treated by TACE with/without hypoxia inhibitor. Left panel: TACE with tyrosine kinase inhibitors (TKI) induces ischemia plus inhibition of angiogenesis *via* blockade of TK receptor phosphorylation, leading to tumor cell death. Some areas of the tumor may remain viable under hypoxic conditions due to embolization and show overexpression of HIF-1α, markers for tumor progression and immunosuppression. Right panel: counteracting the hypoxia (with oxygen release mediated by catalase) downregulates the expression of PD-L1, allowing the activation and infiltration of CD8+ cytotoxic T cells.

a regulator of MMPs through cell–matrix and cell–cell interactions which have been identified as a potential target for cancer therapy (87). In HCC, the chimeric anti-CD147 humanized antibodies inhibited invasion and metastasis by modulation of cytoskeleton rearrangement *via* the FAK–PI3K–AKT signaling pathway (88).

As in HCC, MMP9 detection in VX2 liver tumors is associated with rapid progression of the tumor, especially after locoregional therapies such as TACE and RFA (89, 90). Targeting CD147 with the (131)I-labeled CD147 antibody prolonged survival and inhibited the tumor growth and metastasis spread in VX2 liver tumors (23).

Fibronectin, the main component of the ECM that is particularly abundant in tumors, ligates the integrin α5β1 on both tumor and other cells of ECM, especially vascular endothelial cells. This interaction induces tumor growth and invasion by activation of the Akt and MAPK pathways. Volociximab, a human/mouse chimeric antibody against integrin α5β1, inhibits endothelial cell proliferation and induced cell death. Despite a lower affinity of the antibody to the rabbit antigen, volociximab administered systemically to VX2-bearing animals still resulted in a significant decrease in tumor volume (91).

In the tumor microenvironment, cancer stem-like cells (CSC) are a subpopulation of cells with elevated tumor-initiating potential. They have been identified in both human liver neoplasms and the rabbit tumor (59). It was demonstrated that reducing the genomic instability in VX2 with the use of a protector (aminoethyl isothiourea) decreased tumor-initiating cells. When combined to chemotherapy, this strategy decreased lung metastases and prolonged survival compared to that with the cytotoxic agent alone (92).

Altogether, these reports support the production of tumor-specific antigens after conventional locoregional treatment of liver VX2 and show that immunity against tumor can be developed by adding different types of immunotherapy. Immune response is better in responder animals and may lead to recovery or even tumor rejection upon rechallenging of the animals.

Questions remain regarding the utility of the rabbit VX2 in immuno-oncology compared to other tumor models. Basic knowledge about the cancer immunity is still missing, e.g., immune and non-immune cell populations of the microenvironment are still poorly characterized. While some key mediators of the immune microenvironment have been identified, few molecules have been tested in the model. The

availability of the antibodies used in targeted and IO treatment and the knowledge of their cross-reactivity with the rabbit antigens remain a major challenge. Finally, different pathways probably exist between human and rabbit tumors (carcinogenetic process, interaction with inflamed/healthy liver tissue), despite the similarities demonstrated here. A high-throughput analysis of genomic, transcriptomic, and proteomic data from the tumor could help in specifying their common and unique features.

CONCLUSION

The rabbit VX2 carcinoma has been extensively used as a model of liver tumor to assess various treatment modalities that required animals larger than rodents. Its implantation techniques or growth characteristics have been accurately described, but information about its biology is scattered. The present review aimed at giving a faithful resource to guide teams working in interventional oncology and help them in the design of their future preclinical investigations.

With an appropriate surveillance of biology parameters and metastatic development, survival seems an acceptable endpoint for efficacy studies using the model. Many imaging protocols allow the morphology and functional characterization of the tumor with the same equipment as per clinical practice. With a particular interest in the tumor microenvironment, we showed that similar cells, mediators, mechanisms, and effects can be observed between human cancer and VX2. Of note, therapies aiming at immunizing the rabbit against the tumor are the only treatments that achieved a complete response and no recurrence.

In conclusion, VX2 carcinoma has a place alongside other experimental cancer models and seems to be the most relevant for trials combining locoregional treatments and therapies targeting the tumor microenvironment.

AUTHOR CONTRIBUTIONS

FP is the first author and the corresponding author. JN is the last author. J-PP, MW, SG, J-PS-M, TB, AD, RD, FD, OP, NM, and AL have contributed equally to this work. All authors contributed to the article and approved the submitted version.

FUNDING

The authors declare that this study received funding from Archimmed SARL. The funder was not involved in the study design, collection, analysis, interpretation of data, the writing of this article or the decision to submit it for publication.

REFERENCES

1. Kidd JG, Rous P. A Transplantable Rabbit Carcinoma Originating in a Virus-Induced Papilloma and Containing the Virus in Masked or Altered Form. *J Exp Med* (1940) 71(6):813–38. doi: 10.1084/jem.71.6.813
2. Burgener FA. Peripheral Hepatic Artery Embolization in Rabbits With VX2 Carcinomas of the Liver. *Cancer* (1980) 46(1):56–63. doi: 10.1002/1097-0142(19800701)46:1<56::AID-CNCR2820460113>3.0.CO;2-C
3. Frank JA, Girton M, Dwyer AJ, Cohen PJ, Knop RH, Diggs R, et al. A Reproducible Model of Metastatic Brain and Ocular Tumor by Hematogenous Inoculation of the VX2 Tumor in Rabbits. *J Neurosurg* (1987) 67(1):106–9. doi: 10.3171/jns.1987.67.1.0106
4. de Baere T, Zhang X, Aubert B, Harry G, Lagrange C, Ropers J, et al. Quantification of Tumor Uptake of Iodized Oils and Emulsions of Iodized Oils: Experimental Study. *Radiology* (1996) 201(3):731–5. doi: 10.1148/radiology.201.3.8939223
5. van Es RJ, Nijsen JF, Dullens HF, Kicken M, van der Bilt A, Hennink W, et al. Tumour Embolization of the Vx2 Rabbit Head and Neck Cancer Model With Dextran Hydrogel and Holmium-Poly(L-Lactic Acid) Microspheres: A Radionuclide and Histological Pilot Study. *J Craniomaxillofac Surg* (2001) 29(5):289–97. doi: 10.1054/jcms.2001.0234
6. Lee JM, Kim SW, Chung GH, Lee SY, Han YM, Kim CS. Open Radio-Frequency Thermal Ablation of Renal VX2 Tumors in a Rabbit Model Using a Cooled-Tip Electrode: Feasibility, Safety, and Effectiveness. *Eur Radiol* (2003) 13(6):1324–32. doi: 10.1007/s00330-002-1658-x
7. Duran R, Mirpour S, Pekurovsky V, Ganapathy-Kanniappan S, Brayton CF, Cornish TC, et al. Preclinical Benefit of Hypoxia-Activated Intra-Arterial Therapy With Evofosfamide in Liver Cancer. *Clin Cancer Res* (2017) 23(2):536–48. doi: 10.1158/1078-0432.CCR-16-0725
8. Casak SJ, Donoghue M, Fashoyin-Aje L, Jiang X, Rodriguez L, Shen Y-L, et al. FDA Approval Summary: Atezolizumab Plus Bevacizumab for the Treatment of Patients With Advanced Unresectable or Metastatic Hepatocellular Carcinoma. *Clin Cancer Res* (2021) 27(7):1836–41. doi: 10.1158/1078-0432.CCR-20-3407
9. Greten TF, Mauda-Havakuk M, Heinrich B, Korangy F, Wood BJ. Combined Locoregional-Immunotherapy for Liver Cancer. *J Hepatol* (2019) 70(5):999–1007. doi: 10.1016/j.jhep.2019.01.027
10. Virmani S, Harris KR, Szolc-Kowalska B, Paunesku T, Woloschak GE, Lee FT, et al. Comparison of Two Different Methods for Inoculating VX2 Tumors in Rabbit Livers and Hind Limbs. *J Vasc Interv Radiol* (2008) 19(6):931–6. doi: 10.1016/j.jvir.2008.02.019
11. Parvinian A, Casadaban LC, Gaba RC. Development, Growth, Propagation, and Angiographic Utilization of the Rabbit VX2 Model of Liver Cancer: A Pictorial Primer and "How to" Guide. *Diagn Interv Radiol* (2014) 20(4):335–40. doi: 10.5152/dir.2014.13415
12. Wang Z, Yang G, Nie P, Fu J, Wang X, Liu D. Dynamical Observation on Biological Progression of VX2 Liver Tumors to Identify the Optimal Time for Intervention in Animal Models. *PLoS One* (2013) 8(8):e74327. doi: 10.1371/journal.pone.0074327
13. Burgener FA, Violante MR. Comparison of Hepatic VX2-Carcinomas After Intra-Arterial, Intraportal and Intraparenchymal Tumor Cell Injection. An Angiographic and Computed Tomographic Study in the Rabbit. *Invest Radiol* (1979) 14(5):410–4. doi: 10.1097/00004424-197909000-00005
14. Izumi B, Tashiro S, Miyauchi Y. Anticancer Effects of Local Administration of Mitomycin C *via* the Hepatic Artery or Portal Vein on Implantation and Growth of VX2 Cancer Injected Into Rabbit Liver. *Cancer Res* (1986) 46(8):4167–70.
15. Tanaka H, Taniguchi H, Mugitani T, Koishi Y, Masuyama M, Higashida T, et al. Intra-Arterial Administration of the Angiogenesis Inhibitor TNP-470 Blocks Liver Metastasis in a Rabbit Model. *Br J Cancer* (1995) 72(3):650–3. doi: 10.1038/bjc.1995.389
16. Namur J, Pascale F, Maeda N, Sterba M, Ghegediban SH, Verret V, et al. Safety and Efficacy Compared Between Irinotecan-Loaded Microspheres HepaSphere and DC Bead in a Model of VX2 Liver Metastases in the

Rabbit. *J Vasc Interv Radiol* (2015) 26(7):1067–75.e3. doi: 10.1016/j.jvir.2015.03.014
17. Herath NI, Devun F, Herbette A, Lienafa M-C, Chouteau P, Sun J-S, et al. Potentiation of Doxorubicin Efficacy in Hepatocellular Carcinoma by the DNA Repair Inhibitor DT01 in Preclinical Models. *Eur Radiol* (2017) 27 (10):4435–44. doi: 10.1007/s00330-017-4792-1
18. European Association for the Study of the Liver. EASL Clinical Practice Guidelines: Management of Hepatocellular Carcinoma. *J Hepatol* (2018) 69 (1):182–236. doi: 10.1016/j.jhep.2018.03.019
19. Hoekstra LT, van Lienden KP, Verheij J, van der Loos CM, Heger M, van Gulik TM. Enhanced Tumor Growth After Portal Vein Embolization in a Rabbit Tumor Model. *J Surg Res* (2013) 180(1):89–96. doi: 10.1016/j.jss.2012.10.032
20. Mugitani T, Taniguchi H, Takada A, Yamaguchi A, Masuyama M, Hoshima M, et al. TNP-470 Inhibits Collateralization to Complement the Anti-Tumour Effect of Hepatic Artery Ligation. *Br J Cancer* (1998) 77(4):638–42. doi: 10.1038/bjc.1998.102
21. Niu H, Wang R, Cheng J, Gao S, Liu B. Treatment of (131)I-Labeled Anti-CD147 Monoclonal Antibody in VX2 Carcinoma-Induced Liver Tumors. *Oncol Rep* (2013) 30(1):246–52. doi: 10.3892/or.2013.2418
22. Duran R, Namur J, Pascale F, Czuczman P, Bascal Z, Kilpatrick H, et al. Vandetanib-Eluting Radiopaque Beads: Pharmacokinetics, Safety, and Efficacy in a Rabbit Model of Liver Cancer. *Radiology* (2019) 293(3):695–703. doi: 10.1148/radiol.2019190305
23. Niu C, Wang Z, Lu G, Krupka TM, Sun Y, You Y, et al. Doxorubicin Loaded Superparamagnetic PLGA-Iron Oxide Multifunctional Microbubbles for Dual-Mode US/MR Imaging and Therapy of Metastasis in Lymph Nodes. *Biomaterials* (2013) 34(9):2307–17. doi: 10.1016/j.biomaterials.2012.12.003
24. Tong H, Li X, Zhang CL, Gao JH, Wen SL, Huang ZY, et al. Transcatheter Arterial Embolization Followed by Octreotide and Celecoxib Synergistically Prolongs Survival of Rabbits With Hepatic VX2 Allografts. *J Dig Dis* (2013) 14 (1):29–37. doi: 10.1111/1751-2980.12001
25. Behm B, Di Fazio P, Michl P, Neureiter D, Kemmerling R, Hahn EG, et al. Additive Antitumour Response to the Rabbit VX2 Hepatoma by Combined Radio Frequency Ablation and Toll Like Receptor 9 Stimulation. *Gut* (2016) 65(1):134–43. doi: 10.1136/gutjnl-2014-308286
26. Hough AJ, Hubbard WC, Oates JA. VX2 Carcinoma, Pulmonary Metastases, and Neutrophilic Leukocytosis. Possible Animal Model of Tumor-Associated Granulocytosis. *Am J Pathol* (1983) 112(2):231–7.
27. Zhou Y, Gong Y, Wang M, Xu H, Hou P, Dong J, et al. Spectral Computed Tomographic Parameters Predict the Therapeutic Efficacy and Overall Survival of the Angiogenesis Inhibitor AL3818 in Hepatic Lesions: Preliminary Animal Study. *J Comput Assist Tomogr* (2019) 43(5):721–8. doi: 10.1097/RCT.0000000000000898
28. Tabaru K, Konno T, Oda T, Nagamitsu A, Ishimaru Y, Kitamura N. Treatment of VX2 Carcinoma Implanted in the Liver With Arterial and Intraperitoneal Administration of Oily Anticancer Agents. *Cancer Chemother Pharmacol* (2001) 147(2):149–54. doi: 10.1007/s002800000209
29. Hiatt JR, Gabbay J, Busuttil RW. Surgical Anatomy of the Hepatic Arteries in 1000 Cases. *Ann Surg* (1994) 220(1):50–2. doi: 10.1097/00000658-199407000-00008
30. Tam AL, Melancon MP, Ensor J, Liu Y, Dixon K, McWatters A, et al. Rabbit Hepatic Arterial Anatomy Variations: Implications on Experimental Design. *Acta Radiol* (2014) 55(10):1226–33. doi: 10.1177/0284185113514050
31. Barone R. "Système Lymphatique Du Lapin Dans "Anatomie Comparée Des Mamiferes Domestiques", Page 845". In: *Angiologie*. Paris: Vigot Frères (1996). p. 903 p.
32. Irie T, Kuramochi M, Takahashi N. Diameter of Main Tumor Feeding Artery of a Hepatocellular Carcinoma: Measurement at the Entry Site Into the Nodule. *Hepatol Res* (2016) 46(3):E100–104. doi: 10.1111/hepr.12534
33. Lee K-H, Liapi E, Vossen JA, Buijs M, Ventura VP, Georgiades C, et al. Distribution of Iron Oxide-Containing Embosphere Particles After Transcatheter Arterial Embolization in an Animal Model of Liver Cancer: Evaluation With MR Imaging and Implication for Therapy. *J Vasc Interv Radiol* (2008) 19(10):1490–6. doi: 10.1016/j.jvir.2008.06.008
34. Namur J, Pascale FT, Dinca H, Ghegediban S, Maurice JS, Maeda N, et al. Doxorubicin Eluting Microsphere: Is There a Size Effect ? Comparison of Two Sizes in VX2 Tumor Model. *J Vasc Intervent Radiol* (2014) 25(3):S71–2. doi: 10.1016/j.jvir.2013.12.178
35. Caine M, Chung T, Kilpatrick H, Bascal Z, Willis S, Tang Y, et al. Evaluation of Novel Formulations for Transarterial Chemoembolization: Combining Elements of Lipiodol Emulsions With Drug-Eluting Beads. *Theranostics* (2019) 9(19):5626–41. doi: 10.7150/thno.34778
36. Namur J, Citron SJ, Sellers MT, Dupuis MH, Wassef M, Manfait M, et al. Embolization of Hepatocellular Carcinoma With Drug-Eluting Beads: Doxorubicin Tissue Concentration and Distribution in Patient Liver Explants. *J Hepatol* (2011) 55(6):1332–8. doi: 10.1016/j.jhep.2011.03.024
37. Nicolini D, Svegliati-Baroni G, Candelari R, Mincarelli C, Mandolesi A, Bearzi I, et al. Doxorubicin-Eluting Bead vs Conventional Transcatheter Arterial Chemoembolization for Hepatocellular Carcinoma Before Liver Transplantation. *World J Gastroenterol* (2013) 19(34):5622–32. doi: 10.3748/wjg.v19.i34.5622
38. Vossen JA, Buijs M, Geschwind J-FH, Liapi E, Prieto Ventura V, Lee KH, et al. Diffusion-Weighted and Gd-EOB-DTPA-Contrast-Enhanced Magnetic Resonance Imaging for Characterization of Tumor Necrosis in an Animal Model. *J Comput Assist Tomogr* (2009) 33(4):626–30. doi: 10.1097/RCT.0b013e3181953df3
39. Minami Y, Kudo M. Hepatic Malignancies: Correlation Between Sonographic Findings and Pathological Features. *World J Radiol* (2010) 2(7):249–56. doi: 10.4329/wjr.v2.i7.249
40. Zheng Q, Zhang J-C, Wang Z, Ruan S-M, Li W, Pan F-S, et al. Assessment of Angiogenesis in Rabbit Orthotropic Liver Tumors Using Three-Dimensional Dynamic Contrast-Enhanced Ultrasound Compared With Two-Dimensional DCE-Us. *Jpn J Radiol* (2019) 37(10):701–9. doi: 10.1007/s11604-019-00861-z
41. Shen Z-Y, Liu C, Wu M-F, Shi H-F, Zhou Y-F, Zhuang W, et al. Spiral Computed Tomography Evaluation of Rabbit VX2 Hepatic Tumors Treated With 20 kHz Ultrasound and Microbubbles. *Oncol Lett* (2017) 14(3):3124–30. doi: 10.3892/ol.2017.6557
42. Keller S, Chapiro J, Brangsch J, Reimann C, Collettini F, Sack I, et al. Quantitative MRI for Assessment of Treatment Outcomes in a Rabbit VX2 Hepatic Tumor Model. *J Magn Reson Imaging* (2019) 52(3):668–685. doi: 10.1002/jmri.26968
43. Buijs M, Vossen JA, Geschwind J-FH, Salibi N, Pan L, Ventura VP, et al. Quantitative Proton MR Spectroscopy as a Biomarker of Tumor Necrosis in the Rabbit VX2 Liver Tumor. *J Vasc Interv Radiol* (2011) 22(8):1175–80. doi: 10.1016/j.jvir.2011.03.016
44. Collettini F, Reimann C, Brangsch J, Chapiro J, Savic LJ, Onthank DC, et al. Elastin-Specific MRI of Extracellular Matrix-Remodelling Following Hepatic Radiofrequency-Ablation in a VX2 Liver Tumor Model. *Sci Rep* (2021) 11 (1):6814. doi: 10.1038/s41598-021-86417-6
45. Savic LJ, Schobert IT, Peters D, Walsh JJ, Laage-Gaupp FM, Hamm CA, et al. Molecular Imaging of Extracellular Tumor pH to Reveal Effects of Locoregional Therapy on Liver Cancer Microenvironment. *Clin Cancer Res* (2020) 26(2):428–38. doi: 10.1158/1078-0432.CCR-19-1702
46. Qin H, Zhang M-R, Xie L, Hou Y, Hua Z, Hu M, et al. PET Imaging of Apoptosis in Tumor-Bearing Mice and Rabbits After Paclitaxel Treatment With (18)F(-)Labeled Recombinant Human His10-Annexin V. *Am J Nucl Med Mol Imaging* (2015) 5(1):27–37.
47. van Breugel JMM, Geschwind J-F, Mirpour S, Savic LJ, Zhang X, Duran R, et al. Theranostic Application of Lipiodol for Transarterial Chemoembolization in a VX2 Rabbit Liver Tumor Model. *Theranostics* (2019) 9(13):3674–86. doi: 10.7150/thno.32943
48. Chen J, Qian T, Zhang H, Wei C, Meng F, Yin H. Combining Dynamic Contrast Enhanced Magnetic Resonance Imaging and Microvessel Density to Assess the Angiogenesis After PEI in a Rabbit VX2 Liver Tumor Model. *Magn Reson Imaging* (2016) 34(2):177–82. doi: 10.1016/j.mri.2015.10.013
49. Shao H, Ni Y, Zhang J, Chen F, Dai X, Fan G, et al. Dynamic Contrast-Enhanced and Diffusion-Weighted Magnetic Resonance Imaging Noninvasive Evaluation of Vascular Disrupting Treatment on Rabbit Liver Tumors. *PLoS One* (2013) 8(12):e82649. doi: 10.1371/journal.pone.0082649
50. Zheng L, Li Y, Geng F, Zheng S, Yan R, Han Y, et al. Using Semi-Quantitative Dynamic Contrast-Enhanced Magnetic Resonance Imaging Parameters to Evaluate Tumor Hypoxia: A Preclinical Feasibility Study in a Maxillofacial VX2 Rabbit Model. *Am J Transl Res* (2015) 7(3):535–47.

51. Figini M, Zhou K, Pan L, Sun C, Wang B, Hu S, et al. Transcatheter Intra-Arterial Perfusion (TRIP)-MRI Biomarkers Help Detect Immediate Response to Irreversible Electroporation of Rabbit VX2 Liver Tumor. *Magn Reson Med* (2020) 84(1):365–74. doi: 10.1002/mrm.28104
52. Schmieder AH, Winter PM, Williams TA, Allen JS, Hu G, Zhang H, et al. Molecular MR Imaging of Neovascular Progression in the Vx2 Tumor With αvβ3-Targeted Paramagnetic Nanoparticles. *Radiology* (2013) 268(2):470–80. doi: 10.1148/radiol.13120789
53. Hansen SA, Fink MK, Upendran A, Besch-Williford CL, Livingston RS, Amos-Landgraf JM, et al. Delayed and Aberrant Presentation of VX2 Carcinoma in a Rabbit Model of Hepatic Neoplasia. *Comp Med* (2015) 65 (5):424–8.
54. Pascale F, Ghegediban S-H, Bedouet L, Namur J, Bonneau M, Verret V, et al. bFGF Up-Regulation Reduces Spontaneous Necrosis of VX2 Tumors Without Increasing Tumoral Microvascular Density. *Anticancer Res* (2016) 36 (7):3315–20.
55. Bize P, Duran R, Fuchs K, Dormond O, Namur J, Decosterd LA, et al. Antitumoral Effect of Sunitinib-Eluting Beads in the Rabbit VX2 Tumor Model. *Radiology* (2016) 280(2):425–35. doi: 10.1148/radiol.2016150361
56. Pascale F, Ghegediban S-H, Bonneau M, Bedouet L, Namur J, Verret V, et al. Modified Model of VX2 Tumor Overexpressing Vascular Endothelial Growth Factor. *J Vasc Interv Radiol* (2012) 23(6):809–17.e2. doi: 10.1016/j.jvir.2012.02.003
57. Kreuter KA, El-Abbadi N, Shbeeb A, Tseng L, Mahon SB, Narula N, et al. Development of a Rabbit Pleural Cancer Model by Using VX2 Tumors. *Comp Med* (2008) 58(3):287–93.
58. Esser AK, Schmieder AH, Ross MH, Xiang J, Su X, Cui G, et al. Dual-Therapy With αvβ3-Targeted Sn2 Lipase-Labile Fumagillin-Prodrug Nanoparticles and Zoledronic Acid in the Vx2 Rabbit Tumor Model. *Nanomedicine* (2016) 12(1):201–11. doi: 10.1016/j.nano.2015.10.003
59. Gehlot P, Shukla V, Gupta S, Makidon PE. Detection of ALDH1 Activity in Rabbit Hepatic VX2 Tumors and Isolation of ALDH1 Positive Cancer Stem Cells. *J Transl Med* (2016) 14:49. doi: 10.1186/s12967-016-0785-0
60. Mandic R, Dünne AA, Eikelkamp N, Ramaswamy A, Schulz S, Teymoortash A, et al. Expression of MMP-3, MMP-13, TIMP-2 and TIMP-3 in the VX2 Carcinoma of the New Zealand White Rabbit. *Anticancer Res* (2002) 22 (6A):3281–4.
61. Chen J, Ma L, Zhang N, Zhu Y, Zhang K, Xu Z, et al. Mesenchymal Stem Cells Promote Tumor Progression *via* Inducing Stroma Remodeling on Rabbit VX2 Bladder Tumor Model. *Int J Biol Sci* (2018) 14(9):1012–21. doi: 10.7150/ijbs.25200
62. Winter PM, Schmieder AH, Caruthers SD, Keene JL, Zhang H, Wickline SA, et al. Minute Dosages of Alpha(Nu)Beta3-Targeted Fumagillin Nanoparticles Impair Vx-2 Tumor Angiogenesis and Development in Rabbits. *FASEB J* (2008) 22(8):2758–67. doi: 10.1096/fj.07-103929
63. Sugimoto K, Moriyasu F, Kamiyama N, Metoki R, Iijima H. Parametric Imaging of Contrast Ultrasound for the Evaluation of Neovascularization in Liver Tumors. *Hepatol Res* (2007) 37(6):464–72. doi: 10.1111/j.1872-034X.2007.00060.x
64. Duan X-H, Li T-F, Zhou G-F, Han X-W, Zheng C-S, Chen P-F, et al. Transcatheter Arterial Embolization Combined With Radiofrequency Ablation Activates CD8(+) T-Cell Infiltration Surrounding Residual Tumors in the Rabbit VX2 Liver Tumors. *Onco Targets Ther* (2016) 9:2835–44. doi: 10.2147/OTT.S95973
65. Jin M-Z, Jin W-L. The Updated Landscape of Tumor Microenvironment and Drug Repurposing. *Signal Transduct Target Ther* (2020) 5(1):166. doi: 10.1038/s41392-020-00280-x
66. Makarova-Rusher OV, Medina-Echeverz J, Duffy AG, Greten TF. The Yin and Yang of Evasion and Immune Activation in HCC. *J Hepatol* (2015) 62 (6):1420–9. doi: 10.1016/j.jhep.2015.02.038
67. Verret V, Pascale FT, Marturano A, Ghegediban S, Wassef M, Namur J, et al. Molecular Biology Profile of VX2 Carcinoma in the Rabbit Liver. *J Vasc Intervent Radiol* (2012) 23(3):S96. doi: 10.1016/j.jvir.2011.12.285
68. Roy S, Coulon P-G, Prakash S, Srivastava R, Geertsema R, Dhanushkodi N, et al. Blockade of PD-1 and LAG-3 Immune Checkpoints Combined With Vaccination Restores the Function of Antiviral Tissue-Resident CD8+ TRM Cells and Reduces Ocular Herpes Simplex Infection and Disease in HLA Transgenic Rabbits. *J Virol* (2019) 93(18):e00827-19. doi: 10.1128/JVI.00827-19
69. Shah SA, Dickson JA. Effect of Hyperthermia on the Immunocompetence of VX2 Tumor-Bearing Rabbits. *Cancer Res* (1978) 38(10):3523–31.
70. Wissniowski TT, Hänsler J, Neureiter D, Frieser M, Schaber S, Esslinger B, et al. Activation of Tumor-Specific T Lymphocytes by Radio-Frequency Ablation of the VX2 Hepatoma in Rabbits. *Cancer Res* (2003) 63(19):6496–500.
71. Rossmann A, Mandic R, Heinis J, Hoffken H, Kussner O, Kinscherf R, et al. Intraperitoneal Oxidative Stress in Rabbits With Papillomavirus-Associated Head and Neck Cancer Induces Tumoricidal Immune Response That Is Adoptively Transferable. *Clin Cancer Res* (2014) 20(16):4289–301. doi: 10.1158/1078-0432.CCR-14-0677
72. Park W, Gordon AC, Cho S, Huang X, Harris KR, Larson AC, et al. Immunomodulatory Magnetic Microspheres for Augmenting Tumor-Specific Infiltration of Natural Killer (NK) Cells. *ACS Appl Mater Interf* (2017) 9(16):13819–24. doi: 10.1021/acsami.7b02258
73. Sugiyama Y, Saji S, Miya K, Fukada D, Umemoto T, Kunieda K, et al. Locoregional Therapy for Liver Metastases of Colorectal Cancer. *Gan To Kagaku Ryoho* (1996) 23(11):1433–6.
74. Hamamoto S, Okuma T, Yamamoto A, Kageyama K, Takeshita T, Sakai Y, et al. Radiofrequency Ablation and Immunostimulant OK-432: Combination Therapy Enhances Systemic Antitumor Immunity for Treatment of VX2 Lung Tumors in Rabbits. *Radiology* (2013) 267(2):405–13. doi: 10.1148/radiol.13120249
75. Hamamoto S, Okuma T, Yamamoto A, Kageyama K, Ueki A, Matsuoka T, et al. Combination Radiofrequency Ablation and Local Injection of the Immunostimulant Bacillus Calmette-Guérin Induces Antitumor Immunity in the Lung and at a Distant VX2 Tumor in a Rabbit Model. *J Vasc Interv Radiol* (2015) 26(2):271–8. doi: 10.1016/j.jvir.2014.09.002
76. Vivas I, Iribarren K, Lozano T, Cano D, Lasarte-Cia A, Chocarro S, et al. Therapeutic Effect of Irreversible Electroporation in Combination With Poly-ICLC Adjuvant in Preclinical Models of Hepatocellular Carcinoma. *J Vasc Interv Radiol* (2019) 30(7):1098–105. doi: 10.1016/j.jvir.2019.02.023
77. Shim JH, Park J-W, Kim JH, An M, Kong S-Y, Nam B-H, et al. Association Between Increment of Serum VEGF Level and Prognosis After Transcatheter Arterial Chemoembolization in Hepatocellular Carcinoma Patients. *Cancer Sci* (2008) 99(10):2037–44. doi: 10.1111/j.1349-7006.2008.00909.x
78. Yu H, Zhu G-Y, Xu R-Z, Niu H-Z, Lu Q, Li G-Z, et al. Arterial Embolization Hyperthermia Using As2O3 Nanoparticles in VX2 Carcinoma-Induced Liver Tumors. *PloS One* (2011) 6(3):e17926. doi: 10.1371/journal.pone.0017926
79. Huang Y-W, Zhou Y, Lan C-Y, Wang Y, Feng Y-L, Luo R-Z, et al. Tumor-Induced VEGF-C Overexpression in Retroperitoneal Lymph Nodes in VX2 Carcinoma-Bearing Rabbits. *Drug Des Devel Ther* (2015) 9:5949–56. doi: 10.2147/DDDT.S89810
80. Liang B, Zheng C, Feng G, Wu H, Wang Y, Zhao H, et al. Experimental Evaluation of Inhibitory Effect of 10-Hydroxycamptothecin on Hypoxia-Inducible Factor-1α Expression and Angiogenesis in Liver Tumors After Transcatheter Arterial Embolization. *J Vasc Interv Radiol* (2010) 21(10):1565–72. doi: 10.1016/j.jvir.2010.05.028
81. Liao X-F, Yi J-L, Li X-R, Deng W, Yang Z-F, Tian G. Angiogenesis in Rabbit Hepatic Tumor After Transcatheter Arterial Embolization. *World J Gastroenterol* (2004) 10(13):1885–9. doi: 10.3748/wjg.v10.i13.1885
82. Rhee TK, Young JY, Larson AC, Haines GK, Sato KT, Salem R, et al. Effect of Transcatheter Arterial Embolization on Levels of Hypoxia-Inducible Factor-1alpha in Rabbit VX2 Liver Tumors. *J Vasc Interv Radiol* (2007) 18(5):639–45. doi: 10.1016/j.jvir.2007.02.031
83. Johnson CG, Sharma KV, Levy EB, Woods DL, Morris AH, Bacher JD, et al. Microvascular Perfusion Changes Following Transarterial Hepatic Tumor Embolization. *J Vasc Interv Radiol* (2016) 27(1):133–41.e3. doi: 10.1016/j.jvir.2015.06.036
84. Zhang L, Liu F-Y, Fu J-X, Duan F, Fan Q-S, Wang M-Q. Hepatic Arterial Administration of Sorafenib and Iodized Oil Effectively Attenuates Tumor Growth and Intrahepatic Metastasis in Rabbit VX2 Hepatocellular Carcinoma Model. *Int J Clin Exp Pathol* (2014) 7(11):7775–81.
85. Zhou C, Shi Q, Liu J, Huang S, Yang C, Xiong B. Effect of Inhibiting Tumor Angiogenesis After Embolization in the Treatment of HCC With Apatinib-Loaded P(N-Isopropyl-Acrylamide-Co-Butyl Methyl Acrylate) Temperature-Sensitive Nanogel. *J Hepatocell Carcinoma* (2020) 7:447–56. doi: 10.2147/JHC.S282209

86. Li X, Yu H, Huang Y, Chen Y, Wang J, Xu L, et al. Preparation of Microspheres Encapsulating Sorafenib and Catalase and Their Application in Rabbit VX2 Liver Tumor. *BioMed Pharmacother* (2020) 129:110512. doi: 10.1016/j.biopha.2020.110512
87. Landras A, Reger de Moura C, Jouenne F, Lebbe C, Menashi S, Mourah S. CD147 Is a Promising Target of Tumor Progression and a Prognostic Biomarker. *Cancers (Basel)* (2019) 11(11):E1803. doi: 10.3390/cancers11111803
88. Wang Y, Yuan L, Yang X-M, Wei D, Wang B, Sun X-X, et al. A Chimeric Antibody Targeting CD147 Inhibits Hepatocellular Carcinoma Cell Motility *via* FAK-PI3K-Akt-Girdin Signaling Pathway. *Clin Exp Metastasis* (2015) 32 (1):39–53. doi: 10.1007/s10585-014-9689-7
89. Ke S, Ding X, Kong J, Gao J, Wang S, Cheng Y, et al. Low Temperature of Radiofrequency Ablation at the Target Sites can Facilitate Rapid Progression of Residual Hepatic VX2 Carcinoma. *J Transl Med* (2010) 8:73. doi: 10.1186/1479-5876-8-73
90. Shi Y-L, Xu T, Li L-P, Chen X-P. Over-Expression of VEGF and MMP-9 in Residual Tumor Cells of Hepatocellular Carcinoma After Embolization With Lipidol. *J Huazhong Univ Sci Technolog Med Sci* (2013) 33(1):90–5. doi: 10.1007/s11596-013-1077-z
91. Bhaskar V, Fox M, Breinberg D, Wong MH-L, Wales PE, Rhodes S, et al. Volociximab, a Chimeric Integrin Alpha5beta1 Antibody, Inhibits the Growth of VX2 Tumors in Rabbits. *Invest New Drugs* (2008) 26(1):7–12. doi: 10.1007/s10637-007-9078-z
92. Liang Y, Feng Q, Hong J, Feng F, Sang Y, Hu W, et al. Tumor Growth and Metastasis can be Inhibited by Maintaining Genomic Stability in Cancer Cells. *Front Med* (2015) 9(1):57–62. doi: 10.1007/s11684-015-0389-8

Conflict of Interest: FP, SG, and JN are paid employees of Archimmed SARL. J-PP, MW, AL, and JN are shareholders of Archimmed.

The remaining authors declare that the research was conducted in the absence of any commercial or financial relationships that could be construed as a potential conflict of interest.

Publisher's Note: All claims expressed in this article are solely those of the authors and do not necessarily represent those of their affiliated organizations, or those of the publisher, the editors and the reviewers. Any product that may be evaluated in this article, or claim that may be made by its manufacturer, is not guaranteed or endorsed by the publisher.

frontiers | Frontiers in Oncology

SYSTEMATIC REVIEW
published: 24 June 2022
doi: 10.3389/fonc.2022.907076

Peritumoral Imaging Manifestations on Gd-EOB-DTPA-Enhanced MRI for Preoperative Prediction of Microvascular Invasion in Hepatocellular Carcinoma: A Systematic Review and Meta-Analysis

Ying Wu[1,2†], *Meilin Zhu*[1†], *Yiming Liu*[3], *Xinyue Cao*[1], *Guojin Zhang*[1] *and Longlin Yin*[1*]

[1] Department of Radiology, Sichuan Provincial People's Hospital, University of Electronic Science and Technology of China, Chengdu, China, [2] Department of Radiology, Affiliated Hospital of North Sichuan Medical College, Nanchong, China, [3] Department of Radiology, Affiliated Hospital of Southwest Medical University, Luzhou, China

Purpose: The aim was to investigate the association between microvascular invasion (MVI) and the peritumoral imaging features of gadolinium ethoxybenzyl DTPA-enhanced magnetic resonance imaging (Gd-EOB-DTPA-enhanced MRI) in hepatocellular carcinoma (HCC).

Methods: Up until Feb 24, 2022, the PubMed, Embase, and Cochrane Library databases were carefully searched for relevant material. The software packages utilized for this meta-analysis were Review Manager 5.4.1, Meta-DiSc 1.4, and Stata16.0. Summary results are presented as sensitivity (SEN), specificity (SPE), diagnostic odds ratios (DORs), area under the receiver operating characteristic curve (AUC), and 95% confidence interval (CI). The sources of heterogeneity were investigated using subgroup analysis.

Results: An aggregate of nineteen articles were remembered for this meta-analysis: peritumoral enhancement on the arterial phase (AP) was described in 13 of these studies and peritumoral hypointensity on the hepatobiliary phase (HBP) in all 19 studies. The SEN, SPE, DOR, and AUC of the 13 investigations on peritumoral enhancement on AP were 0.59 (95% CI, 0.41–0.58), 0.80 (95% CI, 0.75–0.85), 4 (95% CI, 3–6), and 0.73 (95% CI, 0.69–0.77), respectively. The SEN, SPE, DOR, and AUC of 19 studies on peritumoral hypointensity on HBP were 0.55 (95% CI, 0.45–0.64), 0.87 (95% CI, 0.81–0.91), 8 (95% CI, 5–12), and 0.80 (95% CI, 0.76–0.83), respectively. The subgroup analysis of two imaging features identified ten and seven potential factors for heterogeneity, respectively.

Conclusion: The results of peritumoral enhancement on the AP and peritumoral hypointensity on HBP showed high SPE but low SEN. This indicates that the peritumoral imaging features on Gd-EOB-DTPA-enhanced MRI can be used as a

OPEN ACCESS

Edited by:
Xiankai Sun,
University of Texas Southwestern Medical Center, United States

Reviewed by:
Alessandro Granito,
University of Bologna, Italy
Zoltan Kovacs,
University of Texas Southwestern Medical Center, United States

***Correspondence:**
Longlin Yin
yinlonglin@163.com

†These authors have contributed equally to this work and share first authorship

Specialty section:
This article was submitted to Cancer Imaging and Image-directed Interventions, a section of the journal Frontiers in Oncology

Received: *29 March 2022*
Accepted: *25 May 2022*
Published: *24 June 2022*

Citation:
Wu Y, Zhu M, Liu Y, Cao X, Zhang G and Yin L (2022) Peritumoral Imaging Manifestations on Gd-EOB-DTPA-Enhanced MRI for Preoperative Prediction of Microvascular Invasion in Hepatocellular Carcinoma: A Systematic Review and Meta-Analysis. Front. Oncol. 12:907076. doi: 10.3389/fonc.2022.907076

noninvasive, excluded diagnosis for predicting hepatic MVI in HCC preoperatively. Moreover, the results of this analysis should be updated when additional data become available. Additionally, in the future, how to improve its SEN will be a new research direction.

Keywords: Gd-EOB-DTPA-enhanced MRI, microvascular invasion, hepatocellular carcinoma, peritumoral enhancement, peritumoral hypointensity, meta-analysis

1 INTRODUCTION

Hepatocellular carcinoma (HCC) is considered the global third highest cause of cancer mortality, ranking second among men (1). However, recurrence is common after surgical treatment. In addition, 5-year recurrence rates reach 70% after surgical resection and 35% after liver transplantation (2). In addition, microvascular invasion (MVI) has been identified as a possible predictor of early recurrence of HCC (3). MVI is considered to be the invasion of tumor cells into the vascular endothelium, which can only be seen under a microscope but not macroscopically. The presence of MVI suggests the aggressive behavior and poor survival outcome of HCC (4). A preoperative risk assessment of HCC patients by surgeons is of great importance. If radical hepatectomy is undertaken in patients at high risk for MVI, larger margins may be preferred; if liver transplantation is performed, the survival outcome of the patient is severely compromised (5). Histopathological examination is the gold standard for diagnosing MVI. However, histopathological examination is an invasive procedure that necessitates extensive sampling. Therefore, a preoperative, noninvasive test for detecting MVI would be extremely helpful in choosing the best treatment options for HCC patients (6). Both clinicians and patients benefit from preoperative noninvasive prediction of MVI.

Gadolinium ethoxybenzyl DTPA-enhanced (Gd-EOB-DTPA-enhanced) MRI uses a liver-specific, intracellular MRI contrast agent called Primovist or Eovist, which is distributed differently in various phases during the course of an MRI. In the arterial phase (AP), Primovist is distributed in vascular and extracellular regions. Gradually, it is distributed in bile ducts and hepatocytes in the hepatobiliary phase (HBP) (7). Gd-EOB-DTPA provides insight into hemodynamic changes in the liver and liver tumors. Gd-EOB-DTPA-enhanced MRI is not only helpful in the diagnosis of HCC but has also been widely applied to the preoperative evaluation and prognostic evaluation of HCC (8, 9). In addition, gadobenate dimeglumine (Gd-BOPTA) is a liver-specific contrast agent. The T1 relaxivity at 1.5T for Primovist and Gd-BOPTA is 6.5–7.3 and 6–6.6, respectively (10). Moreover, the protein-binding capabilities of Gd-BOPTA are weaker than that of Gd-EOB-DTPA, and its uptake by hepatocytes is about one-tenth of the amount of Gd-EOB-DTPA, which might be related to the difference in the lipophilicity of the benzene ring in Gd-BOPTA and the EOB group in Gd-EOB-DTPA (10–12).

Recently, some studies have focused on the imaging findings of HCC tumors themselves to predict the relationship of MVI (13–15). However, based on the altered hemodynamics, peritumoral tissue is the first tissue that is affected by MVI. It is worthy to explore whether peritumoral tissue can directly reflect the relationship between tumor and MVI. Moreover, a high-quality meta-analysis showed that peritumoral enhancement on AP and peritumoral hypointensity on HBP were associated with MVI but with poor diagnostic accuracy (16). However, the number of included literatures in the publication was small, with only four articles about peritumoral hypointensity on HBP, and 2 studies used CT to assess peritumoral enhancement (16). Moreover, the research did not use Primovist as a contrast agent. However, Ahn SJ et al. and Ahn, S Y. et al. found that peritumoral enhancement on AP and peritumoral hypointensity on HBP did not show a statistically significant association with MVI ($P > 0.05$) (17, 18). In addition, the reported SEN and SPE of peritumoral hypointensity on HBP varied widely—0.38–0.81 and 0.56–0.97, respectively (8, 9, 17–33). Yet, as the peritumoral microenvironment has received more attention in recent years, papers on the link between peritumoral imaging and MVI have been updated. Therefore, it is critical to determine the actual accuracy of the two imaging features for predicting the presence of MVI in HCC. As a result, the value of assessing the association between peritumoral imaging features and MVI by taking advantage of Gd-EOB-DTPA-enhanced MRI remains to be investigated.

On the whole, the predictive value of peritumoral enhancement on AP and peritumoral hypointensity on HBP on Gd-EOB-DTPA-enhanced MRI for MVI in HCC patients remains controversial. Furthermore, there has been no systematic evaluation of the diagnostic significance of these imaging findings of preoperative Gd-EOB-DTPA-enhanced MRI for MVI. Hence, this research was performed to determine the diagnostic performance of these features for MVI in HCC patients.

2 METHODS

2.1 Literature Search Strategy

This study was conducted in accordance with the Preferred Reporting Items for Systematic Reviews and Meta-Analyses guidelines (34). Up until Feb 24, 2022, the PubMed, Embase, and Cochrane Library databases were carefully searched for relevant material by two researchers. Medical subject headings, free words, and their variations were employed for retrieval. Literature retrieval has no language restrictions. The full search strategy is described in the Supplementary material.

2.2 Inclusion and Exclusion Criteria

The criteria for selecting the subjects were as follows: 1) studies on preoperative MVI prediction with peritumoral tissue on

disodium gadoxetate–enhanced MRI; 2) studies without treatment before curative hepatectomy; 3) histopathologically proven primary HCC; and 4) studies providing sufficient data to create a diagnostic 2 × 2 table. Further, the following circumstances would be excluded: 1) studieses that did not satisfy any of the aforementioned inclusion criteria; 2) reviews, letters, and reports; 3) studies for involving macrovascular invasion; and 4) studies for which we were unable to get the full text.

2.3 Quality Assessment and Data Extraction

This paper assessed the methodological quality of each study, applying the Quality Assessment of Diagnostic Accuracy Studies (QUADAS-2) tool (35). In addition, a comprehensive evaluation of the bias risk for each research was conducted, including patient selection, index test, reference standard, flow and timing, and applicability concerns. Meanwhile, two researchers independently extracted the data and cross-checked them to arrive at an agreement. In addition, the extracted data from each included study consisted of the first author, year of publication, region, lesion size, sample size of tumors and patients, single tumors or multiple, interval between imaging and surgery, magnetic field strengths, preoperative anti-tumor therapy, microvascular invasion, macrovascular invasion, and blindness to reference and index test. Moreover, the third researcher collated the extracted data as true positives, false positives, false negatives, and true negatives to form a 2 × 2 diagnostic table.

2.4 Definition of Peritumoral Enhancement and Peritumoral Hypointensity

Each study reached a consensus on the definition of peritumoral enhancement on AP and peritumoral hypointensity on HBP. Peritumoral enhancement on AP is defined as a polygonal-shaped or crescent-shaped enhancement outside the cancer edge during the AP, which becomes isointense to background hepatic parenchyma in the delayed phase (21). The definition of peritumoral hypointensity on HBP is considered as a flame-like or wedge-shaped hypointense region of hepatic parenchyma outside the edge of tumor during the HBP (23).

2.5 Statistical Analysis

Review Manager 5.4.1, Meta-DiSc 1.4, and Stata16.0 were used for data analysis and statistics. The evaluation indexes of diagnostic efficiency include SEN, SPE, positive likelihood ratio (PLR), negative likelihood ratio (NLR), diagnostic odds ratio (DOR), and 95% confidence interval (CI). Further, the diagnostic precision of peritumoral imaging features on Gd-EOB-DTPA-enhanced MRI for the prediction of MVI was analyzed using the area under the receiver operating characteristic curve (AUC). The Spearman correlation coefficient in Meta-DiSc1.4 was adopted to evaluate heterogeneity caused by the threshold effect. There was a significant threshold effect, as evidenced by a strong positive association ($P < 0.05$) (36). The heterogeneity of studies was determined by applying Cochran's Q test and I^2 analysis and regarded as $P < 0.1$ or $I^2 > 50\%$ (37). In the case of notable heterogeneity, the random-effects coefficient binary regression model was utilized; otherwise, the fixed-effects coefficient binary regression model was employed (38). In addition, the causes of heterogeneity were investigated by subgroup analysis; the stability of this meta-analysis was estimated by sensitivity analysis, and the publication bias was detected by Deeks' funnel plot asymmetry tests. If the slope coefficient was greater than zero, publication bias was suspected ($P < 0.05$) (39).

3 RESULTS

3.1 Literature Search and Study Selection

Following the research approach, 168 publications were obtained *via* PubMed, Embase, and Cochrane Library databases. Forty-five articles were removed as duplicates (**Figure 1**). Moreover, 91 articles were eliminated after a review of titles and abstracts on the basis of the following reasons: publications were not related to the prediction of MVI or were reviews or report or letters, leaving 32 studies for further screening. After checking for the full text, a review was excluded, and 3 investigations were eliminated due to the unavailability of the full text, 3 for not having valid data, 5 for not using gadoxetic acid as a contrast medium, and one for involving macrovascular invasion. Finally, a total of nineteen articles were involved in this paper and their characteristics are listed in **Table 1**.

3.2 Study Characteristics and Quality Assessment

A total of nineteen articles were included, and all studies examined peritumoral hypointensity on HBP, and 13 studies examined peritumoral enhancement on AP. Furthermore, all articles were retrospective studies. The studies were published between 2011 and 2022. Among these studies, 13 were from China, 5 from South Korea, and 1 from Japan. All 19 studies included 2,699 HCC patients with 2,741 tumors, of which 916 tumors were pathologically diagnosed as MVI-positive and 1,825 tumors as MVI-negative.

Figure 2 depicts the quality of the included investigations as assessed by QUADAS-2 guidelines. As it was not clear whether patients received other treatments before the operation in 2 studies (19, 28), the risk bias arising from patient selection in those studies was determined to be "unclear." Due to the fact that the seven studies did not mention whether there was macrovascular invasion, we also marked it as an unclear risk of patient selection bias (8, 17–19, 24, 27, 28). Moreover, because the lesion size was limited in 4 studies (22, 24, 28, 33), the patient selection bias was considered as "high." Six studies did not mention whether the radiologists were blinded to the pathology data (9, 21, 23, 24, 27, 29) and were therefore marked as unclear risk of index bias domain. The interval between imaging and surgery was unclear in 2 studies (23, 28); hence, the risk bias arising from flow and timing was determined to be "unclear." All tumors were subjected to MRI examination and a histopathological test. Although most articles did not explicitly mention that "pathologists were blinded to the imaging data," they did elaborate on the pathological findings. Accordingly, the risk bias arising from the reference standard was determined to be

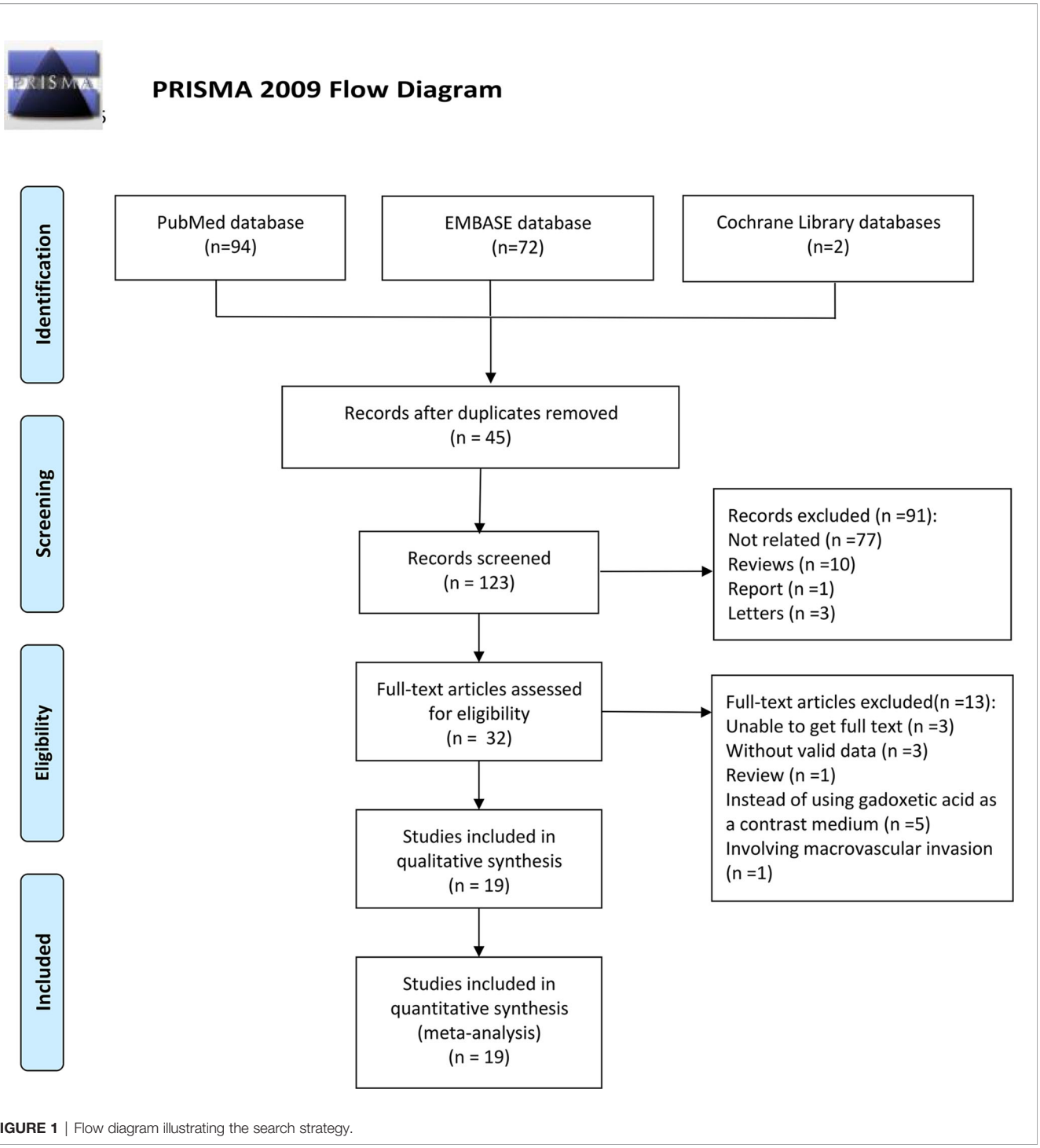

FIGURE 1 | Flow diagram illustrating the search strategy.

"unclear," but in this research, we considered the applicability concerns of reference standard as "low concern."

3.3 Imaging Methods

The characteristics of the imaging methods for the included studies are listed in **Table 2**. Ten studies reported MRI performed with a field strength of 3T, 4 studies used both 1.5T and 3T MRI systems, and 5 studies used 1.5T. In addition, ten articles used Siemens MR devices, while the rest used Philips/GE or two and three devices. Moreover, the scan acquisition time of the AP of 10 studies was performed at 20–35 s following the contrast injection. Three studies scanned AP seven seconds after the contrast media had arrived at the distal thoracic aorta and one when the contrast medium was visible at the level of the celiac trunk of the abdominal aorta. Additionally, the remaining five articles did not illustrate the scan acquisition time of AP. In all studies, the scan acquisition time for

TABLE 1 | Characteristics of the 19 included studies.

Study	Year	Region	Mean age (years)	Patients/Lesions (n)	Lesions	Lesions size	IBIS (days)	PEAP (n)		PHHBP (n)		MVI (n)	
								+	−	+	−	+	−
Ahn SJ. et al (17)	2019	South Korea	56.71	179 (179)	S	NR	≤30	64	115	61	118	68	111
Ahn SY. et al (18)	2015	South Korea	51.94	51 (78)	S/M	NR	≤63	10	68	4	74	18	60
Chen PP. et al (20)	2019	China	58	70 (77)	S/M	NR	≤14	15	62	20	57	27	50
Chen Y. et al (21)	2021	China	51.5	269 (269)	U	NR	≤14	73	196	105	164	111	158
Chong HH. et al (22)	2020	China	54.22	356 (356)	S	≤5 cm	≤30	74	282	54	302	90	266
Chou YC. et al (23)	2019	China	64.76	114 (114)	S	NR	U	27	87	34	80	39	75
Dong SY. et al (24)	2022	China	54.66	214 (214)	S	≤3 cm	≤30	79	135	75	139	49	165
Feng ST. et al (9)	2019	China	54.8	160 (160)	S/M	NR	≤30	44	116	48	112	62	98
Huang M. et al (8)	2018	China	52.2	60 (66)	S/M	NR	≤30	21	45	26	40	17	49
Kim KA. et al (19)	2012	South Korea	55	104 (104)	S/M	NR	≤30	NM	NM	26	78	60	44
Lee S. et al (25)	2020	South Korea	54	122 (122)	S/M	NR	≤30	NM	NM	21	101	21	101
Lu XY. et al (26)	2020	China	57.5	102 (102)	U	NR	≤30	NM	NM	26	76	31	71
Nishie A. et al (27)	2014	Japan	67	61 (61)	S/M	NR	≤30	NM	NM	25	36	25	36
Shin SK. et al (28)	2017	South Korea	57	126 (126)	S	≤5 cm	U	NM	NM	15	111	29	97
Wang LL. et al (29)	2021	China	54.22	113 (113)	S/M	NR	≤14	NM	NM	67	46	50	63
Yang L. et al (30)	2019	China	55.5	208 (208)	S/M	NR	≤30	67	141	30	178	53	155
Yang Y. et al (31)	2021	China	52.4	201 (201)	S	NR	≤30	111	90	82	119	111	90
Zhang K. et al (32)	2022	China	56.4	129 (129)	S	NR	≤30	49	80	43	86	36	93
Zhou M. et al (33)	2021	China	55	60 (62)	S/M	≤3 cm	≤30	14	48	12	50	19	43

IBIS, interval between imaging and surgery; PEAP, peritumoral enhancement on arterial phase; PHHBP, peritumoral hypointensity on hepatobiliary phase; MVI, microvascular invasion; +, positive; -, negative; S, single; M, multiple; U, unclear; NR, no restriction; NM, not mentioned.

HBP was 20 min after the contrast injection. Moreover, the injection dose of Gd-EOB-DTPA was 0.025 mmol/kg body weight in 11 studies and 0.1 ml/kg in 5 studies, and one study injected the contrast in the dose of 0.2 ml/kg. One study used a bolus injection of 10 ml. In addition, one study did not specify the dose of contrast injection. The injection rate was 1 ml/s in 6 studies, 1.5 ml/s in 2 studies, and 1.0–1.5 ml/s in 2 studies. Aditionally, one article injected the contrast agent at a rate of 2 ml/s. The remaining studies did not mention the injection rate.

3.4 Accuracy of Peritumoral Imaging Features of HCC for Predicting MVI

3.4.1 Peritumoral Enhancement on AP

Thirteen studies assessed the relationship between peritumoral enhancement on AP with Gd-EOB-DTPA-enhanced MRI and MVI (8, 9, 17, 18, 20–24, 30–33), including 2,071 HCC patients with 2,113 tumors. Of 2,113 tumors, 700 were pathologically diagnosed as MVI-positive (356 tumors with peritumoral enhancement on AP and 344 tumors without) and 1,413 as MVI-negative (292 tumors with peritumoral enhancement on AP and 1,121 tumors without). The Spearman correlation coefficient was 0.531 (P = 0.062), which indicated that threshold effect–derived heterogeneity was not present. The results of Cochran's Q test and I^2 analysis (P < 0.001, I^2 = 95%) indicated that there was substantial heterogeneity. The pooled SEN was 0.50 (95% CI, 0.41–0.58), and the pooled SPE was 0.80 (95% CI, 0.75–0.85) (**Figure 3**). Moreover, the values of pooled PLR, NLR, and DOR were 2.5 (95% CI, 2.0–3.2), 0.63 (95% CI, 0.54–0.73), and 4 (95% CI, 3–6), respectively. In addition, the SROC curve was plotted (**Figure 4**), resulting in an AUC of 0.73 (95% CI, 0.69–0.77).

3.4.2 Peritumoral Hypointensity on HBP

All 19 studies (8, 9, 17–33) provided the relevant data of peritumoral hypointensity on HBP to predict MVI in HCC with disodium gadoxetate–enhanced MRI, including 2,699 HCC patients with 2,741 tumors. Of 2,741 tumors, 916 were pathologically diagnosed

FIGURE 2 | Methodological quality summary of all included studies by using Quality Assessment of Diagnostic Accuracy Studies.

as MVI-positive (500 tumors with peritumoral hypointensity on HBP and 416 tumors without) and 1,825 as MVI-negative (274 tumors with peritumoral hypointensity on HBP and 1,551 tumors without). Additionally, the Spearman correlation coefficient was 0.318 ($P = 0.185$), indicating the absence of threshold effect–derived heterogeneity. There was, however, significant heterogeneity among the included articles ($P < 0.001$, $I^2 = 98\%$). The results of pooled SEN and SPE were 0.55 (95% CI, 0.45–0.64) and 0.87 (95% CI, 0.81–0.91), respectively (**Figure 5**). In addition, the pooled PLR, NLR, and DOR, separately, were 4.1 (95% CI, 3.0–5.7), 0.52 (95% CI, 0.43–0.63), and 8 (95% CI, 5–12). In addition, the AUC was 0.80 (95% CI, 0.76–0.83) (**Figure 6**).

3.5 Subgroup Analysis

The causes of pooled variability were investigated using subgroup analysis. Based on clinical experience and the classification of basic information from the included literature, subgroups were formed as follows: 1) region (China as "1," others as "0"); 2) the mean age of

TABLE 2 | Characteristics of imaging methods.

Study	MFS (T)	Scanners	Scan acquisition time		Doses of contrast agent	Injection flow rate
			AP	HBP		
Ahn SJ. et al (17)	1.5/3	GE/Siemens/ Philips	Seven seconds after the contrast media had arrived at the distal thoracic aorta	20 min*	0.025 mmol/kg	1.5 ml/s
Ahn SY. et al (18)	1.5/3	GE/Siemens	Seven seconds after the contrast media had arrived at the distal thoracic aorta	20 min*	0.025 mmol/kg	1.5 ml/s
Chen PP. et al (20)	3	Philips	20 s*	20 min*	0.1 ml/kg	1.0–1.5 ml/s
Chen Y. et al (21)	3	Siemens	NM	20 min*	0.2 ml/kg	1 ml/s
Chong HH. et al (22)	1.5	Siemens	20–30 s*	20 min*	0.025 mmol/kg	NM
Chou YC. et al (23)	1.5	Siemens	When the contrast medium was visible at the level of the celiac trunk of the abdominal aorta.	20 min*	Bolus injection of 10 ml	1 ml/s
Dong SY. et al (24)	1.5	Siemens	20–30 s*	20 min*	0.025 mmol/kg	NM
Feng ST. et al (9)	3	Siemens	30–35 s*	20 min*	0.1 ml/kg	1 ml/s
Huang M. et al (8)	3	Siemens	NM	20 min*	NM	NM
Kim KA. et al (19)	3	Siemens	NM	10–20 min*	0.025 mmol/kg	2.0 ml/s
Lee S. et al (25)	1.5/3	Siemens/ Philips	20–35 s*	20 min*	0.025 mmol/kg	1 ml/s
Lu XY. et al (26)	3	Philips	20 s*	10 and 20 min*	0.1 ml/kg	1.0–1.5 ml/s
Nishie A. et al (27)	1.5	Philips	NM	20 min*	0.1 ml/kg (total amount: 4.5–8 ml)	NM
Shin SK. et al (28)	3	Siemens	Seven seconds after the contrast media had arrived at the distal thoracic aorta	20 min*	0.025 mmol/kg	NM
Wang LL. et al (29)	3	Siemens	20–30 s*	20 min*	0.025 mmol/kg	1 ml/s
Yang L. et al (30)	1.5	Siemens	20–30 s*	20 min*	0.025 mmol/kg	NM
Yang Y. et al (31)	1.5/3	GE	20–35 s*	20 min*	0.025 mmol/kg	NM
Zhang K. et al (32)	3	Philips	NM	20 min*	0.025 mmol/kg	NM
Zhou M. et al (33)	3	Philips	25 s*	20 min*	0.1 ml/kg	1 ml/s

**This acquisition time is defined as after contrast media injection. MFS, magnetic field strength; AP, arterial phase; HBP, hepatobiliary phase; NM, no specific time point was mentioned.*

included patients (≥55 years as "1," <55 years as "0"); 3) magnetic field strength (only 3T as "1," 1.5T or mixed as "0"); 4) MRI unit (Siemens as "1," Philips/GE or mixed as "0"); 5) the lesion size of HCC (no restriction as "1," ≤5 cm as "0"); 6) number of included tumors (≥100 as "1," <100 as "0"); 7) only a single HCC (yes as "1," multiple or mixed as "0"); 8) interval between imaging and surgery (≤30 days as "1," >30 days as "0"); 9) without macrovascular invasion (yes as "1," unclear as "0"); 10) blind to pathological

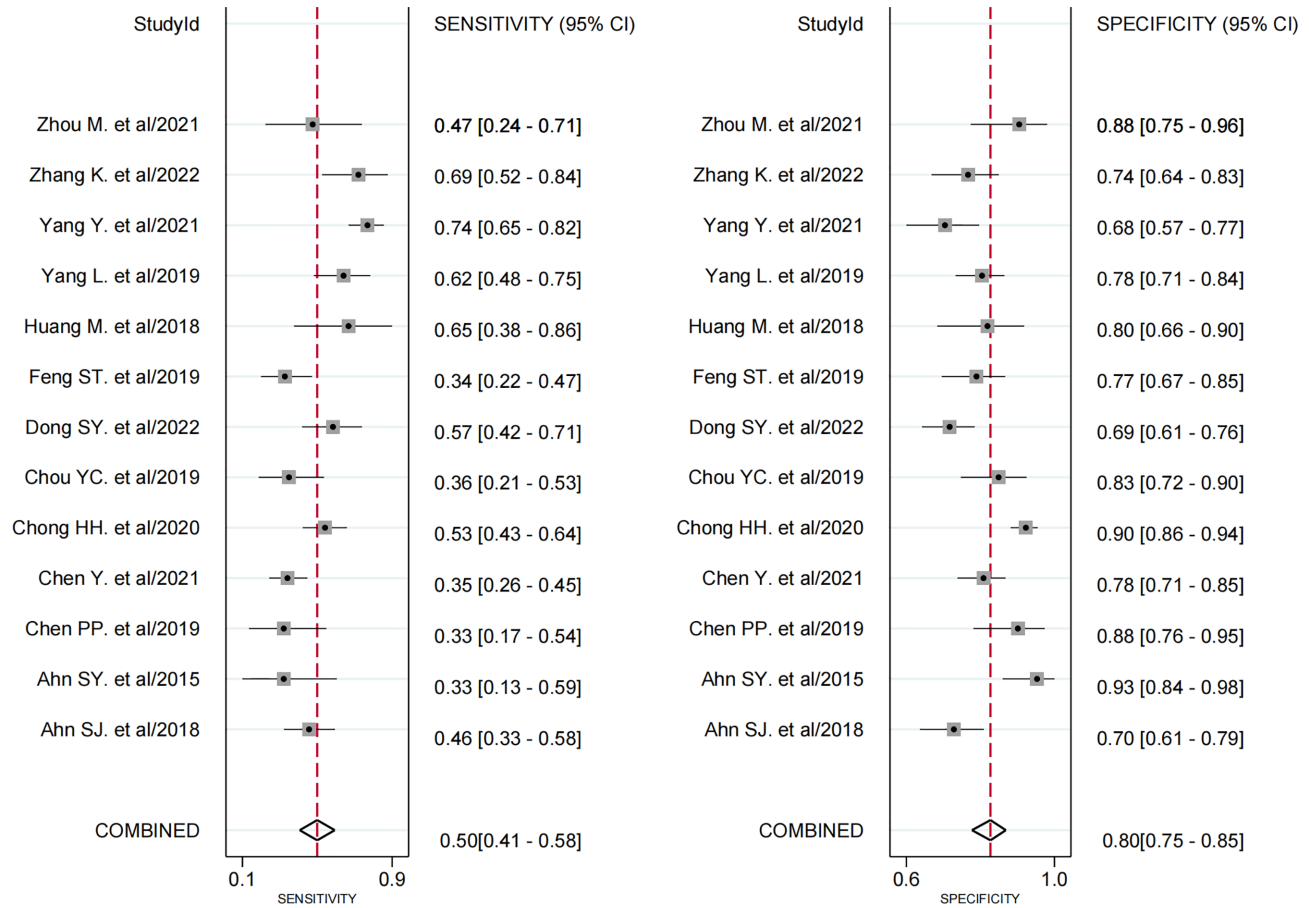

FIGURE 3 | Forest plots demonstrate the pooled sensitivity and specificity of peritumoral enhancement on the arterial phase. The 95% CI are shown around point estimates and the pooled result.

outcomes (yes as "1," unclear as "0"); and 11) blind to imaging diagnosis (yes as "1," unclear as "0").

Tables 3 and **4** present the outcomes of the subgroup analysis. Except for blindness to the index test during the pathological test, the above ten covariates were major determinants in causing heterogeneity, according to the results of peritumoral enhancement on AP ($P < 0.05$). Additionally, in terms of peritumoral hypointensity on HBP, the findings demonstrated that the region, mean age of included patients, magnetic field strength, MRI unit, number of included tumors, and only a single HCC, as well as the interval between imaging and surgery, are significant sources of heterogeneity ($P < 0.05$).

3.6 Sensitivity Analysis and Publication Bias

The results of sensitivity analysis, performed for the two imaging features by eliminating included articles one by one, revealed that none of the articles had any significant effect on the pooled results. There was no significant publication bias in Deeks' funnel plot asymmetry test of peritumoral enhancement on AP ($P = 0.73$) (**Figure 7A**) and peritumoral hypointensity on HBP ($P = 0.58$) (**Figure 7B**).

4 DISCUSSION

MVI is a risk factor for HCC recurrence, and the preoperative noninvasive prediction of MVI remains challenging. In our meta-analysis, based on peritumoral imaging findings, the results revealed that both peritumoral enhancement on AP and peritumoral hypointensity on HBP had high SPE but low SEN, which indicated that Gd-EOB-DTPA-enhanced MRI is helpful as a noninvasive, excluded diagnosis for predicting MVI in HCC preoperatively.

The relationship between peritumoral enhancement and the presence of MVI could be understood as that corona enhancement is a hemodynamic perfusion change due to disturbed portal venous drainage (40–42). Furthermore, the reasons why the peritumoral signal was low during HBP could be explained as follows: the occlusion of the intrahepatic portal

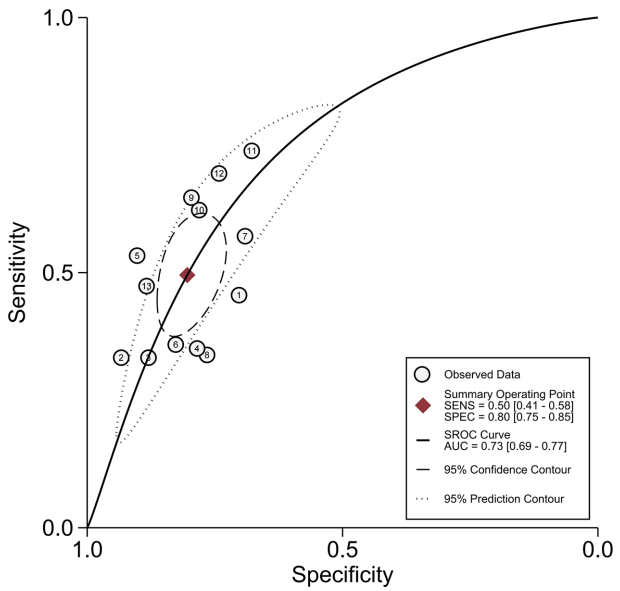

FIGURE 4 | Summary receiver operating characteristic curves of peritumoral enhancement on the arterial phase.

vein and insufficient compensation of the hepatic arterial flow lead to hepatic parenchyma injury, edema, hepatocyte depletion, and fibrosis (43). Moreover, previous articles have confirmed a positive correlation between the enhancement ratio of HCCs in the HBP of Primovist-enhanced MRI and the expression of organic anion–transporting polypeptide (OATPs) and multidrug-resistant proteins (MRPs); of note, gadoxetic acid disodium is absorbed by OATP8 and excreted by MRP3 (44, 45). Additionally, tumor invasion into small portal vein branches probably leads to hemodynamic perfusion changes and then affects the expression of OATP8 and MRP3 in hepatocytes, which may have an impact on hepatic function and decrease gadoxetic acid uptake into hepatocytes near tumors, leading to peritumoral hypointensity on HBP (19, 23).

The preoperative imaging of peritumoral tissue showing MVI has been applied to conventional CT and MRI. However, Chou CT et al. found that peritumoral enhancement on CT was not a significant risk factor for MVI (46). Chun Yang et al. also claimed that peritumoral enhancement did not show a statistically significant association with MVI ($P > 0.05$), when performing MRI scans using non-hepatocyte-specific contrast agents, called Magnevist (47). However, in our study, peritumoral enhancement on Gd-EOB-DTPA-enhanced MRI had an association with MVI and had a high SPE of 87%. This may be related to the imaging principles of CT and non-hepatocyte-specific contrast agents. Moreover, since the drainage of contrast from the tumor vein to the peritumoral parenchymal sinusoids and portal venules is an extremely transient process, it inevitably causes transient and severe respiratory motion. In addition, respiratory motion artifacts affect all dynamic phases, especially during the arterial phase (48). Additionally, Wybranski C et al. suggested that Gd-EOB-DTPA-related respiratory motion could not be improved by a series of standard pre-scan patient preparations including breath-holding training (48). This might be the reason why peritumoral enhancement had a low SEN. As a result, Kim H et al. proposed that a more accurate assessment of peritumoral enhancement should be done by a multi-arterial phase study (49). Although an SEN of 50% of peritumoral enhancement in the present study is low, it has been greatly improved compared with a previous meta-analysis that included traditional CT (a pooled SEN of 0.29) (16). It is undeniable that Gd-EOB-DTPA-enhanced MRI has some advantages in detecting MVI. However, peritumoral enhancement is more often seen in hypervascular progressed HCC. While peritumoral enhancement was not present in many hypovascular HCCs, it is reported that the double hypointensity in the portal/venous and HBP were highly suggestive of hypovascular HCC. However, the diagnostic performance of double hypointensity for MVI has not been reported; therefore, it needs further investigation in the future (50).

There were few studies performed to detect MVI utilizing the peritumoral tissue imaging performance of Gd-EOB-DTPA-enhanced MRI. However, a study conducted by Ahn SY et al. (18) found no significant correlation between peritumoral hypointensity on HBP and MVI ($P > 0.05$). These authors explained that peritumoral hypointensity was not a common observation (it was found in 25% of HCCs) and attributed this discrepancy to the differences in patient populations, small sample size, and low SEN (38.3%) in the research of Kim KA et al. (19). However, in present study, the

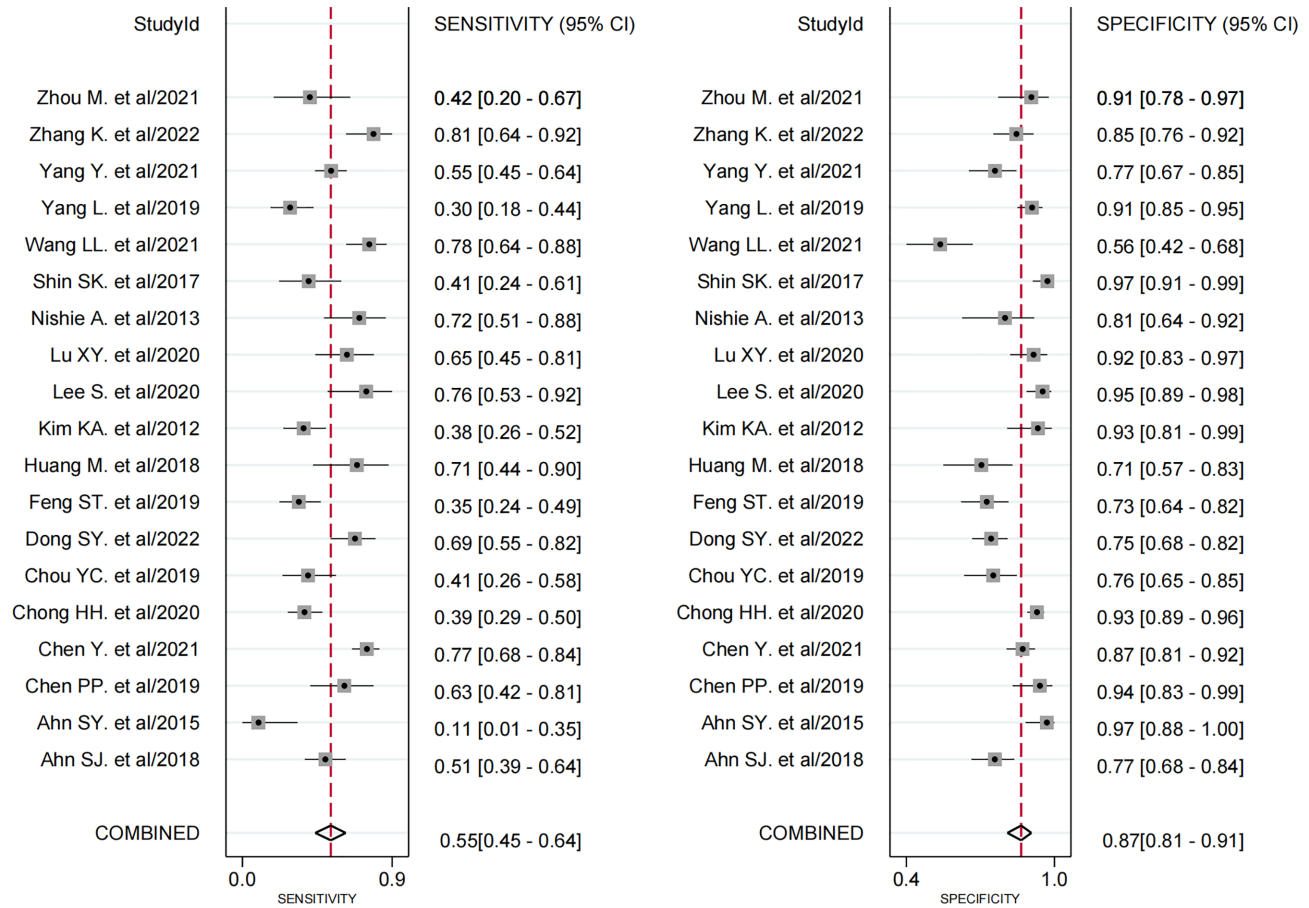

FIGURE 5 | Forest plots demonstrate the pooled sensitivity and specificity of peritumoral hypointensity on the hepatobiliary phase. The 95% CI are shown around point estimates and the pooled result.

SEN and SPE of peritumoral hypointensity were 0.55 and 0.87, respectively, which had some clinical applicability, especially as an exclusionary diagnostic tool. Further, Kim KA et al. (19) suggested that the SEN of detecting MVI with peritumoral hypointensity is relatively low, which may be due to the fact that the prevalence of MVI in certain tumors is not associated with any changes in peritumoral hepatocyte function. We hypothesize that some tumor functional changes occur later. This could also be the cause for the low SEN of peritumoral hypointensity in the current study.

Furthermore, in a high-quality study using Gd-BOPTA-enhanced MRI, the SEN and SPE of peritumoral enhancement on AP and peritumoral hypointensity on HBP were 0.23 and 0.95, respectively, and 0.49 and 0.89, respectively (51). Overall, the gap of peritumoral hypointensity between the study results and the present study was not significant, but the difference in peritumoral enhancement was a little higher. In particular, the results showed that the missed diagnosis rate using Gd-EOB-DTPA was relatively lower compared to Gd-BOPTA, but it needs to be verified by multicenter and large sample studies in the future.

According to our meta-analysis, both peritumoral enhancement and peritumoral hypointensity are key factors in predicting MVI and demonstrate moderate accuracy, which are consistent with the findings of most previous studies (8, 19, 21, 25–29, 32, 33). Different imaging techniques to explore the relationship between MVI with peritumoral imaging all showed a low SEN. In the future, how to improve its SEN will be a new research direction. For example, we speculate on whether the radiomics of peritumoral imaging or quantitative analysis to determine MVI can further improve its accuracy. As shown in the Huang M et al. study, peritumoral enhancement and peritumoral hypointense do not always coexist and a more accurate prediction model for MVI is needed (8). Therefore, whether a model with a combination of multiple imaging presentations has a higher clinical application deserves further investigation.

Assessing accuracy is necessarily preceded by assessing heterogeneity. In our study, ten covariates and seven covariates were found to be significant sources of heterogeneity for peritumoral enhancement and peritumoral

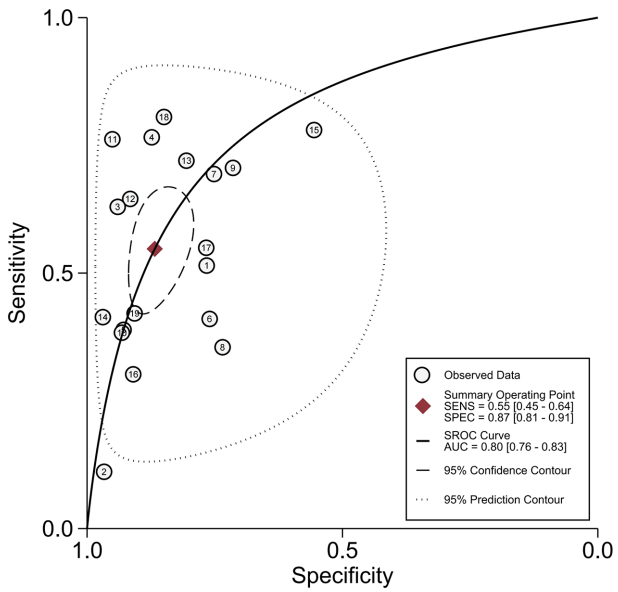

FIGURE 6 | Summary receiver operating characteristic curves of peritumoral hypointensity on the hepatobiliary phase.

hypointensity on HBP, respectively. It indicated that the future articles should pay attention to the basic information of the included patients, including the region, mean age, and number and size of included lesions, and should not ignore the interval between imaging and surgery and blindness to reference tests, so as to improve the quality of research.

In this investigation, there are several flaws. First, the population included in those studies was predominantly Asian, which meant that it was not possible to exclude out the potentiality of selection bias. Second, image interpretation depends on the observer so that subjectivity is inevitable to some extent. Finally, the data provided were inadequate for

TABLE 3 | Subgroup analyses of peritumoral enhancement on arterial phase.

Variable	Subgroups	Studies (n)	Sensitivity	P1	Specificity	P2
Region	China	11	0.51 (0.42–0.60)	0.31	0.80 (0.75–0.85)	0.03
	Others	2	0.39 (0.18–0.59)		0.82 (0.71–0.94)	
Mean age (years)	≥55	6	0.49 (0.36–0.62)	0.96	0.80 (0.73–0.87)	0.00
	<55	7	0.50 (0.39–0.61)		0.80 (0.74–0.87)	
MFS (T)	3	6	0.45 (0.33–0.57)	0.57	0.81 (0.74–0.88)	0.00
	Others	7	0.53 (0.42–0.64)		0.80 (0.74–0.86)	
MRI unit	Siemens	7	0.48 (0.37–0.59)	0.78	0.80 (0.74–0.86)	0.00
	Others	6	0.52 (0.39–0.64)		0.81 (0.74–0.88)	
Lesion size	≤5 cm	3	0.53 (0.36–0.71)	0.76	0.84 (0.76–0.92)	0.03
	NR	10	0.48 (0.39–0.58)		0.79 (0.74–0.85)	
No. of tumors (n)	≥100	9	0.52 (0.43–0.61)	0.48	0.77 (0.72–0.82)	0.00
	<100	4	0.44 (0.27–0.61)		0.88 (0.82–0.94)	
Lesions	S	6	0.57 (0.46–0.67)	0.21	0.77 (0.70–0.84)	0.00
	Others	7	0.43 (0.32–0.53)		0.83 (0.77–0.89)	
IBIS (days)	≤30	11	0.52 (0.44–0.61)	0.14	0.79 (0.74–0.84)	0.00
	>30	2	0.34 (0.14–0.54)		0.88 (0.80–0.96)	
Macro VI	N	9	0.50 (0.40–0.60)	0.91	0.81(0.76–0.86)	0.01
	U	4	0.49 (0.33–0.65)		0.78 (0.69–0.87)	
BR	Y	9	0.55 (0.46–0.64)	0.13	0.82 (0.77–0.88)	0.02
	U	4	0.40 (0.28–0.52)		0.77 (0.68–0.86)	
BI	Y	1	0.34 (0.09–0.58)	0.45	0.77 (0.58–0.95)	0.16
	U	12	0.51 (0.43–0.59)		0.81 (0.76–0.86)	

Data in parentheses are 95% confidence interval (CI). MFS, magnetic field strength; IBIS, interval between imaging and surgery; Macro VI, macrovascular invasion, BR, blindness to reference; BI, blindness to index test; NR, no restrictions; S, single; M, multiple; U, unclear; N, no, Y, yes.

TABLE 4 | Subgroup analyses of peritumoral hypointensity on hepatobiliary phase.

Variable	Subgroups	Studies (n)	Sensitivity	P1	Specificity	P2
Region	China	13	0.58 (0.47–0.69)	0.58	0.84 (0.78–0.90)	0.00
	Others	6	0.48 (0.31–0.64)		0.92 (0.87–0.97)	
Mean age (years)	≥55	10	0.52 (0.40–0.65)	0.48	0.89 (0.84–0.94)	0.03
	<55	9	0.57 (0.44–0.71)		0.84 (0.77–0.91)	
MFS (T)	3	10	0.60 (0.48–0.72)	0.59	0.87 (0.80–0.93)	0.01
	Others	9	0.49 (0.36–0.62)		0.87 (0.80–0.93)	
MRI unit	Siemens	10	0.52 (0.40–0.65)	0.48	0.84 (0.78–0.91)	0.00
	Others	9	0.58 (0.44–0.71)		0.89 (0.84–0.95)	
Lesion size	≤5 cm	4	0.48 (0.28–0.68)	0.52	0.91 (0.84–0.98)	0.18
	NR	15	0.57 (0.46–0.67)		0.85 (0.80–0.91)	
No. of tumors (n)	≥100	14	0.56 (0.45–0.66)	0.97	0.86 (0.80–0.91)	0.01
	<100	5	0.52 (0.33–0.72)		0.89 (0.81–0.97)	
Lesions	S	7	0.54 (0.39–0.69)	0.71	0.85 (0.77–0.93)	0.00
	Others	12	0.55 (0.43–0.67)		0.88 (0.82–0.93)	
IBIS (days)	≤30	15	0.58 (0.48–0.68)	0.28	0.84 (0.79–0.90)	0.00
	>30	4	0.41 (0.21–0.61)		0.93 (0.88–0.99)	
Macro VI	N	13	0.56 (0.45–0.67)	0.97	0.88 (0.82–0.93)	0.05
	U	6	0.52 (0.35–0.69)		0.85 (0.75–0.94)	
BR	Y	13	0.51 (0.40–0.62)	0.17	0.90 (0.87–0.94)	0.26
	U	6	0.63 (0.49–0.78)		0.76 (0.66–0.86)	
BI	Y	2	0.52 (0.24–0.81)	0.81	0.77 (0.56–0.97)	0.05
	U	17	0.55 (0.45–0.65)		0.88 (0.83–0.92)	

Data in parentheses are 95% confidence interval (CI). MFS, magnetic field strength; IBIS, interval between imaging and surgery; Macro VI, macrovascular invasion; BR, blindness to reference; BI, blindness to index test; NR, no restrictions; S, single; M, multiple; U, unclear; N, no; Y, yes.

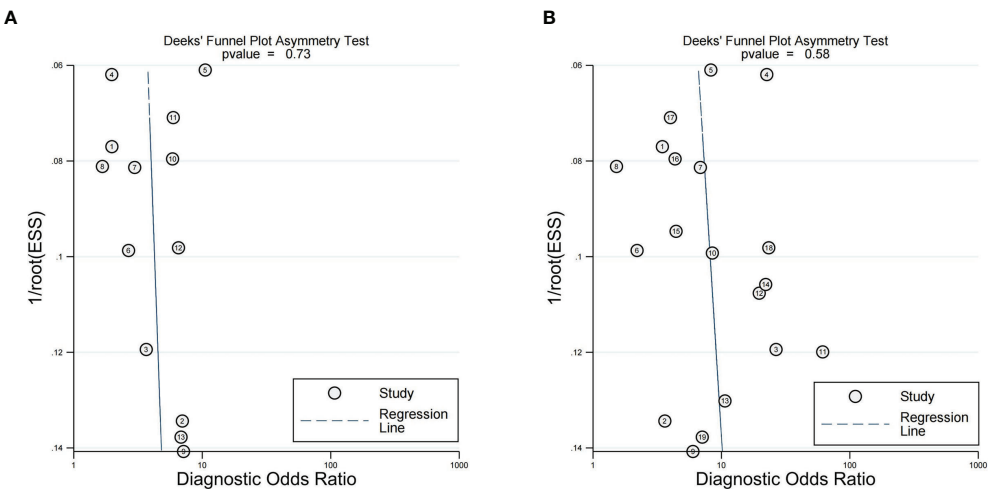

FIGURE 7 | Deeks' functional plots of peritumoral enhancement on the arterial phase **(A)** and peritumoral hypointension on the hepatobiliary phase **(B)**.

further investigation on peritumoral imaging findings. Therefore, larger multicenter studies are required for a more accurate assessment of the ability of Gd-EOB-DTPA-enhanced MRI to predict MVI.

In conclusion, our study found that the results of peritumoral enhancement on AP and peritumoral hypointensity on HBP showed high SPE but low SEN. This indicates that the peritumoral imaging features on Gd-EOB-DTPA-enhanced MRI can be used as a noninvasive, excluded diagnosis for predicting hepatic MVI in HCC preoperatively. Moreover, the results of this analysis should be updated when additional data become available. In the future, how to improve its SEN will be a new research direction.

DATA AVAILABILITY STATEMENT

The original contributions presented in the study are included in the article/**Supplementary Material**. Further inquiries can be directed to the corresponding author.

AUTHOR CONTRIBUTIONS

YW and LY proposed the concepts and designed the study. YW wrote the manuscript. MZ was responsible for the study selection and data extraction. YL and XC contributed to analyze the statistics. GZ and LY revised this manuscript. All authors read and approved the final manuscript.

FUNDING

This study was supported by the Diagnosis and Treatment Projects of Major Digestive System Diseases, the Department of Science and Technology of Sichuan Province (No. 2021YFS0375).

ACKNOWLEDGMENTS

The authors gratefully acknowledge LY for his assistance in study design.

SUPPLEMENTARY MATERIAL

The Supplementary Material for this article can be found online at: https://www.frontiersin.org/articles/10.3389/fonc.2022.907076/full#supplementary-material

REFERENCES

1. Sung H, Ferlay J, RL S, Laversanne M, Soerjomataram I, Jemal A, et al. Global Cancer Statistics 2020: GLOBOCAN Estimates of Incidence and Mortality Worldwide for 36 Cancers in 185 Countries. *CA Cancer J Clin* (2021) 71 (3):209–49. doi: 10.3322/caac.21660
2. Banerjee S, Wang DS, Kim HJ, Sirlin CB, Chan MG, Korn RL, et al. A Computed Tomography Radiogenomic Biomarker Predicts Microvascular Invasion and Clinical Outcomes in Hepatocellular Carcinoma. *Hepatology* (2015) 62(3):792–800. doi: 10.1002/hep.27877
3. Lim KC, Chow PK, Allen JC, Chia GS, Lim M, Cheow PC, et al. Microvascular Invasion is a Better Predictor of Tumor Recurrence and Overall Survival Following Surgical Resection for Hepatocellular Carcinoma Compared to the Milan Criteria. *Ann Surg* (2011) 254(1):108–13. doi: 10.1097/SLA.0b013e31821ad884
4. Roayaie S, Blume IN, Thung SN, Guido M, Fiel MI, Hiotis S, et al. A System of Classifying Microvascular Invasion to Predict Outcome After Resection in Patients With Hepatocellular Carcinoma. *Gastroenterology* (2009) 137 (3):850–5. doi: 10.1053/j.gastro.2009.06.003
5. Hirokawa F, Hayashi M, Miyamoto Y, Asakuma M, Shimizu T, Komeda K, et al. Outcomes and Predictors of Microvascular Invasion of Solitary Hepatocellular Carcinoma. *Hepatol Res* (2014) 44(8):846–53. doi: 10.1111/hepr.12196
6. Hu H, Zheng Q, Huang Y, Huang XW, Lai ZC, Liu J, et al. A non-Smooth Tumor Margin on Preoperative Imaging Assesses Microvascular Invasion of Hepatocellular Carcinoma: A Systematic Review and Meta-Analysis. *Sci Rep* (2017) 7(1):15375. doi: 10.1038/s41598-017-15491-6
7. Murakami T, Sofue K, Hori M. Diagnosis of Hepatocellular Carcinoma Using Gd-EOB-DTPA MR Imaging. *Magn Reson Med Sci* (2022) 21(1):168–81. doi: 10.2463/mrms.rev.2021-0031
8. Huang M, Liao B, Xu P, Cai H, Huang K, Dong Z, et al. Prediction of Microvascular Invasion in Hepatocellular Carcinoma: Preoperative Gd-EOB-DTPA-Dynamic Enhanced MRI and Histopathological Correlation. *Contrast Media Mol Imaging* (2018) 2018:9674565. doi: 10.1155/2018/9674565
9. Feng ST, Jia Y, Liao B, Huang B, Zhou Q, Li X, et al. Preoperative Prediction of Microvascular Invasion in Hepatocellular Cancer: A Radiomics Model Using Gd-EOB-DTPA-Enhanced MRI. *Eur Radiol* (2019) 29(9):4648–59. doi: 10.1007/s00330-018-5935-8
10. Guglielmo FF, Mitchell DG, Gupta S. Gadolinium Contrast Agent Selection and Optimal Use for Body MR Imaging. *Radiol Clin North Am* (2014) 52 (4):637–56. doi: 10.1016/j.rcl.2014.02.004
11. Stroszczynski C, Gaffke G, Gnauck M, Streitparth F, Wieners G, Lopez-Häninnen E. Aktueller Stand Der MRT-Diagnostik Mit Leberspezifischen Kontrastmitteln. Gd-EOB-DTPA Und Gd-BOPTA [Current Status of MRI Diagnostics With Liver-Specific Contrast Agents. Gd-EOB-DTPA and Gd-BOPTA]. *Radiologe* (2004) 44(12):1185–91. doi: 10.1007/s00117-004-1134-5
12. Rohrer M, Bauer H, Mintorovitch J, Requardt M, Weinmann H. Comparison of Magnetic Properties of MRI Contrast Media Solutions at Different Magnetic Field Strengths. *Invest Radiol* (2005) 40(11):715–24. doi: 10.1097/01.rli.0000184756.66360.d3
13. Zhao W, Liu W, Liu H, Yi X, Hou J, Pei Y, et al. Preoperative Prediction of Microvascular Invasion of Hepatocellular Carcinoma With IVIM Diffusion-Weighted MR Imaging and Gd-EOB-DTPA-Enhanced MR Imaging. *PLoS One* (2018) 13(5):e197488. doi: 10.1371/journal.pone.0197488
14. He YZ, He K, Huang RQ, Wang ZL, Ye SW, Liu LW, et al. Preoperative Evaluation and Prediction of Clinical Scores for Hepatocellular Carcinoma Microvascular Invasion: A Single-Center Retrospective Analysis. *Ann Hepatol* (2020) 19(6):654–61. doi: 10.1016/j.aohep.2020.07.002
15. Mule S, Chalaye J, Legou F, Tenenhaus A, Calderaro J, PA G, et al. Hepatobiliary MR Contrast Agent Uptake as a Predictive Biomarker of Aggressive Features on Pathology and Reduced Recurrence-Free Survival in Resectable Hepatocellular Carcinoma: Comparison With Dual-Tracer 18F-FDG and 18F-FCH PET/Ct. *Eur Radiol* (2020) 30(10):5348–57. doi: 10.1007/s00330-020-06923-5
16. Hu HT, SL S, Wang Z, QY S, XW H, Zheng Q, et al. Peritumoral Tissue on Preoperative Imaging Reveals Microvascular Invasion in Hepatocellular Carcinoma: A Systematic Review and Meta-Analysis. *Abdom Radiol (NY)* (2018) 43(12):3324–30. doi: 10.1007/s00261-018-1646-5
17. Ahn SJ, Kim JH, Park SJ, Kim ST, Han JK. Hepatocellular Carcinoma: Preoperative Gadoxetic Acid-Enhanced MR Imaging can Predict Early Recurrence After Curative Resection Using Image Features and Texture Analysis. *Abdom Radiol (NY)* (2019) 44(2):539–48. doi: 10.1007/s00261-018-1768-9
18. Ahn SY, JM L, Joo I, ES L, SJ L, GJ C, et al. Prediction of Microvascular Invasion of Hepatocellular Carcinoma Using Gadoxetic Acid-Enhanced MR and (18)F-FDG PET/Ct. *Abdom Imaging* (2015) 40(4):843–51. doi: 10.1007/s00261-014-0256-0
19. Kim KA, Kim MJ, Jeon HM, Kim KS, Choi JS, Ahn SH, et al. Prediction of Microvascular Invasion of Hepatocellular Carcinoma: Usefulness of Peritumoral Hypointensity Seen on Gadoxetate Disodium-Enhanced Hepatobiliary Phase Images. *J Magn Reson Imaging* (2012) 35(3):629–34. doi: 10.1002/jmri.22876
20. Chen PP, Lu J, Zhang T, Zhang XQ, Liang HW, Miao XF. The Value of Gadolinium-Ethoxybenzyl-Diethylenetriamine Pentaacetic Acid Enhanced MRI in the Prediction of Microvascular Invasion of Hepatocellular Carcinoma. *Chin J Radiol* (2019) 53(2):103–8. doi: 10.3760/cma.j.issn.1005-1201.2019.02.005
21. Chen Y, Xia Y, PP T, Long L, Jiang Z, Huang Z, et al. Comparison of Conventional Gadoxetate Disodium-Enhanced MRI Features and Radiomics Signatures With Machine Learning for Diagnosing Microvascular Invasion. *AJR Am J Roentgenol* (2021) 216(6):1510–20. doi: 10.2214/AJR.20.23255
22. Chong HH, Yang L, RF S, YL Yu, DJ Wu, SX R, et al. Multi-Scale and Multi-Parametric Radiomics of Gadoxetate Disodium-Enhanced MRI Predicts Microvascular Invasion and Outcome in Patients With Solitary Hepatocellular Carcinoma </= 5 Cm. *Eur Radiol* (2021) 31(7):4824–38. doi: 10.1007/s00330-020-07601-2
23. Chou YC, Lao IH, Hsieh PL, Su YY, Mak CW, Sun DP, et al. Gadoxetic Acid-Enhanced Magnetic Resonance Imaging can Predict the Pathologic Stage of Solitary Hepatocellular Carcinoma. *World J Gastroenterol* (2019) 25 (21):2636–49. doi: 10.3748/wjg.v25.i21.2636

24. Dong SY, Wang WT, Chen XS, Yang YT, Zhu S, Zeng MS, et al. Microvascular Invasion of Small Hepatocellular Carcinoma can be Preoperatively Predicted by the 3D Quantification of MRI. *Eur Radiol* (2022) 32(6):4198–209. doi: 10.1007/s00330-021-08495-4
25. Lee S, Kim KW, Jeong WK, Kim MJ, Choi GH, Choi JS, et al. Gadoxetic Acid-Enhanced MRI as a Predictor of Recurrence of HCC After Liver Transplantation. *Eur Radiol* (2020) 30(2):987–95. doi: 10.1007/s00330-019-06424-0
26. Lu XY, Lu J, Zhang T, Zhang XQ, Chen PP, Jiang JF, et al. Predicting Microvascular Invasion of Hepatocellular Carcinoma According to Hepatobiliary Stage Peritumoral Hypointensity During Gadolinium-Ethoxybenzyl-Diethylenetriamine Pentaacetic Aicd Enhanced MRI. *Chin J Med Imaging Technol* (2020) 36(9):1350–4. doi: 10.13929/j.issn.1003-3289.2020.09.018
27. Nishie A, Asayama Y, Ishigami K, Kakihara D, Nakayama T, Ushijima Y, et al. Clinicopathological Significance of the Peritumoral Decreased Uptake Area of Gadolinium Ethoxybenzyl Diethylenetriamine Pentaacetic Acid in Hepatocellular Carcinoma. *J Gastroenterol Hepatol* (2014) 29(3):561–7. doi: 10.1111/jgh.12423
28. Shin SK, Kim YS, Shim YS, Choi SJ, Park SH, Jung DH, et al. Peritumoral Decreased Uptake Area of Gadoxetic Acid Enhanced Magnetic Resonance Imaging and Tumor Recurrence After Surgical Resection in Hepatocellular Carcinoma: A STROBE-Compliant Article. *Med (Baltimore)* (2017) 96(33): e7761. doi: 10.1097/MD.0000000000007761
29. Wang LL, Li JF, Lei JQ, Guo SL, Li JK, Xu YS, et al. The Value of the Signal Intensity of Peritumoral Tissue on Gd-EOB-DTPA Dynamic Enhanced MRI in Assessment of Microvascular Invasion and Pathological Grade of Hepatocellular Carcinoma. *Med (Baltimore)* (2021) 100(20):e25804. doi: 10.1097/MD.0000000000025804
30. Yang L, Gu D, Wei J, Yang C, Rao S, Wang W, et al. A Radiomics Nomogram for Preoperative Prediction of Microvascular Invasion in Hepatocellular Carcinoma. *Liver Cancer* (2019) 8(5):373–86. doi: 10.1159/000494099
31. Yang Y, Fan W, Gu T, Yu L, Chen H, Lv Y, et al. Radiomic Features of Multi-ROI and Multi-Phase MRI for the Prediction of Microvascular Invasion in Solitary Hepatocellular Carcinoma. *Front Oncol* (2021) 11:756216. doi: 10.3389/fonc.2021.756216
32. Zhang K, SS X, WC Li, ZX Ye, ZW S, Shen W. Prediction of Microvascular Invasion in HCC by a Scoring Model Combining Gd-EOB-DTPA MRI and Biochemical Indicators. *Eur Radiol* (2022) 32(6):4186–97. doi: 10.1007/s00330-021-08502-8
33. Zhou M, Shan D, Zhang C, Nie J, Wang G, Zhang Y, et al. Value of Gadoxetic Acid-Enhanced MRI for Microvascular Invasion of Small Hepatocellular Carcinoma: A Retrospective Study. *BMC Med Imaging* (2021) 21(1):40. doi: 10.1186/s12880-021-00572-w
34. Moher D, Liberati A, Tetzlaff J, Altman DG. Preferred Reporting Items for Systematic Reviews and Meta-Analyses: The PRISMA Statement. *PloS Med* (2009) 6(7):e1000097. doi: 10.1371/journal.pmed.1000097
35. Whiting PF, Rutjes AW, Westwood ME, Mallett S, Deeks JJ, Reitsma JB, et al. QUADAS-2: A Revised Tool for the Quality Assessment of Diagnostic Accuracy Studies. *Ann Intern Med* (2011) 155(8):529–36. doi: 10.7326/0003-4819-155-8-201110180-00009
36. Zamora J, Abraira V, Muriel A, Khan K, Coomarasamy A. Meta-DiSc: A Software for Meta-Analysis of Test Accuracy Data. *BMC Med Res Methodol* (2006) 6:31. doi: 10.1186/1471-2288-6-31
37. Higgins JP, SG T, JJ D, Altman DG. Measuring Inconsistency in Meta-Analyses. *BMJ* (2003) 327(7414):557–60. doi: 10.1136/bmj.327.7414.557
38. Leeflang MM, JJ D, Gatsonis C, Bossuyt PM. Systematic Reviews of Diagnostic Test Accuracy. *Ann Intern Med* (2008) 149(12):889–97. doi: 10.7326/0003-4819-149-12-200812160-00008
39. Deeks JJ, Macaskill P, Irwig L. The Performance of Tests of Publication Bias and Other Sample Size Effects in Systematic Reviews of Diagnostic Test Accuracy was Assessed. *J Clin Epidemiol* (2005) 58(9):882–93. doi: 10.1016/j.jclinepi.2005.01.016
40. Matsui O, Kobayashi S, Sanada J, Kouda W, Ryu Y, Kozaka K, et al. Hepatocelluar Nodules in Liver Cirrhosis: Hemodynamic Evaluation (Angiography-Assisted CT) With Special Reference to Multi-Step Hepatocarcinogenesis. *Abdom Imaging* (2011) 36(3):264–72. doi: 10.1007/s00261-011-9685-1
41. Miyayama S, Yamashiro M, Okuda M, Yoshie Y, Nakashima Y, Ikeno H, et al. Detection of Corona Enhancement of Hypervascular Hepatocellular Carcinoma by C-Arm Dual-Phase Cone-Beam CT During Hepatic Arteriography. *Cardiovasc Intervent Radiol* (2011) 34(1):81–6. doi: 10.1007/s00270-010-9835-9
42. Ueda K, Matsui O, Kawamori Y, Nakanuma Y, Kadoya M, Yoshikawa J, et al. Hypervascular Hepatocellular Carcinoma: Evaluation of Hemodynamics With Dynamic CT During Hepatic Arteriography. *Radiology* (1998) 206 (1):161–6. doi: 10.1148/radiology.206.1.9423667
43. Choi BI, Lee KH, Han JK, Lee JM. Hepatic Arterioportal Shunts: Dynamic CT and MR Features. *Korean J Radiol* (2002) 3(1):1–15. doi: 10.3348/kjr.2002.3.1.1
44. Kitao A, Zen Y, Matsui O, Gabata T, Kobayashi S, Koda W, et al. Hepatocellular Carcinoma: Signal Intensity at Gadoxetic Acid-Enhanced MR Imaging–correlation With Molecular Transporters and Histopathologic Features. *Radiology* (2010) 256(3):817–26. doi: 10.1148/radiol.10092214
45. Tsuboyama T, Onishi H, Kim T, Akita H, Hori M, Tatsumi M, et al. Hepatocellular Carcinoma: Hepatocyte-Selective Enhancement at Gadoxetic Acid-Enhanced MR Imaging–Correlation With Expression of Sinusoidal and Canalicular Transporters and Bile Accumulation. *Radiology* (2010) 255 (3):824–33. doi: 10.1148/radiol.10091557
46. Chou CT, Chen RC, Lin WC, Ko CJ, Chen CB, Chen YL. Prediction of Microvascular Invasion of Hepatocellular Carcinoma: Preoperative CT and Histopathologic Correlation. *AJR Am J Roentgenol* (2014) 203(3):W253–9. doi: 10.2214/AJR.13.10595
47. Yang C, Wang H, Sheng R, Ji Y, Rao S, Zeng M. Microvascular Invasion in Hepatocellular Carcinoma: Is it Predictable With a New, Preoperative Application of Diffusion-Weighted Imaging? *Clin Imaging* (2017) 41:101–5. doi: 10.1016/j.clinimag.2016.10.004
48. Wybranski C, Siedek F, Damm R, Gazis A, Wenzel O, Haneder S, et al. Respiratory Motion Artefacts in Gd-EOB-DTPA (Primovist/Eovist) and Gd-DOTA (Dotarem)-Enhanced Dynamic Phase Liver MRI After Intensified and Standard Pre-Scan Patient Preparation: A Bi-Institutional Analysis. *PloS One* (2020) 15(3):e230024. doi: 10.1371/journal.pone.0230024
49. Kim H, Park MS, Choi JY, Park YN, Kim MJ, Kim KS, et al. Can Microvessel Invasion of Hepatocellular Carcinoma be Predicted by Pre-Operative MRI? *Eur Radiol* (2009) 19(7):1744–51. doi: 10.1007/s00330-009-1331-8
50. Granito A, Galassi M, Piscaglia F, Romanini L, Lucidi V, Renzulli M, et al. Impact of Gadoxetic Acid (Gd-EOB-DTPA)-Enhanced Magnetic Resonance on the non-Invasive Diagnosis of Small Hepatocellular Carcinoma: A Prospective Study. *Aliment Pharmacol Ther* (2013) 37(3):355–63. doi: 10.1111/apt.12166
51. Zhang L, Yu X, Wei W, Pan X, Lu L, Xia J, et al. Prediction of HCC Microvascular Invasion With Gadobenate-Enhanced MRI: Correlation With Pathology. *Eur Radiol* (2020) 30(10):5327–36. doi: 10.1007/s00330-020-06895-6

Conflict of Interest: The authors declare that the research was conducted in the absence of any commercial or financial relationships that could be construed as a potential conflict of interest.

frontiers | Frontiers in Oncology

CLINICAL TRIAL
published: 13 July 2022
doi: 10.3389/fonc.2022.869316

The Safety and Efficacy of Nanosecond Pulsed Electric Field in Patients With Hepatocellular Carcinoma: A Prospective Phase 1 Clinical Study Protocol

Min Xu[1,2], Danxia Xu[1,2], Gang Dong[3], Zhigang Ren[4], Wu Zhang[5], Tuerganaili Aji[6], Qiyu Zhao[1,2], Xinhua Chen[2,7†] and Tian'an Jiang[1,2*†]*

[1] Department of Ultrasound Medicine, The First Affiliated Hospital, School of Medicine, Zhejiang University, Hangzhou, China, [2] Key Laboratory of Pulsed Power Translational Medicine of Zhejiang Province, Hangzhou, China, [3] Department of Ultrasound, The First Affiliated Hospital of Zhengzhou University, Zhengzhou, China, [4] Department of Infectious Diseases, The First Affiliated Hospital of Zhengzhou University, Zhengzhou, China, [5] Shulan International Medical College, Shulan (Hangzhou) Hospital Affiliated to Zhejiang Shuren University, Hangzhou, China, [6] Department of Surgery, The First Affiliated Hospital of Xinjiang Medical University, Urumqi, China, [7] Department of Hepatobiliary and Pancreatic Surgery, The First Affiliated Hospital, School of Medicine, Zhejiang University, Hangzhou, China

OPEN ACCESS

Edited by:
Xiankai Sun, University of Texas Southwestern Medical Center, United States

Reviewed by:
Maria Conticchio, Ospedale Generale Regionale Francesco Miulli, Italy
Antonella Argentiero, Bari John Paul II Cancer Institute (IRCCS), Italy

***Correspondence:**
Xinhua Chen
Xinhua_chen@zju.edu.cn
Tian'an Jiang
tiananjiang@zju.edu.cn

†These authors have contributed equally to this work

Specialty section:
This article was submitted to Cancer Imaging and Image-directed Interventions, a section of the journal Frontiers in Oncology

Received: *04 February 2022*
Accepted: *21 June 2022*
Published: *13 July 2022*

Citation:
Xu M, Xu D, Dong G, Ren Z, Zhang W, Aji T, Zhao Q, Chen X and Jiang T (2022) The Safety and Efficacy of Nanosecond Pulsed Electric Field in Patients With Hepatocellular Carcinoma: A Prospective Phase 1 Clinical Study Protocol. Front. Oncol. 12:869316. doi: 10.3389/fonc.2022.869316

Background: Hepatocellular carcinoma (HCC) is a highly aggressive malignancy. Irreversible electroporation (IRE) is an ablative modality that uses high-voltage electrical pulses to permeabilize the cell membrane leading to cell necrosis. Unlike traditional thermal ablation, IRE is hardly affected by the "heat-sink" effect and can prevent damage of the adjacent vital structures. Nanosecond pulsed electric field (nsPEF) is a new IRE technique using ultra-short pulses (nanosecond duration), can not only penetrate the cell membranes, but also act on the organelles. Sufficient preclinical researches have shown that nsPEF can eliminate HCC without damaging vital organs, and elicit potent anti-tumor immune response.

Objective: This is the first clinical study to evaluate feasibility, efficacy, and safety of nsPEF for the treatment of HCC, where thermal ablation is unsuitable due to proximity to critical structures.

Methods and analysis: We will conduct an open-labeled, single-arm, prospective, multicenter, and objective performance criteria trial. One hundred and ninety-two patients with HCC, in which the tumor is located immediately (<0.5 cm) adjacent to the portal vein, hepatic veins, bile duct, gastrointestinal tract, or diaphragm, will be enrolled among 4 academic medical centers. The primary outcomes are the rate of complete ablation at 1 month and adverse events. Secondary outcomes include technical success, technique efficacy, nsPEF procedural characteristics, local tumor progression, and local progression-free survival.

Ethics and dissemination: The trial will be conducted according to the ethical principles of the Declaration of Helsinki and has been approved by the ethics committee of all

participating centers. The results of this study will be published in peer-reviewed scientific journals and presented at relevant academic conferences.

Conclusions: This study is the Phase 1 clinical trial to evaluate the efficacy and safety of nsPEF in patients with HCC at high-risk locations where thermal ablation is contra-indicated. The results may expand the options and offer an alternative therapy for HCC.

Clinical Trial Registration: ClinicalTrials.gov, identifier NCT04309747.

Keywords: nanosecond pulsed electric field (nsPEF), irreversible electroporation (IRE), hepatocellular carcinoma (HCC), ablation, protocol

1 INTRODUCTION

Liver cancer is a major global health challenge that is predicted to affect more than 1 million individuals annually by 2025. Hepatocellular carcinoma (HCC) is the most common type of primary liver cancer (90%) and the fourth leading cause of cancer-related deaths worldwide (1). Local ablation is considered a potentially curative therapy for small HCC, as are surgical resection and liver transplantation (2, 3). Most ablation techniques, effected through radiofrequency, microwave, or laser, are based on thermal changes of the ablated tissue. However, many tumors cannot be treated with thermal ablation owing to hazardous tumor locations, and thermal damage to adjacent non-targeted structures can result in serious complications, such as hemorrhage, biliary fistula or intestinal perforation. Moreover, heat drawn away from the targeted tumor when it is adjacent to vessels, i.e., the heat sink effect, can result in incomplete ablation (4–6).

Irreversible electroporation (IRE) is a non-thermal ablation modality that has been advocated for solid hepato-pancreatico-biliary tumors. IRE delivers high-voltage electric pulses to permeabilize the cell membrane and consequently cause cell death, mostly by apoptosis (7, 8). Unlike thermal ablation, with IRE the extracellular connective tissue stays intact. This enables ablating tumors that are close to or involving vital structures such as the portal vein, hepatic veins, or bile duct. In addition, treatment efficacy of IRE is not impeded by heat sink effect (9–11). Based on these specific properties, IRE should be considered an ideal tool for patients for whom thermal ablation is too aggressive (12, 13).

Traditional IRE applies electric pulses of microsecond duration. Recently, a new type of IRE technique has been introduced, called nanosecond pulsed electric field (nsPEF). Unlike traditional microsecond duration IRE, the nsPEF with the duration from a few nanoseconds to hundreds of nanoseconds and the amplitude from 10 kV/cm to 300 kV/cm has been applied for tumor ablation. Since the duration shorter than the charging time constant of the cell membrane, nsPEF can not only penetrate the cell membranes, but also act on the organelles such as the endoplasmic reticulum, mitochondria, and nucleus (**Figure 1**). Cell responses to nsPEF include calcium mobilization (14), cytoskeleton destruction (15), activation of signaling pathways (16), and induction of apoptosis (17). Moreover,treatment with microsecond pulsed electric field has the undesirable side effect of adjacent skeletal muscle stimulation. Relatively long exposure of the skeletal muscle or its motor nerves to a high exogenous electric field will depolarize the cells and cause intense contractions. Previous studies found that shortening the time of the electric field exposure from microseconds to nanoseconds can reduce pain and involuntary

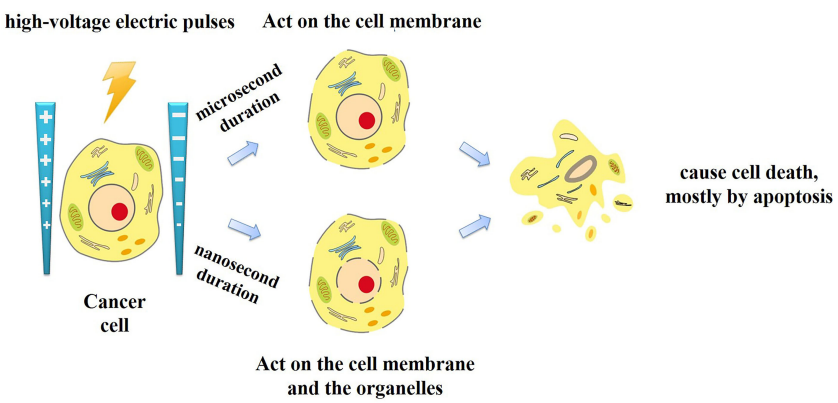

FIGURE 1 | The mechanisms of high-voltage electric pulses with microsecond or nanosecond duration.

muscle contraction (18). Therefore, different interaction mechanisms with traditional IRE, nsPEF expands the options and offers new opportunities for oncological therapy (**Table 1**).

Killing cancer cells *in vitro via* nsPEF has been extensively explored, and successful tumor ablation has been demonstrated in various animal models, including malignant melanoma, skin basal cell carcinoma, lung squamous cell cancer and pancreatic cancer (17, 19–22). Most importantly, a clinical trial showed that nsPEF could successfully treat basal cell carcinoma in human patients, with significant efficacy and minimal invasion (23).

For the treatment of liver cancer, nsPEF has shown promising therapeutic prospects in both cell and animal experiments (**Supplementary Appendix 1**). Our preclinical studies have verified the efficacy of nsPEF, that is, that nsPEF can lead to long-term disease-free survival without recurrence (24, 25). In addition to inducing cell death, nsPEF inhibited cell proliferation and angiogenesis in tumors, triggered an immune response, and prevented secondary tumor growth (26–29).

Here, we propose to conduct the first-in-human trial to evaluate the efficacy and safety of nsPEF in patients with localized HCC, for whom thermal ablation is considered unsuitable.

2 METHODS AND ANALYSIS

2.1 Study Design

This open-labeled, single-arm, prospective, multicenter trial will be conducted in 4 academic medical centers in China, as follows: First Affiliated Hospital, School of Medicine, Zhejiang University, Hangzhou; First Affiliated Hospital of Zhengzhou University, Zhengzhou; Shulan (Hangzhou) Hospital, Hangzhou; and First Affiliated Hospital of Xinjiang Medical University, Xinjiang. This trial has been approved by the committee for medical and health ethics of all the centers and registered on ClinicalTrials.gov (NCT04309747). The trial protocol is in accordance with all the recommendations of the SPIRIT (Standard Protocol Items: Recommendations for Interventional Trials) 2013 statement (30). Written informed consent will be obtained from all participants prior to enrollment. The flow diagram of the study is presented in **Figure 2**.

2.2 Patient Population

Potential trial participants will be identified at an institutional multidisciplinary tumor board, comprised of interventional radiologists, hepatobiliary surgeons, medical oncologist, and diagnostic radiologists. The potential subjects will subsequently be referred for enrollment and eligibility screening. All candidates will be reviewed for safety and eligibility by an experienced interventional radiologist, participating in the research project at each center. All eligible patients will be explained about the study protocol in details. Only those who sign the consent form will enter the trial. The inclusion and exclusion criteria are listed in **Table 2**.

2.3 Baseline Characteristics

Standard evaluation of the patient before the nsPEF procedure should include a general health history review (demographics, past medical history, allergies, and medications), assessment of performance status and pain, general anesthetic review, electrocardiogram, echocardiography, and laboratory tests (blood routine examination, blood coagulation, liver function, tumor marker, and myocardial enzyme). All included patients will have a pre-intervention radiological assessment within 4 weeks before the nsPEF procedure, including abdominal contrast-enhanced magnetic resonance imaging (MRI), CT angiography of the liver, chest computed tomography (CT), contrast-enhanced ultrasound (CEUS) of the liver, and abdominal contrast-enhanced CT when MRI is contraindicated.

2.4 Interventions

The nsPEF procedure will be performed under general anesthesia with endotracheal intubation. Intraoperative nondepolarizing neuromuscular blocking agents (rocuronium or cis-atracurium) will be applied in combination to achieve deep muscle relaxation,

TABLE 1 | Comparison of the mechanism of nsPEF and thermal ablation.

	nsPEF	RFA	MWA	Cryoablation
Fundamental principles	Utilizing high-frequency electric pulses penetrate the cell membranes, and act on the organelles	Utilizing high-frequency alternating current to generate heat	Utilizing electromagnetic waves to generate heat	Utilizing liquefied gases to induce the freezing–thawing cycle of targeted lesions
Treatment temperature	Nonthermal	60–100°C	>100°C	< – 40°C
Mechanism of tumor cell injury	Mainly apoptosis	Mainly necrosis	Mainly necrosis	Mainly necrosis
Advantages	Limited risk of thermal injury to neighbouring critical structures Unsensitive to heat sink effect	Well evaluated treatment	Higher and faster temperature picks reached than with RFA (less sensitive to heat sink effect than RFA)	Easy monitoring with imaging of ice ball progression
Limitations	General anesthesia Muscle contraction	Thermal injury of adjacent structure Heat sink effect	No reliable end point to set the amount of energy deposition	Cryoshock with first device

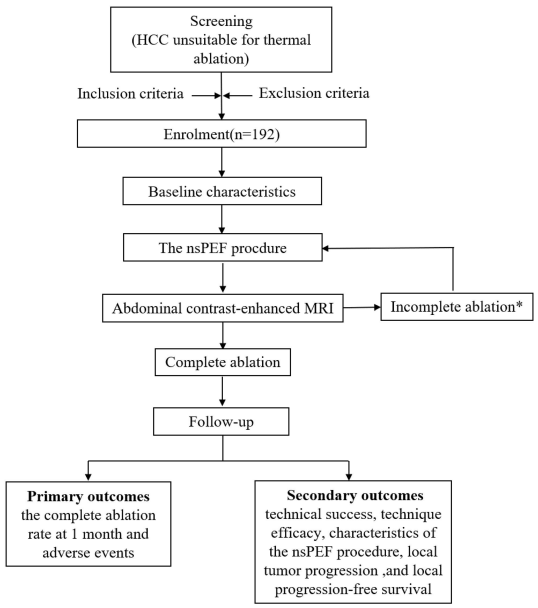

FIGURE 2 | Flow chart of study. *Contrast-enhanced MRI will be performed 1 month after the procedures to evaluate technique efficacy. In the event of incomplete ablation, an additional nsPEF procedure will be conducted with the same technique. If the residual tumor is still viable after the second session, then nsPEF is considered failed, and the patient will be excluded from the trial and referred to other therapies. HCC, hepatocellular carcinoma; nsPEF, nanosecond pulsed electric field; MRI, magnetic resonance imaging.

in which no muscle tremor visible to the naked eye or a train of four stimulations (TOF) is 0. Deep muscle relaxation can eliminate the muscle contractions caused by the high-voltage pulsed electric fields and reduce the injuries of the target organs due to electrode displacements.

The nsPEF procedure will be guided by CT or US. The nsPEF therapeutic apparatus manufactured by the Hangzhou Ruidi Biotech Ltd company (Hangzhou, Zhejiang, China) (**Figure 3**) will be used in this study. All electrodes will be placed parallel by trained interventional radiologists with extensive experience in percutaneous thermal ablation (via radiofrequency, microwave, or laser) and nonthermal ablation (IRE). Depending on the individual tumor size and shape, 2 to 6 19-gauge unipolar nsPEF electrodes with an appropriate active tip length of 1.0 to 2.0 cm will be placed 1.0 to 2.5 cm apart using ultrasound guidance. The nsPEF device generates 15 to 30 kV pulses, and voltage will be determined by a standard algorithm that uses factors such as the intended size of the ablation zone, the number of electrodes, the distance between electrodes, and the length of the active electrode tip (**Figure 4**). Once the electrodes are correctly placed, a test pulse at 5 kV will be delivered. After the test pulse confirms adequate conductivity, nsPEF will be conducted with 800 pulses, a pulse length of 300 ns, with electrocardiographic triggering.

After completion of the pulse applications, CEUS will be performed to confirm sufficient ablation, which is defined as an ablation zone that includes the entire target tumor and a safety margin of at least 0.5 cm. If the extent of the ablation zone is suspected insufficient, additional cycles of energy depositions for overlapped ablations will be performed, preferably after electrodes pullbacks (from 1 to 2 cm partial withdrawal of needles along the axis of the initial puncture) and/or partial or complete electrodes reinsertion (in different axis from initial puncture). A case is shown in **Figure 5** and **Video 1**.

2.5 Postprocedural Follow-Up

After the procedure, all patients will be monitored for at least another day in inpatient department, in accordance with current medical practice. Routine laboratory studies, electrocardiogram, and CEUS will be performed to assess procedure-related complications.

Contrast-enhanced MRI will be performed 1 month after the procedures to evaluate technique efficacy. Complete ablation is considered complete nonenhancement of the treated tumor, and incomplete ablation is the presence of residual tumor on contrast-enhanced MRI. In the event of incomplete ablation, an additional nsPEF procedure will be conducted with the same technique. If the residual tumor is still viable after the second session, then nsPEF is considered failed, and the patient will be excluded from the trial and referred to other therapies.

If efficacy is confirmed, then clinical, biological, and radiological examinations are required every 3 months during the first year, and once every 6 months thereafter. Baseline and follow-up images will be interpreted independently by all experienced diagnostic abdominal radiologists. At the end of the trial, 2 independent radiologists will review all images before and after treatment, and reach a consensus.

TABLE 2 | Patients inclusion and exclusion criteria.

Inclusion criteria	Exclusion criteria
1. HCC diagnosed histologically or clinically according to the guidelines of the American Association for the Study of Liver Diseases	1. Ventricular cardiac arrhythmia
2. tumors located immediately (<0.5 cm) adjacent to the portal vein, hepatic veins, bile duct, gastrointestinal tract, or diaphragm	2. Congestive heart failure, NYHA Class ≥ 3
3. age ≥ 18 years	3. Active coronary artery disease
4. no evidence of extrahepatic metastasis	4. History of epilepsy
5. single tumor with a maximum diameter of ≤5cm, or the number of tumors of ≤3 and a maximum diameter of ≤3cm.	5. Any implanted stimulation device
6. Child-Pugh A or B	6. Other treatment <6 weeks prior to treatment
7. Performance status according to Eastern Cooperative Oncology Group (ECOG) ≤2.	7. presence of vascular invasion or extrahepatic metastasis.
8. written informed consent	8. Severe coagulation abnormalities

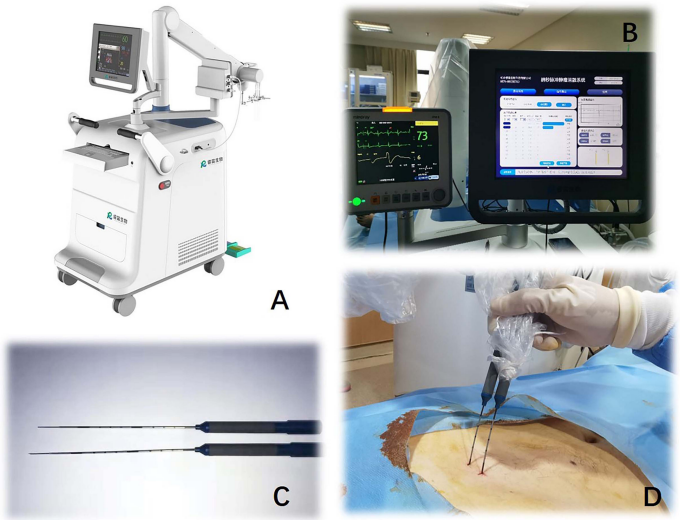

FIGURE 3 | Nanosecond pulsed electric field equipment (Hangzhou Ruidi Biotech Ltd, Hangzhou, Zhejiang, China) **(A)** console. **(B)** displayer. **(C, D)** 19G monopolar needle electrodes.

2.6 Study Outcomes

Treatment outcomes are defined in accordance with the Ahmed et al. (31, 32) proposal for standardization of terms and reporting criteria for imaging-guided ablation.

2.6.1 Primary Outcomes

The primary outcomes are the complete ablation rate at 1 month, and adverse events. The later may be device-related, intraprocedural, postprocedural, or late, and will be reported using the NCI Common Terminology Criteria for Adverse Events (CTCAE) (**Supplementary Appendix 2**).

2.6.2 Secondary Outcomes

The secondary outcomes are the following: technical success, technique efficacy, characteristics of the nsPEF procedure, local tumor progression (LTP), and local progression-free survival (LPFS). Specifically, technical success addresses whether the tumor is treated according to protocol and covered completely by the ablation zone; tumor coverage will be assessed immediately after the nsPEF procedure by CEUS.

Technique efficacy is regarded as radiologic complete ablation achieved after as many as 2 iterative nsPEF procedures. The nsPEF procedure characteristics include the following: number of electrodes used; active tip length of the electrodes; distance

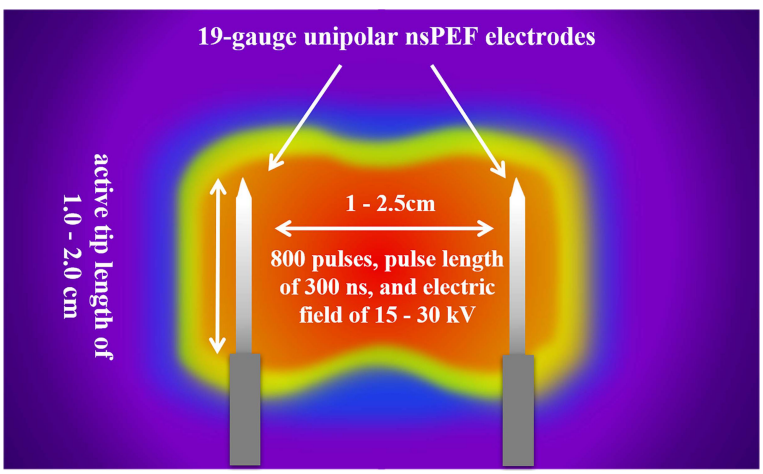

FIGURE 4 | The nsPEF procedure strategy. Depending on the individual tumor size and shape, 2 to 6 19-gauge unipolar electrodes with an appropriate active tip length of 1.0 to 2.0 cm will be placed 1.0 to 2.5 cm apart using ultrasound guidance. The nsPEF will be conducted with 800 pulses of 300ns duration, and an electric field of 15 to 30 kV. nsPEF, nanosecond pulsed electric field.

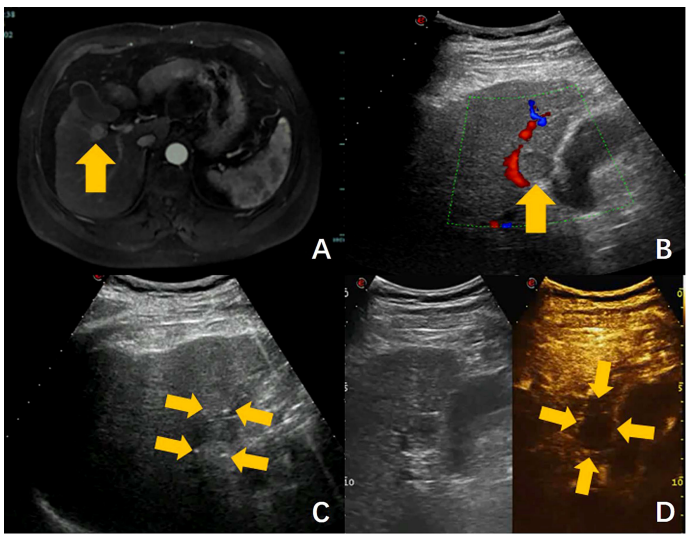

FIGURE 5 | Ultrasound-guided nsPEF procedure for HCC adjacent to gallbladder. **(A)** Pre-ablation contrast-enhanced MRI revealed a hepatocellular carcinoma adjacent to gallbladder. **(B)** Ultrasound showed a hypoecho tumor located in close contact with gallbladder and right portal branch (arrow). **(C)** Ultrasound-guided nsPEF with a two-electrode configuration, and the head and tail end of the active tip of the electrodes can have punctuated enhancements (arrow). **(D)** The contrast-enhanced ultrasound image revealed no enhancement after ablation. (arrow).

between electrodes; rate of pullback applications; total number of pulses delivered per procedure; total procedural time; ablation time; ablation volume; and sufficient ablative margin.

LTP describes the reappearance of HCC adjacent to the ablated zone after successful treatment. LPFS is defined as the time from the commencement date of the nsPEF procedure to the date of local progression. LPFS will be censored at the date of the last follow-up, when the patient has no evidence of local progression.

2.7 Calculation of Sample Size

Because this is a pilot study, there is currently no data on the complete ablation rate of nsPEF for the treatment of HCC. Previous studies showed a 77.3%-86% rate of complete ablation after the first IRE (with a traditional microsecond duration) in patients with HCC that was not appropriate for thermal ablation (11, 33). Our hypothesis is that 80% of tumors treated by nsPEF will achieve complete ablation by the 1-month follow-up. For the single arm OPC hypothesis, employing 80% power and with a 2.5% one-sided α, then 160 patients will be required. Assuming a 20% rate of withdrawal or loss during follow-up, 192 participants should be enrolled.

2.8 Statistical Methods

Continuous data will be expressed as median and range. Categorical variables will be shown as frequency and proportion. Survival curves and cumulative incidence of LTP will be generated using the Kaplan-Meier method. The Cox proportional hazards method will be used for univariate and multivariate analyses to determine prognostic factors. Technical success, technique efficacy, nsPEF procedural characteristics, and local tumor progression will be analyzed per tumor. The rate of adverse events and local progression-free survival will be analyzed per patient. P values < 0.05 will be considered statistically significant. All statistical analyses will be performed with a software package (SPSS, version 23.0; SPSS, Chicago, Ill).

2.9 Adverse Events

Device-related, periprocedural, and postprocedural adverse events will be measured using the CTCAE. Any serious adverse events will be documented in the medical records as well as in the electronic case report form and reported to the institutional review board by the responsible investigator, in accordance with the local regulations.

2.10 Data and Safety Monitoring Board

The DSMB will act in an independent, expert, and advisory capacity to monitor participant safety, and assess the efficacy and overall conduct of the study. The responsibilities of the DSMB are to monitor safety and efficacy data to guide recommendation for continuation of the study or early termination, and to evaluate the overall conduct of the trial. These responsibilities include monitoring: planned sample size assumptions; compliance with the protocol; recruitment figures and losses to follow-up; and continuing appropriateness of patient information. In addition, the DSMB's responsibilities include reports on data quality and completeness of data.

2.11 Ethics and Dissemination

This study is conducted in accordance with the principles of the Declaration of Helsinki. The protocol has been approved by the ethics committee of all participating centers. Informed consent will be obtained from each participating patient in oral and written form. The results of this trial will be disseminated

through peer-reviewed publications and conferences. Data will be available upon reasonable request.

3 DISCUSSION

IRE is primarily a nonthermal ablation technique. The working mechanism of IRE is direct injury caused by high voltage electrical pulses, rather than thermal energy. The major advantage of IRE is its ability to preserve sensitive structures, which is not true of other ablative techniques such as radiofrequency ablation or microwave ablation. Previous clinical trials of IRE revealed encouraging results for the treatment of tumors that are close to major vessels or bile ducts, including those in the liver, pancreas, and kidney (34–36).

With recent developments in electrical engineering technology, IRE devices have gained nanosecond-duration pulses (nsPEF). The charge time constants for the plasma membrane of mammalian cells are characteristically in the order of nanosecond level. In conventional microsecond-duration electrical pulses, the charge of the cell plasma membrane compensates for the external electric field and protects the cell interior. However, for field magnitudes greater than 10 kV/cm, nsPEF can charge smaller intracellular structures to the electroporation threshold faster than the plasma membrane can charge and protect these structures (37, 38). The powerful ability of nsPEF to eradicate tumor has been confirmed by several studies of liver cells and animal models. Moreover, the animal models showed that blood vessels and bile ducts within or directly adjacent to the ablation zone remain undamaged. Hence, we designed this trial to explore and evaluate the feasibility, efficacy, and safety of nsPEF in the treatment of HCC.

This trial is currently recruiting patients. The first patient was enrolled on April 13, 2020. At present, the protocol is effective and 4 centers are actively recruiting patients for the trial. One hundred and eighty-three of 192 patients (95%) have been recruited. It is estimated that recruitment will be completed in December 2022. One case was showed in **Figure 5**, the tumor located in close contact with gallbladder and right portal branch, which had an obvious high risk of thermal damage with RFA or MWA. Thermal damage to adjacent non-targeted structures can result in serious complications, such as hemorrhage, biliary fistula or intestinal perforation. In addition, heat drawn away from the targeted tumor by the surrounding vessel may result in incomplete ablation. For these reasons, the patient was enrolled in the clinical trial and underwent nsPEF treatment.

Based on the preoperative images, the number, size, shape, margins, blood supply, and relationships with adjacent structures of the target tumor were determined. A reasonable arrangement of nsPEF electrodes were designed, including the number of electrodes, active tip length of electrodes, puncture path and distances between the electrodes. Because the maximum diameter of the tumor was 1.9 cm, the two-electrode configuration was selected. Electrodes were inserted along the long axis of the tumor with active tip length of 2.0 cm. The shortest puncture path was selected while avoiding damage to the surrounding important structures. After all the electrodes are precisely placed under ultrasound guidance, a test pulse at 5 kV was delivered. After the test pulse confirms adequate conductivity, nsPEF was conducted with 800 pulses, a pulse length of 300 ns, with electrocardiographic triggering. During nsPEF, the head and tail end of the active tip of the electrodes had punctuated enhancements on ultrasound, which was used to identify the orientation of the electrodes and to further verify the correct placement of the electrodes as planned. The CEUS was performed immediately after nsPEF to evaluate whether the nonenhanced area completely covers the tumor. In this case, the CEUS images after ablation showed the target tumor was covered completely by the ablation zone, and there was no evidence of local complications of biliary or vascular injury. The patient was discharged the next day after nsPEF. As with all ablation techniques, sufficient preoperative preparation, standardized operative procedures, precise positioning, use of reasonable ablation parameter settings and fine postoperative management are important for reducing the incidence of complications. Follow-up MR images on the 16 months after nsPEF revealed adequate shrinkage of the ablation zone was observed, without signs of residual tumor. As showed in this case, the pilot results of our study suggest that nsPEF is an effective and safe technique to treat HCC located close to critical structures, which considered contraindicated to thermal ablation.

Under these challenging inclusion criteria, our initial treatment course of nsPEF achieved 87% complete ablation based on polit data. No collateral thermal damage to the main bile duct or hepatic vascular structures were encountered. In addition, we found that nsPEF induced more slight muscle contraction than traditional IRE. Further analysis with long-term follow-up is required at the end of the recruitment.

The most important limitation of our protocol is its nonrandomized nature. However, nsPEF will be performed in only those patients with tumors close to the portal vein, hepatic veins, bile duct, gastrointestinal tract, or diaphragm (i.e., patients who are not suitable candidates for thermal ablation and surgery). Since these later methods would predictably fail for patients in this study, we favored a single-arm study design with an effectiveness threshold. Along with the scientific and deeper understanding for pathophysiology mechanism of HCC, recent researches have revealed the role of BRAF in HCC, which long non-coding RNA of BRAF may be another mechanism of cancer proliferation and tyrosine kinase inhibitors escape in HCC (39). Targeted therapy combinations, including BRAF pathway, may bring light in new treatment of HCC. With initial promising results of this study, further relevant studies would be useful, such as nsPEF treatment compared to targeted therapy, or nsPEF combined with multi-pathways inhibition therapy. These exploring studies may open the door for better results in the treatment of HCC.

In summary, this study is the first-in-human trial to evaluate the efficacy and safety of nsPEF in patients with HCC who are considered unsuitable for thermal ablation. The design of the trial and its primary, secondary, and exploratory endpoints have

the potential to broaden our understanding of electroporation-based technologies in medicine, and provide new minimally invasive therapeutic pathways for HCC at high-risk locations.

DATA AVAILABILITY STATEMENT

The raw data supporting the conclusions of this article will be made available by the authors, without undue reservation.

ETHICS STATEMENT

The studies involving human participants were reviewed and approved by First Affiliated Hospital of Zhejiang University, First Affiliated Hospital of Zhengzhou University, Shulan Hospital, and First Affiliated Hospital of Xinjiang Medical University. The patients/participants provided their written informed consent to participate in this study.

AUTHOR CONTRIBUTIONS

Conceptualization: T'AJ, XC and MX. Data curation: MX, DX, GD, ZR,WZ,QZ, TA,T'AJ and X-HC. Formal analysis: T'AJ, DX, XC and MX. Investigation: T'AJ, XC and MX. Supervision: T'AJ and XC. Original draft: MX. Review and editing: T'AJ, XC and ZR. All authors contributed to the article and approved the submitted version.

FUNDING

This trial is mainly funded by Hangzhou Ruidi Biotech Ltd. Hangzhou Ruidi Biotech Ltd is a medical company that aims at researching, developing, manufacturing, selling, and renting class III medical devices. This work is also supported by Development Project of National Major Scientific Research Instrument (82027803), National Natural Science Foundation of China (81971623) and Key Project of Natural Science Foundation of Zhejiang Province(LZ20H180001). The funder was not involved in the study design, collection, analysis, interpretation of data, the writing of this article or the decision to submit it for publication.

SUPPLEMENTARY MATERIAL

The Supplementary Material for this article can be found online at: https://www.frontiersin.org/articles/10.3389/fonc.2022.869316/full#supplementary-material

REFERENCES

1. Hepatocellular Carcinoma. *Nat Rev Dis Primers* (2021) 7(1):7. doi: 10.1038/s41572-021-00245-6
2. European Association for the Study of the Liver. Electronic Address Eee, European Association for the Study of the L. EASL Clinical Practice Guidelines: Management of Hepatocellular Carcinoma. *J Hepatol* (2018) 69 (1):182–236. doi: 10.1016/j.jhep.2018.03.019
3. Marrero JA, Kulik LM, Sirlin CB, Zhu AX, Finn RS, Abecassis MM, et al. Diagnosis, Staging, and Management of Hepatocellular Carcinoma: 2018 Practice Guidance by the American Association for the Study of Liver Diseases. *Hepatology* (2018) 68(2):723–50. doi: 10.1002/hep.29913
4. Llovet JM, De Baere T, Kulik L, Haber PK, Greten TF, Meyer T, et al. Locoregional Therapies in the Era of Molecular and Immune Treatments for Hepatocellular Carcinoma. *Nat Rev Gastroenterol Hepatol* (2021) 18(5):293–313. doi: 10.1038/s41575-020-00395-0
5. Lee S, Kang TW, Cha DI, Song KD, Lee MW, Rhim H, et al. Radiofrequency Ablation vs. Surgery for Perivascular Hepatocellular Carcinoma: Propensity Score Analyses of Long-Term Outcomes. *J Hepatol* (2018) 69(1):70–8. doi: 10.1016/j.jhep.2018.02.026
6. Nault JC, Sutter O, Nahon P, Ganne-Carrie N, Seror O. Percutaneous Treatment of Hepatocellular Carcinoma: State of the Art and Innovations. *J Hepatol* (2018) 68(4):783–97. doi: 10.1016/j.jhep.2017.10.004
7. Geboers B, Scheffer HJ, Graybill PM, Ruarus AH, Nieuwenhuizen S, Puijk RS, et al. High-Voltage Electrical Pulses in Oncology: Irreversible Electroporation, Electrochemotherapy, Gene E Lectrotransfer, Electrofusion, and Electroimmunotherapy. *Radiology* (2020) 295(2):254–72. doi: 10.1148/radiol.2020192190
8. Yarmush ML, Golberg A, Sersa G, Kotnik T, Miklavcic D. Electroporation-Based Technologies for Medicine: Principles, Applications, and Challenges. *Annu Rev BioMed Eng* (2014) 16:295–320. doi: 10.1146/annurev-bioeng-071813-104622
9. Distelmaier M, Barabasch A, Heil P, Kraemer NA, Isfort P, Keil S, et al. Midterm Safety and Efficacy of Irreversible Electroporation of Malignant Liver Tumors Located Close to Major Portal or Hepatic Veins. *Radiology* (2017) 285(3):1023–31. doi: 10.1148/radiol.2017161561
10. Niessen C, Thumann S, Beyer L, Pregler B, Kramer J, Lang S, et al. Percutaneous Irreversible Electroporation: Long-Term Survival Analysis of 71 Patients With Inoperable Malignant Hepatic Tumors. *Sci Rep* (2017) 7:43687. doi: 10.1038/srep43687
11. Sutter O, Calvo J, N'Kontchou G, Nault JC, Ourabia R, Nahon P, et al. Safety and Efficacy of Irreversible Electroporation for the Treatment of Hepatocellular Carcinoma Not Amenable to Thermal Ablation Techniques: A Retrospective Single-Center Case Series. *Radiology* (2017) 284(3):877–86. doi: 10.1148/radiol.2017161413
12. Kingham TP, Karkar AM, D'Angelica MI, Allen PJ, Dematteo RP, Getrajdman GI, et al. Ablation of Perivascular Hepatic Malignant Tumors With Irreversible Electroporation. *J Am Coll Surg* (2012) 215(3):379–87. doi: 10.1016/j.jamcollsurg.2012.04.029
13. Gupta P, Maralakunte M, Sagar S, Kumar MP, Bhujade H, Chaluvashetty SB, et al. Efficacy and Safety of Irreversible Electroporation for Malignant Liver Tumors: A Systematic Review and Meta-Analysis. *Eur Radiol* (2021) 31 (9):6511–21. doi: 10.1007/s00330-021-07742-y
14. Craviso GL, Choe S, Chatterjee P, Chatterjee I, Vernier PT. Nanosecond Electric Pulses: A Novel Stimulus for Triggering Ca2+ Influx Into Chromaffin Cells *via* Voltage-Gated Ca2+ Channels. *Cell Mol Neurobiol* (2010) 30 (8):1259–65. doi: 10.1007/s10571-010-9573-1
15. Pakhomov AG, Xiao S, Pakhomova ON, Semenov I, Kuipers MA, Ibey BL. Disassembly of Actin Structures by Nanosecond Pulsed Electric Field is a Downstream Effect of Cell Swelling. *Bioelectrochemistry* (2014) 100:88–95. doi: 10.1016/j.bioelechem.2014.01.004
16. Tolstykh GP, Beier HT, Roth CC, Thompson GL, Payne JA, Kuipers MA, et al. Activation of Intracellular Phosphoinositide Signaling After a Single 600 Nanosecond Electric Pulse. *Bioelectrochemistry* (2013) 94:23–9. doi: 10.1016/j.bioelechem.2013.05.002
17. Liu H, Zhao Y, Yao C, Schmelz EM, Davalos RV. Differential Effects of Nanosecond Pulsed Electric Fields on Cells Representing Progressive Ovarian Cancer. *Bioelectrochemistry* (2021) 142:107942. doi: 10.1016/j.bioelechem.2021.107942

18. Long G, Shires PK, Plescia D, Beebe SJ, Kolb JF, Schoenbach KH. Targeted Tissue Ablation With Nanosecond Pulses. *IEEE Trans BioMed Eng* (2011) 58 (8):2161–7. doi: 10.1109/TBME.2011.2113183
19. Miao X, Yin S, Shao Z, Zhang Y, Chen X. Nanosecond Pulsed Electric Field Inhibits Proliferation and Induces Apoptosis in Human Osteosarcoma. *J Orthop Surg Res* (2015) 10:104. doi: 10.1186/s13018-015-0247-z
20. Gianulis EC, Labib C, Saulis G, Novickij V, Pakhomova ON, Pakhomov AG. Selective Susceptibility to Nanosecond Pulsed Electric Field (nsPEF) Across Different Human Cell Types. *Cell Mol Life Sci* (2017) 74(9):1741–54. doi: 10.1007/s00018-016-2434-4
21. Nuccitelli R, Tran K, Sheikh S, Athos B, Kreis M, Nuccitelli P. Optimized Nanosecond Pulsed Electric Field Therapy can Cause Murine Malignant Melanomas to Self-Destruct With a Single Treatment. *Int J Cancer* (2010) 127(7):1727–36. doi: 10.1002/ijc.25364
22. Zhao J, Chen S, Zhu L, Zhang L, Liu J, Xu D, et al. Antitumor Effect and Immune Response of Nanosecond Pulsed Electric Fields in Pancreatic Cancer. *Front Oncol* (2020) 10:621092. doi: 10.3389/fonc.2020.621092
23. Nuccitelli R, Wood R, Kreis M, Athos B, Huynh J, Lui K, et al. First-In-Human Trial of Nanoelectroablation Therapy for Basal Cell Carcinoma: Proof of Method. *Exp Dermatol* (2014) 23(2):135–7. doi: 10.1111/exd.12303
24. Chen X, Zhuang J, Kolb JF, Schoenbach KH, Beebe SJ. Long Term Survival of Mice With Hepatocellular Carcinoma After Pulse Power Ablation With Nanosecond Pulsed Electric Fields. *Technol Cancer Res Treat* (2012) 11 (1):83–93. doi: 10.7785/tcrt.2012.500237
25. Yin S, Chen X, Hu C, Zhang X, Hu Z, Yu J, et al. Nanosecond Pulsed Electric Field (nsPEF) Treatment for Hepatocellular Carcinoma: A Novel Locoregional Ablation Decreasing Lung Metastasis. *Cancer Lett* (2014) 346 (2):285–91. doi: 10.1016/j.canlet.2014.01.009
26. Liu J, Chen X, Zheng S. Immune Response Triggered by the Ablation of Hepatocellular Carcinoma With Nanosecond Pulsed Electric Field. *Front Med* (2021) 15(2):170–7. doi: 10.1007/s11684-020-0747-z
27. Hu S, Zhu Y, Chen Y, Cheng P, Wang GR, Wang LQ, et al. Nanosecond Pulsed Electric Field Interrupts the Glycogen Metabolism in Hepatocellular Carcinoma by Modifying the Osteopontin Pathway. *Hepatobiliary Pancreat Dis Int* (2021) 21(2):3. doi: 10.1016/j.hbpd.2021.12.001
28. Yin S, Chen X, Xie H, Zhou L, Guo D, Xu Y, et al. Nanosecond Pulsed Electric Field (nsPEF) Enhance Cytotoxicity of Cisplatin to Hepatocellular Cells by Microdomain Disruption on Plasma Membrane. *Exp Cell Res* (2016) 346 (2):233–40. doi: 10.1016/j.yexcr.2016.06.018
29. Qian J, Liu J, Hong L, Lu H, Guo D, Liu Z, et al. Upregulation of PDGF Mediates Robust Liver Regeneration After Nanosecond Pulsed Electric Field Ablation by Promoting the HGF/c-Met Pathway. *BioMed Res Int* (2020) 2020:3635787. doi: 10.1155/2020/3635787
30. Chan AW, Tetzlaff JM, Altman DG, Laupacis A, Gotzsche PC, Krleza-Jeric K, et al. SPIRIT 2013 Statement: Defining Standard Protocol Items for Clinical Trials. *Ann Intern Med* (2013) 158(3):200–7. doi: 10.7326/0003-4819-158-3-201302050-00583
31. Ahmed M, Solbiati L, Brace CL, Breen DJ, Callstrom MR, Charboneau JW, et al. Image-Guided Tumor Ablation: Standardization of Terminology and Reporting Criteria–a 10-Year Update. *Radiology* (2014) 273(1):241–60. doi: 10.1148/radiol.14132958
32. Puijk RS, Ahmed M, Adam A, Arai Y, Arellano R, de Baere T, et al. Consensus Guidelines for the Definition of Time-To-Event End Points in Image-Guided Tumor Ablation: Results of the SIO and DATECAN Initiative. *Radiology* (2021) 301(3):533–40. doi: 10.1148/radiol.2021203715
33. Yu M, Li S. Irreversible Electroporation for Liver Cancer Ablation: A Meta Analysis. *Ejso* (2021) 48(6):1321–30. doi: 10.1016/j.ejso.2021.12.015
34. Al Efishat M, Wolfgang CL, Weiss MJ. Stage III Pancreatic Cancer and the Role of Irreversible Electroporation. *BMJ* (2015) 350:h521. doi: 10.1136/bmj.h521
35. Collettini F, Enders J, Stephan C, Fischer T, Baur ADJ, Penzkofer T, et al. Image-Guided Irreversible Electroporation of Localized Prostate Cancer: Functional and Oncologic Outcomes. *Radiology* (2019) 292(1):250–7. doi: 10.1148/radiol.2019181987
36. Diehl SJ, Rathmann N, Kostrzewa M, Ritter M, Smakic A, Schoenberg SO, et al. Irreversible Electroporation for Surgical Renal Masses in Solitary Kidneys: Short-Term Interventional and Functional Outcome. *J Vasc Interv Radiol* (2016) 27(9):1407–13. doi: 10.1016/j.jvir.2016.03.044
37. Schoenbach KH, Beebe SJ, Buescher ES. Intracellular Effect of Ultrashort Electrical Pulses. *Bioelectromagnetics* (2001) 22(6):440–8. doi: 10.1002/bem.71
38. Tekle E, Oubrahim H, Dzekunov SM, Kolb JF, Schoenbach KH, Chock PB. Selective Field Effects on Intracellular Vacuoles and Vesicle Membranes With Nanosecond Electric Pulses. *Biophys J* (2005) 89(1):274–84. doi: 10.1529/biophysj.104.054494
39. Gnoni A, Licchetta A, Memeo R, Argentiero A, Solimando AG, Longo V, et al. Role of BRAF in Hepatocellular Carcinoma: A Rationale for Future Targeted Cancer Therapies. *Medicina (Kaunas)* (2019) 55(12):754. doi: 10.3390/medicina55120754

Conflict of Interest: The authors declare that the research was conducted in the absence of any commercial or financial relationships that could be construed as a potential conflict of interest.

Publisher's Note: All claims expressed in this article are solely those of the authors and do not necessarily represent those of their affiliated organizations, or those of the publisher, the editors and the reviewers. Any product that may be evaluated in this article, or claim that may be made by its manufacturer, is not guaranteed or endorsed by the publisher.

frontiers | Frontiers in Oncology

TYPE Clinical Trial
PUBLISHED 21 September 2022
DOI 10.3389/fonc.2022.913017

OPEN ACCESS

EDITED BY
Chandan Guha,
Albert Einstein College of Medicine, United States

REVIEWED BY
Cathy Eng,
Vanderbilt University, United States
Weijian Guo,
Fudan University, China
Tianqiang Song,
Tianjin Medical University Cancer Institute and Hospital, China

*CORRESPONDENCE
Xu Zhu
drzhuxu@163.com

SPECIALTY SECTION
This article was submitted to Cancer Imaging and Image-directed Interventions, a section of the journal Frontiers in Oncology

RECEIVED 05 April 2022
ACCEPTED 29 August 2022
PUBLISHED 21 September 2022

CITATION
Feng A-W, Guo J-H, Gao S, Kou F-X, Liu S-X, Liu P, Chen H, Wang X-D, Xu H-F, Cao G and Zhu X (2022) A randomized phase II trial of hepatic arterial infusion of oxaliplatin plus raltitrexed versus oxaliplatin plus 5-fluorouracil for unresectable colorectal cancer liver metastases. *Front. Oncol.* 12:913017. doi: 10.3389/fonc.2022.913017

A randomized phase II trial of hepatic arterial infusion of oxaliplatin plus raltitrexed versus oxaliplatin plus 5-fluorouracil for unresectable colorectal cancer liver metastases

Ai-Wei Feng, Jian-Hai Guo, Song Gao, Fu-Xin Kou, Shao-Xing Liu, Peng Liu, Hui Chen, Xiao-Dong Wang, Hai-Feng Xu, Guang Cao and Xu Zhu*

Department of Interventional Therapy, Key Laboratory of Carcinogenesis and Translational Research (Ministry of Education/Beijing), Peking University Cancer Hospital and Institute, Beijing, China

Background: The purpose was to compare the efficacy and safety of hepatic arterial infusion (HAI) of oxaliplatin plus raltitrexed (TOMOX) to those of oxaliplatin plus 5-fluorouracil (FOLFOX) for unresectable colorectal cancer liver metastases (CRCLM).

Methods: Patients with unresectable CRCLM were randomly assigned to receive HAI of TOMOX or FOLFOX. The primary end points were progression-free survival (PFS) measured from the date of randomisation until the date of disease progression and objective response rate (ORR). The secondary end points were overall survival (OS) measured from the date of randomisation until the date of death from any cause, disease control rate (DCR), and adverse events.

Results: 113 patients were randomly assigned. With a median follow-up of 39.5 months, the PFS was 5.8 months [95% CI, 4.838–6.762]) and 4.6 months [95% CI, 3.419–5.781; P = 0.840], and the median OS was 17.6 months [95% CI, 13.828–21.372] and 13.1 months [95% CI, 11.215–14.985; P = 0.178] for the FOLFOX and TOMOX arm, respectively. The ORR were 26.1% vs 22.4% and DCR were 80.4% vs 71.4% in the FOLFOX and TOMOX arms. The most common severe adverse event was elevation of liver enzymes and pain, which did not differ in the two arms.

Conclusion: HAI chemotherapy was effective for unresectable CRCLM. HAI of FOLFOX has similar efficacy to TOMOX, and HAI of TOMOX had shorter arterial infusion time.

10.3389/fonc.2022.913017

Clinical Trial Registration: https://clinicaltrials.gov/, identifier NCT02557490.

KEYWORDS

hepatic arterial infusion, colorectal cancer, liver metastases, oxaliplatin, raltitrexed, 5-fluorouracil

Background

Colorectal cancer is the third most commonly diagnosed cancer and the second leading cause of cancer death all over the world (1). Approximately 30% of all patients with colorectal cancer develop liver metastases, liver lesions account for at least two-thirds mortality (2). Given that liver resection is associated with improved prognosis, systemic chemotherapies combining with targeted therapies (anti-vascular endothelial growth factor (anti-VEGF) or anti-epidermal growth factor receptor (anti-EGFR) therapy), and HAI chemotherapy has been focused on improving the potential for resection of liver metastases considered unresectable (3–6). The blood supply of liver parenchyma is mainly from portal vein, but the blood supply of liver tumour is mainly from hepatic artery (7). For patients with liver-only or liver-dominant metastases, HAI chemotherapy has evolved as an attractive local therapeutic option because of low systemic toxicity and high local control rates, even when all standard systemic therapy has been used (8–11).

Floxuridine has been widely used for HAI because of the high first-pass hepatic extraction and limited systemic toxic effects noted for the drug, regardless of whether HAI is used alone or in combination with systemic chemotherapy (12–14). The most common adverse events of HAI of floxuridine are biliary toxicity and biliary sclerosis, which are non-interventional and permanent. Several clinical studies showed that the incidence of these adverse events increased when the treatment also included systemic bevacizumab (15–17). Oxaliplatin, irinotecan, 5-fluorouracil, and raltitrexed are the main chemotherapeutic drugs for colorectal cancer; HAI is gradually being used for these drugs, especially in Asia and Europe. Patients who underwent postoperative adjuvant HAI of oxaliplatin combined with systemic chemotherapy showed significantly better 3-year disease-free survival after radical resection of colorectal cancer liver metastases (CRCLM) than patients who underwent adjuvant systemic chemotherapy alone (18). HAI along with doublet or triplet chemotherapy is still extremely effective, even for cases of unresectable CRCLM that have not responded to previous chemotherapy (6, 19).

HAI of FOLFOX has been found to be a feasible treatment option for unresectable CRCLM. 5-fluorouracil is administered intra-arterially for approximately 44 hours every cycle and oxaliplatin is for 4 hours. However, prolonged bed rest increases the incidence of thromboembolic events in some high-risk patients. HAI of TOMOX can help avoid thromboembolic events because raltitrexed requires a short pumping time for only 1 hour. We had previously conducted a retrospective study at our centre, wherein a head-to-head analysis comparing HAI of FOLFOX with TOMOX for unresectable CRCLM had been performed; PFS and OS were found to be similar in both arms (20). Therefore, we expanded on that analysis in the current prospective randomised controlled trial, which aimed to further compare the efficacy and safety of HAI of FOLFOX with TOMOX for unresectable CRCLM.

Patients and methods

Ethics approval

This study was initiated by Beijing Cancer Hospital, China, and registered at ClinicalTrials.gov (identification number, NCT02557490). Informed consent was obtained from the study participants, and the study protocol was approved by the local ethics committee.

Patients

The inclusion criteria were as follows: age ≥ 18 years; histologically confirmed colorectal adenocarcinoma with unresectable liver metastases occupying less than 70% of the liver parenchyma; Eastern Cooperative Oncology Group (ECOG) performance score < 2; life expectancy > 12 weeks; haemoglobin level > 90 g/L; absolute neutrophil count >

1.5×10^9/L; thrombocyte > 80×10^9/L; liver enzyme (including alanine amino transferase and aspartic acid amino transferase) level < five times of the upper limit of the normal range; total bilirubin level < three times of the upper limit of the normal range; serum creatinine level < 1.5 times of the upper limit of the normal range; and prothrombin time < 1.5 times of the upper limit of the normal range; refractory or intolerant to systemic treatment; or unsuitable for systemic treatment. Patients who had extrahepatic metastases were included at the investigators' discretion, provided that the dominant lesion was hepatic.

The main exclusion criteria were as follows: (a) brain metastases, (b) previous trans-arterial chemoembolization (TACE), and (c) other malignancy (within 3 years before study entry).

HAI procedure

For the HAI procedure, a coaxial catheter (Renegade Hi Flo, Boston Scientific, Boston, MA, United States/Stride ASAHI INTECC, Seto, Japan) was inserted through the femoral artery using Seldinger's technique. Based on the tumour location, a microcatheter was placed in the proper hepatic artery or the right or left hepatic arterial branch under arteriography guidance. The peripheral region of the microcatheter that was exposed outside the body was connected with an arterial chemotherapeutic pump. Medication infusion was initiated immediately after catheter insertion. The microcatheter was removed at the end of every treatment cycle.

Medication protocol

The FOLFOX arm consisted of oxaliplatin (85 mg/m^2 *via* 4-h infusion) and 5-Fluorouracil (2000 mg/m^2 *via* 44-h infusion) administered *via* HAI and leucovorin (200 mg/m^2 *via* 2-h infusion initiated at the beginning of the 5-Fluorouracil infusion) administered *via* intravenous infusion. The TOMOX arm consisted of oxaliplatin (85 mg/m^2 *via* 4-h infusion) and raltitrexed (3 mg/m^2 *via* 1-h infusion) administered *via* HAI.

Compared to systemic chemotherapy, HAI can increase the local blood concentration. The incidence of liver injury can be reduced and the treatment tolerance is better improved with the prolonged interval. HAI was regularly performed every 4 weeks, until disease progression, treatment intolerance, or death occurred.

Objectives and assessment

The primary end points were progression-free survival (PFS) defined as the date of randomisation until the date of disease progression and ORR defined as the proportion of patients achieving complete response (CR) or partial response (PR). The secondary end points were overall survival (OS) defined as the date of randomisation until the date of death from any cause, DCR and adverse events. DCR was defined as the proportion of patients achieving CR, PR, or stable disease (SD). Tumour response to treatment was evaluated by imaging analysis according to Response Evaluation Criteria in Solid Tumour (RECIST) version 1.1. Adverse events were categorized on the basis of Common Terminology Criteria for Adverse Events (CTCAE) 5.0.

Pre-treatment evaluation included laboratory tests, chest computed tomography (CT), abdominal CT or magnetic resonance imaging (MRI). Laboratory tests were performed every week during the treatment. Imaging analyses for all lesions (intrahepatic and extrahepatic lesions) were performed for every cycle. Additional imaging analyses were performed to detect potential metastases if clinical symptoms appeared.

Statistical analysis

The assumptions used for size calculation are following: the median PFS in the FOLFOX arm was about 7 months while the median PFS in the TOMOX arm was about 4 months, bilateral α=0.05, power = 80%. The enrollment period was 36 months, the minimal follow up period was 12 months, the total study period was 48 months. Loss to follow-up rate was set as 5%. Using a treatment allocation of 1:1(FOLFOX to TOMOX), total 120 patient in this study and 60 patients per arm were necessary according to the calculation with NCSS-PASS 11 (21, 22).

The χ^2 test or Fisher's exact test was used to analyse differences between categorical variables. Survival time was calculated using the Kaplan–Meier method and compared with the Cox regression model (with hazard ratios [HRs] and 95% confidence intervals [CIs] indicated). The significance of differences in survival was calculated using the log-rank test. Potential prognostic variables were included in the univariate Cox regression model. All statistical tests were two-sided and P-values < 0.05 were considered significant. All statistical analyses were performed using the SPSS software (version 25; IBM SPSS Statistics, Armonk, NY, United States).

Results

Baseline demographic and clinical characteristics

From January 2015 to August 2019, 120 patients were screened, of whom 117 patients were randomly assigned to the TOMOX and FOLFOX cohorts (TOMOX arm, n = 61; FOLFOX arm, n = 56). In the FOLFOX arm, four patients were excluded: one patient was allergic to oxaliplatin, two patients underwent

surgery after the first treatment cycle without tumour assessment, and one patient withdrew informed consent (Figure 1). In the TOMOX and FOLFOX arms, more than 90% of the patients had received oxaliplatin and fluorouracil-based chemotherapy, 78 patients were refractory to systemic therapy, 34 patients were intolerant to systemic therapy. Five untreated patients enrolled in this trial did not have extrahepatic lesion and the hepatic tumour burden was really heavy. After carefully evaluation by multi-disciplinary treatment, HAI was recommended to treat the hepatic metastases without systemic therapy. The patients had also received targeted biologic therapy before HAI, including anti-VEGF therapy (bevacizumab: 26% vs 33%), anti-EGFR therapy (cetuximab: 20% vs 15%), or a combination of both (5% vs 4%) (Table 1). There were 58 patients combined with extrahepatic metastases, including lung metastases (34.5%), lymphatic metastases (16.8%), bone metastases (4.4%) and peritoneal metastases (3.5%). All these patients were strictly evaluated by two senior attending physicians independently, and hepatic metastases were the dominant lesions.

Efficacy

The final analysis included 113 patients (TOMOX arm, n = 61; FOLFOX arm, n = 52). The cut-off date for follow-up was May 16, 2020 (median follow-up duration, 39.5 months), at which time 83 deaths had occurred. The mean HAI treatment cycles were 3.0 and 2.7 in the TOMOX and FOLFOX arms, respectively. The median OS was 17.6 months [95% CI, 13.828–21.372] in the FOLFOX arm and 13.1 months [95% CI, 11.215–14.985; P = 0.178] in the TOMOX arm (Figure 2). The HR for OS was 0.743 for FOLFOX versus TOMOX (95% CI, 0.480–1.149; P = 0.181). The median PFS was 5.8 months [95% CI, 4.838–6.762] in the FOLFOX arm and 4.6 months [95% CI, 3.419–5.781; P = 0.840] in the TOMOX arm (Figure 3). The HR for PFS was 0.962 for FOLFOX versus TOMOX (95% CI, 0.655–1.411; P = 0.842). For the patients received HAI as third-line and above therapy, the median PFS was 5.9 months [95% CI, 4.826–6.974] in the FOLFOX arm and 4.4 months [95% CI, 2.793–6.007; P = 0.969] in the TOMOX arm, the median OS was 17.8 months [95% CI, 6.129–29.471] in the FOLFOX arm and 12.9 months [95% CI, 10.617–15.183; P = 0.091] in the TOMOX arm. Two patients in the FOLFOX arm and one patient in the TOMOX arm achieved CR. The ORR was 26.1% in FOLFOX arm and 22.4% in TOMOX arm. The DCR was 80.4% and 71.4% in the FOLFOX and TOMOX arm, respectively (Table 2). 1 patient received radical resection of liver metastases. 2 patients who achieved CR received targeted therapy as maintenance therapy without radical resection. 6 patients received radical microwave ablation. 1patient received radical radiotherapy. The other 13 patients who achieved PR did not receive local therapy because of advanced age, unresectable extrahepatic metastases, the remaining liver volume cannot be resected after previous partial hepatectomy and heavy tumour burden cannot be radical resection.

Response to HAI was an independent positive prognostic factor for both PFS and OS according to Cox univariate analysis (Table 3). The primary tumour site, primary tumour resection, and histological features were prognostic factors for OS. However, age, sex, synchronous or metachronous liver metastasis, extrahepatic metastasis, KRAS gene status, and systemic therapy before HAI did not show significant correlation with prognosis.

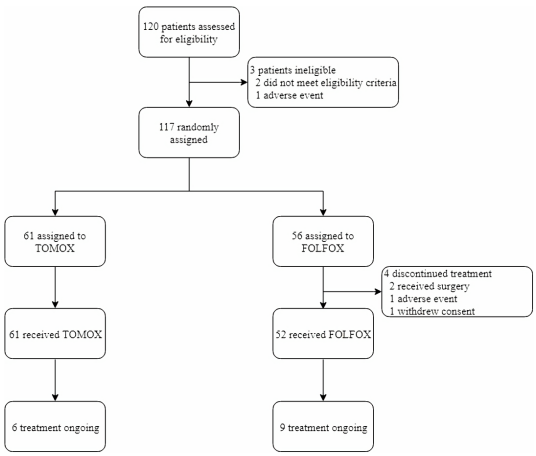

FIGURE 1
Trial Profile.

10.3389/fonc.2022.913017

TABLE 1 Patient demographics and baseline characteristics.

n (%)	TOMOX n = 61	FOLFOX n = 52
Age at diagnosis		
≥65 years	12 (19.7%)	11(21.2%)
<65 years	49 (80.3%)	41(78.8%)
Median age (years [IQR])	58 (31-79)	58(34-83)
Sex		
Male	41 (67.2%)	34(65.4%)
Female	20 (32.8%)	18 (34.6%)
Primary tumour site		
Left hemicolon	41 (67.2%)	41(78.8%)
Right hemicolon	18 (29.5%)	9 (17.3%)
Unknown	2 (3.3%)	2 (3.8%)
Genetic condition		
KRAS mutation	13 (21.3%)	16 (30.8%)
KRAS wild type	14 (23.0%)	11 (21.2%)
Unknown	34(55.7%)	25 (48.1%)
Histology		
Poorly differentiated adenocarcinoma	9 (14.8%)	8 (15.4%)
Well and moderately differentiated adenocarcinoma	40 (65.6%)	33 (63.5%)
Unknown	12 (19.7%)	11 (21.2%)
Mean CEA	616.42ng/ml	604.76ng/ml
Liver metastasis		
Synchronous	50 (82.0%)	47 (90.4%)
Metachronous	11 (18.0%)	5 (9.6%)
Mean size of the biggest liver metastasis	51.2mm	48.7mm
No. of metastatic lesions		
≥3	49 (80.3%)	42 (80.8%)
<3	12 (19.7%)	10 (19.2%)
Primary tumour		
Resection	42 (68.9%)	33 (63.5%)
No resection	14 (23.0%)	15 (28.8%)
Unknown	5 (8.2%)	4 (7.7%)
Extrahepatic metastasis		
Present	31 (50.8%)	27 (51.9%)
Absent	30 (49.2%)	25 (48.1%)
Systemic therapy before HAI		
Untreated	4 (6.6%)	1 (1.9%)
First-line	27 (44.3%)	20 (38.5%)
Second-line	22 (36.1%)	19 (36.5%)
Third-line and above	8 (13.1%)	12 (23.1%)
Previous chemotherapy agents before HAI		
Oxaliplatin	55 (90%)	48 (92%)
Irinotecan	33 (54%)	36 (69%)
Fluorouracil	57 (93%)	51 (98%)
Previous anti-VEGF or anti-EGFR treatment or both before HAI		
Bevacizumab	16 (26%)	17 (33%)
Cetuximab	12 (20%)	8 (15%)
Both	3 (5%)	2 (4%)
None	30 (49%)	25 (48%)

VEGF, vascular endothelial growth factor; EGFR, epidermal growth factor receptor.

Safety

Treatment-related adverse events were evaluated in all patients (Table 4). The most common haematological adverse events were anaemia (34%), leucopenia (33%), and thrombocytopenia (40%) in both arms. The incidence of grade 3 or 4 neutropenia was 2% and 3% in the FOLFOX and TOMOX arms, respectively. Febrile neutropenia was not noted. Elevation of liver enzymes (including alanine amino transferase and aspartic acid amino transferase) was the most frequent non-haematological adverse event, which was seen in 87% and 100% of patients in the FOLFOX and TOMOX arms, respectively; occurrence of grade 3 or 4 elevation of liver enzymes did not significantly differ between the two arms (12% and 18%, respectively; P = 0.432). Bilirubin elevation was seen in 71% and 64% of the patients in the FOLFOX and TOMOX arms, respectively. Grade 3 or 4 hyperbilirubinemia occurred in 4% and 8% of the patients in the FOLFOX and TOMOX arms, respectively, but none of them required biliary stents to relieve jaundice. Approximately half of the patients in both arms experienced severe abdominal pain during agent infusion. Opioid oral administration or lidocaine pumped through the hepatic artery could significantly relieve pain. The incidence of other common clinical adverse events such as nausea, vomiting, fatigue, fever, and diarrhoea was similar in both arms. There were no treatment-related deaths in both arms.

Discussion

HAI of 5-Fluorouracil or oxaliplatin has been proved a safe and feasible treatment even for heavily pre-treated CRCLM (23, 24). However, there is no standard treatment protocol for HAI. The vast majority of studies revolve around the combination of HAI with systemic chemotherapy or targeted therapy, or HAI versus systemic therapy. No head-to-head randomised controlled studies compared two HAI regimens. We had previously performed a retrospective analysis during May 2013 to April 2015 to compare the efficacy and safety of HAI of TOMOX with FOLFOX for patients with unresectable CRCLM. The retrospective analysis showed that the OS was 15.4 versus 20.6 months (P = 0.734) and that the PFS was 6.6 versus 4.9 months (P = 0.215) for the FOLFOX versus TOMOX arms (20). On the basis of that study, we performed this prospective randomised controlled trial for more in-depth analysis of HAI of TOMOX and FOLFOX.

In the current prospective randomised controlled trial, most of the patients had tumours that were refractory to oxaliplatin- and fluorouracil-based chemotherapy, more than 60% patients had tumours that did not response to irinotecan-based therapy and more than half of the patients had exposure to targeted biologic therapy, including bevacizumab and cetuximab. HAI of TOMOX or FOLFOX led to an ORR of 24% for all the patients. The median PFS was 4.6 and 5.8 months in the TOMOX and FOLFOX arms, and the median OS was 13.1 and 17.6 months. The results were consistent with previous studies at other centres. In a randomised phase-II study of HAI of TOMOX for cases of metastatic colorectal cancer wherein the therapy failed or the patients were intolerant to standard systemic therapy, the OS and the PFS were found to be 11.2 and 6.7 months, respectively (19). In this trial, for the patients received HAI as third-line and above therapy, the median PFS was 5.9

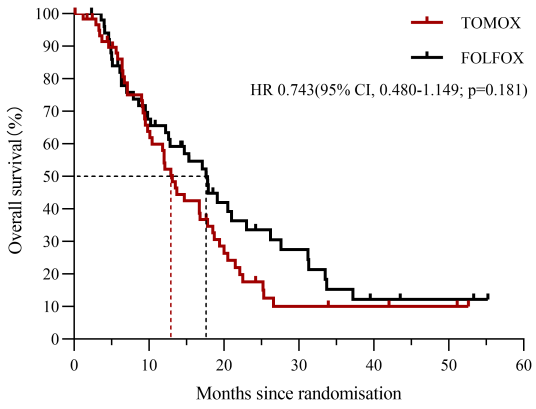

FIGURE 2
OS since randomization for patients receiving HAI of FOLFOX or TOMOX.

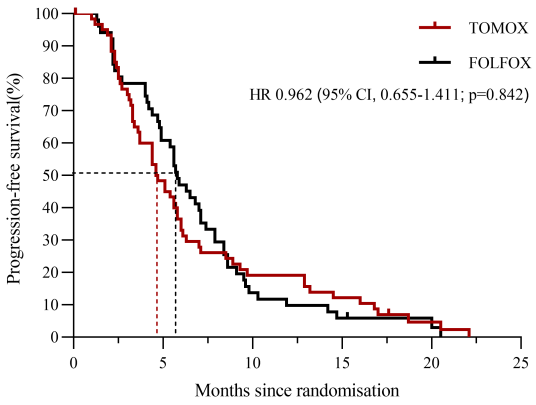

FIGURE 3
PFS since randomization for patients receiving HAI of FOLFOX or TOMOX.

TABLE 2 Response rates to HAI of TOMOX or FOLFOX.

Best response, n (%)	TOMOX n=61	FOLFOX n=52	P-value[a]
CR	1 (1.6)	2 (3.8)	0.621
PR	10 (16.4)	10 (19.2)	
SD	24 (39.3)	25 (48.1)	
PD	14 (23.0)	9 (17.3)	
Unknown	12 (19.7)	6 (11.5)	
ORR	11 (22.4)	12 (26.1)	
DCR	35 (71.4)	37 (80.4)	

[a]P-value calculated using a Fisher exact test.
CR, complete response; PR, partial response; SD, stable disease; PD, progressive disease; ORR, objective response rate; DCR, disease control rate.

months in the FOLFOX arm and 4.4 months in the TOMOX arm, the median OS was 17.8 months in the FOLFOX arm and 12.9 months in the TOMOX arm. For colorectal tumours that are refractory to all the standard first- and second-line systemic therapies, the third-line treatment options are limited. In a prospective phase II study, raltitrexed combined with S-1 treated metastatic colorectal cancer after the failure of conventional chemotherapy demonstrated favourable effects. The median PFS and median OS 2.5 and 8.0 months, respectively (25). Besides, TAS-102 and regorafenib are the recommended third-line systemic therapy. TAS-102 has been reported improve median OS from 5.3 to 7.1 months and median PFS from 1.7 to 2.0 months (26, 27). CORRECT and CONCUR reported that regorafenib versus placebo improved

TABLE 3 Cox univariate analyses of prognostic factors for survival.

Prognostic factor (n)	PFS			OS		
	HR	95% CI	P-value	HR	95% CI	P-value
Age at diagnosis, years						
<65 (90)	1.494	0.931-2.396	0.096	1.157	0.686-1.953	0.585
≥65 (23)	1			1		
Sex						
Male (75)	0.908	0.607-1.357	0.637	0.768	0.489-1.207	0.253
Female (38)	1			1		
Primary tumour site						
Right hemicolon (27)	1.119	0.718-1.743	0.620	1.972	1.200-3.239	0.007
Left hemicolon (82)	1			1		
Liver metastasis						
Synchronous (97)	0.917	0.537-1.565	0.750	0.817	0.459-1.454	0.492
Metachronous (16)	1			1		
Extrahepatic metastasis						
Present (58)	1.193	0.814-1.750	0.366	1.503	0.969-2.329	0.069
Absent (55)	1			1		
Primary tumour						
No resection (29)	1.206	0.764-1.905	0.421	2.553	1.527-4.268	0.000
Resection (75)	1			1		
Genetic condition						
KRAS mutation (29)	0.833	0.478-1.451	0.518	1.298	0.720-2.339	0.386
KRAS wild type (25)	1			1		
Histology						
Poorly differentiated (17)	1.421	0.832-2.427	0.198	2.357	1.304-4.261	0.005
Well and moderately differentiated (73)	1			1		
Systemic therapy before HAI						
≥Third-line (20)	0.757	0.442-1.298	0.312	1.012	0.542-1.888	0.971
Second line (41)	0.942	0.610-1.453	0.787	0.983	0.606-1.594	0.943
First-line (47)	1			1		
Response to HAI						
CR (3)	0.034	0.009-0.127	0.000	0.180	0.041-0.787	0.023
PR (20)	0.052	0.024-0.110	0.000	0.272	0.133-0.558	0.000
SD (49)	0.081	0.042-0.157	0.000	0.397	0.224-0.705	0.002
PD (23)	1			1		

CI, confidence interval; CR, complete response; HAI, hepatic arterial infusion; OS, overall survival; PD, progressive disease; PFS, progression-free survival; PR, partial response; SD, stable disease.

TABLE 4 Summary of safety data.

Adverse event, n (%)	TOMOX (n=61)		FOLFOX (n=52)		P-value[a]
	All Grade	Grade 3-4	All grade	Grade 3-4	
Hematological					
Anaemia	21 (34)	0 (0)	13 (34)	0 (0)	0.290[c]
Leucopenia	17 (28)	3 (5)	16 (31)	1 (2)	0.623[b]
Neutropenia	5 (8)	2 (3)	7 (13)	1 (2)	1.000[b]
Thrombocytopenia	20 (33)	4 (7)	20 (38)	1 (2)	0.372[b]
Nonhematological					
Elevation of liver enzymes	50 (82)	11 (18)	39 (75)	6 (12)	0.432[b]
Elevation of bilirubin	34 (56)	5 (8)	35 (67)	2 (4)	0.449[b]
Nausea	10 (16)	0 (0)	11 (21)	0 (0)	0.629[c]
vomiting	13 (21)	0 (0)	9 (17)	0 (0)	0.853[c]
Fatigue (asthenia)	10 (16)	0 (0)	5 (10)	0 (0)	0.442[c]
Abdominal pain	32 (52)	31 (51)	31 (60)	27 (52)	1.000[b]
Fever	28 (46)	0 (0)	20 (38)	0 (0)	0.533[c]
Diarrhea	5 (8)	0 (0)	9 (15)	1 (2)	0.460[b]

[a]P-value calculated using a $\chi 2$ test; [b]p-value comparing Grade 3-4 adverse events; [c]p-value comparing all Grade adverse events as no patients experienced Grade 3-4 of these adverse events.

the OS from 5.0 to 6.4 months and 6.3 to 8.8 months, respectively (28, 29). HAI has a considerable survival benefit as a third-line treatment for CRCLM, but large prospective randomized controlled studies are needed to compare the efficacy of HAI and the current standard third-line system therapy in liver-dominant metastases.

HAI is a local therapy specific to liver lesions; peripheral blood concentrations in chemotherapeutic regimens decrease because of the hepatic first-pass effect. In this trial, 58 (51.3%) patients had extrahepatic metastases. The limitation of this study was that there was no combination of systemic or targeted therapy to control extrahepatic metastases more effectively. For KRAS wild-type colorectal cancer, cetuximab combined with chemotherapy as first-line therapy can significantly improve survival time (30, 31). BRAF mutant-type colorectal cancer does not benefit from cetuximab therapy (32, 33). Continued anti-angiogenesis therapy with bevacizumab beyond initial progressive disease is closely related to improvement in survival time (34, 35). In a rat model of colorectal liver metastasis, locoregional application of oxaliplatin and bevacizumab was found to be more effective in reducing tumour growth than systemic treatment with these two agents (36, 37). A retrospective study has showed that HAI combined with systemic chemotherapy and targeted therapy is effective in CRCLM (38). Base on the RAS and BRAF gene status, HAI combine with appropriate targeted therapy is a feasible way, especially for the CRCLM patient with extrahepatic metastases.

TOMOX significantly decreased the duration of bed rest, thereby reducing thromboembolic events caused by immobilization. For elderly patients or patients at high risk of thrombosis, HAI of TOMOX was found to be a better choice.

Conclusion

HAI chemotherapy was safe and effective for unresectable CRCLM. HAI of FOLFOX has similar efficacy to TOMOX, and HAI of TOMOX had shorter arterial infusion time.

Data availability statement

The original contributions presented in the study are included in the article. Further inquiries can be directed to the corresponding author.

Ethics statement

The studies involving human participants were reviewed and approved by Beijing Cancer Hospital Medical Ethics Committee. The patients/participants provided their written informed consent to participate in this study.

Author contributions

Contributorship statement: XZ and SG designed the research. A-WF, J-HG, F-XK, S-XL, PL, H-FX, and GC collected the data. A-WF analyzed the data and wrote the original draft. J-HG edited language and proofread this manuscript. XZ, X-DW, and HC critically revised the manuscript for important intellectual content. A-WF and J-HG contributed equally to this work and should be considered co-first authors.

Funding

National Natural Science Foundation of China (81971717).

Conflict of interest

The authors declare that the research was conducted in the absence of any commercial or financial relationships that could be construed as a potential conflict of interest.

Publisher's note

All claims expressed in this article are solely those of the authors and do not necessarily represent those of their affiliated organizations, or those of the publisher, the editors and the reviewers. Any product that may be evaluated in this article, or claim that may be made by its manufacturer, is not guaranteed or endorsed by the publisher.

References

1. Sung H, Ferlay J, Siegel RL, Laversanne M, Soerjomataram I, Jemal A, et al. Global cancer statistics 2020: GLOBOCAN estimates of incidence and mortality worldwide for 36 cancers in 185 countries. *CA Cancer J Clin* (2021) 71:209–49. doi: 10.3322/caac.21660

2. Kopetz S, Chang GJ, Overman MJ, Eng C, Sargent DJ, Larson DW, et al. Improved survival in metastatic colorectal cancer is associated with adoption of hepatic resection and improved chemotherapy. *J Clin Oncol: Off J Am Soc Clin Oncol* (2009) 27:3677–83. doi: 10.1200/jco.2008.20.5278

3. Kemeny NE, Melendez FD, Capanu M, Paty PB, Fong Y, Schwartz LH, et al. Conversion to resectability using hepatic artery infusion plus systemic chemotherapy for the treatment of unresectable liver metastases from colorectal

carcinoma. *J Clin Oncol: Off J Am Soc Clin Oncol* (2009) 27:3465–71. doi: 10.1200/jco.2008.20.1301

4. Goere D, Deshaies I, de Baere T, Boige V, Malka D, Dumont F, et al. Prolonged survival of initially unresectable hepatic colorectal cancer patients treated with hepatic arterial infusion of oxaliplatin followed by radical surgery of metastases. *Ann Surg* (2010) 251:686–91. doi: 10.1097/SLA.0b013e3181d35983

5. D'Angelica MI, Correa-Gallego C, Paty PB, Cercek A, Gewirtz AN, Chou JF, et al. Phase II trial of hepatic artery infusional and systemic chemotherapy for patients with unresectable hepatic metastases from colorectal cancer: conversion to resection and long-term outcomes. *Ann Surg* (2015) 261:353–60. doi: 10.1097/SLA.0000000000000614

6. Lévi FA, Boige V, Hebbar M, Smith D, Lepère C, Focan C, et al. Conversion to resection of liver metastases from colorectal cancer with hepatic artery infusion of combined chemotherapy and systemic cetuximab in multicenter trial OPTILIV. *Ann Oncol* (2016) 27:267–74. doi: 10.1093/annonc/mdv548

7. Ackerman NB. The blood supply of experimental liver metastases. *IV Changes Vasc Increasing Tumor Growth Surg* (1974) 75:589–96.

8. Kemeny NE, Niedzwiecki D, Hollis DR, Lenz H-J, Warren RS, Naughton MJ, et al. Hepatic arterial infusion versus systemic therapy for hepatic metastases from colorectal cancer: A randomized trial of efficacy, quality of life, and molecular markers (CALGB 9481). *J Clin Oncol* (2006) 24:1395–403. doi: 10.1200/jco.2005.03.8166

9. Gallagher DJ, Capanu M, Raggio G, Kemeny N. Hepatic arterial infusion plus systemic irinotecan in patients with unresectable hepatic metastases from colorectal cancer previously treated with systemic oxaliplatin: a retrospective analysis. *Ann Oncol* (2007) 18:1995–9. doi: 10.1093/annonc/mdm405

10. Cercek A, Boucher TM, Gluskin JS, Aguilo A, Chou JF, Connell LC, et al. Response rates of hepatic arterial infusion pump therapy in patients with metastatic colorectal cancer liver metastases refractory to all standard chemotherapies. *J Surg Oncol* (2016) 114:655–63. doi: 10.1002/jso.24399

11. Lim A, Le Sourd S, Senellart H, Luet D, Douane F, Perret C, et al. Hepatic arterial infusion chemotherapy for unresectable liver metastases of colorectal cancer: A multicenter retrospective study. *Clin Colorectal Cancer* (2017) 16:308–15. doi: 10.1016/j.clcc.2017.03.003

12. Ensminger WD, Rosowsky A, Raso V, Levin DC, Glode M, Come S, et al. A clinical-pharmacological evaluation of hepatic arterial infusions of 5-fluoro-2'-deoxyuridine and 5-fluorouracil. *Cancer Res* (1978) 38:3784–92.

13. Kemeny N, Huang Y, Cohen AM, Shi W, Conti JA, Brennan MF, et al. Hepatic arterial infusion of chemotherapy after resection of hepatic metastases from colorectal cancer. *N Engl J Med* (1999) 341:2039–48. doi: 10.1056/nejm199912303412702

14. Groot Koerkamp B, Sadot E, Kemeny NE, Gonen M, Leal JN, Allen PJ, et al. Perioperative hepatic arterial infusion pump chemotherapy is associated with longer survival after resection of colorectal liver metastases: A propensity score analysis. *J Clin Oncol: Off J Am Soc Clin Oncol* (2017) 35:1938–44. doi: 10.1200/jco.2016.71.8346

15. Hohn DC, Stagg RJ, Friedman MA, Hannigan JFJr., Rayner A, Ignoffo RJ, et al. A randomized trial of continuous intravenous versus hepatic intraarterial floxuridine in patients with colorectal cancer metastatic to the liver: the northern California oncology group trial. *J Clin Oncol: Off J Am Soc Clin Oncol* (1989) 7:1646–54. doi: 10.1200/jco.1989.7.11.1646

16. Kemeny NE, Jarnagin WR, Capanu M, Fong Y, Gewirtz AN, Dematteo RP, et al. Randomized phase II trial of adjuvant hepatic arterial infusion and systemic chemotherapy with or without bevacizumab in patients with resected hepatic metastases from colorectal cancer. *J Clin Oncol: Off J Am Soc Clin Oncol* (2011) 29:884–9. doi: 10.1200/JCO.2010.32.5977

17. Cercek A, D'Angelica M, Power D, Capanu M, Gewirtz A, Patel D, et al. Floxuridine hepatic arterial infusion associated biliary toxicity is increased by concurrent administration of systemic bevacizumab. *Ann Surg Oncol* (2014) 21:479–86. doi: 10.1245/s10434-013-3275-0

18. Goéré D, Benhaim L, Bonnet S, Malka D, Faron M, Elias D, et al. Adjuvant chemotherapy after resection of colorectal liver metastases in patients at high risk of hepatic recurrence. *Ann Surg* (2013) 257:114–20. doi: 10.1097/SLA.0b013e31827b9005

19. Ghiringhelli F, Vincent J, Bengrine L, Borg C, Jouve JL, Loffroy R, et al. Hepatic arterial chemotherapy with raltitrexed and oxaliplatin versus standard chemotherapy in unresectable liver metastases from colorectal cancer after conventional chemotherapy failure (HEARTO): a randomized phase-II study. *J Cancer Res Clin Oncol* (2019) 145:2357–63. doi: 10.1007/s00432-019-02970-8

20. Guo JH, Zhang HY, Gao S, Zhang PJ, Li XT, Chen H, et al. Hepatic artery infusion with raltitrexed or 5-fluorouracil for colorectal cancer liver metastasis. *World J Gastroenterol* (2017) 23:1406–11. doi: 10.3748/wjg.v23.i8.1406

21. Lakatos E. Sample sizes based on the log-rank statistic in complex clinical trials. *Biometrics* (1988) 44:229–41. doi: 10.2307/2531910

22. Lakatos E. Designing complex group sequential survival trials. *Stat Med* (2002) 21:1969–89. doi: 10.1002/sim.1193

23. Boige V, Malka D, Elias D, Castaing M, De Baere T, Goere D, et al. Hepatic arterial infusion of oxaliplatin and intravenous LV5FU2 in unresectable liver metastases from colorectal cancer after systemic chemotherapy failure. *Ann Surg Oncol* (2008) 15:219–26. doi: 10.1245/s10434-007-9581-7

24. Tsimberidou AM, Leick MB, Lim J, Fu S, Wheler J, Piha-Paul SA, et al. Dose-finding study of hepatic arterial infusion of oxaliplatin-based treatment in patients with advanced solid tumors metastatic to the liver. *Cancer Chemother Pharmacol* (2013) 71:389–97. doi: 10.1007/s00280-012-2014-8

25. Huang M, Yang Y, Zhu X, Chen Z, Zhang W, Wang C, et al. A prospective phase II study of raltitrexed combined with s-1 as salvage treatment for patients with refractory metastatic colorectal cancer. *Asia Pac J Clin Oncol* (2021) 17:513–21. doi: 10.1111/ajco.13511

26. Longo-Muñoz F, Argiles G, Tabernero J, Cervantes A, Gravalos C, Pericay C, et al. Efficacy of trifluridine and tipiracil (TAS-102) versus placebo, with supportive care, in a randomized, controlled trial of patients with metastatic colorectal cancer from Spain: results of a subgroup analysis of the phase 3 RECOURSE trial. *Clin Trans Oncol: Off Publ Fed Span Oncol Soc Natl Cancer Inst Mex* (2017) 19:227–35. doi: 10.1007/s12094-016-1528-7

27. Mayer RJ, Van Cutsem E, Falcone A, Yoshino T, Garcia-Carbonero R, Mizunuma N, et al. Randomized trial of TAS-102 for refractory metastatic colorectal cancer. *N Engl J Med* (2015) 372:1909–19. doi: 10.1056/NEJMoa1414325

28. Grothey A, Van Cutsem E, Sobrero A, Siena S, Falcone A, Ychou M, et al. Regorafenib monotherapy for previously treated metastatic colorectal cancer (CORRECT): an international, multicentre, randomised, placebo-controlled, phase 3 trial. *Lancet (Lond Engl)* (2013) 381:303–12. doi: 10.1016/s0140-6736(12)61900-x

29. Li J, Qin S, Xu R, Yau TC, Ma B, Pan H, et al. Regorafenib plus best supportive care versus placebo plus best supportive care in Asian patients with previously treated metastatic colorectal cancer (CONCUR): a randomised, double-blind, placebo-controlled, phase 3 trial. *Lancet Oncol* (2015) 16:619–29. doi: 10.1016/s1470-2045(15)70156-7

30. Venook AP, Niedzwiecki D, Lenz H-J, Innocenti F, Mahoney MR, O'Neil BH, et al. CALGB/SWOG 80405: Phase III trial of irinotecan/5-FU/leucovorin (FOLFIRI) or oxaliplatin/5-FU/leucovorin (mFOLFOX6) with bevacizumab (BV) or cetuximab (CET) for patients (pts) with KRAS wild-type (wt) untreated metastatic adenocarcinoma of the colon or rectum (MCRC). *J Clin Oncol* (2014) 32:LBA3–LBA. doi: 10.1200/jco.2014.32.18_suppl.lba3

31. Qin S, Li J, Wang L, Xu J, Cheng Y, Bai Y, et al. Efficacy and tolerability of first-line cetuximab plus leucovorin, fluorouracil, and oxaliplatin (FOLFOX-4) versus FOLFOX-4 in patients with RAS wild-type metastatic colorectal cancer: The open-label, randomized, phase III TAILOR trial. *J Clin Oncol: Off J Am Soc Clin Oncol* (2018) 36:3031–9. doi: 10.1200/jco.2018.78.3183

32. Karapetis CS, Jonker D, Daneshmand M, Hanson JE, O'Callaghan CJ, Marginean C, et al. PIK3CA, BRAF, and PTEN status and benefit from cetuximab in the treatment of advanced colorectal cancer–results from NCIC CTG/AGITG CO. *17 Clin Cancer Res: an Off J Am Assoc Cancer Res* (2014) 20:744–53. doi: 10.1158/1078-0432.ccr-13-0606

33. Pietrantonio F, Petrelli F, Coinu A, Di Bartolomeo M, Borgonovo K, Maggi C, et al. Predictive role of BRAF mutations in patients with advanced colorectal cancer receiving cetuximab and panitumumab: a meta-analysis. *Eur J Cancer (Oxf Engl: 1990)* (2015) 51:587–94. doi: 10.1016/j.ejca.2015.01.054

34. Grothey A, Sugrue MM, Purdie DM, Dong W, Sargent D, Hedrick E, et al. Bevacizumab beyond first progression is associated with prolonged overall survival in metastatic colorectal cancer: Results from a Large observational cohort study (BRiTE). *J Clin Oncol* (2008) 26:5326–34. doi: 10.1200/jco.2008.16.3212

35. Bennouna J, Sastre J, Arnold D, Österlund P, Greil R, Van Cutsem E, et al. Continuation of bevacizumab after first progression in metastatic colorectal cancer (ML18147): a randomised phase 3 trial. *Lancet Oncol* (2013) 14:29–37. doi: 10.1016/s1470-2045(12)70477-1

36. Sperling J, Schäfer T, Ziemann C, Benz-Weiber A, Kollmar O, Schilling MK, et al. Hepatic arterial infusion of bevacizumab in combination with oxaliplatin reduces tumor growth in a rat model of colorectal liver metastases. *Clin Exp Metastasis* (2012) 29:91–9. doi: 10.1007/s10585-011-9432-6

37. Sperling J, Brandhorst D, Schäfer T, Ziemann C, Benz-Weißer A, Scheuer C, et al. Liver-directed chemotherapy of cetuximab and bevacizumab in combination with oxaliplatin is more effective to inhibit tumor growth of CC531 colorectal rat liver metastases than systemic chemotherapy. *Clin Exp Metastasis* (2013) 30:447–55. doi: 10.1007/s10585-012-9550-9

38. Boilève A, De Cuyper A, Larive A, Mahjoubi L, Najdawi M, Tazdait M, et al. Hepatic arterial infusion of oxaliplatin plus systemic chemotherapy and targeted therapy for unresectable colorectal liver metastases. *Eur J Cancer (Oxf Engl: 1990)* (2020) 138:89–98. doi: 10.1016/j.ejca.2020.07.022

frontiers | Frontiers in Oncology

TYPE Original Research
PUBLISHED 14 October 2022
DOI 10.3389/fonc.2022.954445

OPEN ACCESS

EDITED BY
Xiankai Sun,
University of Texas Southwestern Medical Center, United States

REVIEWED BY
Guandou Yuan,
The First Affiliated Hospital of Guangxi Medical University, China
Min Wu,
Sichuan University, China

*CORRESPONDENCE
Baoliang Guo
tomcatccks@163.com
Qiugen Hu
qiugenhu@126.com

†These authors have contributed equally to this work and share first authorship

‡These authors have contributed equally to this work

SPECIALTY SECTION
This article was submitted to Cancer Imaging and Image-directed Interventions, a section of the journal Frontiers in Oncology

RECEIVED 27 May 2022
ACCEPTED 20 September 2022
PUBLISHED 14 October 2022

CITATION
Liu Z, Yang S, Chen X, Luo C, Feng J, Chen H, Ouyang F, Zhang R, Li X, Liu W, Guo B and Hu Q (2022) Nomogram development and validation to predict Ki-67 expression of hepatocellular carcinoma derived from Gd-EOB-DTPA-enhanced MRI combined with T1 mapping. *Front. Oncol.* 12:954445. doi: 10.3389/fonc.2022.954445

Nomogram development and validation to predict Ki-67 expression of hepatocellular carcinoma derived from Gd-EOB-DTPA-enhanced MRI combined with T1 mapping

Ziwei Liu[1†], Shaomin Yang[1,2†], Xinjie Chen[1], Chun Luo[3], Jieying Feng[4], Haixiong Chen[1], Fusheng Ouyang[1], Rong Zhang[1], Xiaohong Li[1], Wei Liu[1], Baoliang Guo[1*‡] and Qiugen Hu[1*‡]

[1]Department of Radiology, Shunde Hospital, Southern Medical University (The First People's Hospital of Shunde), Foshan, China, [2]Department of Radiology, The Affiliated Shunde Hospital of Guangzhou Medical University, Foshan, China, [3]Department of Radiology, The First People's Hospital of Foshan, Foshan, China, [4]Department of Radiology, The Sixth Affiliated Hospital, South China University of Technology, Foshan, China

Objective: As an important biomarker to reflect tumor cell proliferation and tumor aggressiveness, Ki-67 is closely related to the high early recurrence rate and poor prognosis, and pretreatment evaluation of Ki-67 expression possibly provides a more accurate prognosis assessment and more better treatment plan. We aimed to develop a nomogram based on gadolinium ethoxybenzyl diethylenetriamine pentaacetic acid (Gd-EOB-DTPA)-enhanced magnetic resonance imaging (MRI) combined with T1 mapping to predict Ki-67 expression in hepatocellular carcinoma (HCC).

Methods: This two-center study retrospectively enrolled 148 consecutive patients who underwent preoperative Gd-EOB-DTPA-enhanced MRI T1 mapping and surgically confirmed HCC from July 2019 to December 2020. The correlation between quantitative parameters from T1 mapping, ADC, and Ki-67 was explored. Three cohorts were constructed: a training cohort (n = 73) and an internal validation cohort (n = 31) from Shunde Hospital of Southern Medical University, and an external validation cohort (n = 44) from the Sixth Affiliated Hospital, South China University of Technology. The clinical variables and MRI qualitative and quantitative parameters associational with Ki-67 expression were analyzed by univariate and multivariate logistic regression analyses. A nomogram was developed based on these associated with Ki-67 expression in the training cohort and validated in the internal and external validation cohorts.

Results: T1rt-Pre and T1rt-20min were strongly positively correlated with Ki-67 (r = 0.627, r = 0.607, $P < 0.001$); the apparent diffusion coefficient value was

moderately negatively correlated with Ki-67 (r = -0.401, $P < 0.001$). Predictors of Ki-67 expression included in the nomogram were peritumoral enhancement, peritumoral hypointensity, T1rt-20min, and tumor margin, while arterial phase hyperenhancement (APHE) was not a significant predictor even included in the regression model. The nomograms achieved good concordance indices in predicting Ki-67 expression in the training and two validation cohorts (0.919, 0.925, 0.850), respectively.

Conclusions: T1rt-Pre and T1rt-20min had a strong positive correlation with the Ki-67 expression in HCC, and Gd-EOB-DTPA enhanced MRI combined with T1 mapping-based nomogram effectively predicts high Ki-67 expression in HCC.

KEYWORDS

Gd-EOB-DTPA, T1 mapping, hepatocellular carcinoma, Ki-67, nomogram

Introduction

Hepatocellular carcinoma (HCC), as the fifth most common malignancy and the fourth leading cause of cancer-related deaths worldwide, is the most common primary malignant tumor of the liver with increasing incidence (1, 2). The main treatments for HCC include surgical resection, liver transplantation, and transarterial chemoembolization, among others. Surgical resection is recognized as an early radical treatment method, but the recurrence rate of 5 years after surgical resection is as high as 60%–70% (3–5). High early recurrence rate is an important factor affecting the long-term survival and poor prognosis of patients with HCC. The immunohistochemical marker Ki-67 is a nuclear antigen related to cell proliferation activity, and it is a common indicator that reflects the level of cell proliferation. Ki-67 has been proposed as the most valuable independent predictor for evaluating early recurrence and poor prognosis of surgically resected HCC in recent studies (6–8). Ki-67 detection relies on pathological examination. Needle biopsy is a common method to obtain pathological tissue, but it is an invasive examination and has certain disadvantages, such as poor patient compliance, possible surgical risks, and needle tract transfer (9, 10). With the formation of a multidisciplinary and multimethod comprehensive treatment model for liver cancer, a non-invasive preoperative method to predict Ki-67 status is significant in the treatment and prognostic management of patients.

Gadolinium-ethoxybenzyl-diethylenetriamine pentaacetic acid (Gd-EOB-DTPA) is a liver-specific contrast agent, which has dual properties extracellular and hepatobiliary that can be taken up by normal liver cells and is increasingly used in the diagnosis and evaluation of liver diseases. T1 mapping is a non-invasive method of quantitatively analyzing the T1 value of tissue reflecting the T1 relaxation time. T1 mapping combined with GD-EOB-DTPA can provide more accurate and objective magnetic resonance imaging (MRI) quantitative images with functional information. Previous studies have shown that T1 mapping can effectively predict the postoperative histopathological grade and recurrence status of HCC (11, 12) and effectively assess liver fibrosis (13) and liver function (14, 15). These provide a basis for the non-invasive preoperative prediction of Ki-67 expression. To our knowledge, few studies had reported the application of T1 mapping combined with GD-EOB-DTPA for the evaluation of Ki-67 expression in HCC.

Therefore, the purpose of this study was to investigate the correlation between quantitative parameters from T1 mapping, apparent diffusion coefficient (ADC), and Ki-67 expression. We aimed to develop a nomogram based on Gd-EOB-DTPA-enhanced MRI combined with T1 mapping to non-invasive preoperatively predict Ki-67 expression in HCC.

Materials and methods

Patients

This two-center retrospective study was approved by the ethics committee of each participating hospital and was conducted in accordance with the Declaration of Helsinki. The informed consent had a waiver of informed consent. The entire workflow of this retrospective study is shown in Figure 1. A total of 240 patients with surgically and pathologically confirmed HCC from two hospital centers (Shunde Hospital of Southern

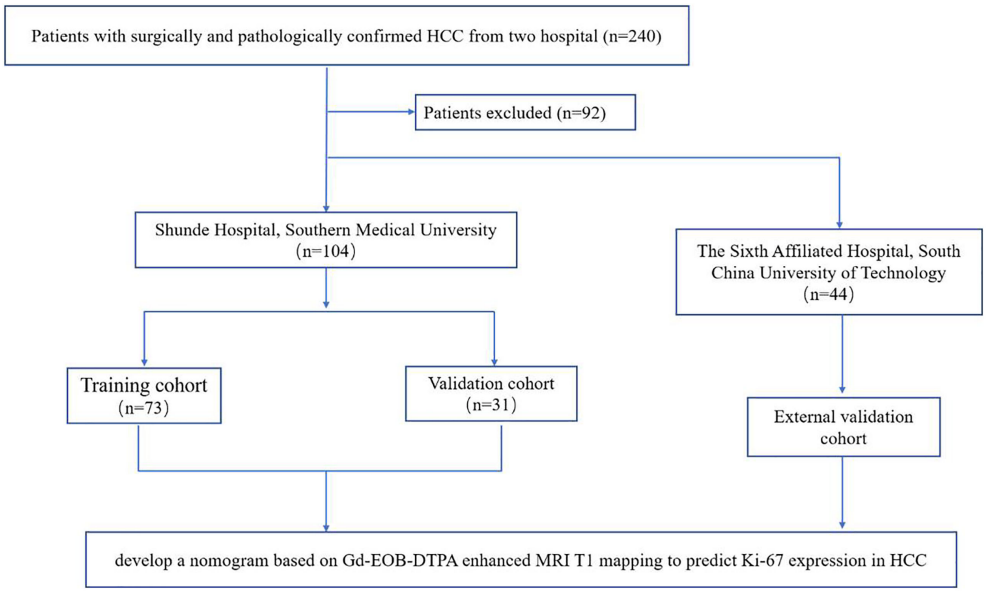

FIGURE 1
Flowchart of patient selection in the study.

Medical University, and the Sixth Affiliated Hospital, South China University of Technology) were collected between July 2019 and December 2020. Finally, 148 patients with preoperative Gd-EOB-DTPA-enhanced MRI T1 mapping and clinical data were included in the final analysis, according to the inclusion and exclusion criteria. Three cohorts were constructed: a training cohort (n = 73) and an internal validation cohort (n = 31) from Shunde Hospital of Southern Medical University, and an external validation cohort (n = 44) from the Sixth Affiliated Hospital, South China University of Technology. The inclusion criteria were as follows: (a) pathologically confirmed solitary HCC; (b) underwent hepatectomy; (c) and received preoperative Gd-EOB-DTPA-enhanced MRI and the interval period between the MRI examination and operation in less than 2 weeks. The exclusion criteria were as follows: (a) received previous treatment; (b) incomplete clinical or pathological information; (c) incomplete T1 mapping image data (pre-enhanced and 20 min after enhancement); (d) incomplete MR images or poor quality with obvious artifact; (e) and multiple HCC (≥2).

One hundred four patients in the internal cohort were followed up. We followed up patients after surgical resection every 3–6 months by contrast-enhanced ultrasound, CT, or MRI. We defined early recurrence (ER) as recurrence within 1 year after surgery.

Histopathological examination

All tissue specimens were sectioned and stained with hematoxylin eosin, and Ki-67 immunohistochemical staining was performed in the pathology department from two hospitals, respectively. The histopathological and immunohistochemical marker Ki-67 was blinded performed by two experienced pathologists from two hospitals (10, 12, 14, and 16 years' experience, respectively). In case of disagreements, a third senior pathologist was consulted.

Histological differentiation was assessed by using the Edmondson–Steiner grading system. If different tumor grades coexist within a tumor, the diagnosis is made with the highest grade. Moreover, Edmondson–Steiner grades were divided into two groups; grades 1 and 2 were defined as high differentiation, and grades 3 and 4 were defined as low differentiation (16). Immunohistochemical staining was checked for Ki-67 expression (Beijing Zhongshan Golden Bridge Biotechnology Company, Beijing, China). Interpretation of Ki-67 by immunohistochemistry was as follows: take five FOVs under a high-power microscope (×400), count 100 cells for each FOV, and count the positively stained cells. Ki-67 was identified as the percentage of positive cells to the total cells, and the average value was used and was classified as low Ki-67 expression (≤25%) or high Ki-67 expression (>25%) according to previous studies (6, 17–19) (Figure 2).

MRI examination

All MRI examinations from two hospitals were performed on a 3.0-T MR scanner (MAGNETOM Skyra or MAGNETOM Verio, Siemens Healthcare, Germany). All patients should be

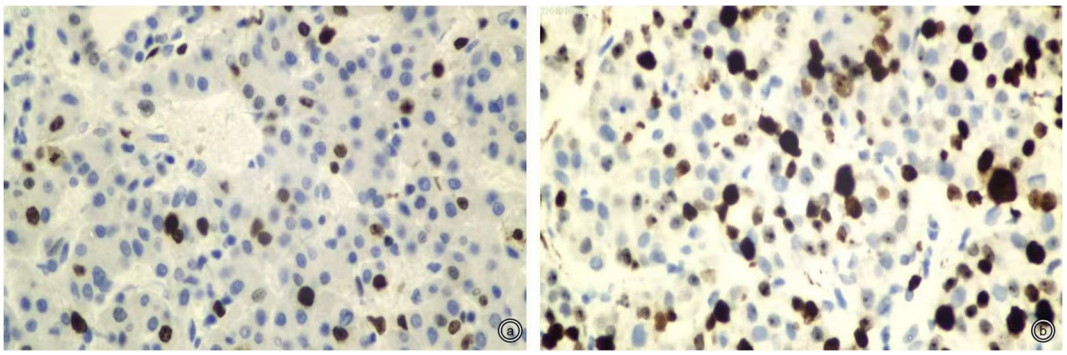

FIGURE 2
Representative staining patterns of Ki-67 (×400). **(A, B)**: Low and high Ki-67 expression (approximately 10% and 50%).

fasted for ≥6 h before the examination, and the patients should be trained in breathing before the scan. The examination range was from the upper edge of the liver to the lower edge of the liver. The main scanning sequence includes T1WI-volumetric interpolated breath-hold examination (VIBE), T1WI-TWIST-VIBE sequence, T2WI-BLADE, T2WI-HASTE (half Fourier single-shot turbo spin echo), diffusion-weighted imaging (DWI), and T1 mapping. The parameters are detailed in Table 1.

GD-EOB-DTPA (Primovist, Bayer Schering Pharma, Berlin, German) was used for enhanced scanning, the dose was 0.1 ml/kg, the flow rate was 1.0 ml/s, and the tube was flushed with 30 ml of physiological saline. The T1WI-VIBE or T1WI-TWIST-VIBE sequence was used for multiphase (two to five phases) arterial phase scanning 10–30 s after spraying, and the T1WI-VIBE sequence was used for portal vein and balance phase scanning 60 and 150 s after spraying. Hepatobiliary imaging after enhancement was performed 20 min later. T1 mapping pre-enhancement was performed before enhancement, and T1 mapping after enhancement was performed 20 min later.

Imaging analysis

The patients' image data were exported from the PACS in the DICOM format, and the RadiAnt DICOM Viewer 2020.2 (https://www.radiantviewer.com) software was used for image reading. All MRI quantitative and qualitative features were independently assessed by two abdominal radiologists from Shunde Hospital of Southern Medical University (8 and 15 years' experience, respectively) who were blinded to the patients' clinical and pathological information. If there is disagreement on the reevaluated image, it was resolved by consensus.

The following qualitative features were evaluated (Figure 3): (1) tumor margin, including smooth (round or oval with smooth

TABLE 1 MRI scan sequence and parameters.

Hospital	Scanner	Sequence	TR (ms)	TE (ms)	Fov (mm)	Matrix	Reverse angle	Seam thickness (mm)	Fat suppression mode
Shunde Hospital, Southern Medical University	Skyra	T1WI-VIBE	4	1.3/2.5	380×380	240×320	9°	3	Dixon
		T1WI-TWIST-VIBE	3.89	1.2/2.5	400×320	216×288	10°	3	Dixon
		T2WI-BLADE	2,000	84	380×380	320×320	90°	5	Spair
		DWI	6,200	50	285×380	128×128	/	5	Spair
		T1 mapping	5.01	2.3	285×380	168×224	3°/15°	4	/
The Sixth Affiliated Hospital, South China University of Technology	Verio	T1WI-VIBE	3.4	1.3/2.6	328×350	228×256	13°	3	Dixon
		T2WI-HASE	1,300	97	360×280	256×320	160°	6	/
		DWI	5,100	73	360×288	154×192	/	5	Fat sat
		T1 mapping	4.2	1.4	273×380	161×320	5°/15°	3	/

VIBE, volumetric interpolated breath-hold examination; DWI, diffusion-weighted imaging; HASE, half Fourier single-shot turbo spin echo.

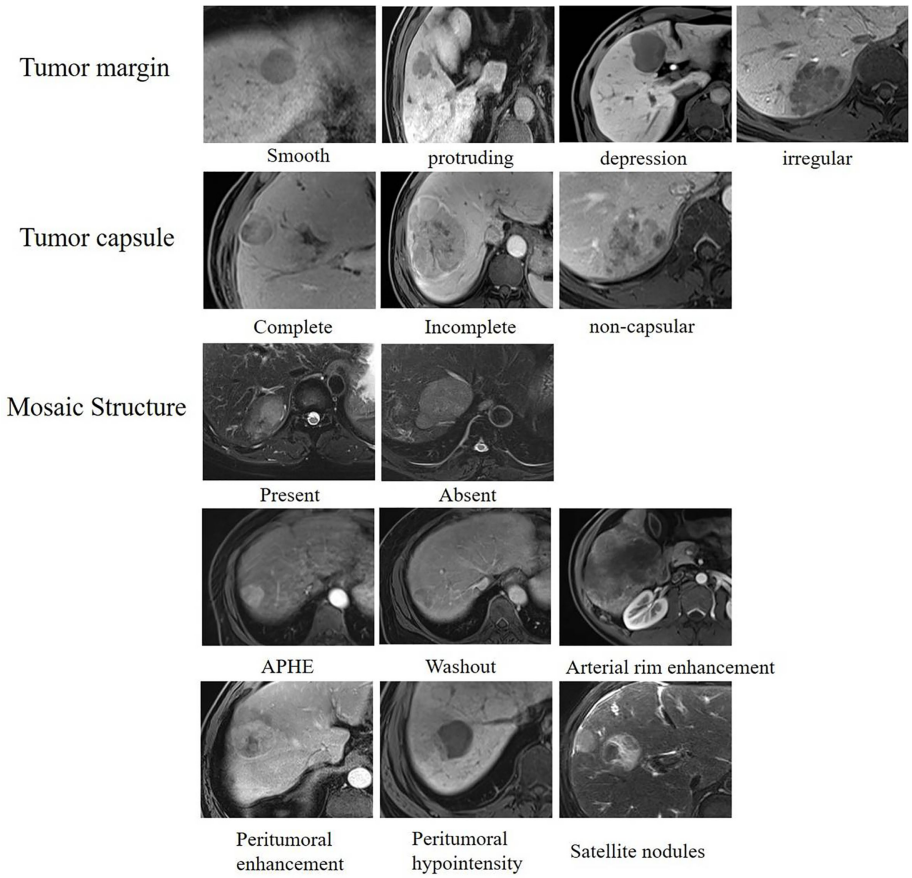

FIGURE 3
Qualitative features of hepatocellular carcinoma. Assessment of qualitative features including tumor margin, tumor capsule, mosaic structure, APHE, washout, arterial rim enhancement, peritumoral enhancement, peritumoral hypointensity, and satellite nodules.

margin) and non-smooth margins (protrusion, depression, or irregular); (2) tumor capsule, defined as the peripheral rim of hyperintensity in the equilibrium phase and classified as complete capsule, and incomplete or non-capsular; (3) mosaic structure, defined as the presence of randomly distributed internal nodules or compartments in the T2-weighted images; (4) arterial phase hyperenhancement (APHE) was defined as enhancement in the arterial phase unequivocally greater in part or in whole than the liver (no non-rim APHE excluded); (5) arterial rim enhancement, defined as the arterial phase enhancement which is most pronounced in the observation periphery; (6) peritumoral enhancement, defined as peri-observation enhancement in the late arterial phase or early portal phase; (7) peritumoral hypointensity, defined as the wedge-shaped area or irregular around the tumor with hypointensity in the HBP (slightly higher signal intensity than the tumor and lower than the surrounding normal liver parenchyma); and (8) satellite nodules, defined as tumors ≤2 cm in size and located ≤2 cm from the main tumor.

The quantitative characteristics included tumor size, T1 relaxation time obtained from T1 mapping pre-enhancement and 20 min after enhancement (T1rt-Pre, T1rt-20min), and ADC value. Selection of the region of interest (ROI) was conducted as follows: (1) select the largest level of measurement as much as possible, and keep the same level of each sequence as much as possible and ROI should be placed as far as possible in the area of obvious enhancement of the lesion; if the tumor is larger than 5 cm, the method of averaging multiple ROIs is used (avoid hemorrhage, cystic area, and blood vessels; Figure 4). (2) The ROIs were not smaller than 1.0 cm^2 (100–150 pixels); the same lesion was measured three times with the same ROI, and then average amounts were calculated. The average values of the measurements of two radiologists were used for further analyses. (3) The following data were measured: T1 relaxation time of pre-enhancement (T1rt-Pre) and T1 relaxation time 20 min after enhancement (T1rt-20min) on the T1 mapping; calculate the reduction rate of T1 relaxation time (rrT1rt): rrT1rt-20min = (T1rt-Pre-T1rt-

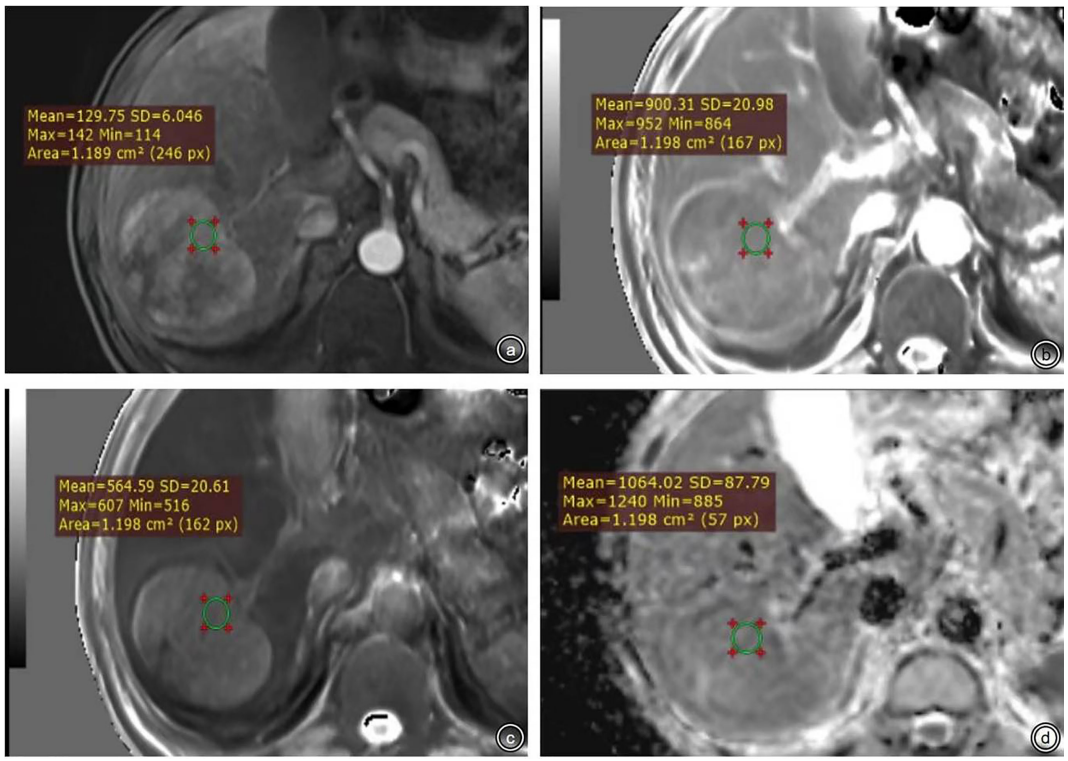

FIGURE 4
(A-D) were ROI measurement methods of T1 relaxation time obtained from pre-enhanced T1 mapping and 20 min after enhancement and the ADC map.

20min)/T1rt-Pre; ADC value on the ADC map; and tumor diameter on the maximum diameter of the tumor measured in the transverse or coronal view.

Statistical analysis

Quantitative variables were expressed as mean and standard deviation (SD) (if normally distributed) and median and range (if non-normally distributed), while categorical data were presented as counts and proportions. The independent-sample t-test or Mann–Whitney U-test were used to assess the continuous variables, while the chi-squared test or Fisher's exact test was used to analyze the categorical variables. Test–retest reliability was assessed using the intraclass correlation coefficient (ICC) for quantitative measurements and kappa for MRI features (>0.75 was considered to represent good agreement). The Spearman correlation analysis method was used to analyze the relationship between quantitative parameters from T1 mapping and ADC and Ki-67 expression in the whole cohort.

Patients from the internal cohort were randomly divided into the training and validation cohorts at a ratio of 7:3. The MRI features and clinical data were compared respectively between the training *vs.* validation cohorts in the internal cohort and between the Ki-67 high expression group and the low expression group in the internal cohort and the external validation cohort. The variables with statistical differences were determined by univariate logistic regression analysis. Then, the above-identified variables were further selected by stepwise regression based on the Akaike information criterion to construct a multivariate logistic regression model for Ki-67 expression. The nomogram was constructed based on the corresponding final logistic model prediction for these features and was separately validated with the same validation dataset and external dataset. We used Harrell's C-index and calibration curves in the training and validation cohorts to test the performance of the model. We also calculated the area under the characteristic operating curves and 95% confidence intervals (CIs), accuracy, sensitivity, specificity, positive predictive value, and negative predictive value. Kaplan–Meier analysis was used to compare early recurrence between high Ki-67 expression groups and low Ki-67 expression groups. Statistical significance was considered as a two-sided p value of less than 0.05. The above statistical analysis was performed by the R software version 3.2.3 (Bell Laboratories; https://cran.r-project.org/bin/windows/base/old/3.2.3).

Results

Correlation analysis of quantitative parameters from T1 mapping, ADC and Ki-67 expression, and histological differentiation

T1rt-Pre and T1rt-20min are strongly positively correlated with Ki-67 (r = 0.627, r = 0.607, $P < 0.001$); the ADC value was moderately negatively correlated with Ki-67 (r = -0.401, $P < 0.001$). rrT1rt-20min was not significantly associated with Ki-67 (r = -0.150, $P = 0.069$). The correlation between T1rt-Pre and T1rt-20min with Ki-67 expression in different histological differentiation patients are shown in Figure 5 (all $P < 0.05$).

Baseline characteristics

From July 2019 to December 2020, 104 consecutive patients were initially enrolled from the internal cohort, with 73 patients assigned to the training cohort and 31 to the validation cohort (Table 2). There was no significant difference between the two cohorts in any of the listed variables in Table 2 (all P > 0.05). Among the internal cohort, 50 patients had a high Ki-67 expression (48.1%) and 54 showed a low Ki-67 expression (51.9%). Regarding quantitative data, patients with a high Ki-67 expression had higher alpha-fetoprotein (AFP) levels, larger tumor size, higher T1rt-pre, higher T1rt-20min, and lower ADC (all $P < 0.05$, Table 3). Regarding qualitative data, patients with high Ki-67 expression more frequently showed APHE, a non-smooth margin, an incomplete or non-complete tumor capsule, a mosaic structure, arterial rim enhancement, peritumoral enhancement, and peritumoral hypointensity (all $P < 0.05$, Table 3). Among the external validation cohort, 20 patients had a high Ki-67 expression (45.5%) and 24 showed a low Ki-67 expression (54.5%). Patients with a high Ki-67 expression had higher albumin levels, larger tumor size, higher T1rt-pre, higher T1rt-20min, and lower ADC (all $P < 0.05$, Table 3). Regarding qualitative data, patients with high Ki-67 expression more frequently showed a non-smooth margin, mosaic structure, arterial rim enhancement, peritumoral enhancement, and peritumoral hypointensity (all $P < 0.05$, Table 3). There were no statistically significant differences in other MR features and clinical indicators between the two groups ($P > 0.05$). The average concordance rate of evaluating MRI features between the two radiologists was 0.877 (95% CI, 0.855–0.899). MRI images of typical cases in the high and low Ki-67 expression groups are shown in Figure 6.

Patients in the internal cohort were followed up until recurrence or at the end point of this study (1 February 2022). The median follow-up time of the patients was 18.96 (range 17.07–20.86) months. The overall early recurrence rate was 34.62% (36/104) and in particular 23.32 (21.44–25.19) months for those with low Ki-67 and 13.84 (11.13–16.56) months for those with high Ki-67 (log-rank test, $P<0.001$; Figure 7).

Performance of predictors and the combined nomogram for predicting high Ki-67 expression

Using multivariable analyses, we found significant independent predictors of Ki-67 expression, including peritumoral enhancement, peritumoral hypointensity, T1rt-20min, and tumor margin, while APHE was marginally significant predictors of Ki-67 expression (Table 4).

For Ki-67 expression, a nomogram was established in the training cohort based on five imaging features: APHE, peritumoral enhancement, peritumoral hypointensity, T1rt-20min, and tumor margin. The nomograms and calibration

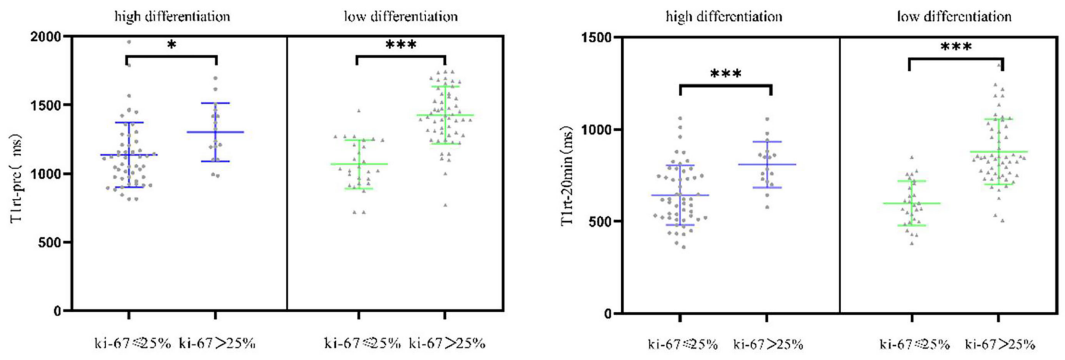

FIGURE 5
Correlation between the quantitative parameters of T1 mapping with Ki-67 expression in different histological differentiation patients (*<0.05; ***<0.001).

TABLE 2 Baseline characteristics between patients in the internal training and validation cohorts.

Variables	Total (n = 104)	Training cohort (n = 73)	Validation cohort (n = 31)	*P* value
Sex				1.000
Male	91 (87.5%)	64 (87.7%)	27 (87.1%)	
Female	13 (12.5%)	9 (12.3%)	4 (12.9%)	
Age (years)				0.543
≤55	39 (37.5%)	21 (28.8%)	18 (58.1%)	
>55	65 (62.5%)	52 (71.2%)	13 (41.9%)	
Hepatitis				0.382
Absent	16 (15.4%)	13 (17.8%)	3 (9.7%)	
Present	88 (84.6%)	60 (82.2%)	28 (90.3%)	
AFP (ng/mL)				0.733
≤20	63 (60.6%)	45 (61.6%)	18 (58.1%)	
>20	41 (39.4%)	28 (38.4%)	13 (41.9%)	
ALT (U/L)	37.50 (23.00, 64.75)	38.00 (23.05, 65.00)	34.00 (18.00, 65.00)	0.520
AST (U/L)	36.00 (26.00, 53.75)	36.00 (26.00, 55.50)	35.00 (22.00, 50.10)	0.534
GGT (U/L)	52.00 (35.25, 99.75)	56.00 (35.00, 109.05)	46.00 (36.00, 64.00)	0.120
PLR	117.70 (78.80, 150.65)	114.29 (72.89, 150.65)	125.49 (90.32, 171.01)	0.117
NLR	2.21 (1.58, 3.14)	2.17 (1.57, 2.90)	2.62 (1.60, 3.79)	0.354
Albumin (g/L)	42.35 (38.30, 44.65)	42.50 (38.65, 44.60)	41.00 (37.60, 44.90)	0.717
Child–Pugh				0.522
A	91 (87.5%)	65 (89.0%)	26 (83.9%)	
B	13 (12.5%)	8 (11.0%)	5 (16.1%)	
APHE				0.547
Absent	14 (13.5%)	11 (15.1%)	3 (9.7%)	
Present	90 (86.5%)	62 (84.9%)	28 (90.3%)	
Washout				0.721
Absent	9 (8.7%)	7 (9.6%)	2 (6.5%)	
Present	95 (91.3%)	66 (90.4%)	29 (93.5)	
Tumor margin				0.834
Smooth	42 (40.4%)	29 (39.7%)	13 (41.9%)	
Non-smooth	62 (59.6%)	44 (60.3%)	18 (58.1%)	
Tumor capsule				0.131
Complete	45 (43.3%)	27 (37.0%)	18 (58.1%)	
Incom-/non	59 (56.7%)	46 (63.0%)	13 (41.9%)	
Mosaic structure				0.759
Absent	46 (44.2%)	33 (45.2%)	13 (41.9%)	
Present	58 (55.8%)	40 (54.8%)	18 (55.8%)	
Arterial rim enhancement				0.821
Absent	79 (76.0%)	55 (75.3%)	24 (77.4%)	
Present	25 (24.0%)	18 (24.7%)	7 (22.6%)	
Peritumoral enhancement				0.733
Absent	63 (60.6%)	45 (61.6%)	18 (58.1%)	
Present	41 (39.4%)	28 (38.4%)	13 (41.9%)	
Peritumoral hypointensity				0.398
Absent	71 (68.3%)	48 (65.8%)	23 (74.2%)	
Present	33 (31.7%)	25 (34.2%)	8 (25.8%)	
Satellite nodules				0.437
Absent	79 (76.0%)	57 (78.1%)	22 (71.0%)	
Present	25 (24.0%)	16 (21.9%)	9 (29.0%)	

(Continued)

TABLE 2 Continued

Variables	Total (n = 104)	Training cohort (n = 73)	Validation cohort (n = 31)	*P* value
Tumor diameter (cm)	3.80 (2.33, 6.05)	3.60 (2.20, 6.30)	3.90 (2.60, 5.90)	0.619
T1rt-pre (ms)	1,232.20 (1014.64, 1450.03)	1,225.63 (1003.68, 1441.25)	1,271.36 (1014.64, 1462.63)	0.402
T1rt-20min (ms)	748.92 ± 201.00	745.65 ± 191.38	755.91 ± 225.22	0.819
rrT1rt-20min	0.396 ± 0.124	0.389 ± 0.117	0.412 ± 0.140	0.384
ADC (mm^2/s)	1,081.86 ± 185.43	1081.23 ± 184.35	1083.33 ± 191.04	0.985
Histological differentiation				0.574
High	48 (46.2%)	35 (47.9%)	13 (41.9%)	
Low	56 (53.8%)	38 (52.1%)	18 (58.1%)	
Ki-67 expression	25.00 (10.00, 40.00)	25.00 (10.00, 40.00)	25.00 (10.00, 45.00)	0.391
Ki-67 group				0.967
≤25%	54 (51.9%)	38 (52.1%)	16 (51.6%)	
>25%	50 (48.1%)	35 (47.95)	15 (48.4%)	

Continuous variables with normal distribution are presented as mean (standard deviation, SD), and those with abnormal distribution as median (interquartile range, IQR). Categorical variables are presented as N (%) according to different levels. (AFP, alpha-fetoprotein; ALT, alanine aminotransferase; AST, aspartate aminotransferase; GGT, galactosyl glucosyltransferase; NLR, neutrophil-to-lymphocyte ratio; PLR, platelet-to-lymphocyte ratio; APHE, arterial phase hyperenhancement; ADC, apparent diffusion coefficient).

curves are presented in Figure 8, which showed that the calibration curves for Ki-67 expression in the three cohorts all well-matched with standard lines. The C-index of the nomogram for Ki-67 expression prediction was 0.919 (95% CI, 0.858–0.970) in the training cohort, 0.925 (95% CI, 0.821–1.000) in the validation cohort, and 0.850 (95% CI, 0.736–0.952) in the external validation cohort (Table 5).

Discussion

Gd-EOB-DTPA can be absorbed by the liver cells through the organic anion transporter polypeptide (OATP) pathway, and it provides structural information of lesions and carries functional information in the hepatobiliary phase, due to its dual extracellular and hepatobiliary properties (20). T1 mapping technology is a non-invasive quantitative analysis method of the tissue T1 value, which has good repeatability and strong operability. Gd-EOB-DTPA-enhanced MR combined T1 mapping is believed to provide abundant diagnostic information. In our study, we retrospectively collected data of 148 consecutive patients with HCC, and we investigated the correlation with T1 mapping, ADC quantification parameters, and Ki-67 expression. Our data showed that T1rt-Pre and T1rt-20min were strongly positively correlated with Ki-67 (r = 0.627, r = 0.607, $P < 0.001$); the ADC value was moderately negatively correlated with Ki-67(r = -0.401, $P < 0.001$), as seen in previous studies (20). However, the ADC values were less correlated with Ki-67 than T1 mapping; the possible explanation could be that the ADC value can be affected by technical parameters, such as limited image quality with poor signal-to-noise ratio and low spatial resolution, motion and air artifacts, and misregistration artifacts on the ADC map (21). T1 mapping reflects the fixed characteristics of the tissue, is not limited by the scan sequence parameters, and is positively correlated with the concentration of the gadolinium contrast agent in the tissue. Therefore, the T1 mapping value is more accurate, which has also been confirmed in the liver function and liver fibrosis assessment (13–15). The author believes that when the proliferation of tumor cells is more active, the tumor cells are arranged more closely per unit volume, which results in a larger T1rt-pre value; when the proliferation of tumor cells is more active, the proportion of normal liver cells contained in the tumor is lower, and the absorption of Gd-EOB-DTPA is also reduced, resulting in a larger value of T1rt-20min. There is a certain correlation between Ki-67 expression and histopathological differentiation (22, 23). Is the T1 mapping value affected by histological differentiation? Therefore, in our study, the correlation between the T1rt-pre, T1rt-20min, and Ki-67 expressions in the different histological differentiations was further obtained. No matter in the low differentiation group or in the high differentiation group, T1rt-Pre and T1rt-20min had statistical difference between high and low expression of Ki-67 ($P < 0.05$). It can be seen that T1 mapping is not affected by the degree of histopathological differentiation when predicting high and low expressions of Ki-67.

The expression of Ki-67 in cancer has been intensively studied, and most studies have shown that Ki-67 is associated with the metabolic, genetic, or clinical-pathological features of HCC (5, 19, 20). Aktas's study showed that Ki-67 was one of the independent prognostic factors of recurrence on patients who underwent liver transplant for HCC (24). Cao et al. revealed that HCC with high Ki-67 expression was more aggressive, and its recurrence-free survival and postoperative overall survival were significantly lower than those of HCC with low Ki-67 expression (6). With the rise of multidisciplinary and multimodal comprehensive treatment of HCC, the high risk of recurrence in HCC patients requires adjuvant therapy and careful follow-up.

TABLE 3 Baseline characteristics of patients in the Ki-67 high and low expression groups.

Variables	Internal cohort (n = 104)				External validation cohort (n = 44)			
	Kappa/ ICC	High Ki-67 group (n = 50)	Low Ki-67 group (n = 54)	*P* value	Kappa/ ICC	High Ki-67 group (n = 20)	Low Ki-67 group (n = 24)	*P* value
Sex	/			0.182	/			0.493
Male		46 (92.0%)	45 (83.3%)			20 (100.0%)	22 (91.7%)	
Female		4 (8.0%)	9 (16.7%)			0 (0.0%)	2 (8.3%)	
Age (years)	/			0.188	/			0.956
≤55		22 (44.0%)	17 (31.5%)			9 (45.0%)	11 (45.8%)	
>55		28 (56.0%)	37 (68.5%)			11 (55.0%)	13 (54.2%)	
Hepatitis	/			0.143	/			0.614
Absent		5 (10.0%)	11 (20.4%)			1 (5.0%)	3 (12.5%)	
Present		45 (90.0%)	43 (79.6%)			19 (95.0%)	21 (87.5%)	
AFP (ng/mL)	/			<0.001	/			0.069
≤20		19 (38.0%)	44 (81.5%)			7 (35.0%)	15 (62.5%)	
>20		31 (62.0%)	10 (18.5%)			13 (65.5%)	9 (37.5%)	
ALT (U/L)	/	39.50 (24.75, 67.00)	32.50 (19.60, 57.50)	0.127	/	34.00 (22.50,68.25)	25.00 (14.25, 43.50)	0.150
AST (U/L)	/	36.00 (27.75, 54.00)	34.50 (23.75, 51.50)	0.276	/	38.50 (26.25,46.00)	39.00 (31.00,49.50)	0.595
GGT (U/L)	/	52.00 (42.00, 90.05)	53.00 (34.75, 101.00)	0.800	/	49.50 (43.25,129.25)	60.00 (33.25, 100.00)	0.724
PLR	/	128.34 (90.17, 150.65)	109.28 (72.83, 152.72)	0.112	/	98.60 (68.57,141.34)	100.86 (59.10, 132.53)	0.671
NLR	/	2.43 (1.59, 3.71)	2.10 (1.54, 2.87)	0.373	/	1.68 (1.15,2.70)	2.15 (1.43, 2.58)	0.289
Albumin (g/L)	/	42.00 (39.00, 43.80)	42.75 (37.80,45.7)	0.524	/	41.45 (38.73,46.63)	37.85 (32.65, 42.65)	0.011
Child–Pugh	/			0.458	/			0.246
A		45 (90.0%)	46 (85.2%)			15 (75.0%)	14 (58.3%)	
B		5 (10.0%)	8 (14.8%)			5 (25.0%)	10 (41.7%)	
APHE	0.922			0.007	0.927			0.117
Absent		2 (4.0%)	12 (22.2%)			2 (10.0%)	7 (29.2%)	
Present		48 (96.0%)	42 (77.8%)			18 (90.0%)	17 (70.8%)	
Washout	0.889			0.819	0.864			0.545
Absent		4 (8.0%)	5 (9.3%)			9 (45.0%)	13 (54.2%)	
Present		46 (92.0%)	49 (90.7%)			11 (55.0%)	11 (45.8%)	
Tumor margin	0.939			<0.001	0.909			<0.001
Smooth		6 (12.0%)	36 (66.7%)			3 (15.0%)	19 (79.2%)	
Non-smooth		44 (88.0%)	18 (33.3%)			17 (85.0%)	5 (20.8%)	
Tumor capsule	0.806			0.027	0.800			0.469
Complete		17 (34.0%)	30 (55.6%)			13 (65.0%)	18 (75.0%)	
Incom-/non		33 (66.0%)	24 (44.4%)			7 (35.0%)	6 (25.0%)	
Mosaic structure	0.942			<0.001	0.909			0.008
Absent		13 (26.0%)	33 (61.1%)			7 (35.0%)	18 (75.0%)	
Present		37 (74.0%)	21 (38.9%)			13 (65.0%)	6 (25.0%)	
Arterial rim enhancement	0.924			<0.001	0.899			0.018
Absent		30 (60.0%)	49 (90.7%)			10 (50.0%)	20 (83.3%)	
Present		20 (40.0%)	5 (9.4%)			10 (50.0%)	4 (16.7%)	
Peritumoral enhancement	0.816			<0.001	0.782			0.016
Absent		18 (36.0%)	45 (83.3%)			11 (55.0%)	21 (87.5%)	
Present		32 (64.0%)	9 (16.7%)			9 (45.0%)	3 (12.5%)	
Peritumoral hypointensity	0.802			<0.001	0.771			0.001
Absent		25 (50.0%)	46 (85.2%)			10 (50.0%)	23 (95.8%)	

(Continued)

TABLE 3 Continued

Variables	Internal cohort (n = 104)				External validation cohort (n = 44)			
	Kappa/ ICC	High Ki-67 group (n = 50)	Low Ki-67 group (n = 54)	*P* value	Kappa/ ICC	High Ki-67 group (n = 20)	Low Ki-67 group (n = 24)	*P* value
resent		25 (50.0%)	8 (14.8%)			10 (50.0%)	1 (4.2%)	
Satellite nodules	0.922			0.068	0.871			0.057
Absent		34 (68.0%)	45 (83.3%)			13 (65.0%)	22 (91.7%)	
Present		16 (32.0%)	9 (16.7%)			7 (35.0%)	2 (8.3%)	
Tumor diameter (cm)	0.986	4.80 (3.32, 7.43)	2.65 (1.60, 4.25)	<0.001	0.950	40.10 (26.28,59.03)	30.95 (19.30, 39.18)	0.044
T1rt-pre (ms)	0.862	1,425.24 (,1244.69, 1,592.75)	1,042.40 (931.58, 1,215.96)	<0.001	0.821	1360.00 (1250.55,1463.00)	1,132.40 (1,037.68, 1,279.00)	0.004
T1rt-20min (ms)	0.872	876.67 ± 157.62	630.63 ± 160.91	<0.001	0.839	825.39 ± 191.03	620.53 ± 121.77	<0.001
rrT1rt-20min	0.920	0.377 ± 0.106	0.414 ± 0.137	0.125	0.894	0.39 ± 0.12	0.46 ± 0.12	0.053
ADC (mm^2/s)	0.839	1,008.02 ± 147.06	1,150.22 ± 192.16	<0.001	0.880	923.30 (844.28,1013.50)	1,081.50 (979.25, 1,286.35)	0.008

Continuous variables with normal distribution are presented as mean (standard deviation, SD), and those with abnormal distribution as median (interquartile range, IQR). Categorical variables are presented as N (%) according to different levels. (AFP, alpha-fetoprotein; ALT, alanine aminotransferase; AST, aspartate aminotransferase; GGT, galactosyl glucosyltransferase; NLR, neutrophil-to-lymphocyte ratio; PLR, platelet-to-lymphocyte ratio; APHE, arterial phase hyperenhancement; ADC, apparent diffusion coefficient).

Hence, a non-invasive preoperative method to predict the Ki-67 status is needed to guide individualized HCC treatment and postoperative surveillance in clinical practice. Many studies have attempted to determine preoperative predictors of HCC with poor prognosis using Ki-67 (6–8), microvascular invasion (MVI) (25, 26), cytokeratin 19 (27, 28), or microvascular density (20). Although the results of these relevant studies have confirmed the relationship between these indicators and prognosis, no consensus has been reached. In terms of the relative molecular mechanism, except for Ki-67 which can be a marker of cellular proliferative activity, few studies have described other mechanisms. Currently, it is more acceptable to use Ki-67 as an important biomarker to reflect tumor cell proliferation and to assess prognosis in patients with HCC and other malignant tumors. However, there is no unified standard for the high and low expression groups of Ki-67 yet. In some studies, 10% (29–31) was used as the cutoff value of Ki-67 expression, but in others, 14% (32) or 35% (7) or 50% (20) was used, and we used 25% (6, 17–19) as the cutoff value because we believe that a cutoff that is too low or too high will lead to selectivity bias for inclusion criteria due to the under- or overestimation of Ki-67 expression. At the same time, our data showed a difference in the overall early recurrence rate between the two groups ($P < 0.001$). The high Ki-67 expression group (>25%) showed a tendency to recur easily within 1 year after surgery.

In our study, MR qualitative characteristics such as APHE, tumor margin, tumor capsule, mosaic structure, arterial rim enhancement, peritumoral hypointensity, and peritumoral enhancement were statistically different between the high Ki-67 group and low Ki-67 group in the internal cohort ($P < 0.05$). However, among the above qualitative characteristics, there was no statistical difference in APHE and tumor capsule between the high Ki-67 expression group and low Ki-67 expression group in the external validation cohort. Among these meaningful MR characteristics in our study, peritumoral hypointensity, peritumoral enhancement, tumor capsule, and tumor margin mainly reflected the relatively dense cell structure and infiltrative growth types of the tumor to the surrounding structures. Peritumoral hypointensity and peritumoral enhancement probably relate to the known hypothesis of invasion of the surrounding structures especially the minute portal branch occlusion and the hemodynamic changes existing in compensatory arterial hyperperfusion and decreased portal flow, which may lead to altered expression of OATP or MRP2 receptors (33, 34). However, the statistically different MR characteristics developed in our study were not included in the regression model, such as mosaic structure, arterial rim enhancement, and tumor capsule. Mosaic structure could be related to the inhomogeneity of the tumor, while arterial rim enhancement pattern is rarely observed in HCCs and is more commonly observed in intrahepatic cholangiocarcinomas or metastases (27). It is noteworthy that APHE was statistically different between the two groups ($P < 0.05$) and included in the nomogram, while it was not a significant predictor of high Ki-67 expression. During hepatocarcinogenesis, changes in the tumor's blood supply often lead to APHE. However, in some benign lesions, such as atypical hemangioma, it can also present with the typical enhancement pattern of APHE (35). This study did not conduct further analysis of the APHE subtypes, but Cunha's study (36) showed that there are still differences in observers' perceptions of APHE subtypes (37), and no unified understanding has been formed. Quantitative assessment can directly reflect histological features. In our study, T1rt-pre and T1rt-20min in the high Ki-67 group were higher than those in

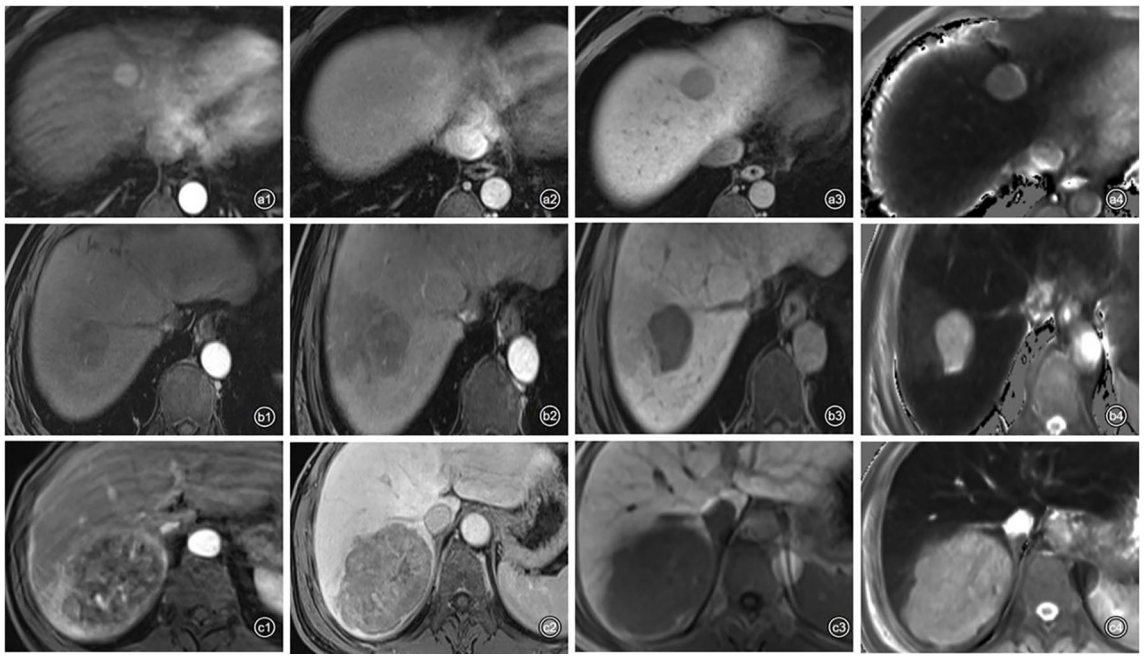

FIGURE 6
Representative images of each phase on Gd-EOB-DTPA-enhanced MRI and T1 mapping 20 min after enhancement in patients with high or low Ki-67 expression. a1–4: A 48-year-old man with Edmondson–Steiner grade II HCC and low expression of Ki-67 (10%). (a1) APHE; (a2), washout and complete capsule; (a3), smooth tumor margin; (a4), T1rt-20 min = 509.92 ms. b1–4: A 58-year-old man with Edmondson–Steiner grade III HCC and high expression of Ki-67 (30%). (b1) no APHE; (b2), peritumoral enhancement; (b3), peritumoral hypointensity and non-smooth tumor margin; (b4), T1rt-20 min = 1,062.86 ms. c1–4: A 59-year-old man with Edmondson–Steiner grade II HCC and high expression of Ki-67 (40%). (c1), rim enhancement and peritumoral enhancement; (c2), washout; (c3), non-smooth tumor margin; (c4), T1rt-20min = 971.84 ms.

the low Ki-67 group ($P < 0.001$), while the ADC value in the high Ki-67 group was lower than that in the low Ki-67 group ($P < 0.001$). However, the ADC value was not included in the regression model.

Finally, the significant independent predictors of Ki-67 expression included peritumoral enhancement, peritumoral hypointensity, T1rt-20min, and tumor margin. Although APHE was included in the regression, it was not an independent predictor. For Ki-67 expression, a nomogram was established based on five imaging features: APHE, peritumoral enhancement, peritumoral hypointensity, T1rt-20min, and tumor margin in the training cohort. The

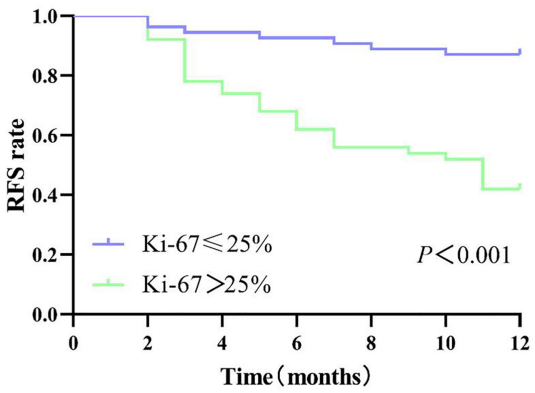

FIGURE 7
Disease-free survival of patients with high Ki-67 expression and low Ki-67 expression.

TABLE 4 Multivariable analyses of preoperative Gd-EOB-DTPA enhanced MRI features in prediction of Ki-67 expression.

Variables	OR	95% CI	*P* value
APHE	17.77	0.48~663.93	0.119
Peritumoral enhancement	7.97	1.24~51.38	0.029
Peritumoral hypointensity	0.09	0.01~0.86	0.037
T1rt-20min (ms)	1.01	1.00~1.02	0.001
Tumor margin	9.52	1.76~51.39	0.009

APHE, arterial phase hyperenhancement.

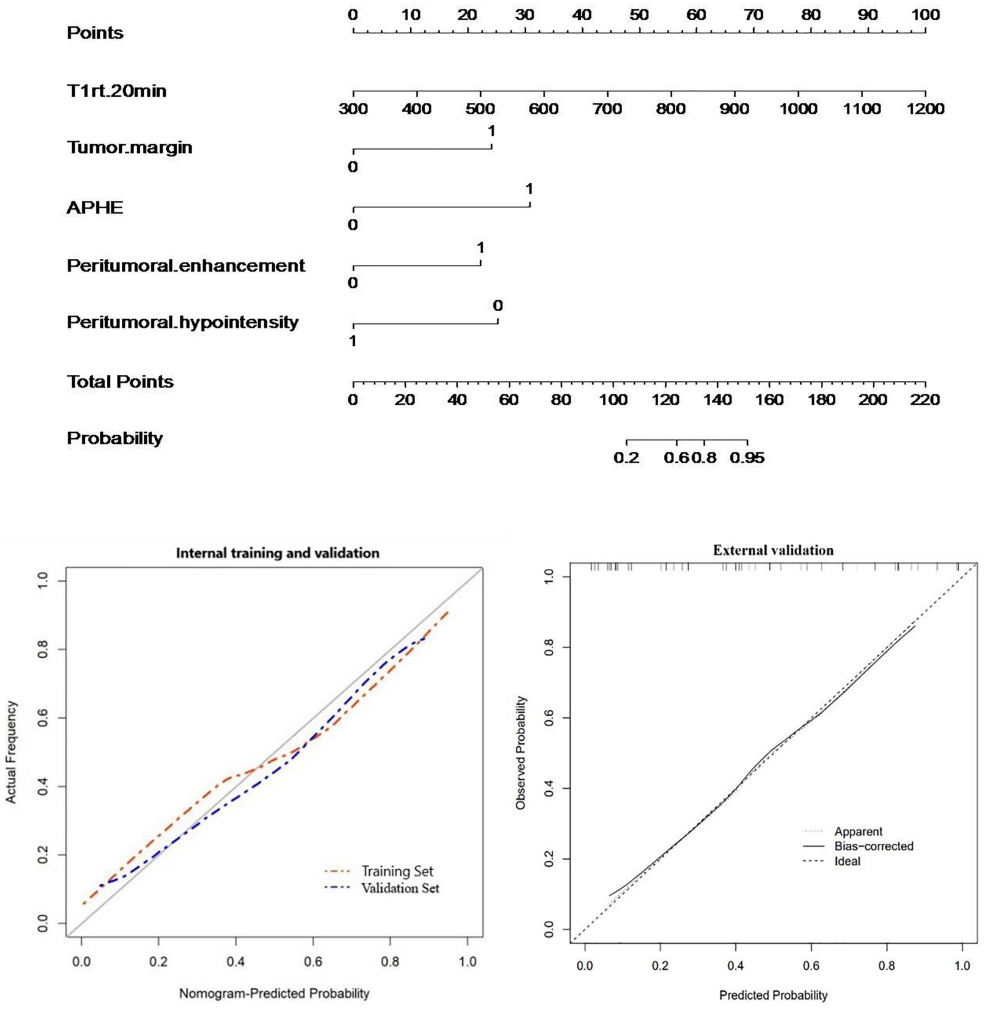

FIGURE 8
Nomogram with calibration curves for predicting Ki-67 expression (internal cohort and external validation cohort).

TABLE 5 Predictive performance of preoperative Gd-EOB-DTPA-enhanced MRI features in Ki-67 expression prediction.

Models	AUC,C-index	Sensitivity (%)	Specificity (%)	Accuracy (%)	PPV (%)	NPV (%)
Training (n = 73)	0.919 (95% CI: 0.858~0.970)	74.3%	94.7%	84.9%	92.8%	80.0%
Validation (n = 31)	0.925 (95% CI: 0.821~1.000)	93.3%	81.2%	87.1%	82.4%	92.9%
External validation (n = 46)	0.850 (95% CI: 0.736~0.952)	80.0%	79.2%	79.5%	76.2%	82.6%

combined nomogram yielded an incremental performance in predicting the Ki-67 expression of HCC; the C-index was 0.919 (95% CI, 0.858–0.970) in the training, 0.925 (95% CI, 0.821–1.000) in the validation cohort, and 0.850 (95% CI, 0.736–0.952) in the external validation group.

In summary, the author believes that gadoxetate disodium-enhanced MRI combined with T1 mapping quantitative technology can better evaluate the expression of Ki-67. However, there are several limitations in this study: (1) This is a retrospective study with a relatively small sample size, and there may be selection bias. (2) At present, there is currently no standardized Ki-67 expression level threshold in HCC and there are differences in various studies that we defined 25% as the cutoff value. Therefore, it is necessary to study the differences of different groups with a large sample of multiple centers and compare the diagnostic efficacy of different groups. (3) ROI is drawn manually, and there may be measurement errors. (4) Multiple liver cancers (>2) were excluded from this study. Because this study is a retrospective study, it is impossible to guarantee the one-to-one correspondence between the imaging images of multiple lesions and the pathological images. However, multiple liver cancers are not uncommon in clinical practice. A prospective study was conducted in conjunction with colleagues from hepatobiliary surgery and pathology departments.

Conclusion

In conclusion, this study shows that the T1 relaxation time measured by Gd-EOB-DTPA-enhanced MRI T1 mapping has a strong positive correlation with Ki-67 expression in HCC, and our established nomogram has good predictive performance for a non-invasive preoperative prediction of Ki-67 expression in HCC.

Data availability statement

The original contributions presented in the study are included in the article/supplementary material. Further inquiries can be directed to the corresponding authors.

Ethics statement

This study was reviewed and approved by the ethics committee of each participating hospital. The patients/participants provided their written informed consent to participate in this study.

Author contributions

Acquisiton of the data of the external validation group of our work: JF. All the other authors listed have made substantial, direct and intellectual contribution to the article and approved the submitted version.

Funding

The study was supported by the grants of the science and technology planning project of Foshan (2020001005216) and Guangdong Medical Science and Technology Research Fund (A2021483).

Acknowledgments

The authors thank the patients and their families for their participation in the study.

Conflict of interest

The authors declare that the research was conducted in the absence of any commercial or financial relationships that could be construed as a potential conflict of interest.

Publisher's note

References

1. Caines A, Selim R, Salgia R. The changing global epidemiology of hepatocellular carcinoma. *Clin Liver Dis* (2020) 24(4):535–47. doi: 10.1016/j.cld.2020.06.001

2. Yang JD, Hainaut P, Gores GJ, Amadou A, Plymoth A, Roberts LR. A global view of hepatocellular carcinoma: trends, risk, prevention and management. *Nat Rev Gastroenterol Hepatol* (2019) 16(10):589–604. doi: 10.1038/s41575-019-0186-y

3. Renzulli M, Brocchi S, Cucchetti A, Federico M, Cristina M, Camilla S, et al. Can current preoperative imaging be used to detect microvascular invasion of hepatocellular carcinoma? *Radiology* (2016) 279(2):432–42. doi: 10.1148/radiol.2015150998

4. Chen B, Wu JX, Cheng SH, Wang LM, Rong WQ, Wu F, et al. Phase 2 study of adjuvant radiotherapy following narrow-margin hepatectomy in patients with HCC. *Hepatology* (2021) 74(5):2595–604. doi: 10.1002/hep.31993

5. Kitamura K, Hatano E, Higashi T, Narita M, Seo S, Nakamoto Y, et al. Proliferative activity in hepatocellular carcinoma is closely correlated with glucose metabolism but not angiogenesis. *J Hepatol* (2011) 55(4):846–57. doi: 10.1016/j.jhep.2011.01.038

6. Cao Y, Ke R, Wang S, Zhu X, Chen J, Huang C, et al. DNA Topoisomerase IIalpha and Ki67 are prognostic factors in patients with hepatocellular carcinoma. *Oncol Lett* (2017) 13(6):4109–16. doi: 10.3892/ol.2017.5999

7. Li HH, Qi LN, Ma L, Chen ZS, Xiang BD, Li LQ. Effect of KI-67 positive cellular index on prognosis after hepatectomy in Barcelona clinic liver cancer stage a and b hepatocellular carcinoma with microvascular invasion. *Onco Targets Ther* (2018) 11:4747–54. doi: 10.2147/OTT.S165244

8. Zhang X, Wu Z, Peng Y, Li D, Jiang Y, Pan F, et al. Correlationship between Ki67, VEGF, and p53 and hepatocellular carcinoma recurrence in liver transplant patients. *BioMed Res Int* (2021) 2021:6651397. doi: 10.1155/2021/6651397

9. Tian G, Kong D, Jiang T, Li L. Complications after percutaneous ultrasound-guided liver biopsy: A systematic review and meta-analysis of a population of more than 12,000 patients from 51 cohort studies. *J Ultrasound Med* (2020) 39(7):1355–65. doi: 10.1002/jum.15229

10. Dube JP, Azzi Z, Semionov A, Sayegh K, Kosiuk J, Presscco J. Imaging of post transthoracic needle biopsy complications. *Can Assoc Radiol J* (2019) 70 (2):156–63. doi: 10.1016/j.carj.2018.08.006

11. Peng Z, Jiang M, Cai H, Chan T, Dong Z, Luo Y, et al. Gd-EOB-DTPA-enhanced magnetic resonance imaging combined with T1 mapping predicts the degree of differentiation in hepatocellular carcinoma. *BMC Cancer* (2016) 16:625. doi: 10.1186/s12885-016-2607-4

12. Wang WT, Zhu S, Ding Y, Yang L, Chen CZ, Ye QH, et al. T1 mapping on gadoxetic acid-enhanced MR imaging predicts recurrence of hepatocellular carcinoma after hepatectomy. *Eur J Radiol* (2018) 103:25–31. doi: 10.1016/j.ejrad.2018.03.027

13. Li Q, Chen T, Shi N, Ye W, Yuan M, Shi Y. Quantitative evaluation of hepatic fibrosis by fibro scan and gd-EOB-DTPA-enhanced T1 mapping magnetic resonance imaging in chronic hepatitis b. *Abdom Radiol (NY)* (2022) 47(2):684–92. doi: 10.1007/s00261-021-03300-8

14. Haimerl M, Fuhrmann I, Poelsterl S, Fellner C, Nickel MD, Weigand K, et al. Gd-EOB-DTPA-enhanced T1 relaxometry for assessment of liver function determined by real-time (13)C-methacetin breath test. *Eur Radiol* (2018) 28 (9):3591–600. doi: 10.1007/s00330-018-5337-y

15. Li J, Cao B, Bi X, Chen W, Wang L, Du Z, et al. Evaluation of liver function in patients with chronic hepatitis b using gd-EOB-DTPA-enhanced T1 mapping at different acquisition time points: A feasibility study. *Radiol Med* (2021) 126 (9):1149–58. doi: 10.1007/s11547-021-01382-4

16. Tang M, Zhou Q, Huang M, Sun K, Wu T, Li X, et al. Nomogram development and validation to predict hepatocellular carcinoma tumor behavior by preoperative gadoxetic acid-enhanced MRI. *Eur Radiol* (2021) 31(11):8615–27. doi: 10.1007/s00330-021-07941-7

17. Bai K, Cao Y, Huang Q, Jiang Y, Lv L. Prognostic value of Ki67 expression for patients with surgically resected hepatocellular carcinoma: Perspectives from a high incidence area. *Clin Lab* (2017) 63(2):355–64. doi: 10.7754/Clin.Lab.2016.160638

18. Yao Z, Dong Y, Wu G, Zhang Q, Yang D, Yu J, et al. Preoperative diagnosis and prediction of hepatocellular carcinoma: Radiomics analysis based on multi-modal ultrasound images. *BMC Cancer* (2018) 18(1):1089. doi: 10.1186/s12885-018-5003-4

19. Yang CK, Yu TD, Han CY, Qin W, Liao XW, Yu L, et al. Genome-wide association study of MKI67 expression and its clinical implications in HBV-related hepatocellular carcinoma in southern China. *Cell Physiol Biochem* (2017) 42(4):1342–57. doi: 10.1159/000478963

20. Chen Y, Qin X, Long L, Zhang L, Huang Z, Jiang Z, et al. Diagnostic value of gd-EOB-DTPA-Enhanced MRI for the expression of Ki67 and microvascular density in hepatocellular carcinoma. *J Magn Reson Imaging* (2020) 51(6):1755–63. doi: 10.1002/jmri.26974

21. Jing M, Cao Y, Zhang P, Zhang B, Lin X, Deng L, et al. The benefit of apparent diffusion coefficient in evaluating the invasiveness of hepatocellular carcinoma. *Front Oncol* (2021) 11:719480. doi: 10.3389/fonc.2021.719480

22. Ding Y, Rao S-X, Zhu T, Chen CZ, Li RC, Zeng MS. Liver fibrosis staging using T1 mapping on gadoxetic acid-enhanced MRI compared with DW imaging. *Clin Radiol* (2015) 70(10):1096–103. doi: 10.1016/j.crad.2015.04.014

23. Ko GH, Go SI, Lee WS, Lee JH, Jeong SH, Lee YJ, et al. Prognostic impact of ki-67 in patients with gastric cancer-the importance of depth of invasion and histologic differentiation. *Med (Baltimore)* (2017) 96(25):e7181. doi: 10.1097/MD.0000000000007181

24. Quaglia A, McStay M, Stoeber K, Loddo M, Caplin M, Fanshawe T, et al. Novel markers of cell kinetics to evaluate progression from cirrhosis to hepatocellular carcinoma. *Liver Int* (2006) 26(4):424–32. doi: 10.1111/j.1478-3231.2006.01242.x

25. Aktas S, Karakayali H, Moray G, Ozdemir H, Haberal M. Effects of risk factors and ki-67 on rates of recurrence on patients who have undergone liver transplant for hepatocellular carcinoma. *Transplant Proc* (2011) 43(10):3807–12. doi: 10.1016/j.transproceed.2011.09.067

26. Erstad DJ, Tanabe KK. Prognostic and therapeutic implications of microvascular invasion in hepatocellular carcinoma. *Ann Surg Oncol* (2019) 26 (5):1474–93. doi: 10.1245/s10434-019-07227-9

27. Wang Y, Lu L, Liu H, Ding Y, Song N, Lin F, et al. Effect of microvascular invasion on the prognosis in hepatocellular carcinoma and analysis of related risk factors: A two-center study. *Front Surg* (2021) 8:733343. doi: 10.3389/fsurg.2021.733343

28. Choi SY, Kim SH, Park CK, Min JH, Lee JE, Choi YH, et al. Imaging features of gadoxetic acid-enhanced and diffusion-weighted MR imaging for identifying cytokeratin 19-positive hepatocellular carcinoma: A retrospective observational study. *Radiology* (2018) 286(3):897–908. doi: 10.1148/radiol.2017162846

29. Yang F, Wan Y, Xu L, Wu Y, Shen X, Wang J, et al. MRI-Radiomics prediction for cytokeratin 19-positive hepatocellular carcinoma: A multicenter study. *Front Oncol* (2021) 11:672126. doi: 10.3389/fonc.2021.672126

30. Wu H, Han X, Wang Z, Mo L, Liu W, Guo Y, et al. Prediction of the ki-67 marker index in hepatocellular carcinoma based on CT radiomics features. *Phys Med Biol* (2020) 65(23):235048. doi: 10.1088/1361-6560/abac9c

31. Hu XX, Yang ZX, Liang HY, Ding Y, Grimm R, Fu CX, et al. Whole-tumor MRI histogram analyses of hepatocellular carcinoma: Correlations with ki-67 labeling index. *J Magn Reson Imaging* (2017) 46(2):383–92. doi: 10.1002/jmri.25555

32. Li Y, Chen J, Weng S, Sun H, Yan C, Xu X, et al. Small hepatocellular carcinoma: using MRI to predict histological grade and ki-67 expression. *Clin Radiol* (2019) 74(8):653.e1–e9. doi: 10.1016/j.crad.2019.05.009

33. Fan Y, Yu Y, Wang X, Hu M, Hu C. Radiomic analysis of gd-EOB-DTPA-enhanced MRI predicts ki-67 expression in hepatocellular carcinoma. *BMC Med Imaging* (2021) 21(1):100. doi: 10.1186/s12880-021-00633-0

34. Kim KA, Kim MJ, Jeon HM, Kim KS, Choi JS, Ahn SH, et al. Prediction of microvascular invasion of hepatocellular carcinoma: usefulness of peritumoral hypointensity seen on gadoxetate disodium-enhanced hepatobiliary phase images. *J Magn Reson Imaging* (2012) 35(3):629–34. doi: 10.1002/jmri.22876

35. Hong SB, Choi SH, Kim SY, Shim JH, Lee SS, Byun JH, et al. MRI Features for predicting microvascular invasion of hepatocellular carcinoma: A systematic review and meta-analysis. *Liver Cancer* (2021) 10(2):94–106. doi: 10.1159/000513704

36. Wei Y, Ye Z, Yuan Y, Huang Z, Wei X, Zhang T, et al. A new diagnostic criterion with gadoxetic acid-enhanced MRI may improve the diagnostic performance for hepatocellular carcinoma. *Liver Cancer* (2020) 9(4):414–25. doi: 10.1159/000505696

37. Cunha GM, Hasenstab KA, Delgado T, Ichikawa S, Lee MH, Medina PM, et al. Multi-arterial phase MRI depicts inconsistent arterial phase hyperenhancement (APHE) subtypes in liver observations of patients at risk for hepatocellular carcinoma. *Eur Radiol* (2021) 31(10):7594–604. doi: 10.1007/s00330-021-07924-8

frontiers | Frontiers in Oncology

TYPE Original Research
PUBLISHED 17 October 2022
DOI 10.3389/fonc.2022.853254

OPEN ACCESS

EDITED BY
Chandan Guha,
Albert Einstein College of Medicine,
United States

REVIEWED BY
Massimo Galia,
University of Palermo, Italy
Kunal Bharat Gala,
Tata Memorial Hospital, India

*CORRESPONDENCE
Jie Peng
sank44@sina.com

†These authors have contributed equally to this work

SPECIALTY SECTION
This article was submitted to Cancer Imaging and Image-directed Interventions, a section of the journal Frontiers in Oncology

RECEIVED 13 January 2022
ACCEPTED 30 September 2022
PUBLISHED 17 October 2022

CITATION
Peng J, Lu F, Huang J, Zhang J, Gong W, Hu Y and Wang J (2022) Development and validation of a pyradiomics signature to predict initial treatment response and prognosis during transarterial chemoembolization in hepatocellular carcinoma. *Front. Oncol.* 12:853254. doi: 10.3389/fonc.2022.853254

Development and validation of a pyradiomics signature to predict initial treatment response and prognosis during transarterial chemoembolization in hepatocellular carcinoma

Jie Peng[1*†], Fangyang Lu[1†], Jinhua Huang[2†], Jing Zhang[3], Wuxing Gong[4], Yong Hu[5] and Jun Wang[6]

[1]Department of Oncology, The Second Affiliated Hospital, GuiZhou Medical University, Kaili, China, [2]Department of Minimal Invasive Interventional Therapy, Sun Yat-Sen University Cancer Center, State Key Laboratory of Oncology in South China, Guangzhou, China, [3]Department of Medical Imaging Center, Nanfang Hospital, Southern Medical University, Guangzhou, China, [4]Department of Oncology, Zhuhai Hospital Affiliated with Jinan University, Jinan University, Zhuhai, China, [5]Department of Oncology, Guiyang Public Health Clinical Center, Guiyang, China, [6]Department of Oncology, The Third Affiliated Hospital, GuiZhou Medical University, Duyun, China

We aimed to develop and validate a pyradiomics model for preoperative prediction of initial treatment response to transarterial chemoembolization (TACE) in patients with hepatocellular carcinoma (HCC). To this end, computed tomography (CT) images were acquired from multi-centers. Numerous pyradiomics features were extracted and machine learning approach was used to build a model for predicting initial response of TACE treatment. The predictive accuracy, overall survival (OS), and progression-free survival (PFS) were analyzed. Gene Set Enrichment Analysis (GSEA) was further used to explore signaling pathways in The Cancer Genome Atlas (TCGA)-HCC cohort. Overall, 24 of the 1,209 pyradiomic features were selected using the least absolute shrinkage and selection operator (LASSO) algorithm. The pyradiomics signature showed high predictive accuracy across the discovery set (AUC: 0.917, 95% confidence interval [CI]: 86.93-96.39), validation set 1 (AUC: 0.902, 95% CI: 84.81-95.59), and validation set 2 (AUC: 0.911; 95% CI: 83.26-98.98). Based on the classification of pyradiomics model, we found that a group with high values base on pyramidomics score showed good PFS and OS (both $P<0.001$) and was negatively correlated with glycolysis pathway. The proposed pyradiomics signature could accurately predict initial treatment response and prognosis, which may be helpful for clinicians to better screen patients who are likely to benefit from TACE.

KEYWORDS

epatocellular carcinoma, therapy response, pyradiomics, TACE, progression-free survival

Introduction

Hepatocellular carcinoma (HCC) is a major cause of cancer-related death worldwide (1). Some patients with HCC are ineligible for liver transplantation and surgical resection because the curative surgery cannot be performed (2–4). For these patients with intermediate and advanced-stage HCC, transarterial chemoembolization (TACE) therapy is a promising treatment method following the National Comprehensive Cancer Network (NCCN) clinical practice guideline (5–7).

Initial treatment response has recently been reported to be a powerful indicator of favorable outcomes, such as longer progression-free survival (PFS) and overall survival (OS) (8–10). Studies on tumor burden were evaluated using magnetic resonance imaging (MRI) or computed tomography (CT) and found associations between imaging features (e.g., tumor size, tumor number) and treatment response to TACE in patients with HCC (11–14). However, imaging features have a limited accuracy of subjective judgment, and they do not reflect intra-tumor heterogeneity. Developing a robust and accurate algorithm to select patients who will show initial response to treatment remains challenging and important. Thus, an accurate model to identify patients with an initial response to TACE could be useful to optimize individualized treatment strategy.

Nowadays, radiomics have been a new and promising field that involves the extraction of large quantitative features from radiographic images (15, 16). The radiomics algorithm offers an unprecedented opportunity to improve cancer decision-making in a low-cost and non-invasive manner. Previous studies have shown that radiomics models of radiology images are significantly associated with clinical outcomes in cancer patients (17–21). We previously found that a radiomics model based on CT images could precisely predict microvascular invasion in HCC patients and the machine learning algorithm could be used to predict clinic outcome in cancer (22, 23). However, the standard method in this field was lacked and the potential mechanism of radiomics model was unclear in the HCC. Radiomics extracting from python package was named pyradiomics and provide the chance. The role of pyradiomics predictive models for initial response or prognosis in TACE treatment, and the association with signal transduction pathway remain unexplored.

In this study, based on the preoperatively CT images and machine learning algorithm, we aimed to develop and validate a robust and accurate pyradiomics signature for a noninvasive pretreatment prediction of initial response to TACE in HCC patients. The mutual relationships between pyradiomics score and clinical factors were further analyzed and validated in other patient cohorts. The subgroup analyses, clinical utility and prognosis of pyradiomics model were estimated. Gene Set Enrichment Analysis (GSEA) tool was used to reveal the association between pyradiomics model and Kyoto Encyclopedia of Genes and Genomes (KEGG), which contributes to interpretation of the potential mechanism but not "black box" of these machine learning models.

Materials and methods

Study design and patients

The flowchart of the machine learning model is presented in detail in Figure 1. This was a retrospective study of 313 patients with Barcelona Clinic Liver Cancer (BCLC) stage B HCC who underwent conventional TACE between February 2010 and December 2020. Patients were recruited from the Nanfang Hospital (n=141 patients, discovery set), Sun Yat-sen University Cancer Center (n=121, validation set 1), and the Second Affiliated Hospital of Gui Zhou Medical University (n=51) (validation set 2). The inclusion criteria were radiologically or pathologically confirmed HCC, initial TACE treatment, BCLC sage B, and arterial-phase CT images availability within 7 days before and 30 days after treatment. Patients who underwent loco-regional or whole-body therapies were excluded. According to the modified Response Evaluation Criteria in Solid Tumors (mRECIST), the initial response to TACE was classified as complete response (CR), partial response (PR), stable disease (SD), and progressive disease (PD) by an experienced radiologist as in the previous study (24). Initial treatment response and non-response were strictly defined as CR+PR and SD+PD, respectively. The OS was defined as the time from the start of TACE or hepatectomy treatment until death or the last contact; PFS was defined as the time between the beginning of TACE treatment and the progression or death of the tumor; disease-free survival (DFS) was defined as the time between the beginning of hepatectomy treatment and disease recurrence or death because of the tumor. This study was approved by the three institutional review boards of Nanfang Hospital, the Second Affiliated Hospital of Gui Zhou Medical University, and Sun Yat-sen University Cancer Center.

Abbreviations: AFP, alpha-fetoprotein; AIC, Akaike information criterion; AUC, area under the curve; BCLC, Barcelona Clinic Liver Cancer; CI, confidence interval; CR, complete response; CT, computed tomography; DFS, disease-free survival; HCC, Hepatocellular carcinoma; HR, hazard ratio; ICCs, inter-correlation coefficients; KEGG, Kyoto Encyclopedia of Genes and Genomes; LASSO, least absolute shrinkage and selection operator; OS, overall survival; PD, progressive disease; PFS, progression-free survival; PR, partial response; PRS, pyradiomics score; ROC, receiver operating characteristic; ROI, regions of interest; SD, stable disease; TACE, trans-arterial chemoembolization; TCGA, The Cancer Genome Atlas; NCCN, National Comprehensive Cancer Network; MRI, magnetic resonance imaging.

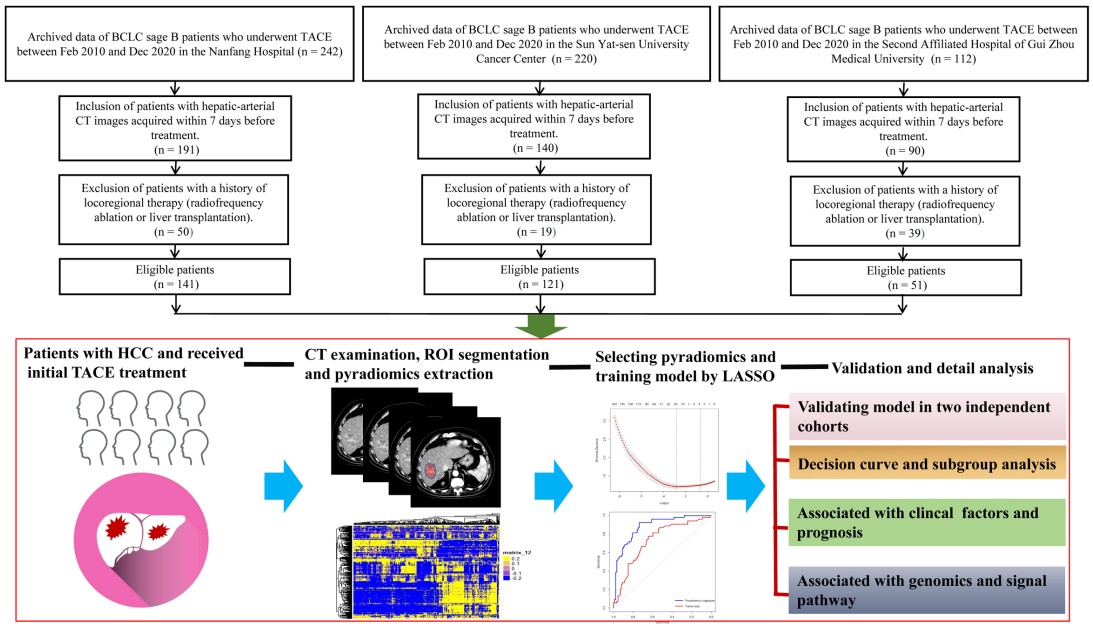

FIGURE 1
Flowchart for the development of the machine learning model. All patients have radiologically or pathologically proven HCC and undergo CT before TACE therapy. The radiologists manually segment the 3D ROIs. Thereafter, 1,167 features are extracted from the hepatic arterial CT images based on the "pyradiomics" package of python. Using LASSO method, 24 features are selected, and the pyradiomics model is built. Model validity is evaluated in two cohorts. The predictive performance of the pyradiomics model is compared with that of clinical factors. The association between the pyradiomics model and cancer signaling pathways is analyzed using the TCGA-HCC cohort. 3D, three-dimensional; HCC, hepatocellular carcinoma; CT, computed tomography; ROI, region of interest; LASSO, least absolute shrinkage and selection operator algorithm; TCGA, The Cancer Genome Atlas.

TACE procedure, CT acquisition and manual segmentation of the region of interest

TACE was performed under local anesthesia using the traditional femoral approach. TACE was performed under the guidance of digital subtraction angiography (Allura Xper FD 20, Philips) through the left and right hepatic arteries directly through the arteries supplying blood to the tumor when technically feasible. Hepatic arteriography, performed using a 5 Fr (RH or Yashiro) catheter, was first used to assess the location, number, size, and blood supply of the target tumor. The embolic emulsion agent, including epirubicin (30–60 mg), lobaplatin (30–50 mg), and lipiodol (10–30 mL), was injected into the artery supplying the tumor through a 2.7/2.8 Fr microcatheter. Thirty days after treatment, according to the modified Response Evaluation Criteria in Solid Tumors (ver. 1.1).

Contrast-enhanced computed tomography scans were performed as previously described (22). Contrast-enhanced computed tomography (CECT) was performed at hospital using an MDCT scanner and the detail information of CT image acquisition was described in the Supplementary Material. After the routine CT scanning, a contrast agent (Ultravist 370, Bayer SchL/s) was delivered *via* an injector (Ulrich CT Plus 150, Ulrich Medical, Ulm, Germany); and CECT was performed immediately after injection. Preoperative CT images were collected on the Picture Archiving and Communication System (PACS; Nanfang Hospital Network Center, China), with an optimal window setting adjustment (window width: 300, window level: 50). The CT images were downloaded through the Picture Archiving and Communication System. Two senior radiologists blinded to the treatment results manually segmented the three-dimensional (3D) regions of interest (ROI) in HCC using the ITK-SNAP (version 3.6, https://sourceforge.net/projects/itksnapx64/). Then, they saved and stored the main images and 3D segmented images for extraction of pyradiomics.

Extraction and reproducibility examination of pyradiomics features

MATLAB 2014b (https://ww2.mathworks.cn/) was used to standardize and reconstruct the segmented 3D ROI image. The thickness of the layer was 1 mm. Python 3.6 (https://www.python.org/downloads/release/python-360/) was used to install the package (https://github.com/Radiomics/pyradiomics) and extract the pyradiomics features from 3D images. These values included the texture, shape, size, and wavelet transform of the CT images.

The intra- and inter-correlation coefficients (ICCs) of 50 hepatic artery CT images between two observers were used to evaluate the repeatability of pyradiomics feature extraction. To evaluate intra-observer reproducibility, two radiologists independently and manually segmented the ROIs of 50 patients. Meanwhile, to assess repeatability between observers, two readers extracted the high-dimensional pyradiomics features twice with at least 1-week interval. ICCs greater than 0.75 were set to indicate favorable consistency in pyradiomics extraction. These values, which described the texture, shape, size, and wavelet transform of the CT images, could be used to analyze the overall consistency and select the robust pyradiomics features with good reproducibility.

Development and validation of the pyradiomics signature for predicting therapy response

The least absolute shrinkage and selection operator (LASSO) is a powerful algorithm to choose the most important variables from high-dimensional features (22, 23). LASSO is a reduction method that shrinks the regression coefficient to a certain area. The main idea in using LASSO is constructing a first-order penalty function to obtain a refined model through the final determination of some variables coefficient 0 for feature screening. The penalty term of LASSO is:

$$\sum_{i=1}^{n} |wi| \leq t$$

This constraint uses the first-order penalty function of absolute value instead of the second-order function of square sum. Although the form is only slightly different, the results are very different. Some of the coefficients would generate to zero. In this study, LASSO based on 5-fold cross-validation was used to select 24 non-zero coefficients. Then, a pyradiomics score (PRS) was calculated based on a logistic method. A pyradiomics signature was consequently developed to predict TACE treatment response. The pyradiomics model's performance was then evaluated in the discovery and two validation sets using receiver operating characteristic (ROC) analysis. The optimal cut-off value for predicting treatment response was calculated using the Youden's index. According to the optimal cut-off PRS value, we divided the patients into two groups. The patients with high values (>-0.14) were defined as RS1, and those with low values (≤-0.14) as RS2. In our study, 112 patients from Nanfang Hospital and 29 from the Second Affiliated Hospital of Gui Zhou Medical University had the information of prognosis.

Gene Set Enrichment Analysis in the TCGA-HCC cohort

The purpose of Gene Set Enrichment Analysis (GSEA) is to explore the relationship between the level of imaging score and tumor-related signaling pathways and gene expression. The GSEA analysis data included four files: 1. The Gene Expression profiling data (Expression dataset) was derived from the mRNA Expression profiles of HCC in The Cancer Genome Atlas (TCGA), and contained 20,533 Gene Expression information; 2. The Gene sets contained 2,074 known Gene sets; 3. Chip annotations listed each probe on the DNA Chip and its matching Hugo gene symbols; 4. Phenotype labels were used to categorize samples into two classes for research purposes and to ensure that the order of the samples was consistent with that of the expression spectrum files. TCGA expression spectrum data were downloaded at: https://www.cancer.gov/about-nci/GDC. The data for a total of 46 HCC patients with preoperative CT images in TCGA database were downloaded from The Cancer Imaging Archive (TCIA) (http://www.Cancer.imaging.archive.net/). In this study, according to the value of PRS, 46 patients with HCC were divided into two groups: RS1 and RS2. The two groups were clustered to identify the distinct genes (fold change ≥2.0, P<0.05). Genes were identified using the "edgR" package. Based on the specific genes, pathway analysis was conducted to determine the potential mechanisms for the machine learning model (DAVID, https://david.ncifcrf.gov/).

Statistical analysis

The "pROC" package was used to plot the receiver operating characteristic (ROC) curves. A confidence interval (CI) of 95% for the area under the curve (AUC) was calculated in all cohorts. PRS was evaluated using the Mann-Whitney U test. The Akaike information criterion (AIC) was used to select the optimal model. The AIC is based on entropy and a measure of the goodness of a statistical model. The smaller the AIC, the better the model. The AIC can be expressed as: AIC = (2k-2L)/n. The Kaplan-Meier curves of DFS, PFS, and OS were analyzed using the "survminer" package. Decision curve analysis (DCA) was used to quantify the probabilities of net benefits at different threshold in patients with HCC, plotted by the "dca.R" package. All statistical analyses were performed using the R statistical software version 3.5.0 (R Core Team, 2018) and GraphPad prism 7.0. Two-sided P values<0.05 were considered significant.

Results

Patient characteristics

In total, 18 (12.76%), 13 (10.75%), and 10 (19.61%) patients in the training set, validation set 1, and validation set 2 were females, respectively. Furthermore, 93 (65.96%), 85 (70.25%), and 33 (64.70%) patients were aged less than 60 years, respectively. The baseline patient characteristics are shown in Table 1. Most patients (82.27, 86.78, and 82.35%) had Child-

Pugh A disease and a low number of tumors (≤3) (85.82, 86.64, and 76.47%) in the training set, validation set 1, and validation set 2, respectively. Overall, 51.06, 52.06, and 49.01% of the patients in the training set, validation set 1, and validation set 2, respectively, had high alpha-fetoprotein (AFP) levels. Patients with small tumor size (≤5 cm) accounted for 13.47, 12.39, and 15.69% of the population in the discovery set, validation set 1, and validation set 2, respectively. There were 56 (39.72%), 51 (42.15%), and 19 (37.25%) patients in these three cohorts, respectively, who achieved CR/PR. There was no significant difference in the treatment response rate between the three sets.

Pyradiomics signature development and associated analysis of clinical factors

Pyradiomics features were extracted as described in previous studies (25–27). A total of 1,167 features were extracted from the hepatic arterial 3D-CT images. A total of 457 pyradiomics features were eliminated in the ICC analysis. The remaining 710 features were then subjected to feature selection and LASSO coefficient analysis. Based on 5-fold cross-validation *via* the maximum criteria, 24 coefficients were selected (Supplemental Figure S1). Twenty-four pyradiomics features were analyzed *via* multi-variable logistic regression and included to develop the pyradiomics signature (PRS) (Table 2).

Treatment responders showed significantly higher PRS than non-responders in the three cohorts (all $P<0.001$) (Figures 2A-C). Tumor size was also associated with treatment response in the three cohorts ($P<0.001$, $P<0.001$, and $P=0.017$, respectively) (Supplemental Figure S2). However, we found there was no association between treatment response and other clinical factors, such as tumor number, AFP level. Meanwhile, PRS was also not correlated with age, sex, Child-Pugh classification, AFP level, and tumor number across all three cohorts (Figures 2D-F). In contrast, PRS was significantly associated with tumor size (r=-0.416, $P<0.001$; r=-0.514, $P<0.001$; r=-0.568, $P<0.001$, respectively) and treatment response (r=0.605, $P<0.001$; r=0.539, $P<0.001$; r=0.588, $P<0.001$, respectively).

Evaluating classifiable accuracy of machine learning model by PRS

The area under the ROC curves of tumor size and the pyradiomics signature were analyzed. We used Youden's index (defining as sum of sensitivity and specificity minus 1) to calculate the optimal cut-off value (-0.14) in the ROC analysis.

TABLE 1 Patient characteristics by study set.

Variable	Discovery set (n = 141)	Validation set 1 (n = 121)	Validation set 2 (n = 51)	*P* value
Sex				0.286
Female	18 (12.7%)	13 (10.7%)	10 (19.6%)	
Male	123 (87.3%)	108 (89.3%)	41 (80.4%)	
Age (years)				0.687
≤60	93 (65.9%)	85 (70.3%)	33 (64.7%)	
>60	48 (34.1%)	36 (29.7%)	18 (35.3%)	
Child–Pugh classification				0.573
A	116 (82.3%)	105 (86.7%)	42 (82.3%)	
B	25 (17.7%)	16 (13.3%)	9 (17.7%)	
AFP (ng/mL)				0.935
≤20	72 (51.1%)	63 (52.1%)	25 (49.1%)	
>20	69 (48.9%)	58 (47.9%)	26 (50.9%)	
Tumor size (cm)				0.967
≤5	19 (13.5%)	15 (12.4%)	8 (15.7%)	
>5, ≤10	62 (44.0%)	57 (47.1%)	23 (45.1%)	
>10	60 (42.5%)	49 (40.5%)	20 (39.2%)	
Tumor number				0.915
≤3	121 (85.8%)	100 (86.6%)	39 (76.5%)	
>3	20 (14.2%)	21 (13.4%)	12 (23.5%)	
Treatment response				0.823
CR/PR	56 (39.7%)	51 (42.2%)	19 (37.3%)	
SD/PD	85 (60.3%)	70 (57.8%)	32 (62.7%)	

P value is derived from the difference between the discovery data set and the two validation data sets. AFP, alpha-fetoprotein; CR, complete response; PR, partial response; SD, stable disease; PD, progressive disease.

TABLE 2 Formula for calculating pyradiomics signature.

Pyradiomic features	Coefficients	*P* value
Intercept	1.479e+02	0.243
exponential_glrlm_Long Run Emphasis	2.502e+04	0.989
exponential_glrlm_Long Run Low Gray Level Emphasis	-2.502e+04	0.989
exponential_glszm_Small Area High Gray Level Emphasis	1.976e+01	0.624
logarithm_first order_Skewness	-9.396e-02	0.046*
logarithm_glcm_Idmn	1.004e+02	0.192
original_gldm_Dependence Variance	-5.060e-02	0.145
original_gldm_Small Dependence High Gray Level Emphasis	-3.662e-02	0.818
original_glszm_Gray Level Non Uniformity	-1.305e-04	0.851
original_shape_Maximum 2D Diameter Slice	4.262e-03	0.732
original_shape_Maximum 3D Diameter	6.609e-03	0.559
original_shape_Sphericity	9.891e+00	0.030*
square_glszm_Small Area Emphasis	-1.362e+00	0.115
wavelet.HHL_firstorder_Skewness	6.523e-01	0.159
wavelet.HHL_glcm_Cluster Prominence	3.869e-05	0.660
wavelet.HHL_glszm_Gray Level Non Uniformity	-2.459e-04	0.308
wavelet.HHL_glszm_Large Area High Gray Level Emphasis	-8.487e-11	0.059
wavelet.HHL_glszm_Low Gray Level Zone Emphasis	2.924e+00	0.001*
wavelet.HLH_gldm_Dependence Non Uniformity Normalized	-2.301e+01	0.030*
wavelet.LHH_first order_Skewness	-4.023e-01	0.072
wavelet.LHL_glszm_Large Area Low Gray Level Emphasis	-4.079e-08	0.252
wavelet.LLH_first order_Median	1.630e+00	0.251
wavelet.LLH_glcm_Cluster Shade	-9.764e-01	0.082
wavelet.LLL_first order_90 Percentile	2.615e-03	0.083
wavelet.LLL_glcm_Idmn	-2.532e+02	0.068

*P<0.05 indicates statistical significance.

The AUCs showed that the tumor size (AUC=0.752, 95% CI: 66.89-83.60, *P*<0.001) and pyradiomics signature (AUC=0.916, 95% CI: 86.93-96.39, *P*<0.001) could be the predictors of treatment response to TACE in patients with HCC (Figure 3A) (Supplemental Table S1). Furthermore, the model of the pyradiomics signature in the validation sets 1 and 2 also demonstrated a high AUC for predicting treatment response, with the AUC consistent with that in the discovery set (AUC=0.902, 95% CI: 84.81-95.59, *P*<0.001; AUC=0.911, 95% CI: 83.26-98.98, *P*<0.001, respectively). The AUCs of the tumor size were 0.778 (95% CI: 52.00-82.60, *P*<0.001) and 0.690 (95% CI: 54.66-83.33, *P*=0.024, Figures 3B, C). Based on boostrap (n=2000) analysis, the efficiency of the pyradiomics signature was significantly higher than that of the tumor size in the discovery (*P*=0.016) and the two validation sets (*P*=0.016 and *P*=0.008). The AIC of the model comprising a combination of the pyradiomics signature and tumor size was not superior to that of the model comprising only the pyradiomics signature in the discovery set (240.53 vs. 238.94). The examples of two patients with response (RS1) or no response (RS2) are shown in our study (Figure 3D). The patient 1 had higher pyradiomics score than patient 2 did (5.44 vs.-3.10).

Clinical utility and subgroup analysis of PRS predictive accuracy

The DCA of the pyradiomics signature showed relatively good performance of the model regarding clinical application (Figure 4A). It was suggested from the DCA curve that when the threshold probability in a patient was 42%, more initial response could be achieved through a pyradiomics signature than either treat-all or treat-none strategies. The probability of acquiring treatment response ranged from 8 to 100%. Thus, a pyradiomics signature accurately identifies the patients who have the initial response and may benefit from TACE therapy. The patients were divided into subgroups based on six clinical variables to estimate the classification performance of the pyradiomics model further (Supplemental Table S2). The AUC was higher in the female patients than that in the male patients (0.966, 95% CI: 92.18-100.00 vs. 0.8985, 95% CI: 86.12-93.59, *P*=0.021) (Figure 4B). Meanwhile, the predictive accuracy was not affected by age, Child–Pugh classification, and AFP levels, compared with bootstrap=2000 (*P*=0.354, *P*=0.998, and *P*=0.424, respectively) (Figures 4C-E). Subgroup analysis by tumor number and tumor size also showed no significant difference in AUCs (*P*=0.443 and *P*=0.597, respectively) (Figures 4F-G).

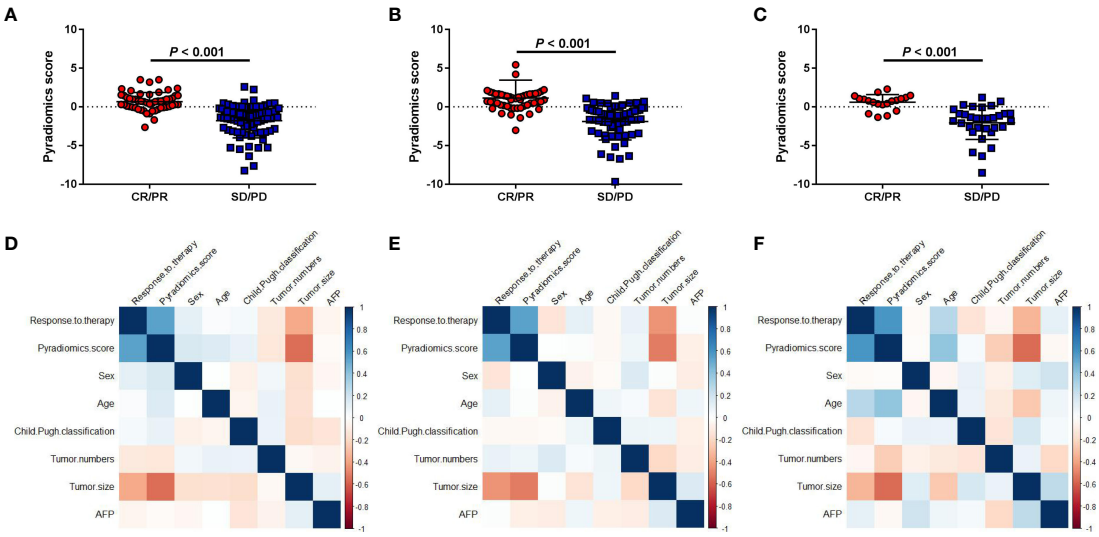

FIGURE 2
Association between the pyradiomics score and clinical factors. **(A-C)** Correlations between the pyradiomics score and object response (CR+PR) in the discovery and two validation sets. **(D-F)** Correlation heatmaps of the pyradiomics score and clinical factors in the three cohorts. SD, stable disease; CR, complete response; PD, progressive disease; PR, partial response.

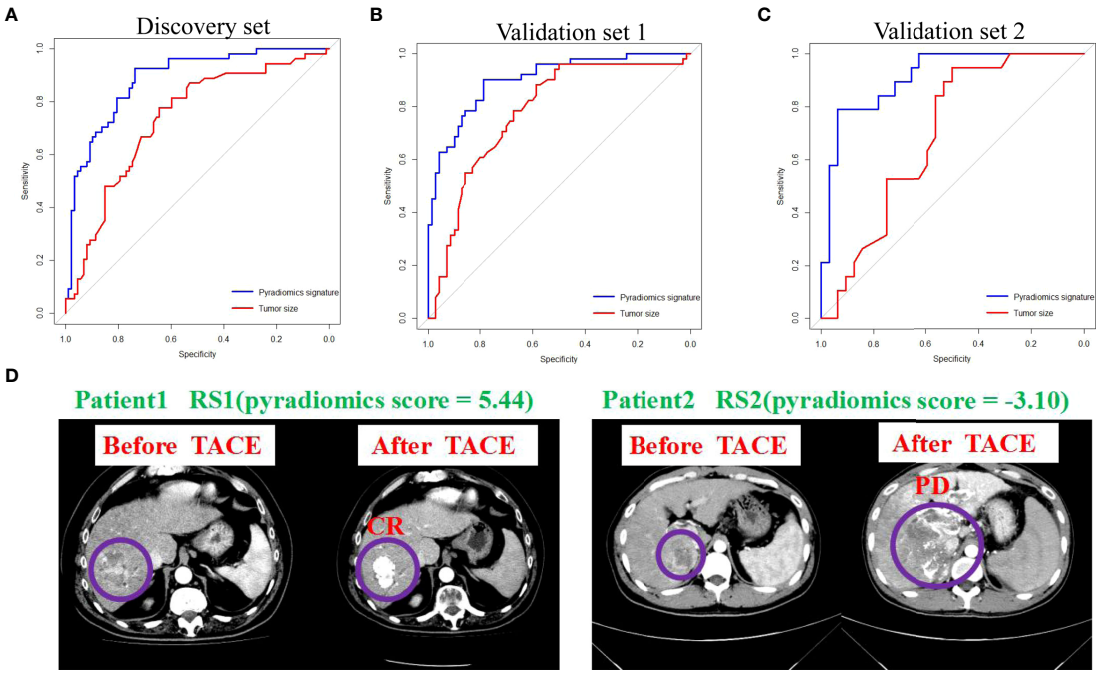

FIGURE 3
Pyradiomics signature and tumor size predict treatment response to TACE. **(A-C)** ROC curves show the predictive performance of pyradiomics signature and tumor size for estimating CR and PR. The bootstrap (n=2000) test results of the two ROC curves indicate that the AUC of the sum of pyradiomics signature is significantly higher than those of the tumor size in the discovery and in validation 1 and 2 sets. **(D)** Examples of two patients with response (RS1) or no response (RS2). ROC, receiver operating characteristic; AUC, area under curve; CR, complete response; PR, partial response.

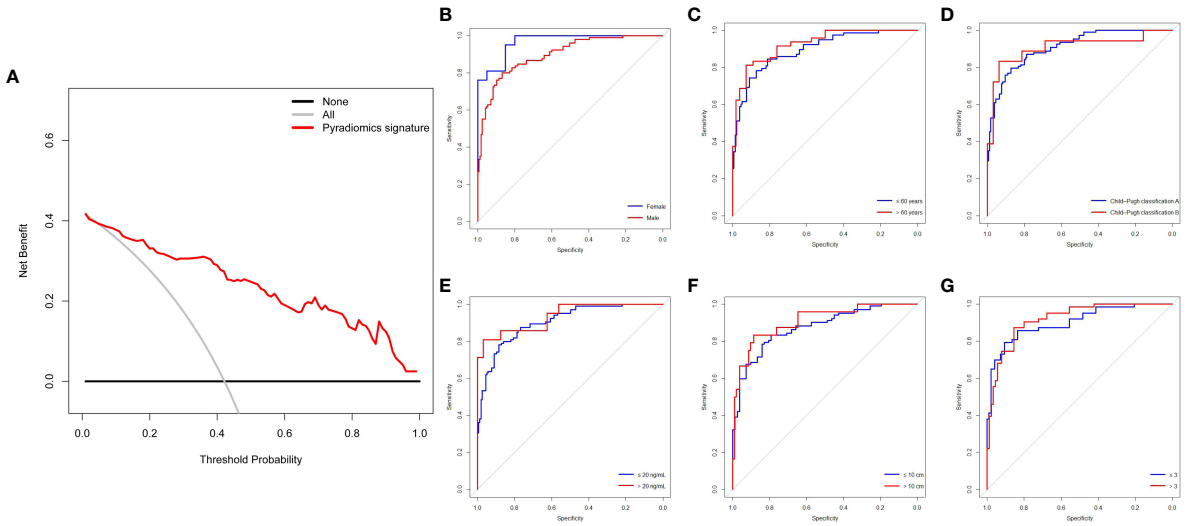

FIGURE 4
DCA and subgroup analysis of the pyradiomics signature for predictive treatment response to TACE. **(A)** DCA of the pyradiomics signature. **(B-G)** Pyradiomics signature of clinical subgroup predicts therapy response in all patients (n=313) undergoing TACE treatment. The two ROC curves are compared using the bootstrap (n=2000) test. DCA, decision curve analysis; ROC, receiver operating characteristic; TACE, transarterial chemoembolization.

The prognostic value of PRS in patients undergoing TACE treatment

According to the optimal cut-off value of PRS, we divided the patients into two groups. The patients with high values (>-0.14) defined as RS1, and the patients with low values (≤-0.14) defined as RS2. In our study, 112 patients from Nanfang Hospital and 29 patients from the Second Affiliated Hospital of Gui Zhou Medical University had the information of prognosis. Therefore, based on stratification of RS1and RS2, PFS and OS were analyzed in a total of 141 patients. We found the patients with RS1 had a longer PFS and OS than those with RS2 (Median PFS: 25 vs. 9 months, hazard ratio [HR]=2.78, 95% CI: 1.93-4.00, P<0.001; Median OS: 49 vs. 22 months, HR=2.23, 95% CI: 1.47-3.38, P<0.001, respectively) (Figures 5A, B). Moreover, we used the biomarkers of RS1 and RS2 to predict the 1-, 3-, and 5-year-OS and PFS rates. In the time-dependent ROC curve estimation from censored survival, the higher accuracies were 1-year-OS/PFS predictions than 3- and 5-year-OS/PFS predictions (0.679 vs.0.676 vs.0.662; 0.737 vs. 0.602 vs.0.617, respectively) (Figures 5C, D).

Association between PRS and glycolysis pathway genes stratify prognosis in TCGA-HCC patients (No-TACE treatment)

The same algorithm of machine learning in the training cohort was used in the CT images of 46 patients with HCC from the TCGA database (TCGA-HCC cohort) and the PRS was calculated by the pyradiomics formulation. According to the above cut-off value of pyradiomics score, all patients were then divided into two groups, which were defined as RS1 group (n=23) and RS2 group (n=23). In this experiment, high pyradiomics scores were mostly observed in the RS2 group and low pyradiomics scores were contrary. Through differential gene expression analysis (RS1 vs. RS2), between-group comparisons showed that 151 genes were significantly downregulated, while 167 genes were upregulated (FDR adjust P<0.05) (Figure 6A) (Supplemental Figure S3). The GSEA found several KEGG pathways were significantly associated with PRS, such as small molecule catabolic process, glycolysis, and recycling of bile acids and salts. In many pathways, we speculated that glycolysis resulting from tumor hypoxia status were mostly associated with TACE treatment. Therefore, we mainly focused on the glycolysis pathway genes and found that RS1 group was negatively associated with *HK2* and *PFKP* presence (Figure 6B) (Supplemental Figure S4). We cound not determine the ability of the PRS in this study to evaluate clinical prognosis in patients with HCC who underwent hepatectomy but did not receive TACE therapy. We subsequently found that RS1 group had significantly longer DFS and OS time than the RS2 group did (P<0.001 and P=0.008, respectively) (Figures 6C, D).

Discussion

Based on preoperatively CT images, this study developed a pyradiomics signature to accurately predict the initial treatment

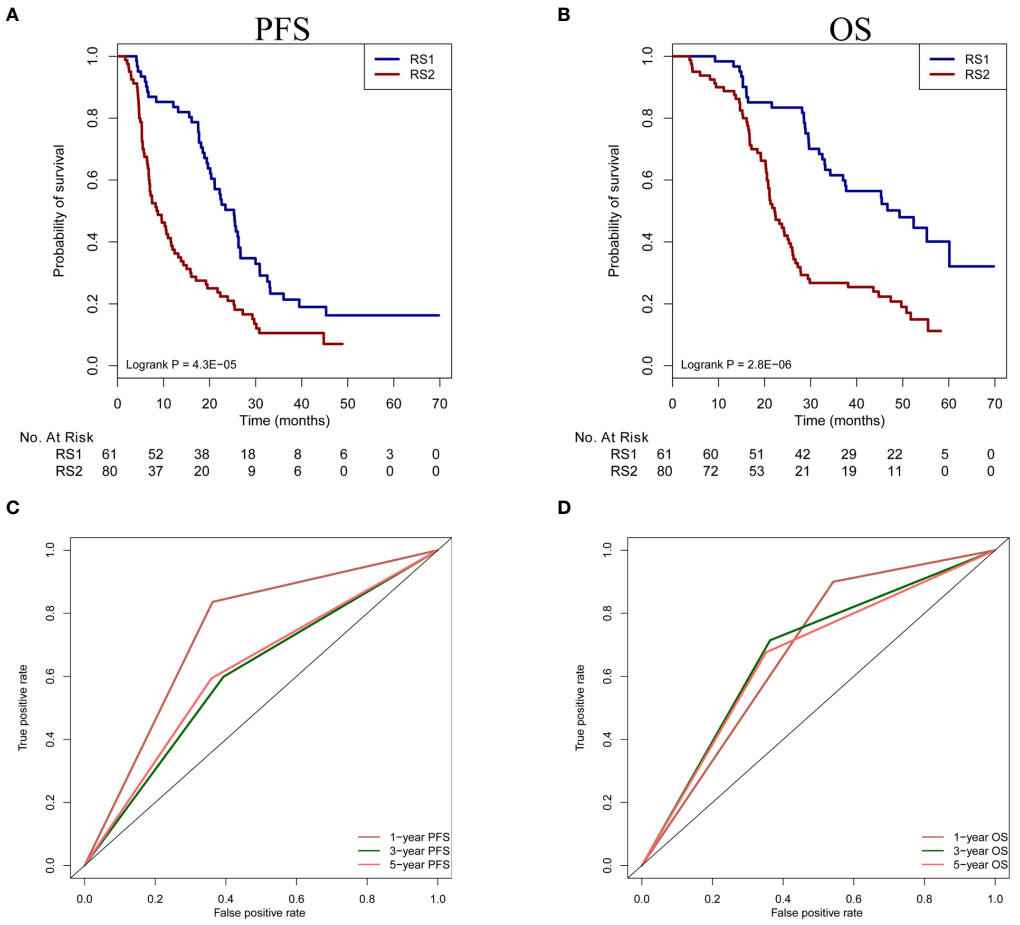

FIGURE 5
Prognosis prediction of PRS in patients undergoing TACE treatment. **(A, B)** The OS and PFS of two classification (RS1 vs. RS2) are compared in the patients. **(C, D)** Time-dependent ROC curve analysis is performed in 1-year-OS/PFS, 3-year-OS/PFS and 5-year-OS/PFS predictions. PFS, progression-free survival; OS, overall survival; PRS, pyradiomics score; TACE, transarterial chemoembolization; ROC, receiver operating characteristic.

response and prognosis in HCC patients who underwent TACE therapy. The DCA and subgroup prediction analysis showed the good clinical performance of the model. We further analyzed the association between the pyradiomics model and KEGG pathway genes in TCGA-HCC database. Our findings provided a novel insight into the interpretability of the machine learning model for predicting therapy response or prognosis in different types of tumors.

TACE is a standard treatment modality for HCC patients with BCLC stage B disease (7). Although recent studies reported that there was a non-superiority of TACE with respect to bland embolization, and direct incremental costs of drug-eluting beads TACE (DEB-TACE) can be acceptable in hepatocarcinoma patients (28, 29), considering the extensiveness of method and health policy in our country, we chose the conventional TACE treatment in this study. Treatment response to the first TACE is a well-known predictor of clinical outcomes in patients with middle-stage HCC. This study used pyradiomics algorithms from the python package to extract features of tumor shape, texture, intensity, and wavelet transform characteristics from three-dimensional CT images in HCC patients who underwent TACE as reported by previous studies (30, 31). In our study, we used LASSO of 5-fold cross-validation to chose pyradiomics features for CT images, and 24 features were finally selected. We then used logistic regression analysis to calculate the pyradiomics score among HCC patients who underwent TACE. The results showed significantly higher pyradiomics scores in the response group. The response group also showed smaller tumor size, which was consistent with previous reports (32, 33). There was a significantly negative correlation between the pyradiomics score and tumor size. Compared with tumor size, the pyradiomics model showed higher accuracies for predicting treatment response. This could be because the pyradiomics model included larger amount of radiology information than the model based on tumor size did (34), and

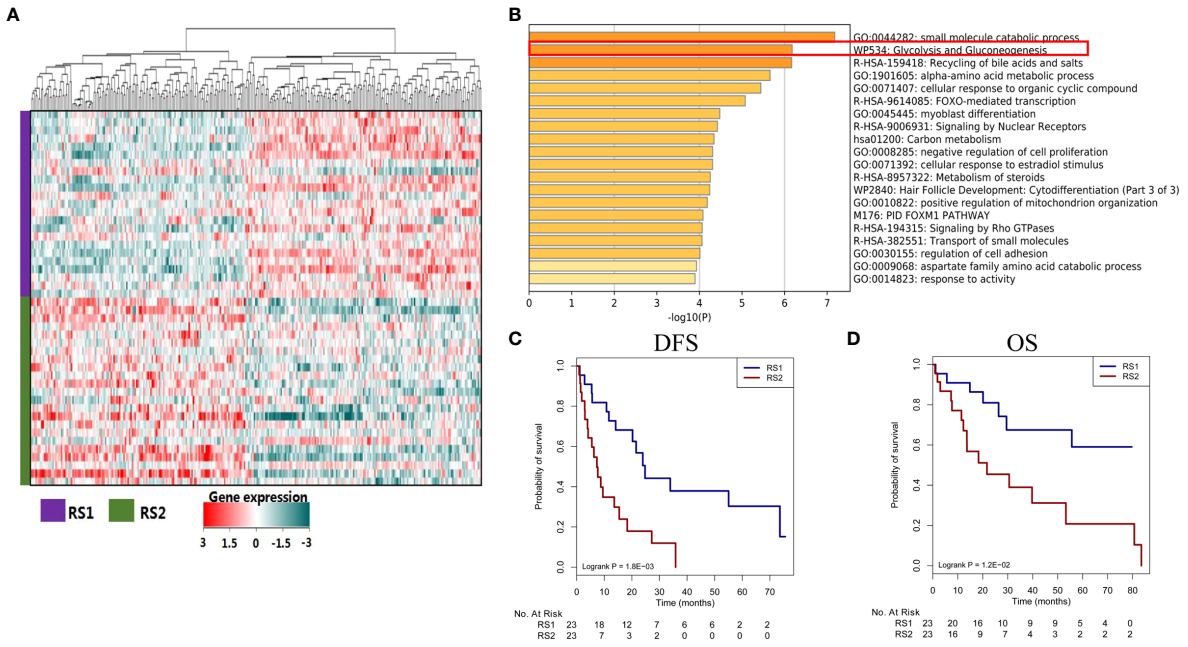

FIGURE 6
Different genes, signaling pathways, and prognosis associated with predicted treatment response. **(A)** The heat map plot of mRNA expression from different genes. Patients with HCC are shown on the *y*-axis, and gene expression is shown on the *x*-axis. **(B)** Some genes are enriched in certain signaling pathways, such as in the glycolysis and gluconeogenesis pathways. **(C, D)** The responder group shows better DFS and OS than the non-responder group does. HCC, hepatocellular carcinoma; DFS, disease-free survival; OS, overall survival.

a machine learning method, such as LASSO, made a great contribution to enhance the predictive ability of diagnosis, therapy response or prognosis in solid tumors. However, the model combining the pyradiomics signature and tumor size did not show superior AIC to that using the pyradiomics signature alone. The machine learning model had a robust accuracy for predicting initial treatment response to TACE and the method could be used as an invasive stool in the other cancers.

The DCA revealed that the pyradiomics model could predict the treatment response when the probability of acquiring treatment response ranged from 8 to 100%. This result indicated that the pyradiomics signature could help determine clinical strategy and identify the patients who had initial treatment response according to the above the optimal cut-off value (>-0.14). Additionally, some clinical variables may affect the predictive accuracy of the pyradiomics model (6, 35), and the model's predictive accuracy in patient subgroups was rarely reported and was still unclear. Interestingly, in this study, our subgroup analysis (Supplemental Table S2) showed that our machine learning model had a better predictive accuracy in females than in male patients. Of note, the sample size of female patients was significantly smaller than that of male patients (41 vs. 272). The different result of TACE treatment in male or female could be further confirmed by large patients. Meanwhile, subgroup analysis by age showed no significant difference in accuracies between patients aged ≤60 years and >60 years. There were also no significant differences in accuracy according to the Child–Pugh classification, AFP, tumor size, and number of tumors. Collectively, these results support that our pyradiomics model can accurately predict individual treatment response to TACE and may help identify patients who will benefit from the treatment. In addition, the correlation between predictive classification of pyradiomics model and prognosis was investigated. We found the RS1 group indicating well response of initial TACE treatment had better OS and PFS than RS2 group did. This result further demonstrated the initial response could improve the OS and PFS in the patients receiving TACE therapy. Moreover, our model based on the series CT images and analysis of time-dependent ROC curve could preoperatively predict the prognosis and to screening of patients who could benefit from TACE treatment among the BCLC stage B patients with HCC.

To explore the potential mechanism of the pyradiomics model, we used CT images from the TCGA-HCC cohort to screen the different genes and related cancer signaling pathways (Supplemental Figure S3). RS1 group was significantly associated with hypoxia. Previous studies have reported that the tumor hypoxia status is associated with resistance to chemotherapy, targeted therapy, and radiation therapy (36–38). This indicates that our machine learning model predicts treatment response to TACE by characterizing the hypoxia change in tumors from CT

images. In the TCGA-HCC patients (No-TACE treatment), RS2 group with severe hypoxia also showed a significantly poorer prognosis than the RS1 group, suggesting the hypoxic status of HCC may be associated with resistant mechanism to TACE treatment, which is consistent with previous findings (39–41). Improving the hypoxic status in tumors is potentially one of the methods to improve the therapy effect and this mechanism should be analyzed in more detail.

Our study has some limitations. First, the number of patients with middle-stage HCC was relatively small. Second, the study was conducted retrospectively. However, we used CT images from four centers, and all the CT images were normalized before extracting pyradiomics features to develop a robust predictive model. Multi-center model analysis also showed robust predictive performance. However, the model still needs to be validated in larger prospective studies. Third, we trained and validated all the pyradiomics signatures in four medical centers. Extracting features from ROI images may have issues in reproducibility. In this study, we evaluated the reproducibility of pyradiomics and found a good agreement (ICC>0.75), markedly improving the predictive model's robustness. Future studies should develop an automatic segmentation model for liver tumors and minimize the discrepancies among pyradiomics features.

In conclusion, the machine learning model based on pyradiomics features from 3D-CT images is a noninvasive yet highly accurate model for predicting the initial response and prognosis to TACE in patients with HCC. Thus, it may be a feasible tool for identifying patients who will benefit from TACE. The association between the pyradiomics model and cancer-related signaling pathways might help clinicians further understand the internal mechanism of machine learning. Finally, this radiology method could be used to improve the accuracy in clinical decision-making for other types of malignant tumors.

Data availability statement

For study involving human sample: The original contributions presented in the study are included in the article/Supplementary Material. Further inquiries can be directed to the corresponding author. For study involving TGCA data: The datasets presented in this study can be found in online repositories. The names of the repository/repositories and accession number(s) can be found in the article/Supplementary Material.

Ethics statement

The studies involving human participants were reviewed and approved by Nanfang Hospital, the Second Affiliated Hospital of Gui Zhou Medical University, and Sun Yat-sen University Cancer Center. The patients/participants provided their written informed consent to participate in this study.

Author contributions

(I)Conception and design: JP. (II) Administrative support: None. (III) Provision of study materials or patients: JH and JP. (IV) Collection and assembly of data: JP, JZ, and FL. (V) Data analysis and interpretation: JP and JH. (VI) Manuscript writing: All authors and (VII) Final approval of manuscript: All authors.

Funding

This work was supported by the Science and Technology Fund Project of Guizhou Provincial Health Commission [gzwjkj2019-1-077], Qian Dong Nan Science and Technology Program [qdnkhJz2019-026], Open Funds of State Key Laboratory of Oncology in South China [HN2020-02], Qian Dong Nan Science and Technology Program [qdnkhJz2020-013], the Guizhou Medical University 2018 academic new talent cultivation and innovation exploration project [Grant No. 20185579-X], Science and Technology Foundation of Guizhou Province [Grant No. Qian ke he ji chu-ZK 2021, yi ban 454], and National Nature Science Foundation of China (Grant Nos. 82060327).

Conflict of interest

The authors declare that the research was conducted in the absence of any commercial or financial relationships that could be construed as a potential conflict of interest.

Publisher's note

Supplementary material

The Supplementary Material for this article can be found online at: https://www.frontiersin.org/articles/10.3389/fonc.2022.853254/full#supplementary-material

References

1. Sung H, Ferlay J, Siegel RL, Laversanne M, Soerjomataram I, Jemal A, et al. Global cancer statistics 2020: GLOBOCAN estimates of incidence and mortality worldwide for 36 cancers in 185 countries. *CA Cancer J Clin* (2021) 71:209–41. doi: 10.3322/caac.21660

2. Shen JY, Li C, Wen TF, Yan LN, Li B, Wang WT, et al. Liver transplantation versus surgical resection for HCC meeting the Milan criteria: A propensity score analysis. *Med (Baltimore)* (2016) 95:e5756. doi: 10.1097/MD.0000000000005756

3. Forner A, Reig M, Bruix J. Hepatocellular carcinoma. *Lancet* (2018) 391:1301–14. doi: 10.1016/S0140-6736(18)30010-2

4. Pinna AD, Yang T, Mazzaferro V, De Carlis L, Zhou J, Roayaie S, et al. Liver transplantation and hepatic resection can achieve cure for hepatocellular carcinoma. *Ann Surg* (2018) 268:868–75. doi: 10.1097/SLA.0000000000002889

5. Chai NX, Chapiro J. Therapy of intermediate-stage hepatocellular carcinoma: Current evidence and clinical practice. *Semin Interv Radiol* (2020) 37:456–65. doi: 10.1055/s-0040-1719186

6. Chen M, Cao J, Hu J, Topatana W, Li S, Juengpanich S, et al. Clinical-radiomic analysis for pretreatment prediction of objective response to first transarterial chemoembolization in hepatocellular carcinoma. *Liver Cancer* (2021) 10:38–51. doi: 10.1159/000512028

7. Prince DA-O, Liu K, Xu W, Chen M, Sun JY, Lu XJ, et al. Management of patients with intermediate stage hepatocellular carcinoma. *Ther Adv Med Oncol* (2020) 12:1758835920970840. doi: 10.1177/1758835920970840

8. Kim BK, Kim SU, Kim KA, Chung YE, Kim MJ, Park MS, et al. Complete response at first chemoembolization is still the most robust predictor for favorable outcome in hepatocellular carcinoma. *J Hepatol* (2015) 62:1304–10. doi: 10.1016/j.jhep.2015.01.022

9. Park C, Chu HH, Kim JH, Kim SY, Alrashidi I, Gwon DI, et al. Clinical significance of the initial and best responses after chemoembolization in the treatment of intermediate-stage hepatocellular carcinoma with preserved liver function. *J Vasc Interv Radiol* (2020) 31:1998–2006.e1. doi: 10.1016/j.jvir.2020.04.017

10. Zhang Y, Zhang M, Chen M, Mei J, Xu L, Guo R, et al. Association of sustained response duration with survival after conventional transarterial chemoembolization in patients with hepatocellular carcinoma. *JAMA Netw Open* (2018) 1:e183213. doi: 10.1001/jamanetworkopen.2018.3213

11. Bae JS, Kim JH, Lee DH, Kim JH, Han JK. Hepatobiliary phase of gadoxetic acid-enhanced MRI in patients with HCC: Prognostic features before resection, ablation, or TACE. *Eur Radiol* (2021) 31:3627–37. doi: 10.1007/s00330-020-07499-w

12. Nam JY, Choe AR, Sinn DH, Lee JH, Kim HY, Yu SJ, et al. A differential risk assessment and decision model for transarterial chemoembolization in hepatocellular carcinoma based on hepatic function. *BMC Cancer* (2020) 20:504. doi: 10.1186/s12885-020-06975-2

13. Vesselle G, Quirier-Leleu C, Velasco S, Charier F, Silvain C, Boucebci S, et al. Predictive factors for complete response of chemoembolization with drug-eluting beads (DEB-TACE) for hepatocellular carcinoma. *Eur Radiol* (2016) 26:1640–8. doi: 10.1007/s00330-015-3982-y

14. Zhang WA-O, Xu AH, Wang W, Wu YH, Sun QL, Shu C. Radiological appearance of hepatocellular carcinoma predicts the response to trans-arterial chemoembolization in patients undergoing liver transplantation. *BMC Cancer* (2019) 19:1041. doi: 10.1186/s12885-019-6265-1

15. Huang Y, Zeng H, Chen L, Luo Y, Ma X, Zhao Y. Exploration of an integrative prognostic model of radiogenomics features with underlying gene expression patterns in clear cell renal cell carcinoma. *Front Oncol* (2021) 11:640881. doi: 10.3389/fonc.2021.640881

16. Shin Y, Nam Y, Shin T, Choi JW, Lee JH, Jung DE, et al. Brain MRI radiomics analysis may predict poor psychomotor outcome in preterm neonates. *Eur Radiol* (2021) 31:6147–55. doi: 10.1007/s00330-021-07836-7

17. Song Z, Tang Z, Liu H, Guo D, Cai J, Zhou Z. A clinical-radiomics nomogram may provide a personalized 90-day functional outcome assessment for spontaneous intracerebral hemorrhage. *Eur Radiol* (2021) 31:4949–59. doi: 10.1007/s00330-021-07828-7

18. Priya S, Agarwal A, Ward C, Locke T, Monga V, Bathla G. Survival prediction in glioblastoma on post-contrast magnetic resonance imaging using filtration based first-order texture analysis: Comparison of multiple machine learning models. *Neuroradiol J* (2021) 34:355–62. doi: 10.1177/1971400921990766

19. Liu C, Gong J, Yu H, Liu Q, Wang S, Wang J. A CT-based radiomics approach to predict nivolumab response in advanced non-small-cell lung cancer. *Front Oncol* (2021) 11:544339. doi: 10.3389/fonc.2021.544339

20. Chen BT, Jin T, Ye N, Mambetsariev I, Wang T, Wong CW, et al. Predicting survival duration with MRI radiomics of brain metastases from non-small cell lung cancer. *Front Oncol* (2021) 11:621088. doi: 10.3389/fonc.2021.621088

21. Carles M, Fechter T, Radicioni G, Schimek-Jasch T, Adebahr S, Zamboglou C, et al. FDG-PET radiomics for response monitoring in non-small-cell lung cancer treated with radiation therapy. *Cancers (Basel)* (2021) 13:814. doi: 10.3390/cancers13040814

22. Peng J, Zhang J, Zhang Q, Xu Y, Zhou J, Liu L. A radiomics nomogram for preoperative prediction of microvascular invasion risk in hepatitis b virus-related hepatocellular carcinoma. *Diagn Interv Radiol* (2018) 24:121–7. doi: 10.5152/dir.2018.17467

23. Han L, Zhao K, Li Y, Han H, Zhou L, Ma P, et al. A gut microbiota score predicting acute graft-versus-host disease following myeloablative allogeneic hematopoietic stem cell transplantation. *Am J Transplant* (2020) 20:1014–27. doi: 10.1111/ajt.15654

24. Tovoli F, Renzulli M, Negrini G, Brocchi S, Ferrarini A, Andreone A, et al. Inter-operator variability and source of errors in tumour response assessment for hepatocellular carcinoma treated with sorafenib. *Eur Radiol* (2018) 28:3611–20. doi: 10.1007/s00330-018-5393-3

25. Cui S, Tang T, Su Q, Wang Y, Shu Z, Yang W, et al. Radiomic nomogram based on MRI to predict grade of branching type intraductal papillary mucinous neoplasms of the pancreas: A multicenter study. *Cancer Imaging* (2021) 21:26. doi: 10.1186/s40644-021-00395-6

26. Wang T, Gao T, Guo H, Wang Y, Zhou X, Tian J, et al. Preoperative prediction of parametrial invasion in early-stage cervical cancer with MRI-based radiomics nomogram. *Eur Radiol* (2020) 30:3585–93. doi: 10.1007/s00330-019-06655-1

27. Zhang W, Fang M, Dong D, Wang X, Ke X, Zhang L, et al. Development and validation of a CT-based radiomic nomogram for preoperative prediction of early recurrence in advanced gastric cancer. *Radiother Oncol* (2020) 145:13–20. doi: 10.1016/j.radonc.2019.11.023

28. Facciorusso A, Bellanti F, Villani R, Salvatore V, Muscatiello N, Piscaglia F, et al. Transarterial chemoembolization vs bland embolization in hepatocellular carcinoma: A meta-analysis of randomized trials. *United Eur Gastroenterol J* (2017) 5:1196. doi: 10.3389/fonc.2020.01196

29. Cucchetti A, Trevisani F, Cappelli A, Mosconi C, Renzulli M, Pinna AD, et al. Cost-effectiveness of doxorubicin-eluting beads versus conventional trans-arterial chemo-embolization for hepatocellular carcinoma. *Dig Liver Dis* (2016) 48:798–805. doi: 10.1016/j.dld.2016.03.031

30. He B, Song Y, Wang L, Wang T, She Y, Hou L, et al. A machine learning-based prediction of the micropapillary/solid growth pattern in invasive lung adenocarcinoma with radiomics. *Transl Lung Cancer Res* (2021) 10:955–64. doi: 10.21037/tlcr-21-44

31. Van Griethuysen JJM, Fedorov A, Parmar C, Hosny A, Aucoin N, Narayan V, et al. Computational radiomics system to decode the radiographic phenotype. *Cancer Res* (2017) 77:e104–7. doi: 10.1158/0008-5472.CAN-17-0339

32. Kim J, Choi SJ, Lee SH, Lee HY, Park H. Predicting survival using pretreatment CT for patients with hepatocellular carcinoma treated with transarterial chemoembolization: Comparison of models using radiomics. *AJR Am J Roentgenol* (2018) 211:1026–34. doi: 10.2214/AJR.18.19507

33. Sheen H, Kim JS, Lee JK, Choi SY, Baek SY, Kim JY. A radiomics nomogram for predicting transcatheter arterial chemoembolization refractoriness of hepatocellular carcinoma without extrahepatic metastasis or macrovascular invasion. *Abdom Radiol (NY)* (2021) 46:2839–49. doi: 10.1007/s00261-020-02884-x

34. Aerts HJ, Velazquez ER, Leijenaar RT, Parmar C, Grossmann P, Carvalho S, et al. Decoding tumour phenotype by noninvasive imaging using a quantitative radiomics approach. *Nat Commun* (2014) 5:4006. doi: 10.1038/ncomms5006

35. Jin Z, Chen L, Zhong B, Zhou H, Zhu H, Zhou H, et al. Machine-learning analysis of contrast-enhanced computed tomography radiomics predicts patients with hepatocellular carcinoma who are unsuitable for initial transarterial chemoembolization monotherapy: A multicenter study. *Transl Oncol* (2021) 14:101034. doi: 10.1016/j.tranon.2021.101034

36. Chen J, Wang X, Yuan Y, Chen H, Zhang L, Xiao H, et al. Exploiting the acquired vulnerability of cisplatin-resistant tumors with a hypoxia-amplifying DNA repair-inhibiting (HYDRI) nanomedicine. *Sci Adv* (2021) 7:eabc5267. doi: 10.1126/sciadv.abc5267

37. Codony VL, Tavassoli M. Hypoxia-induced therapy resistance: Available hypoxia-targeting strategies and current advances in head and neck cancer. *Transl Oncol* (2021) 14:101017. doi: 10.1016/j.tranon.2021.101017

38. Nilsson MB, Robichaux J, Herynk MH, Cascone T, Le X, Elamin Y, et al. Altered regulation of HIF-1α in naive- and drug-resistant EGFR-mutant NSCLC: Implications for a vascular endothelial growth factor-dependent phenotype. *J Thorac Oncol* (2021) 16:439–51. doi: 10.1016/j.jtho.2020.11.022

39. Shou Y, Yang L, Yang Y, Zhu X, Li F, Xu J. Determination of hypoxia signature to predict prognosis and the tumor immune microenvironment in melanoma. *Mol Omics* (2021) 17:307–16. doi: 10.1039/d0mo00159g

40. Zhang Q, Qiao L, Liao J, Liu Q, Liu P, Liu L. A novel hypoxia gene signature indicates prognosis and immune microenvironments characters in patients with hepatocellular carcinoma. *J Cell Mol Med* (2021) 24:3772–84. doi: 10.1111/jcmm.16249

41. Zheng W, Zhang S, Guo H, Chen X, Huang Z, Jiang S, et al. Multi-omics analysis of tumor angiogenesis characteristics and potential epigenetic regulation mechanisms in renal clear cell carcinoma. *Cell Commun Signal* (2021) 19:39. doi: 10.1186/s12964-021-00728-9

frontiers | Frontiers in Oncology

TYPE Original Research
PUBLISHED 23 November 2022
DOI 10.3389/fonc.2022.986713

OPEN ACCESS

EDITED BY
Xiankai Sun,
University of Texas Southwestern Medical Center, United States

REVIEWED BY
Hyungjin Rhee,
Yonsei University, South Korea
Alessandro Granito,
University of Bologna, Italy

*CORRESPONDENCE
Ningyang Jia
ningyangjia@163.com
Wanmin Liu
18389376537@163.com

†These authors have contributed equally to this work and share first authorship

SPECIALTY SECTION
This article was submitted to Cancer Imaging and Image-directed Interventions, a section of the journal Frontiers in Oncology

RECEIVED 05 July 2022
ACCEPTED 07 November 2022
PUBLISHED 23 November 2022

CITATION
Zhang S, Huo L, Feng Y, Zhang J, Wu Y, Liu Y, Lu L, Jia N and Liu W (2022) Preoperative differentiation of hepatocellular carcinoma with peripheral rim-like enhancement from intrahepatic mass-forming cholangiocarcinoma on contrast-enhanced MRI.
Front. Oncol. 12:986713.
doi: 10.3389/fonc.2022.986713

Preoperative differentiation of hepatocellular carcinoma with peripheral rim-like enhancement from intrahepatic mass-forming cholangiocarcinoma on contrast-enhanced MRI

Sisi Zhang[1†], Lei Huo[1†], Yayuan Feng[1], Juan Zhang[1], Yuxian Wu[1], Yiping Liu[1], Lun Lu[1], Ningyang Jia[1*] and Wanmin Liu[2*]

[1]Department of Radiology, Shanghai Eastern Hepatobiliary Surgery Hospital, The Third Affiliated Hospital of Naval Medical University, Shanghai, China, [2]Department of Radiology, Tongji Hospital, School of Medicine, Tongji University, Shanghai, China

Purpose: The present study aimed to determine the reliable imaging features to distinguish atypical hepatocellular carcinoma (HCC) with peripheral rim-like enhancement from intrahepatic mass-forming cholangiocarcinoma (IMCC) on contrast-enhanced magnetic resonance imaging (MRI).

Methods: A total of 168 patients (130 male, 57.10 ± 10.53 years) pathological confirmed HCC or IMCC who underwent contrast-enhanced MRI between July 2019 and February 2022 were retrospectively included. Univariate and multivariate logistic regression analyses were used to determine independent differential factors for distinguishing HCC from IMCC, and the model was established. Bootstrap resampling 1000 times was used to verify the model, which was visualized by nomograms. The predictive performance of the model was evaluated based on discrimination, calibration, and clinical utility.

Results: Radiological capsule (OR 0.024, 95% CI: 0.006, 0.095, P<0.001), heterogeneous signal intensity (SI) on T1WI (OR 0.009, 95%CI: 0.001,0.056, P<0.001) were independent differential factors for predicting HCC over IMCC. A lobulated contour (OR 11.732, 95%CI: 2.928,47.007, P = 0.001), target sign on DP (OR 14.269, 95%CI: 2.849,82.106, P = 0.007), bile duct dilatation (OR 12.856, 95%CI: 2.013, P = 0.001) were independent differential factors for predicting IMCCs over HCCs. The independent differential factors constituted a model to distinguish atypical HCCs and IMCCs. The area under receiver

operating characteristic (ROC) curve, sensitivity, and specificity values of the model were 0.964(0.940,0.987), 0.88, and 0.906, indicating that the model had an excellent differential diagnostic performance. The decision curve analysis (DCA) curve showed that the model obtained a better net clinical benefit.

Conclusion: The present study identified reliable imaging features for distinguishing atypical HCCs with peripheral rim-like enhancement from IMCCs on contrast-enhanced MRI. Our findings may help radiologists provide clinicians with more accurate preoperative imaging diagnoses to select appropriate treatment options.

KEYWORDS

magnetic resonance imaging, hepatocellular carcinoma, liver cancer, intrahepatic cholangiocarcinoma, differential diagnosis

1 Introduction

Hepatocellular carcinoma (HCC) is the sixth most common neoplasm and the third leading cause of death from cancer worldwide (1, 2). HCC is most commonly caused by cirrhosis, with 2-8% of cirrhosis cases developing into HCC each year (3–5). Intrahepatic cholangiocarcinoma (iCCA) is the second most common primary liver malignancy, and its worldwide incidence is increasing (6, 7). As a malignancy, iCCA often shares some common risk factors and clinical manifestations with HCC, which poses a challenge for the differential diagnosis of iCCA and HCC (8, 9). Therefore, it is necessary to find an effective and specific method for the differential diagnosis of HCC and iCCA.

Magnetic resonance imaging (MRI) is widely used for preoperative diagnoses and evaluation of liver tumors (10). HCC can be diagnosed with typical imaging characteristics of hyperenhancement in arterial phase and washout on portal or delayed phase images (10–13), which represent the characteristic vascular profile of HCC on dynamic contrast-enhanced magnetic resonance imaging (13). However, around 40% of HCCs do not show typical imaging features, and they may exhibit arterial phase hypovascularity or peripheral rim-like enhancement (14, 15).

Currently, these HCCs with atypical imaging features pose a significant diagnostic challenge to radiologists. In particular, HCC is difficult to differentiate from intrahepatic mass-forming cholangiocarcinoma (IMCC) if it presents with peripheral rim-like enhancement in the arterial phase followed by gradual filling of the contrast media (16, 17). Several studies have examined the imaging features of atypical HCC (16, 18), although studies focusing on the differentiation between HCC with peripheral rim-like enhancement and IMCC are rare. However, the distinction between HCCs and IMCCs is crucial for clinicians because they have significant differences in prognosis and treatment options (19). Therefore, it is essential to understand and identify reliable imaging features to help accurately differentiate atypical HCCs with peripheral rim-like enhancement from IMCCs.

Accordingly, the purpose of the present study was to determine the reliable imaging features and establish the optimal model to distinguish atypical HCCs with peripheral rim-like enhancement from IMCCs on contrast-enhanced MRI. In order to provide clinicians with more accurate preoperative imaging diagnoses to select appropriate treatment options.

2 Materials and methods

2.1 Patients

This study was approved by the ethics committee of eastern hepatobiliary surgery hospital, the third affiliated hospital of Shanghai naval military medical university, China, and waived the requirement of obtaining written informed consent.

Between July 2019 and February 2022, a total of 168 patients (130 male, 57.10 ± 10.53 years) pathological confirmed HCCs or IMCCs, including 85 patients who were HCCs (74 male, 59.33 ± 10.79 years) and 83 patients were IMCCs (56 male, 54.82 ± 9.81 years) after preoperative Gd-DTPA-enhanced MRI met the following inclusion criteria (Figure 1): (a) complete histopathologic description of HCCs or IMCCs; (b) dynamic contrast-enhanced liver MR examination was performed within one month before operation, including complete scanning phase images (arterial phase, portal phase, delayed phase); (c) HCCs show atypical imaging features of peripheral rim-like enhancement in dynamic contrast-enhanced liver MRI, and (d) no locoregional treatment for tumor before MR examination.

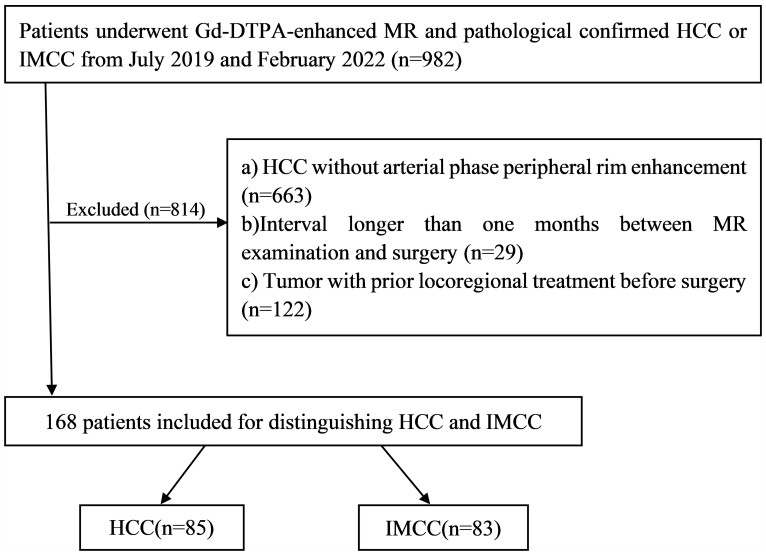

FIGURE 1
The workflow of patient selection for this study.

2.2 Histopathology characteristics

A consensus of two experienced pathologists assessed the histopathological characteristics. All pathological sections were reviewed according to 2019 WHO classification standard (20), and the classification diagnosis of HCC and IMCC was performed. For HCC, histopathological factors for tumors were assessed: gross type, histological type, cell type, nuclear grade, fibrous capsule formation, vascular invasion, bile duct invasion, necrosis or hemorrhage. The nuclear grading scheme proposed by Edmondson-Steiner classified HCC tumors into four grades: I, II, III, and IV (21). For IMCC, the assessment of histopathological factors was evaluated as for HCC.

2.3 MRI examination

MR images were acquired using a GE Optima MR360 1.5T (Optima MR360, GE Healthcare, USA) equipped with an eight-channel abdominal coil. Patients fasted for four hours before the scan. Baseline MRI included T1-weighted turbo field-echo in-phase and opposed sequence (T1WI), Fat -suppressed T2-weighted images (Fs-T2WI). Diffusion-weighted imaging (DWI) was obtained by respiratory-triggered single-shot echo with b-values of 0 and 600 s/mm^2.

Gadolinium meglumine acid (Gd-DTPA) with a total dose of 0.1 mmoL/kg was injected into the median cubitus vein at a rate of 2.0 mL/s with a high-pressure syringe washing with 20 mL of normal saline. The arterial phase (AP), portal venous phase (PVP), and delay phase (DP) scans were performed 20–30 s, 50–60 s, and 90–120 s after the injection of Gd-DTPA, respectively. Detailed scanner and scan parameters can be found in Supplementary Table 1.

2.4 MR imaging analysis

MR imaging analysis was performed by two radiologists (with more than 10 years of abdominal imaging experience) blinded to the histopathology information. Two radiologists independently evaluated imaging features. And inter-observer agreement was used to assess the consistency of the observed imaging features, variables with kappa value < 0.75 were removed. Inter-observer variability for each imaging feature can be found in Supplementary Table 2. Then, if their opinions were not consistent, a consensus decision was made after discussion among three radiologists. The case was included in the study only when the results of the two radiologists' assessments were consistent.

The general imaging features were evaluated as follows: (a) tumor size was measured by selecting the length and diameter of the largest plane according to the liver imaging reporting and data system 2018 standard (22), including the mass capsule, when the mass was shown most clearly in the MRI enhanced portal phase images; (b) shape (round, lobulated or ill-defined); (c) margin, smooth edges (nodular tumors with smooth edges) and non-smooth edges (budding processes on cross-sectional and coronal images (23); (d) signal intensity (SI) on T1WI and T2WI (homogeneous or heterogeneous).

The enhanced imaging features were evaluated as follows: (a) enhancement of the tumor on AP, peripheral thin or thick rim

enhancement (<30%,30–50%hyperintensity area of the tumor surface); (b) signal intensity of the tumor relative to liver parenchyma on PVP and DP; (c) gradual enhancement during dynamic contrast-enhanced phases.

The ancillary features were evaluated as follows: (a) bile duct dilation peripheral to tumor; (b) hepatic surface retraction at tumor attachment; (c) radiological capsule (partial or complete peripheral rim-like enhancement around the tumor on PVP or DP; (d) T2 central brightness (markedly higher than SI of spleen and tumor periphery) (24); (e) T2 central darkness (lower than liver SI) (25); (f) target sign (peripheral hyperintensity compared to central portion) on DWI (b = 600s/mm^2); (g) intralesional fat; (h) portal vein embolus; (i) lymph node enlargement.

2.5 Statistical analysis

IBM SPSS Statistics (version 25; IBM) or R (version 3.6.0; http://www.r-project.org) were used for statistical analyses. Continuous variables conforming to the normal distribution and homogeneity of variance were represented as the means ± standard deviations and were compared using the Student's t-test. Interobserver agreement between two radiologists were compared with the Kappa test. Inconsistent continuous variables were represented using the median (range) and compared with the Mann-Whitney U test. Categorical variables were compared using χ 2 test or Fisher's exact test. The factors with P<0.05 in the univariate logistic regression analysis were included in multivariate logistic regression analysis (forward LR) to identify independent differential factors for distinguishing HCCs and IMCCs.

2.6 Model development and validation, and evaluation

Univariate and multivariate logistic regression (forward LR) were performed to determine the independent differential factors between HCCs and IMCCs. Combining these independent differential factors established the model for discriminating HCCs from IMCCs. Bootstrap resampling 1000 times was used to verify the model, which was visualized by nomograms (26). The differential diagnosis performance of the model was evaluated based on discrimination, calibration, and clinical utility. The discrimination for the model was quantified using the area under the receiver operating characteristic (ROC) curve, sensitivity, and specificity. The calibration curve analysis was performed to evaluate the consistency between the tumor types discriminated by the model and the actual tumor types. Decision curve analysis (DCA) was conducted to determine the clinical utility of the model by quantifying the net benefits at different threshold probabilities.

3 Results

3.1 Demographic and pathological characteristics of HCCs and IMCCs

Among the 168 patients, 85 (74 male, 59.33 ± 10.79 years) were HCC and 83 (56 male, 54.82 ± 9.81 years) were IMCC. The pathological and demographic characteristics of HCCs and IMCCs are shown in Table 1. Patients with HCCs were significantly older than those with IMCCs (59.33 ± 10.79 years

TABLE 1 Demographic and pathological characteristics of HCCs and IMCCs.

Characteristic	HCCs (n=85)	IMCCs (n=83)	P value
Age (y)	59.33 ± 10.79	54.82 ± 9.81	0.004
Sex			
Male	74 (87.1%)	56 (67.5%)	0.003
Female	11 (12.9%)	27 (32.5%)	
HBV/HCV	78 (91.8%)	29 (34.9%)	<0.001
Edmondson-Steiner grade			
I- II	9 (16.5%)	/	/
III-IV	76 (89.4%)	/	
Capsule formation			
Absent	4 (4.7%)	80 (96.4%)	<0.001
Complete	21 (24.7%)	0	
Partial	60 (70.6%)	3 (3.6%)	
Microscopic cirrhosis			
Absent	42 (49.4%)	72 (86.7%)	<0.001
Present	43 (50.6%)	11 (13.3%)	

Data are numbers of patients with percentage in parentheses.
HCC, hepatocellular carcinoma; IMCC, intrahepatic mass-forming cholangiocarcinoma; HBV, hepatitis B virus; HCV, hepatitis C virus.

vs. 54.82 ± 9.81years, P = 0.004). Sex was significantly differently in two groups (87.1% male for HCC vs. 67.5% male for IMCC, P = 0.003). Capsule formation (95.3% vs. 3.6%, P<0.001) and microscopic cirrhosis (50.6% vs. 13.3%, P<0.001) were more frequently present in HCCs than IMCCs.

3.2 MRI characteristics of HCCs and IMCCs

3.2.1 General MRI features

Tumor size, shape, margin, and SI on T1WI or T2WI were significantly different in the two groups. Tumor size of HCCs (7.8cm (5.8,10.2)) was larger than IMCCs size (5.6cm (4.1,7.0)) (P<0.001). A round contour (P<0.001), smooth margin (P = 0.060), and heterogeneous SI on T1WI or T2WI (P<0.001) were more commonly found in HCCs. A lobulated contour (P<0.001), non-smooth margin (P = 0.060), and homogeneous SI on T1WI or T2WI (P<0.001) were more commonly found in IMCCs. Evaluated characteristics for distinguishing HCCs and IMCCs are shown in Table 2.

3.2.2 Enhanced MRI features

HCCs more frequently showed a thick rim on AP images (P<0.001) and diffusely low SI on DP images (P = 0.002). IMCCs more frequently showed a thin rim on AP images (P<0.001), target sign on DP images (P = 0.002), and gradual enhancement (P<0.001).

TABLE 2 MRI characteristics of HCCs and IMCCs.

Characteristic	HCCs (n=85)	IMCCs (n=83)	P value
Gradual MRI features			
Tumor size(cm)	7.8 (5.8,10.2)	5.6 (4.1,7.0)	<0.001
Shape			
Round	68 (80.0%)	42 (50.6%)	<0.001
Lobulated/ill-defined	17 (20.0%)	41 (49.4%)	
Margin			
Smooth	40 (47.1%)	27 (32.5%)	0.060
Non-smooth	45 (52.9%)	56 (67.5%)	
SI on T1WI			
Homogeneous	35 (41.2%)	73 (88.0%)	<0.001
Heterogeneous	50 (58.8)	10 (12.0%)	
SI on T2WI			
Homogeneous	21 (24.7%)	51 (61.4%)	<0.001
Heterogeneous	64 (75.3%)	32 (38.6%)	
Enhancement MRI features			
AP enhancement			
Thick rim	36 (42.4%)	11 (13.3%)	<0.001
Thin rim	49 (57.6%)	72 (86.7%)	
SI on PVP			
Hypo	48 (56.5%)	53 (63.9%)	0.348
Iso/Hyper	37 (43.5%)	30 (36.1%)	
SI on DP			
Diffusely low	27 (31.8%)	8 (9.6%)	0.002
Target	53 (62.4%)	68 (81.9%)	
Iso	5 (5.9%)	7 (8.4%)	
Gradual enhancement	22 (25.9%)	58 (69.9%)	<0.001
Ancillary features			
Surface retraction			
Absent	81(95.3%)	62 (74.7%)	<0.001
Present	4(4.7%)	21 (25.3)	
Bile duct dilation			
Absent	81 (95.3%)	56 (67.5%)	<0.001
Present	4 (4.7%)	27 (32.5%)	

(Continued)

TABLE 2 Continued

Characteristic	HCCs (n=85)	IMCCs (n=83)	P value
Radiological capsule			
Absent	16 (18.8%)	69 (83.1%)	<0.001
Present	69 (81.2%)	14 (16.9%)	
Intralesional fat			
Absent	68 (80.0%)	81 (97.6%)	<0.001
Present	17 (20.0%)	2 (2.4%)	
Central brightness on T2WI			
Absent	46 (54.1%)	68 (81.9%)	<0.001
Present	39 (45.9%)	15 (18.1%)	
Central darkness on T2WI			
Absent	61 (71.8%)	64 (77.1%)	0.482
Present	24 (28.2%)	19 (22.9%)	
Target sign on DWI			
Absent	43 (50.6%)	26 (31.3%)	0.013
Present	42 (49.4%)	57 (68.7%)	
Portal vein embolus			
Absent	65 (76.5%)	83 (100%)	<0.001
Present	20 (23.5%)	0	
Lymph node enlargement			
Absent	75 (88.2%)	57 (68.7%)	
Present	10 (11.8%)	26 (31.3%)	0.002

Data are numbers of patients with percentage in parentheses.
HCC, hepatocellular carcinoma; IMCC, intrahepatic mass-forming cholangiocarcinoma; SI signal intensity; AP, atrial phase; PVP, portal venous phase; DP, delayed phase; T2WI, T2-weighted image; DWI, diffusion-weighted imaging.

3.2.3 Ancillary features

Bile duct dilation (P<0.001), surface retraction (P<0.001), target sign on DWI (P = 0.002), and lymph node enlargement (P = 0.013) were significant imaging features of IMCCs. Radiological capsule (P<0.001), intralesional fat (P<0.001), central brightness on T2WI (P<0.001), and portal vein embolus (P<0.001) were significant imaging features of HCCs (Table 2). The representative images of atypical HCCs with rim-like enhancement cases are displayed in Figures 2 and 3, and IMCC cases are displayed in Figures 4 and 5.

3.3 Univariate and multivariate analysis of independent differences between HCCs and IMCCs

In univariate analysis, 17 features were significantly different between the two groups at a test level of P<0.05 (Table 3). All of the above 17 variables were included in multivariate logistic regression analysis (forward LR), which determined that radiological capsule (odds ratio (OR) 0.024, 95% confidence interval (CI): 0.006, 0.095, P<0.001), heterogeneous SI on T1WI (OR 0.009, 95%CI: 0.001,0.056, P<0.001) were independent differential factors for predicting HCC over IMCC; a lobulated contour (OR 11.732, 95%CI: 2.928,47.007, P = 0.001), target sign on DP (OR 14.269, 95%CI: 2.849,82.106, P = 0.007), bile duct dilatation (OR 12.856, 95%CI: 2.013, P = 0.001) were independent differential factors for predicting IMCC over HCC (Table 4).

3.4 Model development, evaluation and visualization

A nomogram based on the model for distinguishing HCCs and IMCCs is shown in Figure 6A. The area under the ROC curve (AUC), sensitivity, and specificity values for the model were 0.964 (0.940,0.987), 0.880, and 0.906, respectively (Figure 6B). It was further evaluated using calibration curves (Figure 6C), which showed that the discriminated HCC probability from the nomogram is consistent with the estimated value of the actual HCC probability. The model's DCA curve showed an excellent net clinical benefit (Figure 6D). The results demonstrated that the model had an excellent differential diagnosis performance. And two radiologists used the model to diagnose respectively. The area AUC, sensitivity, and specificity values were as follows: 0.943 (0.909,0.976), 0.867, and 0.918 for reviewer1; 0.936(0.897,0.975), 0.880, and 0.906 for reviewer2.

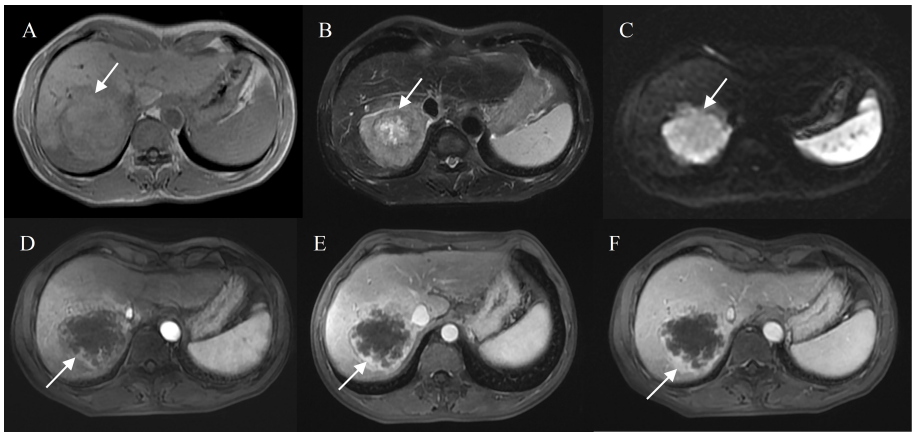

FIGURE 2
Hepatocellular carcinoma with peripheral rim enhancement in a 60-year-old male without chronic viral hepatitis. Gd-DTPA-enhanced MRI detected a round and non-smooth tumor (10.2 cm) with heterogeneous SI on T1WI and T2WI **(A, B)**, restricted diffusion **(C)**. Peripheral rim-like enhancement in the arterial phase **(D)** and sustained rim enhancement in the portal and delayed phase **(E, F)**. Incomplete capsule enhancement on portal venous phase **(E)** and delayed phase images **(F)**.

4 Discussion

The distinction between HCCs and IMCCs is crucial for clinicians because the prognosis and treatment options differ considerably between the two types (19). Thus, a noninvasive way to distinguish iCCA and HCC preoperatively is needed (27). Nowadays, contrast-enhanced MRI is widely used for preoperative diagnoses and evaluation of liver tumors. However, around 40% of HCCs show atypical imaging features such as arterial phase hypovascularity or peripheral rim-like enhancement, which pose a significant diagnostic challenge for radiologists (14, 15). Therefore, the present study aimed to identify reliable imaging features to help accurately differentiate atypical HCC with rim-like enhancement from IMCC.

The study results demonstrated that the radiological capsule, heterogeneous SI on T1WI, a lobulated contour, target sign on

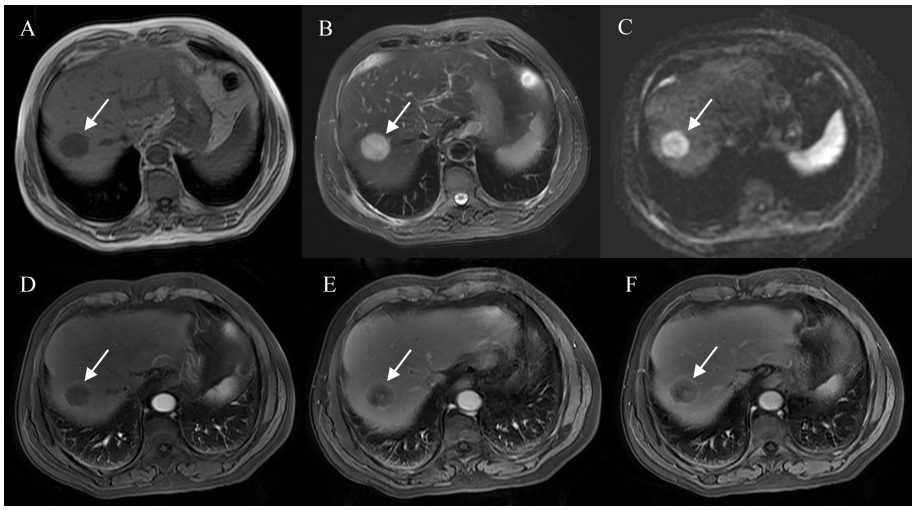

FIGURE 3
Hepatocellular carcinoma with peripheral rim enhancement in a 70-year-old male with hepatitis B virus. Gd-DTPA-enhanced MRI detected a round and smooth tumor (4.8 cm) with heterogeneous SI on T1WI and T2WI **(A, B)**, restricted diffusion **(C)**. Peripheral rim-like enhancement in the arterial phase **(D)**, complete capsule enhancement on portal venous phase **(E)** and delayed phase images **(F)**.

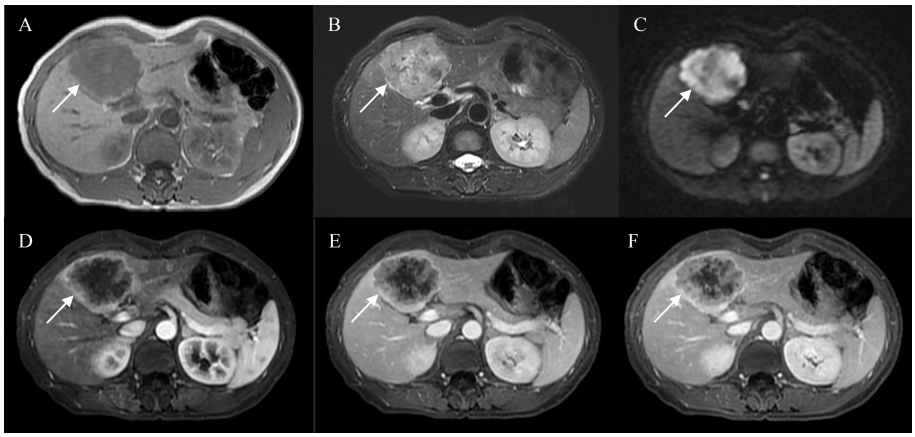

FIGURE 4
Intrahepatic mass-forming cholangiocarcinoma in a 50-year-old female with hepatitis B virus. Gd-DTPA-enhanced MRI detected a lobulated tumor (7.0 cm) with heterogeneous SI on T1WI and T2WI **(A, B)**, restricted diffusion **(C)**. Peripheral rim-like enhancement in the arterial phase **(D)**, followed by progressive filling of the contrast material in the portal and delayed phase **(E, F)**.

DP, and bile duct dilatation were independent differential factors. Combining these independent differential factors established the model for discriminating HCCs from IMCCs. Based on previous research and expert advice, we screened out five independent differential factors to build a model for the simplicity of the model. By verifying and evaluating the model, the model achieved high sensitivity (0.88) and specificity (0.906), indicating that these imaging features could obtain an excellent differential diagnostic performance for distinguishing atypical HCCs with peripheral rim-like enhancement from IMCCs.

In our study, compared to IMCCs, HCCs with peripheral rim-like enhancement more frequently showed heterogeneous SI on T1WI or T2WI, which may be a result of central necrosis and ischemia, or fibrotic component of the tumor. In previous studies, the rim enhancement of the tumor was attributed to the amount of fibrotic component within the tumor or the central necrosis/ischemia of more aggressive tumors (15, 28), which was consistent with our research.

Furthermore, the present study detected the capsule in 81 HCCs (95.3%) and three IMCCs (3.6%) on pathological examination. Histologically, the HCC capsule consists of an

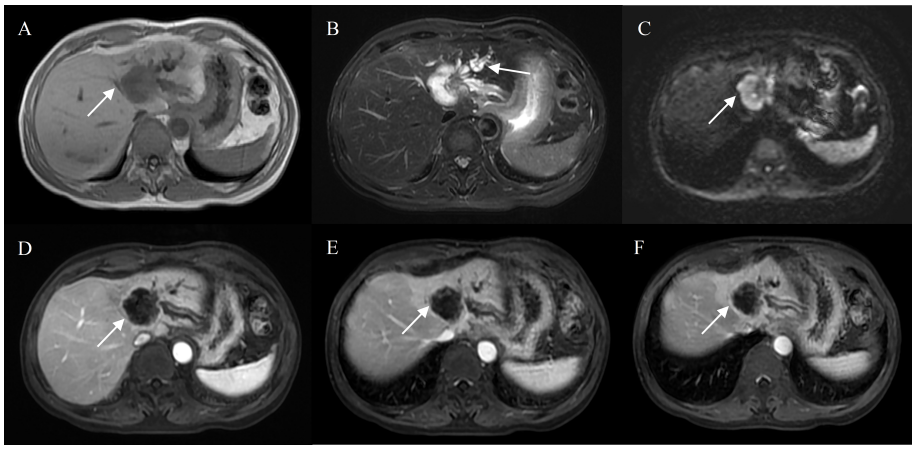

FIGURE 5
Intrahepatic mass-forming cholangiocarcinoma in a 70-year-old male without chronic viral hepatitis. Gd-DTPA-enhanced MRI detected a lobulated tumor (4.3 cm) with homogeneous SI on T1WI and T2WI **(A, B)**, restricted diffusion **(C)**. Peripheral rim-like enhancement in the arterial phase **(D)**, sustained rim enhancement in the portal and delayed phase **(E, F)**. And bile duct dilation peripheral to the tumor **(B)**.

TABLE 3 Univariate analysis for distinguishing HCCs from IMCCs.

Variable	OR	95%CI	P Value
Age	0.958	0.929, 0.988	0.006
Sex(F)	3.244	1.483, 7.092	0.003
Liver disease	0.048	0.020, 0.118	<0.001
Largest diameter	0.746	0.657, 0.847	<0.001
Shape (Lobulated)	3.905	1.971, 7.737	<0.001
Heterogeneous SI on T2WI	0.206	0.106, 0.399	<0.001
Heterogeneous SI on T1WI	0.096	0.044, 0.211	<0.001
Thin rim on AP	4.809	2.234, 10.351	<0.001
SI on DP			0.004
Target	4.330	1.820, 10.3	0.001
Iso	4.725	1.174, 19.02	0.029
Gradual enhancement	6.644	3.383, 13.047	<0.001
Surface retraction	6.859	2.24, 21.005	0.001
Bile duct dilatation	9.763	3.237, 29.446	<0.001
Intrallesional fat	0.099	0.022, 0.443	0.002
Central brightness on T2WI	0.260	0.129, 0.526	<0.001
Radiological capsule	0.047	0.021, 0.104	<0.001
Target on DWI	2.245	1.196, 4.211	0.012
Lymph node enlargement	3.421	1.527, 7.664	0.003

OR, odds ratio; CI, confidence interval. Variables with an odds ratio (OR) higher than 1.0 suggest IMCC, and variables with an OR lower than 1.0 suggest HCC.
Abbreviations can be found in the notes of Table 2.

inner layer that contains fibrous fibers, followed by an outer layer that contains portal venules (or sinusoids) and newly-formed bile ducts (24, 29). Capsule appearance is characteristic of HCC and attributed to tumor growth (25). For this reason, LI-RADS uses capsule appearance as a major imaging feature of HCC. Previous study reported that enhanced "capsule" was a reliable imaging feature to help identify HCC (30). Consistent with previous studies, on imaging analysis, the capsule was more common in HCCs (69,81.2%) than in ICCs (14,16.9%) on Gd-DTPA-enhanced MRI. These results demonstrated the excellent differential diagnostic value of the capsule on imaging.

In the present study, a lobulated contour, target sign on DP, and bile duct dilatation were independent differential factors for predicting IMCC over HCC. A lobulated contour was more common in IMCCs than in HCCs, which was a vital imaging feature of IMCCs. The target sign on DP might be attributable to necrosis/ischemia in tumors or central fibrosis, and peripheral tumor cell components sustained enhancement (16). In addition, bile duct dilatation also was an independent differential factor in distinguishing IMCCs and HCCs. This is mainly because IMCCs originates from the epithelial lining of the intrahepatic bile duct, so IMCCs can occlude intrahepatic bile duct and cause peripheral bile duct dilatation and cholangitis (31, 32).

Our data revealed that approximately 34.9% (29/83) of IMCCs were found in underlying chronic viral hepatitis, and 13.3% (11/83) patients with IMCCs had microscopic cirrhosis. Even though most IMCCs developed in normal liver, several risk

TABLE 4 Multivariate analysis for distinguishing HCCs and IMCCs.

Variable	OR	95%CI	P Value
Radiological capsule	0.024	0.006, 0.095	<0.001
Heterogeneous SI onT1WI	0.009	0.001, 0.056	<0.001
Shape (Lobulated)	11.732	2.928, 47.007	0.001
SI on DP			
Target	14.269	2.849, 71.474	0.001
Iso	4.039	0.42, 38.807	0.227
Bile duct dilatation	12.856	2.013, 82.106	0.007

Variables with an odds ratio (OR) higher than 1.0 suggest IMCC, and variables with an OR lower than 1.0 suggest HCC.
Abbreviations can be found in the notes of Tables 2 and 3.

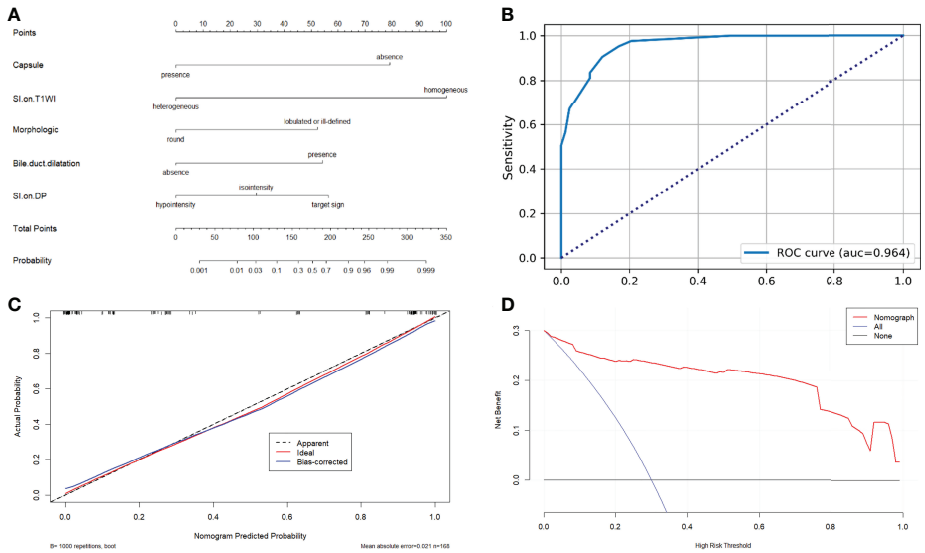

FIGURE 6
(A) Nomograms for distinguishing atypical HCCs with peripheral rim-like enhancement from IMCCs. **(B)** The receiver operating characteristic curve for the model. **(C)** The calibration curve analysis for the model. **(D)** The decision curve analysis (DCA) for the model.

factors have been reported, including chronic viral hepatitis and cirrhosis (33, 34).Moreover, previous studies demonstrated that large HCCs might show atypical enhancement features such as lack or weak arterial or rim-like enhancement (35, 36). We found that the tumor size of HCCs (7.8cm (5.8,10.2)) was larger than IMCCs size (5.6cm (4.1,7.0)) in our study, which was consistent with previous studies.

Previous studies reported that the target sigh in hepatobiliary phase of gadoxetic acid disodium enhanced MRI is a valuable imaging feature to differentiate IMCC from atypical HCC (37, 38). In cirrhotic patients, Hepatobiliary-specific agent enhanced MRI can effectively differentiate small HCC from recurrent nodules, and the hepatobiliary phase has a high diagnostic value for small HCC (39, 40). In the present study, we identified reliable imaging features on Gd-DTPA-enhanced MRI for distinguishing atypical HCCs with peripheral rim-like enhancement from IMCC. It follows that contrast-enhanced MRI remains an effective method for the preoperative diagnosis and evaluation of liver tumors.

The study has several limitations. First, the retrospective single-center nature of the survey might have introduced selection biases. Second, the amount of case is small and we did not conduct external validation. Third, the use of this kind of model is not easy in daily clinical practice, and we will be committed to better applying the research results to clinical practice in the future. Besides, our study only focused on histopathological and MR imaging features. In the future, we will further investigate clinical laboratory indicators to differentiate atypical HCCs from IMCCs.

In conclusion, in the present study, we identified reliable imaging features, including capsule, heterogeneous SI on T1WI, a lobulated contour, target sign on DP, and bile duct dilatation on Gd-DTPA-enhanced MRI, which was helpful for distinguishing atypical HCCs with peripheral rim-like enhancement from IMCC. Our findings may help radiologists better to differentiate HCCs with atypical enhancement patterns from IMCCs, thereby providing clinicians with more accurate preoperative imaging diagnoses to select appropriate treatment options.

Data availability statement

The original contributions presented in the study are included in the article/Supplementary Material. Further inquiries can be directed to the corresponding authors.

Ethics statement

This study was approved by the ethics committee of eastern hepatobiliary surgery hospital, The Third Affiliated Hospital of Shanghai Naval Military Medical University, China, and waived the requirement of obtaining written informed consent. Written informed consent for participation was not required for this study in accordance with the national legislation and the institutional requirements.

Author contributions

SZ, LH, and NJ conceived the project and designed the study. SZ, LH, YF, YL, JZ, and YW performed the data extraction and collection. WL and SZ performed the data analysis. SZ, WL, and NJ wrote and revised the manuscript. All authors contributed to the article and approved the submitted version.

Conflict of interest

The authors declare that the research was conducted in the absence of any commercial or financial relationships that could be construed as a potential conflict of interest.

Publisher's note

Supplementary material

The Supplementary Material for this article can be found online at: https://www.frontiersin.org/articles/10.3389/fonc.2022.986713/full#supplementary-material

References

1. Yang JD, Hainaut P, Gores GJ, Amadou A, Plymoth A, Roberts LR. A global view of hepatocellular carcinoma: trends, risk, prevention and management. *Nat Rev Gastroenterol Hepatol* (2019) 16(10):589–604. doi: 10.1038/s41575-019-0186-y

2. Liu J, Wu Z, Zhang J, Xie Y, Sun P, Wu H, et al. Effect of partial splenic embolization on transarterial chemoembolization for hepatocellular carcinoma with hypersplenism. *Med (Baltimore)* (2021) 100(26):e26441. doi: 10.1097/MD.0000000000026441

3. Forner A, Reig M, Bruix J. Hepatocellular carcinoma. *Lancet* (2018) 391 (10127):1301–14. doi: 10.1016/S0140-6736(18)30010-2

4. European Association for Study of Liver and European Organisation for Research and Treatment of Cancer. EASL-EORTC clinical practice guidelines: management of hepatocellular carcinoma. *Eur J Cancer* (2012) 48(5):599–641. doi: 10.1016/j.ejca.2011.12.021

5. Pan J, Li W, Gu L, Liu C, Zhang K, Hong G. Performance of adding hepatobiliary phase image in magnetic resonance imaging for detection of hepatocellular carcinoma: a meta-analysis. *Eur Radiol* (2022) Epub ahead of print.. doi: 10.1007/s00330-022-08826-z

6. Jing CY, Fu YP, Yi Y, Zhang MX, Zheng SS, Huang JL, et al. HHLA2 in intrahepatic cholangiocarcinoma: an immune checkpoint with prognostic significance and wider expression compared with PD-L1. *J Immunother Cancer* (2019) 7(1):77. doi: 10.1186/s40425-019-0554-8

7. Kelley RK, Bridgewater J, Gores GJ, Zhu AX. Systemic therapies for intrahepatic cholangiocarcinoma. *J Hepatol* (2020) 72(2):353–63. doi: 10.1016/j.jhep.2019.10.009

8. Banales JM, Iñarrairaegui M, Arbelaiz A, Milkiewicz P, Muntané J, Muñoz-Bellvis L, et al. Serum metabolites as diagnostic biomarkers for cholangiocarcinoma, hepatocellular carcinoma, and primary sclerosing cholangitis. *Hepatology* (2019) 70(2):547–62. doi: 10.1002/hep.30319

9. Ejaz A, Cloyd JM, Pawlik TM. Advances in the diagnosis and treatment of patients with intrahepatic cholangiocarcinoma. *Ann Surg Oncol* (2020) 27(2):552–60. doi: 10.1245/s10434-019-07873-z

10. Sung PS, Choi MH, Yang H, Lee SK, Chun HJ, Jang JW, et al. Diffusion-weighted magnetic resonance imaging in hepatocellular carcinoma as a predictor of a response to cisplatin-based hepatic arterial infusion chemotherapy. *Front Oncol* (2020) 10:600233. doi: 10.3389/fonc.2020.600233

11. Lee J, Han JW, Sung PS, Lee SK, Yang H, Nam HC, et al. Comparative analysis of lenvatinib and hepatic arterial infusion chemotherapy in unresectable hepatocellular carcinoma: A multi-center, propensity score study. *J Clin Med* (2021) 10(18):4045. doi: 10.3390/jcm10184045

12. Hartke J, Johnson M, Ghabril M. The diagnosis and treatment of hepatocellular carcinoma. *Semin Diagn Pathol* (2017) 34(2):153–9. doi: 10.1053/j.semdp.2016.12.011

13. Omata M, Cheng AL, Kokudo N, Kudo M, Lee JM, Jia J, et al. Asia-Pacific clinical practice guidelines on the management of hepatocellular carcinoma: a 2017 update. *Hepatol Int* (2017) 11(4):317–70. doi: 10.1007/s12072-017-9799-9

14. Lee JH, Lee JM, Kim SJ, Baek JH, Yun SH, Kim KW, et al. Enhancement patterns of hepatocellular carcinomas on multiphasic multidetector row CT: comparison with pathological differentiation. *Br J Radiol* (2012) 85(1017):e573–83. doi: 10.1259/bjr/86767895

15. Kim JH, Joo I, Lee JM. Atypical appearance of hepatocellular carcinoma and its mimickers: How to solve challenging cases using gadoxetic acid-enhanced liver magnetic resonance imaging. *Korean J Radiol* (2019) 20(7):1019–41. doi: 10.3348/kjr.2018.0636

16. Kovac JD, Ivanovic A, Milovanovic T, Micev M, Alessandrino F, Gore RM. An overview of hepatocellular carcinoma with atypical enhancement pattern: spectrum of magnetic resonance imaging findings with pathologic correlation. *Radiol Oncol* (2021) 55(2):130–43. doi: 10.2478/raon-2021-0004

17. Rimola J, Forner A, Sapena V, Llarch N, Darnell A, Díaz A, et al. Performance of gadoxetic acid MRI and diffusion-weighted imaging for the diagnosis of early recurrence of hepatocellular carcinoma. *Eur Radiol* (2020) 30 (1):186–94. doi: 10.1007/s00330-019-06351-0

18. Renzulli M, Biselli M, Brocchi S, Granito A, Vasuri F, Tovoli F, et al. New hallmark of hepatocellular carcinoma, early hepatocellular carcinoma and high-grade dysplastic nodules on gd-EOB-DTPA MRI in patients with cirrhosis: a new diagnostic algorithm. *Gut* (2018) 67(9):1674–82. doi: 10.1136/gutjnl-2017-315384

19. Vogel A, Cervantes A, Chau I, Daniele B, Llovet JM, Meyer T, et al. ESMO guidelines committee. hepatocellular carcinoma: ESMO clinical practice guidelines for diagnosis, treatment and follow-up. *Ann Oncol* (2018) 29(Suppl 4):iv238–55. doi: 10.1093/annonc/mdy308

20. Nagtegaal ID, Odze RD, Klimstra D, Paradis V, Rugge M, Schirmacher P, et al. WHO classification of tumours editorial board. the 2019 WHO classification of tumours of the digestive system. *Histopathology* (2020) 76(2):182–8. doi: 10.1111/his.13975

21. Zhou L, Rui JA, Zhou WX, Wang SB, Chen SG, Qu Q. Edmondson-Steiner grade: A crucial predictor of recurrence and survival in hepatocellular carcinoma without microvascular invasio. *Pathol Res Pract* (2017) 213(7):824–30. doi: 10.1016/j.prp.2017.03.002

22. Rimola J, Sapena V, Brancatelli G, Darnell A, Forzenigo L, Mähringer-Kunz A, et al. Reliability of extracellular contrast vs. gadoxetic acid in assessing small liver lesions using LI-RADS v.2018 and EASL criteria. *Hepatology* (2022) 76(5):1318–28. doi: 10.1002/hep.32494

23. Romanzi A, Ariizumi S, Kotera Y, Omori A, Yamashita S, Katagiri S, et al. Hepatocellular carcinoma with a non-smooth tumor margin on hepatobiliary-phase gadoxetic acid disodium-enhanced magnetic resonance imaging. is sectionectomy the suitable treatment? *J Hepatobiliary Pancreat Sci* (2020) 27 (12):922–30. doi: 10.1002/jhbp.743

24. Choi SY, Kim YK, Min JH, Kang TW, Jeong WK, Ahn S, et al. Added value of ancillary imaging features for differentiating scirrhous hepatocellular carcinoma from intrahepatic cholangiocarcinoma on gadoxetic acid-enhanced MR imaging. *Eur Radiol* (2018) 28(6):2549–60. doi: 10.1007/s00330-017-5196-y

25. Cruz CR, Carvalho ARMR, Maranhão ACN, Aroucha DB, Foinquinos GA, Carvalho SRC, et al. Clinical and laboratory parameters associated with li-rads as diagnostic of liver nodule in patients with cirrhosis. *Transl Gastroenterol Hepatol* (2021) 6:55. doi: 10.21037/tgh.2020.01.05

26. Ma X, Wei J, Gu D, Zhu Y, Feng B, Liang M, et al. Preoperative radiomics nomogram for microvascular invasion prediction in hepatocellular carcinoma using contrast-enhanced CT. *Eur Radiol* (2019) 29(7):3595–605. doi: 10.1007/s00330-018-5985-y

27. Chen Y, Zhu Y, Chen K, Wang H, Zhang W, Bao J, et al. Differentiation between hepatocellular carcinoma and intrahepatic cholangiocarcinoma using contrast-enhanced ultrasound: A systematic review and meta-analysis. *Clin Hemorheol Microcirc* (2021) 79(2):293–309. doi: 10.3233/CH-211145

28. Kim TH, Kim H, Joo I, Lee JM. Combined hepatocellular-cholangiocarcinoma: Changes in the 2019 world health organization histological classification system and potential impact on imaging-based diagnosis. *Korean J Radiol* (2020) 21(10):1115–25. doi: 10.3348/kjr.2020.0091

29. Yoon JK, Choi JY, Rhee H, Park YN. MRI Features of histologic subtypes of hepatocellular carcinoma: correlation with histologic, genetic, and molecular biologic classification. *Eur Radiol* (2022) 32(8):5119–33. doi: 10.1007/s00330-022-08643-4

30. Zheng W, Huang H, She D, Xiong M, Chen X, Lin X, et al. Added-value of ancillary imaging features for differentiating hepatocellular carcinoma from intrahepatic mass-forming cholangiocarcinoma on gd-BOPTA-enhanced MRI in LI-RADS m. *Abdom Radiol (NY)* (2022) 47(3):957–68. doi: 10.1007/s00261-021-03380-6

31. Ichikawa S, Isoda H, Shimizu T, Tamada D, Taura K, Togashi K, et al. Distinguishing intrahepatic mass-forming biliary carcinomas from hepatocellular carcinoma by computed tomography and magnetic resonance imaging using the Bayesian method: a bi-center study. *Eur Radiol* (2020) 30(11):5992–6002. doi: 10.1007/s00330-020-06972-w

32. Kovač JD, Janković A, Đikić-Rom A, Grubor N, Antić A, Dugalić V. Imaging spectrum of intrahepatic mass-forming cholangiocarcinoma and its mimickers: How to differentiate them using MRI. *Curr Oncol* (2022) 29(2):698–723. doi: 10.3390/curroncol29020061

33. Baidoun F, Sarmini MT, Merjaneh Z, Moustafa MA. Controversial risk factors for cholangiocarcinoma. *Eur J Gastroenterol Hepatol* (2022) 34(3):338–44. doi: 10.1097/MEG.0000000000002313

34. Miyabe K, Chandrasekhara V, Wongjarupong N, Chen J, Yang L, Johnson S, et al. Potential role of inflammation-promoting biliary microbiome in primary sclerosing cholangitis and cholangiocarcinoma. *Cancers (Basel)* (2022) 14(9):2120. doi: 10.3390/cancers14092120

35. Blaschke EM, Rao VL, Xiong L, Te HS, Hart J, Reddy KG, et al. Multiphase multi-detector row computed tomography imaging characteristics of Large (>5 cm) focal hepatocellular carcinoma. *J Comput Assist Tomogr* (2016) 40(3):493–7. doi: 10.1097/RCT.0000000000000379

36. Hwang J, Kim YK, Min JH, Choi SY, Jeong WK, Hong SS, et al. Capsule, septum, and T2 hyperintense foci for differentiation between large hepatocellular carcinoma (≥5 cm) and intrahepatic cholangiocarcinoma on gadoxetic acid MRI. *Eur Radiol* (2017) 27(11):4581–90. doi: 10.1007/s00330-017-4846-4

37. Piscaglia F, Iavarone M, Galassi M, Vavassori S, Renzulli M, Forzenigo LV, et al. Cholangiocarcinoma in cirrhosis: Value of hepatocyte specific magnetic resonance imaging. *Dig Dis* (2015) 33(6):735–44. doi: 10.1159/000439097

38. Mamone G, Marrone G, Caruso S, Carollo V, Gentile G, Crino' F, et al. Intrahepatic mass-forming cholangiocarcinoma: enhancement pattern on gd-BOPTA-MRI with emphasis of hepatobiliary phase. *Abdom Imaging* (2015) 40(7):2313–22. doi: 10.1007/s00261-015-0445-5

39. Leoni S, Piscaglia F, Granito A, Borghi A, Galassi M, Marinelli S, et al. Characterization of primary and recurrent nodules in liver cirrhosis using contrast-enhanced ultrasound: which vascular criteria should be adopted? *Ultraschall Med* (2013) 34(3):280–7. doi: 10.1055/s-0033-1335024

40. Quaia E, De Paoli L, Pizzolato R, Angileri R, Pantano E, Degrassi F, et al. Predictors of dysplastic nodule diagnosis in patients with liver cirrhosis on unenhanced and gadobenate dimeglumine-enhanced MRI with dynamic and hepatobiliary phase. *AJR Am J Roentgenol* (2013) 200(3):553–62. doi: 10.2214/AJR.12.8818

frontiers | Frontiers in Oncology

TYPE Original Research
PUBLISHED 24 November 2022
DOI 10.3389/fonc.2022.1052221

OPEN ACCESS

EDITED BY
Chandan Guha,
Albert Einstein College of Medicine,
United States

REVIEWED BY
Jiann-Ruey Hong,
National Cheng Kung University,
Taiwan
Anita Bakrania,
University Health Network (UHN),
Canada

*CORRESPONDENCE
Ian R. Corbin
ian.corbin@utsouthwestern.edu

†These authors have contributed equally to this work

SPECIALTY SECTION
This article was submitted to Cancer Imaging and Image-directed Interventions, a section of the journal Frontiers in Oncology

RECEIVED 23 September 2022
ACCEPTED 07 November 2022
PUBLISHED 24 November 2022

CITATION
Wang Y, Li J, Vale GDd, Chaudhary J, Anwar A, McDonald JG, Qin T, Zhang H and Corbin IR (2022) Repeated trans-arterial treatments of LDL-DHA nanoparticles induce multiple pathways of tumor cell death in hepatocellular carcinoma bearing rats.
Front. Oncol. 12:1052221.
doi: 10.3389/fonc.2022.1052221

Repeated trans-arterial treatments of LDL-DHA nanoparticles induce multiple pathways of tumor cell death in hepatocellular carcinoma bearing rats

Yuzhu Wang[1,2†], Junjie Li[2†], Goncalo Dias do Vale[3], Jaideep Chaudhary[2], Arnida Anwar[2], Jeffrey G. McDonald[3], Tao Qin[1], Hongwei Zhang[1] and Ian R. Corbin[2,4,5*]

[1]Department of Hepatobiliary and Pancreatic Surgery, Henan Provincial People's Hospital, Zhengzhou University People's Hospital, Henan University People's Hospital, Zhengzhou, Henan, China, [2]Advanced Imaging Research Center, University of Texas Southwestern Medical Center at Dallas, Dallas, TX, United States, [3]Center for Human Nutrition and Department of Molecular Genetics, University of Texas Southwestern Medical Center at Dallas, Dallas, TX, United States, [4]Internal Medicine Division of Liver and Digestive Diseases, University of Texas Southwestern Medical Center at Dallas, Dallas, TX, United States, [5]Radiology, University of Texas Southwestern Medical Center at Dallas, Dallas, TX, United States

Introduction: Repeated hepatic arterial delivery of therapeutic agents to the liver by percutaneously implanted port-catheter systems has been widely used to treat unresectable liver cancer. This approach is applied to assess the therapeutic efficacy of repeated low-density lipoprotein-docosahexaenoic acid (LDL-DHA) nanoparticle treatments in a rat model of hepatocellular carcinoma.

Methods: N1S1 hepatoma bearing rats underwent placement of a percutaneously implanted hepatic artery port-catheter system and were allocated to untreated, control LDL-triolein (LDL-TO) or LDL-DHA nanoparticle infusions groups. Treatments were performed every three days over a nine day study period. MRI was performed at baseline and throughout the study. At the end of the study tissue samples were collected for analyses.

Results and Discussion: Implantation of the port catheters was successful in all rats. MRI showed that repeated infusions of LDL-DHA nanoparticles significantly impaired the growth of the rat hepatomas eventually leading to tumor regression. The tumors in the LDL-TO treated group showed delayed growth, while the untreated tumors grew steadily throughout the study. Histopathology and MRI support these findings demonstrating extensive tumor necrosis in LDL-DHA treated groups while the control groups displayed minor necrosis. Molecular and biochemical analyses also revealed that LDL-DHA treated tumors had increased levels of nuclear factor-kappa B

and lipid peroxidation and depletion of glutathione peroxidase 4 relative to the control groups. Evidence of both ferroptosis and apoptosis tumor cell death was observed following LDL-DHA treatments. In conclusion repeated transarterial infusions of LDL-DHA nanoparticles provides sustained repression of tumor growth in a rat hepatoma model.

KEYWORDS

hepatocellular carcinoma, trans-arterial infusion port, nanoparticle, low-density lipoprotein, docosahexaenoic acid

Introduction

Only an estimated 20% of hepatocellular carcinoma (HCC) patients are diagnosed at early stage, and thus amenable to curative surgical treatments (1). For majority of the patients with more advanced tumors limited within the liver (intermediate/advanced-stage HCC), transarterial therapies are widely used as a palliative treatment (2). This technique takes advantage of the dual blood supply to the liver (80% *via* portal vein and 20% hepatic artery) and the preferential hepatic arterialization of liver tumors (3). Administration of antineoplastic agents through the hepatic artery would enable higher drug concentrations within the tumor while minimizing systemic exposure (4). Current transarterial therapies, which include transarterial chemoembolization (TACE) and hepatic arterial infusion chemotherapy (HAIC). The former involves formulating a cytotoxic anticancer drug with an embolic agent to inflict cytotoxic insult as well as blocking off the blood supply to the tumor (5). HAIC as the name implies infuses chemotherapy through the hepatic artery to deliver high concentrations of drug into the feeding arteries of the HCC. HAIC is more commonly performed in Asian counties, especially Japan, where it has been shown to be an effective treatment for advanced HCC (6). While both methods take advantage of the first-pass effect in the liver, current evidence suggests that single cycle of TACE/HAIC may not be sufficient for effective treatment of HCC, thus repeated transarterial treatments are generally performed to control tumor spread (7–11). Multiple cycles of TACE/HAIC, however, exposes the surrounding healthy liver to repeated bouts of cytotoxic chemotherapy or potential ischemic hepatic injury which often leads to progressive liver failure (12–14). In addition, TACE causes permanent arterial occlusion that restricts transarterial access in future TACE sessions. This approach induces tumor hypoxia, and inadvertently stimulates the development of tumor-feeding collateral vessels, contributing to tumor refractoriness and tumor regrowth (15, 16). These findings highlight the urgent need for novel therapies against HCC.

Preclinical evaluations of rodent models plays a central role anticancer drug discovery. While laboratory rodent models offers practicality, ease and low cost, transarterial drug delivery in these models is challenging. Several labs can achieve one time access of the hepatic artery through abdominal laparotomy (17–19) or catheterization of peripheral arteries (carotid or femoral) followed by fluoroscopy-guided catheter advancement to the hepatic vasculature (20). Repeated administration to the hepatic artery presents an even greater challenge for preclinical investigators. In recent years some progress has been made in this area through the application of percutaneous implantable port-catheter systems in small animal studies (21–23). The port-catheter system allows for facile and safe repeated arterial infusions without the need of repeated invasive surgeries for vascular access.

To this end in the present study we aim to evaluate the therapeutic efficacy of repeated administrations of low density lipoprotein-docosahexaenoic acid (LDL-DHA) nanoparticles in a rat orthotopic model of HCC. Dietary intake of long chain omega 3 fatty acids like DHA has been shown to reduce the risk of HCC development in individuals with known hepatitis infection (24). DHA has been shown to induce multiple cell death pathways in tumor cells (25–28). Conversely, DHA has also been shown to provide anti-inflammatory hepatoprotective benefits in the setting of liver disease (29, 30). Furthermore, studies from our own group has shown that nanoparticle formulations of DHA can elicit marked anticancer effects in cell culture (31, 32), direct tumor injection (33) and *via* hepatic artery injection (HAI) (34). Collectively, these previous finding provide strong rationale and support for the present preclinical investigation.

Materials and methods

Preparation of LDL nanoparticles

Apheresis plasma of patients with familial hypercholesterolemia was collected, LDL was isolated using sequential density gradient ultracentrifugation (35). Triolein (TO) and unesterified DHA (Nu-

chek Prep, Inc) were incorporated into LDL by the reconstitution method as described previously (31).

Cell viability test

The N1S1 rat hepatoma cell line (ATCC, CRL-1603, Manassas, VA, USA) was cultured in Dulbecco's Modified Eagle's Medium (Sigma, D6429) supplemented with 10% fetal bovine serum and 1% penicillin-streptomycin. Cells were incubated at 37°C in a humidified environment containing 5% CO_2. For viability test, cells were seeded in 96-well plates with 30000 cells/well and grown to 80-90% confluency. Prior to treatment all cells were cultured in serum free media overnight (~18 hours). After respective treatments with LDL nanoparticles, cell viability was measured at 72 hours with water soluble tetrazolium salt, WST-8 (CCK-8, Dojindo Molecular Technologies). Briefly, cells were incubated with WST solution for 2 hours at 37°C. A ThermoMax M5 microplate reader was used to measure the absorbance at 450 nm. The relative cell viability was expressed as a percentage of the control.

Chemical and cell death inhibitor studies

To assess the pathway of LDL-DHA mediated cell death cell viability assays were also performed in the presence of selected cell death inhibitors (iron chelator, defiprone (DFP); caspase inhibitor, z-VAD-fmk; ferrroptosis inhibitor, liproxstatin-1. All drugs were purchased from Selleck Chemicals. For this assay all cells were pretreated for 3 hours with the inhibitors prior to the addition of LDL-DHA. Chemicals or cell death inhibitors were used at the following concentrations: DFP, 20-40μM; Z-VAD-FMK, 50-100μM; liproxstatin-1, 50-200nM.

Western blot

Samples were lysed in 1x cell lysis buffer (9803, Cell Signaling) and protein concentration was determined using Pierce™ BCA Protein Assay Kit (Thermo Fisher). Equal amounts of protein were loaded for each sample on a polyacrylamide gel and separated using electrophoresis. Thereafter, proteins were transferred to PVDF Transfer Membrane (Immobilon) and incubated overnight with primary antibodies against Gpx-4 (1:500 dilution, sc-50497), Cleaved Caspase-3(1:1000 dilutions, Abcam ab2302) and β-actin (1: 1000 dilution, Cell Signaling sc-47778). Horseradish peroxidase-conjugated (HRP-conjugated) secondary antibodies were used and western blot signals were detected with ECL (Bio-Rad Laboratories).

Methods of lipid peroxidation measurement for N1S1 cells

N1S1 cells (350,000) in 2 ml media without serum were plated on 6 well plate and incubated overnight. The next day, cells were stained with 1 uM Bodipy C11 581/591 dye (Invitrogen) for 30 minutes at 37°C. After staining, the cells were treated with different concentration of LDL-DHA for 24 hours. Non adherent cells in media were collected and attached cells were trypsinized. All cells were pooled together and then washed with PBS. Bodipy fluorescence of the cells were measured with flow cytometry where green fluorescence indicated oxidized lipid species and red fluorescence indicated unoxidized lipid species. Lipid peroxidation is expressed as a ratio between green and red fluorescence sample signal multiplied by 100.

Animal studies

All procedures involving animals were approved by the Institutional Animal Care and Use Committee of University of Texas Southwestern Medical Center. Eighteen Male, Sprague-Dawley rats, 7 weeks of age, were included in this study. All rats were housed in a temperature-controlled animal room (22± 2°C) under a 12h dark/light cycle, with access to laboratory food and water ad libitum (n=3 rats/plastic cage).

Tumor cell inoculation

At the time of tumor cell inoculation rats were anesthetized with 2% isoflurane and a midline laparotomy incision (2cm) was made to expose the liver. N1S1 rat Hepatoma cells (1 x 10 (7)) in a matrigel suspension was injected into the lower left lobe of the liver. Eight days post implantation tumor growth was monitored using Magnetic resonance image (MRI). Studies were initiated once the tumors reached a diameter of 1.0 - 1.5 cm (approximately 10-12 days post tumor inoculation).

Surgical placement of indwelling hepatic arterial infusion port

Placement of indwelling hepatic arterial infusion port were performed in tumor bearing rats. Anesthetized rats were placed in supine position, and a midline incision (~5 cm) was made to enter the peritoneal cavity. Under a surgical microscope, the hepatic artery was exposed and ligated distal to gastroduodenal artery (GDA) with a 6-0 silk tie. A small arteriotomy was made on GDA and the polyurethane intravascular 2Fr tubing tip end (inner diameter 0.3mm, outer diameter 0.6mm; Access Technologies,

Skokie, Illinois, USA) of the implantable infusion port (silastic PMIN port; Access Technologies, Skokie, Illinois, USA) was inserted at the incision point on the GDA and advanced to the proper hepatic artery. The catheter was then secured by ligatures around the artery. Next a 1-2 cm pocket was created between the skin and muscle layer near the lower part of the abdominal incision to accommodate the implantable infusion port and the connected intra-arterial catheter. The implanted port was sutured and secured to the muscular fascia, followed by closure of the abdominal cavity using standard suture techniques. Thereafter, Taurolidine-Citrate Catheter lock Solution (TCS) (Access Technologies, Skokie, Illinois, USA) was injected into the port to ensure patency and lock the catheter. For the repeated hepatic artery infusion studies, LDL nanoparticles were injected percutaneously through the port, using a 24 gauge Huber point needle (Access Technologies, Skokie, Illinois, USA), followed by a TCS flush.

Repeated hepatic arterial infusions

Rats were randomly allocated into three groups: group I, untreated control rats (n=9); group II, LDL-TO controls (n=4) and group III, LDL-DHA (n=10). Repeated treatments of LDL nanoparticles was performed through the hepatic arterial infusion port at baseline and days 3 and 6. The repeated treatments of LDL-DHA was administered at a dose of 2 mg/kg (DHA) each. LDL-TO treatments were given at an equivalent dose to LDL-DHA. The dose and treatment frequency was selected as a 2mg/kg dose was previous demonstrated to be an effective therapeutic dose for treating tumors and a 3 day dosing frequency was selected as therapeutic responses to HAI of LDL-DHA nanoparticles are near complete in this time frame. Over the course of study the animals' body weights were monitored. All rats were sacrificed on the day 9 at which point blood and various organs were collected for histopathology and biochemical analyses.

Magnetic resonance imaging (MRI)

MRI was performed on all rats at baseline, 3, 6, and 9 days post treatment. A 9.4T MR imaging system (Varian/Agilent, Santa Clara, USA) was used to acquire images with the following parameters: T2: TR/TEesp, 2500/10ms; echo-train length, 8; and T1: TR/TE 250/1.98ms, flip angle 70; the rest parameters of FOV, 64 × 64mm2; matrix size, 256 × 256; 18 slices without gap; section thickness= 2mm, averages= 6. For contrast-enhanced T1 weighted MRI, Magnevist (Bayer Schering Pharma AG, Berlin, Germany) was injected *via* the tail vein at a dose of 100 μL.

Measurements of tumor volume, necrosis ratio and tumor volume doubling time (DT)

N1S1 Tumors appeared hypointense on T1 weighted images, and hyperintense on T2 and contrast-enhanced T1-weighted MR images. ImageJ software (National Institutes of Health, Bethesda, MD, USA) was used to measure the tumor size and necrosis ratio. Tumor area was measured on T1-weighted MR image, by manually circle the tumor lesion on all involved images with T2 image as reference. Tumor volume was calculated using the equation: tumor volume = Σ (tumor area on each slice × slice thickness).

The degree of treatment induced tumor necrosis was measured from the contrast enhanced T1-weighted images. Successful transarterial treatment typically display radiographic features of a non-enhancing core region surrounded by a thin rim enhancement indicative of central tumor necrosis accompanied with a periphery of enhancing cells. The area of central non-enhancing tissue was delineated on ImageJ to estimate necrosis. The necrosis ratio was defined as the volume of tumor necrosis over that of the entire tumor volume, i.e. necrosis ratio = Σ (area of necrosis × slice thickness)/(area of whole tumor × slice thickness) × 100%. Necrosis ratio obtained from MRI was further validated with the corresponding histopathology findings.

Histopathological analysis

At the time of euthanasia, partial excised liver, tumor, and spleen samples were collected, and were fixed with total immersion in 10% neutral buffered formalin for 24h, then embedded in paraffin, and sectioned into 5-μm slices and stained with Hematoxylin and Eosin (H&E). The slides were captured with an optical microscope (CX31, Olympus, Japan) at 100× magnification for histopathology, and micrograph were taken with a microscope digital camera system (DP50, Olympus, Japan). Ki-67 immunohistochemistry was also performed on tissue sections using microwave antigen retrieval and Ki-67 antibody (1:100 dilution; Thermo Fisher Cat # MA5-14520). Tumor tissues from untreated and LDL-TO treated tumor bearing rats serves as controls.

Necrosis ratio determination

H&E slides of control and treated tumors were scanned using a histology slide scanner (PrimeHisto XE) and the images imported into ImageJ. The approximate area of the tumor was marked and

measured. The image was then split into Red, Green and Blue Channels. The viable part of the tissue was most distinctive in the red channel. An intensity threshold was applied until only the viable area was selected. These areas were then selected with the Wand tool and measured. The necrosis tissue ratio was computed for each of the slides percentage necrotic index expressed as (necrotic area)/(total tissue area) × 100.

Serum collection and analysis

Immediately following euthanization, 5mL of blood was collected from inferior vena cava in all rats, and was centrifuged at 2500 rpm for 10 min at 4°C. Separated serum was collected into eppendorf tubes and stored at -20°C until analysis. Plasma liver enzymes alanine aminotransferase (ALT), aspartate aminotransferase (AST), gamma glutamyl transferase (GGT), total bilirubin (TBIL), albumin (ALB), glucose (GLU), alkaline phosphatase (ALKP), Triacylglyceride (TRIG), direct high density lipoprotein (dHDL), Cholesterol (CHOL), creatinine (CREA) and blood urea nitrogen (BUN) were measured with a AU400e automated biochemical analyzer.

Western blot analysis

Frozen samples liver or tumor tissue (~40mg) were homogenized in 500µL Cell Lysis Buffer (Cell signaling technology 9803) with EDTA-free Protease Inhibitor Cocktail (Roche) while on the ice. Samples were then centrifuged for 10 minutes at 14,000 rpm at 4°C, and the collected supernatants were stored at −80°C Protein concentrations were measured by Pierce BCA Protein Assay Kit (prod#23227). Protein concentrations of the collected supernatants were determined using the Pierce BCA Protein Assay Kit (prod#23227). Then, equal amounts of sample (30 µg/lane) were separated on 10% SDS-PAGE and transferred onto Immobilon-FL PVDF membrane (Millipore, USA). After blocking with 5% nonfat milk, Western blotting was performed with primary antibodies against nuclear factor-κβ (NFκB-p65) (SC-514451), interleukin-6 (IL-6) (SC-57315), C reactive protein (CRP) (SC-69770) and glutathione peroxidase 4 (GPX4) (sc-50497) (all of 1:1,000, Santa Cruz) at 4°C overnight, and then incubated with secondary antibodies (all of 1:2500) for 1 h at room temperature. β-Actin (sc-47778)(1:1,000, Santa Cruz) was used as a loading control. The protein bands were detected by ECL detection system and densitometry was quantified using ImageJ software (National Institutes of Health, MD).

Lipid peroxidation analysis

Liver and tumor peroxidative damage was assessed by measuring the malondialdehyde (MDA) level in tissue sample using the TBARs assay as described previously (36). Results were expressed as µM MDA formed/mg protein of tissue.

GSH/GSSG assay

Total soluble glutathione (GSH) and glutathione disulfide (GSSG) were measured in tissue homogenates using the enzymatic recycling method (37). Briefly, about 50mg of tissue were homogenized in 10 volumes of cold 5% metaphosphoric acid and 0.6% sulfosalicylic acid mixture. Protein was precipitated and the supernatant was used to determine GSH and GSSG. Results were expressed in µmoles per gram of tissue.

GC-MS fatty acid analysis

The gas chromatography-mass spectrometry lipidomics analysis of fatty acids in the liver was adapted from the protocol by Val et al. (38). Refer to Supplemental Material for detailed description of methods.

Immunohistochemistry

To examine the contribution of early caspase mediate processes to LDL-DHA tumor killing N1S1-tumor bearing rats receiving a single transarterial infusion of LDL-DHA was examined 3 days post treatment. Tumor tissue was excised and immunohistochemistry was performed as described previously using microwave antigen retrieval and cleaved caspase-3 (1:50 dilution; Abcam, Cambridge, MA). Tumor tissues from untreated tumor bearing rats serves as controls.

Cleaved caspase3 and Ki67 quantification were estimated using IHC by labelling Formalin-fixed, paraffin-embedded (FFPE) tissue sections with respective antibodies and counterstaining with Hematoxylin. The slides were then scanned using the Hamamatsu Nanozoom Scanner and images analyzed by counting percent positive stained cells for antibody compared to total cells in a field of view using ImageJ Cell Count feature.

Statistical analysis

Data were expressed as the mean ± standard error. Analysis of variance (ANOVA) with Tukey's multiple comparison *post hoc* testing was used for evaluation of differences between groups. Differences with a P value less than 0.05 was deemed statistical significance. All statistical analyses were performed using GraphPad Prism Version 5.0 (GraphPad Software, San Diego, CA).

Results

Nanoparticle characterization

Extensive physicochemical and morphological characterization of the LDL- nanoparticles has been reported previously by our group (31, 39). In the following study the LDL-DHA nanoparticles displayed an average hydrodynamic diameter of 30.1 ± 0.5 nm and a negative zeta potential of -23.4 ± 0.9 mV. These particles were monodispersed showing a mean polydispersity index = 0.26 ± 0.1. Each LDL nanoparticle carried an estimated 1,672 ± 219 molecules of DHA. The DHA concentration in the stock solution of LDL-DHA nanoparticles was 9.4 mM.

The LDL-TO (LDL reconstituted with triolein) nanoparticles displayed similar physicochemical characteristics of plasma LDL. LDL-TO maintained a size of 24.5 ± 0.9 nm and average polydispersity index measured 0.30 ± 0.02. The zeta potential for these particles was -6.6 ± 0.5 mV). According to previous preparation each LDL is typically loaded with over 300 molecules of TO (31).

LDL-DHA nanoparticles effects on N1S1 Cells

The cytotoxicity of LDL-DHA nanoparticles was evaluated in the N1S1 hepatoma cell line using a CCK-8 dose response assay. Figure 1A shows that the N1S1 cells were sensitive to the LDL-DHA nanoparticles from concentrations as low as 20μM. Thereafter, their viability dropped precipitously over the dose range from 20μM-50μM to menial levels. Over the second half of the dose response curve the viability of the N1S1 cells was gradually reduced to 0%. Lipid peroxidation was also measured over this dose range and lipid peroxides, as measured by Bodipy-C11 581/591 lipid, showed a dose dependent increase with increasing concentrations of LDL-DHA (Figure 1B). Accompanying this rise of lipid peroxidation was a concomitant depletion of the lipid antioxidant GPX4 (Figure 1C).

Comparative cell viability studies in response to increasing doses of LDL-DHA nanoparticles were performed on primary cultures of Sprague-Dawley rat hepatocytes. These experiments showed that LDL-DHA was not harmful to the primary rat hepatocytes over the dose range examined with the N1S1 cells (Supplementary Figure 1).

Next the mechanism of LDL-DHA induced cytotoxicity was assessed in the N1S1 cells using specific inhibitors of cell death (Figure 2). The radical trapping antioxidant, liproxstatin-1 a potent inhibitor of ferroptosis, was able to significantly protect N1S1 cells from LDL-DHA's cytotoxic effects (Figure 2A). The role of ferroptosis in LDL-DHA mediated tumor cell killing was further validated with the iron chelator, deferiprone (DFP), which was also able to block the cytotoxic activity of LDL-DHA (Figure 2B). In addition to the inhibition of ferroptosis, apoptosis inhibition was also investigated in our study. Surprisingly, ZVad-FMK, the pan-caspase inhibitor of apoptosis, was also shown to effectively rescue N1S1 cells from LDL-DHA killing (Figure 2C). These findings were further validated by increased expression of cleaved caspase-3 among LDL-DHA treated cells (Figure 2D). Collectively these findings indicate that LDL-DHA nanoparticles are able to induce both ferroptotic and apoptotic pathways of cell death in N1S1 hepatoma cells.

To demonstrate that the anticancer response to LDL-DHA was not a murine specific effect we evaluated the well differentiated human HCC cell line HUH7 (Supplementary Figure 2). These HCC cells were shown to have similar sensitivities to LDL-DHA as the N1S1 cells. Furthermore, select ferroptosis and apoptosis inhibition was shown to rescue cells from LDL-DHA cytotoxicity. Similarly, the later was supported by increased protein expression of cleaved caspase 3 following LDL-DHA treatments. Of note at higher concentrations of LDL-DHA treatment (> 40μM) cleaved caspase 3 levels decrease. This likely reflects a predominance of ferroptotic cell killing at these doses of LDL-DHA.

Port placement

MRI was performed approximately 10 days post tumor inoculation in each rat to assess growth of N1S1 tumors. Once tumors were radiologically confirmed rats underwent surgical placement of the arterial port catheter system. Micro CT imaging was performed in a cohort of rats to demonstrate successful surgical implantation of the port-catheter systems (see Figures 3A, B). Multiplane T2-weighted MRI also clearly shows of the orthotopic hepatoma as a hyper-intense lesion (Figure 3C). Corresponding contrast enhanced micro CT, post port placement, shows positioning of the port in the lower abdomen, catheter advancement into the hepatic artery and successful deposition and accumulation of contrast in the rat Hepatoma (Figures 3A, B). The liver is also delineated in this image as contrast also distributes throughout the hepatic arterial circulation (Figure 3A). Having demonstrated placement of the percutaneous port and successful perfusion of hepatomas with CT contrast experiments were initiated and hepatic arterial infusion of LDL nanoparticles commenced in study rats approximately 3 hours post port placement.

Overall, the port placement and repeated infusions were tolerated well by all animals over the course of the study. No observable clinical signs of weakness, restlessness, piloerection, tremors, hair loss or diarrhea appeared in in the study cohort over the 9-day infusion course and all animals survived until the study end-point. Over the course of the study the animals' body weight was documented (see Supplementary Figure 3). Control

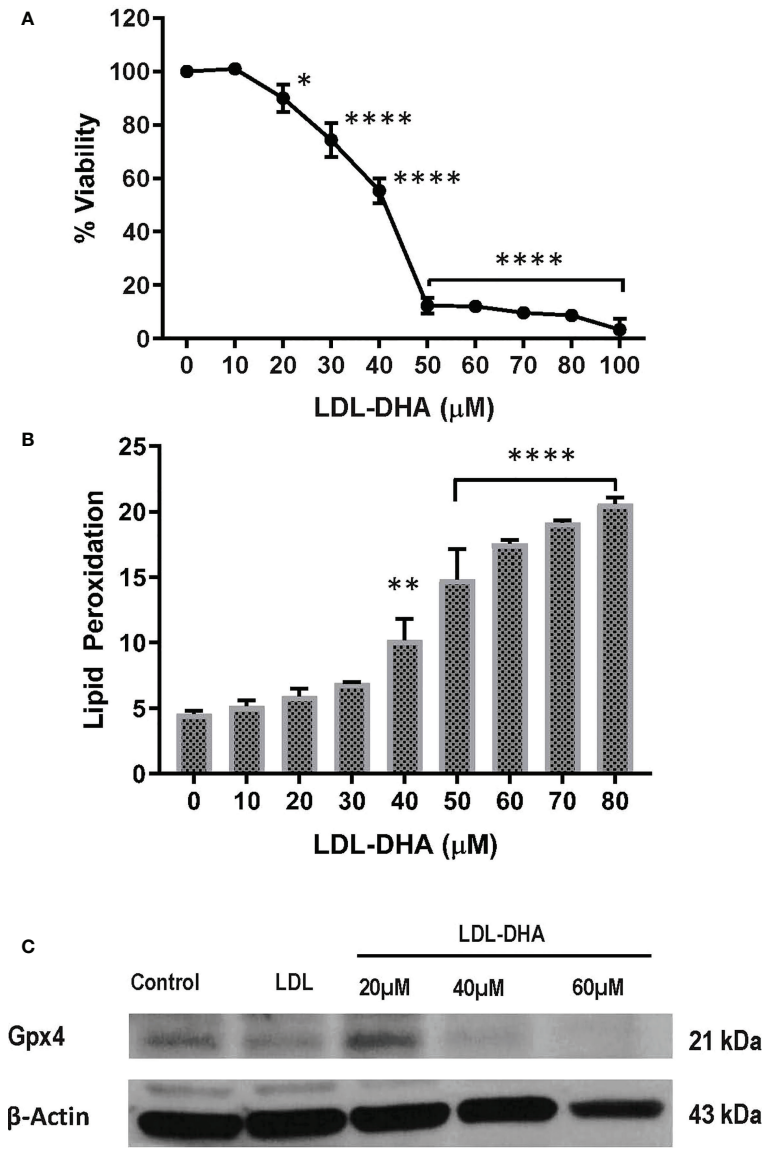

FIGURE 1
LDL-DHA induces toxicity on N1S1 cells through lipid peroxidation. **(A)** N1S1 cells were serum starved overnight, and then treated with LDL nanoparticle (0-100μM). Cell viability was measured by MTS/CCK assay at 72 hours after LDL nanoparticle treatment. Experiments were performed in triplicate wells with 3 independent runs. Results are expressed as mean ± SEM. *, P <0.05; ****, P <0.0001 compared with untreated control. **(B)** N1S1 cells were serum starved overnight, then treated with LDL nanoparticle (0-80μM) for 24 hours. Lipid ROS production was assessed by flow cytometry using C11-BODIPY. Results are expressed as mean ± SEM (n=3). **, P <0.01; ****, P<0.0001 compared with corresponding group (two-way ANOVA). Lipid ROS was not assessed over 80 μM due to inadequate amount of residual cells. **(C)** Immunoblot showing protein expression levels of GPX4 in untreated and treated N1S1 hepatoma cells 24hours after LDL (control) or LDL-DHA (20, 40 and 60 μM) exposure.

rats experienced steady incremental increases in body weight throughout the study, while LDL-DHA and LDL-TO rats showed a 5 and 2% decrease, respectively, in weight in the early post-operative period. Thereafter their body weights gradually increased over the remainder of the study. No significance difference in the mean body weight was observed between the control, LDL-TO and LDL-DHA treated groups.

Treatment results

Noninvasive MRI was used to monitor tumor response following locoregional treatment over the nine day study period (Figure 4A). The margins of the hyperintense orthotopic N1S1 hepatoma can clearly be demarcated from the surrounding liver on the T2 weighted images. Over the course of the nine day study

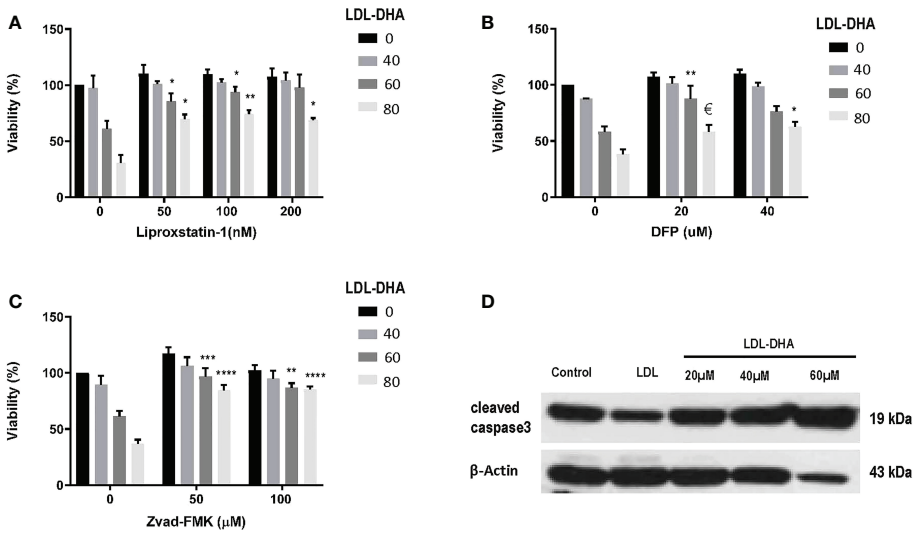

FIGURE 2
Identifying cell death pathways mediated by LDL-DHA cytotoxicity. Cells were treated with LDL-DHA (0, 40, 60, 80 μM) for 24 h in the absence/presence of: **(A)** liproxstatin (0, 50, 100, 200 μM); **(B)** DFO (0, 20, 40 μM); or **(C)** Zvad-FMK (0, 50, 100 μM). Cell viability (left panel) was measured by MTS assay at 24 hours after LDL-DHA treatment. Results are expressed as mean ± SEM (n=3). *, P <0.05; **, P <0.01; ***, P <0.001; ****, P<0.0001, €, P= 0.065 compared with corresponding LDL-DHA only treatment group. **(D)** Immunoblot of protein expression levels of cleaved caspase 3 in untreated and treated N1S1 hepatoma cells 24hours after LDL (control) or LDL-DHA (20, 40 and 60 μM) exposure.

period the untreated tumor grows at an exponential rate (Figures 4B, C). At day 9 the volume of the untreated tumor is close to 9 times its original volume. The LDL-TO treated tumors continued to experience growth over the nine days, however, it was not as rapid as the untreated controls (4 times increase over baseline). The effects of repeated LDL-DHA treatment was evident as the tumor size actually regressed over the study period. At day 9 the tumor volume was less than that at baseline (Day 9/baseline volume ratio=0.83). Image-based growth curves clearly show the dynamics of the treatment effects over the study period.

Specimens taken at the termination of the study also showed drastic histological differences (Figure 5A). The untreated tumors consisted mainly of dark basophilic staining tissues indicative of highly viable and active tumor tissue. LDL-TO treated tumors also displayed large regions of viable tissue, this however, was accompanied with sparse regions of tumor necrosis. In contrast the LDL-DHA treated tumors were composed mainly necrotic non-viable tissue. Histologic estimates of necrosis measured as high as 92% for the LDL-DHA group, while Untreated controls and LDL-TO groups measured 5 and 23% respectively (Figure 5B). Radiologic measurements of necrosis also followed a similar trend with Controls, LDL-TO and LDL-DHA groups averaging 2, 16 and 53% necrosis respectively (Figure 5C).

Complementary Ki67 staining performed on histological specimens also displayed consistent results as the H&E findings (Figure 5A). Untreated control and LDL-TO treated tumor sections were replete with Ki67 positive staining cells, supporting high proliferative and active tumor tissue. Conversely, the LDL-DHA treated tumors were void of Ki-67 staining. This is consistent with the high estimates of tumor necrosis associated with LDL-DHA treatment. Quantification of Ki67 staining confirmed significantly lower levels of Ki67 positive cells within the LDL-DHA treated tumors (12.7 ± 5.2%) relative to untreated (58.5 ± 6.3%) and LDL-TO treated tumors (57.2 ± 1.6%) (Supplementary Figure 4).

Serum biochemistry

The serum biochemistry values were mostly similar between the study groups (Supplementary Table 1). Higher levels of serum alkaline phosphatase were detected in LDL-DHA treated rats compared to the controls. While serum triglycerides were higher in LDL-TO treated rats relative to control and LDL-DHA treated groups. All other measurements of liver, renal and metabolic functions were unremarkable across the groups.

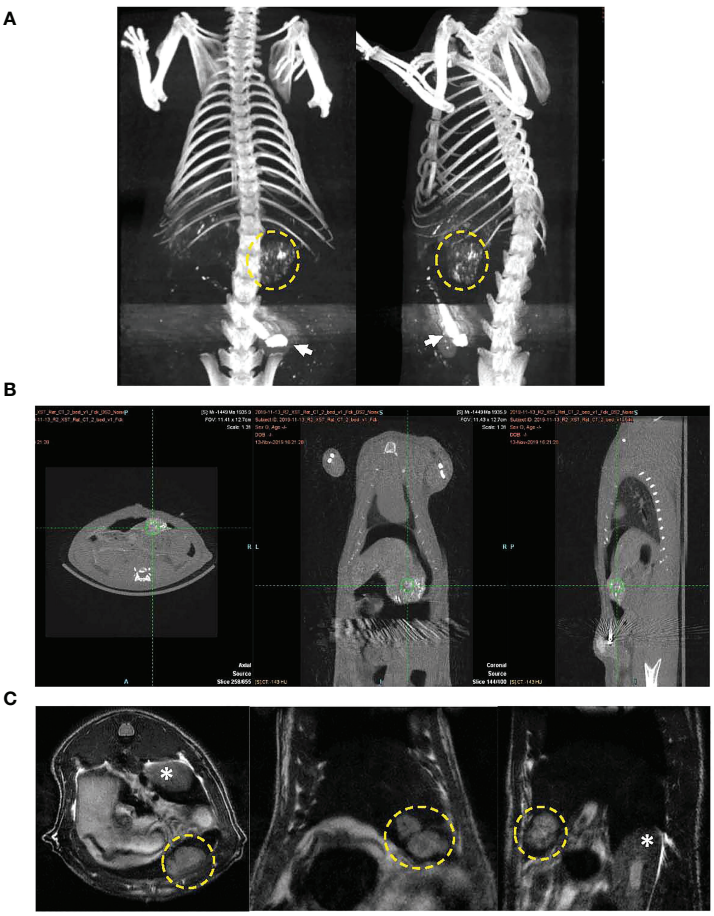

FIGURE 3
CT image of port-catheter system in the N1S1 tumor bearing rat. CT scan of the rat abdomen with three-dimensional reconstructed coronal image. The port system is filled with contrast material (Ethiodized oil) for visualization of the port (arrow) and the catheter line feeding into the gastroduodenal artery. Contrast material was also administered into the animal, some aspects of the liver's contour, hepatic vasculature and tumor (dashed yellow circle) can be seen. **(B)** CT images in three planes showing soft tissue anatomy of tumor bearing rat. Accumulation of contrast material can be seen in the tumor (green hatch marks). **(C)** Multiplane T2 weighted MRI of N1S1 tumor bearing rat. Tumors appear hyper intense on images (dashed yellow circle). * indicates kidney.

Inflammatory regulators

Western blot analyses were performed to assess the liver and corresponding tumor expression of inflammatory regulators, NF-κB, IL-6 and CRP, across the study groups (Figure 6A). The expression levels of the master regulator, NF-κβ, remained constant in the liver regardless of intervention. However, within the tumor the levels of NF-κβ increased dramatically over the untreated and LDL-TO treated groups. Liver CRP expression moderately increased with LDL-DHA treatment over the corresponding controls (1.5 fold). Within the tumor CRP levels remained constant regardless of treatment. Lastly, with regards to IL-6, untreated and LDL-DHA treated livers had similar expression, however LDL-TO treated liver experience a marked decrease in this immune modulator. On the other hand, tumor IL-6 levels were similar for control and the LDL-TO groups, while the LDL-DHA treatment resulted in a precipitous drop in IL-6.

Metabolic evaluation

GPX4 protein expression

We also extended the use of Western blot analyses to investigate tissue levels of the antioxidant GPX4 (Figure 6A). Equivalent expression of GPX4 was detected for control and LDL-DHA treated livers, but moderately lower levels were seen in the livers following LDL-TO infusions. Hepatoma tissues also showed slightly lower levels of GPX4 in LDL-TO group compared to untreated controls, but the LDL-DHA treatment group experienced an even greater diminution of GPX4.

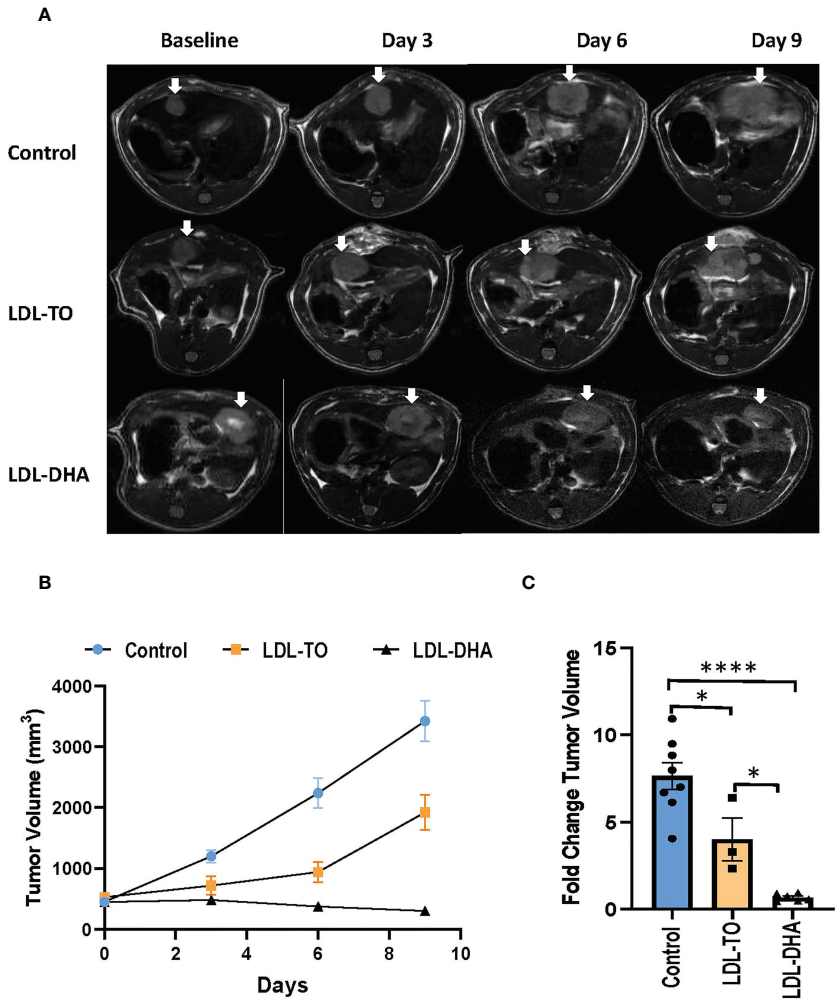

FIGURE 4
Tumor growth over course of repeated LDL nanoparticle treatments. **(A)** MRI assessment of tumor-bearing rats over the course of repeated LDL Nanoparticle treatments. Representative T2-weighted axial images of untreated controls, LDL-TO and LDL-DHA allocated rats at baseline, 3 days, 6 days and 9 days after LDL nanoparticle treatments. Tumor appear hyper-intense on T2-weighted images. White arrow indicates tumor. **(B)** N1S1 tumor volumetric assessment versus time over a course of repeated LDL nanoparticle treatments or no treatments. The average tumor volume for each group is presented in absolute volume (as calculated from MRI) and expressed as mean ± SEM. **(C)** Fold change in tumor volume at day 9 relative to corresponding baseline values. Significant differences between groups is expressed as mean ± SEM. *, P< 0.05; ****, P< 0.0001.

Tissue glutathione

In keeping with the GPX4 response, tissue measurements glutathione revealed that the reduced form of this metabolite (GSH) did not differ in the livers from the different groups (Supplementary Figure 5). Tumor GSH remained at similar levels between control and LDL-TO treatments. LDL-DHA infusion resulted in a greater than 3 fold reduction in tumor GSH, however this decrease did not reach statistical significance. The oxidized glutathione metabolite (GSSG) remained constant regardless of tissue or treatment regime.

Tissue malondialdehyde

The levels of MDA were used to assess the extent of lipid peroxidation experienced by liver and tumor from each study group (Figure 6B). Throughout the study levels of lipid derived aldehyde varied little between untreated and LDL nanoparticle treated livers. Conversely, within the tumor LDL-DHA treatment elicited pronounced increase in lipid peroxidation. MDA concentrations in LDL-DHA treated tumors were approximately 3 and 8 x greater than that in untreated and LDL-TO treated counterparts.

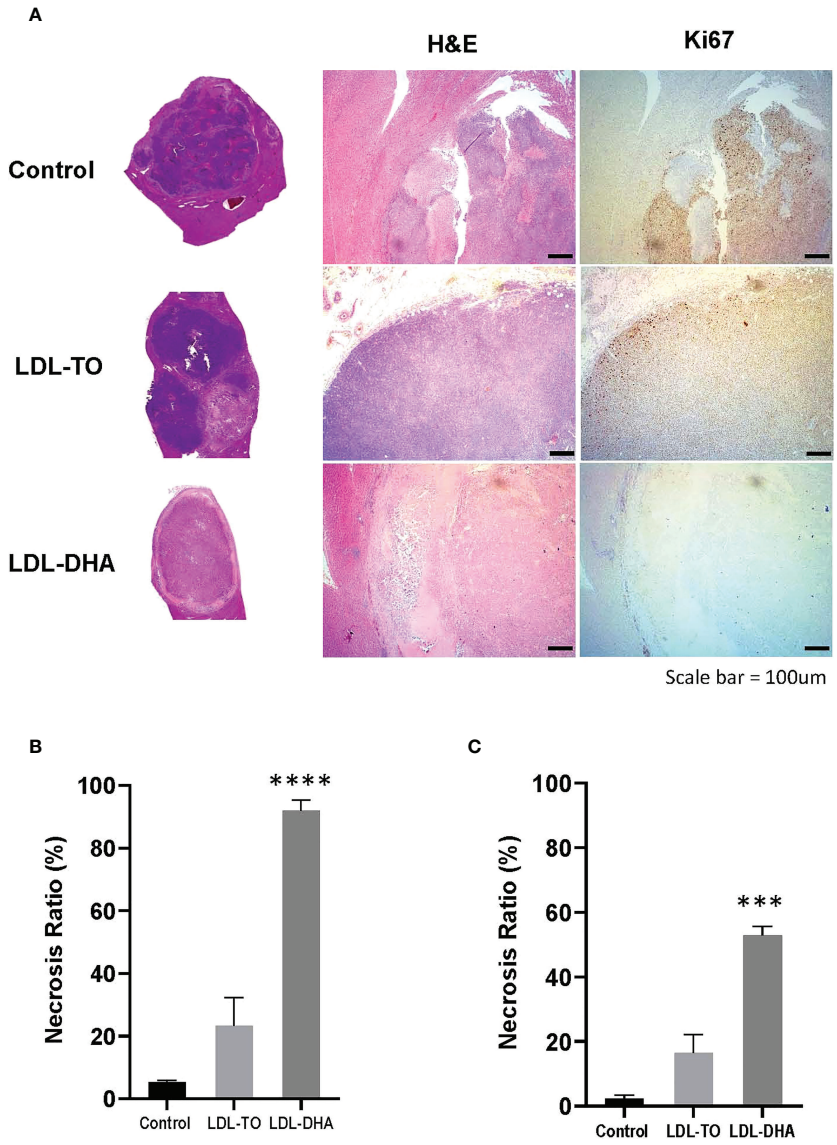

FIGURE 5
Tumor Viability following repeated LDL nanoparticle treatments. **(A)** Liver histology and immunohistochemistry of untreated controls and rats receiving repeated HAI of LDL nanoparticles. Gross tissue micrographs, hematoxylin and Eosin histological sections, corresponding IHC sections stained for stained for the proliferation marker Ki-67 and the apoptosis marker cleaved caspase-3. Images were taken at 20x magnification. Dotted line indicates liver tumor boundary. The LDL-TO sections are entirely composed of tumor tissue. Necrosis ratio measurements subfigure 5B and 5C. Necrosis ratio is defined as the volume of tumor necrosis over that of the entire tumor volume x 100%. **(B)** Necrosis estimates from histopathology. **(C)** Necrosis estimates from T1 weighted MRI. See *Methods* for details. Data is expressed as % mean ± SEM. ***, P<0.001; ****, P< 0.0001 versus untreated or LDL-TO controls.

Lipidomics

Lipidomics was employed to assess alteration in lipid composition and metabolism following HAI of LDL nanoparticles. Organic extraction methods enabled GC-MS investigation of polar (phospholipid) and neutral (triglycerides, cholesterol-ester) lipid fractions (Supplementary Tables 2-5). The composition of the polar lipids in the liver and tumor did not differ significantly between the cohorts of untreated, LDL-TO or LDL-DHA treated rats. Conversely, amongst the neutral lipids the levels of FA(20:2n-6) were elevated in the liver following LDL-DHA treatment relative to untreated and LDL-TO treated livers. For the tumor samples HAI of LDL-DHA lead to accumulation of saturated, mono-and polyunsaturated FAs (16:0, 18:1n-7, 20:4n-6, 20:3n-3, 20:2n-6, 22:6n-3, 22:5n-3) within the neutral lipid pool compared to their untreated and LDL-TO counterparts.

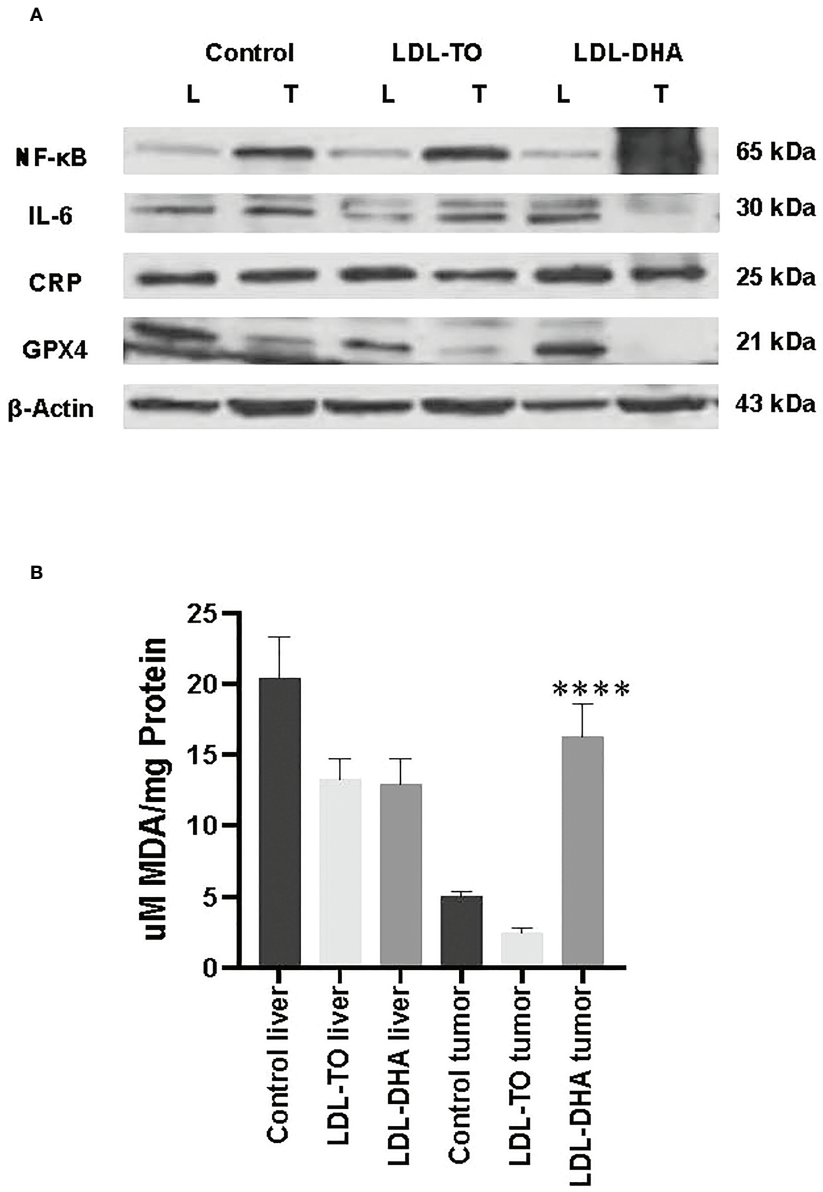

FIGURE 6
Inflammation and lipid peroxidation markers in LDL nanoparticle treated tumors. **(A)** Protein expression levels of inflammatory response marker and glutathione-peroxidase 4. Protein expression of hepatic nuclear factor-κβ (NF-κβ), interleukin-6 (IL-6) C reactive protein (CRP) and glutathione peroxidase 4(GPX4) in liver and tumor samples from untreated controls and rats with repeated HAI of LDL nanoparticles. Representative blots are shown. The data is shown relative to β-actin expression for each treatment group. **(B)** Levels of lipid peroxidation in liver and tumor samples from untreated controls and rats following repeated HAI of LDL nanoparticles. The TBARS assay measured lipid peroxide levels per mg of tissue. The data are expressed as μM malondialdehyde (MDA) per mg of tissue protein (mean ± SEM) for each treatment group **(B)**. ****, $P < 0.0001$ versus untreated and LDL-TO groups.

Cleaved caspase-3 immunohistochemistry

To assess the mechanistic contributions of caspase-mediated processes to LDL-DHA induced tumoricidal effects time points earlier than 10 days post treatment seen in these studies was required. Tumor samples from N1S1 tumor-bearing rats 3 days following a single HAI of LDL-DHA was selected for this study. Tumors showing a partial response with residual viable tumor was examined for cleaved caspase-3 expression (Supplementary Figure 6). Positive staining for cleaved caspase-3 was detected throughout this section, suggesting that caspase mediated processes are active earlier in the course the LDL-DHA tumor cell killing. Caspase-3 expression was also detected in untreated

controls but this was only found around regions of spontaneous necrosis. Quantification of Cleaved caspase-3 positive cells revealed overall similar levels between untreated controls (7.5 ± 1.0%) and LDL-DHA treated tumors (5.1 ± 0.3%) (Supplementary Figure 6).

Discussion

Percutaneous implanted port-catheter systems for intra-arterial infusions hold promise for a growing number of applications in clinical oncology. Repeated hepatic arterial delivery of anticancer agents to the liver by implanted port-catheter systems has been described for the treatment of advanced unresectable liver cancer (40, 41). Even among HCC patients with marked underlying liver disease this approach has been proven efficacious (11). Hepatic arterial infusions provide the benefits of "first pass and increased local concentration effects" within the tumor due to the preferential arterialization of hepatic neoplasms (3). Despite these pharmacokinetic advantages current transarterial therapies remain palliative (42). As such, the five year survival rate for HCC remains less than 12% (43). Innovative and novel therapeutic agents are urgently sought to address this unmet need. Preclinical large animal models, such as pigs, have been avidly used to demonstrate the feasibility of intra-arterial port catheter systems (44, 45), however, laboratory rodents are widely recognized as the primary animal model systems for oncology research. Implanting percutaneous intra-arterial port-catheter systems in rodents is a surgically challenging task, due to their small anatomy, but in recent years several groups have reported successful placement of hepatic artery port-catheter systems in the rat for evaluations of experimental anti-HCC therapies (21–23). Studies from our own group have also demonstrated the utility of hepatic artery port catheter systems in the rat (46). We assessed the safety of repeated transarterial infusions of LDL-DHA to the normal rat liver. Repeated infusions of LDL-DHA nanoparticles did not elicit hepatotoxicities and was concluded to be safe (46). Precedence for investigating the anticancer benefits of natural n-3 PUFAs stem from the seminal work of Sawada and others who reported that dietary intake of n-3 PUFAs among populations with chronic hepatitis significantly reduced the risk of HCC development (24). Other reports have also confirmed these findings (47). Within our own group formulation of DHA into LDL carriers has been shown to effectively kill hepatoma cells in culture by the induction of ferroptosis (33). Similar antitumor effects were also witnessed *in vivo* either by direct tumor injection or by transarterial injection (33, 34). In the present study, we sought to determine whether repeated infusions of LDL-DHA nanoparticles, through an indwelling cannula surgically implanted in the hepatic artery, would provide sustained tumor suppression in a syngeneic rat model of HCC.

Our investigations first examined the anticancer effects of LDL-DHA nanoparticles on *in vitro* cultures of the rat N1S1 and human HUH7 hepatoma cells. Similar to previous studies the LDL-DHA nanoparticles displayed a dose dependent cytotoxicity against the N1S1 and HUH7 cells, while primary Sprague Dawley rat hepatocytes remained fully viable over a similar treatment range. Accompanying the tumor cell cytotoxicity was a dose dependent accumulation of lipid peroxides. This finding (along with the depletion of GPX4 expression) point to ferroptosis as the mechanism whereby LDL-DHA induces tumor cell death. Rescue experiments with the radical-trapping antioxidant, liproxstatin-1 or ferrostatin, further confirmed the role of ferroptosis in the LDL-DHA's cytotoxicity. Surprisingly, the apoptosis inhibitor, Z-vad-fmk, was also able to effectively protect the tumor cells from LDL-DHA killing. These findings of dual ferroptosis–apoptosis tumor cell killing was also observed in human HUH7 HCC cells following treatment with LDL-DHA. Collectively, these findings suggest that the LDL-DHA nanoparticles induce a mixed pattern of tumor cell killing which involve both ferroptotic and apoptotic pathways. Similar responses were also found *in vivo* and will be discussed later.

Selective tumoricidal activity against N1S1 hepatoma of was also observed following repeated transarterial infusions of LDL-DHA nanoparticles. Both radiologic and histological analyses confirmed striking therapeutic effects from the locoregional nanoparticle treatment on the rat tumors. Although some discrepancy was noted between the two analyses. While contrast-enhanced MRI is used to determine viable tumor tissue (enhancing portions of the tumor are presumed to be viable, whereas non-perfused portions are presumed to be necrotic) (48), it is unable to distinguish viable cells from permeable reactive granulation tissue (49). Hence, enhancing granulation tissue remains a potential confounding factor for radiologic-based measures of tumor necrosis. Contrast enhancing granulation tissue is often noted at the periphery of tumors following locoregional treatment (50) and thus likely explains the lower MRI measures of tumor necrosis in the present study. Histological analysis, the gold standard of treatment assessment, revealed near complete necrosis (~92%) of the hepatomas after 3 courses of the LDL-DHA nanoparticle treatment. Complementary immunohistochemistry also supported these measurements as Ki-67 staining was near absent in the LDL-DHA treated tumors (12.7 ± 5.2%), but abundant in corresponding untreated (58.5 ± 6.3%) and LDL-TO controls (57.2 ± 1.6%). Tumor volumes measurements also corroborated these histology findings as the LDL-DHA treated tumors did not show signs of growth over the study. In fact, the volume of LDL-DHA treated tumors decreased in this study suggesting evidence of treatment induced tumor regression. Conversely, the untreated cohort of untreated rat showed exponential tumor growth. The control LDL-TO treated group also displayed tumors growth, although it was at a delayed rate.

Tumors from these animals presented varied degrees of necrosis (23.4 ± 9.0%) which were significantly greater than that seen in the untreated group (5.2 ± 0.7%). Given that the LDL-TO nanoparticles are known to support and not impede tumor growth these results revealed that other confounding factors were at play (34, 51). Positioning of the distal end of the fixed catheter that advances from the gastroduodenal artery into the hepatic artery proper could potentially obstruct arterial blood flow to the liver. The outer diameter of the catheter is 0.6 mm while that of the hepatic artery in the rat is 0.2 - 0.5 mm (52). Such impediment in hepatic artery blood flow would potentiate ischemic injury to the N1S1 liver tumors. As such, the LDL-TO treated tumors experienced some damage in the early post op period following port implantation, but soon after that the tumor growth resumed reaching exponential rates towards the end of the study. It stands to reason that the LDL-DHA treated tumors also experienced some obstructed hepatic arterial flow and ischemic injury as a result of the implanted port, however, the repeated administration of LDL-DHA nanoparticles appear to predominantly account for the observed tumoricidal effect. The biochemical and molecular disturbances that characterized the LDL-DHA treated tumors were absent in the tumors from the untreated and LDL-TO treated groups. Striking depletions in GSH and GPX4 accompanied by increasing levels of lipid peroxidation showcase the hallmark features of LDL-DHA induced ferroptosis (53). These tumors also significantly overexpressed NF-ƙβ indicating marked inflammatory activity following LDL-DHA treatment. We observed a significant accumulation of mononuclear inflammatory cells within the rim of the necrotic tumor mass after repeated LDL-DHA administration. Innate immune responses, including the recruitment and activation of mononuclear cells of the phagocytic system, likely contribute to the enhanced tumoricidal effects observed in this study.

The selective cytotoxic effects of LDL-DHA is also evident in the altered neutral lipid profile of treated tumors. The increased tissue levels of saturated, mono- and polyunsaturated FA moieties of neutral lipids suggest the intracellular accumulation of lipid droplets. Tumor accumulation of lipid droplets has been widely reported to correlate with chemotherapy treatments (54). Apoptosis-inducing anticancer drugs, like etoposide and doxorubicin, have been shown cause lipid droplet accumulation in tumor cells likely through the activation of p53 and the inhibition of mTOR and MYC which leads to lipid accretion as a result of mitochondrial impairment, inhibition of fatty acid oxidation and the subsequent redirection of fatty acids towards lipid storage (55, 56). Increased lipid droplet formation during chemotherapy may also be a consequence of non-apoptotic cell death pathways, as ferroptosis-induced cell death is known to perturb FA metabolism (57). Regardless of the mechanism of cytotoxicity stressed tumor cells respond by accumulating fatty acids and depositing lipid droplets (58). Similar to other anticancer agents LDL-DHA nanoparticle tumor cell killing is also characterized by the accumulation of neutral lipids. Further studies will be designed to elucidate how neutral lipid accumulation assist in mediating LDL-DHA induced tumor cell death.

Consistent with the *in vitro* findings the N1S1 tumors also displayed signs of caspase activated pathways/apoptosis following LDL-DHA treatments. In recent years several small molecules and natural products have also demonstrated the capacity to induce multiple pathways of cell death (59–61). Seiler and others have reported that the depletion of GPX4 is not only a potent activator of ferroptosis but may also be involved in potentiating apoptosis (62). Other potential mechanisms for co-stimulatory cell death pathways include the induction of pro-apoptotic protein PUMA by ferroptotic agents (59). The unique mixed pattern of LDL-DHA induced ferroptosis and apoptosis is intriguing and certainly requires further mechanistic exploration.

In conclusion, the percutaneous placement of a port-catheter system for repeated drug infusion is technically safe and provides a viable approach for accessing the hepatic artery. However, for laboratory small animal applications, smaller diameter catheters are recommended to prevent any complications of obstructive arterial blood flow. In spite of this mishap, repeated infusions of LDL-DHA proved to be highly effective at delivering DHA to rat hepatomas. The tumor deposited DHA was able to induce pronounce destruction of tumor tissue *via* ferroptosis and apoptotic pathways. Collectively, the results from this study demonstrates that repeated administrations of LDL-DHA nanoparticles through the hepatic artery provides sustained repression of malignant tumors in the rat.

Data availability statement

The original contributions presented in the study are included in the article/Supplementary Material. Further inquiries can be directed to the corresponding author.

Ethics statement

The animal study was reviewed and approved by Institutional Animal Care and Use Committee, UT Southwestern Medical Center.

Author contributions

YW: Acquisition and analysis of data; study design; draft article; JL: Acquisition and analysis of data; study design; draft article; GD: Acquisition and analysis of data; critical revision of content; JC: Acquisition and analysis of data; draft article; critical revision of content; AA: Acquisition of data; critical revision of content; JM: Data curation, formal analysis, methodology; TQ: Contribution and support for the study; HZ: Contribution and support for the study; IC: Contribution to conception and design; Analysis and interpretation of data; Draft article and critical revision; Final approval for publication; Accountable for all aspects of work. All authors contributed to the article and approved the submitted version.

Funding

This work was supported in part by Remeditex ventures LCC OTD-109946; NCI, National Institutes of Health (NIH), Grant R01CA215702; Provincial Ministry Co-Construction Key Project, Medical Scientific and Technological Research Program of Henan Province (SBGJ202002012); NIH HL020948 and the UTSW Cancer Center Support Grant (5P30 CA 142543-05).

Conflict of interest

The authors declare that the research was conducted in the absence of any commercial or financial relationships that could be construed as a potential conflict of interest.

Publisher's note

All claims expressed in this article are solely those of the authors and do not necessarily represent those of their affiliated organizations, or those of the publisher, the editors and the reviewers. Any product that may be evaluated in this article, or claim that may be made by its manufacturer, is not guaranteed or endorsed by the publisher.

Supplementary material

The Supplementary Material for this article can be found online at: https://www.frontiersin.org/articles/10.3389/fonc.2022.1052221/full#supplementary-material

SUPPLEMENTARY FIGURE 1
Effects of LDL nanoparticles on Sprague Dawley rat primary hepatocytes. **(A)** MTS dose response assay of rat primary hepatocytes to LDL-DHA (0-100 μM). Experiments were performed in triplicate wells with six independent runs. Results are expressed as mean ± SEM. ***, P<0.001 versus untreated control.

SUPPLEMENTARY FIGURE 2
Identifying cell death pathways in human HUH7 cells mediated by LDL-DHA cytotoxicity. **(A)** HUH7 cells were serum starved overnight, and then treated with LDL nanoparticle (0-100μM). Cell viability was measured by MTS/CCK assay at 72 hours after LDL nanoparticle treatment. Experiments were performed in triplicate wells with 3 independent runs. Cells were treated with LDL-DHA (0, 40, 60, 80 μM) for 24 h in the absence/presence of: **(B)** ferrostatin (0, 20, 40 μM); **(C)** Zvad-FMK (0, 50, 100 μM). Cell viability (left panel) was measured by MTS assay at 24 hours after LDL-DHA treatment. Results are expressed as mean ± SEM (n=3). *, P <0.05; **, P <0.01; ***, P <0.001; ****, P<0.0001, Ψ, P= 0.07-0.08 compared with corresponding LDL-DHA only treatment group. **(D)** Immunoblot of protein expression levels of cleaved caspase 3 in untreated and treated HUH7 hepatoma cells 24hours after LDL (control) or LDL-DHA (20, 40 and 60 μM) exposure.

SUPPLEMENTARY FIGURE 3
Mean body weight of tumor bearing rats with implanted hepatic artery port-catheters receiving repeated infusions of saline or LDL nanoparticles over a 9 day study period. Arrows indicate time of HAI.

SUPPLEMENTARY FIGURE 4
Quantification of KI-67 immunohistochemistry in untreated controls, LDL-TO and LDL-DHA treated animals. Results are expressed as mean ± SEM.

SUPPLEMENTARY FIGURE 5
Concentrations of reduced and oxidized glutathione in liver and tumor samples from untreated controls and rats following repeated HAI of LDL nanoparticles. The data is expressed as μmoles of glutathione per mg of tissue (mean ± SEM) for each treatment group.

SUPPLEMENTARY FIGURE 6
H&E and Immunohistochemistry of N1S1 tumors after Sham and HAI treatment of LDL-DHA (2 mg/kg). N1S1 tumor tissue samples were collected 72 hours post-treatment. Corresponding tissue sections were stained for H&E and the apoptosis marker cleaved caspase-3. **(A)** Sham; **(B)** LDL-DHA. Images were taken at 20x magnification. Quantification of cleaved caspase-3 immunohistochemistry in untreated controls and LDL-DHA treated animals. Results are expressed as mean ± SEM.

References

1. Salem R, Gilbertsen M, Butt Z, Memon K, Vouche M, Hickey R, et al. Increased quality of life among hepatocellular carcinoma patients treated with radioembolization, compared with chemoembolization. *Clin Gastroenterol Hepatol* (2013) 11:1358–65.e1. doi: 10.1016/j.cgh.2013.04.028

2. Bruix J, Sherman M. Management of hepatocellular carcinoma. *Hepatology* (2005) 42:1208–36. doi: 10.1002/hep.20933

3. Breedis C, Young G. The blood supply of neoplasms in the liver. *Am J Pathol* (1954) 30:969–77.

4. Arai Y, Takeuchi Y, Inaba Y, Yamaura H, Sato Y, Aramaki T, et al. Percutaneous catheter placement for hepatic arterial infusion chemotherapy. *Tech Vasc Interv Radiol* (2007) 10:30–7. doi: 10.1053/j.tvir.2007.08.007

5. Tsochatzis EA, Fatourou EM, Triantos CK, Burroughs AK. Transarterial therapies for hepatocellular carcinoma. In: Vauthey JN, Brouquet A, editors. *Multidisciplinary treatment of hepatocellular carcinoma*. Berlin, Heidelberg: Springer Berlin Heidelberg (2013). p. 195–206. doi: 10.1586/14737140.6.10.1377

6. Hendi M, Mou Y, Lv J, Zhang B, Cai X. Hepatic arterial infusion chemotherapy is a feasible treatment option for hepatocellular carcinoma: A new update. *Gastrointest Tumors* (2021) 8:145–52. doi: 10.1159/000516405

7. Bruix J, Llovet JM, Castells A, Montañá X, Brú C, Ayuso MDC, et al. Transarterial embolization versus symptomatic treatment in patients with advanced hepatocellular carcinoma: Results of a randomized, controlled trial in a single institution. *Hepatology* (1998) 27:1578–83. doi: 10.1002/hep.510270617

8. Lin D-Y, Liaw Y-F, Lee T-Y, Lai C-M. Hepatic arterial embolization in patients with unresectable hepatocellular carcinoma–a randomized controlled trial. *Gastroenterology* (1988) 94:453–6. doi: 10.1016/0016-5085(88)90436-2

9. Saccheri S, Lovaria A, Sangiovanni A, Nicolini A, De Fazio C, Ronchi G, et al. Segmental transcatheter arterial chemoembolization treatment in patients with cirrhosis and inoperable hepatocellular carcinomas. *J Vasc Intervent Radiol* (2002) 13:995–9. doi: 10.1016/S1051-0443(07)61863-6

10. Ikeda K, Kumada H, Saitoh S, Arase Y, Chayama K. Effect of repeated transcatheter arterial embolization on the survival time in patients with hepatocellular carcinoma. *Anal by cox proportional hazard Model Cancer* (1991) 68:2150–4. doi: 10.1002/1097-0142(19911115)68:10<2150::Aid-cncr2820681011>3.0.Co;2-f.

11. Park JY, Ahn SH, Yoon YJ, Kim JK, Lee HW, Lee DY, et al. Repetitive short-course hepatic arterial infusion chemotherapy with high-dose 5-fluorouracil and cisplatin in patients with advanced hepatocellular carcinoma. *Cancer* (2007) 110:129–37. doi: 10.1002/cncr.22759

12. Hiraoka A, Kumada T, Kudo M, Hirooka M, Koizumi Y, Hiasa Y, et al. Hepatic function during repeated TACE procedures and prognosis after introducing sorafenib in patients with unresectable hepatocellular carcinoma: Multicenter analysis. *Dig Dis* (2017) 35:602–10. doi: 10.1159/000480256

13. Hsin IF, Hsu CY, Huang HC, Huang YH, Lin HC, Lee RC, et al. Liver failure after transarterial chemoembolization for patients with hepatocellular carcinoma and ascites: incidence, risk factors, and prognostic prediction. *J Clin Gastroenterol* (2011) 45:556–62. doi: 10.1097/MCG.0b013e318210ff17

14. Grigorian A, O'Brien CB. Hepatotoxicity secondary to chemotherapy. *J Clin Trans Hepatol* (2014) 2:95–102. doi: 10.14218/JCTH.2014.00011

15. Sergio A, Cristofori C, Cardin R, Pivetta G, Ragazzi R, Baldan A, et al. Transcatheter arterial chemoembolization (TACE) in hepatocellular carcinoma (HCC): the role of angiogenesis and invasiveness. *Am J Gastroenterol* (2008) 103:914–21. doi: 10.1111/j.1572-0241.2007.01712.x

16. Virmani S, Rhee TK, Ryu RK, Sato KT, Lewandowski RJ, Mulcahy MF, et al. Comparison of hypoxia-inducible factor-1α expression before and after transcatheter arterial embolization in rabbit VX2 liver tumors. *J Vasc Intervent Radiol* (2008) 19:1483–9. doi: 10.1016/j.jvir.2008.06.017

17. Than TT, Sitzmann JV, Li SS, Lin PW, Grochow LB.. A method for hepatic arterial perfusion studies in the rat. *J Surg Res* (1989) 47:251–4. doi: 10.1016/0022-4804(89)90116-9

18. Garin E, Denizot B, Roux J, Noiret N, Lepareur N, Moreau M, et al. Description and technical pitfalls of a hepatoma model and of intra-arterial injection of radiolabelled lipiodol in the rat. *Lab Anim* (2005) 39(3):314–20. doi: 10.1258/0023677054307051

19. Sheu AY, Zhang Z, Omary RA, Larson AC. Invasive catheterization of the hepatic artery for preclinical investigation of liver-directed therapies in rodent models of liver cancer. *Am J Transl Res* (2013) 5:269–78.

20. Gade TPF, Hunt SJ, Harrison N, Nadolski GJ, Weber C, Pickup S, et al. Segmental transarterial embolization in a translational rat model of hepatocellular carcinoma. *J Vasc Intervent Radiol* (2015) 26:1229–37. doi: 10.1016/j.jvir.2015.02.006

21. Altomonte J, Braren R, Schulz S, Marozin S, Rummeny EJ, Schmid RM, et al. Synergistic antitumor effects of transarterial viroembolization for multifocal hepatocellular carcinoma in rats. *Hepatology* (2008) 48:1864–73. doi: 10.1002/hep.22546

22. Shinozaki K, Ebert O, Woo SL. Eradication of advanced hepatocellular carcinoma in rats *via* repeated hepatic arterial infusions of recombinant VSV. *Hepatology* (2005) 41:196–203. doi: 10.1002/hep.20536

23. Smoot RL, Blechacz BR, Werneburg NW, Bronk SF, Sinicrope FA, Sirica AE, et al. A bax-mediated mechanism for obatoclax-induced apoptosis of cholangiocarcinoma cells. *Cancer Res* (2010) 70:1960–9. doi: 10.1158/0008-5472.CAN-09-3535

24. Sawada N, Inoue M, Iwasaki M, Sasazuki S, Shimazu T, Yamaji T, et al. Consumption of n-3 fatty acids and fish reduces risk of hepatocellular carcinoma. *Gastroenterology* (2012) 142:1468–75. doi: 10.1053/j.gastro.2012.02.018

25. Jeong S, Jing K, Kim N, Shin S, Kim S, Song KS, et al. Docosahexaenoic acid-induced apoptosis is mediated by activation of mitogen-activated protein kinases in human cancer cells. *BMC Cancer* (2014) 14:481. doi: 10.1186/1471-2407-14-481

26. Newell M, Goruk S, Schueler J, Mazurak V, Postovit L-M, Field CJ., et al. Docosahexaenoic acid enrichment of tumor phospholipid membranes increases tumor necroptosis in mice bearing triple negative breast cancer patient-derived xenografts. *J Nutr Biochem* (2022) 107:109018. doi: 10.1016/j.jnutbio.2022.109018

27. Shan K, Feng N, Zhu D, Qu H, Fu G, Li J, et al. Free docosahexaenoic acid promotes ferroptotic cell death via lipoxygenase dependent and independent pathways in cancer cells. *Eur J Nutr* (2022) 61(8):4059–75. doi: 10.1007/s00394-022-02940-w

28. Jing K, Song K-S, Shin S, Kim N, Jeong S, Oh H-R, et al. Docosahexaenoic acid induces autophagy through p53/AMPK/mTOR signaling and promotes apoptosis in human cancer cells harboring wild-type p53. *Autophagy* (2011) 7:1348–58. doi: 10.4161/auto.7.11.16658

29. Nobili V, Carpino G, Alisi A, De Vito R, Franchitto A, Alpini G, et al. Role of docosahexaenoic acid treatment in improving liver histology in pediatric nonalcoholic fatty liver disease. *PloS One* (2014) 9:e88005. doi: 10.1371/journal.pone.0088005

30. Enguita M, Razquin N, Pamplona R, Quiroga J, Prieto J, Fortes P.. The cirrhotic liver is depleted of docosahexaenoic acid (DHA), a key modulator of NF-κB and TGFβ pathways in hepatic stellate cells. *Cell Death Dis* (2019) 10:14. doi: 10.1038/s41419-018-1243-0

31. Reynolds L, Mulik RS, Wen X, Dilip A, Corbin IR. Low-density lipoprotein-mediated delivery of docosahexaenoic acid selectively kills murine liver cancer cells. *Nanomed (Lond)* (2014) 9:2123–41. doi: 10.2217/nnm.13.187

32. Moss LR, Mulik RS, Van Treuren T, Treuren T, Kim SY, Corbin IR.. Investigation into the distinct subcellular effects of docosahexaenoic acid loaded low-density lipoprotein nanoparticles in normal and malignant murine liver cells. *Biochim Biophys Acta (BBA) - Gen Subj* 1860:2363–76. doi: 10.1016/j.bbagen.2016.07.004.

33. Ou W, Mulik RS, Anwar A, McDonald JG, He X, Corbin IR.. Low-density lipoprotein docosahexaenoic acid nanoparticles induce ferroptotic cell death in hepatocellular carcinoma. *Free Radic Biol Med* (2017) 112:597–607. doi: 10.1016/j.freeradbiomed.2017.09.002

34. Wen X, Reynolds L, Mulik RS, Kim SY, Van Treuren T, Nguyen LH, et al. Hepatic arterial infusion of low-density lipoprotein docosahexaenoic acid nanoparticles selectively disrupts redox balance in hepatoma cells and reduces growth of orthotopic liver tumors in rats. *Gastroenterology* (2016) 150:488–98. 10.1053/j.gastro.2015.10.008.

35. Lund-Katz S, Laplaud PM, Phillips MC, Chapman MJ. Apolipoprotein b-100 conformation and particle surface charge in human LDL subspecies: implication for LDL receptor interaction. *Biochemistry* (1998) 37:12867–74. doi: 10.1021/bi980828m

36. Draper HH, Hadley M. Malondialdehyde determination as index of lipid peroxidation. *Methods Enzymol* (1990) 186:421–31. doi: 10.1016/0076-6879(90)86135-I

37. Rahman I, Kode A, Biswas SK. Assay for quantitative determination of glutathione and glutathione disulfide levels using enzymatic recycling method. *Nat Protoc* (2006) 1:3159–65. doi: 10.1038/nprot.2006.378

38. Vale G, Martin SA, Mitsche MA, Thompson BM, Eckert KM, McDonald JG., et al. Three phase liquid extraction (3PLE): A simple, and fast method for lipidomic workflows. *J Lipid Res* (2019) 60(3):694–706. doi: 10.1194/jlr.D090795

39. Mulik RS, Zheng H, Pichumani K, Ratnakar J, Jiang QX, Corbin IR., et al. Elucidating the structural organization of a novel low-density lipoprotein nanoparticle reconstituted with docosahexaenoic acid. *Chem Phys Lipids* (2017) 204:65–75. doi: 10.1016/j.chemphyslip.2017.03.007

40. Lorenz M, Muller HH. Randomized, multicenter trial of fluorouracil plus leucovorin administered either *via* hepatic arterial or intravenous infusion versus fluorodeoxyuridine administered *via* hepatic arterial infusion in patients with nonresectable liver metastases from colorectal carcinoma. *J Clin Oncol* (2000) 18:243–54. doi: 10.1200/JCO.2000.18.2.243

41. Allen-Mersh TG, Earlam S, Fordy C, Abrams K, Houghton J. Quality of life and survival with continuous hepatic-artery floxuridine infusion for colorectal liver metastases. *Lancet* (1994) 344:1255–60. doi: 10.1016/S0140-6736(94)90750-1

42. Llovet JM, Brú C, Bruix J. Prognosis of hepatocellular carcinoma: the BCLC staging classification. *Semin Liver Dis* (1999) 19:329–38. doi: 10.1055/s-2007-1007122

43. El-Serag HB. Hepatocellular carcinoma. *N Engl J Med* (2011) 365:1118–27. doi: 10.1056/NEJMra1001683

44. Clark TW, Bilo JM, Beecroft JR. Arterial port catheter system placement using a translumbar aortic route. *Invest Radiol* (2002) 37:7–12. doi: 10.1097/00004424-200201000-00003

45. Fukuoka Y, Tanaka T, Nishiofuku H, Sato T, Masada T, Tatsumoto S, et al. Development of repeatable microcatheter access port for intra-arterial therapy of liver cancer. *Cardiovasc Intervent Radiol* (2019) 42:298–303. doi: 10.1007/s00270-018-2111-0

46. Wang Y, Li J, Subramaniyan I, do Vale GD, Chaudhary J, Anwar A, et al. An implanted port-catheter system for repeated hepatic arterial infusion of low-density

lipoprotein-docosahexaenoic acid nanoparticles in normal rats: A safety study. *Toxicol Appl Pharmacol* (2020) 400:115037. doi: 10.1016/j.taap.2020.115037

47. Gao M, Sun K, Guo M, Gao H, Liu K, Yang C, et al. Fish consumption and n-3 polyunsaturated fatty acids, and risk of hepatocellular carcinoma: systematic review and meta-analysis. *Cancer Causes Control* (2015) 26:367–76. doi: 10.1007/s10552-014-0512-1

48. Murakami T, Nakamura H, Hori S, Tomoda K, Mitani T, Nakanishi K, et al. Detection of viable tumor cells in hepatocellular carcinoma following transcatheter arterial chemoembolization with iodized oil. pathologic correlation with dynamic turbo-FLASH MR imaging with gd-DTPA. *Acta Radiol* (1993) 34:399–403. doi: 10.1177/028418519303400419

49. Kamel IR, Bluemke DA, Eng J, Liapi E, Messersmith W, Reyes DK, et al. The role of functional MR imaging in the assessment of tumor response after chemoembolization in patients with hepatocellular carcinoma. *J Vasc Interventional Radiol* (2006) 17:505–12. doi: 10.1097/01.RVI.0000200052.02183.92

50. Voizard N, Cerny M, Assad A, Billiard J-S, Olivié D, Perreault P, et al. Assessment of hepatocellular carcinoma treatment response with LI-RADS: a pictorial review. *Insights Imaging* (2019) 10:121. doi: 10.1186/s13244-019-0801-z

51. Li S, Zhou T, Li C, Dai Z, Che D, Yao Y, et al. High metastaticgastric and breast cancer cells consume oleic acid in an AMPK dependent manner. *PloS One* (2014) 9:e97330. doi: 10.1371/journal.pone.0097330

52. Martins PNA, Neuhaus P. Surgical anatomy of the liver, hepatic vasculature and bile ducts in the rat. *Liver Int* (2007) 27:384–92. doi: 10.1111/j.1478-3231.2006.01414.x

53. Dixon SJ, Stockwell BR. The hallmarks of ferroptosis. *Annu Rev Cancer Biol* (2019) 3:35–54. doi: 10.1146/annurev-cancerbio-030518-055844

54. Mehdizadeh A, Bonyadi M, Darabi M, Rahbarghazi R, Montazersaheb S, Velaei K, et al. Common chemotherapeutic agents modulate fatty acid distribution in human hepatocellular carcinoma and colorectal cancer cells. *BioImpacts BI* (2017) 7:31–9. doi: 10.15171/bi.2017.05

55. Boren J, Brindle KM. Apoptosis-induced mitochondrial dysfunction causes cytoplasmic lipid droplet formation. *Cell Death Differ* (2012) 19:1561–70. doi: 10.1038/cdd.2012.34

56. Zirath H, Frenzel A, Oliynyk G, Segerström L, Westermark UK, Larsson K, et al. MYC inhibition induces metabolic changes leading to accumulation of lipid droplets in tumor cells. *Proc Natl Acad Sci USA* (2013) 110:10258–63. 10.1073/pnas.1222404110

57. Magtanong L, Ko PJ, Dixon SJ. Emerging roles for lipids in non-apoptotic cell death. *Cell Death Differ* (2016) 23:1099–109. doi: 10.1038/cdd.2016.25

58. Shyu PJr., Wong XFA, Crasta K, Thibault G. Dropping in on lipid droplets: insights into cellular stress and cancer. *Biosci Rep* (2018) 38:BSR20180764. doi: 10.1042/BSR20180764.

59. Hoon Hong S, Lee DH, Lee YS, Jee Jo M, Jeong YA, Kwon WT, et al. Correction: Molecular crosstalk between ferroptosis and apoptosis: Emerging role of ER stress-induced p53-independent PUMA expression. *Oncotarget* (2018) 9:24869. doi: 10.18632/oncotarget.25365

60. Yang L, Chen X, Yang Q, Chen J, Huang Q, Yao L, et al. Broad spectrum deubiquitinase inhibition induces both apoptosis and ferroptosis in cancer cells. *Front Oncol* (2020) 10:949–9. doi: 10.3389/fonc.2020.00949

61. Mbaveng AT, Bitchagno GTM, Kuete V, Kuete V, Tane P, Efferth T., et al. Cytotoxicity of ungeremine towards multi-factorial drug resistant cancer cells and induction of apoptosis, ferroptosis, necroptosis and autophagy. *Phytomedicine* (2019) 60:152832. doi: 10.1016/j.phymed.2019.152832.

62. Seiler A, Schneider M, Förster H, Roth S, Wirth EK, Culmsee C, et al. Glutathione peroxidase 4 senses and translates oxidative stress into 12/15-lipoxygenase dependent- and AIF-mediated cell death. *Cell Metab* (2008) 8:237–48. doi: 10.1016/j.cmet.2008.07.005

frontiers | Frontiers in Oncology

TYPE Original Research
PUBLISHED 16 January 2023
DOI 10.3389/fonc.2023.977160

OPEN ACCESS

EDITED BY
Xiankai Sun,
University of Texas Southwestern Medical Center, United States

REVIEWED BY
William Dezarn,
Wake Forest University, United States
Carlo Chiesa,
National Cancer Institute Foundation (IRCCS), Italy

*CORRESPONDENCE
Gyoung Min Kim
kimgm@yonsei.ac.kr

SPECIALTY SECTION
This article was submitted to Cancer Imaging and Image-directed Interventions, a section of the journal Frontiers in Oncology

RECEIVED 24 June 2022
ACCEPTED 04 January 2023
PUBLISHED 16 January 2023

CITATION
Kim H-C and Kim GM (2023) Radiation pneumonitis following Yttrium-90 radioembolization: A Korean multicenter study.
Front. Oncol. 13:977160.
doi: 10.3389/fonc.2023.977160

Radiation pneumonitis following Yttrium-90 radioembolization: A Korean multicenter study

Hyo-Cheol Kim[1] and Gyoung Min Kim[2*]

[1]Department of Radiology, Seoul National University Hospital, Seoul National University College of Medicine, Seoul, Republic of Korea, [2]Department of Radiology, Yonsei University College of Medicine, Seoul, Republic of Korea

Objective: To report the incidence of radiation pneumonitis after radioembolization.

Methods: In this retrospective study, from May 2009 to July 2021, 782 consecutive patients underwent radioembolization in two institutes. Medical internal radiation dose dosimetry and partition dosimetry were used for glass and resin Yttrium-90-labeled microspheres (^{90}Y-microspheres), respectively. Medical records and radiological findings were retrospectively evaluated with emphasis on the symptomatic radiation pneumonitis.

Results: Of the 732 patients with lung shunt study and follow-up, 13 (1.8%) had symptomatic radiation pneumonitis and six patients died due to radiation pneumonitis. Of the 721 patients whose lung doses were calculated, 10 patients who were treated with glass (n = 5) and resin (n = 5) ^{90}Y-microspheres had radiation pneumonitis. No significant statistical difference between glass and resin ^{90}Y-microspheres (p = 0.304) was noted in terms of radiation pneumonitis incidence. Among the patients with radiation pneumonitis, all five patients treated with glass ^{90}Y-microspheres had estimated lung doses > 29 Gy, whereas five patients treated with resin ^{90}Y-microspheres had relatively wide range of lung dose reaching much lower value (13.21Gy).

Conclusion: The present study suggests that radiation pneumonitis after radioembolization may occur even though the manufacturer's instructions are followed.

KEYWORDS

hepatocellular carcinoma, radioembolization, radiation pneumonitis, dosimetry, dyspnea

1 Introduction

Radioembolization, using ^{90}Y-microspheres, are used for the treatment of malignant liver tumors (e.g., hepatocellular carcinomas (HCCs) and colorectal liver metastases) (1). Radioactive ^{90}Y-microspheres are small enough to pass through tumoral vessels in rare patients, resulting in radiation pneumonitis. For this reason, planning angiography and

simulating ^{90}Y-microsphere delivery by infusing ^{99m}Tc-macroaggregated albumin (^{99m}Tc-MAA) into the hepatic artery are used to measure the lung shunt fraction (LSF) and the estimated lung dose (2). The 25-Gy estimated lung dose by partition dosimetry is believed to be the safe upper limit for resin ^{90}Y-microspheres (3, 4). However, for glass ^{90}Y-microspheres, radioembolization is relatively contraindicated when the estimated lung dose is >30 Gy in a session and 50 Gy in a lifetime by medical internal radiation dose (MIRD) dosimetry (5).

Radiation pneumonitis is a rare but serious radioembolization complication that can occur 1–6 months after the procedure. Several case reports of radiation pneumonitis have been noted in the literature (6–8). This study, herein, reports the incidence ofradiation pneumonitis after radioembolization in the Asian population.

2 Materials and methods

2.1 Patients

From May 2009 to July 2021, 782 consecutive patients underwent radioembolization in two institutes. The inclusion criteria were (a) patients who underwent planning angiography and ^{99m}Tc-MAA scan and (b) patients whose information regarding lung dose was available. Exclusion criteria were (a) no lung shunt study (n = 37) and (b) no follow-up imaging for at least 2 months (n = 13). Consequently, 732 patients (mean age, 62.8 ± 12.4 years [range, 21–92 years]), which comprised 592 men and 140 women, were included in the present study. Among these patients, 664 and 68 had hepatocellular carcinoma and other cancers, respectively (Table 1). Moreover, 493 and 239 patients were treated with glass and resin ^{90}Y-microspheres, respectively. Furthermore, 36 patients received two sessions and 10 patients received three sessions of radioembolization.

2.2 Planning angiography and 99mTc-macroaggregated albumin imaging

Planning angiography includes celiac and superior mesenteric angiography, and depending on the need, right and/or left hepatic angiograms are also included. The operator advanced a microcatheter into the lobar artery supplying the primary target tumor, and 185 MBq of ^{99m}Tc-MAA was injected into the lobar hepatic artery. After injecting ^{99m}Tc-MAA, planar body scans that conjugated the anterior and posterior images were obtained for 10 min and were used to calculate the LSF.

2.3 Volume measurement and lung dose calculation

Total liver volume, target volume, and tumor volume of each patient were measured from the most recent cross-sectional imaging study before treatment, including computed tomography (CT) scan and magnetic resonance imaging using Aquarius Intuition (Terarecon, Durham, NC).

For Therasphere, single compartment dosimetry (MIRD) was used to calculate the estimated lung dose as provided by the manufacturer, and the lung mass was set as 1,000g for all patients. For SIR-Spheres, partition dosimetry provided by the manufacturer was used, and the lung weight was set as 800 and 600 g for men and women, respectively.

2.4 Analysis

Medical records and radiological findings were retrospectively evaluated. Radiation pneumonitis was diagnosed when patients presented with restrictive ventilatory dysfunction and typical

TABLE 1 Baseline characteristics in 732 patients who received radioembolization.

		Total (n = 732)	Radiation pneumonitis (n = 13)
Sex	Men	592	11
	Women	140	2
^{90}Y-Microspheres	glass	493	6
	resin	239	7
Tumor type	HCC	664	13
	Colorectal cancer	31	
	Cholangiocarcinoma	23	
	Neuroendocrine tumor	7	
	Breast cancer	2	
	Gallbladder cancer	1	
	Gastrointestinal stromal tumor	1	
	Ampular of vater cancer	1	
	Gastric cancer	1	
	Hepatoblastoma	1	

bilateral lung infiltrates with exertional dyspnea and dry cough (9), and pathogens causing similar presentation such as pneumocystis carinii were not revealed. Severity was graded by Common Terminology Criteria for Adverse Events (CTCAE) v5.0. The chi-square test was used to compare the radiation pneumonitis incidences between the groups. A p value <0.05 was considered statistically significant. All statistical analyses were performed with SPSS version 25.0 software (SPSS, Inc., Chicago, IL, USA).

3 Results

Of the 732 patients, 13 (1.8%) had symptomatic radiation pneumonitis and were treated with steroids (Table 2) (Figure 1). All 13 patients did not receive systemic chemotherapy. All 13 patients had HCCs which were treated with glass (n = 6) and resin (n = 7) ^{90}Y-microspheres. Dyspnea (n = 12) and cough (n = 6) were the common symptoms. The time interval between radioembolization and symptom onset ranged from 1.1 to 6.7 months (mean, 3.5 months; median, 3.3 months). Six patients died due to respiratory failure without tumor progression. Only one patient (patient no. 12) had radiation pneumonitis after second session of radioembolization, among the 46 patients who received multiple sessions.

Lung dose was not accurately calculated in 11 patients (three and eight with and without radiation pneumonitis, respectively). Radioembolization was performed by placing a balloon catheter in the right hepatic vein to reduce lung shunt in eight of 719 patients without radiation pneumonitis. Lung dose was not precisely estimated in the following three patients with radiation pneumonitis. Patient no. 11 had HCC, which was supplied by both the hepatic and right inferior phrenic artery. ^{99m}Tc-MAA was injected into the right hepatic artery, and the LSF was 7.65%. The right inferior phrenic angiogram showed tumor blush and pulmonary shunt, and ^{90}Y-microspheres were injected into both the right hepatic and right inferior phrenic arteries without arteriovenous shunt embolization. Patient no. 12 had received two radioembolization sessions. The LSF was 14.38% at the first radioembolization session. The second radioembolization session was performed 6 months after the first session, and the LSF was assumed as 14.38% without repeating the lung shunt study. Patient no.13 had a large arteriovenous shunt, and the LSF was 49.32%. ^{90}Y-microspheres were injected into the hepatic artery after complete arteriovenous shunt embolization.

TABLE 2 Treatment factors, symptom and outcome of radiation pneumonitis.

Sex/ Age	^{90}Y-microspheres used	Total radiation activity delivered (GBq)	Lung shunt fraction (%)	Estimated lung dose (Gy)	Symptom	Symptom onset after radioembolization (months)	Outcome	CTCAE grade	Follow-up period after diagnosis of radiation pneumonitis (months)
M/61	Glass	12.99	4.57	29.12	Dyspnea, cough	3.3	Improved	3	8
M/78	Glass	3.14	19.4	29.78	Dyspnea	1.3	Died	5	1
F/62	Glass	7.23	8.93	31.61	Dyspnea, cough	6.1	Died	5	2.5
M/84	Glass	7.37	10.0	36.15	Cough	6.0	improved	3	18
M/65	Glass	5.89	13.21	38.14	Dyspnea	5.5	Improved	3	12
F/71	Resin	2.7	5.91	13.21	Dyspnea, cough	1.6	Died	5	0.7
M/55	Resin	2.5	12.15	18.86	Dyspnea	4.3	improved	3	16
M/65	Resin	2.4	14.1	21.01	Dyspnea	3.8	improved	3	27
M/47	Resin	3.0	16.23	30.23	Dyspnea	1.1	Died	5	0.6
M/78	Resin	3.0	18.22	33.94	Dyspnea	6.7	improved	3	26
M/60	Glass	3.45	7.65	12.95*	Dyspnea, cough	2.8	Improved	3	9
M/91	Resin	1.8/1.5	14.38/not measured	16.07/13.39#	Dyspnea	3.6	Died	5	0.4
M/76	Resin	2.0	49.32	61.24$	Dyspnea, cough	3.3	Died	5	0.7

* The tumor was supplied by both the right hepatic artery and right inferior phrenic artery. ^{99m}Tc-MAA was injected into only the right hepatic artery. Right inferior phrenic angiogram showed tumor blush and pulmonary shunt. ^{90}Y-microspheres were injected into both right hepatic and right inferior phrenic arteries, assuming that the lung shunt fraction from the right inferior phrenic artery was same as that of the right hepatic artery.
# 2nd session of radioembolization was performed 6 months after 1st session of radioembolization without lung shunt study. It was assumed that lung shunt fraction at 2nd session was 14.38%.
$ Hepatic angiogram shows a large arteriovenous shunt. ^{99m}Tc-MAA was injected without embolization of arteriovenous shunt. ^{90}Y-microspheres were injected after embolization of arteriovenous shunt.

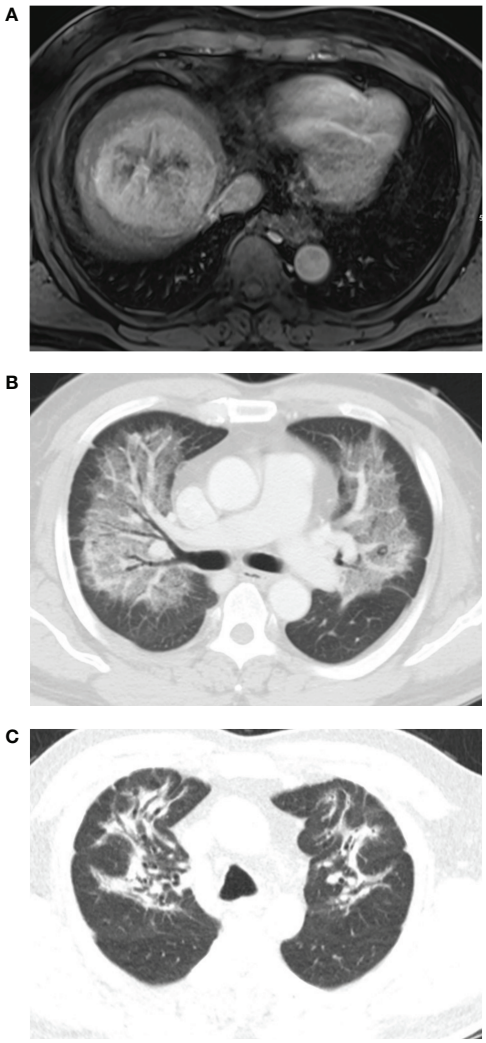

FIGURE 1
A 65-year-old man had a 9cm single mass in the right lobe. The lung shunt fraction was 14.1%, and 2.4 GBq of resin ^{90}Y-microspheres were delivered into the right hepatic artery. The estimated lung dose was 21.01 Gy. **(A)** Magnetic resonance shows a mass in right lobe. **(B)** Chest CT scan 3.8 months after radioembolization shows diffuse consolidation and ground-glass opacity in both the lungs with subpleural sparing. **(C)** Chest CT scan 4 months after steroid therapy shows fibrotic changes in both the lungs.

The lung dose could be calculated in 721 patients, which ranged from 0.013 to 38.14 Gy (Table 3). The estimated lung dose was >30 and >25 Gy in 24 and 20 patients who were treated with glass and resin ^{90}Y-microspheres, respectively. Of the 721 patients, 10 who were treated with glass (n = 5) and resin (n = 5) ^{90}Y-microspheres had radiation pneumonitis. No significant statistical difference between glass and resin ^{90}Y-microspheres (p = 0.304) was noted in terms of radiation pneumonitis incidence. For glass ^{90}Y-microspheres, radiation pneumonitis was more frequent in patients whose lung dose was >30 Gy than in patients whose lung dose was ≤30 Gy (p = 0.001). The same trend was obtained for resin ^{90}Y-microsphere, though the difference was not statistically significant (p = 0.061) probably for an insufficient number of patients. Notably, all five radiation pneumonitis patients treated with glass ^{90}Y-microspheres had estimated lung dose >29 Gy (29.12 ~ 38.14Gy). In contrast, five radiation pneumonitis patients treated with resin ^{90}Y-microspheres had relatively wide range of lung dose reaching much lower level (13.21Gy).

4 Discussion

Radiation pneumonitis is rare but could be a fatal complication after radioembolization (6–8). Exertional dyspnea and dry cough are common clinical manifestations. CT scan commonly shows bilateral symmetric ground-glass opacity and consolidation with relative peripheral/hilar sparing, which is the so-called "bat wing appearance." In addition, steroid therapy is the treatment mainstay.

MIRD dosimetry for glass ^{90}Y-microspheres is used, and 30 Gy of lung dose is considered as an upper limit. Salem et al. reported no case of radiation pneumonitis in 403 patients treated with glass ^{90}Y-microspheres (10) even if 18 and 58 patients had >30 and >30 Gy of single and cumulative lung doses, respectively. The estimated lung dose in patients with radiation pneumonitis ranged from 29.12 to 38.14 Gy in this study. The 30 Gy cutoff value should be reconsidered. For resin ^{90}Y-microspheres, body surface area (BSA) method and partition dosimetry are commonly used in western and in eastern countries, respectively. In BSA method, LSF >20% is an absolute contraindication and dose reductions of 20% and 40% are recommended if LSF exceeds 10% or 15%, respectively (3, 4). In

TABLE 3 Baseline characteristics in 721 patients whose lung dose was able to be calculated.

			Total (n = 721)	Radiation pneumonitis (n = 10)	P value
Sex		Men	581	8	1.0
		Women	140	2	
^{90}Y-Microspheres		glass	490	5	0.304
		resin	231	5	
Lung dose	Glass ^{90}Y-microspheres	≤ 30 Gy	466	2	0.001
		> 30 Gy	24	3	
	Resin ^{90}Y-microspheres	≤ 25 Gy	211	3	0.061
		> 25 Gy	20	2	

partition dosimetry, 25 Gy of the estimated lung dose is considered as an upper limit. Lung mass was previously regarded as 1,000 g. Lung mass was set as 800 and 600 g for men and women, respectively, for the Asian population since 2019 as recommended by the manufacturer (4). In all patients treated with resin ^{90}Y-microspheres in this study, lung dose was recalculated with reduced lung mass (800 and 600 g for men and women, respectively). Three patients had radiation pneumonitis with a low estimated lung dose (13.21–21.01 Gy). These three patients did not have any underlying lung disease such as emphysema and did not undergo chemotherapy.

Six patients had estimated lung dose above the recommended lung dose limit in our series. In early study period, some patients were treated using glass ^{90}Y-microsphere with predicted lung dose above 30 Gy, referring to Salem's article (10) which had reported the safety of radioembolization with high predicted lung dose (patient no. 3, 4 and 5). In late study period, the recommended lung dose limit has been strictly followed. Two patients (patient no. 9 and 10) were treated using resin ^{90}Y-microsphere before the revised recommendation by the manufacturer was applied, when the suggested lung dose limit was 30Gy and lung mass was set as 1,000g. Patient no. 13 was treated after embolization of arteriovenous shunt, as mentioned above.

Current dosimetry has limitations; planar scintigraphy using ^{99m}Tc-MAA is not adequate to simulate biodistribution of ^{90}Y-microsphere, especially in lung (11). Individual lung mass is not taken into account in these models. In addition, the lung dose limitations proposed by manufacturers are not validated with proper methodology.Thus, radiation pneumonitis after radioembolization seems to be able to occur, even though the lung dose limitation suggested by the manufacturers was followed in most patients. Consequently, the authors modified the lung dose cutoff value (i.e., 25 Gy for men and 20 Gy for women with glass ^{90}Y-microspheres and 20 Gy with resin ^{90}Y-microspheres).

This study has several limitations. First, the dosimetry between glass and resin ^{90}Y-microspheres is different. Lung mass was considered as 1,000 and 600–800 g for glass and resin ^{90}Y-microspheres, respectively. Second, superselective radioembolization *via* multiple target vessels is a common form of daily clinical practice. However, ^{99m}Tc-MAA was injected into the lobar hepatic artery in most cases. Thus, the different injection sites of radioactive ^{90}Y-microspheres and ^{99m}Tc-MAA may affect the lung dose.

In conclusion, the present study suggests that radiation pneumonitis after radioembolization may occur even though the manufacturer's instructions are followed, and the recommended cutoff value of the estimated lung dose may be adjusted to a slightly lower value.

Data availability statement

The raw data supporting the conclusions of this article will be made available by the authors, without undue reservation.

Ethics statement

The studies involving human participants were reviewed and approved by Institutional Review Board, Severance Hospital, Yonsei University Health System. Written informed consent for participation was not required for this study in accordance with the national legislation and the institutional requirements.

Author contributions

Guarantor of integrity of the entire study: GK. Study concepts and design: H-CK. Literature research: H-CK, GK. Clinical studies: H-CK, GK. Data analysis: H-CK, GK. Manuscript preparation: H-CK. Manuscript editing: GK. All authors contributed to the article and approved the submitted version.

Conflict of interest

The authors declare that the research was conducted in the absence of any commercial or financial relationships that could be construed as a potential conflict of interest.

Publisher's note

References

1. Weber M, Lam M, Chiesa C, Konijnenberg M, Cremonesi M, Flamen P, et al. EANM procedure guideline for the treatment of liver cancer and liver metastases with intra-arterial radioactive compounds. *EJNMMI* (2022) 49(5):1682–99. doi: 10.1007/s00259-021-05600-z

2. Salem R, Thurston KG. Radioembolization with 90yttrium microspheres: A state-of-the-Art brachytherapy treatment for primary and secondary liver malignancies. part 1: Technical and methodologic considerations. *J Vasc Interv Radiol* (2006) 17(8):1251–78. doi: 10.1097/01.RVI.0000233785.75257.9A

3. Lau WY, Kennedy AS, Kim YH, Lai HK, Lee RC, Leung TW, et al. Patient selection and activity planning guide for selective internal radiotherapy with yttrium-90 resin microspheres. *Int J Radiat Oncol Biol Phys* (2012) 82(1):401–7. doi: 10.1016/j.ijrobp.2010.08.015

4. Ltd SMP. *Package inserted for sir-spheres® y-90 resin microspheres* (2019). Available at: https://www.sirtex.com/media/169278/pi-ec-13-spheres-ifu-eu-row.pdf.

5. Kallini JR, Gabr A, Salem R, Lewandowski RJ. Transarterial radioembolization with yttrium-90 for the treatment of hepatocellular carcinoma. *Adv Ther* (2016) 33(5):699–714. doi: 10.1007/s12325-016-0324-7

6. Lin M. Radiation pneumonitis caused by yttrium-90 microspheres: Radiologic findings. *AJR Am J Roentgenol* (1994) 162(6):1300–2. doi: 10.2214/ajr.162.6.8191985

7. Leung TW, Lau WY, Ho SK, Ward SC, Chow JH, Chan MS, et al. Radiation pneumonitis after selective internal radiation treatment with intraarterial 90yttrium-microspheres for inoperable hepatic tumors. *Int J Radiat Oncol Biol Phys* (1995) 33 (4):919–24. doi: 10.1016/0360-3016(95)00039-3

8. Wright CL, Werner JD, Tran JM, Gates VL, Rikabi AA, Shah MH, et al. Radiation pneumonitis following yttrium-90 radioembolization: Case report and literature review. *J Vasc Interv Radiol* (2012) 23(5):669–74. doi: 10.1016/j.jvir.2012.01.059

9. Sangro B, Martinez-Urbistondo D, Bester L, Bilbao JI, Coldwell DM, Flamen P, et al. Prevention and treatment of complications of selective internal radiation therapy: expert guidance and systemic review. *Hepatology* (2017) 66(3):969–82. doi: 10.1002/hep.29207

10. Salem R, Parikh P, Atassi B, Lewandowski RJ, Ryu RK, Sato KT, et al. Incidence of radiation pneumonitis after hepatic intra-arterial radiotherapy with yttrium-90 microspheres assuming uniform lung distribution. *Am J Clin Oncol* (2008) 31(5):431–8. doi: 10.1097/COC.0b013e318168ef65

11. Chiesa C, Sjogreen-Gleisner K, Walrand S, Strigari L, Flux G, Gear J, et al. EANM dosimetry committee series on standard operational procedures: a unified methodology for ^{99m}Tc-MAA pre- and ^{90}Y peri-therapy dosimetry in liver radioembolization with ^{90}Y microspheres. *EJNMMI* (2021) 8(1):77–120. doi: 10.1186/s40658-021-00394-3

frontiers | Frontiers in Oncology

TYPE Original Research
PUBLISHED 02 February 2023
DOI 10.3389/fonc.2023.975216

OPEN ACCESS

EDITED BY
Xiankai Sun,
University of Texas Southwestern Medical Center, United States

REVIEWED BY
Vishal G. Shelat,
Tan Tock Seng Hospital, Singapore
Alessandro Granito,
University of Bologna Department of Medical and Surgical Sciences, Italy
Antonio Giovanni Solimando,
University of Bari Aldo Moro, Italy

*CORRESPONDENCE
Xia Du
duxia05@126.com
Ming Li
ming_li@fudan.edu.cn

SPECIALTY SECTION
This article was submitted to Cancer Imaging and Image-directed Interventions, a section of the journal Frontiers in Oncology

RECEIVED 22 June 2022
ACCEPTED 12 January 2023
PUBLISHED 02 February 2023

CITATION
Wang R, Xu H, Chen W, Jin L, Ma Z, Wen L, Wang H, Cao K, Du X and Li M (2023) Gadoxetic acid–enhanced MRI with a focus on LI-RADS v2018 imaging features predicts the prognosis after radiofrequency ablation in small hepatocellular carcinoma. *Front. Oncol.* 13:975216. doi: 10.3389/fonc.2023.975216

Gadoxetic acid–enhanced MRI with a focus on LI-RADS v2018 imaging features predicts the prognosis after radiofrequency ablation in small hepatocellular carcinoma

Ruizhi Wang[1], Hengtian Xu[2], Wufei Chen[1], Liang Jin[1], Zhuangxuan Ma[1], Lei Wen[2], Hongwei Wang[3], Kun Cao[4], Xia Du[2*] and Ming Li[1*]

[1]Department of Radiology, Huadong Hospital, Fudan University, Shanghai, China, [2]Department of Radiology, The Affiliated Hospital of Guizhou Medical University, Guiyang, China, [3]Department of General Surgery, Huadong Hospital, Fudan University, Shanghai, China, [4]Department of Hepatobiliary Surgery, The Affiliated Hospital of Guizhou Medical University, Guiyang, China

Introduction: Gadoxetic acid–enhanced magnetic resonance imaging (MRI) contributes to evaluating the prognosis of small hepatocellular carcinoma (sHCC) following treatment. We have investigated the potential role of gadoxetic acid–enhanced MRI based on LI-RADS (Liver Imaging Reporting and Data System) v2018 imaging features in the prognosis prediction of patients with sHCC treated with radiofrequency ablation (RFA) as the first-line treatment and formulated a predictive nomogram.

Methods: A total of 204 patients with sHCC who all received RFA as the first-line therapy were enrolled. All patients had undergone gadoxetic acid–enhanced MRI examinations before RFA. Uni- and multivariable analyses for RFS were assessing using a Cox proportional hazards model. A novel nomogram was further constructed for predicting RFS. The clinical capacity of the model was validated according to calibration curves, the concordance index (C-index), and decision curve analyses.

Results: Alpha fetoprotein (AFP) > 100 ng/ml (HR, 2.006; 95% CI, 1.111–3.621; P = 0.021), rim arterial phase hyperenhancement (APHE) (HR, 2.751; 95% CI, 1.511–5.011; P = 0.001), and targetoid restriction on diffusion-weighted imaging (DWI) (HR, 3.289; 95% CI, 1.832–5.906; P < 0.001) were considered as the independent risk features for recurrence in patients with sHCC treated with RFA. The calibration curves and C-indexes (C-index values of 0.758 and 0.807) showed the superior predictive performance of the integrated nomogram in both the training and validation groups.

Discussion: The gadoxetic acid–enhanced MRI features based on LI-RADS v2018, including rim APHE, targetoid restriction on DWI, and the AFP level, are the

independent risk factors of recurrence in patients with sHCC treated with RFA as the first-line therapy. The predictive clinical-radiological nomogram model was constructed for clinicians to develop individualized treatment and surveillance strategies.

KEYWORDS

small hepatocellular carcinoma, radiofrequency ablation, gadoxetic acid-enhanced MRI, nomogram, prognosis

Introduction

Hepatocellular carcinoma (HCC), the sixth leading cause of cancer-related deaths in the world, is also one of the most common malignant tumors (1). Nowadays, not only surgical resection but also more treatment strategies, such as transarterial chemoembolization (TACE), ablation therapy, cryotherapy, and immune checkpoint inhibitors therapy, can be applied to HCC (2–4). Among them, radiofrequency ablation (RFA) has become one of the most commonly used first-line therapies for small HCC (sHCC) (5–7). There are increasingly more studies showing the safety and effectiveness of RFA for small or early-stage HCC (8, 9). However, recurrence and metastasis have still been occurred in the patients with sHCC treated with RFA. Several previous literature studies have reported that the 1-year recurrence rate of patients with sHCC treated with ablation was approximately from 10% to 30% (10, 11). However, another study recently reported by Joo Hyun Oh showed that recurrence-free survival (RFS) and overall survival (OS) at 5-year are only 72.3% and 22.0% for patients with sHCC treated with RFA (12). Thus, preoperative prognosis evaluation for patients treated with RFA as first-line therapy is urgently needed to formulate further individual treatment strategies.

Preoperative imaging examinations, especially magnetic resonance imaging (MRI), play an important role in the prognosis prediction of patients with HCC treated with surgical resection or interventional therapy (12–14). More interestingly, a kind of hepatocyte-specific contrast agents, gadoxetic acid (Gd-EOB-DTPA or Primovist), has been emerged and widely applied, showing an extremely promising value in the diagnosis and prognosis assessment of liver tumors (15, 16). In addition, compared with traditional contrast agent, gadoxetic acid–enhanced MRI is beneficial for the accurate and early diagnosis of sHCC nodules during surveillance as previously demonstrated (17, 18). Emerging pieces of studies suggested that several imaging features and ready availability from the gadoxetic acid–enhanced MRI make it an excellent candidate parameter for prognosis prediction of patients with HCC treated with surgical resection or interventional therapy (19). Unfortunately, the standard use and repeatability of various imaging features from gadoxetic acid–enhanced MRI in the prognosis assessment of HCC are still lacking, which is one of the reasons why these so-called imaging features cannot be formally recognized and applied in clinical practice. The LI-RADS (Liver Imaging Reporting and Data System) was formulated, aiming to promote a standard imaging-based diagnosis of HCC. Several emerging studies have reported that the LI-RADS system is associated with the prognosis of patients with primary HCC treated with surgical resection, independent of the pathologic diagnosis (20, 21). The establishment of the prognostic model based on standard imaging features is of great significance for radiologists/clinicians to routinely use and popularize in clinic. However, to our knowledge, few studies have focused on the gadoxetic acid–enhanced MRI based on LI-RADS v2018 (a latest version) imaging features that predict the prognosis after RFA as a first-line therapy in sHCC.

Hence, the purpose of our study was to mainly evaluate the potential role of LI-RADS v2018 (a latest version) imaging features from gadoxetic acid–enhanced MRI in the prediction of prognosis in patients with sHCC treated with RFA as first-line treatment. Furthermore, a nomogram model integrating standard imaging parameters and clinical parameters was developed for improving the practicability and repeatability of imaging in prognosis evaluation of patients with sHCC treated with ablation.

Methods

Patient selection

The retrospective study was approved by the institutional review board of our institution. The corresponding requirement for informed consent was waived. Between January 2017 and December 2020, a total of 386 patients treated with RFA were retrospectively analyzed. The inclusion criteria are as follows: (1) patients who underwent preoperative gadoxetic acid–enhanced MRI were diagnosed with HCC, and the MRI examinations were conducted within 2 weeks prior to RFA; (2) a single HCC ≤ 5 cm in diameter or up to three HCCs that were each ≤ 3 cm in diameter without portal vein thrombosis or extrahepatic metastases; (3) the coagulation function met the operation requirements; and (4) patients who did not undergo other treatment prior to surgery and have no history of extrahepatic cancer. The exclusion criteria are as follows: (a) MR images with poor-quality or incomplete clinical data; (b) patients treated with surgery, chemoradiotherapy, or TACE prior to RFA; (c) number of nodules > 3 or diameter of nodules > 5 cm; (d) patients with a short-term follow-up (<3 months); and (e) pathological diagnosis was not HCC. The first-line therapy was defined as no prior therapy for patients with sHCCs at the time of the first diagnosis. Finally, 204 patients with sHCCs treated with RFA as first-line therapy were enrolled in this study. The flow chart is shown in detail in Figure 1.

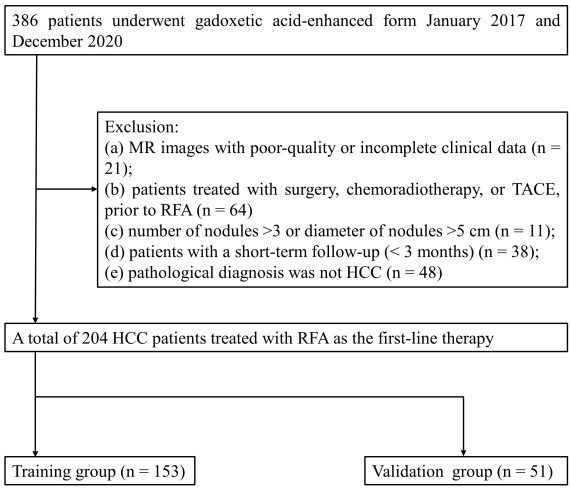

FIGURE 1
The flowchart of selection of patients with sHCC.

MRI protocols

All patients in this study were examined in a 3.0-T MRI scanner (Canon Vantege Titan) equipped with a phased-array body coil before RFA. MRI sequences contained conventional in- and opposed-phase sequences, T1WI, fat-suppressed T2WI, and diffusion-weighted imaging (DWI, b = 0, 1000). Dynamic contrast-enhanced MR imaging with a T1-weighted fat-suppressed sequence was obtained once before and four times after intravenous administration. Acquisitions were performed at 25, 90, and 180 s and 20 min after injection gadoxetic acid (Primovist; Bayer Healthcare, Berlin, Germany). During the contrast-enhanced MRI, all patients were treated with Primovist at a rate of 3 ml/s and at a dose of 0.0025 mmol/kg, immediately followed by a 25-ml saline flush using a power injector.

RFA procedures

Percutaneous RFA was performed by under general anesthesia using an S-1500 radiofrequency therapeutic apparatus (MedSphere® International, Shanghai, China). All interventional procedures were conducted by one of the two interventional radiologists who had 11 and 8 years of interventional operation experience, respectively. The negative patch was pasted to the skin of back, thigh, or waist because of sparse hair. The different models and specifications of ablation needles were chosen according to the size of tumor. Then, the needle tip was sent to distal edge of tumor, and the active umbrella-like structure of needle tip was put up to a certain degree based on the location of the tumor and needle. The initial power was set at 30 to 50 watts, and the ablation time was 6 to 10 min according to the chosen needles. The radiofrequency therapeutic apparatus would automatically stop when the targeted tissue impedance reached 500 Ω, and the tissue temperature reached 70°C to 100°C. If necessary, the position of the needle tip was adjusted, and the procedure was repeated to ensure the complete ablation of the tumor. The needle track was ablated to prevent track implantation and bleeding before the needle was pulled out. The RFA was finished when the hyperechoic ablation surrounding was large enough to cover the entire tumor and the ablative margin (at least 5 mm of normal liver parenchyma surrounding the tumor).

Follow-up and outcome analysis

After RFA, the ultrasound (US), contrast-enhanced CT/MRI, and serum alpha fetoprotein (AFP) examination were performed every 3 months for the first year and then every 4–6 months thereafter. The outcome in this study was assessed by RFS. According to previous literature, the RFS was considered as the interval between the initial date of interventional therapy and the date of the first tumor recurrence or last follow-up visit before 1 October 2021. In our study, the tumor recurrence was defined as local recurrence (LR) and intrahepatic distant recurrence (IDR), and extrahepatic metastasis. Among them, LR was considered as the appearance of new tumor nodules at the surrounding of ablation zone, and IDR was considered as the appearance of new tumor nodules not around the ablation area.

Clinical-radiological characteristics analysis

In this study, various clinical data—including age, sex, cause of underlying liver disease (chronic hepatitis B/chronic hepatitis C/alcoholic liver disease), Child–Pugh score (A/B), number of tumors, and tumor size—were recorded. In addition, a series of laboratory findings—including albumin, total bilirubin, prothrombin time–international normalized ratio (PT-INR), AFP, and protein induced by vitamin K absence or antagonist-II (PIVKA-II)—were simultaneously analyzed.

As for radiological findings, two radiologists (with 12 and 19 years of experience in abdominal imaging, respectively) evaluated the MRI images on a picture archiving communication system based on the LI-RADS v2018, which represented a standard description of terminology and criteria for interpretation of liver observations. Another observer (with more than 30 years of experience in abdominal diagnostic) was invited for an opinion when there was inconsistency, and a majority decision was finally obtained and served for further study.

According to LI-RADS v2108 diagnostic algorithm, arterial phase hyperenhancement (APHE) (rim/non-rim), washout (not peripheral/peripheral), enhancing capsule, delayed central enhancement, targetoid restriction on DWI and targetoid hepatobiliary phase (HBP) appearance, ancillary imaging features (including corona enhancement, fat sparing in solid mass, restricted diffusion, mild-moderate T2 hyperintensity, iron sparing in solid mass, HBP hypointensity, nodule-in-nodule architecture, mosaic architecture, fat in mass, more than adjacent liver, and blood products in mass), and LI-RADS categorization (LR-3/4/5/M) were analyzed and recorded. Moreover, tumor size (the maximum diameter of the tumor); tumor margins (well-/ill-defined); signal intensity (SI) on T1-weighted, T2-weighted; and arterial, portal venous, and delayed phase images were also analyzed. The SI in this study was recognized as hyperintense, hypointense, or isointense compared with the adjacent hepatic parenchyma.

Construction and validation of the nomogram

Gadoxetic acid–enhanced MRI features based on LI-RADS v2018 diagnostic algorithm, served as predictive risk factors, were build the preliminary predictive model of the prognostic of sHCC after RFA. In addition, the utility of the preliminary MRI-based nomogram was verified by the calibration curve and concordance index (C-index). Moreover, the decision curve analysis (DCA) was conducted to determine the clinical utility of the nomogram *via* calculating the net benefits at various threshold probabilities.

Statistical analysis

Statistical analysis was conducted using SPSS 26.0 (IBM, Armonk, NY) and R project version 4.1.2 (http://www.r-project.org/). The categorical variables were showed as numbers (percentages). Uni- and multivariable analyses for RFS were assessed using the Cox proportional hazards model, and multicollinearity test was simultaneously conducted. The survival curve was conducted by Kaplan–Meier analyses *via* the log-rank test. Moreover, the interobserver agreement on LI-RADS v2018 imaging features in our study was valuated using the Cohen κ coefficient. The agreement was divided as five levels according to κ values as follows: poor (< 0.20), fair (0.21–0.40), moderate (0.41–0.60) and well (0.61–0.80), and excellent (0.81–1.00).

The predictive nomogram integrating LI-RADS v2018 imaging features and clinical parameters was formulated using in R project. The predictive performance of the constructed nomogram was evaluated by calibration curves and C-index. All tests were two-sided, and P-value < 0.05 was considered as statistically significance.

Results

Patients characteristics in both training and validation groups

This study enrolled 204 patients, which were divided into training (n = 153) and validation (n = 51) groups. There were no significant differences in age, sex, cause of underlying liver disease, Child–Pugh score, number of tumors, tumor sized, various laboratory data, and various conventional imaging features and LI-RADS v2018 imaging findings between the training and validation groups. All detailed data about patient characteristics in both groups are presented in Table 1. In addition, there was no significant difference between the training and validation groups. Among the overall cohort, the median follow-up was 20.3 months (range from 3.4 to 36.0 months). During the follow-up, the recurrence rate was 36.7% (75/204), observed in all patients, among which 10 patients (13.3%) showed LR, 57 patients (72.1%) showed IDR, and 6 (7.6%) had extrahepatic recurrence. Moreover, the 1- and 2-year RFS rates were 87.7% and 75.4%, respectively.

TABLE 1 The clinical, pathological, and radiological characteristics of the study population.

Variables	Training group (n = 153)	Validation group (n = 51)	P-value
Age (years)			0.290
<60	65 (42.5)	26 (51.0)	
≥60	88 (57.5)	25 (49.0)	
Sex (M/W)			0.686
Woman	76 (49.7)	27 (52.9)	
Man	77 (50.3)	24 (47.1)	
Cause of underlying liver disease			0.105
Chronic hepatitis B	101 (66.0)	26 (51.0)	
Chronic hepatitis C	47 (30.7)	22 (43.1)	
Alcoholic liver disease	5 (3.3)	3 (5.9)	
Child–Pugh score			0.620
A	122 (79.7)	39 (76.5)	
B	31 (20.3)	12 (23.5)	
Number of tumors			0.656
1	110 (71.9)	35 (68.6)	
2–3	43 (28.1)	16 (31.4)	
Tumor size (cm)			0.417
≤3	108 (70.6)	39 (76.5)	
3–5	45 (29.4)	12 (23.5)	
Laboratory finding			
Albumin (g/dl)			0.169
Normal	76 (49.7)	31 (60.8)	
Abnormal	77 (50.3)	20 (39.2)	
Total bilirubin (mg/dl)			0.514
Normal	64 (41.8)	24 (47.1)	
Abnormal	89 (58.2)	27 (52.9)	
PT-INR			0.146
Normal	72 (47.1)	30 (58.8)	
Abnormal	81 (52.9)	21 (41.2)	
AFP (>100 ng/ml)			0.124
Normal	77 (50.3)	32 (62.7)	
Abnormal	76 (49.7)	19 (37.3)	
PIVKA-II (>40 mAU/ml)			0.808
Normal	75 (49.0)	26 (51.0)	
Abnormal	78 (51.0)	25 (49.0)	

(Continued)

10.3389/fonc.2023.975216

TABLE 1 Continued

Variables	Training group (n = 153)	Validation group (n = 51)	P-value
Conventional imaging features			
Tumor margin			0.073
Well-defined	62 (40.5)	28 (54.9)	
Ill-defined	91 (59.5)	23 (45.1)	
Diffusion-weighted imaging			0.322
Hyperintense	113 (73.9)	34 (66.7)	
Iso-intense	40 (26.1)	17 (33.3)	
Hypointense	0 (0%)	0 (0%)	
Signal on arterial phase			0.354
Hypointense	47 (30.7)	11 (21.6)	
Isointense	50 (32.7)	18 (35.3)	
Hyperintense	56 (36.6)	22 (43.1)	
Signal on portal phase			0.590
Hypointense	52 (34.0)	20 (39.2)	
Isointense	51 (33.3)	16 (31.4)	
Hyperintense	50 (32.7)	15 (29.4)	
Signal on delayed phase			0.262
Hypointense	45 (29.4)	18 (35.3)	
Isointense	62 (40.5)	16 (31.4)	
Hyperintense	46 (30.1)	17 (33.3)	
LI-RADS v2018 imaging findings			
APHE			0.727
Non-rim APHE	104 (68.0)	36 (70.6)	
Rim APHE	49 (32.0)	15 (29.4)	
Washout			0.851
Not peripheral Washout	115 (75.2)	39 (76.5)	
Peripheral Washout	38 (24.8)	12 (23.5)	
Enhancing capsule			0.195
Presence	77 (50.3)	31 (60.8)	
Absence	76 (49.7)	20 (39.2)	
Delayed central enhancement			1.000
Presence	114 (74.5)	38 (74.5)	
Absence	39 (25.5)	13 (25.5)	
Targetoid restriction on DWI			0.667
Presence	104 (68.0)	33 (64.7)	
Absence	49 (32.0)	18 (35.3)	
Targetoid HBP appearance			0.703
Presence	118 (77.1)	38 (74.5)	
Absence	35 (22.9)	13 (25.5)	
Corona enhancement			1.000
Presence	120 (78.4)	40 (78.4)	
Absence	33 (21.6)	11 (21.6)	
Fat sparing in solid mass			0.920
Presence	122 (79.7)	41 (80.4)	
Absence	31 (20.3)	10 (19.6)	
Restrict diffusion			0.627
Presence	72 (47.1)	26 (51.0)	
Absence	81 (52.9)	25 (49.0)	
Mild-moderate T2 hyperintensity			0.284
Presence	122 (79.7)	37 (72.5)	
Absence	31 (20.3)	14 (27.5)	
Iron sparing in solid mass			0.766
Presence	120 (78.4)	41 (80.4)	
Absence	33 (21.6)	10 (19.6)	
Hepatobiliary phase hypointensity			0.513
Presence	113 (73.9)	40 (78.4)	
Absence	40 (26.1)	11 (21.6)	
Nodule-in-nodule architecture			0.092
Presence	125 (81.7)	36 (70.6)	
Absence	28 (18.3)	15 (29.4)	
Mosaic architecture			0.284
Presence	122 (79.7)	37 (72.5)	
Absence	31 (20.3)	14 (27.5)	
Fat in mass, more than adjacent liver			0.458
Presence	116 (75.8)	36 (70.6)	
Absence	37 (24.2)	15 (29.4)	
Blood products in mass			0.508
Presence	118 (77.1)	37 (72.5)	
Absence	35 (22.9)	14 (27.5)	
LI-RADS categorization			0.657

(Continued)

TABLE 1 Continued

Variables	Training group (n = 153)	Validation group (n = 51)	P-value
LR-3	29 (19.0)	8 (15.7)	
LR-4	34 (22.2)	12 (23.5)	
LR-5	63 (41.2)	21 (41.2)	
LR-M	27 (17.6)	10 (19.6)	

PT-INR, prothrombin time-international normalized ratio; alphafetoprotein, AFP, PIVKA-II, protein induced by vitamin K absence or antagonist-II; APHE, arterial phase hyperenhancement; DWI, diffusion weighted imaging; HBP, hepatobiliary phase; LI-RADS, Liver Imaging Reporting and Data System.

Independent predictive radiological-clinical factors for RFS in patients with sHCC with RFA

In univariate logistic regression analysis, it is shown that tumor size, AFP level, rim APHE, targetoid restriction on DWI, and number of tumors were correlated with recurrence in the training group. Then, in the multivariate logistic regression analysis, AFP > 100 ng/ml (HR, 2.006; 95% CI, 1.111–3.621; P = 0.021), rim APHE (HR, 2.751; 95% CI, 1.511–5.011; P = 0.001), and targetoid restriction on DWI (HR, 3.289; 95% CI, 1.832–5.906; P < 0.001) were considered as the independent risk characteristics for recurrence in patients with sHCC treated with RFA as the first-line therapy (Figures 2, 3). The detailed information is listed in Table 2. Moreover, to verify the complex collinearity among the variables, the multicollinearity test was performed, which showed that there was no multicollinearity among three variables. The variance inflation factors were 1.33, 1.21, and 1.17, respectively, which are all less than 5.

In terms of the assessment of interobserver agreement of LI-RADS v2018 imaging features, the results showed that APHE (κ = 0.881), washout (κ = 0.910), enhancing "capsule" (κ = 0.811), delayed central enhancement (κ = 0.832), targetoid restriction on DWI (κ = 0.890), targetoid HBP appearance (κ = 0.865), mild-moderate T2 hyperintensity (κ = 0.882), HBP hypointensity (κ = 0.878), restricted diffusion (κ = 0.911), and blood products in mass (κ = 0.812) exhibited excellent interobserver agreement. Corona enhancement (κ = 0.871), fat sparing in solid mass (κ = 0.773), iron sparing in solid mass (κ = 0.767), nodule-in-nodule architecture (κ = 0.756), mosaic architecture (κ = 0.723), fat in mass, more than adjacent liver (κ = 0.798), and LI-RADS categorization (κ = 0.760) exhibited well interobserver agreement.

Construction and validation of predictive nomogram for RFS

In this study, a predictive nomogram model including LI-RADS v2018 imaging findings and clinical features was established, which contains AFP > 100 ng/ml, rim APHE, and targetoid restriction on DWI for RFS after patients with sHCC treated with RFA as the first-line therapy (Figure 4A). The calibration curves of the developed nomogram for both the training and validation groups exhibited a good consistency between estimation and observation at 12 and 24 months after RFA (Figures 4B–E). As for C-index in the training group, the C-index for RFS prediction with the integrated nomogram (AFP + rim APHE + targetoid restriction on DWI) was 0.758 (95% CI, 0.679–0.837), which was higher than the C-index by other independent risk features. Similarly, in the validation group, the C-index for RFS prediction with the integrated nomogram (AFP + rim APHE + targetoid restriction on DWI) was 0.807 (95% CI, 0.712–0.904), showing the best prediction capacity (Table 3).

On DCA, the developed nomogram showed a best net benefit with a wider range of threshold probability compared with the separate LI-RADS v2018 imaging findings and clinical features, indicating improved performance for predicting 12- and 24-month RFS (Figure 5).

Discussion

In this study, we found that the clinical feature (AFP) and LI-RADS v2018 imaging features on gadoxetic acid–enhanced MRI (rim APHE and targetoid restriction on DWI) are the independent risk factors for recurrence of sHCC after RFA. Moreover, a novel integrated nomogram based on clinical parameters and MRI

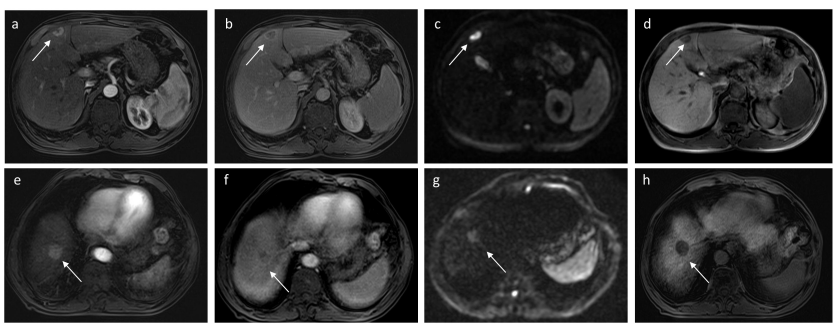

FIGURE 2
A 56-year-old man with sHCC was observed with early IDR after receiving RFA as the first-line therapy. Axial arterial **(A)** and delayed phases **(B)** show a well-defined tumor (white arrow) with rim APHE in hepatic segment IV. On the DWI **(C)**, the tumor exhibits targetoid restriction and the tumors showed targetoid HBP appearance on hepatobiliary phase **(D)**. Another 76-year-old man with HCC was observed with no recurrence after RFA during 13 months of the follow-up period. Axial arterial **(E)** and delayed phases **(F)** show a well-defined tumor (white arrow) with APHE in hepatic segment VIII. On the DWI **(G)**, the tumor exhibits appeared restriction, and the tumors exhibit completely hypointense on hepatobiliary phase **(H)**.

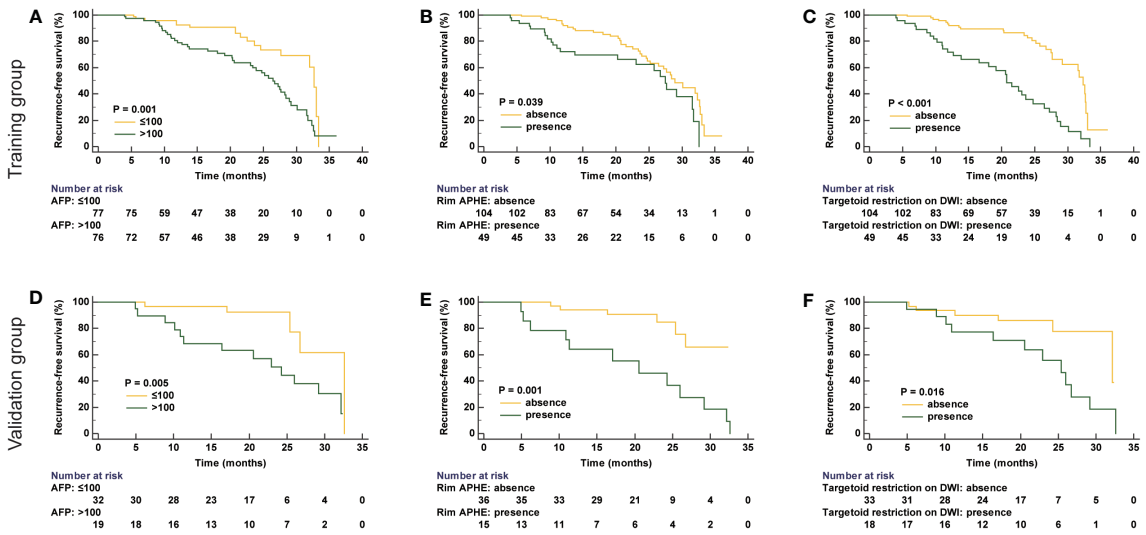

FIGURE 3
The RFS of each group in both training **(A–C)** and validation groups **(D–F)**.

features was constructed to predict 12- and 24-month RFS of patients with sHCC after curative RFA as the first-line therapy.

As is known, LI-RADS category, a means of standard imaging-based diagnosis of HCC, has recently been applied in the classification or differentiation diagnosis of liver tumors (22). Intriguingly, in several previous studies, HCC with several imaging appearances from LI-RADS category, such as target-like imaging morphology is often closely associated with unfavorable biomarkers (9, 23). However, few studies have focused on the application of the LI-RADS category on the prognosis evaluation of sHCC treated with RFA as the first-line therapy. In our study, on the basis of LI-RADS v2018 category, we found that targetoid imaging features including rim APHE and targetoid restriction on gadoxetic acid–enhanced MRI were two of the valuable risk factors for recurrence of patients with sHCC following RFA. In addition, a combined nomogram model integrating LI-RADS imaging features in this study was constructed to enable clinicians to handily assess the individually recurrence risk of patients with sHCC, avoiding vague recurrence risk assessments or overly complicated recurrence risk calculations. According to the presented nomogram model, patients with a low recurrence risk are the optimal candidates of RFA as the first-line treatment. As to patients with HCC with a high recurrence risk, more therapies such as combined TACE and surgical resection may be the first choice. In addition, the postoperative follow-up needs to be earlier and more frequent for those patients.

In this study, rim APHE was one of the significant LI-RADS v2018 imaging features predictive of post-RFA recurrence of patients with sHCC. According to LI-RADS category, rim APHE was not a major feature of HCC, rather an imaging feature of cholangiocarcinoma or combined hepatocellular cholangiocarcinoma. In our study, 31.4% of patients in this cohort were showed rim APHE, which is slightly higher than 5%–13% reported in the previous literature (24). Although HCC presenting with rim APHE is relatively rare, HCC with rim APHE seems to be more invasive. A previous study has reported HCC with rim APHE expresses higher carbonic anhydrase IX and epithelial cell adhesion molecule levels, which are hypoxia- and stemness-related markers, respectively (25). Moreover, sHCCs presenting with rim APHE may be frequently associated with growth patterns and invasive pathophysiological features, such as microvascular invasion, abundant intratumoral fibrous stroma, tumor necrosis, and low microvascular density (25). As such, these aforementioned studies may explain our results that rim APHE was an independent recurrence predictor for patients with sHCC treated with RFA as the first-line therapy. In addition, similar results have been reported in some surgically resected HCC studies. For instance, Moon et al. have reported that HCCs categorized as LR-M with rim APHE often showed worst prognosis after surgical resection, meaning that rim APHE was helpful for assessing the postoperative prognosis of HCC after further stratification of LR-M on preoperative MRI (12). Moreover, in another recent study reported by Kang et al., rim APHE at gadoxetate-enhanced MRI was used to distinguish non-proliferative class HCC from proliferative class HCC, which was an independent factor for poor survival of HCC (26). In addition, this imaging feature can also be used to assess OS and incidence of extrahepatic metastasis in the proliferative class HCC.

Targetoid restriction on DWI was another LI-RADS v2018 imaging feature predictive of post-RFA recurrence of patients with sHCC. Similar to rim APHE, targetoid restriction on DWI, as one of the targetoid imaging appearances, was another typical imaging feature of non-HCC malignancies (27). Such imaging feature was showed as restricted diffusion in tumor periphery on DWI with less restricted diffusion in tumor center, which may reflect peripheral hypercellularity and central stromal fibrosis or ischemia (28). Moreover, the increased diffusivity of the loose fibrotic component with necrosis could be the main contributor for central darkness on DWI. Thus, the above histopathologic properties are highly correlated with targetoid restriction on DWI and consistent with our results showing that targetoid restriction was another independent risk factor for recurrence of sHCC after RFA. On the other hand, some studies have also shown that the targetoid restriction on DWI may be associated with some biologically invasive characteristics, such as CK-19. For example, Hu et al. have reported that MR features with targetoid appearances based on LI-RDAS v2017, such as targetoid appearance on DWI (P = 0.001), were more frequently observed in

10.3389/fonc.2023.975216

TABLE 2 Uni- and multivariate Cox analyses for risk factors for RFS in sHCC after RFA.

Parameters		Univariate analysis		Multivariate analysis	
		HR (95% CI)	P-value	HR (95% CI)	P-value
Age (years)	<60	Reference			
	≥60	1.395 (0.829–2.346)	0.210		
Sex	Female	Reference			
	Male	0.730 (0.439–1.214)	0.225		
Cause of underlying liver disease	Chronic hepatitis B	Reference			
	Chronic hepatitis C	0.880 (0.520–1.491)	0.635		
	Alcoholic liver disease	0.572 (0.134–2.437)	0.450		
Child–Pugh score	A	Reference			
	B	1.316 (0.706–2.453)	0.388		
Number of tumors	1	Reference			
	2–3	1.692 (1.004–2.852)	**0.048***	0.916 (0.516–1.626)	0.765
Tumor size (cm)	≤3	Reference			
	3–5	1.872 (1.110–3.158)	**0.019***	1.576 (0.927–2.680)	0.093
Laboratory finding					
Albumin (g/dl)	Normal	Reference			
	Abnormal	0.781 (0.468–1.303)	0.344		
Total bilirubin (mg/dl)	Normal	Reference			
	Abnormal	1.051 (0.623–1.772)	0.852		
PT-INR	Normal	Reference			
	Abnormal	1.189 (0.713–1.985)	0.507		
AFP (>100 ng/ml)	Normal	Reference			
	Abnormal	2.614 (1.473–4.640)	**0.001***	2.006 (1.111–3.621)	**0.021***
PIVKA-II (>40 mAU/mL)	Normal	Reference			
	Abnormal	1.158 (0.690–1.944)	0.579		
Conventional imaging features					
Tumor margin	Well-defined	Reference			
	Ill-defined	0.666 (0.398–1.114)	0.122		
Diffusion-weighted imaging	Hypointense	Reference			
	Hyperintense	0.872 (0.485-1.567)	0.646		
Signal on arterial phase	Hypointense	Reference			
	Isointense	0.771 (0.405–1.468)	0.429		
	Hyperintense	0.681 (0.373–1.245)	0.213		
Signal on portal phase	Hypointense	Reference			
	Isointense	1.088 (0.583–2.029)	0.791		
	Hyperintense	1.179 (0.623–2.231)	0.614		
Signal on delayed phase	Hypointense	Reference			
	Isointense	1.113 (0.591–2.097)	0.740		
	Hyperintense	1.164 (0.589–2.303)	0.662		

(Continued)

10.3389/fonc.2023.975216

TABLE 2 Continued

Parameters		Univariate analysis		Multivariate analysis	
		HR (95% CI)	P-value	HR (95% CI)	P-value
LI-RADS v2018 imaging findings					
APHE	Non-rim APHE	Reference			
	Rim APHE	2.047 (1.192–3.516)	**0.009***	2.751 (1.511–5.011)	**0.001***
Washout	Not peripheral washout	Reference			
	Peripheral washout	1.157 (0.653–2.053)	0.617		
Enhancing capsule	Presence	Reference			
	Absence	0.955 (0.571–1.596)	0.859		
Delayed central enhancement	Presence	Reference			
	Absence	1.381 (0.774–2.464)	0.275		
Targetoid restriction on DWI	Presence	Reference			
	Absence	2.833 (1.693–4.743)	< **0.001***	3.289 (1.832–5.906)	<**0.001***
Targetoid HBP appearance	Presence	Reference			
	Absence	1.420 (0.806–2.504)	0.225		
Corona enhancement	Presence	Eeference			
	Absence	0.886 (0.478–1.642)	0.700		
Fat sparing in solid mass	Presence	Reference			
	Absence	1.588 (0.891–2.831)	0.117		
Restrict diffusion	Presence	Reference			
	Absence	1.043 (0.625–1.741)	0.872		
Mild-moderate T2 hyperintensity	Presence	Reference			
	Absence	0.702 (0.363–1.359)	0.294		
Iron sparing in solid mass	Presence	Reference			
	Absence	0.957 (0.509–1.798)	0.891		
Hepatobiliary phase hypointensity	Presence	Reference			
	Absence	0.890 (0.495–1.600)	0.697		
Nodule-in-nodule architecture	Presence	Reference			
	Absence	0.968 (0.475–1.975)	0.929		
Mosaic architecture	Presence	Reference			
	Absence	1.278 (0.697–2.346)	0.428		
Fat in mass, more than adjacent liver	Presence	Reference			
	Absence	1.071 (0.576–1.990)	0.829		
Blood products in mass	Presence	Reference			
	Absence	1.017 (0.561–1.845)	0.955		
LI-RADS categorization	LR-3	Reference			
	LR-4	1.062 (0.472–2.390)	0.885		
	LR-5	1.455 (0.709–2.986)	0.307		
	LR-M	0.990 (0.429–2.288)	0.982		

Bold represents statistically significant.

RFS, recurrence-free survival; sHCC, small hepatocellular carcinoma; RFA, radiofrequency ablation; PT-INR, prothrombin time-international normalized ratio; alphafetoprotein, AFP, PIVKA-II, protein induced by vitamin K absence or antagonist-II; APHE, arterial phase hyperenhancement; DWI, diffusion weighted imaging; HBP, hepatobiliary phase; LI-RADS, Liver Imaging Reporting and Data System.

10.3389/fonc.2023.975216

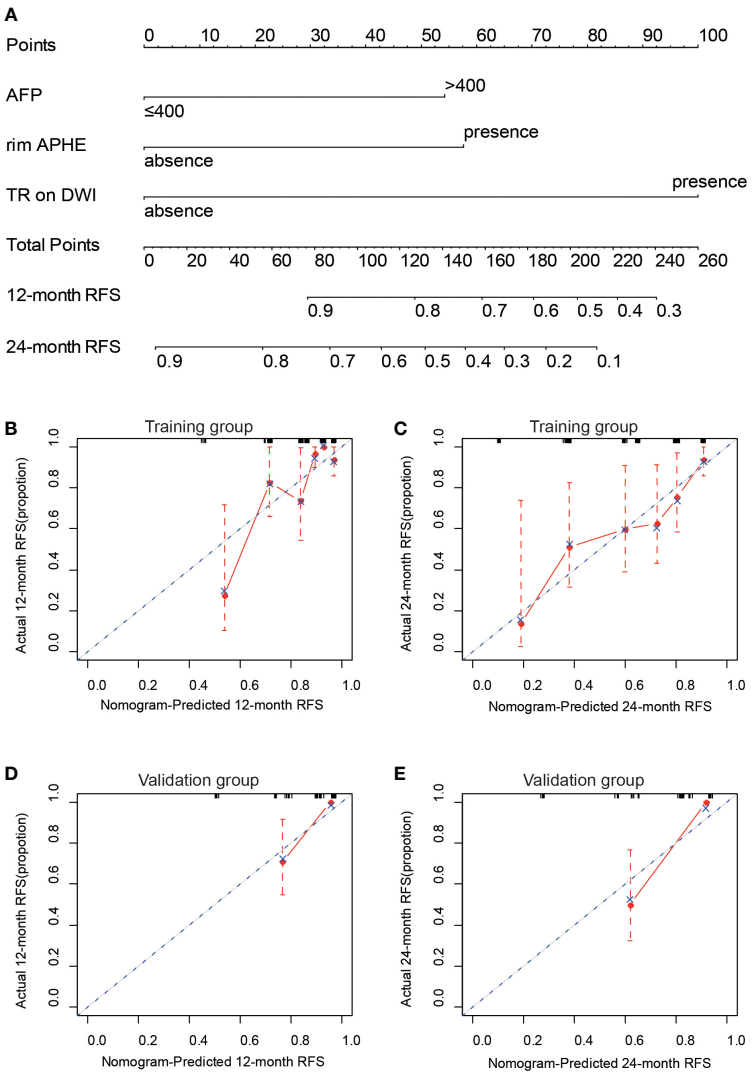

FIGURE 4
Construction and validation of nomogram for predicting RFS of patients with sHCC with RFA as the first-line therapy. **(A)** Integrated nomogram for predicting probability of 12- and 24-month after RFA of sHCC. The calibration curves for the nomogram-predicted 12-month RFS **(B)** and the nomogram-predicted 24-month RFS **(C)** in the training cohort and the nomogram-predicted 12-month RFS **(D)** and the nomogram-predicted 24-month RFS **(E)** in the validation cohort.

comparison with CK19-negative HCCs. These results may be the potential reason for worse post-RFA outcomes of patients with HCC presenting with targetoid restriction on DWI (25).

In addition to imaging features based on LI-RDAS v2018 in this study, clinical characteristics were incorporated into the predictive model for further improve the practicality and predictive efficiency of the developed nomogram in clinic. In our study, AFP (>100 ng/ml)

TABLE 3 Prediction performance of nomogram and independent risk factors in training and validation cohort.

Factors	Training group		Validation group	
	C-index	95% CI	C-index	95% CI
AFP	0.613	0.543–0.683	0.706	0.588–0.825
Rim APHE	0.585	0.511–0.659	0.709	0.584–0.833
Targetoid restriction on DWI	0.679	0.612–0.746	0.634	0.499–0.768
Nomogram (AFP + rim APHE)	0.653	0.569–0.736	0.794	0.703–0.885
Nomogram (AFP + targetoid restriction on DWI)	0.734	0.664–0.804	0.739	0.601–0.876
Nomogram (AFP + rim APHE + targetoid restriction on DWI)	0.758	0.679–0.837	0.807	0.712–0.904

C-index, concordance index; AFP, alphafetoprotein; APHE, arterial phase hyperenhancement; DWI, diffusion weighted imaging.

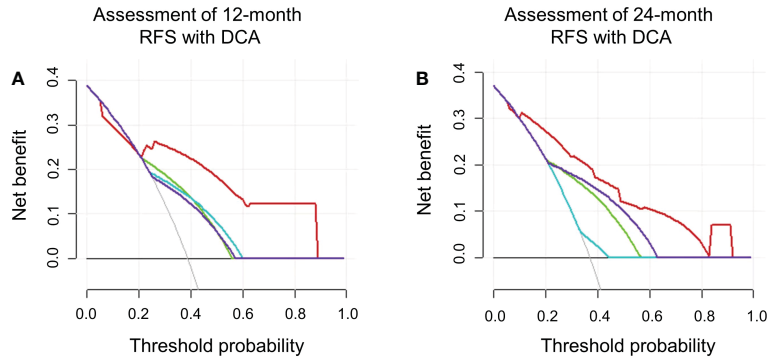

FIGURE 5
The decision curve analyses in terms of 12 **(A)** and 24 **(B)** months. RFS depicted integrated nomogram comprising the clinical feature (AFP) and LI-RADS v2018 imaging features on gadoxetic acid–enhanced MRI (rim APHE and targetoid restriction on DWI). Red line represents integrated nomogram (AFP + rim APHE + targetoid restriction on DWI); purple line represents targetoid restriction on DWI; green line represents AFP; blue line represents rim APHE.

was considered as a clinical independent risk factor for post-RFA recurrence of patients with sHCC. As is well known, AFP is one of the most commonly used markers of HCC in clinic (29, 30). Several present studies have increasingly showed that the AFP level was closely associated with the cellular differentiation, microvascular invasion, and tumor prognosis. For example, in a recent study, Hu et al. have reported that the AFP level was identified as one of the independent risk factors for early recurrence after ablation (10). However, in their study, the risk of postoperative recurrence was greatest when AFP was greater than 400 ng/ml. Similar results were seen in the assessment of outcomes after TACE of HCC (31). Song and coworkers have demonstrated that the AFP level (>13.2 ng/ml) was identified as clinical risk factor for recurrence after TACE of HCC (32). Note that AFP (≤100 ng/ml) was normal in more than 50% of patients in our cohort. With different cutoff values of AFP, the effectiveness of the AFP level in the prediction model will also change.

There were several limitations in this study. First, the present study is a retrospective and single-center study; therefore, reselection and verification biases were inevitable. Only patients with sHCC that fully met RFA as the first-line therapy were enrolled, and patients with poor-quality MR images or incomplete clinical data were excluded; thus, the results in our study may not represent the true spectrum of HCC after RFA. Moreover, in this study, sHCC (<5 cm) was included in the study. If we only conducted RFA treatment for patients with sHCC (<3 cm), then the clinical effect might be better (33). For patients with HCC of 3–5 cm, TACE + RFA may achieve better efficacy (34). Second, we only focused on the MRI features according to the LI-RDAS v2018 several MRI features reported in the previous literature such as peritumoral signal on different sequences that were not analyzed in our study. Further sophisticated investigations with more samples in the multicenters should be conducted. Third, only pre-RFA clinical-radiological features were analyzed, and the correlation analysis between detailed pathological characteristics and prognosis of HCC after RFA was lacking. Finally, for practicability in clinic and easy popularity, the predictive models were only integrating the conventional and standard MRI features. In addition, genomic directed stratifications in clinical trial design are needed to be considered in future study.

In conclusion, the predictive model based on LI-RADS v2018 MRI features and clinical factors could be used to assess the prognosis of patients before RFA as the first-line treatment, which contributed to screening out the high probability of recurrence in patients with sHCC treated with RFA. Moreover, such an integrated nomogram may be used as a convenient method for facilitating clinicians to make precise and personalized management decisions.

Data availability statement

The original contributions presented in the study are included in the article/supplementary material. Further inquiries can be directed to the corresponding authors.

Author contributions

RW, HX, and ML designed this study. RW, HX, WC, LJ, and ZM collected the patients' data. LW, HW, and KC conducted the statistical analysis of this study. RW and HX wrote the manuscript. ML revised and supervised the manuscript. All authors contributed to the article and agreed to the submitted version.

Funding

This study has received funding by National Natural Science Foundation of China (no. 61976238), Shanghai "Rising Stars of Medical Talent" Youth Development Program "Outstanding Youth Medical Talents" [SHWJRS (2021)-99], Scientific Research Program of Shanghai Science and Technology Commission (Reference: 20Y11902900), and the "Future Star" of famous doctors' training plan of Fudan University.

Conflict of interest

The authors declare that the research was conducted in the absence of any commercial or financial relationships that could be construed as a potential conflict of interest.

Publisher's note

References

1. Llovet JM, Montal R, Sia D, Finn RS. Molecular therapies and precision medicine for hepatocellular carcinoma. *Nat Rev Clin Oncol* (2018) 15:599–616. doi: 10.1038/s41571-018-0073-4

2. Raoul JL, Forner A, Bolondi L, Cheung TT, Kloeckner R, de Baere T. Updated use of TACE for hepatocellular carcinoma treatment: How and when to use it based on clinical evidence. *Cancer Treat Rev* (2019) 72:28–36. doi: 10.1016/j.ctrv.2018.11.002

3. Lee DH, Lee JM, Lee JY, Kim SH, Yoon JH, Kim YJ, et al. Radiofrequency ablation of hepatocellular carcinoma as first-line treatment: Long-term results and prognostic factors in 162 patients with cirrhosis. *Radiology* (2014) 270:900–9. doi: 10.1148/radiol.13130940

4. Leone P, Solimando AG, Fasano R, Argentiero A, Malerba E, Buonavoglia A, et al. The evolving role of immune checkpoint inhibitors in hepatocellular carcinoma treatment. *Vaccines* (2021) 9(5):532. doi: 10.3390/vaccines9050532

5. Awad T, Thorlund K, Gluud C. Cryotherapy for hepatocellular carcinoma. *Cochrane Database Syst Rev* (2009) 7(4):D7611. doi: 10.1002/14651858.CD007611.pub2

6. Zongyi Y, Xiaowu L. Immunotherapy for hepatocellular carcinoma. *Cancer Lett* (2020) 470:8–17. doi: 10.1016/j.canlet.2019.12.002

7. Dai Y, Qiang W, Lin K, Gui Y, Lan X, Wang D. An immune-related gene signature for predicting survival and immunotherapy efficacy in hepatocellular carcinoma. *Cancer Immunol Immunother* (2021) 70:967–79. doi: 10.1007/s00262-020-02743-0

8. Song KD, Rhim H, Lee MW, Kim YS, Kang TW. Intrahepatic distant recurrence after radiofrequency ablation for hepatocellular carcinoma: Precursor nodules on pre-procedural gadoxetic acid-enhanced liver magnetic resonance imaging. *Acta Radiol* (2017) 58:778–85. doi: 10.1177/0284185116673122

9. Lee DH, Lee JM, Lee JY, Kim SH, Kim JH, Yoon JH, et al. Non-hypervascular hepatobiliary phase hypointense nodules on gadoxetic acid-enhanced MRI: Risk of HCC recurrence after radiofrequency ablation. *J Hepatol* (2015) 62:1122–30. doi: 10.1016/j.jhep.2014.12.015

10. Hu C, Song Y, Zhang J, Dai L, Tang C, Li M, et al. Preoperative gadoxetic acid-enhanced MRI based nomogram improves prediction of early HCC recurrence after ablation therapy. *Front Oncol* (2021) 11:649682. doi: 10.3389/fonc.2021.649682

11. Yang Y, Chen Y, Ye F, Cao X, Xin Y, Wang Y, et al. Late recurrence of hepatocellular carcinoma after radiofrequency ablation: A multicenter study of risk factors, patterns, and survival. *Eur Radiol* (2021) 31:3053–64. doi: 10.1007/s00330-020-07460-x

12. Moon JY, Min JH, Kim YK, Cha D, Hwang JA, Ko SE, et al. Prognosis after curative resection of single hepatocellular carcinoma with a focus on LI-RADS targetoid appearance on preoperative gadoxetic acid-enhanced MRI. *Korean J Radiol* (2021) 22:1786. doi: 10.3348/kjr.2020.1428

13. Cha DI, Jang KM, Kim SH, Kang TW, Song KD. Liver imaging reporting and data system on CT and gadoxetic acid-enhanced MRI with diffusion-weighted imaging. *Eur Radiol* (2017) 27:4394–405. doi: 10.1007/s00330-017-4804-1

14. Morisaka H, Seno D, Sakurai Y, Sano K, Akamine Y, Ichikawa T, et al. Quantitative analysis of gadoxetic acid-enhanced MRI for the differential diagnosis of focal liver lesions: Comparison between estimated intralesional gadoxetic acid retention by T1 mapping and conventional processing methods. *Eur J Radiol* (2021) 138:109620. doi: 10.1016/j.ejrad.2021.109620

15. Choi SH, Lee SS, Park SH, Kim KM, Yu E, Park Y, et al. LI-RADS classification and prognosis of primary liver cancers at gadoxetic acid-enhanced MRI. *Radiology* (2019) 290:388–97. doi: 10.1148/radiol.2018181290

16. Park S, Joo I, Lee DH, Bae JS, Yoo J, Kim SW, et al. Diagnostic performance of LI-RADS treatment response algorithm for hepatocellular carcinoma: Adding ancillary features to MRI compared with enhancement patterns at CT and MRI. *Radiology* (2020) 296:554–61. doi: 10.1148/radiol.2020192797

17. Granito A, Galassi M, Piscaglia F, Romanini L, Lucidi V, Renzulli M, et al. Impact of gadoxetic acid (gd-eob-dtpa)-enhanced magnetic resonance on the non-invasive diagnosis of small hepatocellular carcinoma: a prospective study. *Aliment Pharmacol Ther* (2013) 37(3):355–63. doi: 10.1111/apt.12166

18. Renzulli M, Biselli M, Brocchi S, Granito A, Vasuri F, Tovoli F, et al. New hallmark of hepatocellular carcinoma, early hepatocellular carcinoma and high-grade dysplastic nodules on gd-eob-dtpa mri in patients with cirrhosis: A new diagnostic algorithm. *Gut* (2018) 67(9):1674–82. doi: 10.1136/gutjnl-2017-315384

19. Kim SW, Joo I, Kim HC, Ahn SJ, Kang HJ, Jeon SK, et al. LI-RADS treatment response categorization on gadoxetic acid-enhanced MRI: Diagnostic performance compared to mRECIST and added value of ancillary features. *Eur Radiol* (2020) 30:2861–70. doi: 10.1007/s00330-019-06623-9

20. Kim MY, Joo I, Kang HJ, Bae JS, Jeon SK, Lee JM. LI-RADS m (LR-m) criteria and reporting algorithm of v2018: Diagnostic values in the assessment of primary liver cancers on gadoxetic acid-enhanced MRI. *Abdom Radiol (NY)* (2020) 45:2440–8. doi: 10.1007/s00261-020-02545-z

21. Jeon SK, Joo I, Lee DH, Lee SM, Kang HJ, Lee KB, et al. Combined hepatocellular cholangiocarcinoma: LI-RADS v2017 categorisation for differential diagnosis and prognostication on gadoxetic acid-enhanced MR imaging. *Eur Radiol* (2019) 29:373–82. doi: 10.1007/s00330-018-5605-x

22. Min JH, Kim SH, Hwang JA, Hyun SH, Ha SY, Choi SY, et al. Prognostic value of LI-RADS category on gadoxetic acid-enhanced MRI and 18F-FDG PET-CT in patients with primary liver carcinomas. *Eur Radiol* (2021) 31:3649–60. doi: 10.1007/s00330-020-07378-4

23. Bae JS, Kim JH, Lee DH, Kim JH, Han JK. Hepatobiliary phase of gadoxetic acid-enhanced MRI in patients with HCC: Prognostic features before resection, ablation, or TACE. *Eur Radiol* (2021) 31:3627–37. doi: 10.1007/s00330-020-07499-w

24. Wei H, Jiang H, Zheng T, Zhang Z, Yang C, Ye Z, et al. LI-RADS category 5 hepatocellular carcinoma: Preoperative gadoxetic acid-enhanced MRI for early recurrence risk stratification after curative resection. *Eur Radiol* (2021) 31:2289–302. doi: 10.1007/s00330-020-07303-9

25. Hu XX, Wang WT, Yang L, Yang ZX, Liang HY, Ding Y, et al. MR features based on LI-RADS identify cytokeratin 19 status of hepatocellular carcinomas. *Eur J Radiol* (2019) 113:7–14. doi: 10.1016/j.ejrad.2019.01.036

26. Kang HJ, Kim H, Lee DH, Hur BY, Hwang YJ, Suh KS, et al. Gadoxetate-enhanced MRI features of proliferative hepatocellular carcinoma are prognostic after surgery. *Radiology* (2021) 300:572–82. doi: 10.1148/radiol.2021204352

27. Park HJ, Kim YK, Cha DI, Ko SE, Kim S, Lee ES, et al. Targetoid hepatic observations on gadoxetic acid-enhanced MRI using LI-RADS version 2018: Emphasis on hepatocellular carcinomas assigned to the LR-m category. *Clin Radiol* (2020) 75:413–78. doi: 10.1016/j.crad.2020.01.002

28. Cannella R, Fraum TJ, Ludwig DR, Borhani AA, Tsung A, Furlan A, et al. Targetoid appearance on T2-weighted imaging and signs of tumor vascular involvement: Diagnostic value for differentiating HCC from other primary liver carcinomas. *Eur Radiol* (2021) 31:6868–78. doi: 10.1007/s00330-021-07743-x

29. Harrison LE, Koneru B, Baramipour P, Fisher A, Barone A, Wilson D, et al. Locoregional recurrences are frequent after radiofrequency ablation for hepatocellular carcinoma. *J Am Coll Surgeons* (2003) 197:759–64. doi: 10.1016/S1072-7515(03)00750-6

30. Wu YC, Xiao ZB, Lin XH, Zheng XY, Cao DR, Zhang ZS. Dynamic contrast-enhanced magnetic resonance imaging and diffusion-weighted imaging in the activity staging of terminal ileum crohn's disease. *World J Gastroenterol* (2020) 26:6057–73. doi: 10.3748/wjg.v26.i39.6057

31. Wu L, Rao S, Xu P, Yang L, Chen C, Liu H, et al. Pre-TACE kurtosis of ADCtotal derived from histogram analysis for diffusion-weighted imaging is the best independent predictor of prognosis in hepatocellular carcinoma. *Eur Radiol* (2019) 29(1):213–23. doi: 10.1007/s00330-018-5482-3

32. Song W, Yu X, Guo D, Liu H, Tang Z, Liu X, et al. MRI-Based radiomics: Associations with the recurrence-free survival of patients with hepatocellular carcinoma treated with conventional transcatheter arterial chemoembolization. *J Magn Reson Imaging* (2020) 52:461–73. doi: 10.1002/jmri.26977

33. Chan KS, Shelat VG. Clinical utility of advances in radiofrequency ablation for small hepatocellular carcinoma. *J Invest Surg* (2022) 35(4):888–90. doi: 10.1080/08941939.2021.1944404

34. Gui CH, Baey S, D'Cruz RT, Shelat VG. Trans-arterial chemoembolization + radiofrequency ablation versus surgical resection in hepatocellular carcinoma – a meta-analysis. *Eur J Surg Oncol* (2020) 46(5):763–71. doi: 10.1016/j.ejso.2020.01.004

frontiers | Frontiers in Oncology

TYPE Original Research
PUBLISHED 28 February 2023
DOI 10.3389/fonc.2023.1114406

OPEN ACCESS

EDITED BY
Xiankai Sun,
University of Texas Southwestern Medical Center, United States

REVIEWED BY
Qun Tang,
Nanchang University, China
Xiongwen Lv,
Anhui Medical University, China

*CORRESPONDENCE
Shi Zhou
zhou_shi89@21cn.com
Shuai Zhang
zhangshuai476900@gmc.edu.cn

†These authors have contributed equally to this work and share first authorship

SPECIALTY SECTION
This article was submitted to Cancer Imaging and Image-directed Interventions, a section of the journal Frontiers in Oncology

RECEIVED 02 December 2022
ACCEPTED 08 February 2023
PUBLISHED 28 February 2023

CITATION
Cheng Z, Qin H, Cao W, He H, Zhang S, Yang Y, Wang Z, Zou X, Wang L, Huang X, Zhou S and Zhang S (2023) Intravoxel incoherent motion imaging used to assess tumor microvascular changes after transarterial chemoembolization in a rabbit VX2 liver tumor model.
Front. Oncol. 13:1114406.
doi: 10.3389/fonc.2023.1114406

Intravoxel incoherent motion imaging used to assess tumor microvascular changes after transarterial chemoembolization in a rabbit VX2 liver tumor model

Zhimei Cheng[1†], Huanrong Qin[1†], Wei Cao[2†], Huizhou He[1], Shuling Zhang[3], Yushi Yang[4], Zhenmin Wang[5], Xun Zou[5], Lizhou Wang[1], Xueqing Huang[1], Shi Zhou[1*] and Shuai Zhang[1*]

[1]Department of Interventional Radiology, the Affiliated Hospital of Guizhou Medical University, China Branch of National Clinical Research Center for Interventional Medicine, Guiyang, China, [2]Department of Interventional Radiology, The Affiliated Cancer Hospital of Guizhou Medical University, Guiyang, China, [3]The Affiliated Hospital of Guizhou Medical University & Key Laboratory of Environmental Pollution Monitoring and Disease Control, Ministry of Education, School of Public Health, Guizhou Medical University, Guiyang, China, [4]Department of Pathology, The Affiliated Hospital of Guizhou Medical University, Guiyang, Guizhou, China, [5]Department of Radiology, The Affiliated Hospital of Guizhou Medical University, Guiyang, Guizhou, China

Purpose: To evaluate the correlation between microvascular density (MVD) and intravoxel incoherent motion (IVIM) magnetic resonance imaging (MRI) parameters and the effect of glycolytic flux after transarterial chemoembolization (TACE) in a rabbit VX2 liver tumor.

Materials and methods: VX2 liver tumor allografts in 15 New Zealand white rabbits were treated with sterile saline (control group, n = 5) or lipiodol-doxorubicin emulsion (experimental group, n = 10). MRI was performed 2 weeks after the procedure to evaluate IVIM parameters, including apparent diffusion coefficient (ADC), pure diffusion coefficient (D), pseudodiffusion coefficient (D*), and perfusion fraction (PF). All animal samples were taken of the tumor and surrounding liver. Immunostaining for CD31, CD34, CD105, and VEGF was used to evaluate MVD. The protein expression of Glut4, HK2, PKM2, LDHA, and MCT1 was determined using western blotting. Pearson correlation tests were used to analyze the relationship between MVD and IVIM parameters.

Results: D* value in the peritumoral region was negatively correlated with CD34 ($r = -0.71$, $P = 0.01$). PF value positively correlated with CD34 ($r = 0.68$, $P = 0.015$), CD105 ($r = 0.76$, $P = 0.004$) and VEGF ($r = 0.72$, $P = 0.008$) in the peritumoral region. Glut4, HK2, PKM2, and MCT1 in the peritumoral regions were higher in the experimental group than in the control group (all $P < 0.05$).

Conclusion: IVIM parameters were correlated with MVD in the intratumoral and peritumoral regions after TACE in a rabbit liver tumor model. The angiogenesis reflected by MVD may be related to changes of glycolytic flux.

KEYWORDS

rabbit VX2 liver tumor, transarterial chemoembolization, microvessel density, intravoxel incoherent motion imaging, glycolytic flux

Introduction

Transarterial chemoembolization (TACE) is often used for the treatment of unresectable hepatocellular carcinoma (HCC) (1). Although the short-term effect of this treatment has been demonstrated in multiple studies, its long-term efficacy is poor, with a 5-year survival rate of less than 30% (2, 3). This limited efficacy over the long term is mainly due to a high rate of tumor recurrence and intrahepatic and extrahepatic metastasis (4, 5). Among factors affecting the efficacy of TACE, tumor microenvironment (TME) changes are of particular importance. For example, hypoxia is a key condition affecting the TME of HCC, and research has shown that the modulation of hypoxia inducible factor-1α can reduce sorafenib resistance and improve the prognosis of patients treated with TACE (6). Another study has similarly shown that elevated pyruvate kinase muscle isozyme M2 (PKM2) expression is associated with treatment resistance and reduced survival in patients receiving TACE (7). A recent meta-analysis demonstrated that higher expression levels of glycolysis markers in tumor tissues are correlated with poorer overall survival (8).

These changes in TME result in the formation of new tumor microvessels, eventually leading to tumor recurrence and metastasis (9). Tumor microvessel density (MVD) is a marker that can be used to evaluate tumor angiogenesis. For instance, cluster designation 34 (CD34) staining has been used to evaluate the growth of neovascularization in HepG2 xenograft tumor-bearing mice (10), and CD31 staining can be used to identify the stages of HCC (11). Other research has shown that CD105 staining is useful in quantifying the formation of new microvessels in HCC (12). It is essential to accurately identify these MVD changes after TACE treatment for HCC.

Magnetic resonance imaging (MRI) is a noninvasive method that can be used to assess various tumor characteristics. More specifically, intravoxel incoherent motion (IVIM) imaging is of particular use. In 1986, researchers proposed using a bi-exponential model to separate the diffusion of water molecules and the perfusion of microcirculation (13). With this method, researchers could obtain the apparent diffusion coefficient (ADC), the pure diffusion coefficient (D), the pseudodiffusion coefficient (D*), and the perfusion fraction (PF), parameters that not only reflect tissue diffusion more accurately but also provide information about tissue microcirculation perfusion (13). However, studies assessing IVIM imaging have differed in their conclusions regarding the role of these parameters in predicting treatment efficacy and assessing tumor MVD. For example, one study found that PF value is associated with MVD in ovarian epithelial tumors (14), and another study found that both PF value and D* value are significantly and positively correlated with CD31 and VEGF staining in A549 tumor-bearing mice (15). Other research has shown that PF values are positively correlated with tumor MVD but that ADC and D* values are not correlated with tumor MVD after treatment with transcatheter arterial embolization and apatinib (16).

In this study, we therefore sought to further evaluate the correlation between IVIM parameters and histopathological MVD after TACE treatment in a rabbit VX2 liver tumor allograft model. Through this research, we hoped to determine the potential value of IVIM imaging in evaluating the therapeutic effect of TACE treatment.

Abbreviations: ADC, apparent diffusion coefficient; ALT, alanine aminotransferase; AST, aspartate aminotransferase; CD31, cluster designation 31; CD34, cluster designation 34; CD105, cluster designation 105; CT, computed tomography; D, pure diffusion coefficient; D*, pseudodiffusion coefficient; DSA, digital subtraction angiography; Glut4, glucose transporter 4; HCC, hepatocellular carcinoma; H&E, hematoxylin and eosin; HK2, hexokinase 2; HRP, horseradish peroxidase; IVIM, intravoxel incoherent motion; LDHA, lactate dehydrogenase A; MCT1, monocarboxylate transporter 1; MRI, magnetic resonance imaging; MVD, microvessel density; PF, perfusion fraction; PKM2, pyruvate kinase muscle isozyme M2; ROI, region of interest; SD, standard deviation; TACE, transarterial chemoembolization; TME, tumor microenvironment; VEGF, vascular endothelial growth factor.

Materials and methods

Animals

Male New Zealand white rabbits (aged 8 weeks, weighing 2.0-2.5 kg) were purchased from the Animal Center of Guizhou Medical University (license: SYXK 20180001). Of these rabbits, a total of 16 rabbits with similar growth status were selected for this study. All experiments in animal models were conducted following the experimental program approved by the Animal Ethics Committee of Guizhou Medical University and following institutional norms (ethics number: 1900932). All animals were maintained in laminar flow rooms at constant temperature and humidity, with free access to food and water.

Implantation of VX2 liver tumor

VX2 tumor tissues purchased from Guangzhou Gineo Biotechnology Co. (Guangzhou, Guangdong, China) were implanted into the muscle layer of the hindlimb of one carrier rabbit (n = 1) and were grown for 2 to 3 weeks as described in previous study (17). The tumor tissues harvested from the carrier rabbit were then divided and subsequently implanted into the left liver lobe of the remaining rabbits (n = 15) under ultrasound guidance (M6Vet, Shenzhen Mindray Bio-Medical Electronics Co., Guangdong, China) *via* percutaneous puncture. The growth of VX2 tumors was monitored by ultrasonography (Figure 1A).

Experimental and control procedures

All animals underwent either the control or experimental procedure 2 to 3 weeks after tumor implantation, once a well-delineated solitary tumor (1.5-2.0 cm in diameter) could be detected on ultrasound images (18, 19). For these procedures, anesthesia was administered at a concentration of 2.5% to 3.5%, with an oxygen flow rate of 1 L/min. Each rabbit was placed on an operating table

10.3389/fonc.2023.1114406

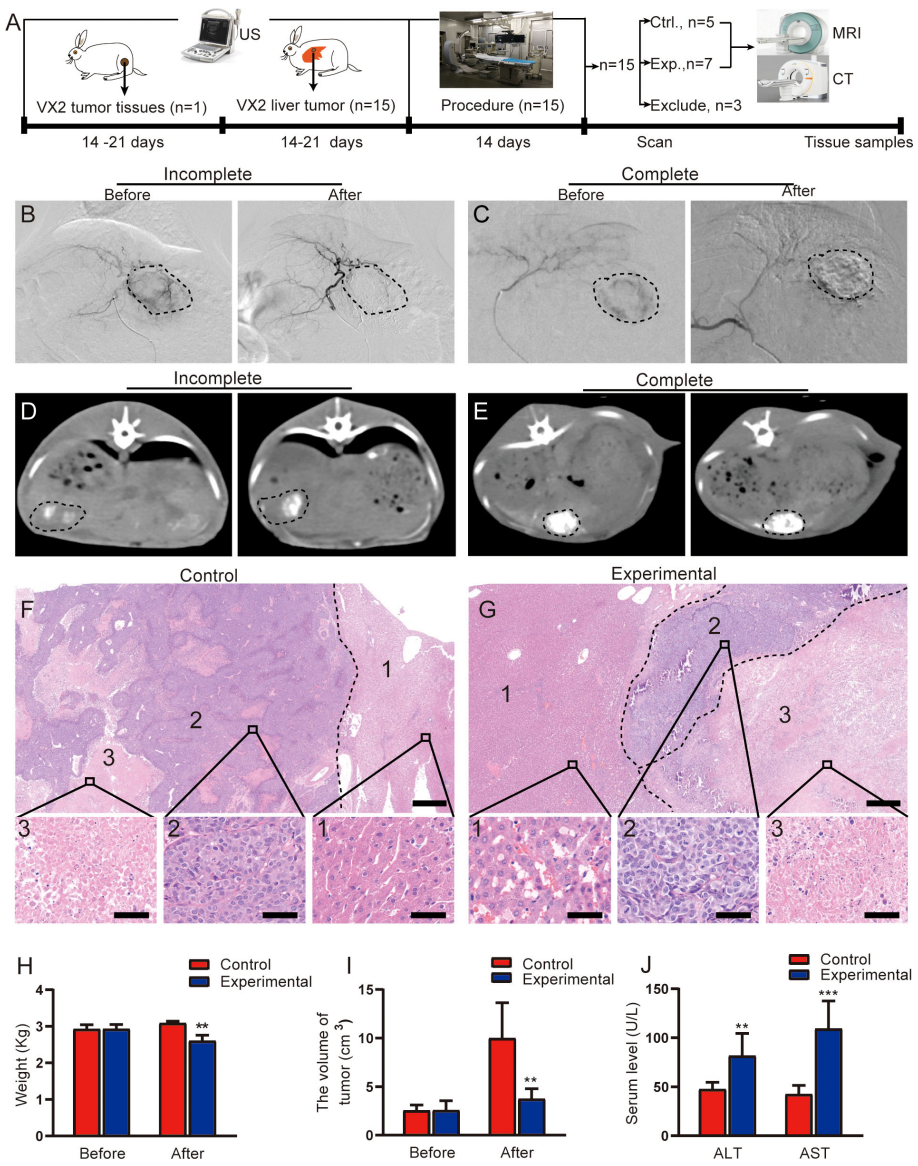

FIGURE 1
Evaluation of TACE treatment in rabbit VX2 liver tumor models. **(A)** Overview of the experimental design. **(B, C)** Representative angiographic images show the tumor staining before and after embolization in the experimental group. **(D, E)** Representative CT images in the experimental group obtained 2 weeks after TACE. **(D)** shows incomplete lipiodol deposition within the tumor, whereas **(E)** shows complete lipiodol deposition within the tumor. **(F, G)** Representative H&E staining of resected tumor lesions after procedure in the control and experimental groups, consisting of the liver (1), the viable tumor (2), and the necrotic tumor (3). Scale for large image, 500 μm; scale for small image, 50 μm. **(H)** Quantitative analysis of rabbit weight before and after procedure in two groups. **(I)** Quantitative analysis of tumor volume before and after procedure in two groups. **(J)** Quantitative analysis of serum ALT and AST levels after procedure in two groups. Data represent mean ± SD. $^{**}P < 0.01$; $^{***}P < 0.001$. Ctrl., control; Exp., experimental; MRI, magnetic resonance imaging; CT, computed tomography.

containing a digital subtraction angiography (DSA) machine (MEGALIX Cat Plus 125/20/40/80, Siemens Healthcare GmbH, Erlangen, Germany). The procedure was then performed under fluoroscopic guidance as described in a previous study (19). Briefly, the right femoral artery was selected and punctured with a 20G blood vessel puncture needle. A steerable guidewire (M001508110, FATHOMTM-14, Boston Scientific, Marlborough, MA, USA) and microcatheter (1055091150, Micro Therapeutics, Irvine, CA, USA) were advanced through the right femoral artery to the celiac axis. The proper hepatic artery was then selectively catheterized off the common hepatic artery with the aid of a steerable guidewire. A mixture of lipiodol and doxorubicin (up to 1.0 mL; experimental group) or sterile water (control group) was slowly infused under fluoroscopic guidance. Hepatic arteriography was performed to detect staining of the tumor before and after embolization. All rabbits can be weighed before and 2 weeks after procedure.

Inclusion criteria and study groups

Rabbits were eligible for inclusion if the implanted tumor was located in the liver parenchyma and extensive extrahepatic metastasis was not seen. Animals were excluded if significant tumor staining was still observed after infusion with a mixture of lipiodol and doxorubicin (experimental group).

MR acquisition and image analysis

All MR examinations were performed with the rabbits under deep sedation. A 3.0T scanner (750 W Discovery, GE Medical Systems, Fayetteville, Wisconsin, USA) with an 8-channel rabbit coil (Wankang Medical Technology Co., Jiangsu, China) was used to scan rabbits in the prone position 2 weeks after treatment, as described previously (19). In brief, an axial T2−weighted HASTE sequence was performed using the following parameters: repetition time/echo time, 4454.0/98.7 ms; field of view, 140 × 140 mm; matrix size, 140 × 140; section thickness, 4 mm; gap, 0 mm; and bandwidth, 41.67 Hz/pixel. IVIM imaging was performed in the transverse plane using an echo−planar imaging sequence with diffusion −gradient encoding in three orthogonal directions; scans were performed with single excitation in a free-breathing state. The b values were 0, 10, 20, 50, 80, 100, 150, 200, 400, 800, and 1000 mm^2/s. The scan parameters for IVIM imaging were as follows: repetition time/echo time, 3585/66.1 ms; slice thickness/layer interval, 4/0 mm; layer number, 16; field of view, 140 × 140 mm; frequency, 64; phase, 2; bandwidth, 166.7 Hz/pixel; frequency coding direction, R/L; matrix, 64 × 80; and acquisition time, ~1 minute and 30 seconds.

One radiologist with 5 years of experience in abdominal MR imaging evaluated all MR images on a GE Healthcare Advantage Workstation; the radiologist was blinded to the histopathological results. The ADC, D, D*, and PF maps derived from IVIM imaging were extracted after fitting with a bi-exponential model. Parametric values were automatically output by measuring the region of interest (ROI) using incorporated software on a commercial workstation (Syngo, Siemens Healthcare). The largest three sections were chosen, and three ROIs measuring 5 to 15 mm^2 were drawn manually on each section to measure the ADC, D, D*, and PF values of the intratumoral region, peritumoral region, and liver region. The peritumoral region was defined as an area around the tumor of approximately 2 mm (20); the liver region was defined as an area 2 cm away from the tumor margin. The average values of all ROIs were used for statistical analyses. The tumor size was estimated by calculating its largest (L) and smallest (S) diameters using the following formula: Tumor volume/mm^3 = $(L \times S^2)/2$ (21).

CT scan

After MR imaging, computed tomography (CT) imaging was performed to assess lipiodol deposition (22). Each rabbit was sedated and then scanned, in the prone position, on a 128-slice Multislice CT scanner (SOMATOM definition AS+, Siemens Healthcare). The volumetric scanning parameters were as follows: field of view, 22 cm; tube voltage, 120 kVp; tube current, 250 Ma; and slice thickness, 1.0 mm, as described in a previous study (23).

Conventional liver function tests

Once imaging was complete, blood was collected from an artery in each rabbit's ear. For each sample, the supernatant was collected after centrifugation at 3000 rotations per minute for 15 minutes at 4°. The levels of alanine aminotransferase (ALT) and aspartate aminotransferase (AST) were assessed using an automatic biochemical analyzer (Chemray 240, Shenzhen Life Science & Technology).

Pathology

Immediately after blood collection, the rabbits were euthanized under deep anesthesia with isoflurane. Tumor and adjacent liver samples were then collected and fixed in a 10% formalin solution. Paraffin blocks were cut and stained with hematoxylin and eosin (H&E) and immunohistochemistry stains for CD31, CD34, CD105, and vascular endothelial growth factor (VEGF). The sections were placed in boiling citrate buffer for 20 minutes for antigen repair. Tissue sections were incubated in endogenous peroxidase reagent (ORIGENE, Beijing, China) for 10 minutes at room temperature to block the endogenous peroxidase of cells, and the samples were then incubated with 10% goat serum for 20 minutes at 37°. Incubation with primary antibodies occurred at 4° in hydration chambers overnight. The anti-mouse CD31, CD34, CD105, and VEGF antibodies were purchased from Aifang Biological Co. (Hunan Province, China).

Image J software (Wayne Rasband National Institutes of Health, USA) was used to quantify CD31, CD34, CD105, and VEGF staining. The percentage of staining in each region was determined by dividing the area of staining by the total area of the region. The percentage of positively stained area was calculated in at least six fields per section. All sections were analyzed and evaluated independently by two double-blinded pathologists, and the results were reconfirmed by a third pathologist once inconsistent.

Western blotting

RIPA lysate (Solarbia, Beijing, China) was used to extract the total protein from the intratumoral, peritumoral and liver regions respectively. Equal amounts of protein were separated on 10% SDS-PAGE gels and transferred to a PVDF membrane (Amersham Hybond, GE Healthcare). Protein detection was performed using anti-glucose transporter 4 (Glut4, Abcam Cat# ab33780, RRID : AB_2191441), anti-hexokinase 2 (HK2, LSBio (LifeSpan) Cat# LS-B3571-50, RRID : AB_10622121), anti-PKM2 (Novus Cat# NBP1-

48308, RRID : AB_10011057), anti-lactate dehydrogenase A antibody (LDHA, Abcam Cat# ab47010, RRID : AB_1952042), anti-monocarborxylate transporter 1 (MCT1, Absin, Shanghai, China, cat# abs120479), anti-β-actin (Enogene, Nanjing, China, cat# E12-041), anti-mouse-horseradish peroxidase (HRP, Absin, Shanghai, China, cat# abs20001ss), anti-rabbit-HRP (Absin, cat# abs20040), and anti-goat-HRP (Bioss, Wuhan, China, cat# bs-0294D-HRP). Protein detection was performed using ECL Western blotting substrate (Affinity Biosciences, KF003, Jiangsu, China). β-actin was used as a loading control. Blots were quantified using Image J, and intensities of the protein of interest were normalized to β-actin.

Statistical analysis

SPSS software (version 26; IBM, Armonk, NY, USA) was used for data analysis. Descriptive statistics were reported as mean ± standard deviation (SD). Groups were compared using independent sample *t* tests. A Pearson correlation test was used to analyze the correlation between IVIM parameters and MVD. *P* values < 0.05 were considered statistically significant.

Results

TACE treatment in rabbit VX2 liver tumor model

The process of tumor implantation and subsequent tumor formation was successful in all 15 rabbits. No periprocedural complications occurred in any of the study animals. Under DSA fluoroscopy, 3 rabbits in the experimental group were found to still have tumor staining after embolization in the experimental group (Figure 1B); these animals were therefore excluded from the analysis. The remaining 7 rabbits in the experimental group had no obvious tumor staining (Figure 1C). Of these 7 rabbits, 3 demonstrated incomplete lipiodol deposition in tumors on CT imaging (Figure 1D), and the remaining 4 demonstrated relatively complete lipiodol deposition (Figure 1E).

In the control group (n = 5), H&E staining demonstrated a large number of viable tumor cells in the intratumoral region, with disordered arrangement, large cell volume, and imbalanced ratio of nucleus to cytoplasm small irregular necrotic areas were also seen in the viable tumor region (Figure 1F). In the experimental group, H&E staining demonstrated complete tumor necrosis in 2 of the 7 rabbits; staining in the remaining 5 rabbits demonstrated a few viable tumor cells in the necrotic tumor rim (Figure 1G). The liver lobular architecture in the control group was well preserved, and no edema, congestion, or centrilobular necrosis was observed. The experimental group displayed focal hepatocyte necrosis and infiltration of inflammatory cells, as well as sinusoidal congestion.

The body weight of the rabbits was significantly lower in the experimental group than in the control group (t = 3.98, $P = 0.003$; Figure 1H). This may be related to little or no food consumption in rabbits after TACE. The tumor volume in the experimental group was also significantly lower than the volume in the control group (t = 3.724, $P = 0.017$; Figure 1I. TACE treatment inhibited tumor growth.

Postoperative changes in serum ALT and AST levels are shown in Figure 1J. Serum ALT and AST significantly higher in the experimental group than in the control group (ALT: t = 3.708, $P = 0.007$; AST: t = 5.863, $P < 0.001$).

Quantitative analysis of tumor and liver using MR IVIM parameters

On T2-weighted imaging, central necrosis demonstrated low T2 signal intensity, whereas viable tumor tissue demonstrated slight T2 hyperintensity (Figures 2A, B). In the experimental group, an uneven signal intensity was seen in the intratumoral region (Figure 2B). IVIM sequence color maps are shown in Figures 2C, D, and the scale of the color maps and the fitting curves with IVIM sequences are shown in Figures 2E, F. Compared with the control group, the intratumoral ADC and D values in the experimental group were significantly increased (t = 23.256, $P < 0.001$; t = 13.53, $P < 0.001$, respectively), and the D* and PF values were significantly decreased (t = 23.256, $P < 0.001$; t = 13.53, $P < 0.001$, respectively) (Figure 2G), which means that the expansion of water molecules in the intratumoral region increases, and the blood flow and velocity in the capillaries decrease after TACE. Compared with the control group, the D* value in the peritumoral region was significantly decreased in the experimental group (t = 2.478, $P = 0.033$), and the PF value was significantly increased (t = 4.069, $P = 0.004$) (Figure 2H), which means that may be related to the increase of peritumoral new microvessels. The ADC, D, D*, and PF values in the liver parenchyma were similar between the two groups (Figure 2I).

The correlation between MVD and IVIM parameters after treatment

CD31, CD34, CD105, and VEGF staining results, which are widely used to characterize MVD, are shown in Figure 3A. The percentage of CD31 and VEGF staining in the intratumoral and peritumoral regions was significantly higher in the experimental group than in the control group (t = 8.607, $P < 0.001$; t = 7.992, $P < 0.001$, respectively); there were no differences in the liver parenchyma between the two groups. The percentage of CD34 and CD105 staining in the peritumoral region was significantly higher in the experimental group than in the control group (t = 10.101, $P < 0.001$); there were no significant differences between the two groups in the intratumoral region or in the liver parenchyma (Figures 3B-E).

Analysis of the correlation between immunohistochemistry staining and IVIM parameters is shown in Table 1. In the peritumoral region, the D* value was negatively correlated with CD34 (Figure 4A), and the PF value was positively correlated with CD34, CD105, and VEGF (Figures 4B-D). In the intratumoral region, the ADC and D values were positively correlated with CD31 and VEGF, and D* and PF values were negatively correlated with CD 31 and VEGF (Figures 4E–L) and the D* value was positively correlated with CD105 (Figure 4M).

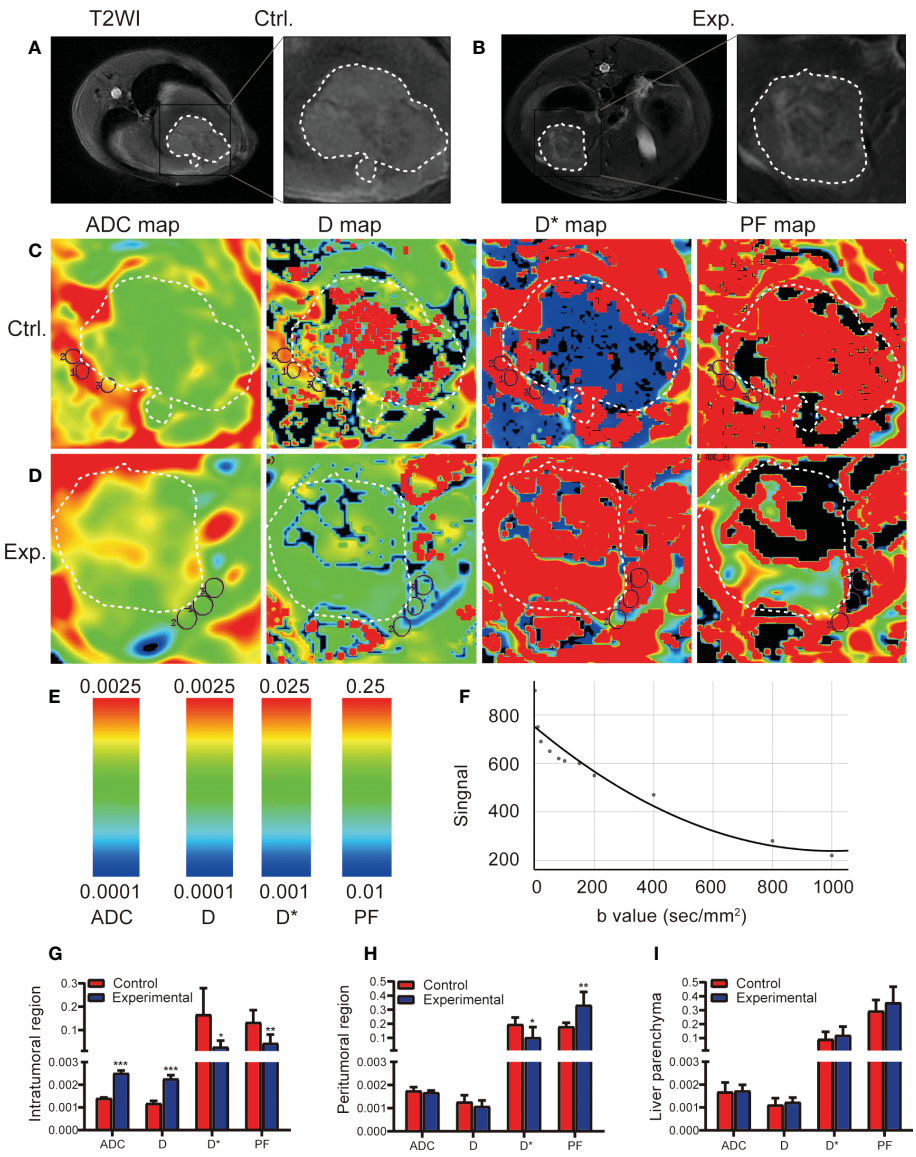

FIGURE 2
IVIM MRI was used to scan the rabbit VX2 liver tumor model 2 weeks after the control or experimental procedure. **(A, B)** Representative axial T2-weighted images (T2WI) of the tumor in the control and experimental groups delineate the tumor area 2 weeks after the procedure. **(C, D)** ADC, D, D*, and PF maps derived from the IVIM sequence for the control and experimental groups. **(E)** Scale of IVIM parameter value. **(F)** IVIM fitting curve. **(G-I)** Quantitative analysis of IVIM parameters for the intratumoral, region, peritumoral region, and liver parenchyma in the control and experimental groups. Data represent mean ± SD. *$P < 0.05$; **$P < 0.01$; ***$P < 0.001$. Ctrl., control; Exp., experimental; ADC, apparent diffusion coefficient; D, pure diffusion coefficient; D*, pseudodiffusion coefficient; PF, perfusion fraction.

The protein expression of glycolytic flux was increased after TACE treatment

As a key enzyme in glycolytic metabolic, the expression levels of Glut4, HK2, PKM2, and MCT1 were significantly higher in the experimental group than in the control group in the intratumoral ($t = 2.58$, $P = 0.027$; $t = 3.47$, $P = 0.013$; $t = 5.91$, $P = 0.001$; $t = 4.21$, $P = 0.002$, respectively) and peritumoral ($t = 3.07$, $P = 0.012$; $t = 3.77$, $P = 0.005$; $t = 3.07$, $P = 0.012$; $t = 3.34$, $P = 0.009$, respectively) regions. LDHA expression increased slightly after TACE treatment, but this increase was not significant in the intratumoral region or in the peritumoral region (Figures 5A-D). The expression levels of Glut4, HK2, PKM2, LDHA, and MCT1 in the liver parenchyma were similar between the two groups (Figures 5E, F).

Discussion

In this study, we found that the IVIM parameters ADC, D, D*, and PF were associated with MVD changes in the intratumoral and peritumoral regions after TACE treatment in a rabbit VX2 liver tumor model. These parameters, especially PF value, were particularly useful in the evaluation of neovascularization of the peritumoral region. The expression of the protein enzymes of

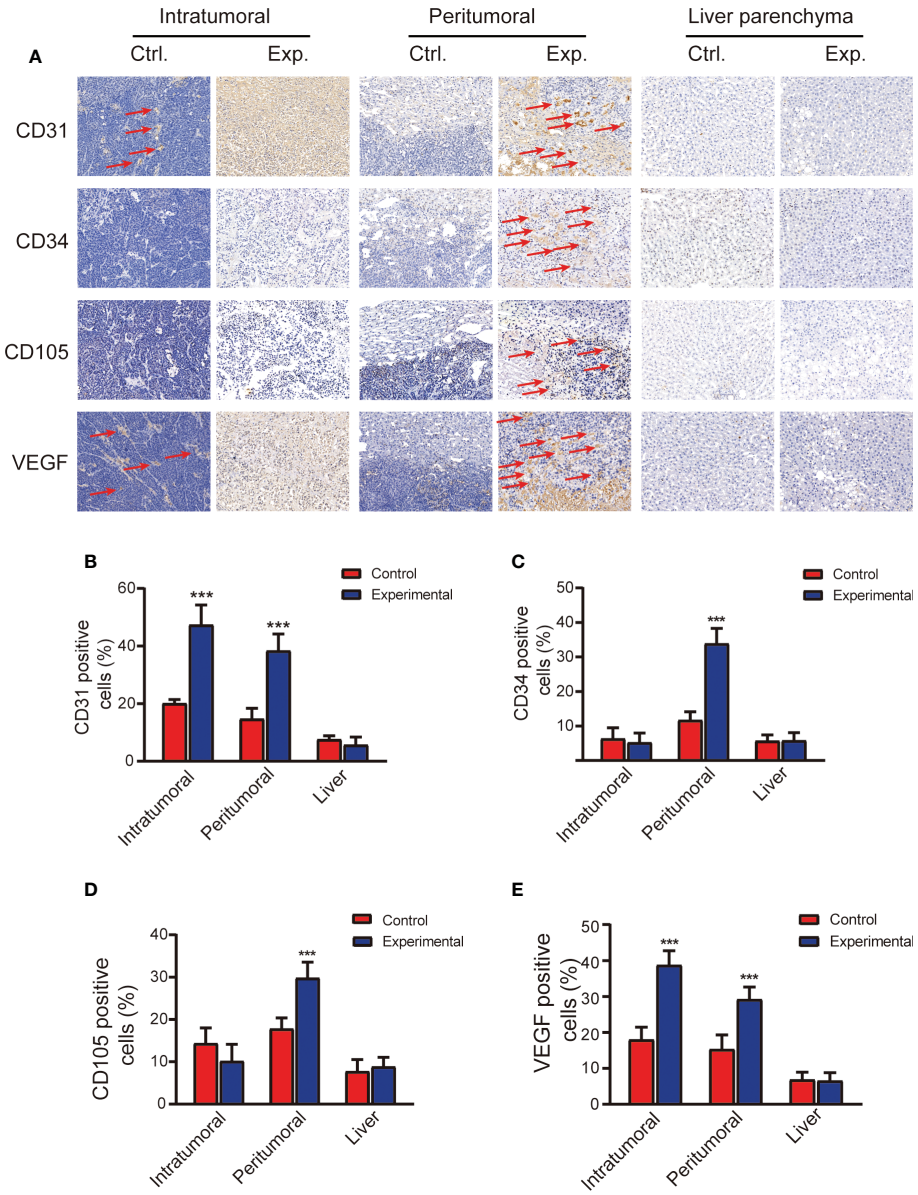

FIGURE 3
Immunohistopathology staining demonstrating microvasculature in the tumor and liver 2 weeks after the control or experimental procedure. **(A)** Representative images of the intratumoral, peritumoral, and liver regions stained with anti-CD31, anti-CD34, anti-CD105, and anti-VEGF. Scale bars, 100 μm. **(B-E)** Quantitative analysis of CD31, CD34, CD105, and VEGF staining. Data represent mean ± SD. ***P < 0.001. Ctrl, control; Exp., experimental; VEGF, vascular endothelial growth factor.

TABLE 1 The correlation between MVD and IVIM parameters.

Region	Parameter	CD31		CD34		CD105		VEGF	
		r	*P*-value	r	*P*-value	r	*P*-value	r	*P*-value
Intratumoral	ADC	0.957	<0.001***	−0.184	0.567	−0.44	0.152	0.950	<0.001***
	D	0.924	<0.001***	−0.0258	0.418	−0.418	0.177	0.927	<0.001***
	D star	−0.673	0.016*	0.294	0.354	0.652	0.022*	−0.795	0.002**
	PF	−0.662	0.019*	0.325	0.303	0.184	0.567	−0.614	0.034*

(Continued)

TABLE 1 Continued

Region	Parameter	CD31		CD34		CD105		VEGF	
		r	*P*-value	r	*P*-value	r	*P*-value	r	*P*-value
Peritumoral	ADC	−0.317	0.316	−0.269	0.397	−0.246	0.441	0.283	0.373
	D	−0.214	0.504	−0.255	0.425	−0.418	0.176	−0.265	0.406
	D star	−0.565	0.055	−0.706	0.01*	−0.477	0.117	−0.371	0.236
	PF	0.528	0.078	0.68	0.015*	0.761	0.004**	0.72	0.008**
Liver parenchyma	ADC	0.345	0.272	−0.275	0.387	−0.088	0.786	−0.159	0.622
	D	−0.059	0.855	−0.548	0.065	−0.269	0.398	0.176	0.584
	D star	−0.286	0.367	0.315	0.319	−0.007	0.984	0.490	0.106
	PF	−0.006	0.986	−0.391	0.209	−0.125	0.698	−0.547	0.066

MVD, microvessel density; IVIM, intravoxel incoherent motion; CD31, cluster designation 31; CD34, cluster designation 34; CD105, cluster designation 105; VEGF, vascular endothelial growth factor; ADC, apparent diffusion coefficient; D, pure diffusion coefficient; D star, pseudodiffusion coefficient; PF, perfusion fraction. *P < 0.05; **P < 0.01; ***P < 0.001.

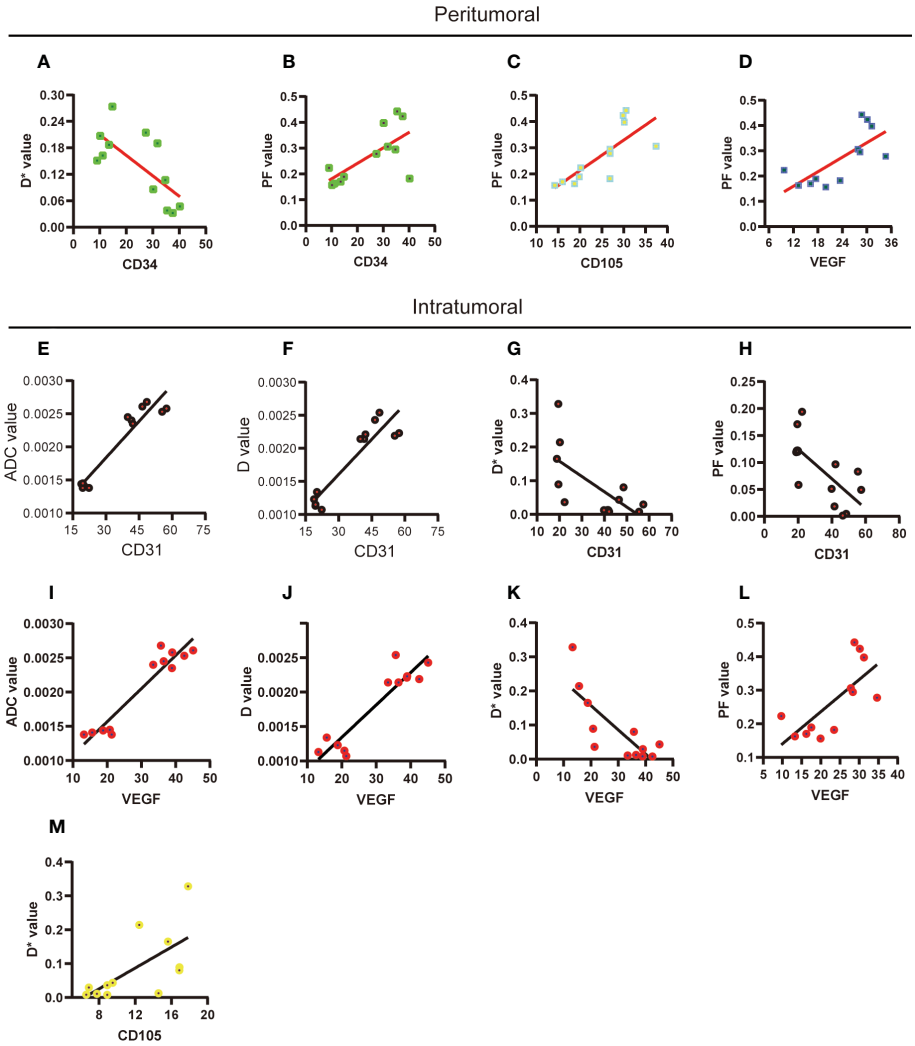

FIGURE 4
Correlations between the quantitative results of histological staining and IVIM parameters. **(A-D)** The significant correlation between histological staining and IVIM parameters in peritumoral region was performed. **(E-M)** The significant correlation between histological staining and IVIM parameters in intratumoral region was performed. ADC, apparent diffusion coefficient; D, pure diffusion coefficient; D*, pseudodiffusion coefficient; PF, perfusion fraction.

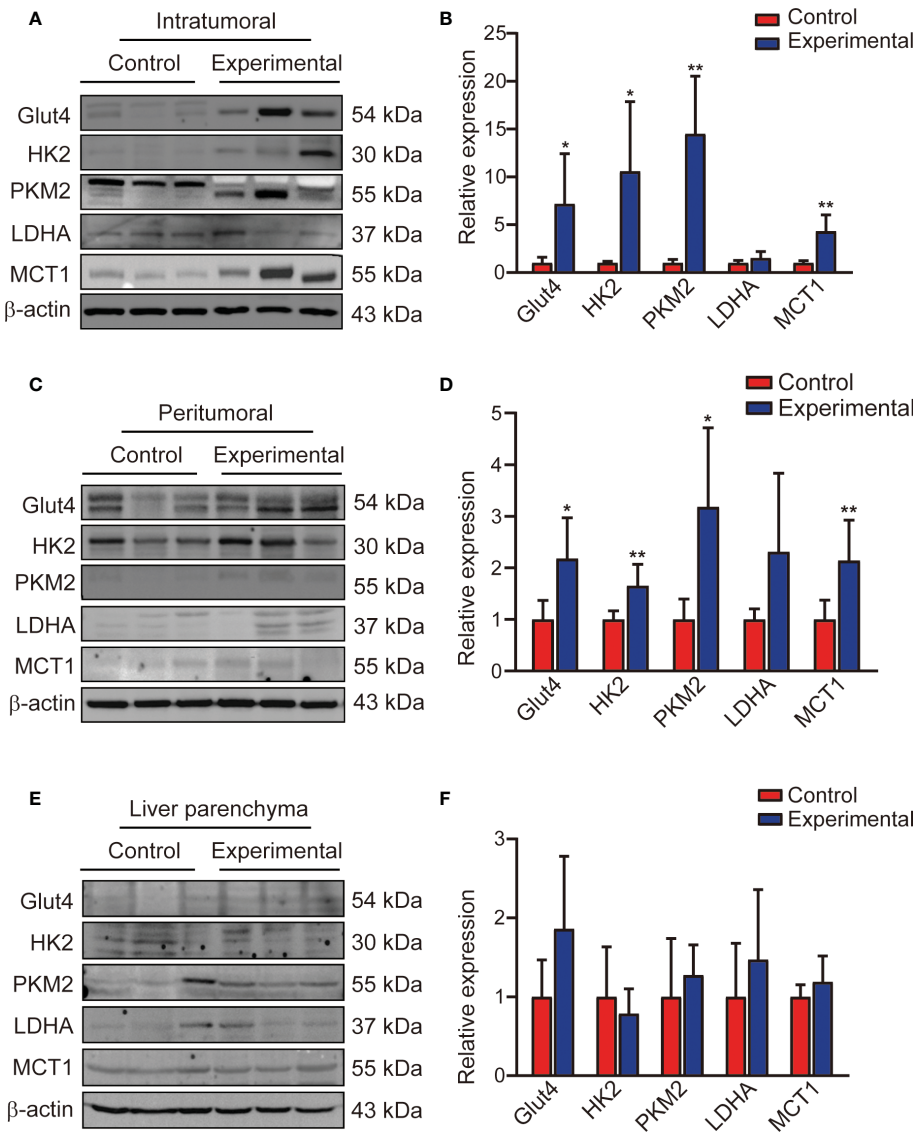

FIGURE 5
Expression of glycolysis flux protein in the intratumoral region, peritumoral region, and liver parenchyma. **(A, B)** Western blotting and corresponding bar chart for the intratumoral region, **(C, D)** the peritumoral region, **(E, F)** and the liver parenchyma. Data represent mean ± SD. *P< 0.05; **P < 0.01. Glut4, glucose transporter 4; HK2, hexokinase 2; PKM2, pyruvate kinase muscle isozyme M2; LDHA, lactate dehydrogenase A; MCT1, monocarboxylate transporter 1.

glycolytic flux in the intratumoral and peritumoral regions was also enhanced after TACE treatment.

Previous studies have shown that many factors can negatively affect the long-term efficacy of TACE, including incomplete tumor-supplying arterial embolization, establishment of complex trophic arterial collateral circulation, involvement of the portal vein, residual tumor blood supply, and tumor hypoxia after embolization. All of these factors can lead to tumor angiogenesis (24–26). The degree of angiogenesis can be assessed most directly by using immunohistochemistry staining to evaluate MVD. Previous research in a rabbit VX2 liver tumor model demonstrated that tumor angiogenesis begins to appear in the residual tumor and tumor junction 14 days after chemoembolization with lipiodol (27). In this study, MVD in the intratumoral and peritumoral regions was significantly higher in the experimental group than in the control group, especially in the peritumoral region; these findings are consistent with the results of previous research (27, 28).

In this study, the D values in the liver and tumor were lower than the ADC values in any group in any area, consistent with previous reports (29). This suggests that the ADC value is affected by the diffusion movement of microcirculatory perfusion. Previous research has demonstrated that the diffusion of water molecules is limited by the presence of viable tumor cells, leading to restricted cellular space (30), and that the vascular structure is destroyed and the blood supply is blocked after TACE (31). In this study, we found that the ADC and D values of the intratumoral region in the experimental group were higher than those in the control group, whereas the D* and PF values were lower. The presence of massive necrotic cells in the experimental group after TACE increased water

movement and reduced microcirculatory perfusion. Interestingly, the D* value of the peritumoral region was significantly lower in the experimental group than in the control group, whereas the PF value was significantly higher. The D* value mainly characterizes changes in hemodynamics, which depend on the length and flow rate of blood vessels (32). Although the number of new microvessels in the peritumoral area increased, the immature blood vessels still lacked the typical vascular structure and had high vascular permeability, so the blood flow of the microvessels in this area was slow, as has been shown previously (22). The PF value is defined as the fractional volume of capillary blood flowing in each imaging voxel. Our data demonstrated that PF value can be illuminated with abundant new neovascularization in the peritumoral region after TACE.

From an angiogenic standpoint, CD31, CD34, CD105, and VEGF are widely used to characterize MVD in the field of tumor research. Previous research in a VX2 tumor model demonstrated that the expression of CD31 is significantly increased at 20 days after TACE (22). In this study, VEGF and CD31 were strongly expressed in the intratumoral and peritumoral tissues. We found that most of the CD34 and CD105 expressed in the peritumoral tissue represented new tumor vessels after TACE treatment; these factors were barely expressed in the intratumoral region in the experimental group. Similarly, a previous study demonstrated that CD105 was highly correlated with postoperative recurrence and metastasis in HCC (12). Overall, these findings suggest that MVD, especially CD105, is a navel marker for tumor angiogenesis in liver VX2 tumor model after TACE.

Previous studies have shown that PF is associated with CD31 staining of the tumor (14, 33) and that D* and PF values are positively correlated with CD31 and VEGF (15, 34). In the current study, ADC, D, D*, and PF values were positively correlated with CD31 and VEGF in the intratumoral region, and the D* value was also associated with CD105 in the intratumoral region. Other research has demonstrated that D and PF values are positively correlated with CD34 staining after transcatheter arterial embolization combined with apatinib in a VX2 liver tumor model (16). However, in a study of human gastric cancer-bearing nude mice, ADC and D values were found to be associated with tumor necrosis and apoptosis (35). In our study, H&E staining demonstrated a large amount of tumor cell necrosis as a result of TACE treatment. The PF value was also positively correlated with CD34, CD105, and VEGF in the peritumoral region, representing the active and viable area; this finding is consistent with previous results (15, 36). Because the state of microvessels is directly related to tumor growth, invasion, metastasis, and prognosis (37), our study suggests that PF values derived from IVIM imaging may theoretically be useful as a marker of these variables.

Previous studies regarding tumor glycolysis have found that tumor tissues preferentially use glycolytic metabolism and that tumor recurrence and metastasis are associated with enhanced glycolytic metabolism; thus, antiglycolytic key enzymes could potentially play a role in antitumor treatment (7, 38–41). In one study, elevated PKM2 was found to be associated with treatment resistance and shortened survival in patients undergoing TACE treatment, suggesting that PKM2 knockdown could improve TACE efficacy (7). In the current study, TACE was found to induce the expression of glycolytic proteins, including HK2 and PKM2. In addition, the high expression of Glut4 was found to mediate increased glucose uptake, and the high expression of MCT1 was found to induce acidification of the TME. Several studies have shown that acidification of the TME is related to a metabolic shift of cancer cells to a hyperglycolytic phenotype, which is associated with poor survival (42, 43). Therefore, high glycolytic flux may be associated with a poorer prognosis.

This study had several limitations. Performing MRI under free breathing may have affected the accuracy of the results. In addition, a rabbit's stomach cavity is large, potentially leading to artifacts in images of the liver parenchyma near the stomach. Considering the 3-dimensional structure of the liver and tumor, parameters measured in only part of the transverse position of the tumor likely do not represent the parameters in the entire tumor, and it is difficult to correlate these results with pathologic findings. Finally, tumors in the experimental group had varying degrees of necrosis, complicating the analysis.

In conclusion, this study demonstrated that the IVIM parameters ADC, D, D*, and PF are associated with tumor MVD after TACE in a rabbit VX2 liver tumor model. These results suggest that IVIM parameters may be useful as quantitative biomarkers for the characterization of angiogenesis and that these parameters could potentially be used to evaluate changes in tumor microcirculation after TACE in patients with HCC. In addition, our findings suggest that changes in the protein enzymes of glycolytic flux induced by TACE treatment may be associated with tumor angiogenesis.

Data availability statement

The original contributions presented in the study are included in the article/supplementary material. Further inquiries can be directed to the corresponding author.

Ethics statement

The animal study was reviewed and approved by the Animal Ethics Committee of Guizhou Medical University and following institutional norms (ethics number: 1900932).

Author contributions

ShiZ and ShuaZ contributed to the experiment design, and data analysis. HQ and WC contributed to the experiment implementation, ZC contributed to manuscript draft and data analysis. All authors contributed to the article and approved the submitted version.

Funding

This study was supported by funds from the Natural Science Foundation of China (no. 81860320; no.81960328), the Funding for innovation and Entrepreneurship of high-level overseas students in Guizhou Province [2019 01] and the China Postdoctoral Science Foundation (no.2020M683660XB), and the Science and Technology Project of Guizhou Provincial Health Commission (gzwkj2022-186).

Acknowledgments

We thank the members of technical assistance in the imaging and ultrasound department of Affiliated Hospital of Guizhou Medical University.

Conflict of interest

The authors declare that the research was conducted in the absence of any commercial or financial relationships that could be construed as a potential conflict of interest.

Publisher's note

All claims expressed in this article are solely those of the authors and do not necessarily represent those of their affiliated organizations, or those of the publisher, the editors and the reviewers. Any product that may be evaluated in this article, or claim that may be made by its manufacturer, is not guaranteed or endorsed by the publisher.

References

1. Lencioni R, de Baere T, Soulen MC, Rilling WS, Geschwind JF. Lipiodol transarterial chemoembolization for hepatocellular carcinoma: A systematic review of efficacy and safety data. *Hepatology* (2016) 64(1):106–16. doi: 10.1002/hep.28453

2. Takayasu K, Arii S, Ikai I, Omata M, Okita K, Ichida T, et al. Liver cancer study group of japan. prospective cohort study of transarterial chemoembolization for unresectable hepatocellular carcinoma in 8510 patients. *Gastroenterology* (2006) 131 (2):461–9. doi: 10.1053/j.gastro.2006.05.021

3. Daniels JR. Overall survival after transarterial lipiodol infusion chemotherapy with or without embolization for unresectable hepatocellular carcinoma: Propensity score analysis. *AJR Am J Roentgenol* (2011) 196(2):W220. doi: 10.2214/AJR.10.4558

4. Kudo M, Han G, Finn RS, Poon RT, Blanc JF, Yan L, et al. Brivanib as adjuvant therapy to transarterial chemoembolization in patients with hepatocellular carcinoma: A randomized phase III trial. *Hepatology* (2014) 60(5):1697–707. doi: 10.1002/hep.27290

5. Han G, Berhane S, Toyoda H, Bettinger D, Elshaarawy O, Chan AWH, et al. Prediction of survival among patients receiving transarterial chemoembolization for hepatocellular carcinoma: A response-based approach. *Hepatology* (2020) 72(1):198–212. doi: 10.1002/hep.31022

6. Chen H, Chen J, Yuan H, Li X, Li W. Hypoxia-inducible factor-1α: A critical target for inhibiting the metastasis of hepatocellular carcinoma. *Oncol Lett* (2022) 24 (2):284. doi: 10.3892/ol.2022.13404

7. Martin SP, Fako V, Dang H, Dominguez DA, Khatib S, Ma L, et al. PKM2 inhibition may reverse therapeutic resistance to transarterial chemoembolization in hepatocellular carcinoma. *J Exp Clin Cancer Res* (2020) 3;39(1):99. doi: 10.1186/s13046-020-01605-y

8. Wang Y, Li Y, Jiang L, Ren X, Cheng B, Xia J. Prognostic value of glycolysis markers in head and neck squamous cell carcinoma: A meta-analysis. *Aging (Albany NY)* (2021) 13(5):7284–99. doi: 10.18632/aging.202583

9. Ranieri G, Ammendola M, Marech I, Laterza A, Abbate I, Oakley C, et al. Vascular endothelial growth factor and tryptase changes after chemoembolization in hepatocarcinoma patients. *World J Gastroenterol* (2015) 21;21(19):6018–25. doi: 10.3748/wjg.v21.i19.6018

10. Liao ZH, Zhu HQ, Chen YY, Chen RL, Fu LX, Li L, et al. The epigallocatechin gallate derivative Y6 inhibits human hepatocellular carcinoma by inhibiting angiogenesis in MAPK/ERK1/2 and PI3K/AKT/ HIF-1α/VEGF dependent pathways. *J Ethnopharmacol* (2020) 15(259):112852. doi: 10.1016/j.jep.2020.112852

11. Phan C, Zheng Z, Wang J, Wang Q, Hu X, Tang G, et al. Enhanced antitumour effect for hepatocellular carcinoma in the advanced stage using a cyclodextrin-sorafenib-chaperoned inclusion complex. *Biomater Sci* (2019) 7(11):4758–68. doi: 10.1039/c9bm01190k

12. Yang LY, Lu WQ, Huang GW, Wang W. Correlation between CD105 expression and postoperative recurrence and metastasis of hepatocellular carcinoma. *BMC Cancer* (2006) 2(6):110. doi: 10.1186/1471-2407-6-110

13. Le Bihan D, Breton E, Lallemand D, Grenier P, Cabanis E, Laval-Jeantet M. MR imaging of intravoxel incoherent motions: Application to diffusion and perfusion in neurologic disorders. *Radiology* (1986) 161(2):401–7. doi: 10.1148/radiology.161.2.3763909

14. Song XL, Wang L, Ren H, Wei R, Ren JL, Niu J. Intravoxel incoherent motion imaging in differentiation borderline from malignant ovarian epithelial tumors: Correlation with histological cell proliferation and vessel characteristics. *J Magn Reson Imaging* (2020) 51(3):928–35. doi: 10.1002/jmri.26885

15. Gao P, Liu Y, Shi C, Liu Y, Luo L. Performing IVIM-DWI using the multifunctional nanosystem for the evaluation of the antitumor microcirculation changes. *MAGMA* (2020) 33(4):517–26. doi: 10.1007/s10334-019-00814-7

16. Chen C, Liu X, Deng L, Liao Y, Liu S, Hu P, et al. Evaluation of the efficacy of transcatheter arterial embolization combined with apatinib on rabbit VX2 liver tumors by intravoxel incoherent motion diffusion-weighted MR imaging. *Front Oncol* (2022) 13:951587(12). doi: 10.3389/fonc.2022.951587

17. Cheng Z, Zhang S, Wang L, Huang Z, Wang P, Zhu H, et al. Ultrasound-guided percutaneous implantation of rabbit VX2 carcinoma, using a coaxial technique and gelfoam pellet injection combination to establish a rabbit liver tumor model. *Diagn Interv Radiol* (2022) 28(1):103–7. doi: 10.5152/dir.2021.20533

18. Luo W, Zhou X, Zheng X, He G, Yu M, Li Q, et al. Role of sonography for implantation and sequential evaluation of a VX2 rabbit liver tumor model. *J Ultrasound Med* (2010) 29(1):51–60. doi: 10.7863/jum.2010.29.1.51

19. Cheng Z, Yang Q, He H, Li R, Li X, Jiang H, et al. Intravoxel incoherent motion diffusion-weighted imaging and shear wave elastography for evaluating peritumoral liver fibrosis after transarterial chemoembolization in a VX2 rabbit liver tumor model. *Front Physiol* (2022) 13:893925. doi: 10.3389/fphys.2022.893925

20. Keller S, Borde T, Brangsch J, Adams LC, Kader A, Reimann C, et al. Native T1 mapping magnetic resonance imaging as a quantitative biomarker for characterization of the extracellular matrix in a rabbit hepatic cancer model. *Biomedicines* (2020) 8 (10):412. doi: 10.3390/biomedicines8100412

21. He P, Ren E, Chen B, Chen H, Cheng H, Gao X, et al. A super-stable homogeneous lipiodol-hydrophilic chemodrug formulation for treatment of hepatocellular carcinoma. *Theranostics* (2022) 12(4):1769–82. doi: 10.7150/thno.68456

22. van Breugel JMM, Geschwind JF, Mirpour S, Savic LJ, Zhang X, Duran R, et al. Theranostic application of lipiodol for transarterial chemoembolization in a VX2 rabbit liver tumor model. *Theranostics* (2019) 9(13):3674–86. doi: 10.7150/thno.32943

23. Lei P, Jiao J, Li H, Wang P, Duan Q, Liu J, et al. NAFLD evaluation: Which is more appropriate, multislice computed tomography or ultrasound real-time shear wave elastography? *J Xray Sci Technol* (2019) 27(5):871–83. doi: 10.3233/XST-190502

24. Rammohan A, Sathyanesan J, Ramaswami S, Lakshmanan A, Senthil-Kumar P, Srinivasan UP, et al. Embolization of liver tumors: Past, present and future. *World J Radiol* (2012) 28;4(9):405–12. doi: 10.4329/wjr.v4.i9.405

25. Sergio A, Cristofori C, Cardin R, Pivetta G, Ragazzi R, Baldan A, et al. Transcatheter arterial chemoembolization (TACE) in hepatocellular carcinoma (HCC): the role of angiogenesis and invasiveness. *Am J Gastroenterol* (2008) 103 (4):914–21. doi: 10.1111/j.1572-0241.2007.01712.x

26. Kim YB, Park YN, Park C. Increased proliferation activities of vascular endothelial cells and tumour cells in residual hepatocellular carcinoma following transcatheter arterial embolization. *Histopathology* (2001) 38(2):160–6. doi: 10.1046/j.1365-2559.2001.01064.x

27. Zhang L, Liu FY, Fu JX, Duan F, Fan QS, Wang MQ. Hepatic arterial administration of sorafenib and iodized oil effectively attenuates tumor growth and intrahepatic metastasis in rabbit VX2 hepatocellular carcinoma model. *Int J Clin Exp Pathol* (2014) 7(11):7775–81.

28. Li W, Kong S, Su J, Huang J, Xue H. Efficacy of transcatheter arterial chemoembolization combined with sorafenib in inhibiting tumor angiogenesis in a rabbit VX2 liver cancer model. *J Interv Med* (2020) 3(1):27–33. doi: 10.1016/j.jimed.2020.01.003

29. Kovač JD, Daković M, Janković A, Mitrović M, Dugalić V, Galun D, et al. The role of quantitative diffusion-weighted imaging in characterization of hypovascular liver lesions: A prospective comparison of intravoxel incoherent motion derived parameters and apparent diffusion coefficient. *PloS One* (2021) 16(2):e0247301. doi: 10.1371/journal.pone.0247301

30. Han Y, Ma J, Sun X, Li Y. The value of intraventricular incoherent motion diffusion weighted imaging in the diagnosis of primary liver cancer. *Minerva Med* (2020) 15. doi: 10.23736/S0026-4806.20.07169-4

31. Lin M, Tian MM, Zhang WP, Xu L, Jin P. Predictive values of diffusion-weighted imaging and perfusion-weighted imaging in evaluating the efficacy of transcatheter arterial chemoembolization for hepatocellular carcinoma. *Onco Targets Ther* (2016) 14 (9):7029–37. doi: 10.2147/OTT.S112555

32. Sigmund EE, Vivier PH, Sui D, Lamparello NA, Tantillo K, Mikheev A, et al. Intravoxel incoherent motion and diffusion-tensor imaging in renal tissue under hydration and furosemide flow challenges. *Radiology* (2012) 263(3):758–69. doi: 10.1148/radiol.12111327

33. Meyer HJ, Höhn AK, Woidacki K, Andric M, Powerski M, Pech M, et al. Associations between IVIM histogram parameters and histopathology in rectal cancer. *Magn Reson Imaging* (2021) 77:21–7. doi: 10.1016/j.mri.2020.12.008

34. Liang J, Li Z, Li J, Peng C, Dai W, He H, et al. Application of IVIM-DWI in detecting the tumor vasculogenic mimicry under antiangiogenesis combined with oxaliplatin treatment. *Front Oncol* (2020) 10:1376. doi: 10.3389/fonc.2020.01376

35. Song XL, Kang HK, Jeong GW, Ahn KY, Jeong YY, Kang YJ, et al. Intravoxel incoherent motion diffusion-weighted imaging for monitoring chemotherapeutic efficacy in gastric cancer. *World J Gastroenterol* (2016) 22(24):5520–31. doi: 10.3748/wjg.v22.i24.5520

36. Song Q, Guo Y, Yao X, Rao S, Qian C, Ye D, et al. Comparative study of evaluating the microcirculatory function status of primary small HCC between the CE (DCE-MRI) and non-CE (IVIM-DWI) MR perfusion imaging. *Abdom Radiol (NY)* (2021) 46(6):2575–83. doi: 10.1007/s00261-020-02945-1

37. Yoneda N, Matsui O, Kobayashi S, Kitao A, Kozaka K, Inoue D, et al. Current status of imaging biomarkers predicting the biological nature of hepatocellular carcinoma. *Jpn J Radiol* (2019) 37(3):191–208. doi: 10.1007/s11604-019-00817-3

38. Feng J, Li J, Wu L, Yu Q, Ji J, Wu J, et al. Emerging roles and the regulation of aerobic glycolysis in hepatocellular carcinoma. *J Exp Clin Cancer Res* (2020) 39(1):126. doi: 10.1186/s13046-020-01629-4

39. Fan Q, Yang L, Zhang X, Ma Y, Li Y, Dong L, et al. Autophagy promotes metastasis and glycolysis by upregulating MCT1 expression and wnt/β-catenin signaling pathway activation in hepatocellular carcinoma cells. *J Exp Clin Cancer Res* (2018) 37(1):9. doi: 10.1186/s13046-018-0673-y

40. Li J, Hu ZQ, Yu SY, Mao L, Zhou ZJ, Wang PC, et al. CircRPN2 inhibits aerobic glycolysis and metastasis in hepatocellular carcinoma. *Cancer Res* (2022) 82(6):1055–69. doi: 10.1158/0008-5472.CAN-21-1259

41. Xu Q, Tu J, Dou C, Zhang J, Yang L, Liu X, et al. HSP90 promotes cell glycolysis, proliferation and inhibits apoptosis by regulating PKM2 abundance *via* thr-328 phosphorylation in hepatocellular carcinoma. *Mol Cancer* (2017) 16(1):178. doi: 10.1186/s12943-017-0748-y

42. Hanahan D, Weinberg RA. Hallmarks of cancer: the next generation. *Cell* (2011) 144(5):646–74. doi: 10.1016/j.cell.2011.02.013

43. Warburg O. On respiratory impairment in cancer cells. *Science* (1956) 124 (3215):269–70. doi: 10.1126/science.124.3215.269

frontiers | Frontiers in Oncology

TYPE Review
PUBLISHED 30 May 2023
DOI 10.3389/fonc.2023.963966

OPEN ACCESS

EDITED BY
Xiankai Sun,
University of Texas Southwestern Medical Center, United States

REVIEWED BY
Vlastimil Válek,
University Hospital Brno, Czechia
Aimin Jiang,
The First Affiliated Hospital of Xi'an Jiaotong University, China
Hridayesh Prakash,
Amity University, India

*CORRESPONDENCE
Sanjeeva P. Kalva
skalva@partners.org

RECEIVED 08 June 2022
ACCEPTED 19 May 2023
PUBLISHED 30 May 2023

CITATION
Vulasala SSR, Sutphin PD, Kethu S, Onteddu NK and Kalva SP (2023) Interventional radiological therapies in colorectal hepatic metastases.
Front. Oncol. 13:963966.
doi: 10.3389/fonc.2023.963966

Interventional radiological therapies in colorectal hepatic metastases

Sai Swarupa R. Vulasala[1], Patrick D. Sutphin[2], Samira Kethu[3], Nirmal K. Onteddu[4] and Sanjeeva P. Kalva[2]*

[1]Department of Radiology, University of Florida College of Medicine, Jacksonville, FL, United States, [2]Division of Interventional Radiology, Department of Radiology, Massachusetts General Hospital and Harvard Medical School, Boston, MA, United States, [3]Department of Microbiology and Immunology, College of Arts and Sciences, University of Miami, Coral Gables, FL, United States, [4]Department of Hospital Medicine, Flowers Hospital, Dothan, AL, United States

Colorectal malignancy is the third most common cancer and one of the prevalent causes of death globally. Around 20-25% of patients present with metastases at the time of diagnosis, and 50-60% of patients develop metastases in due course of the disease. Liver, followed by lung and lymph nodes, are the most common sites of colorectal cancer metastases. In such patients, the 5-year survival rate is approximately 19.2%. Although surgical resection is the primary mode of managing colorectal cancer metastases, only 10-25% of patients are competent for curative therapy. Hepatic insufficiency may be the aftermath of extensive surgical hepatectomy. Hence formal assessment of future liver remnant volume (FLR) is imperative prior to surgery to prevent hepatic failure. The evolution of minimally invasive interventional radiological techniques has enhanced the treatment algorithm of patients with colorectal cancer metastases. Studies have demonstrated that these techniques may address the limitations of curative resection, such as insufficient FLR, bi-lobar disease, and patients at higher risk for surgery. This review focuses on curative and palliative role through procedures including portal vein embolization, radioembolization, and ablation. Alongside, we deliberate various studies on conventional chemoembolization and chemoembolization with irinotecan-loaded drug-eluting beads. The radioembolization with Yttrium-90 microspheres has evolved as salvage therapy in surgically unresectable and chemo-resistant metastases.

KEYWORDS

colorectal metastases, hepatic colorectal metastases, interventional oncology, interventions in colorectal metastases, TARE, TACE, percutaneous ablation, DEBIRI-TACE

1 Introduction

Colorectal cancer (CRC) is the third most prevalent malignancy in the United States and the third most common cause of death pertinent to cancer (1). The incidence of CRC has been increasing by approximately 3.2% per year and 2.5 million cases are estimated to be diagnosed in 2035 (2, 3). Around 56% of the patients lose their life from CRC (4). The mortality could be

attributed to distant organ metastases noticed in 25% of patients at the time of initial diagnosis and in 50% of patients during disease progression (5). The 5-year survival rate of CRC confined to primary location is 88-91.1%, while the rate falls to 13.3-14% in metastatic CRC (6). Liver (68-75%) followed by lung (21-33%), distant lymph nodes (16-26%), bone (10.7-23.7%), peritoneum (11-15%), brain (0.3-0.6%), adrenal glands and spleen are the most to least common sites of CRC metastases (7, 8).

Synchronous colorectal cancer liver metastases (CRLM) are encountered in 20-25% of CRC patients whereas metachronous CRLM is observed in 20-30% of CRC patients (9, 10). Untreated CRLM has worse prognosis with a median survival of 4.5 to 12 months subject to the extent of disease at diagnosis (10). The intention of any curative treatment is to achieve the R0 resection of both the primary and metastatic tumor. Surgical resection is the potential curative and gold standard treatment for CRLM (11). It has improved the 5-year overall survival (OS) rate to 24-58% and a 10-year survival rate to 28% (10, 12–16). Although 50-60% of patients benefit from curative surgical resection of CRLM, only 10-25% of patients are suitable for surgery owing to tumor anatomy, extrahepatic involvement and general health status (10, 17, 18). Neoadjuvant systemic chemotherapy allows for sufficient tumor shrinkage for resection in merely 10-30% of non-surgical candidates (19). Current chemotherapy regimens include 5-fluorouracil and oxaliplatin (FOLFOX), 5-FU and irinotecan (FOLFIRI), and capecitabine and oxaliplatin (CapOx). These regimens have a response rate of 40% and an OS of 57% at 15-20 months (20). The addition of biologic agents to systemic chemotherapy such as anti-vascular endothelial and anti-epidermal growth factors inhibitors has improved the OS to >24 months (20). However, these systemic therapies are intolerable to a 1/3rd of patients resulting in discontinuation of treatment. A few patients may experience chemotherapy-associated liver injury (CALI) including sinusoidal obstruction syndrome and steatohepatitis (20). Hence, the demand for locoregional therapies has increased to make the tumor amenable to resection in addition to mitigating unwanted side effects of chemotherapy. Minimally invasive interventional therapies such as percutaneous ablation, trans-arterial chemoembolization (TACE), trans-arterial radioembolization (TARE) and portal vein embolization (PVE) have transformed the management algorithms of CRLM. These therapies improve the candidacy for surgical resection, provide curative treatment options for non-surgical candidates, and improve the survival of patients undergoing palliative care (Table 1).

2 Therapies to improve surgical candidacy

2.1 Portal vein embolization

One of the main limitations of curative surgical resection is the presence of low volume of the future liver remnant (FLR), which might lead to hepatic insufficiency following the surgery (21). In the last few decades, various techniques have been introduced to induce hypertrophy of the FLR, thereby preventing the liver failure. In 1980s, Masatoshi Makuuchi introduced PVE of right portal vein to cause hypertrophy of the left lobe of the liver (22). PVE diverts blood flow to the healthy liver through embolization of the portal vein branches of the diseased liver. This results in atrophy of the embolized liver and hypertrophy of the non-embolized liver (Figure 1). The resultant increased FLR makes it possible to resect the large or multiple liver tumors. The exact mechanism of liver atrophy-hypertrophy following PVE remains unclear. However, it is hypothesized to be due to (i) upregulated cytokines and growth factors during liver regeneration, (ii) restituted increase in hepatic arterial perfusion and (iii) cellular host response enhancing the local tumor growth (23).

PVE has become the standard of practice for patients with inadequate FLR prior to extensive hepatic resection. The FLR of <20% in the normal liver, <30% in the liver with chemotherapeutic exposure, and <40% in the cirrhotic liver is usually considered an indication of PVE (11, 24–27). The liver regenerates by 20-46% in 6-8 weeks following the procedure (28). The resection rate after PVE is reported to be around 60-80%, 20% of patients may present with insufficient FLR hypertrophy or tumor progression (29–31). Other complications include tumor recurrence and accelerated tumor growth following the procedure (11). Tumor progression is the major concern as it affects the clinical and survival outcomes and may lead to unresectable disease. Pamecha et al. reported increased tumor growth rate among post-PVE cases compared to controls (0.36± 0.68 ml/day vs. 0.05± 0.25 ml/day; P=0.06) (Table 2) (29). For patients with high tumor load, defined as ≥ 9 CRLM or ≥ 5.5 cm diameter for the largest metastatic lesion, a liver transplant may be the preferred management for improved survival (32). Dueland et al. reported a 5-year survival rates of 33.4% and 6.7% in patients who underwent liver transplant and post-PVE liver resection respectively (32).

2.2 Lobar trans-arterial radioembolization

The external beam radiotherapy (EBRT) of the liver exposes the normal hepatic parenchyma to radiation, in addition to the target tumor tissue. Even 35-45Gy, a dose inadequate to induce tumor cell death, can cause radiation-induced liver disease in 50% of the patients due to the low radiation toxicity threshold of normal hepatic parenchyma (40, 41). TARE, also known as selective internal radiation therapy (SIRT) deploys microspheres made of

TABLE 1 Interventional Therapies for CRLM.

Indication	Treatment Options
Improve surgical candidacy	Portal vein embolization
	Lobar TARE
	Combine ablation with surgical resection
Therapies with Curative Intent	Ablation +/- Systemic chemotherapy
	Radiation Segmentectomy
	Firstline Chemotherapy plus TARE
Therapies with Palliate Intent	TARE
	TACE

CRLM, Colorectal liver metastases; TARE, Trans-arterial radioembolization; TACE, Trans-arterial chemoembolization.

10.3389/fonc.2023.963966

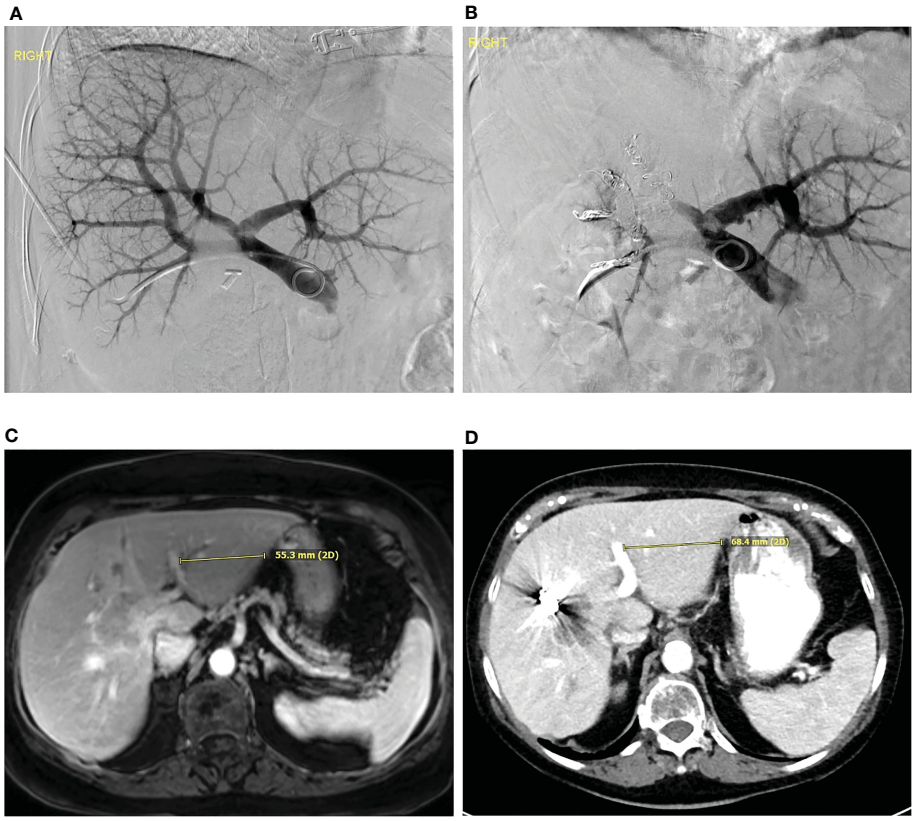

FIGURE 1
Portal vein embolization **(A)** Digitally subtracted percutaneous transhepatic portovenogram demonstrates patent main, left and right portal veins. The portal vein was embolized with particles followed by coil embolization. **(B)** Digitally subtracted portovenogram after portal vein embolization demonstrates flow only to the left hepatic lobe. **(C)** Pre-procedure MRI and **(D)** post portal vein embolization CT demonstrates hypertrophy of the left hepatic lobe.

TABLE 2 Data on PVE for CRLM.

Study	Study design	Country/ region	Sample size	Treatment	Follow up time/ Inclusion period	Outcome
Dueland et al., 2021 (32)	Retrospective study	Norway	53	PVE prior to liver resection compared with liver transplantation	Included the patients between 2006-2019	5-year OS for patients with PVE + Liver resection: 44.6%; 5-year OS for HTL patients was 33.4% and 6.7% in liver transplant and PVE groups respectively; 5-year OS rate for patients with HTL+ left-sided primary tumors was 45.3% and 12.5% in liver transplant and PVE groups respectively. Median OS from the PVE and liver resection was 32.7 months
Huiskens et al., 2017 (33)	Retrospective study	Netherlands	Cases: 46 PVE patients who underwent liver resection; controls: 46 non-PVE patients who underwent liver resection	PVE followed by liver resection vs. liver resection alone	Included the patients between 2000-2015	No significant difference in 3-year DFS (16% vs. 9%; P=0.776) and 5-year OS (14% vs. 14%; P= 0.866)

(Continued)

TABLE 2 Continued

Study	Study design	Country/ region	Sample size	Treatment	Follow up time/ Inclusion period	Outcome
Ironside et al., 2017 (34)	Systematic review	–	1345	Liver resection in PVE vs. non-PVE patients	Included the studies until 2016	Post-operative morbidity: 42% in PVE and 35% in non-PVE patients; Median OS in PVE and non-PVE patients following resection was 38.9 months and 45.6 months respectively; Median DFS in PVE and non-PVE patients was 15.7 months and 21.4 months respectively.
Giglio et al., 2015 (35)	Meta-analysis	–	688	Liver resection in PVE vs. non-PVE patients	Included the studies until 2015	No significant difference was observed between PVE and non-PVE groups in tumor recurrence (OR: 0.78; 95% CI: 0.42-1.44), 3-year OS (OR: 0.80; 95% CI: 0.56-1.14) and 5-year OS (OR: 1.12; 95% CI: 0.40-3.11)
Hoekstra et al., 2012 (36)	Retrospective study	United States	28	Liver resection in PVE vs. non-PVE patients	Included the patients between 2004-2011; After liver resection, median follow up of 6 months in PVE group and 40 months in non-PVE group.	25% of patients developed new lesions in FLR and 42% had tumor recurrence post PVE; 11% of the tumors were not resectable post PVE. 3-yr OS was 77% vs. 26% in non-PVE vs. PVE groups respectively.
Simoneau et al., 2012 (37)	Prospective study	Montreal, Quebec	109 cases and 11 controls	Liver regeneration in PVE vs. non-PVE group	Included the patients between 2003-2011	33.4% increase in TV in right lobe and 49.9% increase in TV in left lobe post-PVE; Growth rate: no statistical significance; Median FLR was similar in test group and control (28.8% vs. 28.7%)
Pamecha et al., 2009 (29)	Prospective study	United Kingdom	22	Liver growth rate after PVE vs. non-PVE; All patients had chemotherapy (5FU, folinic acid, oxaliplatin/irinotecan) before and after PVE.	Included patients between 1999 to 2005.	Tumor volume at resection (P=0.98), time from presentation to resection and tumor growth rate after PVE (P=0.06), (P=0.19) were not statistically significant among PVE group compared to controls. Ki67 proliferation index (P= 0.048) was significantly higher than in controls. The 5-year survival rate in PVE vs control group: 25% vs. 55%; The median DFS in PVE vs control groups: 12 months vs. 24 months.
Pamecha et al., 2009 (38)	Retrospective study	United Kingdom	101	Cases: 36 patients underwent preoperative PVE Controls: 65 patients	Included patients between 1999 to 2005	The median volume of FLR increased from 22% to 32% following PVE; Overall morbidity in cases and controls was 36% and 20% respectively; 1-, 3- and 5-year survival following PVE was 70%, 30% and 25% respectively; 3- and 5-year survival after liver resection in cases vs. controls was 52% vs. 65% and 25% vs. 50% respectively. No significant difference in recurrence rates between cases and controls.
Mueller et al., 2008 (24)	Retrospective study	Germany	107	Outcomes after liver resection in PVE vs. non-PVE patients	Included patients between 1995 to 2004	81% of patients were unresectable due to tumor progression post PVE; Progressive metastases: 52.4%; 5-year survival rate: 43.66%
Kokudo et al., 2003 (39)	Retrospective study	Japan	47	Cases: 18 patients who underwent pre-operative PVE Controls: 29 patients without PVE	Included patients between 1996 to 2000	Tumor volume increased by 20.8% and percent tumor volume increased by 18.5% post PVE; OS in PVE group: 59.7% and 47.8% at 2 and 4 years respectively; whereas in control group: 67.8% and 50.2% at 2 and 4 years respectively (P= 0.421); DFS in PVE group: 15.2% and 0% at 2 and 4 years respectively; in control group: 45.8% and 34.4% at 2 and 4 years respectively.

PVE, Portal vein embolization; CRLM, Colorectal liver metastases; OS, Overall survival; HTL, High tumor load; DFS, Disease free survival; FLR, Future liver remnant; TV, Tumor volume; 5FU, 5-Fluorouracil.

glass or resin and loaded with Yttrium-90 (Y-90) into the hepatic tumor vasculature. The Y-90 TARE emits beta radiation to the selective tumor tissue in contrast to the whole hepatic parenchyma in EBRT. As the radiation is achieved through the infusion of Y-90 microspheres into the hepatic artery, the TARE technique is often referred to as "inside-out radiation" or brachytherapy (42). The Y-90 TARE delivers the radiation with a mean penetration of 2.5 mm, mean energy of 0.94 MeV and targeted radiation dose of 80-150 Gy to the tumors (43).

The concept of lobar TARE as a method to increase the FLR while also controlling the tumor growth in the diseased liver is recently popularized (Table 3). Teo et al. studied seven retrospective clinical studies involving the patients undergoing lobar TARE and reported a FLR hypertrophy of 26-47% within 1.5-9 months of the procedure (47). However, Nebelung et al. reported a significantly greater hypertrophy in patients after PVE than lobar TARE (25.3% vs. 7.4%; P<0.001) (45). However, the post-TARE hypertrophy was substantial with a minimized risk of tumor progression in the embolized lobe (48). Edeline et al. stated that the increase in FLR was similar after TARE as well as PVE procedures (49). Kurilova et al. reported two cases reports in which the patients had insufficient FLR post PVE and underwent lobar TARE. They observed 13% increase in FLR at 4-week follow up in the first patient and 59% increase in FLR at 7-week follow-up in the second patient (50). Liebl et al. studied the FLR hypertrophy in pigs and reported that although PVE induced rapid FLR hypertrophy, it reached a plateau after I month of procedure, whereas, TARE resulted in FLR comparable to PVE within 3-6 months of procedure (51). Vouche et al. studied 83 patients with unilobar disease and observed a reduction in the tumor volume from 134 cc to 56 cc during >9 month follow up period (46). Another study by Edeline et al., including 34 patients, delivered a median lobar dose of 122 Gy and observed a complete response rate of 0%, partial response rate of 26%, stable disease in 63%, and progression of disease in 3% of patients based on RECIST criteria (49). However, CR, PR, SD and PD of 30, 33, 30 and 2% were reported based on mRECIST criteria. Edeline et al. also reported a median OS of 13.5 months and a median time to tumor progression of 21.7 months (49). The lobar TARE has the advantage of tumor control and biological test of time for extrahepatic tumor progression prior to liver resection. Lobar TARE is a well-tolerated procedure with very minimal side effects such as pain and nausea. A few studies reported an increase in Child-Pugh score from 6 to 7 during the first 6 months follow-up which improved later during the >6-9 month follow up period (52). A > 20% increase in the splenic volume was reported without any signs of hypersplenism or additional findings of portal hypertension (52). Serious toxicities including irreversible ascites, temporary and progressive hyperbilirubinemia, and variceal hemorrhage may be observed following the procedure (49).

2.3 Combined RFA and surgical resection

A few studies recommend the combination therapy of RFA with surgical resection to slightly improve the survival and recurrence risk compared to RFA alone (Table 4). Mima et al. studied the

TABLE 3 Data on lobar TARE in CRLM.

Study	Study design	Country/ region	Sample size	Treatment	Follow up time/ Inclusion period	Results
Chiu et al. (44) 2023	Retrospective study	United States	16	Radiation segmentectomy with Y90 in oligometastatic disease (well-controlled primary tumor, ≤ 3 metastases, absence of active extrahepatic tumor burden.	Included patients between 2009 and 2020	Disease control rate was 93%; 13.3% achieved complete response and 47% had partial response. 40% of the patients required subsequent systemic or local tumor therapy while 60% underwent additional chemotherapy. Median time-to-progression was 72.9 months.
Nebelung et al., 2021 (45)	Retrospective study	Germany	73	Lobar TARE: 24 patients; PVE: 49 patients	Included patients who underwent PVE between 2015 to 2019 and TARE between 2013 to 2019	Hypertrophy after PVE was significantly greater than that after TARE (25.3% vs. 7.4%; P<0.001); When stratified by the presence of cirrhosis, the difference in hypertrophy was statistically significant in those without cirrhosis but not statistically significant in cirrhotic patients.
Vouche et al., 2013 (46)	Retrospective study	United States	83	83 patients with uni-lobar disease treated with Y90 microspheres; HCC: 67 patients; CRLM: 8 patients (6 patients had ≥1 cycle of chemotherapy); Cholangiocarcinoma: 8 patients	Included patients between 2003 to 2012	FLR hypertrophy increased from 7% at one month to 45% at 9 month follow up; Median FLR hypertrophy: 26%; Reduction in tumor volume was observed from 134 cc to 99 cc at 3-month period and to 56 cc at > 9-month period
Teo et al., 2016 (47)	Systematic review	Singapore	312	312 patients (HCC: 215 patients; intrahepatic cholangiocarcinoma: 12 patients; CRLM: 85 patients)	Included studies between 2000 to 2014	FLR hypertrophy ranged from 26-47% over a period of 44 days to 9 months
Garlipp et al., 2013 (48)	Retrospective study	Germany	176	Lobar TARE: 35 patients; PVE: 141 patients	Included patients between 2006 and 2012	FLR hypertrophy was significantly greater in PVE group than TARE group (61.5% vs. 29%; P<0.001)

TARE, Trans-arterial radioembolization; PVE, Portal vein embolization; HCC, Hepatocellular carcinoma; CRLM, Colorectal liver metastases; FLR, Future liver remnant.

TABLE 4 Data on combined percutaneous ablation and surgical resection.

Study	Study design	Country/ Region	Sample size	Treatment	Follow up/ Inclusion period	Results
Mima et al., 2013 (53)	Prospective study	Japan	153	118 patients with unresectable CRLM treated preoperatively with FOLFOX ± bevacizumab; HR alone: 35 patients; HR + RFA: 13 patients	Included patients between 2005 to 2010	Postoperative morbidity: 17% in HR group and 23% in HR +RFA group (P= 0.640); Local tumor recurrence at RFA site in only one tumor (7.7% of patients); 3-year PFS: 45.3% in HR group and 12.8% in HR+RFA group (P= 0.472); 3-year OS rate: 70.4% in HR group and 77.1% in HR+RFA group (P=0.627)
Sasaki et al., 2016 (54)	Retrospective study	United States	485	Resection + RFA: 86 patients; Resection alone: 399 patients	Included patients between 2003 to 2015	R1 resection was more frequent in surgical resection + RFA group than the resection-alone group (15.1% vs. 8.5%; P= 0.071); Median OS for combined and resection alone groups: 20.7-61.8 months and 75.3 months respectively; 5-year OS for combined and resection alone groups: 52.7% and 58.7% respectively.

CRLM, Colorectal liver metastases; FOLFOX, 5-fluorouracil and oxaliplatin; HR, Hepatic resection; RFA, Radiofrequency ablation; PFS, Progression free survival; OS, Overall Survival.

efficacy of RFA alone and RFA combined with hepatic resection in unresectable CRLM (53). RFA was mainly performed alongside hepatic resection in those patients who had an effective clinical response to preoperative chemotherapy (FOLFOX). Metastatic nodules smaller than 2 cm was the main indication for RFA while the contralateral tumor was for the hepatic resection. The 3-year recurrence free survival was 33.2% in hepatic resection alone group and 18.5% in combined hepatic resection+ RFA group. Although tumor recurrence was reported in both the group of patients, it was not statistically significant (P=0.154). The 3-year PFS was 45.3% in hepatic resection alone group compared to 12.8% in hepatic resection + RFA group (P= 0.472). The 3- and 5-year OS was 70.4% and 62.6% in hepatic resection group and 77.1% and 64.3% in the hepatic resection + RFA group (P= 0.627) (53). Mima et al. concluded that hepatic resection combined with RFA may be a safe and effective alternative after responsive chemotherapy (53) The similar conclusion was observed in a retrospective study by Sasaki et al. (54). They observed improved resection rates in the resection +RFA group compared to resection alone group (15.1% vs. 8.5%; P= 0.071) (54).

3 Therapies with curative intent

3.1 Ablation +/- systemic chemotherapy

Percutaneous thermal ablation is a tumor-destructive technique and is based on exposing the tumor cells to a targeted temperature of > 60^0 C or < -40^0 C. Ablation can be accomplished through thermal techniques such as radiofrequency, microwave, cryoablation, laser ablation, and focused ultrasound ablation. The irreversible electroporation (IRE), a nonthermal ablation technique utilizes an electrical field to induce tumor death without damaging the tissue protein architecture of vessels and the bile-ducts (55). Either thermal or non-thermal, ablation techniques have the advantages of being minimally invasive and less morbid than surgical resection and can be delivered as an out-patient treatment. The open or percutaneous approach to thermal ablation has been studied in the literature. Puijk et al., reported significantly improving liver tumor PFS following percutaneous ablation (2010-2013: 37.7%; 2014-2017: 69%; 2018-2021: 86.3%; P< 0.0001) whereas the PFS was stable following open ablations (2010-2013: 87.1%; 2014-2017: 92.7%; 2018-2021: 90.2%; P= 0.12) (56). The complications were less severe in percutaneous rather than open approach (2010-2013: P=0.69; 2014-2017: P= 0.129; 2018-2021: P= 0.02) (56). The tissue damage secondary to ablation is low when compared to surgical resection, which is the most important requisite in patients with underlying liver disease or those who already had extensive liver resection (55).

RFA is a well-studied and most widely used ablative modality in colorectal metastases. The monopolar or bipolar radiofrequency ablation (RFA) systems produce ionic oscillation by a high-frequency alternating current resulting in frictional heating and tissue damage (57). The level of thermal tissue damage varies depending on the achieved temperature. For instance, a 50-55^0 C for a period of 4-6 minutes induces irreversible cellular damage, 60-100^0 C leads to irreversible coagulation of the cells and 100-110^0 C results in vaporization and carbonization of tissue (58). The 1, 3, 5,10-year survival rates of CRLM following RFA are 98%, 69%, 48%, and 18% in a study by Solbiati et al. (59). Local tumor progression (LTP) after RFA, seen in 2-60% of cases, is an important factor to consider while ablating the CRLM. There are many factors that attribute to LTP including tumor size, tumor number, ablation zonal geometry, ablative margin, extrahepatic disease, location adjacent to large vessels and subcapsular tumors (60, 61). Radiofrequency ablation (RFA) is usually recommended in patients with ≤ 3-5 metastases of size ≤ 3-3.5 cm, not involving bile ducts or large vessels (≥3 mm), and not located centrally (62, 63).

Tumor size is critical in selecting patients for RFA as the commercially available devices can deliver the ablation to about 4-5 cm in one session and the studies reported high success rates of RFA in tumors ≤ 3-4 cm. In a study by Nielsen et al., the local recurrence after ablation was reported in 9%, 26.5%, and 45% of metastases measuring 0-3 cm, 3-5 cm and > 5 cm respectively (64). Compared to surgical resection, RFA has a lower complication rate

(9.5%) and minimal risk of death (10, 65). However, it cannot replace surgical resection, especially in tumors > 3 cm size (57). The number of CRLM is also an important criterion when selecting the patients for RFA. Solitary CRLM is associated with high tumor control and survival rates. Kim et al. reported the 5-year survival and disease-free survival rates as 51% and 34% respectively in patients with solitary CRLM of size < 3 cm (66). Similarly, Gillams et al. studied the 5-year survival rate of solitary CRLM of size 2.3 cm to be 54% with a median survival of 63 months (67). Wang et al. studied the emphasis of ablative and tumor margins and reported that the risk of LTP decreases by 46% for every 5-mm increase in ablative margin size and increases by 22% with every 5 mm increase in tumor size (68). The tumor abutting large vessels causes convective heat loss termed as "heat-sink effect", hence preventing heat accumulation in the tumor (63). A study by Elias et al. reported that 23% of CRLM, close to the large vessels, recured compared to 3% of CRLM located away from the vessels (69). In such situations, percutaneous balloon occlusion of large vessels during RFA has demonstrated improved tumor progression rates (62). Van Tilborg et al. studied that the centrally located CRLM recur more often compared to peripheral CRLM (21.4% vs. 6.5%; P= 0.009) (10).

Local tumor progression following RFA can be re-treated with repeat RFA, stereotactic body radiation therapy (SBRT), TACE, hepatic resection, and ultimately transplantation; however, with a high failure risk (70). The optimal choice among these techniques is still debatable, and a study by Xie et al. compared the repeat RFA with TACE and transplantation (70). In their study, repeat RFA has comparable outcomes with transplantation; hence the former is the primary choice, while the latter can be performed in patients where RFA failed or is inapplicable (70). Recently, CT-guided I^{125} brachytherapy has been studied in patients with recurrent HCC after thermal ablation. Its validation in recurrent CRLM is yet to be determined.

Other ablation techniques include microwave ablation (MWA), irreversible electroporation (IRE), and cryoablation. MWA has shown to be effective as an alternative to RFA and in a few cases, it is the preferred modality. The MWA generates heat by utilizing electromagnetic signals. Current machines operate between 900-2450 MHz, a frequency at which the microwaves cause coagulation necrosis by the oscillation of polarized water molecules which produce friction and heat (Figure 2) (57, 71). Compared to RFA, the size and zone of MWA are consistent and less affected by the heat-sink effect, impedance, penetrability, and thermal conductivity (72, 73). Gravante et al. examined the histopathological sample of MWA tissue and found no viable cells 6 cm away from the ablation zone in 93% of cases (74). Ierardi et al. included patients who are

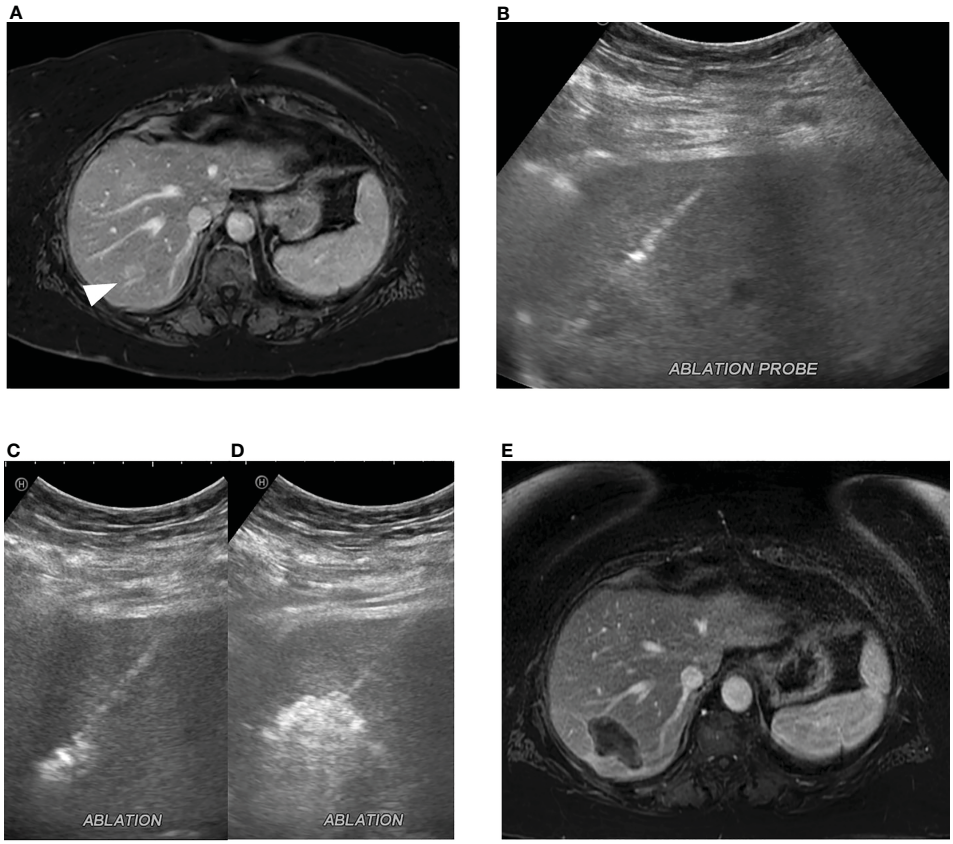

FIGURE 2
Microwave ablation of colorectal cancer liver metastasis. **(A)** A 2.0 cm colorectal cancer metastasis in segment 7 (white arrowhead). **(B)** Ultrasound-guided microwave ablation probe placement in the segment 7 lesion which was confirmed with CT (not shown). Continuous monitoring of ablation was performed with ultrasound with **(C)** early and **(D)** late ablation images obtained. **(E)** Post-ablation MRI, 1 month post procedure, demonstrates ablation zone without evidence of residual disease.

unfeasible to RFA such as those with tumors > 3 cm and are abutting larger vessels (> 3 mm) (73). They reported that the local recurrence was observed in 13% of patients with a disease-free OS of 20.5 months. Although no major complications were noticed, approximately 45% of patients had minor complications such as abdominal pain, fever with malaise, nausea, vomiting and elevated serum bilirubin levels (73). Pathak et al. reviewed various studies on RFA and MWA and reported that the local recurrence rates of CRLM after RFA and MWA to be ranging from 10-36% and 5-13% respectively (71). IRE is a non-thermal ablative technique that induces high-voltage electrical pulse waves between the electrodes (75). It is a safer ablation method in case of tumors close to the vascular or biliary structures due to the absence of the heat-sink effect (76, 77). The COLDFIRE-1 is a Phase-I study that demonstrated CRLM death and necrosis when exposed to IRE (78). COLDFIRE-2 is a Phase-II study including the patients with ≤ 5 cm CRLM, and it reported a 1-year PFS of 68%. Around 74% of the patients achieved local tumor control after the repeat IRE procedure (79). In a study by Schicho et al., 67% of patients achieved tumor control after the first IRE and 96% after re-intervention (80). Complications during IRE were reported to be observed in 40% of patients, with the most severe being arrhythmias, portal vein thrombosis, and biliary obstruction (79).

Laser ablation uses micrometer optical fiber to produce heat by transmitting infrared light. The optical fiber is connected to a generator or diode made of neodymium: yttrium aluminum garnet (ND: YAG), which emits a precise wavelength. The size of the fiber, the wavelength used, conduction and penetration of surrounding tissue, and the power and duration of the ablation are the factors that affect the size of the ablation zone (81). The lesions located within 1 cm of the main biliary duct, untreatable coagulopathy, and ascites interposed along the path of the applicator are considered contraindications to the thermal ablation (82). Patients may experience side effects after the procedure including pain, and post-ablation syndrome. Pain is self-limiting and depends on the size of the ablation zone. Post-ablation syndrome presents with flu-like illness with low-grade fever, nausea, vomiting and malaise, and can be managed symptomatically (72). Complications of the ablation procedure can be secondary to the injury to surrounding structures or the ablation itself, such as pneumothorax, intraperitoneal bleeding, hemothorax, portal vein thrombosis, gastrointestinal tract perforation, strictures, bile duct injury, cholecystitis, and liver abscess (72, 82).

The EORTC-CLOCC trial was a phase-II clinical trial that studied the efficacy of systemic chemotherapy with or without RFA in 119 patients diagnosed with unresectable CRLM (83). The trial randomized patients to receive systemic treatment alone or in combination with RFA. A significant improvement in OS and PFS was reported in the combined modality group rather than the systemic chemotherapy alone group (83). Improved OS in the combined modality group compared to the systemic treatment alone group (HR: 0.58; P=0.01) was observed. The 3-, 5- and 8-year OS rates were 56.9%, 43.1%, and 35.9% respectively in the combined modality group, and 55.2%, 30.3%, and 8.9% respectively in the systemic chemotherapy alone group. The median OS was 45.6 months in the combined modality group and 40.5 months in the systemic chemotherapy alone group. There was a prolonged PFS in the combined modality group (HR: 0.57; P=0.05). The liver as the first site of recurrence was noticed in 46.7% of the combined modality group and 78% of the systemic chemotherapy alone group (83). Another study, the ARF2003, included 52 unresectable CRLM treated with neoadjuvant chemotherapy and RFA. The study reported complete hepatic response in 75% of patients at their 3-month follow-up. The OS at 1-, and 5-years was 94% and 43% respectively, whereas PFS was 46% and 19% (84). Furthermore, another study reported that the combination of RFA and systemic chemotherapy has shown improved 3-year progression-free survival in comparison to systemic chemotherapy alone (27.6% vs. 10.6%; hazard ratio= 0.63; CI: 0.42-0.95; P=0.025) (85).

SBRT delivers the radiation to a specified region of interest with millimetric accuracy and reduces the irradiation to surrounding parenchyma. Unlike RFA and MWA, the SBRT is the better technique to access the perihilar, periampullary, or subcapsular lesions (86). SBRT can be considered, in combination with surgical resection, for oligometastatic liver disease that failed local therapies (87). Candidates with ≤ 5 CRLM involving <700 cc of the liver, an expected survival of > 3 months, curative extrahepatic disease, no chemotherapy received before two weeks of planned SBRT, and ≤ 2 Eastern Cooperative Oncology Group performance status are suitable for SBRT (87). A radiotherapy dose of ≥ 100-110 Gy can achieve local tumor control in 80-90% of the patients, while a higher dose may be required in case of larger tumors to attain similar outcomes (86–88). A study by Petrelli et al. included 656 patients and reported that the SBRT provides an overall survival of 67% and 57% and local tumor control of 67% and 59% at 1 and 2 years, respectively (89, 90). Compared to RFA, SBRT achieves greater 2-year local tumor control (84% vs. 60%); however, both the techniques had similar OS rates (91). The OLIVER trial compares the SBRT and chemotherapy alone and may provide further validations for its application (NCT03296839).

3.2 Radiation segmentectomy

Radiation segmentectomy (RS) delivers a very high ablative radiation dose (>190 Gray) confined to one or two liver segments, thus limiting the radiation-related complications (92, 93). The dose is based on the available literature for RS in patients with HCC which demonstrated a correlation between the level of tumor necrosis and the radiation exposure (93). The major intent of RS is to achieve cure in patients with CRLM, similar to the ablation or ablative external radiation therapy (94, 95). Diagnostic and therapeutic advancements through proper patient selection, imaging and radiation dosimetry allowed transition of lobar salvage to segmental curative radioembolization, especially in patients with features including (i) solitary tumor of size ≤ 5 cm (ii) primary or secondary liver tumor without other organ involvement and (iii) a tumor that can be targeted angiographically such that ≤ 2 liver segments receive the ablative dose of radiation (92, 96).

RECIST criteria have been widely employed to evaluate the response to TARE, however, PRECIST has proved to be more

accurate in CRLM (97–99). Among all the parameters included in PRECIST, metabolic tumor volume and total lesional glycolysis are observed to be the significant predictors of OS (100). Recently, Choi criteria based on tumoral attenuation and diameter on CT imaging was identified to be a reliable criterion in CRLM to predict the PFS (101). Kurilova et al. observed that the RS of ≤ 3 hepatic segments can provide a 2-year tumor control rate of 83% in patients with limited therapeutic options and limited metastatic disease (Table 5) (102). They also reported that the tumor progression occurred in 21% of their study population which is similar to the study by Padia et al. (103) who reported tumor progression in 28% (102). In a study by Meiers et al, the authors included 10 patients of which 7 patients had inoperable CRLM confined to ≤ 2 liver segments (104). The procedure was unsuccessful in one among 7 patients due to attenuated hepatic vasculature. Of the remaining 6 patients with CRLM, four had a complete response or stable disease at their follow-up evaluation ranging from 1-14 months. Two of six patients had progressive disease after 7- and 18-months period. There were no reported adverse events. The mean PFS was 7.1 months for the entire cohort (92, 104).

Although RS has a promising role in the treatment of HCC that cannot be resected or ablated, the literature on CRLM is limited (93, 105–107). In addition, as the most of the CRLM patients may have been pre-treated with chemotherapeutic regimens, the hepatic vasculature can be altered limiting the ability to perform the super-selective RS. Furthermore, the hypovascular nature of CRLM results in difficulty targeting the tumor. Based on the available data, RS appears to provide local tumor control with acceptable toxicity in patients with CRLM. Further studies on patient selection and tumor response are required to emphasize the application of RS in patients with CRLM.

3.3 Firstline chemotherapy plus TARE

Combined therapy with radioembolization and systemic chemotherapy has been studied in the literature. Haber et al. reported 38-month and 25-month median survival of CRLM patients treated with combined systemic chemotherapy plus TARE and systemic chemotherapy alone groups, respectively from the date of primary diagnosis (108). Three phase-III clinical trials, SIRFLOX, FOXFIRE and FOXFIRE-Global, studied the efficacy of combined chemotherapy with Y90 TARE over chemotherapy alone among 1103 patients in total (109–111). SIRFLOX trial by Van Hazel et al. concluded that the addition of TARE to the chemotherapy did not improve the PFS, however delayed the tumor progression significantly (Table 6) (110). A combined analysis of FOXFIRE, SIRFLOX and FOXFIRE-Global was performed by Wasan et al. with a total of 1103 patients (113). The patients were randomized to receive FOLFOX alone (549) or in combination with single cycle of TARE (554). Higher overall response rate was reported in the combined group (72% vs. 63%) however no differences were identified in median OS (22.6 months vs. 23.3 months; P=0.61). Radiological progression of the tumor was observed in 49% of FOLFOX alone group and 31% of the combined group. The cumulative incidence of tumor progression in the first 12 months follow up period was 22% in the combined group compared to 39% in FOLFOX alone group. An objective response rate was reported in 72% of the combined group and 63% of FOLFOX alone group (P= 0.0012). The study also reported high odds of grade 3 or worse adverse events in the combined group (74%) than the FOLFOX alone group (67%) (OR: 1.42; P= 0.008) (113). Wasan et al. reported 17% resectablity rate in TARE + chemotherapy group and 16% in chemotherapy alone group (P=0.67) (113). Garlipp et al. reported an improved resectability rate of the lesions after TARE+ chemotherapy compared to chemotherapy alone (38.1% vs. 28.9%; P<0.001) (115). The subgroup analyses of the FOXFIRE, SIRFLOX and FOXFIRE-Global trials reported no significant difference in OS between the combined and FOLFOX alone group (112, 114). However, when tumors are stratified based on location, the addition of SIRT improved the OS in right-sided but not left-sided primary CRC (Table 6) (112, 114).

TABLE 5 Studies describing the efficacy of radiation segmentectomy.

Study	Study design	Country/ Region	Sample size	Patient characteristics	Follow-up/ Inclusion period	Results
Kurilova et al., 2021 (102)	Retrospective study	United States	10 patients	14 tumors treated with 12 RS sessions; Each patient has ≤ 3 tumors of median size 3 cm; Median radiation dose delivered: 293 Gy	Included the patients between 2015 and 2017; median follow up of 17.8 months (Range: 1.6-37.3)	Tumor response as per Choi and RECIST criteria: 100% and 44% respectively; Tumor progression: 33%; 1-, 2- and 3-year PFS: 83%, 83%, and 69% respectively; Median OS: 41.5 months
Padia et al., 2020 (103)	Retrospective study	United States	36	36 patients; 81% had prior chemotherapy; CRC: 31%; NEN: 28%; Sarcoma: 19%; Miscellaneous: 22%	Included patients between 2013 and 2018	Disease control rate was 92% according to RECIST criteria in all tumors and 100% according to mRECIST criteria in hypervascular tumors; Tumor progression: 28%; OS at 6 and 12 months was 96% and 83% respectively.
Jia et al., 2019 (96)	Systematic review	Multiregional	155	HCC: 145; CRC: 7; Others: 3	Included patients between 1991 and 2018	CR, PR, SD and PD was observed in 20-82%, 10-70%, 1.8-40% and 0-8% respectively. Disease control rate: 92-100%.

PFS, Progression free survival; OS, Overall survival; CRC, Colorectal cancer; NEN, Neuroendocrine neoplasm; HCC, hepatocellular carcinoma; CR, Complete response PR, Partial response; SD, Stable disease; PD, Progression of disease.

TABLE 6 Data on the efficacy of combined chemotherapy and TARE.

Study	Study design	Country/ Region	Sample size	Patient characteristics	Follow up/ Inclusion period	Results
Gibbs et al., 2018 (112)	Combined analysis of two randomized control trials FOLFOX and SIRFLOX	Multiregional study	739	FOLFOX + SIRT: 372 patients; FOLFOX alone: 367 patients	Included patients from 2006 to 2015; median follow-up period was 22.2 months	TARE has significant impact on OS in patients with right-sided (22 months vs. 17.1 months; P= 0.008) but not left-sided primary tumor (24.6 months vs. 26.6 months; P= 0.264).
Wasan et al., 2017 (113)	Combined analysis of three trials FOXFIRE, SIRFLOX, FOXFIRE-Global	Multiregional study	1103	FOLFOX+ SIRT: 554 patients; FOLFOX: 549 patients	Included patients between 2006 and 2014; Median follow-up was 43.3 months	No difference in median OS and median PFS; ORR: 72% (FOLFOX+SIRT) and 63% (FOLFOX alone); Tumor progression: 31% (FOLFOX +SIRT) and 49% (FOLFOX alone)
Van Hazel et al., 2017 (114)	Combined analysis of FOXFIRE-Global and SIRFLOX trials	Multiregional study	739	739 patients were randomized to receive either FOLFOX alone or in combination with SIRT with Y-90 microspheres	–	SIRT improved OS in right sided primary tumors (22 vs. 17 months; P= 0.007) and the difference in OS was not significant in left-sided primary tumors (24.6 vs. 25.6 months; P= 0.279)
Van Hazel et al., 2016 (110)	Randomized Phase III trial	Multiregional study	530	530 patients randomized to FOLFOX + SIRT +/- bevacizumab or FOLFOX	Included patients between 2006 and 2013;	Median PFS at any site: 10.2 (FOLFOX alone) vs. 10.7 (FOLFOX+SIRT) months (P= 0.43); Median PFS in the liver: 12.6 (FOLFOX alone) vs. 20.5 (FOLFOX+SIRT) months (P= 0.002); ORR at any site: 68.1% (FOLFOX alone) vs. 76.4% (FOLFOX+SIRT) (P= 0.113); ORR in the liver: 68.8% (FOLFOX alone) vs. 78.7% (FOLFOX +SIRT) (P= 0.042); Grade ≥ 2 adverse events observed in 73.4% (FOLFOX alone) and 85.4% (FOLFOX+SIRT) of patients.

FOLFOX, 5-fluorouracil and oxaliplatin; SIRT, Selective internal radiation therapy; TARE, Trans-arterial radioembolization; OS, Overall survival; ORR, Objective response rate; PFS, Progression free survival.

4 Therapies with palliative intent

4.1 TACE

Approximately 80% of blood supply to CRLM is derived from the hepatic artery while it is from the portal vein to the normal liver parenchyma (42, 116). Transarterial therapies utilize the advantage of dual blood supply of the liver and hence the cytotoxic agents infused through the hepatic artery selectively target tumor over normal cells. In addition, the first pass metabolism of the chemotherapeutic agents can be bypassed in the intra-arterial therapies. TACE is a catheter-based infusion of one or more chemotherapeutic medications and embolizing material into the hepatic artery. Embolizing material can be either temporary or permanent. The former includes collagen, gelatin sponge and degradable starch microspheres, while the latter include polyvinyl alcohol particles. Lipiodol has both the vaso-occlusive effect and the ability to enhance the effect of cytotoxic agents (117). TACE procedure was first introduced by Yamada et al. in late 1970s (118). In general, TACE is indicated as a second-line modality of treatment in patients who are refractory to systemic chemotherapy or in inoperable CRLM (119). Conventional TACE (cTACE) represents the injection of lipiodol + chemotherapy and embolizing agents. Recently, the drug-eluting beads are being used as embolic materials termed as DEB-TACE. The efficacy of cTACE and DEB-TACE have been extensively studied in the management of CRLM.

4.1.1 Conventional TACE

The chemotherapeutic regimen and embolic materials are variable in the published studies. Albert et al. studied the efficacy of TACE with doxorubicin, cisplatin, mitomycin C and lipiodol mixture followed by embolization material- polyvinyl alcohol particles, in 245 unresectable CRLM in 121 patients who were refractory to systemic chemotherapy (120). Median survival from initial CRLM diagnosis and TACE was 27 months and 9 months, respectively. The study described that the OS was better with TACE after first- or second-line systemic chemotherapy than after three to five lines of systemic chemotherapy (11-12 months vs. 6 months; P= 0.03) (120). Vogl et al. studied 463 patients with unresectable CRLM (117). Patients were divided into three groups with each receiving mitomycin C alone, mitomycin C plus gemcitabine, or mitomycin C plus irinotecan and followed by embolization with starch microspheres. The authors reported that 1-year and 2-year survival rates were 62% and 28% respectively with no significant difference among the patient groups (117). A study by Gruber-Rouh et al. involved 564 patients who were infused with mitomycin C, gemcitabine, irinotecan or cisplatin depending on the prior

systemic chemotherapy regimen (Table 7) (123). For instance, patients treated with systemic FOLFOX or FOLFIRI were treated with mitomycin alone. Embolization was performed with iodized oil and starch microspheres. The study reported survival of 14.3 months from the start of first cTACE (123).

Vogl et al. studied on patients treated with cTACE as a palliative or a neoadjuvant option (Table 7) (122). The cTACE was followed by ablation in the neoadjuvant group. All the patients were refractory to prior systemic chemotherapy. Vogl et al. reported significant improvement in OS and PFS in palliative (12.6 and 5.9

TABLE 7 Studies describing the role of TACE in CRLM.

Study	Study design	Country/ Region	Sample Size	Patients	Follow up/ Inclusion period	Results	Additional data
Maraj et al. (121) 2023	Retrospective study	Canada	120	328 procedures of irinotecan-eluting microspheres TACE was performed in unresectable CRLM with <75% hepatic parenchymal disease, limited extrahepatic tumor burden and previous locoregional treatment.	Included patients between 2012 to 2020	Technical success rate was 85%; Median OS of 12.7 months; The OS improved if the patient has prior ablation (P<0.05), <25% hepatic tumor burden (P<0.001), and previously resected primary disease (P<0.05)	5% intraprocedural adverse events including groin hematoma without pseudoaneurysm, periprocedural pain and hepatic artery dissection; 6% post-procedural adverse events including post embolic cholecystitis, perforated gastric ulcer, bleeding duodenal ulcer and biloma.
Vogl et al. (122) 2018	Retrospective study	Germany	452	Total: 452 patients with CRLM unresponsive to systemic chemotherapy; TACE as palliative option: 233 patients; TACE followed by ablation as neoadjuvant therapy: 219 patients	Included patients between 2001 and 2015	OS and PFS in palliative group were 12.6 and 5.9 months respectively and in neoadjuvant group was 25.8 and 10.8 months respectively.	Extrahepatic metastases in both palliative and neoadjuvant group; Tumor number, location, average size of metastases in neoadjuvant group.
Gruber-Rouh et al. (123)2013	Retrospective study	Germany	564	564 patients underwent TACE; Mean number of sessions:6	Included patients between 1999 and 2011	Partial response: 16.7%; Stable disease: 48.2%; Progressive disease: 16.7%; 1-, 2-, and 3-year survival rates: 62%, 28%, and 7% respectively; Median survival from the start of TACE: 14.3 months	Predictors of survival: Indication of TACE and initial tumor response
Nishiofuku et al. (124) 2013	Prospective trial	Japan	24	24 patients treated with FOLFOX prior to TACE	Phase I patient recruitment from February 2008 to July 2008; Phase II patient recruitment from September 2008 to January 2010; Mean follow up duration was 17.4 months	Tumor response rate: 61.1%; Median hepatic PFS: 8.8 months; OS: 21.1 months	Grade 3 thrombocytopenia: 12.5%; Grade 3 AST elevation: 33.3%; Grade 3 ALT elevation: 12.5%; Grade 3 hyponatremia: 8.3%; Grade 3 cholecystitis: 4.2%
Albert et al. (120) 2011	Retrospective study	United States	121	121 patients were treated with TACE comprising cisplatin, mitomycin C, doxorubicin, ethiodized oil and polyvinyl alcohol particles	Included patients between 1992 and 2008	Partial response: 2%; Stable disease: 41%; Progressive disease: 57%; Median time to disease progression: 5 months; Median survival: 27 months from development of hepatic metastases and 9 months from chemoembolization; Survival was better when cTACE was performed prior to third line systemic chemotherapy	

(Continued)

TABLE 7 Continued

Study	Study design	Country/ Region	Sample Size	Patients	Follow up/ Inclusion period	Results	Additional data
Muller et al. (125) 2007	Prospective study	Germany	66	66 patients; 5-FU and GM-CSF infusion followed by embolization with Melphalan, lipiodol, and gelfoam; 54% of patients received prior systemic chemotherapy	–	Complete response: 1%; partial response: 42.4%; Stable disease: 18.2%; No response: 12.1%; Two-year survival: 66%; Time to progression: 8 months	Almost all patients experienced self-limiting side effects such as upper abdominal pain, vomiting and leukopenia
Wasser et al., 2005 (126)	Randomized prospective trial	Germany	21	21 patients with CRLM patients treated with TACE	Total follow up duration was 12-18 weeks	Median survival was 13.8 months; therapeutic response in three patients; progression free interval of 5.8 months	

TACE, Trans- arterial radioembolization; CRLM, Colorectal liver metastases; OS, Overall survival; PFS, Progression free survival; FOLFOX, 5-fluorouracil and oxaliplatin; AST, Aspartate transaminase; ALT, Alanine transaminase; 5-FU, 5-Fluorouracil; GM-CSF, Granulocyte monocyte- colony stimulating factor.

months, respectively) and neoadjuvant (25.8 and 10.8 months, respectively) groups (122). The presence of extrahepatic metastases was described as the significant factor for OS and PFS in both palliative and neoadjuvant groups (122). Vogl et al. concluded that cTACE was effective in unresectable advanced CRLM and further improves survival, if followed by ablation (122). Nishiofuku et al. studied the efficacy of TACE with cisplatin powder and degradable starch microspheres (DSM) and a reported tumor response rate in 61.1% of patients (124). They also reported the median OS, PFS, and hepatic-PFS as 21.1 months, 5.8 months, and 8.8 months (124). However, majority of patients became eligible for surgical resection post-TACE, which might overestimate the OS benefit of TACE. The authors studied the tumor response rate in wild-type and mutated KRAS tumors to be around 75% and 66.7%, respectively (124). The study concluded that cisplatin, at a dose of 80 mg/m2 with the DSM, can provide a high tumor response rate and prolonged survival time for patients with unresectable CRLM refractory to FOLFOX systemic chemotherapy (124). Short embolization effect and good tumor response are the two main advantages of DSM-TACE over conventional TACE (127). In summary, all the described studies demonstrate that cTACE is a feasible treatment modality in patients who are unresponsive to conventional therapy.

The TACE in combination with RFA is studied to improve the survival and outcomes in single HCC lesion >5 cm and multiple HCC lesions >3 cm (128). The same has also been applied in CRLM by Faiella et al., who discovered a positive impact on the patient survival (129). However, the data is limited as the protocol for TACE is quite different from RFA. Regular TACE protocol is for widespread CRLM, while targeted TACE, along with RFA, can be used for focal metastases (128).

4.1.2 DEBIRI-TACE

A current area of research involves the use of irinotecan drug-eluting beads (DEBIRI-TACE) to treat CRLM. The initial results of a Phase II clinical trial comprising 20 patients reported an 80% response rate with reduction of contrast enhancement of treated tumors following treatment with irinotecan drug-eluting beads [37]. Similarly, Aliberti et al. reported 78% tumor response rate at three months in a phase II study comprising 82 patients (130). All the patients had at least two failed systemic chemotherapy lines. The study also described the OS and PFS as 25 months and 8 months respectively (130). Martin et al. studied the efficacy of DEBIRI in patients refractory to oxaliplatin- and irinotecan-based systemic chemotherapy. The study concluded that DEBIRI was safe with minimal complications and 75% tumor response rate (131). This promising treatment for patients with colorectal metastases merits further study both as a salvage agent and potentially in combination with systemic chemotherapy. Fiorentini et al. compared the efficacy of FOLFIRI and DEBIRI-TACE (132). Median OS was longer for DEBIRI-TACE group (22 vs. 15 months). In addition, DEBIRI-TACE group had better quality of life (8 vs. 3 months) and objective tumor response (69% vs. 20%) (132). However, the study was limited by the omission of bevacizumab, oxaliplatin, panitumumab or cetuximab in the standard care of treatment (132). Martin et al. overcame this limitation by comparing DEBIRI plus systemic FOLFOX and bevacizumab with systemic FOLFOX plus bevacizumab alone (133). The study observed a significantly greater response rate in DEBIRI-FOLFOX arm compared to FOLFOX/bevacizumab arm at the end of 2 months (78% vs. 54%) and 6 months (76% vs. 60%) (133). Th significant tumor downsizing was observed in DEBIRI-FOLFOX arm than the comparison arm (35% vs. 16%) (133). The median PFS of 15.3 months was reported in DEBIRI-FOLFOX arm and 7.6 months in FOLFOX/bevacizumab arm (133). Nonetheless, the study by Martin et al. did not demonstrate improvement in OS compared to cTACE studies that excluded systemic chemotherapy (Table 8) (133). Recently, a systematic review by Akinwande et al. included 13 studies comprising a total of 850 patients (135). The weighted average PFS and OS were 8.1 months and 16.8 months respectively (135).

The most common complications following TACE procedure include post-embolization syndrome (PES) (15-90%), cholecystitis, and hepatic insufficiency (134, 136). Complications such as segmental biliary dilatation, thrombocytopenia, leukopenia, hepatic artery thrombosis, embolus migration are less common (134). The etiology of PES is not entirely determined but several

TABLE 8 Studies describing the role of DEBIRI-TACE in CRLM.

Study	Study design	Country/ Region	Sample size	Patient characteristics	Follow up/ Inclusion period	Results
Szemitko et al. (134) 2021	Retrospective study	Poland	52	52 patients underwent 202 DEBIRI-TACE	Included the patients between 2016 and 2019	Median survival: 13 months; 1-year survival: 63%; 2-year survival: 33%; Significant complications: 7.4%; PES: 51%;
Akinwande et al. (135) 2017	Systematic review	United States	850	13 studies with a total of 850 patients treated with systemic chemotherapy	Included patients until 2016	Average all-grade toxicity: 35.2%; Average response rate: 56.2% and 51.1% according to RECIST and modified RECIST/EASL response criteria; PFS: 8.1 months; OS: 16.8 months.
Martin et al. (133) 2015	Randomized control trial	United States	70	70 patients randomized to DEBIRI/FOLFOX group and FOLFOX/bevacizumab group	Median follow up of 19 months (range 17-38 months)	DEBIRI/FOLFOX vs. FOLFOX/bevacizumab: Grade 3/4 adverse events- 54% vs. 46%; Overall response rate: 78% vs. 54% at 2 months and 76% vs. 60% at 6 months; Tumor downsizing: 35% vs 16%; Median PFS: 15.3 months vs. 7.6 months (P=0.18).
Fiorentini et al. (132) 2012	Prospective study	Italy	74	74 patients randomized to FOLFIRI and DEBIRI-TACE	Included patients presenting between 2006 and 2008; Median follow up at 50 months	Median survival for DEBIRI and FOLFIRI: 22 vs. 15 months; PFS: 7 vs. 4 months; Quality of life: 8 vs. 3 months
Martin et al. (131) 2009	Prospective study	United States, Canada, Europe, and Australia	55	55 patients treated with DEBIRI-TACE with 2 as the median number of treatments per patient	Included patients between 2007 and2008	Median DFS and OS were 247 days and 343 days respectively; Downstaged disease in 10% of patients; Response rate at 6 and 12 months was 66% and 75%, respectively; Predictors of OS: extrahepatic disease and extent of prior chemotherapy

DEBIRI, irinotecan drug-eluting beads; TACE, Trans-arterial chemoembolization; PFS, progression free survival; OS, Overall survival; FOLFOX, 5-fluorouracil and oxaliplatin; DFS, Disease free survival.

theories have been proposed including hepatic capsular distention, tumor necrosis, hepatic ischemia, anti-inflammatory response to chemotherapeutic medications and gallbladder infarction (136, 137). Paye et al. studied that the PES following TACE is due to injury to the non-tumoral hepatic cells (138). Risk factors for the adverse effects include complete flow stasis during embolization, lack of pre-treatment with lidocaine, infusion of > 100 mg of DEBIRI, bilirubin > 2 ug/dl, with > 50% liver involvement, and achievement of complete stasis (131). Hence, patients with extrahepatic metastases, tumor burden of >70% liver parenchyma, increased bilirubin levels (> 3mg/dl), renal dysfunction (serum creatinine, > 2 mg/dl), and complete portal venous thrombosis are usually excluded from TACE (123).

DEB-TACE has certain limitations including (i) inability to identify the beads in real-time which in turn prevents the visualization of intraoperative precise delivery and post-operative effects (ii) as the DEBs load only positively charged chemotherapeutic medications, the options of drugs are restricted (139). Hence, new drug carriers are being studied to overcome the limitations. Iodine-containing and superparamagnetic iron oxide- containing microspheres are studied to visualize on the X-ray and MR imaging respectively.

4.2 TARE

Guidelines support TARE as a treatment option in patients with CRLM who are refractory to ≥ 2 lines of systemic chemotherapy (Figure 3) (category 2A and Grade B recommendation as per European Society for Medical Oncology and National

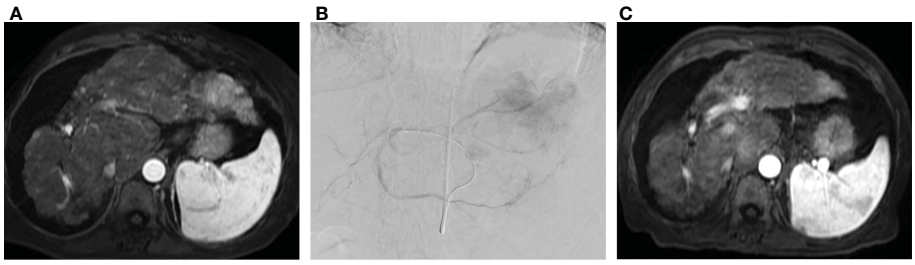

FIGURE 3
Radioembolization as salvage therapy. **(A)** Pre-procedure MRI in patient with metastatic colorectal cancer to the liver following three lines of chemotherapy demonstrating multifocal metastatic disease involving the left hepatic lobe. **(B)** Transradial radioembolization of the left hepatic lobe with Yttrium-90 resin microspheres *via* a replaced left hepatic artery arising from a left gastric artery. **(C)** Post procedure MRI with interval reduction in size and enhancement of left hepatic lobe tumor.

Comprehensive Cancer Network, respectively) (57, 140, 141). The application of TARE as a second-line therapy in unresectable CRLM refractory to first-line systemic chemotherapy require endorsement from further studies. Ideal candidates for Y90-TARE shall be ≥ 18 years old, Eastern Cooperative Oncology group (ECOG) score ≤ 2, serum bilirubin < 3 mg/dl, serum creatinine < 2 mg/dl, and with adequate lung function (140). Mulcahy et al. reported tumor response rate of 40.3% in unresectable CRLM when exposed to a median dose of 118Gy (Table 9) (148). The MORE study included 606 patients with CRLM who had two lines of prior systemic chemotherapy. The study reported OS of 9.6 months (144). Hickey et al. reported OS of 10.6 months in their study which involved 531 patients who were refractory to prior systemic chemotherapy or locoregional therapies (143). Absence of extrahepatic metastases, <25% tumor burden, albumin > 3 g/dl, good performance status and receipt of < 2 chemotherapeutic medications are the independent predictors of survival (143). In a prospective study by Helmberger et al. involving 1027 patients who underwent Y90-TARE for primary or metastatic hepatic tumors, the authors reported the OS of 9.8 months in CRLM (150). Wu et al. compared the survival outcomes with Y90-TARE in right versus left sided primary tumor location. They observed that patients with right sided primary tumors had decreased OS compared to left sided primary tumors (5.4 vs. 6.2 months; P=0.03) (151). However, no significant difference in hepatic PFS, tumor response and disease progression were observed (151). Lahti et al. studied the KRAS status as the prognostic factor in unresectable CRLM who underwent Y-90 TARE. They reported that median OS was greater in patients with KRAS wild-type genes than

TABLE 9 Studies describing the application of TARE in CRLM.

Study	Study design	Country/ region	Sample size	Patient characteristics	Follow up/ Inclusion period	Results	Additional data
Kalva et al. (142) 2017	Retrospective study	United States	45	45 patients with CRLM, who are unresponsive to chemotherapy	Included patients between 2005 to 2011	Technical success rate: 100%; Partial response: 2%; Stable disease (71%); Progressive disease (13%); PET response rate: 46%; Median survival: 186 days	Grade-3 toxicities: 13%; PET response was the independent predictor of OS; OS in PET responsive and non-responsive patients: 317 days vs. 163 days respectively.
Hickey et al. (143) 2016	Retrospective study	United States	531	531 patients who underwent radioembolization of CRLM	Included patients between 2001 and 2014	Median OS: 10.6 months; Median OS for patients who received three chemotherapeutics was shorter than those who received ≤ 2 chemotherapeutics (9.2 vs. 14.7 months)	Adverse events: Fatigue- 55%; Abdominal pain- 34%; Nausea- 19%; Grade 3/4 hyperbilirubinemia- 13%. Independent predictors of survival: Performance status, < 25% tumor burden, no extrahepatic metastases, albumin > 3 g/dl, and no more than two lines of chemotherapy.
Kennedy et al. (144) 2015	Retrospective study	United States	606	606 patients, with a prior history of two lines of chemotherapy, who underwent radioembolization for CRLM	Included patients between 2002 and 2011	Median survival following 2^{nd} -, 3^{rd} -, and 4^{th} - line chemotherapy was 13, 9, and 8.1 months respectively.	Garde ≥ 3 adverse events: Abdominal pain- 6.1%; Fatigue- 5.5%; Hyperbilirubinemia- 5.4%; Ascites- 3.6%; Gastrointestinal ulceration- 1.7%. Independent variables for survival: Stage of tumor, tumor to treated liver ratio, LFTs, leukocytes and prior history of chemotherapy.
Saxena et al. (145) 2014	Systematic review	Australia	979	20 studies with a total of 979 patients who failed atleast 3 lines of chemotherapy and underwent radioembolization	Included the studies performed before 2012	Complete radiological response: 0%; partial response: 31%; stable disease: 40.5%; OS: 12 months	Acute toxicity: 11-100%; Factors associated with poor survival: ≥ 3 lines of chemotherapy, extrahepatic disease, poor radiological response and extensive liver disease
Evans et al. (146) 2010	Retrospective study	Australia	140	140 patients with CRLM who are unresponsive to chemotherapy and underwent radioembolization	Included patients between 2006 to 2009	OS: 7.9 months;	Minor complications in the form of abdominal pain, nausea and vomiting.

(Continued)

TABLE 9 Continued

Study	Study design	Country/ region	Sample size	Patient characteristics	Follow up/ Inclusion period	Results	Additional data
Cianni et al. (147) 2009	Retrospective study	Italy	41	Patients with CRLM who are unresponsive to chemotherapy and underwent radioembolization	Included patients between 2005 and 2008	Complete response: 4.8%; partial response: 41.5%; Stable disease: 36.2%; Progressive disease: 19.5%; CEA reduced from 4.2 ug/L before treatment to 2.1 ug/L after treatment; Technical success rate: 98%; Median survival: 354 days; PFS: 279 days	Hepatic failure: 2%; Grade-2 gastritis: 4%; Grade-2 cholecystitis: 2%
Mulcahy et al. (148) 2009	Prospective study	United States	72	Patients with unresectable CRLM who ultimately underwent radioembolization	Included patients between 2003 and 2007	Tumor response rate: 40.3%; PET response rate: 77%; OS from the date of hepatic metastases: 34.6 months; OS from first Y90 treatment: 14.5 months; Patients with ECOG status 0 had a median survival of 42.8 months and 23.5 months from the date of hepatic metastases and Y90 treatment, respectively.	Fatigue (61%), nausea (21%), abdominal pain (25%), grade 3 & 4 bilirubin toxicities (12.6%).
Kennedy et al. (149) 2006	Prospective study	United States	208	Unresectable CRLM refractory to Oxaliplatin and Irinotecan	Included patients between 2002 and 2005; Median follow-up: 13 months; Median survival: 10.5 month in responders and 4.5 months in non-responders	CT partial response rate: 35%, PET response rate: 91%; CEA reduced by 70%	Nausea (9-10%), abdominal pain (11-13%), grade 2 & 3 bilirubin toxicity (3-4.5%), grade 2 & 3 ALP toxicity (20-20.5%)

CRLM, Colorectal liver metastases; PET, Positron emission tomography; OS, Overall survival; LFT, Liver function tests; CEA, Carcinoembryonic antigen; PFS, progression free survival; ECOG, Eastern cooperative oncology group; CT, Computed tomography.

mutant genes (9.5 months vs. 4.8 months; P= 0.04) (152). The KRAS status, carcinoembryonic antigen levels, and Child-Pugh class were found to be the prognostic factors for OS (152). Narsinh et al. described the importance of hepatopulmonary shunting as a prognostic indicator of survival in their study of 606 patients who underwent Y90-TARE for CRLM. They reported that increased liver shunt fraction (LSF) indicated worse prognosis in CRLM. The LSF > 10% was associated with reduced survival rate compared to LSF < 10% (6.9 months vs. 10 months; HR: 1.60; P<0.001) (153).

Dendy et al. studied the survival predictive biomarkers in patients who underwent Y90-TARE for CRLM (140). They described that low tumor burden, sufficient calculated Y90 dose, increased albumin, and low ECOG score are the pre-interventional biomarkers which indicate favorable outcome (140). Likewise, after the procedure, decreased tumor burden, reduced tumor glycolysis, radiological tumor response and reduced expression of surviving, p53, Bcl-2 are indicative of favorable outcome (140). Irrespective of timing of biomarker evaluation, the increased HMGB1(High mobility group box 1), nucleosome expression, increased carcinoembryonic antigen, CA 19-9, CYFRA 21-1 (Cytokeratin 19 fragment), lactate dehydrogenase, aspartate transaminase, choline esterase, gamma glutamyl transferase, alkaline phosphatase, amylase are the indicators of unfavorable response (140). Usually, Y90 radioembolization is safe with minor complications and post-embolization syndrome. Gastric ulceration (<5%), portal hypertension (<1%), radiation induced liver fibrosis (<4%), pancreatitis (<1%), biloma (<1%), cholecystitis (<1%), abscess formation (<1%), and radiation induced pneumonitis (<1%) are the few of reported complications secondary to radioembolization (154). The post-embolization syndrome can be observed in 50% of the patients within 2 weeks of the procedure. In contrast to post-embolic syndrome, it rarely requires patient hospitalization.

5 Other hepatic metastases

Very few studies have been performed on the interventional management of non-CRLM. In liver metastases secondary to gastric tumors, RFA is proven beneficial only in cases of single metastases limited to a single lobe and without extrahepatic disease (155). Combined systemic chemotherapy is also recommended in addition to RFA to prolong the OS (155). RFA in liver metastases secondary to breast cancer has also been studied to improve OS; however, the extrahepatic metastases (P=0.013) and age >60 years (P=0.025) are considered worse prognostic factors for OS (156). MWA has equal benefits to RFA and can be an alternate therapy in patients with liver metastases originating from ovarian, pancreatic, esophageal, and neuroendocrine neoplasms (157). Further broad studies are required for more data on patient outcomes and efficacy. Arterial

interventions such as TACE with raltitrexed eluting beads are studied to be safe and efficient in hepatic metastases due to gastric adenocarcinoma (158). In contrast to CRLM, the focus of arterial interventions in neuroendocrine liver metastases (NELM) is on the controlling the endocrine secretions (159). NELM are hypervascular tumors, and the studies show that the embolization alone has good efficacy on patient outcomes, unlike colorectal metastases, requiring chemotherapeutic embolization (160, 161). Elf et al. demonstrated that the NELM has optimal response rates to embolization therapies compared to SIRT (162). Other than CRLM and NELM, the literature is limited to other hepatic metastases. Saxena et al. studied that SIRT in chemoresistant hepatic metastases due to breast cancer has improved 24-month survival rates to 39% (163). Despite this, prospective trials on optimal patient selection and survival data are necessary for further validation.

6 Future directions

The combination of immunotherapy and targeted ablation is a new revolutionizing concept based on enhanced exposure of the tumor antigen. Ablated and dead tumor cells release tumor antigens into the bloodstream which augments the T-cell response, enhancing the efficacy of immunotherapy (164). Both the pro-inflammatory cytokines such as IL-6, and the anti-inflammatory cytokines, such as IL-10, get elevated after the ablation procedure. So far, cryoablation has been proven to induce a higher (4.6 fold) IL-10 release compared to heat-based techniques such as RFA (1,7 fold) and MWA (1.2 fold) (165, 166). Shi et al. reported that the PD-L1-PD-1 axis inhibits the T-cell response; hence monoclonal antibodies against the PD-1 are used to increase the feasibility of an anti-tumor immune response (167). The stronger T-cell response, robust anti-tumor immunity, and improved survival rates were observed in mice after combining anti-PD1 monoclonal antibodies with an ablation procedure (167). Likely, the TACE procedure triggers tissue hypoxia and the release of vascular endothelial growth factor, which could be used as the target for bevacizumab and tyrosine kinase inhibitors. Tumor-associated macrophages (TAMs) are responsible for tumor nurture and metastasization by inducing the epithelial-to-mesenchymal transition (EMT) and vascular disruption. Current studies are targeting TGF-beta signaling pathway, which is responsible for the EMT. The collagen triple helix repeat containing 1 (CTHRC1) is secreted by the colorectal cancer cells, stabilizing the TGF-beta signaling and activation. Studies show that the monoclonal antibodies against CTHRC1 combined with PD-1/PD-L1 blockade have led to the shrinkage of CRLM (168). Similarly, strategies targeting the TAMs reprogramming, depletion, and inhibition were studied (169). However, stronger validations are not yet provided due to the heterogenous behavior of the TAMs.

7 Conclusion

Tremendous evolution has occurred over the last two decades in the locoregional interventional therapies for CRLM. Surgical resection is the curative treatment for patients with CRLM. In case of unresectable tumors or non-surgical candidates, evaluation for ablation is recommended. Transarterial therapies are indicated as a salvage therapy and Y90-TARE is the FDA approved therapy for CRLM. DEBIRI-TACE or cTACE is considered in patients with progressive liver disease after Y90-TARE.

Author contributions

SV, PS, SK, NO and SPK have contributed equally to this work. All authors contributed to the article and approved the submitted version.

Conflict of interest

SPK reports grants from NIH, BD, Black Swan, and Trisalus for Institution; reports royalties from Elsevier, Springer, and Thieme for himself; reports consulting fees from Penumbra, Okami Medical, Boston Scientific, Medtronic, Covidien, US Vascular, Dova Pharmaceuticals, Instylla, and BD for himself; reports payment from Stony Brook University, American Institute of Biology, UT Houston, and NACCME for himself; reports payment for expert testimony from Southern Institute for Medical and Legal Affairs LLC for himself; reports participation from NIH for institution; reports leadership from Chief, Interventional Radiology, Massachusetts General Hospital, Boston, MA; Chair, Vascular Panel, ACR Appropriateness Criteria; International Editor, Journal of Clinical Interventional Radiology ISVIR; Assistant Editor, Radiology – Cardiothoracic, RSNA; reports stock from Biogen Inc, Clover Health Investments Corp, Inovio Pharmaceuticals, Moderna Inc, Pfizer Inc, Novavax Inc, Orphazyme, Cassava Sciences Inc, Vivos Therapeutics Inc, Ardelyx Inc, Althea Health, Sarepta Therapeutics, Clover Health Investments Corp, CureVac BV, Immunoprecise Antibodies Ltd, Infinity Pharmaceuticals Inc, Zymergen Inc, BioNTech SE, Trillium Therapeutics Inc, Theravance Biopharma Inc, Doximity Inc, Eargo Inc, Allogent Therapeutics Inc, NRx Pharmaceuticals Inc, Atea pharmaceuticals Inc, for himself and spouse; and reports financial or nonfinancial interests as Adjunct Associate Professor from University of Texas Southwestern Medical Center and Professor of Radiology at Harvard medical school.

The remaining authors declare that the research was conducted in the absence of any commercial or financial relationships that could be construed as a potential conflict of interest.

Publisher's note

References

1. Piawah S, Venook AP. Targeted therapy for colorectal cancer metastases: a review of current methods of molecularly targeted therapy and the use of tumor biomarkers in the treatment of metastatic colorectal cancer. *Cancer* (2019) 125(23):4139–47. doi: 10.1002/cncr.32163

2. Zhou H, Liu Z, Wang Y, Wen X, Amador EH, Yuan L, et al. Colorectal liver metastasis: molecular mechanism and interventional therapy. *Signal Transduct Target Ther* (2022) 7(1):70. doi: 10.1038/s41392-022-00922-2

3. Dekker E, Tanis PJ, Vleugels JLA, Kasi PM, Wallace MB. Colorectal cancer. *Lancet* (2019) 394(10207):1467–80. doi: 10.1016/S0140-6736(19)32319-0

4. Riihimäki M, Hemminki A, Sundquist J, Hemminki K. Patterns of metastasis in colon and rectal cancer. *Sci Rep* (2016) 6(1):1–9. doi: 10.1038/srep29765

5. Van Cutsem E, Oliveira J. Advanced colorectal cancer: ESMO clinical recommendations for diagnosis, treatment and follow-up. *Ann Oncol* (2009) 20: iv61–iv3. doi: 10.1093/annonc/mdp130

6. Siegel RL, Miller KD, Fedewa SA, Ahnen DJ, Meester RGS, Barzi A, et al. Colorectal cancer statistics, 2017. *CA Cancer J Clin* (2017) 67(3):177–93. doi: 10.3322/caac.21395

7. Vatandoust S, Price TJ, Karapetis CS. Colorectal cancer: metastases to a single organ. *World J Gastroenterol* (2015) 21(41):11767. doi: 10.3748/wjg.v21.i41.11767

8. Osterlund P, Salminen T, Soveri LM, Kallio R, Kellokumpu I, Lamminmäki A, et al. Repeated centralized multidisciplinary team assessment of resectability, clinical behavior, and outcomes in 1086 Finnish metastatic colorectal cancer patients (RAXO): a nationwide prospective intervention study. *Lancet Reg Health Eur* (2021) 3:100049. doi: 10.1016/j.lanepe.2021.100049

9. Leporrier J, Maurel J, Chiche L, Bara S, Segol P, Launoy G. A population-based study of the incidence, management and prognosis of hepatic metastases from colorectal cancer. *J Br Surg* (2006) 93(4):465–74. doi: 10.1002/bjs.5278

10. Van Tilborg A, Meijerink M, Sietses C, Van Waesberghe J, Mackintosh M, Meijer S, et al. Long-term results of radiofrequency ablation for unresectable colorectal liver metastases: a potentially curative intervention. *Br J Radiol* (2011) 84(1002):556–65. doi: 10.1259/bjr/78268814

11. Al-Sharif E, Simoneau E, Hassanain M. Portal vein embolization effect on colorectal cancer liver metastasis progression: lessons learned. *World J Clin Oncol* (2015) 6(5):142–6. doi: 10.5306/wjco.v6.i5.142

12. Andreou A, Aloia TA, Brouquet A, Vauthey J-N. Recent advances in the curative treatment of colorectal liver metastases. *Gastrointest Cancer Res: GCR* (2011) 4(4 Suppl 1):S2.

13. Fernandez FG, Drebin JA, Linehan DC, Dehdashti F, Siegel BA, Strasberg SM. Five-year survival after resection of hepatic metastases from colorectal cancer in patients screened by positron emission tomography with f-18 fluorodeoxyglucose (FDG-PET). *Ann Surg* (2004) 240(3):438. doi: 10.1097/01.sla.0000138076.72547.b1

14. Abdalla EK, Vauthey J-N, Ellis LM, Ellis V, Pollock R, Broglio KR, et al. Recurrence and outcomes following hepatic resection, radiofrequency ablation, and combined resection/ablation for colorectal liver metastases. *Ann Surg* (2004) 239 (6):818. doi: 10.1097/01.sla.0000128305.90650.71

15. Wei AC, Greig PD, Grant D, Taylor B, Langer B, Gallinger S. Survival after hepatic resection for colorectal metastases: a 10-year experience. *Ann Surg Oncol* (2006) 13(5):668–76. doi: 10.1245/ASO.2006.05.039

16. Adam R, Avisar E, Ariche A, Giachetti S, Azoulay D, Castaing D, et al. Five-year survival following hepatic resection after neoadjuvant therapy for nonresectable colorectal [liver] metastases. *Ann Surg Oncol* (2001) 8(4):347–53. doi: 10.1007/s10434-001-0347-3

17. Deschamps F, Ronot M, Gelli M, Durand-Labrunie J, Tazdait M, Hollebecque A, et al. Interventional radiology for colorectal liver metastases. *Curr Colorectal Cancer Rep* (2020) 16(2):29–37. doi: 10.1007/s11888-020-00449-0

18. Raoux L, Maulat C, Mokrane F-Z, Fares N, Suc B, Muscari F. Impact of the strategy for curative treatment of synchronous colorectal cancer liver metastases. *J Visceral Surg* (2020) 157(4):289–99. doi: 10.1016/j.jviscsurg.2019.10.007

19. Xing M, Kooby DA, El-Rayes BF, Kokabi N, Camacho JC, Kim HS. Locoregional therapies for metastatic colorectal carcinoma to the liver–an evidence-based review. *J Surg Oncol* (2014) 110(2):182–96. doi: 10.1002/jso.23619

20. Fairchild AH, White SB. Decision making in interventional oncology: intra-arterial therapies for metastatic colorectal cancer-Y90 and chemoembolization. *Semin Intervent Radiol* (2017) 34(2):87–91. doi: 10.1055/s-0037-1601854

21. Mahnken AH, Pereira PL, de Baère T. Interventional oncologic approaches to liver metastases. *Radiology* (2013) 266(2):407–30. doi: 10.1148/radiol.12112544

22. Makuuchi M, Thai BL, Takayasu K, Takayama T, Kosuge T, Gunvén P, et al. Preoperative portal embolization to increase safety of major hepatectomy for hilar bile duct carcinoma: a preliminary report. *Surgery* (1990) 107(5):521–7.

23. de Graaf W, van den Esschert JW, van Lienden KP, van Gulik TM. Induction of tumor growth after preoperative portal vein embolization: is it a real problem? *Ann Surg Oncol* (2009) 16(2):423–30. doi: 10.1245/s10434-008-0222-6

24. Mueller L, Hillert C, Möller L, Krupski-Berdien G, Rogiers X, Broering DC. Major hepatectomy for colorectal metastases: is preoperative portal occlusion an oncological risk factor? *Ann Surg Oncol* (2008) 15(7):1908–17. doi: 10.1245/s10434-008-9925-y

25. Shindoh J, Tzeng CW, Aloia TA, Curley SA, Zimmitti G, Wei SH, et al. Optimal future liver remnant in patients treated with extensive preoperative chemotherapy for colorectal liver metastases. *Ann Surg Oncol* (2013) 20(8):2493–500. doi: 10.1245/s10434-012-2864-7

26. Ribero D, Abdalla EK, Madoff DC, Donadon M, Loyer EM, Vauthey JN. Portal vein embolization before major hepatectomy and its effects on regeneration, resectability and outcome. *Br J Surg* (2007) 94(11):1386–94. doi: 10.1002/bjs.5836

27. Abdalla EK, Barnett CC, Doherty D, Curley SA, Vauthey JN. Extended hepatectomy in patients with hepatobiliary malignancies with and without preoperative portal vein embolization. *Arch Surg* (2002) 137(6):675–80. doi: 10.1001/archsurg.137.6.675

28. Wen XD, Xiao L. Associating liver partition and portal vein ligation for staged hepatectomy in the treatment of colorectal cancer liver metastases. *World J Gastrointest Surg* (2021) 13(8):814–21. doi: 10.4240/wjgs.v13.i8.814

29. Pamecha V, Levene A, Grillo F, Woodward N, Dhillon A, Davidson BR. Effect of portal vein embolisation on the growth rate of colorectal liver metastases. *Br J Cancer* (2009) 100(4):617–22. doi: 10.1038/sj.bjc.6604872

30. Collin Y, Paré A, Belblidia A, Létourneau R, Plasse M, Dagenais M, et al. Portal vein embolization does not affect the long-term survival and risk of cancer recurrence among colorectal liver metastases patients: a prospective cohort study. *Int J Surg* (2019) 61:42–7. doi: 10.1016/j.ijsu.2018.11.029

31. Coco D, Leanza S. Associating liver partition and portal vein ligation for staged hepatectomy (ALPPS) in colorectal liver metastases: review of the literature. *Clin Exp Hepatol* (2021) 7(2):125–33. doi: 10.5114/ceh.2021.106521

32. Dueland S, Yaqub S, Syversveen T, Carling U, Hagness M, Brudvik KW, et al. Survival outcomes after portal vein embolization and liver resection compared with liver transplant for patients with extensive colorectal cancer liver metastases. *JAMA Surg* (2021) 156(6):550–7. doi: 10.1001/jamasurg.2021.0267

33. Huiskens J, Olthof PB, van der Stok EP, Bais T, van Lienden KP, Moelker A, et al. Does portal vein embolization prior to liver resection influence the oncological outcomes - a propensity score matched comparison. *Eur J Surg Oncol* (2018) 44 (1):108–14. doi: 10.1016/j.ejso.2017.09.017

34. Ironside N, Bell R, Bartlett A, McCall J, Powell J, Pandanaboyana S. Systematic review of perioperative and survival outcomes of liver resections with and without preoperative portal vein embolization for colorectal metastases. *HPB (Oxford)* (2017) 19(7):559–66. doi: 10.1016/j.hpb.2017.03.003

35. Giglio MC, Giakoustidis A, Draz A, Jawad ZAR, Pai M, Habib NA, et al. Oncological outcomes of major liver resection following portal vein embolization: a systematic review and meta-analysis. *Ann Surg Oncol* (2016) 23(11):3709–17. doi: 10.1245/s10434-016-5264-6

36. Hoekstra LT, van Lienden KP, Doets A, Busch OR, Gouma DJ, van Gulik TM. Tumor progression after preoperative portal vein embolization. *Ann Surg* (2012) 256 (5):812–7. doi: 10.1097/SLA.0b013e3182733f09

37. Simoneau E, Aljiffry M, Salman A, Abualhassan N, Cabrera T, Valenti D, et al. Portal vein embolization stimulates tumour growth in patients with colorectal cancer liver metastases. *HPB (Oxford)* (2012) 14(7):461–8. doi: 10.1111/j.1477-2574.2012.00476.x

38. Pamecha V, Glantzounis G, Davies N, Fusai G, Sharma D, Davidson B. Long-term survival and disease recurrence following portal vein embolisation prior to major hepatectomy for colorectal metastases. *Ann Surg Oncol* (2009) 16(5):1202–7. doi: 10.1245/s10434-008-0269-4

39. Kokudo N, Tada K, Seki M, Ohta H, Azekura K, Ueno M, et al. Proliferative activity of intrahepatic colorectal metastases after preoperative hemihepatic portal vein embolization. *Hepatology* (2001) 34(2):267–72. doi: 10.1053/jhep.2001.26513

40. Geschwind JFH, Salem R, Carr BI, Soulen MC, Thurston KG, Goin KA, et al. Yttrium-90 microspheres for the treatment of hepatocellular carcinoma. *Gastroenterology* (2004) 127(5):S194–205. doi: 10.1053/j.gastro.2004.09.034

41. Dawson LA, Normolle D, Balter JM, McGinn CJ, Lawrence TS, Ten Haken RK. Analysis of radiation-induced liver disease using the Lyman NTCP model. *Int J Radiat Oncol Biol Physics* (2002) 53(4):810–21. doi: 10.1016/S0360-3016(02)02846-8

42. Raval M, Bande D, Pillai AK, Blaszkowsky LS, Ganguli S, Beg MS, et al. Yttrium-90 radioembolization of hepatic metastases from colorectal cancer. *Front Oncol* (2014) 4:120. doi: 10.3389/fonc.2014.00120

43. Kalva SP, Thabet A, Wicky S. Recent advances in transarterial therapy of primary and secondary liver malignancies. *Radiographics* (2008) 28(1):101–17. doi: 10.1148/rg.281075115

44. Chiu AM, Savoor R, Gordon AC, Riaz A, Sato KT, Hohlastos E, et al. Yttrium-90 radiation segmentectomy in oligometastatic secondary hepatic malignancies. *J Vasc Interv Radiol* (2023) 34(3):362–8. doi: 10.1016/j.jvir.2022.12.021

45. Nebelung H, Wolf T, Bund S, Radosa CG, Plodeck V, Grosche-Schlee S, et al. Radioembolization versus portal vein embolization for contralateral liver lobe hypertrophy: effect of cirrhosis. *Abdom Radiol (NY)* (2021) 46(8):4046–55. doi: 10.1007/s00261-021-03048-1

46. Vouche M, Lewandowski RJ, Atassi R, Memon K, Gates VL, Ryu RK, et al. Radiation lobectomy: time-dependent analysis of future liver remnant volume in unresectable liver cancer as a bridge to resection. *J Hepatol* (2013) 59(5):1029–36. doi: 10.1016/j.jhep.2013.06.015

47. Teo JY, Allen JCJr., Ng DC, Choo SP, Tai DW, Chang JP, et al. A systematic review of contralateral liver lobe hypertrophy after unilobar selective internal radiation therapy with Y90. *HPB (Oxford)* (2016) 18(1):7–12. doi: 10.1016/j.hpb.2015.07.002

48. Garlipp B, de Baere T, Damm R, Irmscher R, van Buskirk M, Stübs P, et al. Left-liver hypertrophy after therapeutic right-liver radioembolization is substantial but less than after portal vein embolization. *Hepatology* (2014) 59(5):1864–73. doi: 10.1002/hep.26947

49. Edeline J, Lenoir L, Boudjema K, Rolland Y, Boulic A, Le Du F, et al. Volumetric changes after (90)y radioembolization for hepatocellular carcinoma in cirrhosis: an option to portal vein embolization in a preoperative setting? *Ann Surg Oncol* (2013) 20 (8):2518–25. doi: 10.1245/s10434-013-2906-9

50. Kurilova I, Pompa V, Guerrero R, Tapias MA, Calatayud MD, Fondevila C, et al. (90)Y-radioembolization after failed portal vein embolization for colorectal liver metastases: a case report. *Cardiovasc Intervent Radiol* (2020) 43(8):1232–6. doi: 10.1007/s00270-020-02537-y

51. Liebl M, Pedersoli F, Zimmermann M, Schulze-Hagen M, Truhn D, Sieben P, et al. Induction of contralateral hepatic hypertrophy by unilobar yttrium-90 transarterial radioembolization versus portal vein embolization: an animal study. *J Vasc Interv Radiol* (2021) 32(6):836–42.e2. doi: 10.1016/j.jvir.2021.01.281

52. Fernández-Ros N, Silva N, Bilbao JI, Iñarrairaegui M, Benito A, D'Avola D, et al. Partial liver volume radioembolization induces hypertrophy in the spared hemiliver and no major signs of portal hypertension. *HPB (Oxford)* (2014) 16(3):243–9. doi: 10.1111/hpb.12095

53. Mima K, Beppu T, Chikamoto A, Miyamoto Y, Nakagawa S, Kuroki H, et al. Hepatic resection combined with radiofrequency ablation for initially unresectable colorectal liver metastases after effective chemotherapy is a safe procedure with a low incidence of local recurrence. *Int J Clin Oncol* (2013) 18(5):847–55. doi: 10.1007/s10147-012-0471-z

54. Sasaki K, Margonis GA, Andreatos N, Kim Y, Wilson A, Gani F, et al. Combined resection and RFA in colorectal liver metastases: stratification of long-term outcomes. *J Surg Res* (2016) 206(1):182–9. doi: 10.1016/j.jss.2016.06.098

55. Petre EN, Sofocleous CT, Solomon SB. Ablative and catheter-directed therapies for colorectal liver and lung metastases. *Hematol Oncol Clin North Am* (2015) 29 (1):117–33. doi: 10.1016/j.hoc.2014.09.007

56. Puijk RS, Dijkstra M, van den Bemd BAT, Ruarus AH, Nieuwenhuizen S, Geboers B, et al. Improved outcomes of thermal ablation for colorectal liver metastases: a 10-year analysis from the prospective Amsterdam CORE registry (AmCORE). *Cardiovasc Intervent Radiol* (2022) 45:1074–89. doi: 10.1007/s00270-022-03152-9

57. Tsitskari M, Filippiadis D, Kostantos C, Palialexis K, Zavridis P, Kelekis N, et al. The role of interventional oncology in the treatment of colorectal cancer liver metastases. *Ann Gastroenterol* (2019) 32(2):147. doi: 10.20524/aog.2019.0338

58. Rhim H, Goldberg SN, Dodd GD, Solbiati L, Lim HK, Tonolini M, et al. Essential techniques for successful radio-frequency thermal ablation of malignant hepatic tumors. *Radiographics* (2001) 21(suppl_1):S17–35. doi: 10.1148/radiographics.21.suppl_1.g01oc11s17

59. Solbiati L, Ahmed M, Cova L, Ierace T, Brioschi M, Goldberg SN. Small liver colorectal metastases treated with percutaneous radiofrequency ablation: local response rate and long-term survival with up to 10-year follow-up. *Radiology* (2012) 265(3):958–68. doi: 10.1148/radiol.12111851

60. Kei SK, Rhim H, Choi D, Lee WJ, Lim HK, Kim Y-s. Local tumor progression after radiofrequency ablation of liver tumors: analysis of morphologic pattern and site of recurrence. *Am J Roentgenol* (2008) 190(6):1544–51. doi: 10.2214/AJR.07.2798

61. Wang C-Z, Yan G-X, Xin H, Liu Z-Y. Oncological outcomes and predictors of radiofrequency ablation of colorectal cancer liver metastases. *World J Gastrointest Oncol* (2020) 12(9):1044. doi: 10.4251/wjgo.v12.i9.1044

62. de Baere T, Deschamps F, Briggs P, Dromain C, Boige V, Hechelhammer L, et al. Hepatic malignancies: percutaneous radiofrequency ablation during percutaneous portal or hepatic vein occlusion. *Radiology* (2008) 248(3):1056–66. doi: 10.1148/radiol.2483070222

63. Lu DS, Raman SS, Limanond P, Aziz D, Economou J, Busuttil R, et al. Influence of large peritumoral vessels on outcome of radiofrequency ablation of liver tumors. *J Vasc Interv Radiol* (2003) 14(10):1267–74. doi: 10.1097/01.RVI.0000092666.72261.6B

64. Nielsen K, van Tilborg AA, Meijerink MR, Macintosh MO, Zonderhuis BM, de Lange ES, et al. Incidence and treatment of local site recurrences following RFA of colorectal liver metastases. *World J Surg* (2013) 37(6):1340–7. doi: 10.1007/s00268-013-1997-6

65. Curley SA, Marra P, Beaty K, Ellis LM, Vauthey JN, Abdalla EK, et al. Early and late complications after radiofrequency ablation of malignant liver tumors in 608 patients. *Ann Surg* (2004) 239(4):450. doi: 10.1097/01.sla.0000118373.31781.f2

66. Kim KH, Yoon YS, Yu CS, Kim TW, Kim HJ, Kim PN, et al. Comparative analysis of radiofrequency ablation and surgical resection for colorectal liver metastases. *J Korean Surg Society* (2011) 81(1):25–34. doi: 10.4174/jkss.2011.81.1.25

67. Gillams AR, Lees WR. Five-year survival following radiofrequency ablation of small, solitary, hepatic colorectal metastases. *J Vasc Interv Radiol* (2008) 19(5):712–7. doi: 10.1016/j.jvir.2008.01.016

68. Wang X, Sofocleous CT, Erinjeri JP, Petre EN, Gonen M, Do KG, et al. Margin size is an independent predictor of local tumor progression after ablation of colon cancer liver metastases. *Cardiovasc Interv Radiol* (2013) 36(1):166–75. doi: 10.1007/s00270-012-0377-1

69. Elias D, Baton O, Sideris L, Matsuhisa T, Pocard M, Lasser P. Local recurrences after intraoperative radiofrequency ablation of liver metastases: a comparative study with anatomic and wedge resections. *Ann Surg Oncol* (2004) 11(5):500–5. doi: 10.1245/ASO.2004.08.019

70. Xie X, Jiang C, Peng Z, Liu B, Hu W, Wang Y, et al. Local recurrence after radiofrequency ablation of hepatocellular carcinoma: treatment choice and outcome. *J Gastrointest Surg* (2015) 19(8):1466–75. doi: 10.1007/s11605-015-2850-z

71. Pathak S, Jones R, Tang J, Parmar C, Fenwick S, Malik H, et al. Ablative therapies for colorectal liver metastases: a systematic review. *Colorectal Dis* (2011) 13 (9):e252–e65. doi: 10.1111/j.1463-1318.2011.02695.x

72. Filippiadis DK, Velonakis G, Kelekis A, Sofocleous CT. The role of percutaneous ablation in the management of colorectal cancer liver metastatic disease. *Diagnost (Basel)* (2021) 11(2):308. doi: 10.3390/diagnostics11020308

73. Ierardi AM, Floridi C, Fontana F, Chini C, Giorlando F, Piacentino F, et al. Microwave ablation of liver metastases to overcome the limitations of radiofrequency ablation. *La Radiol Medica* (2013) 118(6):949–61. doi: 10.1007/s11547-013-0968-1

74. Gravante G, Ong SL, Metcalfe MS, Strickland A, Dennison AR, Lloyd DM. Hepatic microwave ablation: a review of the histological changes following thermal damage. *Liver Int* (2008) 28(7):911–21. doi: 10.1111/j.1478-3231.2008.01810.x

75. Spiers HV, Lancellotti F, de Liguori Carino N, Pandanaboyana S, Frampton AE, Jegatheeswaran S, et al. Irreversible electroporation for liver metastases from colorectal cancer: a systematic review. *Cancers* (2023) 15(9):2428. doi: 10.3390/cancers15092428

76. Nieuwenhuizen S, Dijkstra M, Puijk RS, Geboers B, Ruarus AH, Schouten EA, et al. Microwave ablation, radiofrequency ablation, irreversible electroporation, and stereotactic ablative body radiotherapy for intermediate size (3-5 cm) unresectable colorectal liver metastases: a systematic review and meta-analysis. *Curr Oncol Rep* (2022) 24(6):793–808. doi: 10.1007/s11912-022-01248-6

77. Torres-Jiménez J, Esteban-Villarrubia J, Ferreiro-Monteagudo R, Carrato A. Local treatments in the unresectable patient with colorectal cancer metastasis: a review from the point of view of the medical oncologist. *Cancers (Basel)* (2021) 13(23):5938. doi: 10.3390/cancers13235938

78. Scheffer HJ, Nielsen K, van Tilborg AA, Vieveen JM, Bouwman RA, Kazemier G, et al. Ablation of colorectal liver metastases by irreversible electroporation: results of the COLDFIRE-I ablate-and-resect study. *Eur Radiol* (2014) 24(10):2467–75. doi: 10.1007/s00330-014-3259-x

79. Meijerink MR, Ruarus AH, Vroomen LGPH, Puijk RS, Geboers B, Nieuwenhuizen S, et al. Irreversible electroporation to treat unresectable colorectal liver metastases (COLDFIRE-2): a phase II, two-center, single-arm clinical trial. *Radiology* (2021) 299(2):470–80. doi: 10.1148/radiol.2021203089

80. Schicho A, Niessen C, Haimerl M, Wiesinger I, Stroszczynski C, Beyer LP, et al. Long-term survival after percutaneous irreversible electroporation of inoperable colorectal liver metastases. *Cancer Manag Res* (2019) 11:317–22. doi: 10.2147/CMAR.S182091

81. Filippiadis D, Mauri G, Marra P, Charalampopoulos G, Gennaro N, De Cobelli F. Percutaneous ablation techniques for renal cell carcinoma: current status and future trends. *Int J Hyperthermia* (2019) 36(2):21–30. doi: 10.1080/02656736.2019.1647352

82. Crocetti L, de Baére T, Pereira PL, Tarantino FP. CIRSE standards of practice on thermal ablation of liver tumours. *Cardiovasc Intervent Radiol* (2020) 43(7):951–62. doi: 10.1007/s00270-020-02471-z

83. Ruers T, Van Coevorden F, Punt CJ, Pierie J-PE, Borel-Rinkes I, Ledermann JA, et al. Local treatment of unresectable colorectal liver metastases: results of a randomized phase II trial. *JNCI: J Natl Cancer Institute* (2017) 109(9):djx015. doi: 10.1093/jnci/djx015

84. Kazemier G. Unresectable colorectal cancer liver metastases treated by intraoperative radiofrequency ablation with or without resection (Br J surg 2012; 99: 558–565). *Br J Surg* (2012) 99(4):566. doi: 10.1002/bjs.8724

85. Ruers T, Punt C, Van Coevorden F, Pierie J, Borel-Rinkes I, Ledermann J, et al. Radiofrequency ablation combined with systemic treatment versus systemic treatment alone in patients with non-resectable colorectal liver metastases: a randomized EORTC intergroup phase II study (EORTC 40004). *Ann Oncol* (2012) 23(10):2619–26. doi: 10.1093/annonc/mds053

86. Lee SL, Bassetti MF, Rusthoven CG. The role of stereotactic body radiation therapy in the management of liver metastases. *Semin Radiat Oncol* (2023) 33(2):181–92. doi: 10.1016/j.semradonc.2022.11.008

87. Mohamad I, Barry A, Dawson L, Hosni A. Stereotactic body radiation therapy for colorectal liver metastases. *Int J Hyperthermia* (2022) 39(1):611–9. doi: 10.1080/02656736.2021.1923836

88. Tubin S, Gupta S, Grusch M, Popper HH, Brcic L, Ashdown ML, et al. Shifting the immune-suppressive to predominant immune-stimulatory radiation effects by SBRT-PArtial tumor irradiation targeting HYpoxic segment (SBRT-PATHY). *Cancers (Basel)* (2020) 13(1):50. doi: 10.3390/cancers13010050

89. Morris VK, Kennedy EB, Baxter NN, Benson AB, Cercek A, Cho M, et al. Treatment of metastatic colorectal cancer: ASCO guideline. *J Clin Oncol* (2023) 41 (3):678–700. doi: 10.1200/JCO.22.01690

90. Petrelli F, Comito T, Barni S, Pancera G, Scorsetti M, Ghidini A, et al. Stereotactic body radiotherapy for colorectal cancer liver metastases: a systematic review. *Radiother Oncol* (2018) 129(3):427–34. doi: 10.1016/j.radonc.2018.06.035

91. Lee J, Shin IS, Yoon WS, Koom WS, Rim CH. Comparisons between radiofrequency ablation and stereotactic body radiotherapy for liver malignancies: meta-analyses and a systematic review. *Radiother Oncol* (2020) 145:63–70. doi: 10.1016/j.radonc.2019.12.004

92. Entezari P, Gabr A, Salem R, Lewandowski RJ. Yttrium-90 for colorectal liver metastasis - the promising role of radiation segmentectomy as an alternative local cure. *Int J Hyperthermia* (2022) 39(1):620–6. doi: 10.1080/02656736.2021.1933215

93. Vouche M, Habib A, Ward TJ, Kim E, Kulik L, Ganger D, et al. Unresectable solitary hepatocellular carcinoma not amenable to radiofrequency ablation: multicenter radiology-pathology correlation and survival of radiation segmentectomy. *Hepatology* (2014) 60(1):192–201. doi: 10.1002/hep.27057

94. Dupré A, Jones RP, Diaz-Nieto R, Fenwick SW, Poston GJ, Malik HZ. Curative-intent treatment of recurrent colorectal liver metastases: a comparison between ablation and resection. *Eur J Surg Oncol* (2017) 43(10):1901–7. doi: 10.1016/j.ejso.2017.08.008

95. He X, Zhang P, Li Z, Bi F, Xu F, Wang X, et al. Curative-intent radiotherapy in patients with oligometastatic lesions from colorectal cancer: a single-center study. *Med (Baltimore)* (2018) 97(40):e12601. doi: 10.1097/MD.0000000000012601

96. Jia Z, Wang C, Paz-Fumagalli R, Wang W. Radiation segmentectomy for hepatic malignancies: indications, devices, dosimetry, procedure, clinical outcomes, and toxicity of yttrium-90 microspheres. *J Interv Med* (2019) 2(1):1–4. doi: 10.1016/j.jimed.2019.05.001

97. Zerizer I, Al-Nahhas A, Towey D, Tait P, Ariff B, Wasan H, et al. The role of early ^{18}F-FDG PET/CT in prediction of progression-free survival after ^{90}Y radioembolization: comparison with RECIST and tumour density criteria. *Eur J Nucl Med Mol Imag* (2012) 39(9):1391–9. doi: 10.1007/s00259-012-2149-1

98. Jongen JMJ, Rosenbaum C, Braat M, van den Bosch M, Sze DY, Kranenburg O, et al. Anatomic versus metabolic tumor response assessment after radioembolization treatment. *J Vasc Interv Radiol* (2018) 29(2):244–53.e2. doi: 10.1016/j.jvir.2017.09.024

99. Sager S, Akgün E, Uslu-Beşli L, Asa S, Akovali B, Sahin O, et al. Comparison of PERCIST and RECIST criteria for evaluation of therapy response after yttrium-90 microsphere therapy in patients with hepatocellular carcinoma and those with metastatic colorectal carcinoma. *Nucl Med Commun* (2019) 40(5):461–8. doi: 10.1097/MNM.0000000000001014

100. Shady W, Kishore S, Gavane S, Do RK, Osborne JR, Ulaner GA, et al. Metabolic tumor volume and total lesion glycolysis on FDG-PET/CT can predict overall survival after (90)Y radioembolization of colorectal liver metastases: a comparison with SUVmax, SUVpeak, and RECIST 1.0. *Eur J Radiol* (2016) 85(6):1224–31. doi: 10.1016/j.ejrad.2016.03.029

101. Shady W, Sotirchos VS, Do RK, Pandit-Taskar N, Carrasquillo JA, Gonen M, et al. Surrogate imaging biomarkers of response of colorectal liver metastases after salvage radioembolization using 90Y-loaded resin microspheres. *AJR Am J Roentgenol* (2016) 207(3):661–70. doi: 10.2214/AJR.15.15202

102. Kurilova I, Bendet A, Fung EK, Petre EN, Humm JL, Boas FE, et al. Radiation segmentectomy of hepatic metastases with y-90 glass microspheres. *Abdom Radiol (NY)* (2021) 46(7):3428–36. doi: 10.1007/s00261-021-02956-6

103. Padia SA, Johnson GE, Agopian VG, DiNorcia J, Srinivasa RN, Sayre J, et al. Yttrium-90 radiation segmentectomy for hepatic metastases: a multi-institutional study of safety and efficacy. *J Surg Oncol* (2021) 123(1):172–8. doi: 10.1002/jso.26223

104. Meiers C, Taylor A, Geller B, Toskich B. Safety and initial efficacy of radiation segmentectomy for the treatment of hepatic metastases. *J Gastrointest Oncol* (2018) 9 (2):311–5. doi: 10.21037/jgo.2017.11.02

105. Padia SA, Kwan SW, Roudsari B, Monsky WL, Coveler A, Harris WP. Superselective yttrium-90 radioembolization for hepatocellular carcinoma yields high response rates with minimal toxicity. *J Vasc Interv Radiol* (2014) 25(7):1067–73. doi: 10.1016/j.jvir.2014.03.030

106. Biederman DM, Titano JJ, Korff RA, Fischman AM, Patel RS, Nowakowski FS, et al. Radiation segmentectomy versus selective chemoembolization in the treatment of early-stage hepatocellular carcinoma. *J Vasc Interv Radiol* (2018) 29(1):30–7.e2. doi: 10.1016/j.jvir.2017.08.026

107. Lewandowski RJ, Gabr A, Abouchaleh N, Ali R, Al Asadi A, Mora RA, et al. Radiation segmentectomy: potential curative therapy for early hepatocellular carcinoma. *Radiology* (2018) 287(3):1050–8. doi: 10.1148/radiol.2018171768

108. Haber Z, Lee EW, Price M, Wainberg Z, Hecht JR, Sayre J, et al. Survival advantage of yttrium-90 radioembolization to systemic therapy in patients with hepatic metastases from colorectal cancer in the salvage setting: results of a matched pair study. *Acad Radiol* (2021) 28:S210–S7. doi: 10.1016/j.acra.2021.03.033

109. Gibbs P, Gebski V, Van Buskirk M, Thurston K, Cade DN, Van Hazel GA. Selective internal radiation therapy (SIRT) with yttrium-90 resin microspheres plus standard systemic chemotherapy regimen of FOLFOX versus FOLFOX alone as first-line treatment of non-resectable liver metastases from colorectal cancer: the SIRFLOX study. *BMC Cancer* (2014) 14:897. doi: 10.1186/1471-2407-14-897

110. Van Hazel GA, Heinemann V, Sharma NK, Peeters M. SIRFLOX: randomized phase III trial comparing first-line mFOLFOX6 (plus or minus bevacizumab) versus mFOLFOX6 (plus or minus bevacizumab) plus selective internal radiation therapy in patients with metastatic colorectal cancer. *J Clin Oncol -New York* (2016) 34(15):1723–31. doi: 10.1200/JCO.2015.66.1181

111. Dutton SJ, Kenealy N, Love SB, Wasan HS, Sharma RA. FOXFIRE protocol: an open-label, randomised, phase III trial of 5-fluorouracil, oxaliplatin and folinic acid (OxMdG) with or without interventional selective internal radiation therapy (SIRT) as first-line treatment for patients with unresectable liver-only or liver-dominant metastatic colorectal cancer. *BMC Cancer* (2014) 14:497. doi: 10.1186/1471-2407-14-497

112. Gibbs P, Heinemann V, Sharma NK, Taieb J, Ricke J, Peeters M, et al. Effect of primary tumor side on survival outcomes in untreated patients with metastatic colorectal cancer when selective internal radiation therapy is added to chemotherapy: combined analysis of two randomized controlled studies. *Clin Colorectal Cancer* (2018) 17(4):e617–e29. doi: 10.1016/j.clcc.2018.06.001

113. Wasan HS, Gibbs P, Sharma NK, Taieb J, Heinemann V, Ricke J, et al. First-line selective internal radiotherapy plus chemotherapy versus chemotherapy alone in patients with liver metastases from colorectal cancer (FOXFIRE, SIRFLOX, and FOXFIRE-global): a combined analysis of three multicentre, randomised, phase 3 trials. *Lancet Oncol* (2017) 18(9):1159–71. doi: 10.1016/S1470-2045(17)30457-6

114. van Hazel G, Heinemann V, Sharma N, Taieb J, Ricke J, Peeters M, et al. Impact of primary tumour location on survival in patients with metastatic colorectal cancer receiving selective internal radiation therapy and chemotherapy as first-line therapy. *Ann Oncol* (2017) 28:iii152. doi: 10.1093/annonc/mdx302.005

115. Garlipp B, Gibbs P, Van Hazel GA, Jeyarajah R, Martin RCG, Bruns CJ, et al. Secondary technical resectability of colorectal cancer liver metastases after chemotherapy with or without selective internal radiotherapy in the randomized SIRFLOX trial. *Br J Surg* (2019) 106(13):1837–46. doi: 10.1002/bjs.11283

116. Breedis C, Young G. The blood supply of neoplasms in the liver. *Am J Pathol* (1954) 30(5):969.

117. Vogl TJ, Zangos S, Eichler K, Yakoub D, Nabil M. Colorectal liver metastases: regional chemotherapy *via* transarterial chemoembolization (TACE) and hepatic chemoperfusion: an update. *Eur Radiol* (2007) 17(4):1025–34. doi: 10.1007/s00330-006-0372-5

118. Yamada R, Sato M, Kawabata M, Nakatsuka H, Nakamura K, Takashima S. Hepatic artery embolization in 120 patients with unresectable hepatoma. *Radiology* (1983) 148(2):397–401. doi: 10.1148/radiology.148.2.6306721

119. Gruber-Rouh T, Marko C, Thalhammer A, Nour-Eldin NE, Langenbach M, Beeres M, et al. Current strategies in interventional oncology of colorectal liver metastases. *Br J Radiol* (2016) 89(1064):20151060. doi: 10.1259/bjr.20151060

120. Albert M, Kiefer MV, Sun W, Haller D, Fraker DL, Tuite CM, et al. Chemoembolization of colorectal liver metastases with cisplatin, doxorubicin, mitomycin c, ethiodol, and polyvinyl alcohol. *Cancer* (2011) 117(2):343–52. doi: 10.1002/cncr.25387

121. Maraj T, Mirrahimi A, Dey C. Survival of patients with colorectal liver metastases after transarterial chemoembolization using irinotecan-eluting microspheres: a single-center retrospective analysis comparing RECIST 1.1 and choi criteria. *J Vasc Interv Radiol* (2023). doi: 10.1016/j.jvir.2023.02.005

122. Vogl TJ, Lahrsow M, Albrecht MH, Hammerstingl R, Thompson ZM, Gruber-Rouh T. Survival of patients with non-resectable, chemotherapy-resistant colorectal cancer liver metastases undergoing conventional lipiodol-based transarterial chemoembolization (cTACE) palliatively versus neoadjuvantly prior to percutaneous thermal ablation. *Eur J Radiol* (2018) 102:138–45. doi: 10.1016/j.ejrad.2018.03.015

123. Gruber-Rouh T, Naguib NN, Eichler K, Ackermann H, Zangos S, Trojan J, et al. Transarterial chemoembolization of unresectable systemic chemotherapy-refractory liver metastases from colorectal cancer: long-term results over a 10-year period. *Int J Cancer* (2014) 134(5):1225–31. doi: 10.1002/ijc.28443

124. Nishiofuku H, Tanaka T, Matsuoka M, Otsuji T, Anai H, Sueyoshi S, et al. Transcatheter arterial chemoembolization using cisplatin powder mixed with degradable starch microspheres for colorectal liver metastases after FOLFOX failure: results of a phase I/II study. *J Vasc Interv Radiol* (2013) 24(1):56–65. doi: 10.1016/j.jvir.2012.09.010

125. Müller H, Nakchbandi V, Chatzisavvidis I, von Voigt C. Repetitive chemoembolization with melphalan plus intra-arterial immuno-chemotherapy within 5-fluorouracil and granulocyte-macrophage colony-stimulating factor (GM-CSF) as effective first- and second-line treatment of disseminated colorectal liver metastases. *Hepatogastroenterology* (2003) 50(54):1919–26.

126. Wasser K, Giebel F, Fischbach R, Tesch H, Landwehr P. [Transarterial chemoembolization of liver metastases of colorectal carcinoma using degradable starch microspheres (Spherex): personal investigations and review of the literature]. *Radiologe* (2005) 45(7):633–43. doi: 10.1007/s00117-004-1061-5

127. Vogl TJ, Marko C, Langenbach MC, Naguib NNN, Filmann N, Hammerstingl R, et al. Transarterial chemoembolization of colorectal cancer liver metastasis: improved tumor response by DSM-TACE versus conventional TACE, a prospective, randomized, single-center trial. *Eur Radiol* (2021) 31(4):2242–51. doi: 10.1007/s00330-020-07253-2

128. Seager MJ, Jakobs TF, Sharma RA, Bandula S. Combination of ablation and embolization for intermediate-sized liver metastases from colorectal cancer: what can we learn from treating primary liver cancer? *Diagn Interv Radiol* (2021) 27(5):677–83. doi: 10.5152/dir.2021.20520

129. Faiella E, Calabrese A, Santucci D, de Felice C, Pusceddu C, Fior D, et al. Combined trans-arterial embolization and ablation for the treatment of Large (>3 cm) liver metastases: review of the literature. *J Clin Med* (2022) 11(19):5576. doi: 10.3390/jcm11195576

130. Aliberti C, Fiorentini G, Muzzio PC, Pomerri F, Tilli M, Dallara S, et al. Trans-arterial chemoembolization of metastatic colorectal carcinoma to the liver adopting DC bead®, drug-eluting bead loaded with irinotecan: results of a phase II clinical study. *Anticancer Res* (2011) 31(12):4581–7.

131. Martin RC, Robbins K, Tomalty D, O'Hara R, Bosnjakovic P, Padr R, et al. Transarterial chemoembolisation (TACE) using irinotecan-loaded beads for the treatment of unresectable metastases to the liver in patients with colorectal cancer: an interim report. *World J Surg Oncol* (2009) 7:80. doi: 10.1186/1477-7819-7-80

132. Fiorentini G, Aliberti C, Tilli M, Mulazzani L, Graziano F, Giordani P, et al. Intra-arterial infusion of irinotecan-loaded drug-eluting beads (DEBIRI) versus intravenous therapy (FOLFIRI) for hepatic metastases from colorectal cancer: final results of a phase III study. *Anticancer Res* (2012) 32(4):1387–95.

133. Martin RC2nd, Scoggins CR, Schreeder M, Rilling WS, Laing CJ, Tatum CM, et al. Randomized controlled trial of irinotecan drug-eluting beads with simultaneous FOLFOX and bevacizumab for patients with unresectable colorectal liver-limited metastasis. *Cancer* (2015) 121(20):3649–58. doi: 10.1002/cncr.29534

134. Szemitko M, Golubinska-Szemitko E, Sienko J, Falkowski A. Complications following irinotecan-loaded microsphere chemoembolization of colorectal metastatic liver lesions associated with hepatic-artery branch temporary stasis. *Curr Oncol* (2021) 28(3):2296–307. doi: 10.3390/curroncol28030211

135. Akinwande O, Dendy M, Ludwig JM, Kim HS. Hepatic intra-arterial injection of irinotecan drug eluting beads (DEBIRI) for patients with unresectable colorectal liver metastases: a systematic review. *Surg Oncol* (2017) 26(3):268–75. doi: 10.1016/j.suronc.2017.05.003

136. Dhand S, Gupta R. Hepatic transcatheter arterial chemoembolization complicated by postembolization syndrome. *Semin Intervent Radiol* (2011) 28 (2):207–11. doi: 10.1055/s-0031-1280666

137. Gonsalves CF, Brown DB. Chemoembolization of hepatic malignancy. *Abdom Imag* (2009) 34(5):557–65. doi: 10.1007/s00261-008-9446-y

138. Paye F, Farges O, Dahmane M, Vilgrain V, Flejou JF, Belghiti J. Cytolysis following chemoembolization for hepatocellular carcinoma. *Br J Surg* (1999) 86 (2):176–80. doi: 10.1046/j.1365-2168.1999.01014.x

139. He Y, Zhang Y, Gong Y, Zhang Z, Xu T, Tian L, et al. Multimodal imaging of nano-assembled microspheres loaded with doxorubicin and cisplatin for liver tumor therapy. *Front Bioeng Biotechnol* (2022) 10:1024174. doi: 10.3389/fbioe.2022.1024174

140. Dendy MS, Ludwig JM, Kim HS. Predictors and prognosticators for survival with yttrium-90 radioembolization therapy for unresectable colorectal cancer liver metastasis. *Oncotarget* (2017) 8(23):37912–22. doi: 10.18632/oncotarget.16007

141. Wang DS, Louie JD, Sze DY. Evidence-based integration of yttrium-90 radioembolization in the contemporary management of hepatic metastases from colorectal cancer. *Tech Vasc Interv Radiol* (2019) 22(2):74–80. doi: 10.1053/j.tvir.2019.02.007

142. Kalva SP, Rana RS, Liu R, Rachamreddy N, Dave B, Sharma A, et al. Yttrium-90 radioembolization as salvage therapy for liver metastases from colorectal cancer. *Am J Clin Oncol* (2017) 40(3):288–93. doi: 10.1097/COC.0000000000000151

143. Hickey R, Lewandowski RJ, Prudhomme T, Ehrenwald E, Baigorri B, Critchfield J, et al. 90Y radioembolization of colorectal hepatic metastases using glass microspheres: safety and survival outcomes from a 531-patient multicenter study. *J Nucl Med* (2016) 57(5):665–71. doi: 10.2967/jnumed.115.166082

144. Kennedy AS, Ball D, Cohen SJ, Cohn M, Coldwell DM, Drooz A, et al. Multicenter evaluation of the safety and efficacy of radioembolization in patients with unresectable colorectal liver metastases selected as candidates for (90)Y resin microspheres. *J Gastrointest Oncol* (2015) 6(2):134–42. doi: 10.3978/j.issn.2078-6891.2014.109

145. Saxena A, Bester L, Shan L, Perera M, Gibbs P, Meteling B, et al. A systematic review on the safety and efficacy of yttrium-90 radioembolization for unresectable, chemorefractory colorectal cancer liver metastases. *J Cancer Res Clin Oncol* (2014) 140 (4):537–47. doi: 10.1007/s00432-013-1564-4

146. Evans KA, Richardson MG, Pavlakis N, Morris DL, Liauw W, Bester L. Survival outcomes of a salvage patient population after radioembolization of hepatic metastases with yttrium-90 microspheres. *J Vasc Interv Radiol* (2010) 21(10):1521–6. doi: 10.1016/j.jvir.2010.06.018

147. Cianni R, Urigo C, Notarianni E, Saltarelli A, Salvatori R, Pasqualini V, et al. Selective internal radiation therapy with SIR-spheres for the treatment of unresectable colorectal hepatic metastases. *Cardiovasc Intervent Radiol* (2009) 32(6):1179–86. doi: 10.1007/s00270-009-9658-8

148. Mulcahy MF, Lewandowski RJ, Ibrahim SM, Sato KT, Ryu RK, Atassi B, et al. Radioembolization of colorectal hepatic metastases using yttrium-90 microspheres. *Cancer* (2009) 115(9):1849–58. doi: 10.1002/cncr.24224

149. Kennedy AS, Coldwell D, Nutting C, Murthy R, Wertman DEJr., Loehr SP, et al. Resin 90Y-microsphere brachytherapy for unresectable colorectal liver metastases: modern USA experience. *Int J Radiat Oncol Biol Phys* (2006) 65(2):412–25. doi: 10.1016/j.ijrobp.2005.12.051

150. Helmberger T, Golfieri R, Pech M, Pfammatter T, Arnold D, Cianni R, et al. Clinical application of trans-arterial radioembolization in hepatic malignancies in Europe: first results from the prospective multicentre observational study CIRSE registry for SIR-spheres therapy (CIRT). *Cardiovasc Intervent Radiol* (2021) 44 (1):21–35. doi: 10.1007/s00270-020-02642-y

151. Wu V, Li MD, Goodwin JS, Wehrenberg-Klee EP, Zurkiya O, Kalva SP, et al. Yttrium-90 hepatic radioembolization for advanced chemorefractory metastatic colorectal cancer: survival outcomes based on right- versus left-sided primary tumor location. *AJR Am J Roentgenol* (2021) 217(5):1141–52. doi: 10.2214/AJR.20.25315

152. Lahti SJ, Xing M, Zhang D, Lee JJ, Magnetta MJ, Kim HS. KRAS status as an independent prognostic factor for survival after yttrium-90 radioembolization therapy for unresectable colorectal cancer liver metastases. *J Vasc Interv Radiol* (2015) 26 (8):1102–11. doi: 10.1016/j.jvir.2015.05.032

153. Narsinh KH, Van Buskirk M, Kennedy AS, Suhail M, Alsaikhan N, Hoh CK, et al. Hepatopulmonary shunting: a prognostic indicator of survival in patients with metastatic colorectal adenocarcinoma treated with (90)Y radioembolization. *Radiology* (2017) 282(1):281–8. doi: 10.1148/radiol.2016152100

154. Riaz A, Lewandowski RJ, Kulik LM, Mulcahy MF, Sato KT, Ryu RK, et al. Complications following radioembolization with yttrium-90 microspheres: a comprehensive literature review. *J Vasc Interv Radiol* (2009) 20(9):1121–30. doi: 10.1016/j.jvir.2009.05.030

155. Hwang JE, Kim SH, Jin J, Hong JY, Kim MJ, Jung SH, et al. Combination of percutaneous radiofrequency ablation and systemic chemotherapy are effective treatment modalities for metachronous liver metastases from gastric cancer. *Clin Exp Metastasis* (2014) 31(1):25–32. doi: 10.1007/s10585-013-9606-5

156. Schullian P, Johnston E, Laimer G, Putzer D, Eberle G, Scharll Y, et al. Stereotactic radiofrequency ablation of breast cancer liver metastases: short- and long-term results with predicting factors for survival. *Cardiovasc Intervent Radiol* (2021) 44 (8):1184–93. doi: 10.1007/s00270-021-02820-6

157. Vogl TJ, Jaraysa Y, Martin SS, Gruber-Rouh T, Savage RH, Nour-Eldin NA, et al. A prospective randomized trial comparing microwave and radiofrequency ablation for the treatment of liver metastases using a dual ablation system — the Mira study. *Eur J Radiol Open* (2022) 9:100399. doi: 10.1016/j.ejro.2022.100399

158. Bi Y, Jiao D, Wang Y, Han X, Ren J. Preliminary outcomes of raltitrexed eluting bead-transarterial chemoembolization using callispheres® beads for gastrointestinal adenocarcinoma liver metastasis. *World J Surg Oncol* (2022) 20(1):229. doi: 10.1186/s12957-022-02696-x

159. Barat M, Cottereau AS, Kedra A, Dermine S, Palmieri LJ, Coriat R, et al. The role of interventional radiology for the treatment of hepatic metastases from neuroendocrine tumor: an updated review. *J Clin Med* (2020) 9(7):2302. doi: 10.3390/jcm9072302

160. Fiorentini G, Sarti D, Nani R, Aliberti C, Fiorentini C, Guadagni S. Updates of colorectal cancer liver metastases therapy: review on DEBIRI. *Hepat Oncol* (2020) 7(1): HEP16. doi: 10.2217/hep-2019-0010

161. Maire F, Lombard-Bohas C, O'Toole D, Vullierme MP, Rebours V, Couvelard A, et al. Hepatic arterial embolization versus chemoembolization in the treatment of liver metastases from well-differentiated midgut endocrine tumors: a prospective randomized study. *Neuroendocrinology* (2012) 96(4):294–300. doi: 10.1159/000336941

162. Elf AK, Andersson M, Henrikson O, Jalnefjord O, Ljungberg M, Svensson J, et al. Radioembolization versus bland embolization for hepatic metastases from small intestinal neuroendocrine tumors: short-term results of a randomized clinical trial. *World J Surg* (2018) 42(2):506–13. doi: 10.1007/s00268-017-4324-9

163. Saxena A, Kapoor J, Meteling B, Morris DL, Bester L. Yttrium-90 radioembolization for unresectable, chemoresistant breast cancer liver metastases: a large single-center experience of 40 patients. *Ann Surg Oncol* (2014) 21(4):1296–303. doi: 10.1245/s10434-013-3436-1

164. Dai Y, Zhao W, Yue L, Dai X, Rong D, Wu F, et al. Perspectives on immunotherapy of metastatic colorectal cancer. *Front Oncol* (2021) 11:659964. doi: 10.3389/fonc.2021.659964

165. Erinjeri JP, Fine GC, Adema GJ, Ahmed M, Chapiro J, den Brok M, et al. Immunotherapy and the interventional oncologist: challenges and opportunities-a society of interventional oncology white paper. *Radiology* (2019) 292(1):25–34. doi: 10.1148/radiol.2019182326

166. Adnan A, Sheth RA, Tam A. Oligometastatic disease in the liver: the role of interventional oncology. *Br J Radiol* (2022) 95(1138):20211350. doi: 10.1259/bjr.20211350

167. Shi L, Chen L, Wu C, Zhu Y, Xu B, Zheng X, et al. PD-1 blockade boosts radiofrequency ablation-elicited adaptive immune responses against tumor. *Clin Cancer Res* (2016) 22(5):1173–84. doi: 10.1158/1078-0432.CCR-15-1352

168. Zhang XL, Hu LP, Yang Q, Qin WT, Wang X, Xu CJ, et al. CTHRC1 promotes liver metastasis by reshaping infiltrated macrophages through physical interactions with TGF-β receptors in colorectal cancer. *Oncogene* (2021) 40(23):3959–73. doi: 10.1038/s41388-021-01827-0

169. Gazzillo A, Polidoro MA, Soldani C, Franceschini B, Lleo A, Donadon M. Relationship between epithelial-to-Mesenchymal transition and tumor-associated macrophages in colorectal liver metastases. *Int J Mol Sci* (2022) 23(24):16197. doi: 10.3390/ijms232416197

Frontiers in Oncology

Advances knowledge of carcinogenesis and tumor progression for better treatment and management

The third most-cited oncology journal, which highlights research in carcinogenesis and tumor progression, bridging the gap between basic research and applications to imrpove diagnosis, therapeutics and management strategies.

Discover the latest Research Topics

See more →

Frontiers

Avenue du Tribunal-Fédéral 34
1005 Lausanne, Switzerland
frontiersin.org

Contact us

+41 (0)21 510 17 00
frontiersin.org/about/contact